e-ISSN : 2320-0847
p-ISSN : 2320-0936

American Journal of Engineering Research (AJER)

Volume 2 Issue 11 - November 2013

www.ajer.org ajer.research@gmail.com

Editorial Board

American Journal of Engineering Research (AJER)

Dr. Moinuddin Sarker,
Qualification :PhD, MCIC, FICER, MInstP, MRSC (P), VP of R & D
Affiliation : Head of Science / Technology Team, Corporate Officer (CO)
Natural State Research, Inc.
37 Brown House Road (2nd Floor)
Stamford, CT-06902, USA.

Dr. June II A. Kiblasan
Qualification : Phd
Specialization: Management, applied sciences
Country: PHIILIPPINES

Dr. Jonathan Okeke Chimakonam
Qualification: PHD
Affiliation: University of Calabar
Specialization: Logic, Philosophy of Maths and African Science,
Country: Nigeria

Dr. Narendra Kumar Sharma
Qualification: PHD
Affiliation: Defence Institute of Physiology and Allied Science, DRDO
Specialization: Proteomics, Molecular biology, hypoxia
Country: India

Dr. ABDUL KAREEM
Qualification: MBBS, DMRD, FCIP, FAGE
Affiliation: UNIVERSITI SAINS Malaysia
Country: Malaysia

Prof. Dr. Shafique Ahmed Arain
Qualification: Postdoc fellow, Phd
Affiliation: Shah abdul Latif University Khairpur (Mirs),
Specialization: Polymer science
Country: Pakistan

Dr. sukhmander singh
Qualification: Phd
Affiliation: Indian Institute Of Technology, Delhi
Specialization : PLASMA PHYSICS
Country: India

Dr. Alcides Chaux
Qualification: MD
Affiliation: Norte University, Paraguay, South America
Specialization: Genitourinary Tumors
Country: Paraguay, South America

Dr. Nwachukwu Eugene Nnamdi
Qualification: Phd
Affiliation: Michael Okpara University of Agriculture, Umudike, Nigeria
Specialization: Animal Genetics and Breeding
Country: Nigeria

Dr. Md. Nazrul Islam Mondal
Qualification: Phd
Affiliation: Rajshahi University, Bangladesh
Specialization: Health and Epidemiology
Country: Bangladesh

Volume-2 Issue-11

American Journal of Engineering Research (AJER)
e-ISSN : 2320-0847 p-ISSN : 2320-0936
Volume-02, Issue-11, pp-01-13
www.ajer.org

Research Paper Open Access

Reuse of Waste Plastics Coated Aggregates-Bitumen Mix Composite For Road Application – Green Method

S.Rajasekaran[1*], Dr. R. Vasudevan[2], Dr. Samuvel Paulraj[3]

1. C-MET, Athani, Thrissur 2. Dept. of Chemistry, TCE, MDU, 3. Head (Rtd), Environ. Science, MKU, MDU

Abstract: - Waste plastics both by domestic and industrial sectors can be used in the production of asphalt mix. Waste plastics, mainly used for packing are made up of Polyethylene Polypropylene polystyrene. Their softening varies between 110^{o}C – 140^{0}C and they do not produce any toxic gases during heating but the softened plastics have tendency to form a film like structure over the aggregate, when it is sprayed over the hot aggregate at 160^{0}C. The Plastics Coated Aggregates (PCA) is a better raw material for the construction of flexible pavement. PCA was then mixed with hot bitumen of different types and the mixes were used for road construction. PCA - Bitumen mix showed improved binding property and less wetting property. The sample showed higher Marshall Stability value in the range of 18-20KN and the load bearing capacity of the road is increased by 100%. The roads laid since 2002 using PCA-Bitumen mixes are performing well. A detailed study on the performances of these roads shows that the constructed with PCA –Bitumen mix are performing well. This process is eco-friendly and economical too.

Abbreviations:

1. PE: Poly Ethylene
2. PS: Poly Styrene
3. PP: Poly Propylene
4. PCA: Polymer-Coated Aggregate/ Plastic Coated Aggregate
5. PVC: Poly Vinyl Chloride
6. IRC: Indian Road Congress
7. ASTM: American Society for Testing and Materials
8. PET: Poly ethylene Terephthalate
9. DTA: Differential Thermal Analysis
10. TGA: Thermo Gravimetric Analysis
11. AC: Asphalt Concrete
12. EVA: Ethylene Vinyl Acetate
13. SBS: Styrene Butadiene Styrene
14. LAR: Los Angeles Abrasion Value
15. TCE: Tri Chloro Ethylene
16. AIV: Aggregate Impact Value
17. ACT: Aggregate Crushing Test
18. PMB: Polymer-Modified Bitumen
19. LDPE: Low Density Polyethylene
20. MSV: Marshall Stability Value
21. FV: Flow Value
22. MQ: Marshall Quotient
23. IS: Indian Standards
24. BS: British Standards
25. DRDA: Department of Rural Development Agency
26. SDBC: Semi Dense Bituminous Concrete
27. Bitumen Types: Pen Grade 80/100 and 60/70

Key Words: Waste Plastics, Plastic Coated Aggregate, Bitumen, Plastic Tar road, Roads, Monitoring

I. INTRODUCTION

1.1. PLASTIC WASTE SCENARIO

Plastics waste scenario in the world, of the various waste materials, plastics and municipal solid waste are great concern. Finding proper use for the disposed plastics waste is the need of the hour. On the other side, the road traffic is increasing, hence the need to increase the load bearing capacities of the roads.

The use of plastics (be consistent in the use of polymer or plastic, since the focus is on plastic waste) coated aggregate for asphalt pavement allows the reuse of plastics waste. Plastics, are versatile packing materials and commonly used by man but they become problem to the environment. After using them mostly used plastics products are bags, cups, films and foams, made up of polyethylene, polypropylene or polystyrene. India

consumption of Plastics will grow 15 million tonnes by 2015* and is set to be the third largest consumer of plastics in the world. Around 55% is being used for packing. They are mostly dropped and left to litter the environment, after the contents have been consumed. The littered plastics, a non biodegradable material, get mixed with domestic waste and make the disposal of municipal solid waste difficult. The municipal solid waste is either incinerated or land filled. Both disposal methods are not the best ways to dispose the waste and it causes both land and air pollution [1, 2, 3]. Moreover, if municipal solid waste, contains PVC waste, when burnt, it produces toxic gases like dioxins[1]. Disposal of plastic wastes in an eco friendly way is the main thrust area of today's research works. The author has developed innovative [4] technique to use the waste plastics for the construction of asphalt pavement. This process is eco friendly and can promote value addition to the waste plastic.

* Plastindia 8th International plastics Exhibition & Conference Feb. 1-6 , 2012, New Delhi.

1.2. LITERATURE REVIEW

In the construction of asphalt pavement, hot bitumen is coated over hot stone aggregate mixed, laid and rolled. Bitumen acts as a binder. Yet when water is stagnated over road, it penetrates and results in pot holes, a defective spot on the pavement. The use of anti stripping agents are having limited use only and the process also increases the cost of road construction[5]. Use of plastic (virgin as well as waste) to modify the bitumen and also the use of plastic coated aggregates are being studied to improve performance of the pavement.

Bituminous mixes used in the surface course of the bituminous pavements are being improved in their performance by incorporating various types of additives to bitumen such as rubber latex, crumb rubber, styrene, butadiene styrene, styrene – ethylene –butylenes, recycled Polypropylene ,low density polyethylene [6] Polyethylene [7], Ethylene vinyl acetate (EVA) (5%) [8] and polyolefin [9, 10]. Some of the properties improved are durability, fatigue life [12, 13], resistance to rutting, softening point, visco elastic property [11], etc.

The major obstacle to widespread usage of polymer modified bitumen in paving practice has been their tendency towards gross phase separation under quiescent conditions [16].

2.0. Present Study:

Plastics waste like PE, PP and PS is coated over stone aggregates and the PCA was mixed with bitumen and the mix was used for flexible pavement construction. Higher percentage of plastic waste (10-15%) can be used without separation. Detailed studies are going on this direction [17&4]. Various tests were carried out to find the characterization of the following.

1. Different waste plastics used for coating over the aggregates
2. Plastics coated aggregate
3. Plastics coated aggregate mix with bitumen
4. Plastics coated bituminous road scrap

All the tests were carried out using standard procedures

2.1.0 CHARACTERIZATION OF WASTE PLASTICS

2.1.1. THERMAL CHARACTERISTICS

The thermal behavior of the polymers namely Polyethylene, Polypropylene and Polystyrene was studied using Thermo Gravimetry Analyzer TGA-50 and Differential Scanning Calorimeter DSC-60 to find out the decomposition temperature and the softening point of the polymers (Table-1& Fig.1).

II. PHYSICAL PROPERTIES

Most of the packing materials* used are made up of PE, PP, PS. These materials were characterized for their thickness, solubility and softening temperature (Table -2). All these materials can be shredded and used for road construction.

Common food packaging plastics and their uses: Table- 2a

Full name	Abbreviation	Examples of use
High density polyethylene	HDPE	Bottles and films
Linear low density Polyethylene	LLDPE	Film
Low density polyethylene	LDPE	Film
Polypropylene	PP	Containers, film
Polyvinylchloride	PVC	Blister packs and bottles
Polyethylene terephthalate	PET	Bottles for soft drinks, films etc.
Polysyrene	PS	Pots , thermo -Cole, trays, toys etc.

*Introduction to Plastics Science Teaching Resources. American Chemistry Council, Inc. Retrieved 24 December 2012.

2.1. CHARACTERISTICS OF PLASTIC COATED AGGREGATE

For the asphalt pavement, stone aggregate with specific characteristics is used for road laying. The aggregate is chosen on the basis of its strength, porosity and moisture absorption capacity. The aggregate was coated with waste plastic material by the following process. The waste plastics namely films, cups and foams shredded to the required size of 2.5mm – 4.36mm. The aggregate is heated to 170^{o}C. The shredded waste plastic was sprayed over the hot aggregate. Plastics got softened and coated over the aggregate. The extent of coating was varied by using different percentage of plastics. Higher percentage of plastics was used up to 25% to evaluate the binding property, whereas lower percentage of plastics like 1% to 5% to evaluate the properties like moisture absorption and soundness.

2.2.0. BINDING PROPERTIES

The hot plastics coated aggregates was compacted into a block using compacting machine operated hydraulically and cooled. Then the block was subjected to a compressive test using universal testing machine. (Table -3)

2.2.1. MOISTURE ABSORPTION AASHTO T 96 (2001)**:**

A known quantity of plastics coated aggregate was taken. It was then immersed in water for 24hrs. Then the aggregate was dried using dry clothes and the weight was determined. The water absorbed by the aggregate was determined from the weight difference. The test was repeated with plain aggregate for comparison of results. Table-4.

2.2.2. SOUNDNESS TEST AASHTO T 96 (2001)

Soundness is mainly to test the stability towards weathering of the aggregates and its chemical resistance. The plain aggregate when exposed to stagnation of water, the water penetrates easily inside the pores of the aggregates. Since the water contains dissolved salts, the salt gets crystallized and expands inside the pores during evaporation resulting in the breaking of the aggregates. The low soundness property directly depends upon the amount of voids and porosity of the aggregates . This is evaluated by conducting accelerated weathering test cycle. The average loss in weight of aggregate for 5 cycles should not exceed 12 % when tested with sodium sulphate. The plain aggregates and PCA were subjected to this test and the results are tabulated in Table-4 for comparison.

2.2.3. AGGREGATE IMPACT TEST(AASHTO T 96 (2001))

It is used to evaluate the toughness of stone or the resistance of the aggregate to fracture under repeated impacts. The aggregates were subjected to 15 blows with a hammer of weight 14kg and the crushed aggregates were sieved on 2.26mm sieve. The aggregate impact value is the percentage of fine (passing through the 2.36mm sieve size) to the total weight of the sample. The aggregate impact value should not exceed 30% for use in wearing course of pavements. Maximum permissible values are 35% for bituminous macadam and 40 % for water bound macadam. The plastic coated aggregates were subjected to this test and the results are tabulated in Table-4.

2.2.4. LOS ANGELES ABRASION TEST AASHTO T 96 (2001)

The principle of Los Angeles abrasion (L.A.R) test is to find the percentage wear due to relative rubbing action between the aggregate and the steel balls used as abrasive. LAR value should be less than 30% for pavements. For the L.A. abrasion test, the portion of a plastics coated aggregate sample retained on the 1.70 mm (No. 12) sieve was placed in a large rotating drum that contains a shelf plate attached to the outer wall. A specified number of steel spheres were then placed in the machine and the drum was rotated for 500 revolutions at a speed of 30 - 33 revolutions per minute (rpm). The material was then extracted and separated into material passing the 1.70 mm (No. 12) sieve and material retained on the 1.70 mm (No. 12) sieve. The retained material (larger particles) was then weighed and compared to the original sample weight. The difference in weight was reported as a percent of the original weight and called the percentage loss. LAR value should be less than 30 percent for pavements. The results are tabulated in Table-4.

2.3. CHARACTERISTICS OF "PCA-BITUMEN MIX"

The hot plastic coated aggregate was mixed with 80/100 bitumen at 160^{0}C. The bitumen polymer coated aggregate mix was subjected to tests like Stripping test, Bitumen extraction test and Marshall Value determination test

2.3.1. STRIPPING (IS: 6241-1971)

Stripping value is the determination of binding strength of the aggregate and the bitumen. It is tested by immersing bitumen coated aggregate in water for 24hrs at 40^0C. When bitumen coated aggregate was immersed in water, the water penetrates into the pore and voids of the stone resulting in the peeling of the bitumen. This in turn results in the loosening of the aggregate and forming potholes. 200gm of PCA- bitumen mix was taken and cooled to room temperature and weighed. The mixture was immersed in water bath maintained at 40^0C for 24hrs. After 24hrs the stripping was observed and the percentage of stripping was noted and the results are tabulated in Table -5

2.3.2. BITUMEN EXTRACTION TEST ASTM D2172

The extraction tests were carried out in the following order.

1. Bitumen coated aggregate was treated with TCE and the bitumen was extracted. Here the extraction was almost complete
2. PCA bitumen mix was first treated with TCE and the bitumen extracted was separated and estimated. Complete removal of bitumen did not take place
3. So further extraction was carried out using another solvent, namely decaline, which can act as a solvent to extract plastics also.
4. The PCA bitumen mix obtained from step 2 is then treated with decaline for another 30 minutes and separated bitumen was estimated.
5. The extraction was again repeated after refluxing the mix for 5 minutes. Further separation took place.

The process was repeated using aggregate, coated with different percentage of plastics. The results are tabulated (Table-6).

2.3.3. MARSHALL STABILITY ASTM: D 1559 - 1979

Marshall Stability value is the basic study on the stability of the mix with application of load. The standard mixture was prepared in accordance with IRC specifications . The aggregates were coated with plastics waste as described earlier. This plastics coated aggregates mix was then mixed with 5% of total quantity of 80/100 bitumen. The mixture was transferred to the mould. It was compacted with 75 blows on either side. The specimens (64 mm height and 10.2 mm diameter) were prepared by 1. Varying the percentage of plastics waste and 2. by varying bitumen quantity. These specimens were tested. The voids present in the mix also play an important role in deciding the performance of the mix. The following properties were determined: Voids filled with Mineral Aggregate, Air Voids, Voids filled with bitumen, Bulk Density, Specific Gravity and Voids in Mix. The results are reported in the Table-8.

Marshal Stability Value is indicative of load withstanding property of the flexible pavement. The minimum value is fixed as 4KN by IRC with 5% of bitumen and 95% of stone aggregate Table (7 &8).

III. DISCUSSION OF RESULTS WASTE PLASTICS CHARACTERIZATION

3.1. THERMAL ANALYSIS

The results obtained from the thermal analysis using DSC and TGA (Table-1) show that polymers namely PE, PP and PS softened easily around 130 – 140 Deg C without any evolution of gas and around 270 deg. C. They decomposed, releasing gases like methane, ethane etc. and above 700 Deg.C. They undergo combustion, producing gases like CO and CO_2. Hence it is safe to use molten waste plastics below 100-150^0C. This is supported by TGA and DSC graphs shown in Figure1. (Table.1)

3.2. Binding Property

The aggregate coated with higher percentage of plastics was compacted into a block and compacted blocks showed a compressive strength not less than 12 N/$mm^{2.}$ This shows that the molten plastics have a good adhesion property. The increase in the values of the compression strength and bending strength show that the plastics can be used as a binder. Moreover the strength increases with the increase in the percentage of plastics used for coating. It is also depended on the types of plastics used like PE, PP and PS (Table-2a). The following is the increasing order of strength of block produced PS<PE<PP<Laminated films<BOPP. This order is in agreement of the chemical nature of the above polymers[1] Table- 3.

3.3. Aggregate characterization:

It was found that there is significant improvement in the strength properties of the aggregates change to coated with molten plastics. This is due to the fact that when the plastic was coated over the aggregate, the aggregate surface is covered with the thin film of polymer. The film of polymer also fills the pores at the surface and there is no water absorption. Hence there is significant improvement in the general properties of the

aggregate like soundness, abrasion resistance, etc., Moreover, the PCA mixed with bitumen shows better stripping property.

- **Soundness:** Plastics coated aggregate showed no value for soundness. This can be explained as follows. The coating of plastics fills the pores and voids present at the surface of the aggregate. There is no penetration of water and there is no salt deposition. Hence there was no disintegration. (Table-4).
- In **Los Angeles Abrasion,** the hardness of aggregate is measured. Plastics coated aggregates show better resistance to higher wear and tear load (Table-4). The resistance increases with the increase of coating thickness of the plastics coated. This is because coating of polymers over aggregate gives better adhesion over the surface particles. It reduces the roughness of the aggregate and thus resulting in the reduction of abrasion over the surface of aggregate.
- **Impact value**. The brittleness of the aggregate is measured as Impact value. Coating of waste polymers over the aggregate reduces the voids and the air cavities present in the aggregates (Table-4). The film formed helps in preventing the cracking The toughness of the stones is also increased. Hence, the impact value of the plastics coated aggregate is lower when compared with the plain aggregate.

IV. PLASTIC COATED AGGREGATE - BITUMEN MIX CHARACTERIZATION

3.4. Extraction Characteristics:

The experimental results of extraction of bitumen (Table- 6) from the PCA - bitumen mix clearly show explain the bonding nature of the mixture. It was observed that the TCE could remove bitumen almost from the plain bitumen coated aggregates , whereas in the PCA- bitumen mix the removal of the bitumen by TCE was a slow process and not all the bitumen was removed. The TCE cannot remove completely all the bitumen from PCA- bitumen mix. Decaline, an organic solvent remove both bitumen and plastic on further treatment. Complete removal is possible only by refluxing the PCA -bitumen mix with decaline for more than 30 minutes.
The following observations were made from the results of extraction test. In the case of PCA bitumen mix, TCE removed only loosely bonded bitumen. It could not remove the bitumen bonded with the aggregate through the plastics. Decaline (being a solvent to plastic) could remove the bonded bitumen further. Only after refluxing was complete removal of Bitumen and plastic achieved. Moreover, when the percentage of coating of plastics was more, the extent of bitumen removal was correspondingly less. This observation helps to conclude the bonding of bitumen over plastic coated aggregate is strong.

3.5. Stripping Value:

In the case of polymer coated aggregates (Table-4), the surface is covered by the polymer film and there are no pores. The molten polymer not only fills the voids of the aggregate and binds the aggregate together but also strongly binds with bitumen forming an organic bonding. Water cannot penetrate over polymer coated aggregate, hence peeling out of bitumen from the PCA was zero even after 96 hours (Table-5), thus having better stripping value.

3.6. Marshall Stability Value:

Marshall Stability Value (kN), Flow Value (mm) and Marshall quotient (kN/mm) were obtained for plain aggregate bituminous mixes and polymer coated aggregate bituminous mixes of varied compositions.(Table 7&8)

For an effective asphalt pavement, the flow values should be in the range 2-5 and the ratio of MSV and FV (referred to as Marshall Quotient) should not not more than 500. The results obtained for the PCA are within this range. Voids filled with bitumen (VFB) are expected to be around 65%. The observed value is around 58%. The reduction is attributed to the reduction in the use of percentage of bitumen (90%) and the reduction in voids. The data (Table 7 & 8) also suggest that with the use of plastics waste coated aggregate, the quantity of bitumen needed for a good mix can be reduced by 0.5% of the total weight. This accounts for 10% reduction in the quantity of bitumen needed to be used. It is a good saving of natural resource.
The following observations are made

- The use of PCA increases the MSV of the mix
- As the percentage of the waste plastics coated increases the MSV is also increased
- Higher percentage of plastics (more than 15%) results in lesser compatibility with bitumen and lesser bonding resulting in lower MSV.
- The use of PP gives higher MSV value than PE
- The foams of PP and PE also gives better MSV results
- The waste plastics available as foams or films can also be used
- The use of optimum percentage of plastics was arrived using mathematical modelling and it is found to be 10% of bitumen used.

- The flow value and the voids filled with bitumen are within the tolerance value
- The MSV of PCA - bitumen mix is compared with PMB mix. It was observed that the values of the PCA bitumen mix are 50% to 60% higher than that of the PMB mix(Table-8), showing that the binding strength is higher in the case of PCA bitumen mix.

3.7. Theoretical Explanation:

The shredded plastics on spraying over the hot aggregate melted and spread over the aggregate giving a thin coating at the surface. When the aggregate temperature is around 140^0 C to 160^oC the coated plastics remains in the softened state. Over this, hot bitumen (160^oC) is added. The added bitumen spreads over the aggregate. At this temperature both the coated plastics and bitumen are in the liquid state, capable of easy diffusion at the inter phase. This process is further helped by the increase in the contact area (increased surface area).

These observations may be explained as follows. Waste polymers namely PE, PP and PS are hydrocarbons with long chains. The bitumen is a complex mixture of asphaltenes and maltenes which are also long chain hydro carbon. When bitumen was mixed with plastic coated aggregate a portion of bitumen diffuse through the plastic layer and binds with aggregate. The plastic layer has already bonded strongly with aggregate. During this process three dimensional internal cross linked net work structure results between polymer molecules and bitumen constitutes. Therefore the bond becomes stronger and the removal of bonded bitumen becomes difficult as explained earlier in section 3.4

The results of the studies on the extraction of bitumen (Table - 6) by dry process showed that the bonding between stone aggregate and bitumen is improved due to the presence of polymers. This may be explained by the following structural models. Using these models the extraction pattern is explained.

A plastic aggregate bitumen interaction model for the Plastics waste coated aggregate bitumen mix (Not to Scale)

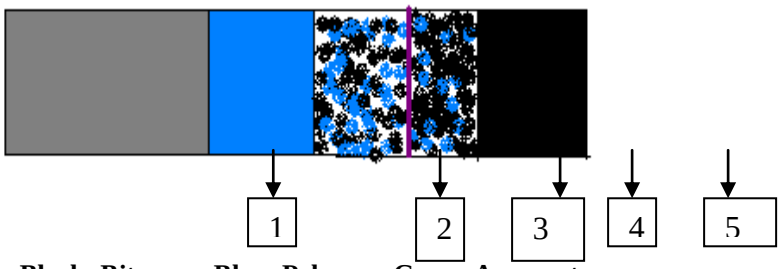

Key: Black- Bitumen; Blue- Polymer; Grey - Aggregate

Aggregate

1. Area of Plastics bonded with aggregate (polymer coating)
2. Area of Bitumen–plastics blend (due to diffusion between molten plastics & hot bitumen)
3. Area of Loosely bonded bitumen with dispersed plastics
4. Area of Plain bitumen layer

On the whole, the coating of plastics over the stone aggregate helps bitumen to have a strong bonding at the surface.

Basing on the above observations, the increased value of MSV, nil stripping and improved strength of road is explained

3.6. Reduction of Carbon dioxide Emission:

Littered waste plastics are otherwise burnt along with domestic waste resulting in the production of green house gases thus aiding global warming.

In the Dry process, waste plastics are used as a coating material by softening the plastic and not by burning. Hence there is no evolution of gases like carbon dioxide. For a distance of one Kilometer single lane plastic bitumen road, a minimum of one ton of waste plastics is used. This accounts for a reduction of Carbon Dioxide to a tune of 3 tons. Using this technology we have laid more than 2500kms of plastic bitumen road at various places in India. This amounts to a prevention of burning of waste plastics to an extent of 2500tonnes. This means that the process prevented the formation of Carbon Dioxide to an extent of 7500tonnes. (If this waste plastic is burnt along with MSW, nearly 2, 50,000tonnes of Carbon Dioxide would have been produced)

Chemical Reaction (700^0C)

PE, PP,PS $\xrightarrow{\triangle}$ C, CO,CO_2 but no Cl_2

Use of PE, PP and PS cannot liberate dioxin even on burning (Table-1).

PVC $\xrightarrow[\text{Cu II catalyst}]{\text{C+O}_2\text{+Cl}_2,\ 300\text{-}350\ ^{o}\text{C}}$ C, CO, CO_2 and Cl_2 and HCl

PVC alone on heating may result in dioxin formation (300-350^{0}C) (reverse cooling).

V. FIELD STUDY

4.1. Performance Study:

This work is intended to examine several aspects related to the use of polymer coated aggregate for strengthening of flexible pavement. The objective of the work is to have functional evaluation and structural evaluation of polymer coated aggregate flexible pavement. This is achieved by performing the following specific tasks:

4.1.1Non Destructive Test:

a. Structural Evaluation

I. Carrying out structural evaluation of flexible pavement for the strength of the pavement by deflection measurement using Benkelman beam
II. Measuring the field density of the road using sand pouring cylinder

III. b. Functional Evaluation

IV. Measuring the roughness of the pavement surface using Bump integrator / Merlin
V. Examining the pavement condition of the road (cracks, raveling, potholes, rutting, corrugation edge break etc) by carrying out visual inspection of road surface
VI. Measuring the resistance offered by the pavement surface against skidding of vehicles using portable skid resistance tester
VII. Measuring the pavement macro texture for the geometrical deposition of individual aggregates. Texture depth was measured using sand patch method

4.1.2. Destructive Test:

i. Studying the gradation of the laid road.
ii. Carrying out different tests on recovered bitumen.
iii. Investigation of the properties of Plain aggregate and Polymer modified aggregate

VI. CONSTRUCTION OF THE TEST ROADS

Six sites were chosen (Table -10). Sites 1 to 5 for roads constructed using plastic coated aggregates and the site 6 road constructed with conventional bituminous mixtures . The above tests were conducted as per the specification (IRC) and the values were compared with standard values which are given in the Table-6 as tolerance value. The tests were conducted periodically from Jan 2007 to Dec'12. The average values are tabulated (Table 9)

It is observed from the results that the plastic roads laid since 2002 to 2012 are showing results which are the characteristics of a good road. They are showing better results and maintain good quality compared to the plain bitumen roads laid in 2002 .Hence it can be concluded that the plastic tar roads are performing much better than the plain bitumen road.

In addition to this, the physical surface condition survey of the plastic tar road (procedure adopted by Central Road Research Institute, New Delhi) shows that there is no pot hole formation, cracking, deformation, rutting, raveling and edge flaw. The photos of these roads taken recently are also attached for having a visual exhibition (Table -10). Hence it can be concluded that the plastic tar roads are having good skid resistance values, good texture values, good surface evenness, reasonably good strength and field density with least change.

VII. ECONOMY OF THE PROCESS

Based on the experimental evidences and the amount of raw materials used for 25mm Semi Dense Bituminous Concrete (SDBC- this top layer of the bituminous road. 10M^2 SDBC road the following calculation has been arrived

Material needed	Plain bitumen process	Plastics coated aggregate (PCA)

80/100 Bitumen	11250Kg	10125Kg
Plastic waste	-----	1125Kg
Cost	Rs. 393750	(BIT)Rs.354375+(plastic) Rs.13500 = Rs. 367875
Cost Reduced	NIL	Rs. 25875.00
Carbon Credit Achieved on avoiding burning of plastics		3.5tonnes

- Cost Bitumen Approx: 35,000/ton and Waste Plastic : Rs. 12000/tons
- Savings of bitumen = 1 ton
- Use of Plastics waste – (11,25, 000) carry bags (1.125 ton)
- Bitumen needed– 10125kg
- Plastics waste needed – 1125 kg.

Three kilograms of bitumen were saved and three kilograms of waste plastics were used. The cost of bitumen is much higher than that of plastics and this process also helps to save the natural resources. There is no maintenance cost for a minimum period of five years. Hence the process is cheap and eco friendly.

VIII. CONCLUSION

In Dry process, the aggregate is modified by coating with polymers and producing a new modified raw material for flexible pavement. Patent has been obtained for this process (Fig-2). Coating of polymers on the surface of the aggregate has resulted in many advantages and ultimately helps to improve the quality of flexible pavement. The coating of plastics over aggregate also improves the quality of the aggregate.

In addition to the improvement of the quality of the road, this technology has helped to use the waste plastics obtained from domestic and industrial packing materials. This has added more value to the dry process as this process helps to dispose 80 percentages of the waste polymers usefully by an eco-friendly method. This has already been accepted by the Central Pollution Control Board, New Delhi. They have already released a guideline on the technique of the road laying by dry process and its advantage.

By this technique, which is in-situ, waste polymer like carry bags, foam, laminated sheets, cups are all used for road laying.

Moreover, the use of polymers helps to reduce equivalent quantity of bitumen, thus reducing the cost of the road laying.

In a net shell the Dry Process thus helps to

1. Use higher percentage of plastics waste.
2. Reduce the need of bitumen by around 10%.
3. Increase the strength and performance of the road.
4. Avoid the use of anti stripping agents.
5. Reduce the cost to around Rs. 30000/ km of single lane road as on date.
6. Carry the process in situ.
7. Avoid industrial involvement.
8. Avoid disposal of plastics waste by incineration and land filling.
9. Generate jobs for rag pickers.
10. Add value to plastics waste.
11. Develop a technology, which is eco-friendly.

Our studies on the performance of plastic tar road conclusively proves that it is good for heavy traffic due to better binding , increased strength and better surface condition for a prolonged period of exposure to variation in climatic changes Above all, the process helps to dispose waste plastics usefully and easily.

REFERENCES

[1] Nabil Mustafa, " Plastics Waste Management " Canadian Plastics Institute, Toronto, Ontario, Canada, Marcel Dekker, Inc 1993.
[2] A support manual for Municipal Solid Wastes, Central Pollution Control Board, July 2003.
[3] S.K.Garg, Environmental Engineering, Vol.II Khanna Publishers, 1999.
[4] R.Vasudevan, S.Rajasekaran, S.Saravanavel, "Reuse of Waste plastics for Road Laying" Indian Highways, (Journal of Indian Roads Congress) Vol. 34. Issue 7 ,Page No: 5 – 20 July 2006.
[5] Shuler, T.S, Collins J.H., and Kirkpoatrick, J.P, "Polymer Modified Asphalt Properties Related to asphalt concrete performance", Asphalt Rheology Relationship to Mixture, ASTM: STP: 941, O.E, Briscoe Ed ASTM, Philadelphia, 1987.

[6] Zoorab S.E, and Suparma L.B, "Laboratory Design and Performance of Improved Bituminous Composites Utilizing Recycled Plastics Packaging waste", Presented at technology Watch and Innovation in the Construction Industry, Palais Descongres, Brussels, Belgium 5-6, April 2000, pp. 203-209.
[7] Denning,J.H, and Carswell.j., " Improvements in rolled Asphalt Surfacing by the Addition of organic Polymers ", Department of the Environment Department of Transport. Report LR 989. Transportation Road Research Laboratory (TRRL), Crow throne, 1981.
[8] Salter, R.J., and Rafati-Afshar, F., "Effect of Additives on Bituminous Highway Pavement Materials Evaluated by the Indirect Tensile Test", Transportation Research Record 1115, 1987. pp 183-195.
[9] Dallas, N. Little : AN Additive of Asphalt Additives to Reduce Permanent Deformation and Cracking in Asphalt Pavements: A brief Synopsis of On going Research", Proceedings of the Association of Asphalt Paving Technologists(AAPT), Vol. 55, 1986, pp 314-320.
[10] Walter j. Tappeinier , " Performance and Economical Advantage of Polymer Modified Asphalt", Richard Felisinger, Vienna, Austria 1999.
[11] King, G.N., Muncy, H.W., and Prudhome, J.B., " Polymer Modification: Binder's Effect on Mix Properties", Proceedings of the Association of Asphalt Paving Technologists(AAPT), Vol. 55 , 1986 pp 519-540.
[12] Sunil Bose, and Jain, P.K," Laboratory Studies on the Use of Organic Polymers in Improvement of Bituminous Road Surfacing", Highway Research Bulletin 38, 1989, New Delhi.
[13] Sunil Bose, and Jain, P.K, Sangita, and Arya, I.R., "Characterization of Polymer Modified Asphalt Binders for Roads and Air Field Surfacing, Polymer Modified Asphalt Binders", ASTM: S.T.P:1108, American Society of Testing Materials, Philadelphia, USA, 19923. Pp.331-355.
[14] Mahabir Panda and Mayajit Muzumdar, "Development and Evaluation of a Bituminous Paving Binder Containing Reclaimed Polyethylene", Indian Highways, Indian Roads Congress, New Delhi, Vol. 25(5), 1997.
[15] Punith .V.S. and Dr. Veeraragavan.A "Fatigue characteristics of Recycled Plastics Modified Bituminous Concrete Mixes". Highways Research Bulletin, Indian Road Congress, Nov.2004.
[16] Rheological Properties of Bitumen Modified with Polyethylene and Polyethylene Based Blends, Oscar González Uranga, Department de cynical Technologic de Polymers. Faulted de Química, Universidad del País Vasco. Spain. 2000.
[17] Dr. R. Vasudevan, S.Rajasekaran & S.Saravanavel, " Utilization of plastics waste in construction of flexible pavement" Proceeding of the National Seminar on " Integrated Development of Rural & Arterial Road Network for Socio-Economic Growth"Dec.2003. P-II. 243 and Journal of IRC July'2006
[18] Indicative Operational Guidelines on the construction of Polymer – Bitumen roads, Probes/101/ 2005-2006; Central Pollution Control Board, New Delhi.
[19] Performance Evaluation of polymer coated bitumen built roads; Probes/121/2008-2009; Central Pollution Control Board, New Delhi.
[20] AASHTO T 96-2001- "Standard Method of Test for Resistance to Degradation of Small-Size Coarse Aggregate by Abrasion and Impact in the Los Angeles Machine
[21] ASTM D2172 Standard Test Methods for Quantitative Extraction of Bitumen From Bituminous Paving Mixtures
[22] IRC 82-1982 Tentative Guidelines for Strengthening of Flexible Road Pavements Using Benkelman Beam Deflection Technique
[23] IS 6241-1971 Method For Test For Determination Of Stripping Value Of Road Aggregate.

TABLES AND FIGURES

Table 1. Thermal properties of polymers

Polymer	Solubility		Softening Temperature range in Deg.C	Products reported	Decomposition Temp. range in Deg.C	Products reported	Ignition temp. range in Deg. C	Products reported
	Water	EPT *						
PE	Nil	Nil	100-120	No gas	270-350	CH_4, C_2H_6	>700	CO,CO_2
PP	Nil	Nil	140 - 160	No gas	270-300	C_2H_6	>700	CO,CO_2
PS	Nil	Nil	110-140	No gas	300-350	C_6H_6	>700	CO,CO_2
PVC	Nil	Nil	200-220	HCl	320-350	C_2H_6, HCl	>700	CO,CO_2, Cl_2& HCl

* 5% Acetic acid

Type of plastics and variation in Bending Strength:

Table 3

Type of Plastic	Percentage of Plastics	Bending Strength in Kg	Compression Strength Tons
Poly ethylene	10 20 25	325 340 350	250 270 290
Poly propylene	10 20 25	350 370 385	280 290 310
Polystyrene	10 20 25	200 210 215	155 165 170
Polyethylene Foam	10 20 25	310 325 335	250 265 290
Polypropylene Foam	10 20 25	340 360 365	270 290 310
Laminated Plastics	10 20 25	360 385 400	290 310 335
BOPP	10 20 25	380 400 410	300 310 330

Physical properties of waste plastics Table – 2

Commercial Plastic material	Nature of Plastics	Thickness μ	Softening Point Deg.C
Cup	Poly ethylene	150	100-120
Carry bag	Poly ethylene	10	100-120
Water bottle	PET	210	170-180
Cool drinks bottle	PET	210	170-180
Chocolate covers	Poly ester+Poly ethylene+metalised polyester	20	155
Parcel cover	Poly ethylene	50	100-120
Supari cover	Polyester+Poly ethylene	60	120-135
Milk Pouch	LDPE	60	100-120
Biscuit covers	Polyester+Poly ethylene	40	170
Decoration papers	BOPP	100	110
Film	Polyethylene	50	120-130
Foam	Polyethylene	NA	100-110
Foam	Polystyrene	NA	110

Table 4. Aggregate technical properties

Stone Aggregate	Plastic content	Moisture Absorption	Soundness	A I V	A C T	L AR	Voids
Without plastic coating	0	4%	5+/- 1 %	25.4	26%	37%	4%
With plastic coating	1%	2%	Nil	21.20	21%	32%	2.2%
With plastic coating	2%	1.1%	Nil	18.50	20%	29%	1%
With plastic coating	3%	traces	Nil	17.00	18%	26%	Nil

Table – 5. Stripping Value of PCA bitumen Mix (Percentage of Plastic – 10%)

		Plain aggregate				Plastic coated Aggregate			
PCA+ Bitumen Mix	Stripping Value	2 hrs	24 hrs	72 hrs	96 hrs	2 hrs	24 hrs	72 hrs	96 hrs
		0	0	2	5	0	0	0	0

Table -6. Results of the bitumen extraction test for the bitumen mix containing the PCA

Plastic content (% by weight)	Bitumen extracted after 5 min %	Bitumen extracted after 10 min %	Bitumen extracted after 15 min %
0	96.0	98.0	99.0
0.5	63.5	88.7	92.3
0.75	63.2	86.7	90.7
1.0	61.3	76.7	83.6

Table -7. Marshall Stability Value for Polymer Coated Aggregate

% of Bitumen	% of Polymer w.r.t wt of bitumen	Type of Polymer	PCA	Marshall Value (kN)	Flow Value (X 0.25mm)	Void Percentage	Marshall Quotient kN/mm
4.5	5	PP	PCA	16	4	53	4
4.5	10	PP	PCA	20	5	55	4
4.5	5	LDPE	PCA	16	4	55	4
4.5	10	LDPE	PCA	17.5	4	55	4.38
4.5	10	PE Foam	PCA	20	4	58	5
4.5	15	PE Foam	PCA	22.5	4	56	5.63
4.5	20	PE Foam	PCA	26.5	4	56	6.62

Table -8. Marshall Stability Value for Polymer Modified Bitumen

% of Bitumen	% of Polymer w.r.t wt of bitumen	Type of Polymer	PMB	Marshall Value (kN)	Flow Value (x 0.25mm)	Void Percentage	Marshall Quotient kN/mm
4.5	**5**	PP	PMB	14.50	3	56	4.83
4.5	**10**	PP	PMB	17.00	3.3	62	5.15
4.5	**10**	PE FOAM	PMB	18.00	3.4	66	5.29
4.5	**5**	LDPE	PMB	15.00	3.3	62	4.55
4.5	**10**	LDPE	PMB	17.00	3.5	62	4.86

Table-9. Summary of Results

Road	Year laid	Unevenness (mm /km)	Skid number	Texture Depth (mm)	Field Density Kg/M^3	Rebound Deflection (mm)
Jambulingam Street	**2002**	**2700**	**41**	**0.63**	**2.55**	**0.85**
Veerabadhra Street	**2003**	**3785**	**45**	**0.70**	**2.62**	**0.60**
Vandiyur road,	**2004**	**3005**	**41**	**0.66**	**2.75**	**0.84**
Vilachery Road, mai	**2005**	**3891**	**45**	**0.50**	**2.89**	**0.86**
Canteen Road, TCE	**2006**	**3100**	**45**	**0.65**	**2.86**	**0.86**
Plain Bitumen Road*	**2002**	**5200**	**76**	**0.83**	**2.33**	**1.55**
Tolerance Value**	------	**4000**	**<65**	**0.6-0.8**	**2.86**	**0.5-1**

*** - Reference road constructed with plain bitumen**
****- Theoretical value for the effective performance of a good road**

Table -10. SURFACE CONDITION SURVEY:

Site Name	Surface Condition Survey	Photo
Jumbulingam road, Chennai (2002) Photo Date: 21-12-2012	1. No Pothole 2. No Cracking 3. No Deformation 4. No Edge Flaw	
Veerbadhra Street, Erode(2003) Photo Date: 04-01-2013	1. No Pothole 2. No Cracking 3. No Deformation 4. No Edge Flaw	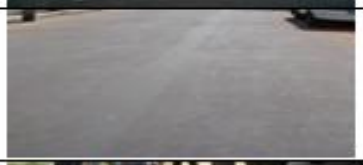
Vandiyur Main road (2004) Photo Date: 01-02-2013	1. No Pothole 2. No Cracking 3. No Deformation 4. No Edge Flaw	
Vilachery Main road (2005) Photo Date: 11-02-2013	1. No Pothole 2. No Cracking 3. No Deformation 4. No Edge Flaw	
Canteen road (2006) Photo Date: 05-01-2013	1. No Pothole 2. No Cracking 3. No Deformation 4. No Edge Flaw	
Plain bituminous road (2002) Photo date: 21.12.2012	1. Pothole developed 2. Cracking is there. 3. Deformation is there 4. Edge Fault	

Fig I. Thermal Analysis Graph

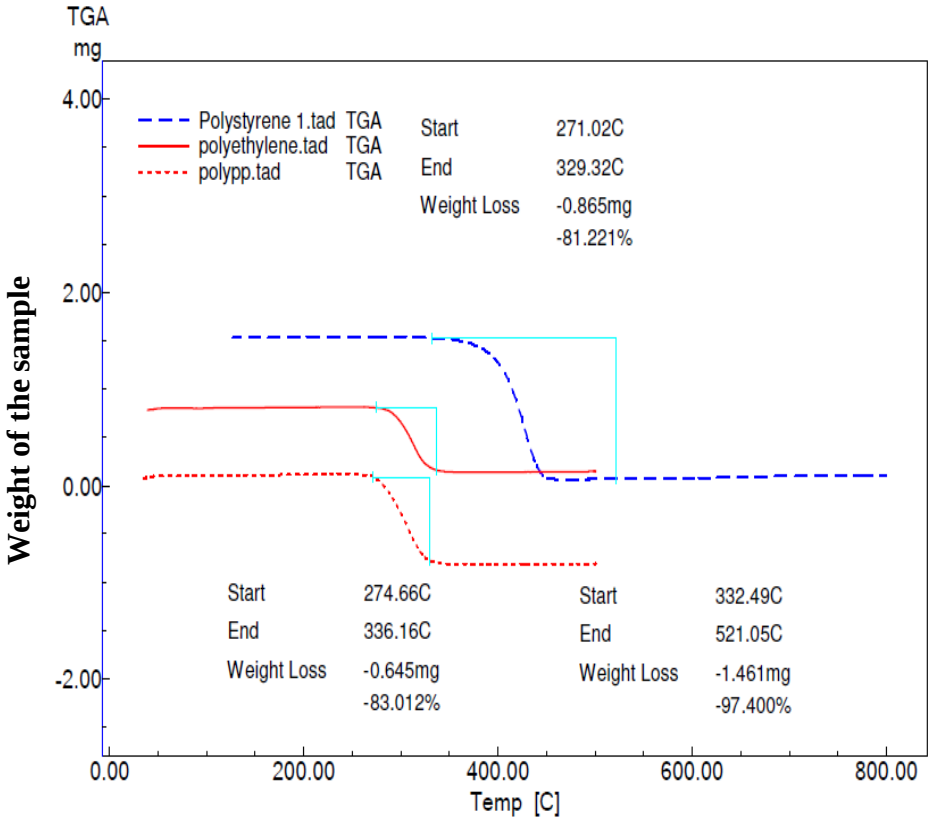

Thermo Gravimetric Analysis

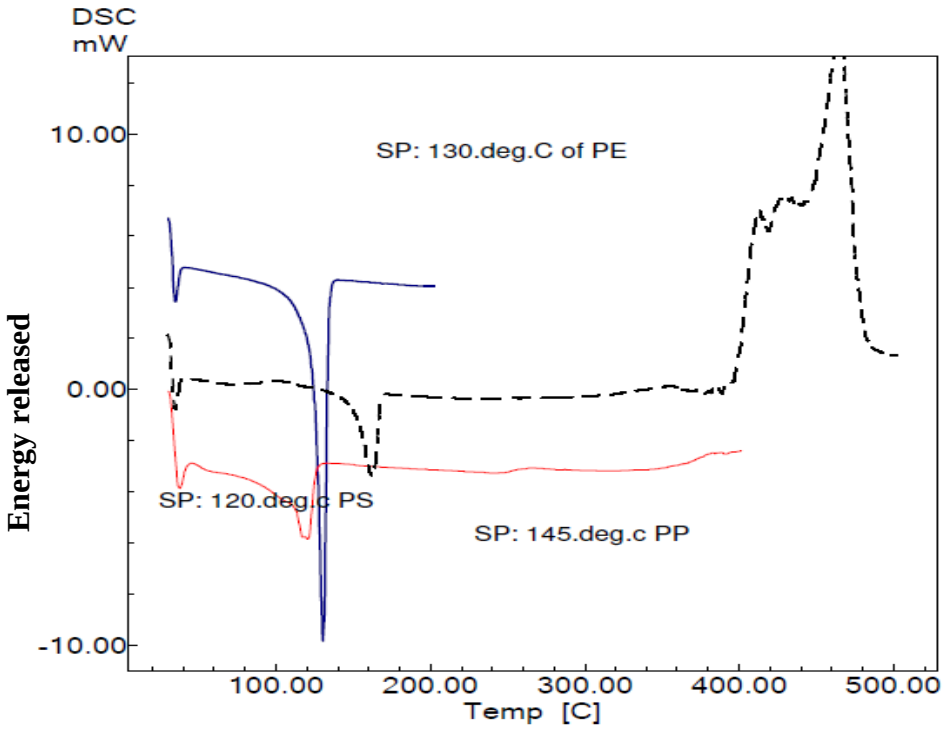

Differential Scanning Calorimeter

Fig.2

American Journal of Engineering Research (AJER)
e-ISSN : 2320-0847 p-ISSN : 2320-0936
Volume-02, Issue-11, pp-14-24
www.ajer.org

Research Paper Open Access

Economic Viability of Coal based Power Generation for Nigeria

Ujam, A. J., and Diyoke C.
a. Department of Mechanical & Production Engineering, Enugu State University of science and Technology (ESUT), Enugu, Nigeria

Abstract: - Coal is an abundant and widely spread fossil energy resource in Nigeria that has not been properly harnessed. It has a potential to meet the current and future energy needs of Nigeria if security and diversity of supply remain fundamental. Supercritical Pulverised coal technology is the power plant of choice for most countries in Europe, USA and Asia. This paper examines the economic viability of the deployment of supercritical pulverised coal technology for power generation in Nigeria. The economic viability of the technology was accessed by three major economic parameters; the Net present value (NPV), the levelized generation cost (LGC) and the internal rate of return (IRR). LGC is determined by taking the net sum of expenses and dividing by the discounted value of the electrical energy generated (kWh) throughout the life of the power plant. The NPV is estimated by subtracting the discounted values of the various expenses of the investment from the discounted value of the income generated from the sale of the electricity generated by the plant over its useful life. Company tax of 32% and annual depreciation rate of 33.3% as recommended by Nigeria Electricity Regulatory Council (NERC) were allowed for in the calculation. The results of the study show that supercritical pulverised coal combustion technology is economically, less risk and technically viable option for power generation in Nigeria generating electricity at a levelized cost of 0.045 dollars per kWh at a net present value of $1.13 billion.

Keywords*: - Coal, SC PCC, Economic analysis, Electricity, kWh, Power Generation*

I. INTRODUCTION

In Nigeria, 93% of electric power generation is provided by fossil fuel (gas), the remainder is from Hydro sources **[1].** There is over 8.6 GW **[2]** of installed capacity of generating plant made of government owned and Independent power plants, details in tables 1.1 and 1.2. Despite the large number of installed power generation capacity, Nigeria could still not meet up with the electricity demand of its populace which is estimated at 10 GW **[3]** because of old age of the power plants and the lack of new generation plants addition. Actual electricity generation is only between 2.5-3.6 GW

Table 1 Installed and Generating capacities of Government owned Power stations in Nigeria **[2]**

S/N	Station name	Type	Year Built	Location	Installed capacity (MW)	Available capacity (MW)
1	Kainji/Jebba	Hydro	1968	Niger state	760	480
2	Shiroro	hydro	1989	Niger state	600	450
3	Kainji/jebba	Hydro	1985	Niger state	540	450
4	Egbin power Plc	Thermal	1986	Egbin, lagos	1320	1100
5	Geregu Power Plc	Thermal	2007	Kogi state	414	276
6	Omotosho Power Plc	Thermal	2007	Ondo state	304	76
7	Delta Power Plc	Thermal	1966	Delta state	900	300
8	Sapele Power Plc	Thermal	1978	Delta State	1020	90
9	Afam (IV-V)	Thermal	1963/01	Rivers state	726	60
10	Calaber Thermal station	Thermal	1934	Cross River state	6.6	nil
11	Oji River	Thermal	1956	Enugu state	10	nil
12	Olorunsago Power Plc	Thermal	2008	Ogun statae	304	76
				Total	**6904.6**	**3558**

Table 2 Installed and Generating capacities of Independent Power projects (IPPs) in Nigeria **[2]**

S/No	Station name	Location	Installed capacity (MW)	Available capacity (MW)
1	AES Power Station	Egbin lagos	224	224
2	SHELL- Afan VI Power station	Rivers state	650	650
3	Agip Okpai Power Station	Delta state	480	650
4	ASG Ibom Power Station	Akwa Ibom	155	76
5	RSG – Trans Amadi Power Station	PH,Rivers State	100	24
6	RSG Omoku Power Station	Omoku, Rivers state	150	30
		Total	**1759**	**1484**

Even if new power plant additions were to be made, it is our concern that the longer term sustainability of fossil fuel-based generation cannot be guaranteed due to the frequent agitation for resource control from the Niger Deltans and vandalism of power plant gas supply infrastructure. More over there is an urgent need for a good energy mix in the nation's energy generation infrastructure due to the so many benefits derivable from it. Globally the energy industry is driving toward sustainable, low carbon emitting, renewable energy sources. However, renewable as at now are still in their infant stage of commercialisation and cannot help to meet Nigeria's base load electricity demand deficit. Coal which is evenly spread across Nigerian states with an estimated reserve of 2.734 billion tonnes **[2]** holds the key to Nigerian's present and even future energy security.

1.2 Coal use for electric power generation

Coal is an important energy resource for the world, principally for electricity generation. It is the world's most abundant and widely distributed fossil fuel, with global proven reserves totalling nearly 1000 billion tonnes **[4].** Within the last decade, in the global market the demand for coal has grown rapidly, exceeding that for gas, oil, nuclear and renewable energy sources, although this comes at a cost **[4].** On the average, 40% of the world's electricity is generated from coal. Nevertheless this figure is even much greater in many countries, like in South Africa, coal fuels about 93% of their electricity generation; it is 92%, in Poland, 79% in China, 69% in India and 49% in the United States of America just to mention a few **[4].** As can be inferred from the above, most developed and developing countries that have coal deposits meet their energy demands through coal based generation. Nigeria can also bridge its energy demand and supply deficit by leveraging on its abundant coal deposit resource. The potential role coal stands to play in meeting Nigeria energy needs can further be buttressed by the following quotes.... '' The growing energy needs of the developing world are likely to ensure that coal remains a key component of the power generation mix in the foreseeable future, regardless of climate change policy **[4].**'' The onus is now for Nigerian government to find better ways of utilising coal in power generation while causing minimal environmental consequences. A retinue of clean coal technologies (CCTs) have been developed to ensure that **[5].**

Advanced or clean Coal based power generation technologies (CCTs) are technically proven and draws on a cheaply available energy resource. Carbon emissions and greenhouse gas impacts are controlled.

An enormous amount of capital investment will be required to reach the development goals for new electricity capacity investment in Nigeria. It is estimated that Projected Electricity Supply by Fuel Mix (Coal) for 7% growth rate scenario for the years 2015, 2020, 2025 and 2030 are 2393, 6515, 9305 , and 15, 815 mega watt (MW) respectively **[2].** An enormous financial investment will be needed to actualise that and Obtaining the required capital investment from government will be a major problem especially now that government funding of the power sector is becoming more difficult since there is intense competition for funds between different industry sectors. As a result, private participation in power projects is emerging, introducing IPP (independent power producer) projects into the market. For an IPP investor to invest in coal power plant in Nigeria, he needs to be sure he can recoup his investment with some satisfactory interest on time. Another drawback is revealed when it is understood that current low electricity tariffs result in financial shortfalls in the utilities with a consequent lack of capital for new investment.

In order to make a rational decision about choice of an alternative coal fired power plant technology to adopt in Nigeria, there is the need not just for the consideration of the environmental and technical or technological advantage of the alternatives but also the evaluation of the cost and benefits of the technology to know whether it is economically viable. This study therefore examines the economic viability of a Supercritical pulverised coal combustion y (SC PCC) power generation technology option for electricity generation in Nigeria.

1.3 Approach to the study

The economic analysis study investigates clean coal based power generation options, carries out a brief analysis of those that could reasonably be considered suitable for both long and short term commercial power generation in Nigeria and identifies a choice technology for adoption that can be evaluated economically. The evaluation and selection of a favoured technology consist of;

- An assessment of the possible technologies
- Consideration of the level commercialisation of the technologies
- Consideration of the ability or flexibility of the technologies to burn Nigeria coal
- Immediate Nigerian environmental requirements and future stricter emission legislation requirements
- Consideration of costs (both capital, LGC and O&M cost) and efficiency
- Consideration of risks involved.

The economic viability of the technology selected was accessed by three major economic parameters; the NPV, the LGC and the IRR. LGC is determined by taking the net sum of the discounted O&M cost, replacement costs, fuel costs, investment costs, and dividing by the discounted value of the electrical energy generated (kWh) throughout the life of the power plant. The NPV is estimated by subtracting the discounted values of the various expenses of the investment from the discounted value of the income generated from the sale of the electricity generated by the plant over its useful life. Company tax of 32% and annual depreciation rate of 33.3% as recommended by Nigeria Electricity Regulatory Council (NERC) **[6]** were allowed for in the calculation.

II. CLEAN COAL GENERATION TECHNOLOGY (CCT) OPTIONS

The coal based electricity technologies considered for this study; the subcritical pulverised coal combustion (Sub PCC) technology, the supercritical pulverised coal combustion (SC PCC and the circulating fluidised bed combustion (CFBC) technology are presented in this section. Integrated gasification combined cycle (IGCC), Pressurised fluidised bed combustion (PFBC), and ultra supercritical pulverised coal combustion (USC PCC) are clean coal technologies, but were not considered for selection because they are still in their infant stage of commercialisation and development.

2.1 Sub Critical Pulverised coal Technology (Sub PCT)

Subcritical operation refers to steam pressure below 22.0 MPa (critical point of steam) and temperature of about 540^{o}C. Sub PCC is one of the most predominant, conventional and commercialised method of coal conversion to electricity with over 40 years of experience **[7].** Sub critical PCC owes its predominant position to its good all round performance and high availability. It is technically proven and commercially viable. The main barriers to its continued use are its relatively low thermal efficiency and environmental performance.

2.2 Supper Critical (SC) Pulverised Coal Technology (SC PCT)

This is an improvement over the conventional sub critical pulverised coal combustion. Cycle generating efficiency is improved beyond that of sub critical PCC power plants by modifying the unit to operate at higher (above critical) steam temperature and pressure. Higher efficiency means less emission for every MWh of electricity generated by burning coal **[7].** It is reported than more than 400 SC PCT plants are in operation globally **[8; 9]**

2.3 Circulating Fluidised Bed Combustion (CFBC)

The CFB is a variant of the PCT plant. It is environmentally friendly, flexible to burn a wide spectrum of coals including blends of coal and coke. CFBC is efficient and one of the promising CCTs. The technology is proven in small capacity. Good technical and superb environmental performance without the aid of complex flue gas treatment units is responsible for its rapid development. Take up of CFBC at utility scale has been limited but this is mostly due to the fact that the technology is new and the largest single capacity boiler in operation is 460 MWe, although other high capacity plants are being commissioned **[9].**

2.4 Comparison of coal based generation options

A summary of comparison of the options at 500 MWh is presented in Table 3. This shows Sub PCT to have the lowest total plant cost (TPC) price option with a levelized electricity cost of $47.7/kWh. It represents the lowest risk of the options because of its maturity and long years of experience. SC PCC is marginally more expensive than Sub PCC in this assessment, but with better efficiency and environmental performance. However less mature, there is a high potential that it will be more cost competitive in the long run.

III. SELECTION OF APPROPRIATE TECHNOLOGY

In an earlier work by the authors, Super critical pulverised coal combustion (SC PCC) technology is identified as the appropriate technology for Nigeria. This is because of its more advanced commercial status compared with other options, and its significantly lower levelized generation cost and O&M cost compared to sub PCC technology. Additionally there is known commercial experience of generating power using SC PCC in some African countries like South Africa; this confers on SC PCC the best technology of choice in Nigeria.

This technology continues to be selected as a power plant of choice in China, India, Japan and Europe by commercial investors ahead of other CCTs **[4].** Being a highly efficient technology, it can meet the current short term Nigerian electricity requirements with minimal emissions and it has a great potential to meet whatever future long term policy of emission legislation that Nigeria may become obliged to tomorrow like Carbon capture and storage (CCS).

Table 3 Summary of the clean Coal technologies based on a 500 MWe capacity Plant burning Sub-Bituminous coal **[10, 11]**

Parameter	Sub critical PCC	Super-Critical PCC	CFBC
Maturity	Completely mature	Substantially mature	Proven at small scale(<200 MWe)
Range of Unit size	50-1000 MW	250-1000 MW	40-400 MW
Fuel flexibility	Burns wide range of coals but less better than AFBC at extreme moisture/ash	Burns wide range of coals but less better than AFBC at extreme moisture/ash	Burns practically any fuel
Thermal efficiency	Lowest (33-37%) HHV	High (37-42%) HHV	Low (35%)
Environmental performance	Low efficiency and FGD solids disposal problem	Better than sub-PCC because of higher efficiency	Low efficiency and large volume of solids
Availability	Excellent (85%)	Good (85%)	Limited experience
Capacity factor (%)	80	80	80
TPC ($/kW) HHV	1266	1306	1386
Capital cost ($/kWh)	25.7	26.5	28.1
O&M Cost ($/kWh)	8	8	10.4
Fuel Cost ($/kWh)	14	13	9.5
LGC ($/kWh)	47.7	47.5	48

CFBC is a good and competitive option for low calorific value fuels but its capacity and the type of coal in Nigeria limits its selection. The highest commercial capacity of a CFB plant in operation is approximately 460 MWe Lagisza plant in Poland **[12]** which is less than the capacity of 500 MW being proposed. Installation of multiple boilers of CFB to make up the capacity of 500 MW would make the LGC and capital and O&M cost higher by about 50-70%. USC PCC and IGCC were screened out and not considered for selection because they were judged not to have been proven commercial for a cost effective, competitive and reliable power generation in Nigeria within the next ten years. Besides, there is no technological knowhow in Nigeria to operate those kinds of high tech power plants. There is also greater potential for this technology's costs to be driven down over time and performance improved as a result of the developments in new boiler materials now under way.

3.1 Economic viability of SC PCC power plant

Although diverse ways exist for checking economic viability, the most often and commonly applied methodology in the electricity industry for this purpose is employed below, i.e., the estimation of the levelized generation cost (LGC) , the internal rate of return (IRR) and the net present value (NPV) of the investment.

In any given electricity generation project, the levelized generation costs (LGC) represents the constant stream of costs or electricity price (usually in dollars) over the life of the plant, which is needed to cover all operating expenses, payment of debts and accumulated interests on expenses made by the project initially, and the payment of an acceptable return to the investors.

Levelized cost is estimated by converting the net cash flows of the project to the equivalent net present value costs at the first year the plant commenced operation and dividing the result by the yearly revenue of electricity sales over the project life time. The levelized cost of electricity is made up of three basic components; total capital requirement also called the investment cost, operation and maintenance cost and cost of fuel.

3.2 Investment cost (I) or total plant cost (TCR)

TCR as used here is the sum of all the costs incurred in buying, supplying and building the plant including the cost of land accounted for as if they were spent instantaneously TCR consists of costs as: the PC boiler and accessories cost, cost of flue gas clean up systems, cost of ducting and stack, steam T-G plant, including cooling water system, accessory electric plant, and cost of balance of plant, engineering services, and some allowance for uncertainty **[9].** TCR is usually provided by a mixture of loans, that is, debt contribution through bonds, and equity contribution. In calculating LGC, provision is made so that these costs are paid back with some interests to the owners and lenders over the useful life of the project. TPC are added and divided over the yearly generated output to get the average cost per kWh. Total plant costs of coal fired power plants vary depending on location, supplier, type of plant and type of fuel burnt and environmental requirements. The variation is however less than 10 % as observed in MIT cost estimates **[10].**

3.3 Bond and Equity

A bond is an interest-carrying instrument or discounted government or corporate security that compels the user to pay the bondholder a specific sum of interest. However, equity financing is contributed by the owners of the project and usually paid back from the remaining revenues left after meeting all other obligations and, hence, posses a higher risk of not being completely recouped in comparison to the debt proportion. In LGC estimation investigation, it is assumed that the bond and equity contributions are recouped on a fixed yearly basis irrespective of the quantity of generated output.

3.4 Annual operations and maintenance (O&M) costs

As the name suggests, O&M costs represent the costs incurred in operating and maintaining the plant annually throughout its useful life. These costs are dependent on operation of the plant but are not essentially in direct proportion with the quantity of output, but will stop if plant stops operation. Operational costs include labour and management costs, insurance and other services, and certain types of consumables. Maintenance costs include cost of scheduled overhauls and periodic upkeep. As with TCR, these costs are summed and divided by the yearly generated output to come at the mean cost per kWh. However, unlike Investment costs that are relatively independent of mode of operation, the operating mode significantly influence these types of costs. For instance much less labour will be needed for a power plant that generates electricity only during peak periods of the season, as opposed to one that is used as a base-load power plant. Nevertheless, the condition of power plant working seasonally will not arise in Nigeria any sooner as the demand for power has continuously increased for some years now and is expected to go on in coming years. Moreover, O&M costs naturally rise after some time as the plant ages, as against the investment costs that are presumed steady and fixed as soon as the initial investment is made.

3.5 Fuel and other variable and costs (F)

Fuel cost is the cost of coal, and depends on the plant loading and calorific value. Variable costs are estimated from fuel consumption, maintenance expenditures for forced outages, and other input costs driven directly by hourly plant operations.

IV. FINANCIAL MODELLING

The financial evaluation used discounted cash flow (DCF) to calculate a levelized cost of generation and a net present value (NPV) analysis to assist in the economic analysis of the preferred coal based generation technology. Key project assumptions on which the study was based are:

- The Nigerian average rate of inflation (consumer prices) within the last eight years is 12%. This inflation rate will be used for O&M escalation to protect the investors against future uncertainties in price escalation.
- The price of Nigeria coal was $40 per tonne in 2005 and was forecasted to be $42 per tonne in 2010 **[13].** Annual coal price of $42 forecasted above is assumed and fuel escalation rate equivalent of the inflation rate of 12% was used in fuel price escalation.
- The capital financing for the project was assumed to be 70% borrowed through bonds at a cost of 19.29% and 30% owners equities at a cost of 20.9% and a company tax rate of 32% as recommended by NERC in multi tariff order for the determination of charges **[6]** for power generation in Nigeria.

- Although the average life of a coal power plant is between 30-40 years, a conservative economic life of 30 years was assumed for the coal power plant so the investors can recoup their investment on time.
- The estimation did not account for site specific factors like transmission line additions, transformer or fuel delivery
- The investment cost is escalated at 3% to reflect the forecasts by power plants/equipment cost index **[14].**
- Since money has time value, and the plant will come online in 2016, all currencies are expressed in 2016 $.

4.1 Analysis of costs

Levelized generation cost (LGC). The cash flow diagram for the project throughout its 35 years life cycle is shown in figure 4.2. The levelized generation cost is estimated using equation 1 **[9, 15],** adapted to model the various inputs and assumptions

$$LGC = \frac{Total\ life\ cycle\ cost}{total\ life\ energy\ production}$$

$$LGC = \frac{I + (1-T)\{O + R + F\} - TD}{(1-T).G_1{}_\circ C \sum_{t=1}^{k} \left\{\frac{1+h}{1+i}\right\}^t} \quad \left[\frac{\$}{kWh}\right] \qquad (1)$$

Discounted cost of investment (I).The relationship between the present (I_t) and (I) future value of income at discount rate i, is given by

$$\frac{I}{I_t} = (1+i)^{-N} \qquad (2)$$

Accommodating the rate of cost escalation as a result of inflation (h) into equation (2),
The discounted value of I after N years becomes **[16].**

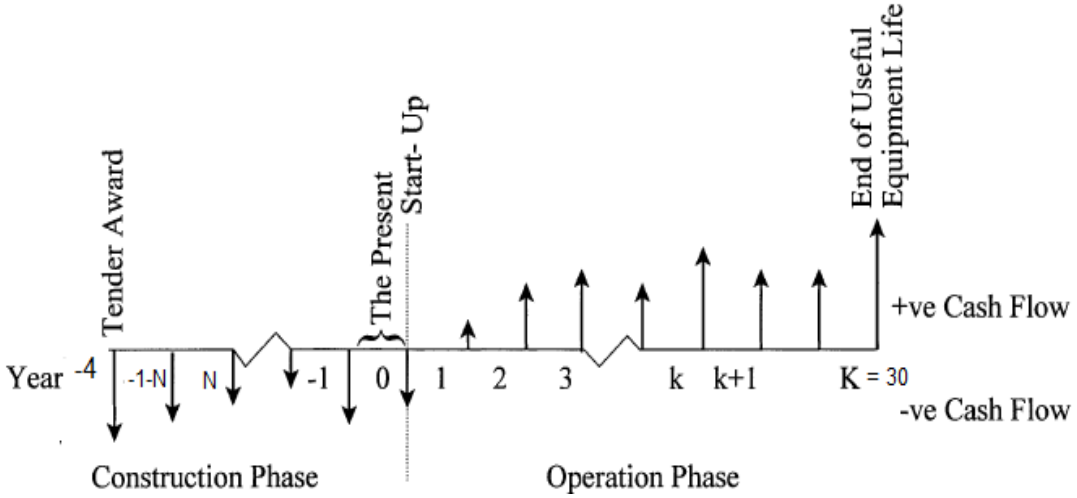

Figure.1 Investment and economic life cycle for the power plant

$$I = \sum_{t=1-N}^{0} I_t \left\{\frac{1+h}{1+i}\right\}^N = I_o + I_1 \left\{\frac{1+h}{1+i}\right\}^1 + I_2 \left\{\frac{1+h}{1+i}\right\}^2 + \ldots + I_N \left\{\frac{1+h}{1+i}\right\}^N \qquad (3)$$

Similarly discounted O&M is calculated using the expression

$$O = \sum_{t=1}^{k} O_{annual} \left\{\frac{1+h}{1+i}\right\}^t \qquad (4)$$

and discounted fuel cost (F) is given by

$$F = \sum_{t=1}^{k} F_t \left\{\frac{1+h}{1+i}\right\}^t \qquad (5)$$

Discounted revenue (E) from electricity generated (G_A) is

$$E = G_A.C + G_A.C\left\{\frac{1+h}{1+i}\right\}^1 + G_A.C\left\{\frac{1+h}{1+i}\right\}^2 + \cdots + G_A.C\left\{\frac{1+h}{1+i}\right\}^k \quad (6)$$

Discounted replacement cost R is;

$$R = \sum_{t=1}^{k} R_{1°annual}\left\{\frac{1+\mathrm{h}}{1+\mathrm{i}}\right\}^{\mathrm{t}} \quad (7)$$

Discounted depreciation (D) is given by;

$$D = D_A \sum_{t=1}^{k}\left\{\frac{1+h}{1+i}\right\}^t \quad (8)$$

The discount rate (i) also called the post tax weighted average cost of capital is calculated from equation (9) **[17]**

$$i = WACC = \frac{E_C \times C_E}{E_C + D_C} + \frac{D_C \times C_D}{E_C + D_C}(1 - T) \quad (9)$$

where,

$$C_E = R_F + \beta\{R_M - R_F\} \quad (10)$$

4.2 Plant input data calculation.

The specification of the plant and the method for calculating some of the plant input data used in the financial model are summarised in table 4

Table 4 Plant input data used in excel calculation

S/No	Calculation input data	Unit	Value	remarks
1a	Construction period	years	5	
b	Project economic life	years	30	
2a	Generation capacity	MW	500	
b	Efficiency (HHV)	%	37.5	
3	Capacity factor	%	85	
4	Availability	%	90	
5a	Investment cost	$/kW	1800	
b	Total investment cost	$ million	900	2ax5a
6	One yr calendar period	hr	8760	
7a	Annual gen. output	kWh/yr	3350700000	2ax3x4x6
b	Electricity tariff	$/kWh	0.07	[6]
c	Annual revenues	$ million	234.54	7ax7b
8	Calorific value of fuel	kJ/kg	31600	
9	Coal feed	tonne/hr	152	(2ax3600)/(8x2b)
10	Annual fuel use	tonne/yr	1,131,792	3x6x9
11	Coal price	$/tonne	42	
12	Annual fuel cost	$ million	47.5	10x11
13	O&M cost	$/kWe	15.6	[18]
14	Annual O&M cost	$ million	7.8	7x13
15	Capital from Debt (D)	%	70	[6]
16	Capital from equity	%	30	[6]
17	Cost of debt (R_D)	%	19.29	[6]
18	Asset beta (β)	%	50	[6]
19	Risk free rate (R_F)	%	14.8	[6]
20	Market return or ROR (R_M)	%	27	[6]
21	Cost of equity (R_E)	%	20.9	$R_F - \beta(R_M - R_F)$
22	WACC (i)	%	15.34	See Eqn. 9
23	Inflation rate (h)	%	12	[6]
24	Company tax rate (T)	%	32	[6]

4.3 Discounted Cost of investment (I).

The investment cost (I) of the coal fired power plant with NO_x combustion controls (low NO_x burner & OFA) and without SO_2 is estimated to be $1,800 per kW. Construction time for coal power plants is usually 4 or 5 years **[18]**. Since there is no coal fired power plant construction experience in Nigeria, the schedule for construction of coal fired power plant in South Africa as shown in table 5 is applied here. The discounted cost of total plant investment (I) as determined from equation (3) using excel model, adapted to model the various inputs and assumptions is $1344.97 million

Table **5** Economic requirements for generation in Nigeria (NERC, 2008)

Project economy	
▪ Construction time:	5 years
▪ Economic life:	30 years
▪ Company Tax rate:	32%
▪ Financing policy:	Equity and debt (30:70%)
▪ Asset beta (β)	0.5
▪ Risk free rate (R_F)	14.8%
▪ Cost of debt (R_D)	19.29%
▪ Market return (R_M)	27%

4.4 Discounted value of O&M Cost (O).

Annual O&M cost for coal fired power plant of capacity 500 MWe in South Africa for the year 2010 was estimated as $17.38 per kWe (2007 $) [18] which is $19.56 in 2016 $. In Nigeria, cost of labour is assumed to be cheaper due to disparity in the economy of South Africa and Nigeria. The annual O&M cost in Nigeria is assumed to be 80% of South Africans' O&M (i.e. 20% less). Therefore the annual O&M cost in Nigeria at the first year of plant operation is

O_{annual} = 0.8 x $19.56 = $15.64 per kWe.

O_{annual} = $15.64 x 500000 million = $7.82 million.

Applying equation (4) in the excel model, the discounted value of O&M is

O = $157.74 million

4.5 Discounted fuel cost (F). Annual fuel cost (F_A) as estimated in the cost input data estimation in table 4 is $47.54 million. Applying equation (5), Discounted fuel cost over the 30 years life of the power plant (as in table 4) is F = $961.3 million

4.6 Discounted value of the revenue from electricity produced annually.

At a capacity factor of 85% and availability of 90%, the coal fired power plant will generate an annual net output of 3.3507 GWh. From table 6, the average electricity tariff in Nigeria per kWh is ₦8.95 ($0.07 per kWh) at an exchange rate of 1$ for N135.

Therefore, $E_{annual=} G_A.C= 3.3507x10^3x0.07$ = $234.55 million

Applying equation (6) in the Excel model,

Discounted value of E_{annual}=$4743.3 million

4.7 Replacement cost (R).

The power plant will definitely need some of its major parts changed or refurbished during its life time. . Assuming 15% of the total plant investment is used for the replacement. We also assume that this is evenly spaced over 28 years of its life time. Hence, annual replacement cost (R_A) is

$$R_A = 0.15 \times \frac{900}{30} = \$4.5\ million$$

Using equation (7), discounted replacement cost R is $87.11 million

Table 6 Nigeria electricity tariffs Schedule for 2010 (NERC, 2008)

Type of load	Tariff code	categories	Energy charge (₦:K/kWh)
Residential	R1-R5 (MD)	<5kVA to < 20 MVA	1.80-12.50
Commercial	C1-C4 (MD)	<5kVA to < 20 MVA	9.40-12.30
Industrial	D1-D5	<5 kVA to > 20 MVA	9.80-12.90
Special tariff class	A1-A6	<15 kVA to < 20 MVA	8.60
Street lightening	SI	1ph, 3ph	6.60
		Average	7.28-10.62($0.07)

Exchange rate used: $1 = ₦135

4.8 Discounted value of depreciation expense (D).

The power plant will depreciate in value with use. Hence a depreciation allowance is usually allowed for the replacement of the plant at the end of its economic life. Annual depreciation expense D_A is given by

$$D_A = \frac{total\ plant\ cost}{depreciation\ period} = \frac{900}{30} = \$30\ million$$

Applying equation (8),

Discounted depreciation cost (D) is D = $222.4 million.

4.9 Net Present value (NPV).

This is the net cash flow throughout the life of the power plant. It is the difference between benefits accruing from the investment and costs or expenses incurred in running the business.

NPV after tax is calculated by the expression **[15]**

$$NPV\ after\ tax\ at\ T\% = (1-T)\{E-(F+O+R)\}+T\times D-I \qquad (11)$$

Applying equation (11) in Excel model adapted

NPV at a tax of 32% is 1131.44 million dollars.

4.10 Levelized generation cost (LGC).

Applying equation 1 in the excel model, the levelized generation cost of the power plant is estimated thus,

LGC= $0.045 per kWh (₦6.1 per kWh)

Allowing 30% for profit, the tariff for power from the power plant will be $0.059 per kWh (₦7.8 per kWh).

4.11 Pay back period (PB) and Internal rate of return (IRR).

The payback period is 19 years while internal rate of return of the project is 20.8%

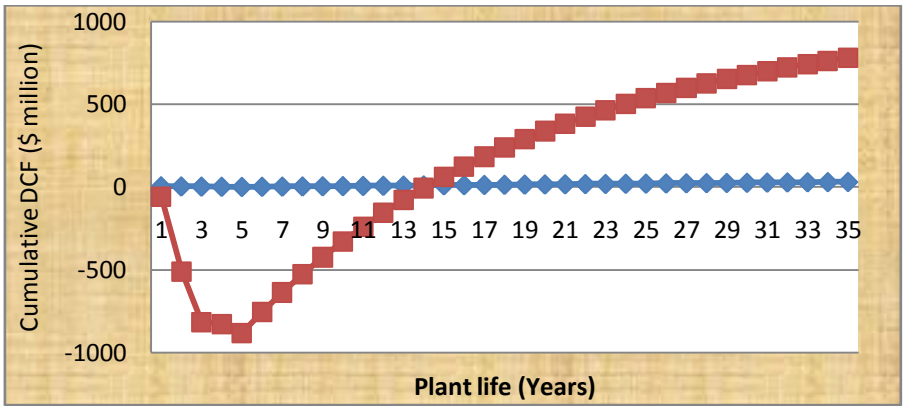

Figure 2 Graph of Plant life VS cumulative DCF

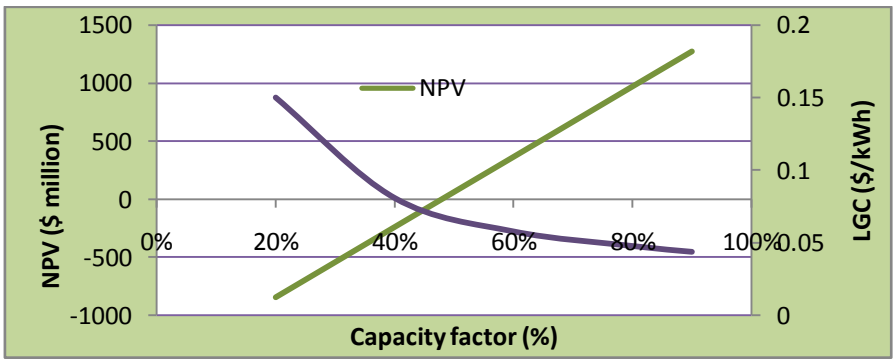

Figure 3 Sensitivity of NPVand LGC on Capacity factor

4.12 Sensitivity/Risk Analysis: Impacts of Major Factors on LGC.

The LGC and other economic performance indicators (NPV, IRR, PB) estimated are determined majorly by four cost parameters; the investment cost, the O&M cost, the capacity factor and the cost of fuel. Since some of these cost are estimated and assumptions in future values are difficult to predict accurately, there would always be some uncertainty about the projects results. To reveal the potential risks that may be associated with the input factors and proffer solutions, the SC PCC study was subjected to further sensitivity analysis of the plant capital, O&M and capacity factor. Three alternative scenarios were created, one being the original plant capital of $1800/kW (Identified as the base case) and the other two scenarios. For each scenario the plant cost, O&M cost and capacity factor were further increased by a percentage until the NPV becomes negative and that point becomes the switching value of the project. The other scenario is cost reduction by 10% and then 15% to demonstrate the effect of a 10% and 15% subsidy of plant capital cost, O&M cost, and fuel cost. The main inputs and results for the sensitivity analysis are shown in table 7.

Table 7: Sensitivity analysis inputs and results

Item	Unit	Base case	Switching value/Bad trend	Favourable trend	
				Good	Better
Installation cost	$/kW	1800	Up by 85%	Down by 10%	Down by 15%
			3328	1620	1530
Installation cost	$ million	900	1664	810	765
LGC	$/kWh/$	0.045	0.07	0.042	0.041
NPV	$ million	1131.4	-0.16	1264.8	1331.4
Fuel cost	$/tonne	42	Up by 173.1%	Down by 10%	Down by 15%
			114.7	37.8	35.7
Fuel cost	$ million/year	47.54	129.8	42.79	48.91
LGC	$/kWh	0.045	0.070	0.044	0.043
NPV	$ million	1131.4	-0.06	1196.8	1229.5
Capacity factor	%	85%	47.6%	Up by 5.9%	Up by 11.8%
				90	95
Impacted fuel cost	$million/year	47.54	26.62	50.33	53.13
LGC	$/kWh	0.045	0.071	0.044	0.042
NPV	$ million	1131.4	-0.012	1282	1434

An investment cost of $1800 per kWe at a tax rate of 32% and discount rate of 15.4% translates in the analysis of this study to LGC of $0.045 per kWh which is very well below the tariff benchmark of $0.07 per kWh set by the Nigeria electricity regulation council (NERC, 2008). With all other factors remaining constant, a capital cost increase by about 50-65% will still give good returns on investment. However, cost above $3327 per kWh (i.e. increase above 65%) will change the Npv to a negative value.

The discount rate is the interest rate used to determine the present value of the future streams of income from the project. The relationship between discount rate and LGC or NPV will reveal to investors what range of discount rates will produce a positive cash flow and hence electricity tariff below the benchmark of $0.07 per kWe. A discount rate below 20% will give a positive NPV and electricity with tariff rate within the limits set by NERC. However, a discount rate of above 20.7% is the switching value and will change the project to a non profitable one.

The capacity factor is another important factor in the analysis of a power plant performance economically. The NPV drops progressively as the capacity factor is decreased from 85 through 70 t0 65% and becomes negative at a capacity factor of 47.6%.

An increase in fuel cost to about 150-165% of the base fuel cost will l not change the NPV of the project to a negative value, but the lower the fuel cost, the lesser the cost of electricity. However, fuel cost increase to about 170% will switch the NPV of the project to negative.

V. SUMMARY OF MODELLING

A summary of a levelized unit cost of generation and NPV cost analysis performed, using a DCF model, adapted to model the various inputs and assumptions attributable to the selected alternative is shown in table 8.

Table 8 Summary of computed results for 500 MWe net coal power plant

Variable	Discounted value	LGC ($/kWh)	% of total
Investment cost (I)	$1344.97 million	0.0290	64%
O&M cost (O)	$157.74 million	0.0023	5%
Fuel cost (F)	$961.30 million	0.0142	31%
Replacement cost (R)	$87.11 million	0.0011	2%
LGC		0.045	100%
Sale price of a kWh of electricity (30% profit)		0.059 USD/kWh	
Sum of discounted revenue over 30 years.		$4,743.28 million	
NPV		$782.09 million	
PBT		19 years	
IRR		20.8%	

VI. CONCLUSIONS

Coal based electricity has been a major source of power in so many countries especially those that have coal deposits. It is a major contributor of the power sectors of USA, China, South Africa, Australia to mention just a few. Nigeria has plentiful coal deposits but cannot meet its power needs presently because it has been depending solely on oil and hydro sources for its power needs. The gap between Nigeria's electricity demand and supply continues to widen, reinforcing the rising pace of economic and social development.

The integration of coal power generation in the Nigeria electricity mix will not only guarantee the steady and interruptible power supply that has eluded it for centuries, but will ensure security of energy supply, stability in

prices of electricity by removing unnecessary monopoly in the electricity sector and also ensure survival and continued operation of companies in the Nigerian environment while also attracting new ones. This will have a general multiplier effect of creating additional employment opportunities for the teeming unemployed youths while also setting the pace for the attainment and sustainability of growth and development of Nigeria economy. The outcome of the economic evaluation of the selected SC PCC technology assuming 70% equity and 30% debt funding at a company tax rate of 32%, inflation rate of 12% and discount rate of 19.6% (WACC) is as follows;

- The project would cost $1.34 billion (2016 $) over the 5 years construction period and would generate a net present value of $1.13 billion over the thirty years of its economic life.
- The LGC of the electricity from the SC PCC Plant is estimated as 0.045 dollars per kWh at an internal rate of return of 20.8% which means the cost of the electricity supplied to the grid could be up by about 50% and still be within the limit set by Nigeria electricity regulation council (NERC) which is $0.07 per kWh.

VII. REFERENCES

[1] Energy Information and administration, EIA, (2009b). "Nigeria energy data, statistics and analysis". Available at: http://www.eia.doe.gov/emeu/cabs/Nigeria/pdf.pdf (accessed 05/2010).

[2] A. S. Sambo (2009), "The challenges of sustainable energy development in Nigeria", Energy commission of Nigeria.

[3] Tallapragada, P.V (2009). "Nigeria electricity sector –Electricity and gas pricing barriers". International Association of Energy Economics, first quater, 2009. Available at: https://www.iaee.org/en/publications/newsletterdl.aspx?id=72. (accessed 08/10).

[4] International Energy Agency IEA, (2011) "Power Generation from Coal'' Ongoing Developments and Outlook.

[5] Alessandro Franco, Ana R. Diaz. (2009) "The future challenges for clean coal Technologies: Joining efficiency increase and pollutant emission control" Energy 34348–354.

[6] NERC, (2008). "Multi year tariff order for the determination of charges and tariffs for electricity generation, transmission and retail tariffs 2009". Available at: http://www.nercng.org/index. php?option=com_content&task=view&id=69&Itemid=84. (accessed 08/10).

[7] National Technical Energy Laboratory, NTEL (2007). "Cost and performance baseline for fossil energy plants", DOE/NETL-2007/1281. Available at: http://www.netl.doe.gov/energy- analyses/pubs/Bituminous %20Baseline_Final%20Report.pdf

[8] Lusica. N., Xie. T and Lu.Y. (2008). "Technology status and project development risks of advanced coal power generation technologies in APEC developing countries",(prepared for APEC, EWG/06/2007A, Oct., 2008) available at http://www.egcfe.ewg.apec.org/projects/EWG_06-2007_Report%20_2008-10-01.pdf (accessed 5/6/2010

[9] NETL, (2010). "Investment decision for base load power plants". Available at: http://www.netl.doe.gov/energy-analyses/pubs/InvestmtDecsnsBsldPP4.pdf

[10] MIT (2007), "The Future of Coal – options for a carbon-constrained world", MIT, Cambridge, MA, USA. Available at: http://web.mit.edu/coal/The_Future_of_Coal.pdf

[11] EPA (2006) : Nexant, Inc., "The environmental footprints and Cost of coal-based Integrated gasification combined cycle and pulverized coal technologies". (prepared for the US Environmental Protection Agency, EPA_430/R-06-006, july, 2006) Available at: http://www.epa.gov/airmarkets/resource/emissions-resource.html. (Accessed 05/2010

[12] Chen, W. and Xu, R. (2009), "Clean Coal Technology development in China", Energy Policy, vol. 38, no. 5, pp. 2123-2130.

[13] Gujba, H. Mulugetta, Y., and Azapagic, C. (2010). "Environmental and economic appraisal of power generation capacity expansion plan in Nigeria". Energy policy (2010), (in press)

[14] IHS Inc. (2009)."Steam generation plant cost index". Available at: http://www.ihsglobalinsight.com/ gcpath/PowerPlanner.pdf

[15] Short, W., Packey, D. and Holt, T. (1995) "A manual for the economic analysis of energy efficiency and renewable energy technologies", National Renewable Energy Laboratory available at*:* http://www.nrel.gov/csp/troughnet

[16] Fuller, S.K. and Petersen, S.R. (1995). "Life cycle costing manual for the federal and energy management programme: National institute of standards and technology USA". Available at: http://www.wbdg.org/ccb/NIST/hdbk_135.pdf

[17] Chelson, J.V., Payne, A.C., and Reavill, L.R. (2005). "Management for Engineers Scientists and Technologists". 2nd edition. John Willey & Sons ,England.

[18] IEA, (2008). "Clean Coal Technologies: accelerating commercial and Policy drivers for development".Available :http://www.iea.org/publications/free_new_Desc.asp?PUBS_ID=2011(accessed 2010/02)

American Journal of Engineering Research (AJER)
e-ISSN : 2320-0847 p-ISSN : 2320-0936
Volume-02, Issue-11, pp-25-32
www.ajer.org

Research Paper Open Access

The Effects of Superficial Gas Velocity and Liquid Phase Properties on Gas Holdup and Mass Transfer In An Airlift Reactor

Ali Abdul Rahman–Al Ezzi, Ghazi Faisal Najmuldeen
[a]*Faculty of Chemical & Natural Resources Engineering, Universiti Malaysia Pahang Pahang, Malaysia*
[d]*Department of Chemical Engineering, University of Technology, Baghdad, Iraq*

***Abstract*: -** Mass transfer coefficient (K_{La}) and gas hold up (ε_g) were characterized in 8 liter internal air lift loop reactor (down comer-to-riser cross-sectional area ratio = 0.249) as function of the superficial gas velocity in the riser (V_{gr}). Data were obtained in air–water, air-50% glycerol solution, air-10%acetic acid solution, air-10%NaCL solution and air-2% carboxyl methyl cellulose solution (CMC) systems. Extent different gas velocity ranges 0.01-0.1 m/s and air dispersed into the center of riser by using porous gas distributor. The results showed that(ε_g) and (K_{La}) increased with increasing gas velocity and coalescence inhibition in liquid , in (CMC) solution (K_{La}) is approximately similar to that in water while the increasing in coalescence and liquid viscosity reduces (ε_g) and (K_{La}) .

***Keywords*: -** *Airlift reactor; Mass transfer; Gas hold up; Liquid-phase properties*

I. INTRODUCTION

Airlift reactors (ALRs) are suitable for many different processes. They are mainly used as bioreactors in fermentation processes and in the biotransformation of many substances [1, 2]. In wastewater treatment ALRs are increasingly being developed [3, 4, 5, 6]. Airlift loop reactors find extensive applications in many areas of chemical engineering, especially for homogeneous as well as heterogeneous single and multiphase systems due to their simple construction and operation, directed circulation flow, good mixing and favorable ratio of interfacial area to energy dissipation rate per unit volume, low investment, operational costs and relatively lower power requirements [7]. Based on their configurations, airlift reactors can be classified into two groups: internal-loop (IL- ALR) and external-loop airlift reactors (EL-ALR). An internal-loop airlift reactor contains a vertical baffle or a draft tube by which a loop channel for fluid circulation is formed in the reactor. An external-loop airlift reactor consists of two vertical tubes (a riser and a down comer) which are connected by horizontal connections at the top and bottom. [8]. The intrinsic complicated hydrodynamic structures induced by bubble motion and associated with wake interaction, have been recognized to be the key factors responsible for heat and mass transfers. Because bubble-induced flows in the airlift reactor are identified to be dynamic in nature, the time averaged flow properties cannot well represent the dynamic governing mechanisms of flow structures. IL-ALR and EL-ALR have been widely studied experimentally. Some of these studies focus on liquid velocity circulation, gas and solid phase hold-ups [5] and on mass transfer [9]. To design and operate ALRs with confidence, the knowledge of gas-liquid mass transfer is required to characterize the performance of the ALR. The main parameter used as an indicator for gas-liquid mass transfer rate is the gas-liquid mass transfer coefficient (K_{La}). A large number of researchers [10, 11, 12, 13, 14, 15, 16] have investigated the mass transfer performance in the ALRs together with their hydrodynamic behavior. It was found that the knowledge of hydrodynamic behavior is critical for design purposes because of their strong influence on mass transfer. Although a large number of investigations contributed to the knowledge of the effect of various parameters on hydrodynamic and mass transfer characteristics in ALRs, available information frequently showed wide variations and conflicting claims. The contradiction is regularly attributed to the difference in the reactor geometries, experimental conditions and experimental techniques. However the present knowledge suggests that this contradiction is brought about by some complicated phenomena taking place in ALR, such as the bubble

size distribution, internal liquid circulation, etc [17, 18, 19, 20,21]. The purpose of this study is to clarify experimentally the effects of the gas velocity and liquid phase properties(viscosity and coalescing behavior) on gas hold-up, and mass transfer coefficient(K_{la}) in concentric-tube airlift loop reactor when the ratio of draught tube diameter to column diameter is equal to 0.5 and the air is sparged into the center of the riser.

II. EXPERIMENTAL SECTION

A schematic diagram of the experimental set-up used in this work is shown in Figures 1a and 1b. Aconcentric aplexiglass tube airlift reactor of an inside diameter of 0.9 m and about a total height of 1.30 m with draught tube dimensions inside diameter of 0.045m and a total height 0.90 m was used. The volume of the reactor was 8 liter and Ad /Ar=0.249,where Ad is the downcomer superficial area(m^2)and Ar is the riser superficial area (m^2). The water level in the reactor was 0.75 m. The draught tube was fitted with three support legs at the upper and the lower end of the column so as to locate it in central position at any distance above the base. The column consists of two main sections, namely: the gas inlet section and the liquid recycling testing section. The gas inlet section consists of a gas distributor. At the bottom of this section, two lines are connected together before entering the distributor section each line has a valve to be opened or closed as required. One of these lines is the air inlet flow. Air compressor supplied the line with the desired amount of air needed; for the experiment, the amount of air was measured using a gas meter. The other line is the nitrogen gas inlet flow. The nitrogen was supplied from a cylinder. A gate valve was used in the nitrogen flow, which must be shut off when air was sparged to the column, and must be opened during desorption process. The liquid testing section contains two openings, one for liquid out-flow and the other for liquid in flow. The circulation of liquid in the column was achieved using a dosing pump placed in the recycling line. A ball valve placed in the middle of the recycling line was used to take various samples at various times to measure the concentration of the dissolved oxygen during the operation. The water is fed to the top of the column and discharged from the bottom of the column using adosing pump. Compressed air at (100-150)psig was supplied using a reciprocating compressor.The desired air flow rate was set-up using gate valve and the amount was measured with a gas meter. The dissolved oxygen concentration in the liquid phase was measured using oxygen meter device type a (YSI-5100),which consists of a probe metal electrode. The liquid phase (batch) consists of the following systems (only water, water- glycerol, water-CMC) the chemicals used in the present study were procured from Permula Chemicals SDN.BHD., Malaysia. The gas distributor in Fig 1.c was constructed from a ceramic material and the type is a multi hole tuyere. The distributor has equivalent pore diameter of 0.15 mm and a free section of 80%.

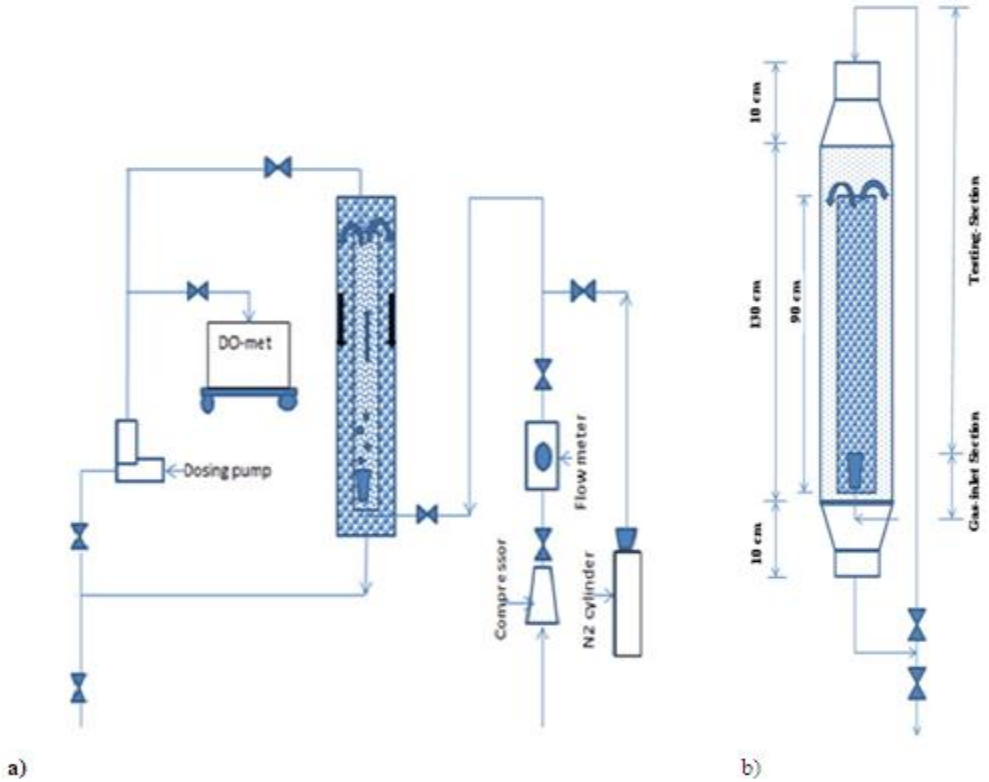

Figure 1: (a) Experimental apparatus; (b) column; (c) gas distributor

TABLE A1-Physical-properties for pure liquids at T = 20 ^{o}C

	ρ (Kg/m^3)10^3	μ (CP)	σ (dyn/cm)	ν_L (cm^2/sec)
Water	0.998	1.002	72.86	1.004
Glycerol	1.261	1.005	6304	0.796
CMC	1.008	K=0.012 ps.s^n n=0.8	73	1.23
Acetic-Acid	1.049	1.219	27.6	1.162
NaCL	2.165	1.295	72	0.598

The solution of CMC (carboxy methyl celluose) shows non newtonian, pseudo plastic behavior, which can be described by the power law of ostwald and deweale:
$t = K \gamma^{n}$
Where:-
K: ostwald factor (consistency index)
n: flow behavior index
γ : shear rate 1/sec
t: shear stress
$\mu_{eff} = \gamma^{n-1}$
where μ_{eff}: effective liquid phase viscosity Pa.s
Y = 5000 Vg [22]
Where Vg: gas velocity m/sec.

TABLE A2- Physical properties for mixtures used with various concentration at T=20^{o}C

	ρ (kg/m^3)10^3	μ (CP)	σ (dyn/cm)	ν_L (cm^2/sec)
Water-Acetic Acid 10 %	1.026	0.916	22.225	0.8932
Water-glycerol 50%	1.126	6.00	64	0.8905
Water-CMC 2%	1.009	K=1.320 Pas^n n=0.5	69	0.09051
Water-NaCL 10%	1.0216	0.9247	48.375	0.9051

III. MEASUREMENTS OF GAS HOLD-UP AND VOLUMETRIC OXYGEN TRANSFER COEFFICIENT

The overall gas hold up ε_g in the reactor was determined by visual measurements of the static liquid height H_L and the aerated height H_F. The gas holdup ε_g was calculated from the following equation.

$$\varepsilon_g = \frac{H_F - H_L}{H_F - (V_i / S_o)} \quad (1)$$

(V_i / S_o) In Eq. (1) is a correction term for the volume of the draft tube [23].

The physical absorption of oxygen in the air by the liquid was employed to determine the mass transfer coefficient. A material balance of oxygen in the liquid gives:-

$$K_{La} = \frac{-2.303(1-\varepsilon_g)}{t}.Log\frac{C_{Sa}-C_i}{C_{Sa}-C_o} \quad (2)$$

Rearranging Eq. (3) gives

$$Log\frac{C_{Sa}-C_i}{C_{Sa}-C_i} = \frac{K_{La}}{2.303(1-\varepsilon_g)}.t \quad (3)$$

Plotting the left hand side of Eq. (3) with(t),the avarge slope of the plot will give the term $K_{La}/2.303(1-\varepsilon_g)$ The values of (ε_g) were determine as mentioned in (1), then (k_{La}) can be calculated.

GASHOLD UP AND MASS TRANSFER COEFFICIENT RESULTS .IV

Fig 2 shows the influence of gas velocity for different liquid phase systems (water, water-glycerol, water-CMC) on gas hold-up when the down comer-to-riser cross-sectional area ratio = 0.249. The gas hold-up increases with increasing gas through put (gas velocity), but interact mutually, depending on liquid phase properties. Many Literatures revealed that increasing superficial gas velocity increased the gas holdup [24,25,19,21]. The viscous solutions of glycerol and CMC show only slightly higher gas hold-ups than water. In spite of similar a flow property of the CMC and glycerol solutions, gas hold-up in the CMC solution is somewhat larger, due to accompanying coalescence inhibiting. In general, low viscosity liquid exhibit bubble disintegration behavior. whereas, a trend towards bubble coalescing behavior has been observed with increasing the viscosity of the liquid media, as shown by many investigators [26, 27].

Fig 3 shows the effect of using different liquid phase (water, water-acetic acid, water-NaCl), on gas hold up. Low electrolyte concentrations have no noticeable effect on the surface tension of the solution. However the ionic forces in the liquid bulk reduce the bubble rise velocity and the bubble coalescence. As a result, the gas holds- up increase. For high electrolyte concentration, the interfacial tension increases, resulting in increased bubble size and reduce gas holdup.

Fig 4 shows the influence of gas velocity for different liquid phase systems (water, water-glycerol, water-CMC) on (K_{La}) when the down comer-to-riser cross-sectional area ratio = 0.249. The volumetric-mass transfer coefficient (K_{La}) is a function of gas hold-up and mean bubble size. The K_{la} values for water increases with increasing gas velocity because of the increase of the axial dispersion coefficient D_L. The mass transfer coefficient in (water-glycerol) system reaches its maximum value at gas velocity of about 0.02 m/sec; owing to the strong coalescence promoting properties of highly viscous liquid, large bubbles are formed already at very small gas throughputs. The reduction of bubble size with increasing gas velocity is a characteristic feature of pseudo-plastic (water-CMC) system [28], therefore the mass transfer coefficient are smaller than that in water, and larger than in (water-glycerol) system.

Fig 5 shows the effect of using different liquid phase (water, water-acetic acid, water-NaCl), on (K_{La}) when the down comer-to-riser cross-sectional area ratio = 0.249. For electrolytes as mentioned before, the ionic forces in the liquid bulk reduce the bubble rise velocity and the bubbles coalescence, so that the mass transfer coefficient is increased.

V. CONCLUSIONS

From the present study the following conclusions were made:

1. The gas hold-up and mass transfer coefficient in air lift loop reactor, where gas is dispersed into the center of base of inner draught tube using a porous multi hole distributor and the reactor volume equal to 8 liters increase with increasing gas velocity, for *Vg* equal or less than 0.1m/sec, only for the case of (water, glycerol) system, the mass transfer coefficient reaches its maximum at gas velocity of 0.02 m/sec. This observation is in agreement with many experimental works [29, 25, 30, 17, 15, 21].
2. Gas hold-up and mass transfer coefficient decrease with increasing liquid phase viscosity and liquid surface tension.

VI. NOMENCLATURE

a	Specific gas-liquid interfacial area based on aerated liquid volume m^{-1}
C_i	Concentration of dissolved oxygen at any time p.p.m
C_0	Initial Concentration of dissolved oxygen p.p.m
C_{Sa}	Saturated concentration of dissolved oxygen p.p.m
D_C	Column diameter.
D_i	Diffusivity of oxygen in solution m^2/sec
D_L	Axial dispersion coefficient (liquid) m^2/sec

g	Acceleration of gravity m/sec^2
H_L	Static slurry height (m)
H_F	Level of aerated slurry (m)
K_{La}	Overall mass transfer coefficient, based on aerated slurry volume. (Sec^{-1})
t	Time (min)
V_g	Gas velocity (m/sec)

Greek letters

ε_g	Gas hold up
ρ_L	Liquid phase density kg/m^3
μ_L	Liquid phase viscosity (C_p)
v_L	Kinematic viscosity of liquid phase (cm^2/sec)
σ_L	Liquid phase surface tension dyn/cm

Subscripts

G	gas
L	liquid

VII. REFERENCES

[1] A Sánchez, M. Cerón, F. García, E. Molina, and Y. Chisti, Growth and biochemical characterization of microalgal biomass produced in bubble column and airlift photo bioreactors: Studies in fed-batch culture, *Enzyme Microbial Technol*, 31, 2002, 1015–1023.

[2] G Acién, M. Sevilla, A. Sánchez, E. Molina, and Y. Chisti, Airlift-driven external-loop tubular photo bioreactors for outdoor production of microalgae: assessment of design and performance, *Chemical Engineering Science*, 56, 2001, 2721–2732.

[3] J Frijters, H. Eikelboom, A. Mulder, and R. Mulder, Treatment of municipal wastewater in a CIRCOX® airlift reactor with integrated denitrification, *Water Science and Technology*, 36 (1),1997, 173–181.

[4] J Heijnen, J. Hols, M.Van der Lans, M.Van Leeuwen, A. Mulder, and R. Weltevrede, A simple hydrodynamic model for the liquid circulation velocity in a full-scale two-and three-phase internal airlift reactor operating in the gas recirculation regime, *Chemical Engineering Science*, 52 (15), 1997, 2527–2540.

[5] J Van, M.Van der Lans, M. Van Loosdrecht, and J. Heijnen, The biofilm airlift suspension extension reactor-II: three-phase hydrodynamics, *Chemical Engineering Science*, 55 (3), 2000, 699–711.

[6] J Beun, M. Van Loosdrecht, and J. Heijnen, Aerobic granulation in a sequencing batch airlift reactor, *Water Research*, 36 (3), 2002,702–712.

[7] C Merchuk, and H. Siegel, *Chemical Technology and Biotechnology*. 41, (2), 1988, 105–120.

[8] M Chisti, *Airlift Bioreactors*, Elsevier, New York, 1989.

[9] C Nicollela, M.van Loodrecht, and J. Heijnen, Identification of mass transfer parameters in three-phase biofilm reactors, *Chemical Engineering Science*, 541,1999, 3143–3152.

[10] K Koide, S. Hiroyuki, and I. Shinji, Gas holdup and volumetric liquid phase mass transfer coefficient in bubble column with draught tube and with gas dispersion into annulus, *Journal of Chemical Engineering of Japan*, 16(5), 1983a, 407–413.

[11] Y Chisti, and M. Moo-Young, Hydrodynamics and oxygen transfer in pneumatic devices, *Biotechnology & Bioengineering*, 31, 1988, 487–494.

[12] H Choi, and W. Lee, Circulation liquid velocity, gas holdup and volumetric oxygen transfer coefficient in external-loop airlift reactors, *Journal of Chemical Technology and Biotechnology*, 56,1993,51–58.

[13] C Merchuk, N. Ladwa, A.Cameron, M.Bulmer, and a Pickett, Concentric-Tube Airlift Reactors: Effects of Geometrical Design on Performance, *AIChE Journal*. 40(7), 1994, 1105–1117.

[14] K Shimizu, S. Takada, T.Takahashi, and Y. Kawase, Phenomenological simulation model for gas holdups and volumetric mass transfer coefficients in external-loop airlift reactors, *Chemical Engineering Journal*, 84,2001,599–603.

[15] T Zhang, B. Zhao, and J. Wang, Mathematical models for macro-scale mass transfer in airlift loop reactors, *Chemical Engineering Journal*, 119, 2006, 19–26.

[16] T Zhang, T.Wang, and J. Wang, Analysis and measurement of mass transfer in airlift loop reactors, *Chinese Journal of Chemical Engineering*, 14 (5),2006, 604–610.

[17] T Samuel, x. Arnaud, and L. Alain, , Global modeling of a gas–liquid–solid airlift reactor, *Chemical Engineering Science*, 60, 2005,5991–6003.

[18] S Sarkar, and C. Kaustubha, Hydrodynamic modeling of a novel multi-stage gas–liquid external loop airlift reactor, *Chemical Engineering Journal*, 145, 200869–77.
[19] W Wei, L. Malin, and W. Zhanwen, Bubble circulation regimes in a multi-stage internal-loop airlift reactor, *Chemical Engineering Journal*, 142, 2008, 301–308.
[20] P Giovannettonea, E. Tsaib, and S. Gulliver, Gas void ratio and bubble diameter inside a deep airlift reactor, *Chemical Engineering Journal*, 149, 2009, 301–310.
[21] D Zhonghuo, T. Wang, N. Zhang, and Z. Wang, Gas holdup, bubble behavior and mass transfer in a 5m high internal-loop airlift reactor with non -Newtonian fluid, *Chemical Engineering Journal*, 160, 2010, 729–737.
[22] M Nishikawa, H. Kato, and K. Hashimoto, *Ind. Eng. Chem. Process Des. Dev*, 16, 1977, 133–137.
[23] K Koide, K. Katsumi, I. Shinji, I. Yutaka, and H. Kazuyoshi, Gas holdup and volumetric liquid-phase mass transfer coefficient in bubble column with draught tube and with gas dispersion into tube, *Journal of Chemical Engineering of Japan*, 16(5), 1983b, 413–419.
[24] H Vial, S. Poncin, G. Wild, and N. Midoux, Experimental and theoretical analysis of the hydrodynamics in the riser of an external loop airlift reactor, *Chemical Engineering Science*, 57, 2002, 4745–4762.
[25] M Peter, A. Argyrios, Y. JunTang, and Y.Qin, Influence of the baffle clearance design on hydrodynamics of a two riser rectangular airlift reactor with inverse internal loop and expanded gas–liquid separator, *Chemical Engineering Journal*, 121, 2006, 17–26.
[26] H Calderbank, *Chemical Engineer*, 45, 1976, 225.
[27] L Hanning, and A. Prakash, Heat transfer and hydrodynamics in a three-phase slurry bubble column, *Industrial & engineering chemistry research*, 36**(**11),1997, 4688–4694.
[28] W Haque, P. Nigam, K. Viswanathan, and B. Joshi,.Studies on Gas Hold-up and Bubble Parameter in Bubble Columns with Pseuodoplastic, Carboxy methel Cellulose, *Industrial & Engineering Chemistry Research*, 26(1):, 1987, 86–91 .
[29] E Carvalho, E. Camarasa, C. Meleiro, R. Maciel, A. Domingues, h. Vial, G.Wild, S.Poncin, N. Midoux, and J. Bouillard, Development of a hydrodynamic model for air-lift reactors, *Brazilian Journal of Chemical Engineering*, **17** , 2000, 4–7.
[30] M Blažej, J. Annus, and J. Markoš, Comparison of gassing -out and pressure-step dynamic methods for k_{la} measurement in an Airlift reactor with internal loop, *Chemical Engineering Research And Design*, 82, 2004,1375–1382.

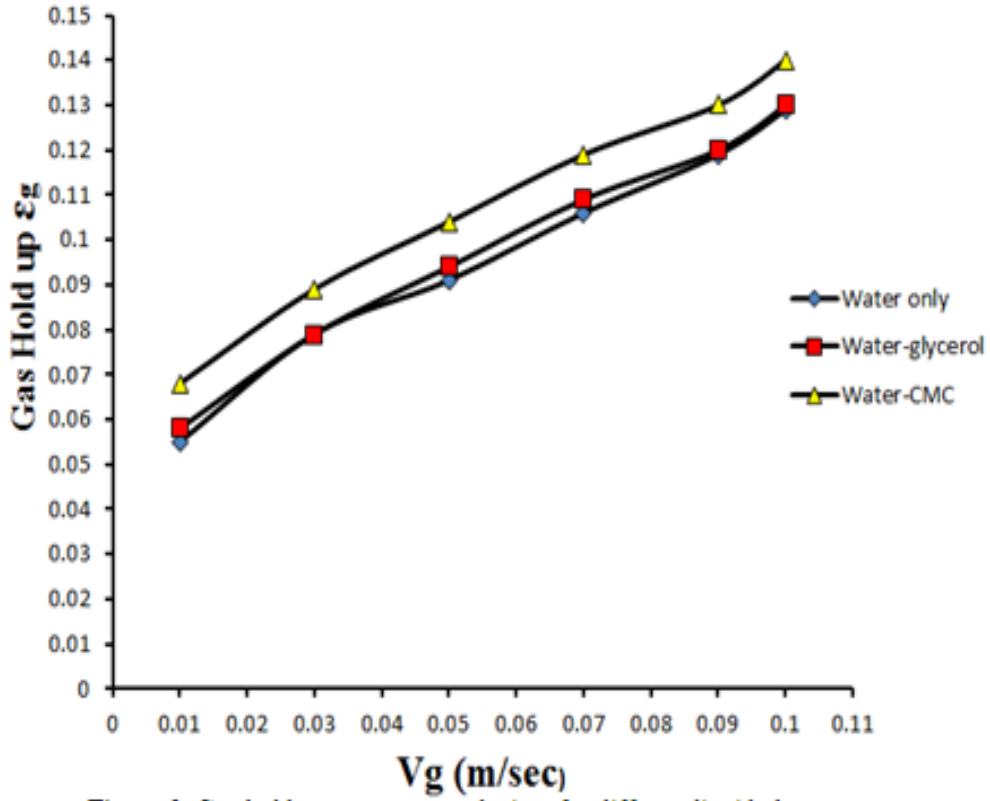

Figure 2: Gas hold up versus gas velocity for different liquid phase system.

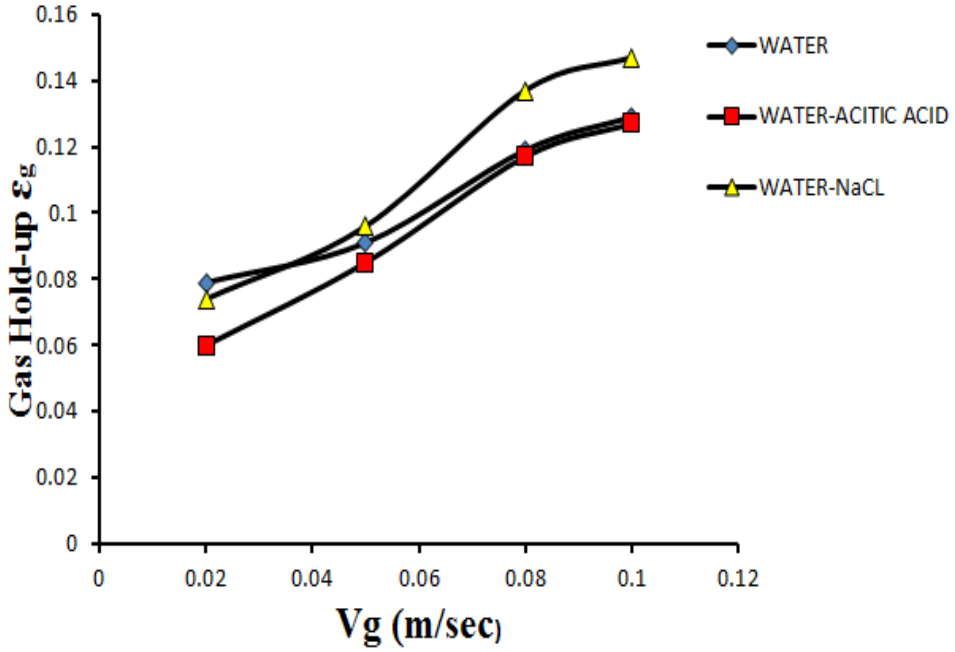

Figure 3: Gas hold up versus gas velocity for different liquid phase system.

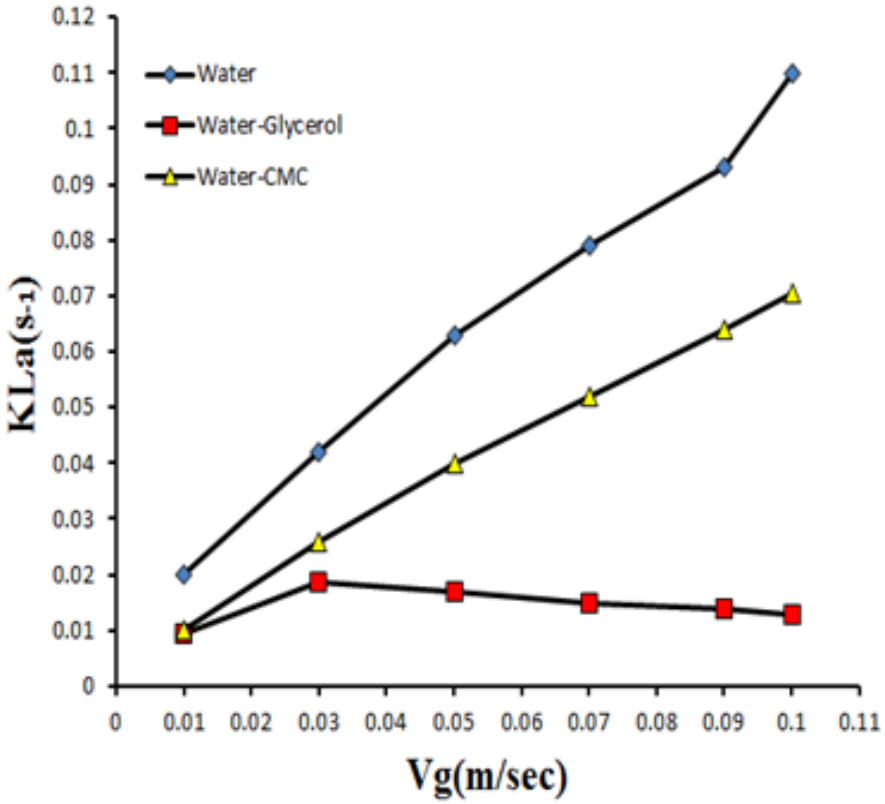

Figure 4: Mass transfer coefficient versus gas velocity for different liquid phase system.

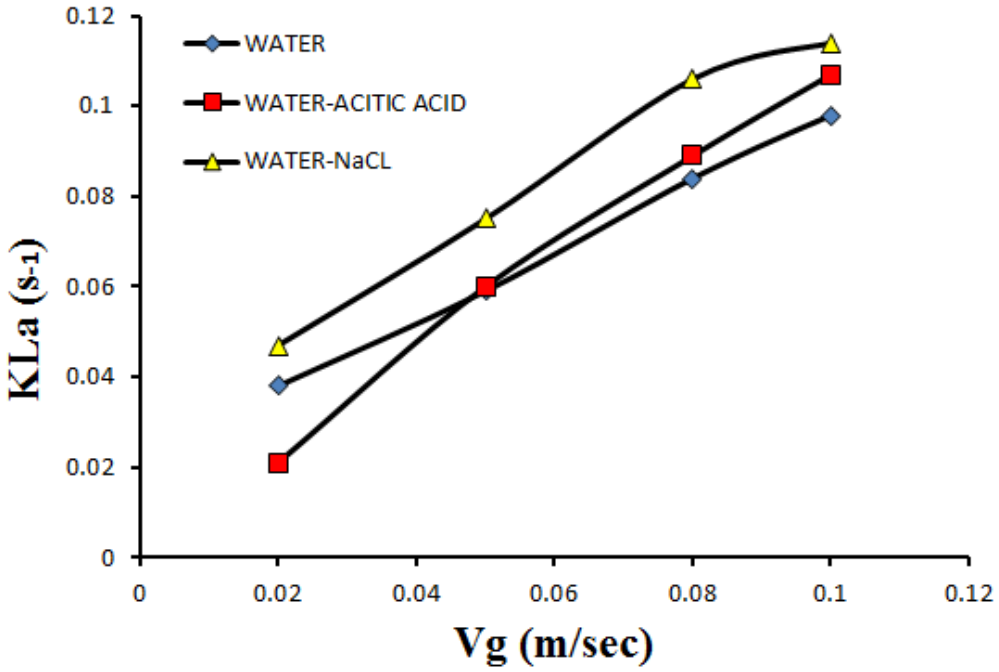

Figure 5: Mass transfer coefficient versus gas velocity for different liquid phase system.

American Journal of Engineering Research (AJER)
e-ISSN : 2320-0847 p-ISSN : 2320-0936
Volume-02, Issue-11, pp-33-42
www.ajer.org

Research Paper Open Access

Poiseuille Flow in a Vertical Tubular and Porous Membrane for Solar Air Gap Membrane Desalination of Brackish Water.

M. Sene, Y. Mandiang, D. Azilinon
Laboratoire d'Energétique Appliquée (LEA), Ecole Supérieure Polytechnique (ESP) de Dakar, BP 5085
Université Cheikh Anta Diop (UCAD) de Dakar, SENEGAL

Abstract: - Membrane distillation is an emerging technology for desalination that differs from other membrane technologies and in which the driving force for desalination is the difference in vapor pressure of water across the membrane, rather than total pressure. The membrane is hydrophobic material that allows water vapor only to pass across. The vapor pressure gradient is created by heating the source water, thereby elevating its vapor pressure. The major energy requirement is for low-grade solar energy.

The technique used to desalinate water is the Air Gap Membrane Distillation (AGMD), which is more compact, less energy-consuming and required lower temperature (between 40 °C to 80 °C) than conventional distillation processes. In this paper, the work aims to establish a mathematical model of the Navier-Stockes equation applied to a porous membrane of polytetrafluoroethylene. PTFE nanofiber membrane could be used in membrane distillation to produce drinking water from a saline water of NaCl.

Keywords: - *tubular membrane, distillation, brackish water, Poiseuille flow, porous, Darcy's law, Navier-Stockes, desalination*

I. INTRODUCTION

The population of the world is increasing, and fresh water is the primary requirement for life in the universe. However, while water covers about three-quarters of the earth's surface, only 3 % is fresh water from various sources, and not all of this limited quantity is suitable for drinking.

Thus, water treatment is usually needed, and desalination is the most efficient method for providing fresh water from brackish and/or seawater. However, desalination is energy- intensive process. And because of scarce availability of wood and oil and high capital and operational cost, the desalination based on renewable, safe, free and clean solar energy is the promise for a cost-effective solution.

The steady flow in a long channel or in a long tube of circular section under the action the pressure gradient imposed at the two ends, usually known as Poiseuille flow or Hagen Poiseuille flow, is a typical textbook example in fluid dynamics. In the last few years, numerous authors [1-9] have analyzed this problem with the channel geometry when the pressure difference is replaced by a constant external field.
The objective of this work is to analyze theoretically the effect of membrane pore size and porosity.

II. MEMBRANE DISTILLATION CONFIGURATIONS

Membrane distillation (MD) is an emerging technology for desalination. Membrane distillation differs from other membrane technologies, the fact that the driving force for desalination is the difference in vapor pressure of water across the membrane, rather than total pressure. The membranes for MD are hydrophobic, which allows water vapor (but not liquid water) to pass. The vapor pressure gradient is created by heating the source water, thereby elevating its vapor pressure. The major energy requirement is for low-grade thermal energy.

A variety of methods have been employed to impose the vapor pressure difference across the hydrophobic membranes [1]. In every case, the raw water to be desalted directly contacts the hot side of the membrane. The four classes of membrane distillation are therefore (Fig. 1) [2]:

• Direct-Contact Membrane Distillation (DCMD). The cool condensing solution directly contacts the membrane and flows in a countercurrent system to the raw water. This is the simplest configuration. It is well suited for applications such as desalination and concentration of aqueous solutions.
• Air-Gap Membrane Distillation (AGMD) in which an air layer is interposed between the membrane and the condensation surface.
• Sweep-Gas Membrane Distillation (SGMD). A sweep gas pulls the water vapor and/or volatilizes from the system. Useful when volatile salts can be removed from an aqueous solution.
• Vacuum Membrane Distillation (VMD). A vacuum is used to pull the water vapor out of the system. Useful when volatile salts can be removed from an aqueous solution.
Membranes with lower thermal conductivities and higher porosities improve the performance of single-membrane designs while thinner membranes improve the performance of air-gap designs. This device can be used with a solar heating system which already uses concentrated salt solutions.

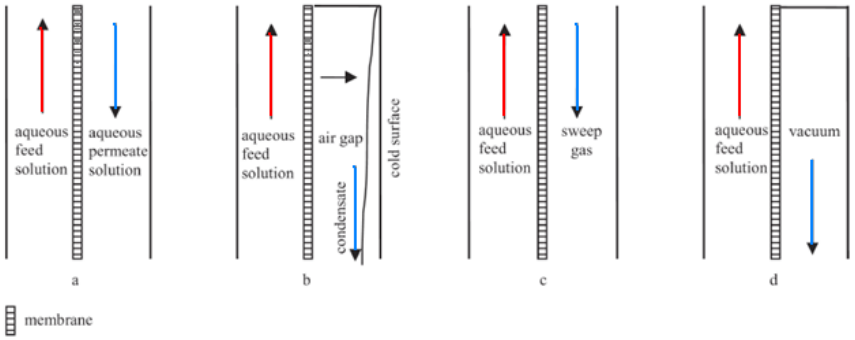

Figure 1 - Membrane distillation configurations (a) DCMD, (b) AGMD, (c) SGMG, and (d) VMD

The advantages of membrane distillation are:
• It produces high-quality distillate.
• Water can be distilled at relatively low temperatures (40 °C to 90 °C).
• Low-grade heat (solar, industrial waste heat or desalination waste heat) may be used.
• The water does not require extensive pretreatment as in pressure-based membrane treatment.

III. PHENOMENA DESCRIPTION OF AGMD

Out of all the different MD processes, AGMD was selected for modeling because the model was more general than for some other MD processes, and is therefore easier to modify for modeling other types of MD processes. A schematic of an air-gap membrane distillation unit is shown in figure 2. The brackish or saline water to be distilled is heated and passed by one side of the membrane. Water vapor diffuses across the membrane and air gap to the other side, where it condenses on the cooler surface. The right side of the air gap is kept cool by a flow of cooling water. The overall process is driven by a gradient in water vapor pressure, rather than a difference in total pressure. Thermal energy is required to elevate the vapor pressure of water in the hot stream. Figure 3 illustrates the scheme of a cylindered membrane PTFE.

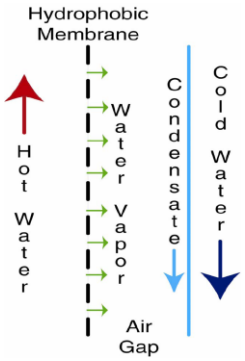

Figure 2 - Schematic of air-gap membrane distillation.

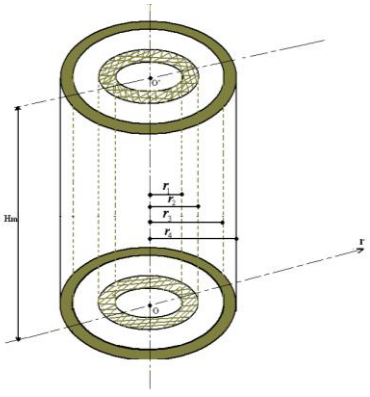

Figure 3 - Vertical and cylindered membrane PTFE

The membrane itself is hydrophobic with pore sizes r_p, usually in the range of 0.05 μm to 0.2 μm. Lawson and Lloyd (1997) [3], for example, used polypropylene membranes with maximum pore sizes r_p ranging from 0.3 μm to 1.1 μm. Water is kept from penetrating the pores by surface tension and capillary

pressure. Table 1 summarizes surface energy of some membrane materials and table 2 recapitulates characteristics of commercial materials commonly used in membrane distillation.

Table 1 - Experimental surface energy of some material membranes used in MD [4]

Membrane materials	Surface tension γ_{LV} (N/m)
PTFE	0.0191
PP	0.0300
PVDF	0.0303
PE	0.0332

Table 2- Characteristics commercial materials commonly used in membrane distillation **[5]**

Membrane Trade Name	Manufacturer	Material	Thickness (µm)	pore size y (µm)	Conductivities k ($W^{-1}K^{-1}$)	Porosity ε (%)
TF200	Gelman	PTFE	55	0.20	0.0382	75-85
TF450	Gelman	PTFE/PP	178	0.45		80
TF1000	Sartorious	PTFE		1.00		75-80
GVHP	Millipore	PVDF	118	0.22	0.041	70
HVHP	Millipore	PVDF	140	0.45	0.040	75
S6/MD020CP2N	Akzo Nobel Microdyn	PP	450	0.2		70

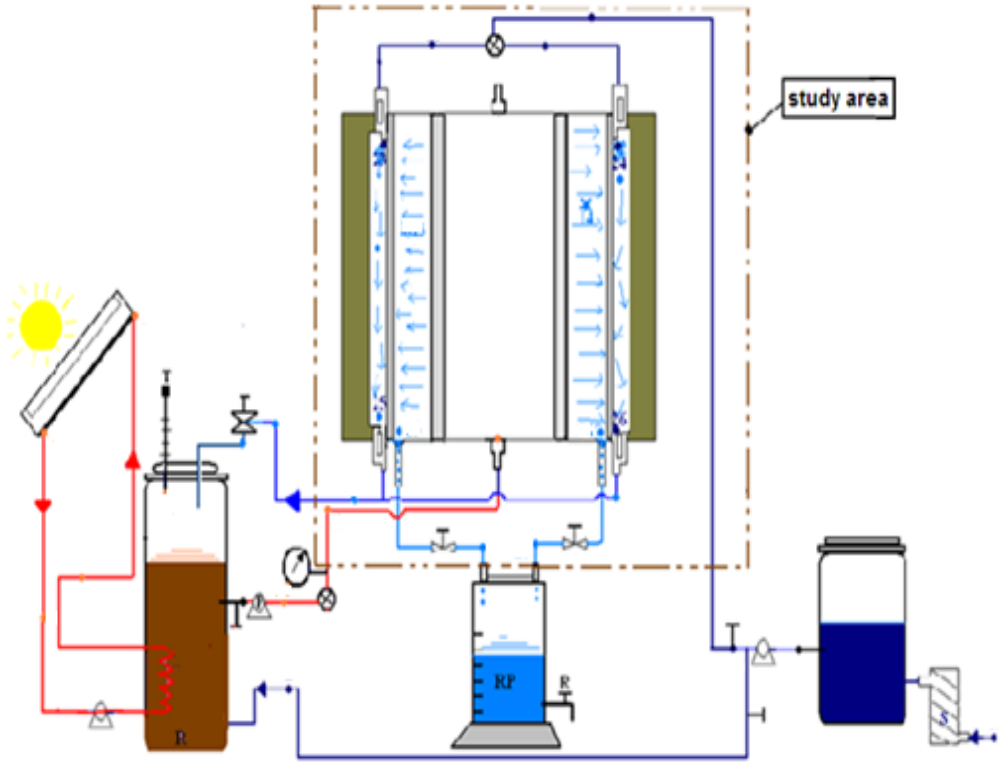

Figure 4 - Scheme of an operating modular solar system of the membrane distillation

To study the performance of the modular solar thermal desalination system, analytical calculations have been made as illustrated (Fig.4). The salt-water supply is heated from a set (solar collector (7-8), conventional heat exchanger (5-6)). In the tubular porous membrane, the temperature of the brine is between 30 °C and 90 °C [**4**]. The wall of the tube is hydrophobic allowing only radial diffusion of the vapor. Steam generated through the membrane and the air gap condenses on the inner wall of the second pipe to be collected. The energy balance equations will be presented in next sections.

IV. THE POISEUILLE MODEL FLOW: THEORETICAL APPROACH

The Poiseuille flow model is based on viscous flow through a cylindrical capillary wall (Fig.5). When the capillary diameter is large compared with mean free path lengths and a pure substance is present in the capillary we have the classical Poiseuille's problem.

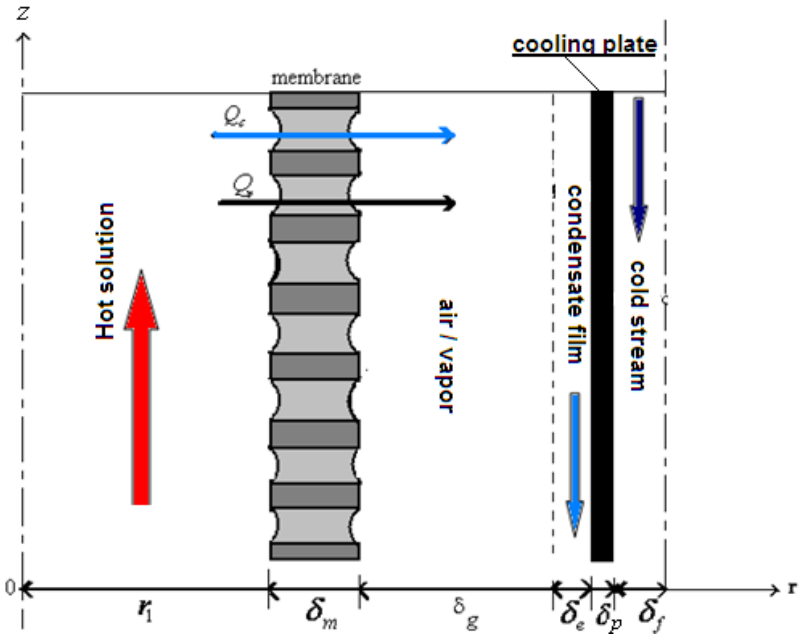

Figure 5- AGMD cell configurations

4.1. Mathematical and physical modeling at steady state

A steady state, laminar, incompressible, viscous and isothermal flow in a cylindrical tube with a permeable wall is considered. The velocity profile in laminar flow in a tubular membrane is plotted as illustrated (Fig.6).

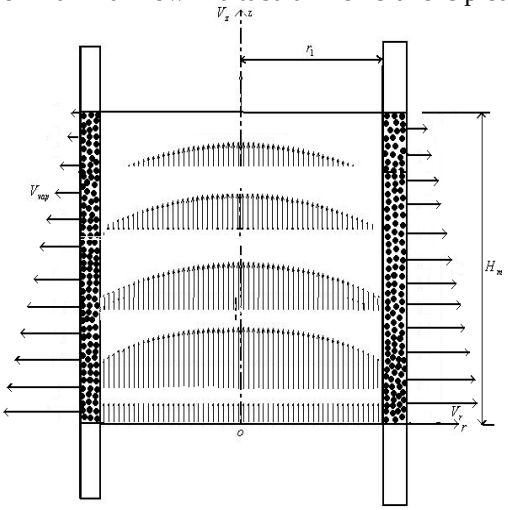

Figure 6 - Plot of velocity profile for laminar flow in a tubular membrane

For micro porous membrane, the viscous flow equation may be written as:

$$J_v = \dot{m}_p n_p \tag{1}$$

where

$$n_P = \frac{1}{\pi}\frac{\varepsilon}{r_p^2} \tag{2}$$

assuming the pore is a uniform circular tube.

Balancing the viscous shear forces acting over the surface, the velocity distribution over the cross section of the pore is given by:

$$V_{(r)} = \frac{r^2 - r_p^2}{4\mu}\frac{\partial p}{\partial r} \tag{3}$$

The mass flow rate through the pore can be obtained by integrating equation (3) over the cross section of the pore size.

$$\dot{m}_p = \frac{\pi}{8}\frac{r_p^4}{\delta_m}\frac{\rho_v}{\mu_v} \tag{4}$$

Substituting equation (4) and (2) into (1) we have

$$J_v = \frac{1}{8}\frac{r_p^2\varepsilon}{\delta_m\tau}\frac{\bar{p}}{R\bar{T}}\frac{M_v}{\mu_v}\Delta p_v \tag{5}$$

where T_{hm} and T_{cm} are the temperatures of the hot and cold sides of the membrane.
And in general, equation (5) may be written as:

$$J_v = K_p.p_v \tag{6}$$

where K_p, the permeability of the membrane due to Poiseuille flow, is expressed by

$$K_p = \frac{1}{8}\frac{r_p^2\varepsilon}{\delta_m\tau}\frac{\bar{p}}{R\bar{T}}\frac{M_v}{\mu_v} \tag{7}$$

The vapor pressure (p_v) were calculated using the Antoine equation [1] as

$$ln\, p_v = 23.328 - \frac{3841}{T - 45} \tag{8}$$

The effect of the presence of salt in the solution on the vapor pressure at the hot surface onto the membrane side has been accounted by using the empirical correlation for the boiling point elevation. Raoul's Law can be used to express the vapor pressure at the hot side of the membrane (p_{hm}) as

$$p_{hm} = (1 - C_{s,hm})p_v(T_{hm}) \tag{9}$$

4.2. Velocity problem

Consideration is given to a constant property fluid flowing in a straight tube of circular cross section, at the walls of which there is a uniform mass transfer.
The mass conservation and momentum equations, Navier-Stokes equations expressed in cylindered coordinates with axisymetric assumption are:

$$\rho\left(V_r\frac{\partial V_r}{\partial r} + V_z\frac{\partial V_r}{\partial z}\right) = -\frac{\partial P}{\partial r} + \mu\left[\frac{\partial}{\partial r}\left(\frac{1}{r}\frac{\partial}{\partial r}(rV_r)\right) + \frac{\partial^2 V_r}{\partial z^2}\right] \tag{10}$$

$$\rho\left(V_z\frac{\partial V_z}{\partial z} + V_r\frac{\partial V_z}{\partial \bar{r}}\right) = -\frac{\partial P}{\partial z} - \rho g + \mu\left[\frac{1}{r}\frac{\partial}{\partial r}(rV_z) + \frac{\partial^2 V_z}{\partial z^2}\right] \tag{11}$$

where V_r and V_z are the velocity components.
At the permeable, porous, homogeneous and isotropic wall, the wall suction velocity is given by Darcy's law as mentioned in the previous section. Considering the boundary conditions, at the inlet developed laminar profile is considered, ie, Poiseuille flow which leads to:

$$V_z = 2V_e\left[1 - \left(\frac{r}{r_1}\right)^2\right]\exp\left[-4\sqrt{\frac{J_v r_1}{\mu}}\left(\frac{z}{r_1}\right)\right] \tag{12}$$

$$V_r = 4V_e\sqrt{\frac{J_v r_1}{\mu}}\left[\left(\frac{r}{r_1}\right)^2 - \frac{1}{2}\left(\frac{r}{r_1}\right)^4\right]\exp\left[-4\sqrt{\frac{J_v r_1}{\mu}}\left(\frac{z}{r_1}\right)\right] \tag{13}$$

In the entrance region the flow is not developed, and the following equation has been recommended for turbulent flow in tubes. The solution depends on both the Reynolds axial and filtration number.

$$N_u = 0.097 R_e^{0.73} . P_r^{0.13} \quad \text{laminar flow} \qquad (14)$$

$$N_u = 0.036 R_e^{0.96} . P_r^{\frac{1}{3}} \left(\frac{D}{L}\right)^{0.055} \quad \text{for} \quad 10 \le \frac{L}{D} \le 400 \quad \text{turbulent flow} \qquad (15)$$

where D is the equivalent diameter of the flow channel and L is the tube length

$$Pr = \frac{\mu C_p}{\lambda} \quad \text{Prandtl number}$$

$$Re_{r1} = \frac{\rho V_e r_1}{\mu} \quad \text{Reynolds number}$$

V. RESULTS AND DISCUSSIONS

Simulations have been carried out for following data:

- the analysis is made for the inlet temperature of the feed solution (T_{hi}) in the range (40 to 80) °C computed at 5 °C increments;
- Steady state: feed solution inlet velocities (V_e) of 0.1 m.s^{-1} to 0.8 m.s^{-1} ;
- cooling solution inlet temperatures (Tci) of 5 °C to 20 °C at 5 °C increments;
- air/vapor gap widths (δg) of 1 mm to 5 mm at 1 mm increments;
-membrane thermal conductivities (k_m) of (0.05 to 0.3) Wm^{-1}.K^{-1} at 0.05 Wm^{-1}.K^{-1} increments;
- membrane porosities (ε = 0.70 to 0.80);
-membrane tortuosity (τ = 1.7).

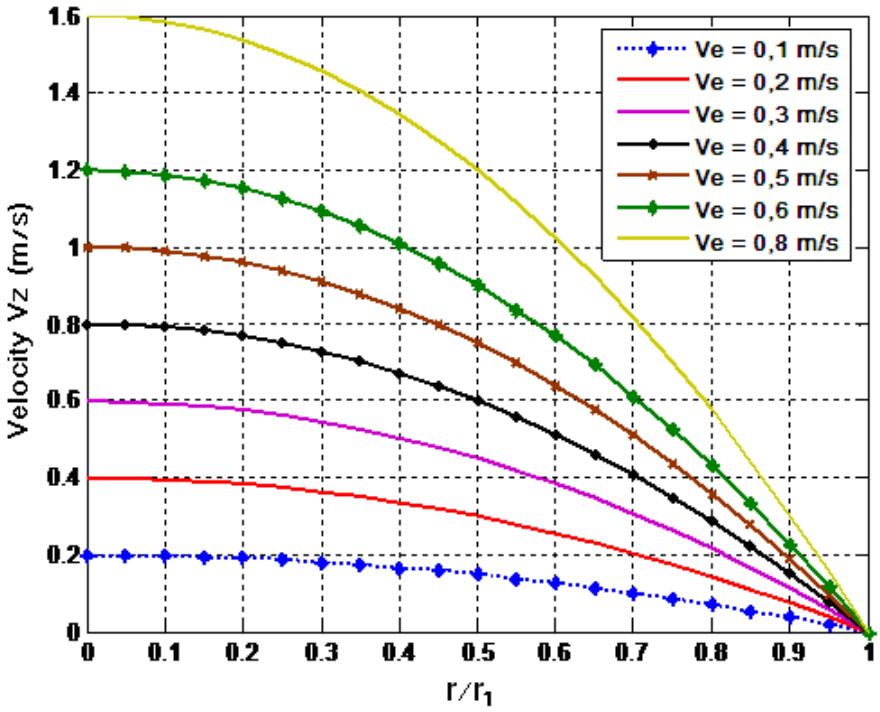

Figure 7 - Plot of velocity along the membrane length

It is observed (Fig.7) the boundary layer grows with a faster rate near-by the entrance of the channels. This implies that the heat transfer coefficient, and thus the local permeate flux, are (as expected) higher near-by the hot channel entrance.

The velocity increases along the radius of the membrane with the input speed of the hot solutions (0.1 m/s to 0.8 m/s). We observe that (Fig.8) it is higher in the wall of the membrane, which allows a relatively large water production. This effect can reduce the resistance time of the steam within the membrane. The velocity

affects the process by reducing the boundary layer thicknesses of the temperature and concentration of the hot solution and the temperature of the cold solution.

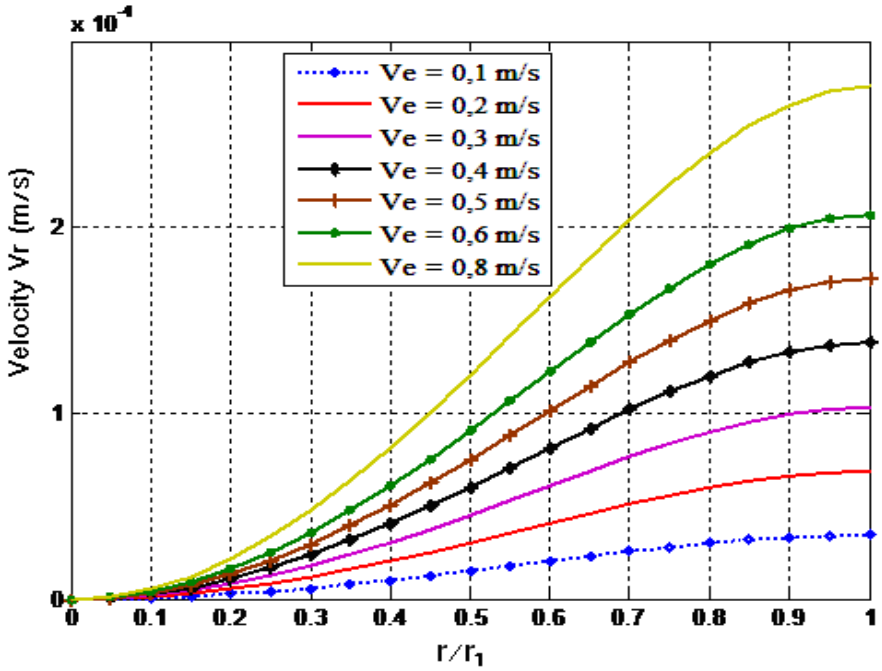

Figure 8 - Plot of velocity through the radial axis

The feed solution temperature has a major effect on the permeate flux. This increase is larger at higher temperatures because the vapor pressure increases exponentially with increasing temperature.
Figure 9 shows the permeate flux (J) as a function of both the hot and the cold solutions inlet velocities. The improvement is because higher velocities reduce the z-direction temperature drop in the solutions, increasing the driving temperature difference, and that has a higher effect on the vapor pressure in the hot solution.

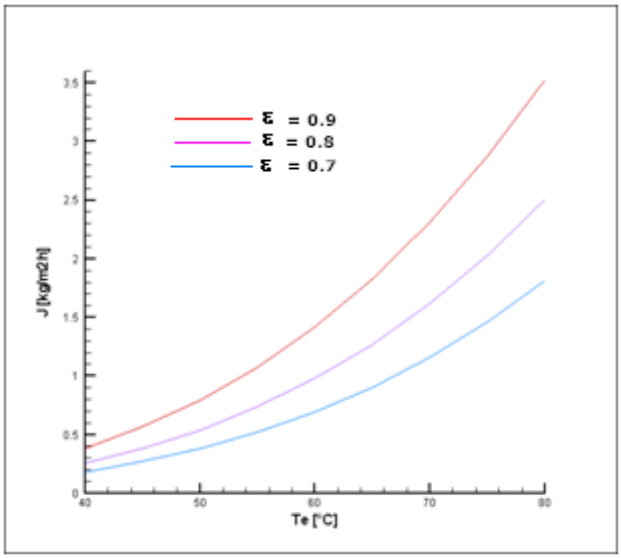

Figure 9 - Effect of the average temperature of feed and permeate side solution of the commercial. PTFE membranes [T_{ci} = 20 °C, u_{hi} = 0.1 m.s^{-1} , ε = 0.7 to 0.9].

Figure 10 shows that the permeate flux from the interior of the membrane increases as a function of porosity. Depending on the value of dimensionless radius it decreases slightly, indicating that the appearance of the membrane permeable and selective.

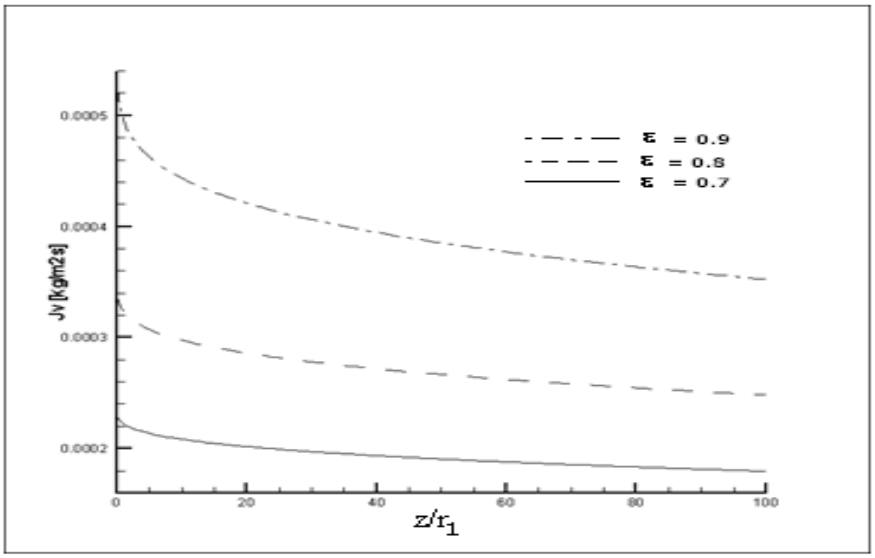

Figure 10 - The effect of membrane radius on the permeate flux.

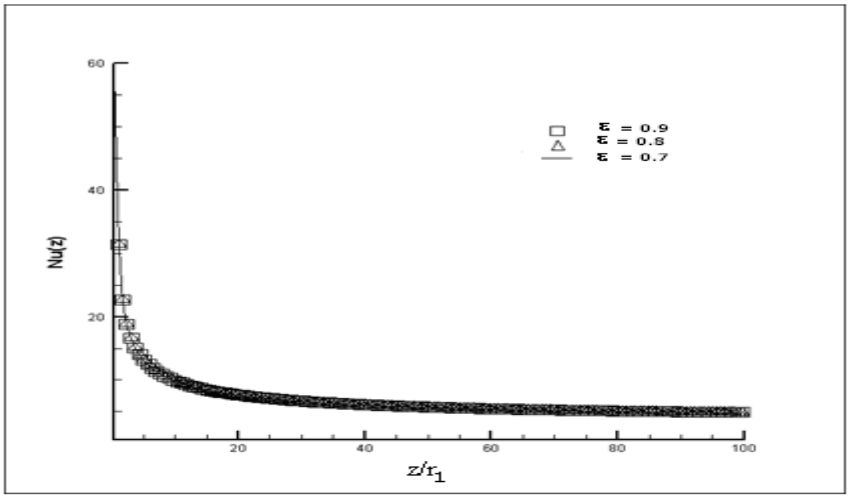

Figure 11 - The effect of distance on the Nusselt number.

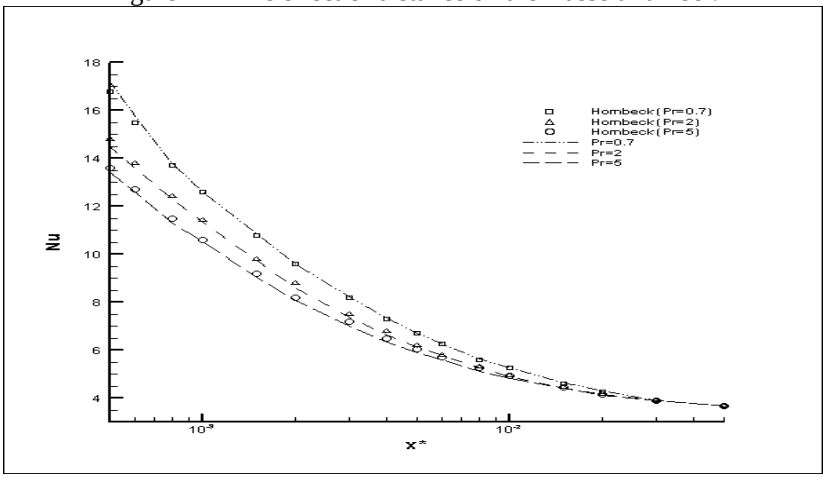

Figure 12 - Hombeck solution in comparison to our model

To validate our model, we compared it with the experimental work of Hombeck (Fig.12). The Nusselt number characterizes energy heat transfer between a solid surface and a fluid in motion. The Prandlt number compares the speed of the thermal and hydrodynamic phenomena in a fluid. A high Prandlt (Pr = 5) indicates that the temperature profile.

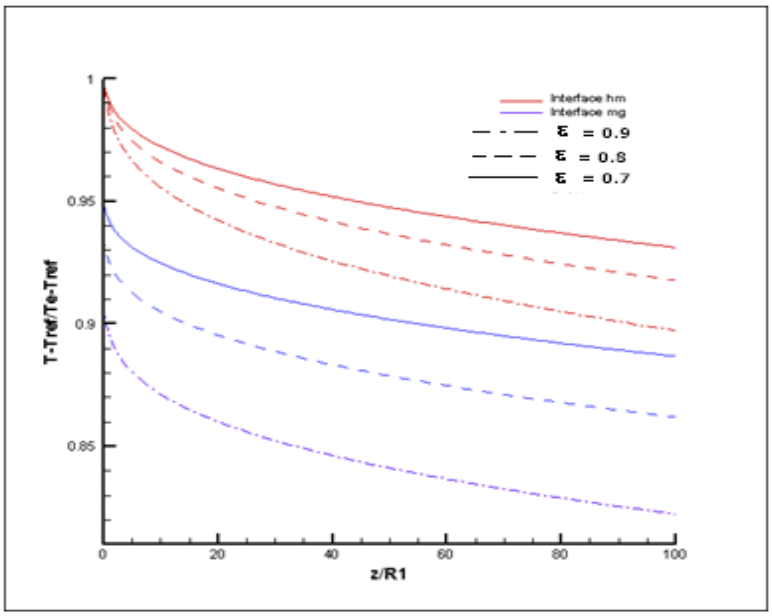

Figure 13 - Effect of polarization of temperature

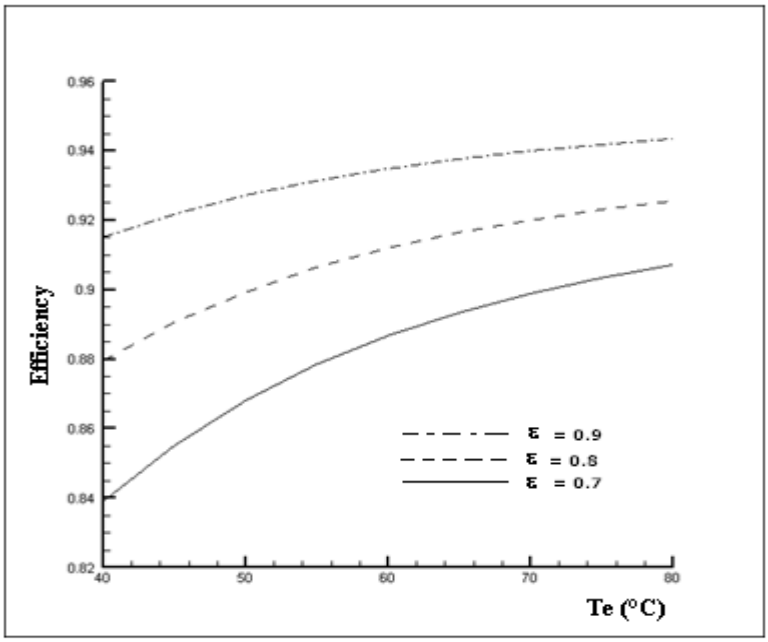

Figure 14 - Efficiency of the AGMD model

The performance of the proposed model is the order of 0.94 % for different porosities (0.7, 0.8 and 0.9) on this curve, it increases with the operating temperature of the system that is to say from 40 °C to 80 °C.

VI. CONCLUSIONS

This paper describes Poiseuille flow model to simulate the permeate flux of water in cross flow filtration tubular membrane. The flow in the hot fluid region and in the porous medium is described by the Navier-Stokes equations and Darcy's law. First the model was carefully validated by Hombeck experimental model.

The effectiveness and efficiency of the model have been assessed, however, understanding of the physical phenomena and the behavior of the model should require the pursuit and deepening of this work.
But we think that Poiseuille flow should not be neglected in the process of desalination since it intervenes largely depending on the type of membrane used.

VII. LIST OF SYMBOLS

C_s mole fraction of NaCl
d_h half-width of the flow channel, m
g acceleration of gravity, $m.s^{-2}$
H_m membrane length, m
J length-averaged permeate flux at the hot side of the membrane, $kg.m^{-2}.s^{-1}$
K membrane Permeability, $m^{-1}.s$
J_v local permeate flux at the hot side of membrane, in vapor phase, $kg.m^{-2}.s^{-1}$
K_m mass transfer coefficient, $J.m^{-2}.s^{-1}.K^{-1}$
M molar mass, $kg.mol^{-1}$
m mass, kg
$\dot{m}$ mass flow rate, $kg.s^{-1}$
Nu Nusselt number
P pressure, Pa
Pr Prandlt number
P_v water vapor pressure, Pa
R_e Reynolds number of the hot solution channel
R Universal gas constant, $J.kmol^{-1}.K$
r_p membrane pore size, m
r_1 largest membrane pore , m
T temperature, ^oC
T_{ci} inlet temperature of cold solution, ^oC
T_{hi} inlet temperature of hot solution, ^oC
$\bar{T}$ Average temperature, ^oC
V velocity, $m.s^{-1}$
V_e velocity of feed solution, $m.s^{-1}$
Vr the velocity in radius direction, $m.s^{-1}$
r coordinate normal to the solution flow
z coordinate along the solution flow

Greek letters

ΔP water vapor pressure difference, Pa
δ Thickness or width, m
ε porosity of the membrane
γ_l surface tension of water, $N.m^{-1}$
μ dynamic viscosity, $kg.m^{-1}.s^{-1}$
ρ density, $kg.m^{-3}$
τ tortuosity

Subscripts

a Air
atm Atmosphere
Avg Average
c cold solution
f condensate film
fp condensate film/cooling plate interface
g vapor/air gap
gf air gap/condensate film interface
h hot solution
hi inlet of the hot channel
hm hot liquid/membrane interface
i inlet of the channel or ith domain
m membrane
mc membrane cold side
mg membrane/air gap interface

REFERENCES

[1] L. MARTINEZ, F.J.FLORIDO-DIAZ, A.HERNANDEZ, P. PRADANOS « *Characterisation of three hydrophobic porous membranes used in membrane distillation: Modelling and evaluation of their water vapour permeabilities* » - Journal of membrane science 203 (2003) 15-27.

[2] A.EL-ABASSI, A.HAFIDI, M.C.GARCIA-PAYO, M. KHAYET "*Concentration of olive mill wastewater by membrane distillation for polyphenols recovery*",- Semlalia, Marrakech, Morroco, February 2009.

[3] K. CHARFI , M. KHAYET, M.J. SAFI , "*Numerical simulation and experimental studies on heat and mass transfer using sweeping gas membrane distillation*", - 28040 Madrid, Spain

[4] M.SENE, « *Transferts de chaleur et de masse dans des procédés de dessalement par distillation membranaire, type AGMD - valorisation des ressources en eau dans le delta du saloum* ». - Thèse de doctorat, Université Cheikh Anta Diop de Dakar Sénégal (2010).

[5] 5.J. PHATTANARAWIK, R JIRARATANANON, A.G.FANE, « *Effect of pore size distribution and air flux on mass transport in direct contact membrane distillation*» - Toogkru, Bangkok, Thailand, 2002

[6] JULIÁN BLANCO GÁLVEZA, LOURDES GARCÍA-RODRÍGUEZ, ISABEL MARTÍN-MATEOS, "*Seawater desalination by an innovative solar-powered membrane distillation system: the MEDESOL project*", - Tabernas, Almería, Spain

[7] E. MATHIOULAKIS, V. BELESSIOTIS, E. DELYANNIS, "*Desalination by using alternative energy:Review and state-of-the-art*", - Aghia Paraskevi, 153-10, Athens, Greece

[8] HAZIM MOHAMEED QIBLAWEY, FAWZI BANAT, "*Solar thermal desalination technologies*", 22110 Irbid, Jordan

[9] S. MIDDLMANN « *An introduction to fluid dynamics : principles of analysis and design* » - University of California, San Diego pp 261-267.

[10] K. DAMAK, A. AYADI, B. ZEGHMATI, P. SCHMITH, « *A new Navier-Stokes and Darcy's law combined model for fluid flow in crossflow filtration tubular membranes* » - Laboratoire Radio Analyse et Environnement, Ecole nationale d'ingénieurs de Sfax, TunisieDesalination 161 (2004) 67-77.

[11] M.S. El-BOURAWI, Z. DING, R. MA, M. KHAYET, « *A framework for better understanding membrane distillation separation process* », - State Key Laboratory of Chemical Resource Engineering, Beijing University of Chemical Technology, Beijing 100029, PR China , Journal of Membrane Science 285 (2006) 4-29.

[12] A.M. ALKAIBI, N. LIOR, « *Transport analysis of air gap membrane distillation* » - Department of Mechanical engineering and Applied of Pennsylvania, USA. Journal of Membrane Science 255 (2005) 239-253.

American Journal of Engineering Research (AJER)
e-ISSN : 2320-0847 p-ISSN : 2320-0936
Volume-02, Issue-11, pp-43-47
www.ajer.org

Research Paper Open Access

Improving inward luggage flow using Simulation: Case Study at a Private Medium-scale Airport

Mayank Kumar, Tarun Gupta, Akhilesh Jha

Abstract: - Loading luggages in the aircraft is the primary step in Air Travel. The flow time involved in the movement of passengers and luggage from parking to the Aircraft reflects the Airport Management as well as is a primary metric to determine customer satisfaction. This paper presents a case wherein the time involved in the loading of luggage from parking to Aircraft from both customer and service provider's point of view is analyzed. Simulation is used to model the existing system and find alternate ways to reduce the overall time taken in loading luggage. Simulation results showed that by using alternate process of loading operation, the overall time can be reduced along with lower congestion and delays. Implementation of the proposed operational model would result in greater customer satisfaction as the overall time spent in loading luggages onto the aircraft would be reduced.

Keywords: - *simulation, flow time, loading, Airport management.*

I. INTRODUCTION TO EXISTING SYSTEM

The flight can only take-off after all the luggages are loaded onto the Aircraft. Thus loading is one of the most critical activities in Air Journey. Delays in flights due to high flow time of loading luggages in aircraft reflect poor Airport Management. This paper presents a case study at a medium scale private Airport wherein the process of loading luggages is analyzed. The present Operational set-up is associated with delay of flights, congestion, and panic during peak load i.e. when the number of luggages is high. The number of flights that take off and the number of luggages handled during takeoff is shown in figure-1.

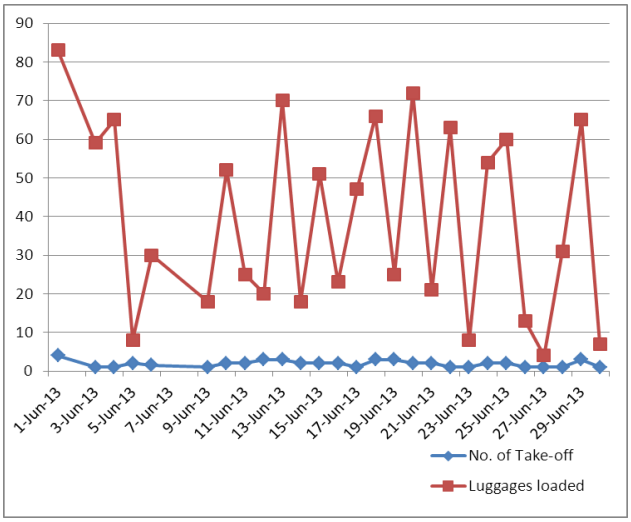

Figure-1: Number of luggages handled and number of take-offs. Figure shows the fluctuation in number of luggages and the peak number of luggages handled per day

The overall loading process starts from the moment the passenger arrives at the parking lot and ends when the passenger as well as the luggage is loaded onto the Aircraft. The passenger hands over the luggage to the loaders (manpower responsible for loading to aircraft) and subsequently signs the luggage tag. All the other activities such as movement of luggages to x-ray machine, loading/ unloading from x-ray machine, loading luggages to aircraft etc. is done by the loaders. The flow of luggages and passengers during the loading operation is shown in Figure-2.

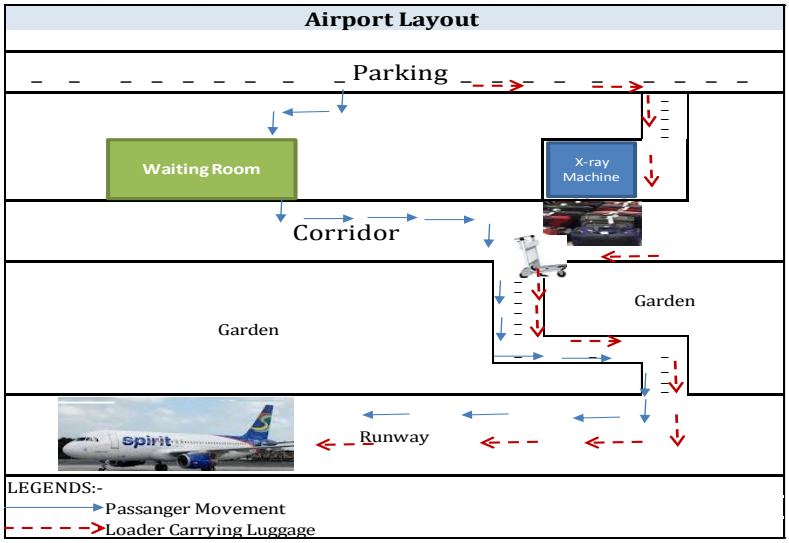

Figure-2: Flow of luggages and passengers during loading operation

The present operational set up is able to handle about 30-35 luggages in 60 minutes. However, it is been forecasted that the number of passengers and thereby the number of loaders may increase. The present operational setup can cater more number of luggages only if a certain set of manpower is increased or the time duration in loading in increased. However, the outcomes of this study show that by redesigning some operational practices, greater luggages can be handled in a lower time span with reduced work-load.

II. MODELLING APPROACH

To analyze the movement of the luggages in the as-is situation, the entire loading process is simulated in the software package ARENA. The simulation is then run by changing some parameters through which an optimal solution is output. The methodology used in this paper for simulation and deriving an optimal solution shown in figure-3.

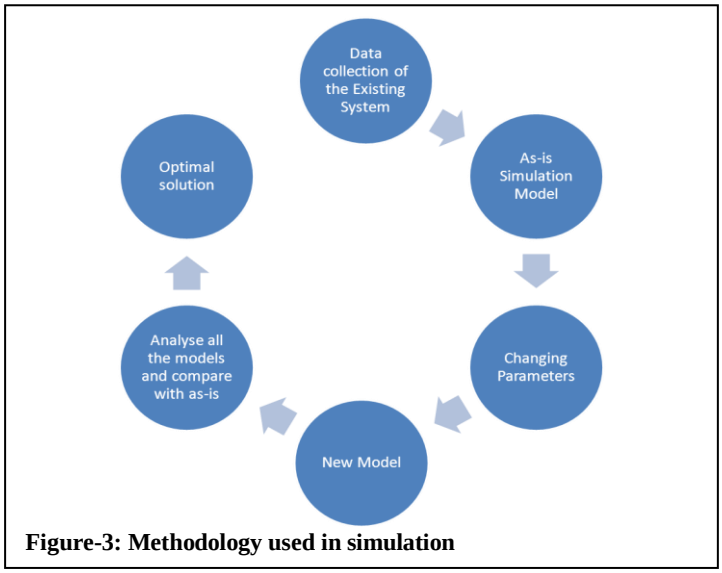

Figure-3: Methodology used in simulation

III. DATA COLLECTION

Data collection is an important aspect in simulation modeling for accurately representing the actual system. The data that were collected includes arrival pattern of the passengers, number of luggages handled, lot size of luggages, time taken in each activity and the overall time taken in the entire loading operation. The simulation should take into account all these parameters. ARENA software was used for building the simulations. Data collection of the existing system is done by direct field observations, video recording and data analysis. The parameters that are analyzed are value added time, waiting time of entity, number of luggages handled and overall time taken in the entire loading operation. The activities involved in the entire loading process and the average time taken per luggage is shown in Figure-3.

IV. MODELLING THE AS-IS SYSTEM

The as-is scenario is modeled in ARENA software package. The model is compared with the data collected from field observation in order to validate the model developed in the package. The arrival pattern showed that the average arrival rate of passengers start from about 45 minutes to 60 minutes prior to the take-off of flight. This implies the entire loading activity is to be done within a time span of 60 minutes for a batch size of 35-40 luggages. Time span greater than 60 minutes would result in delay of the take-off of the flight.

The existing system is modeled in ARENA as shown in Figure-5. The outcomes of the model matched the direct field observations. The results of the as-is model is shown below:

Table-1: Simulation results for each entity in As-is Model

PARTICULARS	TIME (Mins)
Total Value Added time	2.5
Waiting time	7.9
Transfer time	4.5
Total Time	14.9
Number of Luggages handled	36

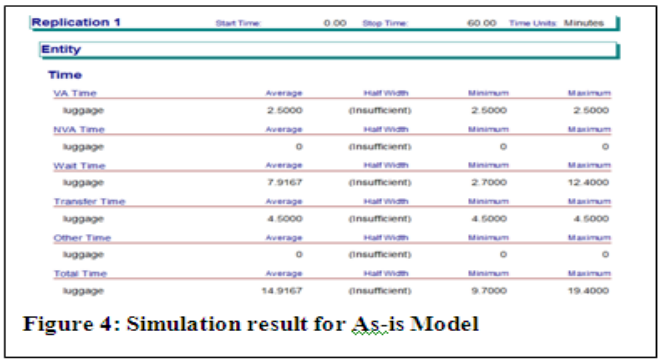

Figure 4: Simulation result for As-is Model

V. RE-DESIGNING OPERATIONAL PRACTICE:

1. Model-1: Self Service Concept:

This model introduces Self-service concept similar to the operational practice followed in commercial flights. In the as-is system, all the activities from tagging luggages to loading the luggage in Aircraft is done by loaders (manpower involved in loading activity). The existing system results in delays when there are greater number of luggages and uncertainty in the number of luggages leads to greater flow time of luggages. Model-1 suggests introduction of self-service i.e. all the activities up to loading the luggage in trolley is to be done by the passengers themselves. For this to be operational, certain sign boards and display monitors may be used so that the passengers can do the activities such as tagging, x-raying and loading luggages in trolley without confusion. Secondly a proper pathway is proposed to be constructed so that the trolley carrying luggages may be moved from trolley near x-ray to aircraft directly. The results obtained after simulating this system is shown in table-2.

Table-2: Simulation results for each entity in Model-1

PARTICULARS	TIME (Mins)
Total Value Added time	2.5
Waiting time	5.2
Transfer time	4.5
Total Time	12.2
Number of Luggages handled	42

2. Model-2: LMV Trolley (Batch size-4):

Model-2 suggests introduction of self-service as in model-1 as well as using a LMV (Light motor vehicle) to transfer the luggages from x-ray to aircraft. Further, a batch size of 4 luggages per trip is considered in this model. This model is simulated for one hour prior to the take-off. The results obtained after simulating this system is shown in table-3

Table-3: Simulation results for each entity in Model-2

PARTICULARS	TIME (Mins.)
Total Value Added time	2.5
Waiting time	5.2
Transfer time	1.5
Total Time	9.2
Number of Luggages handled	42

3. Model-3: LMV Trolley (Batch size-6):

Model-2 suggests introduction of self-service as in model-1 as well as using a LMV (Light motor vehicle) to transfer the luggages from x-ray to aircraft. Further a batch size of 6 luggages per trip is considered in this model. The results obtained after simulating this system is shown in table-4.

Table-4: Simulation results for each entity in Model-3

PARTICULARS	TIME (Mins)
Total Value Added time	2.5
Waiting time	3.4
Transfer time	1.5
Total Time	7.4
Number of Luggages handled	45

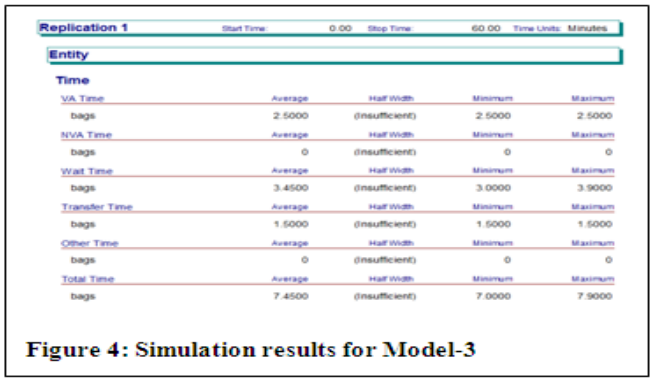

Figure 4: Simulation results for Model-3

4. Model-4: LMV Trolley (Batch size-8):

Model-2 suggests introduction of self-service as in model-1 as well as using a LMV (Light motor vehicle) to transfer the luggages from x-ray to aircraft. Further a batch size of 8 luggages per trip is considered in this model. The results obtained after simulating this system is shown in table-5.

Table-5: Simulation results for each entity in Model-3

PARTICULARS	TIME (Mins)
Total Value Added time	2.5
Waiting time	6.55
Transfer time	1.5
Total Time	10.55
Number of Luggages handled	40

VI. SENARIO ANALYSIS AND RESULTS

Out of the four models the overall value added time per entity is the same for all models. However, maximum number of luggages that can be handled in one hour is maximum for Model -3. The overall time per entity is also the least for Model-3. Therefore, model-3 i.e. using self-service system along with a LMV that can carry 6 luggages is suggested to be implemented

VII. CONCLUSION

Results show that on implementation of Model-3, the overall time per luggage in loading can be decreased by about 50 % and the capacity of handling luggages can be increased by about 25% with the same number of workforce. The implementation of the model suggested will lower the delays occurring due to the wait time involved for the loading of luggages to take place.

ACKNOWLEDGMENT

We would like to thank our guide Mr. Dalbir Singh Rekhi (GM-Industrial Engineering) for his immense support and research inputs. We would also like to extend our sincere thanks to Mr. Ankit Jain (Jr. Manager-Industrial Engineering) for providing his valuable insight in simulation modeling.

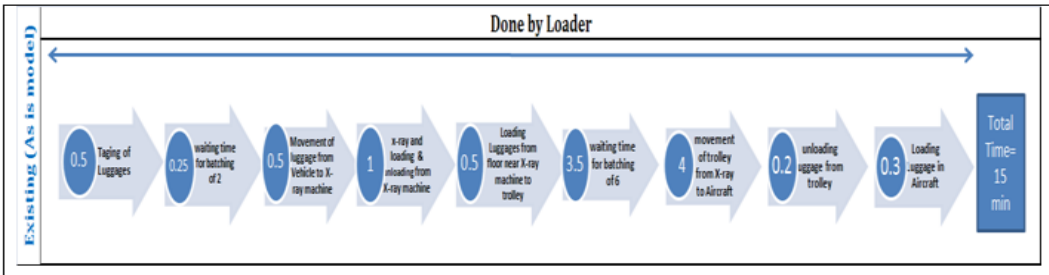

Figure 6: Process flow of As-is system. The overall time per luggage is about 15 minutes.

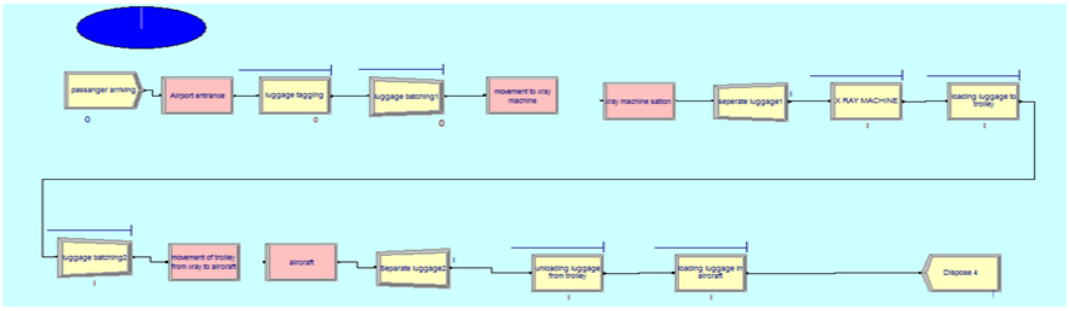

Figure 7: As-is process flow and simulation in arena. The results show that about 36 luggages can be handled in one hour with the existing workforce

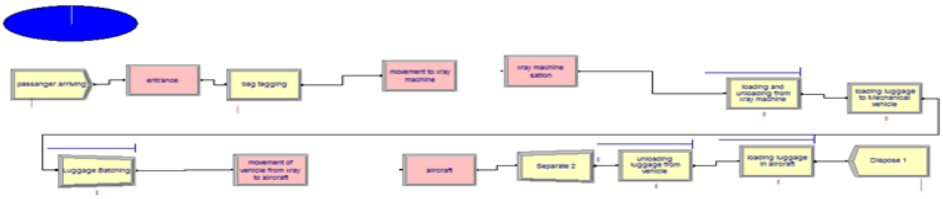

Figure 8: MODEL-3 simulation in arena. The results show that about 45 luggages can be handled in one hour with the existing workforce

REFERENCES

[1] KatalinEmese Bite (2003) 'IMPROVING ON PASSENGER AND BAGGAGE PROCESS AT AIRPORTS WITH RFID'.

[2] Lorenzo Brunetta and Giorgio (2010) 'Passenger and baggage flow in an airport terminal:A flexible simulation model'.

[3] Mihails, Alexander and Elena (2007) 'Riga airport baggage handling system simulation'

[4] Central Statistical Bureau of Latvia 2007.Transport in 2006 Riga Latvia.

[5] Simone Appelt, ranjan and Li Lin (2007) 'Simulation of passenger check-in at a medium size US airport'.

[6] U. Vandebona and P. Thananupappaisan (2003) 'Modeling of composite of baggage screening system at airport'

[7] Jim and Chang, (1998). 'The luggage is sorted in accordance with the flights, and the loading operation begins'.

American Journal of Engineering Research (AJER)
e-ISSN : 2320-0847 p-ISSN : 2320-0936
Volume-02, Issue-11, pp-48-60
www.ajer.org

Research Paper Open Access

Improvement of Transient stability in Power Systems with Neuro-Fuzzy UPFC

Gundala Srinivasa Rao, Venugopal Reddy Bodha

Abstract: - Low Frequency Oscillations (LFO) occur in power systems because of lack of the damping torque in order to dominance to power system disturbances as an example of change in mechanical input power. In the recent past Power System Stabilizer (PSS) was used to damp LFO. FACTs devices, such as Unified Power Flow Controller (UPFC), can control power flow, reduce sub-synchronous resonance and increase transient stability. So UPFC may be used to damp LFO instead of PSS. UPFC damps LFO through direct control of voltage and power. In this paper the linearized model of synchronous machine (Heffron-Philips) connected to infinite bus (Single Machine-Infinite Bus: SMIB) with UPFC is used and also in order to damp LFO, adaptive neuro-fuzzy controller for UPFC is designed and simulated. Simulation is performed for various types of loads and for different disturbances. Simulation results show good performance of neuro-fuzzy controller in damping LFO.

Keywords: - *Neuro-Fuzzy Controller, Low Frequency Oscillations (LFO), Unified Power Flow Controller (UPFC), Single Machine-Infinite Bus (SMIB)*

I. INTRODUCTION

The Benefits of Flexible AC Transmission Systems (FACTs) usage to improve power systems stability is well known. The growth of the demand for electrical energy leads to loading the transmission system near their limits. Thus, the occurrence of the LFO has increased. FACTs Controllers has capability to control network conditions quickly and this feature of FACTs can be used to improve power system stability. The UPFC is a FACTS device that can be used to the LFO. The primarily use of UPFC is to control the power flow in power systems. The UPFC consists of two voltage source converters (VSC) each of them has two control parameters namely m_e, δ_e, m_b and δ_b. The UPFC used for power flow control, enhancement of transient stability, mitigation of system oscillations and voltage regulation. For systems which are without power system stabilizer (PSS), excellent damping can be achieved via proper controller design for UPFC parameters. By designing a suitable UPFC controller, an effective damping can be achieved. It is usual that Heffron-Philips model is used in power system to study small signal stability. This model has been used for many years providing reliable results.
In recent years, the study of UPFC control methods has attracted attentions so that different control approaches are presented for UPFC control such as Fuzzy control, conventional lead-lag control, Genetic algorithm approach, and robust control methods.

In this study, the class of adaptive networks that of the same as fuzzy inference system in terms of performance is used. The controller utilized with the above structure is called Adaptive Neuro Fuzzy Inference System or briefly ANFIS. Applying neural networks has many advantages such as the ability of adapting to changes, fault tolerance capability, recovery capability, High-speed processing because of parallel processing and ability to build a DSP chip with VLSI Technology. To show performance of the designed adaptive neuro-fuzzy controller, a conventional lead-lag controller that is used and the simulation results for the power system including these two controllers are compared with each other.

II. FLEXIBLE AC TRANSMISSION SYSTEMS (FACTS)

Flexible AC Transmission Systems, called FACTS, got in the recent years a well known term for higher controllability in power systems by means of power electronic devices. Several FACTS-devices have been introduced for various applications worldwide. A number of new types of devices are in the stage of being introduced in practice.

In most of the applications the controllability is used to avoid cost intensive or landscape requiring extensions of power systems, for instance like upgrades or additions of substations and power lines. FACTS-devices provide a better adaptation to varying operational conditions and improve the usage of existing installations. The basic applications of FACTS-devices are:

Power flow control, Increase of transmission capability, Voltage control, Reactive power compensation, Stability improvement, Power quality improvement, Power conditioning, Flicker mitigation, Interconnection of renewable and distributed generation and storages.

The development of FACTS-devices has started with the growing capabilities of power electronic components. Devices for high power levels have been made available in converters for high and even highest voltage levels.

The overall starting points are network elements influencing the reactive power or the impedance of a part of the power system. Figure 1.2 shows a number of basic devices separated into the conventional ones and the FACTS-devices.

For the FACTS side the taxonomy in terms of 'dynamic' and 'static' needs some explanation. The term 'dynamic' is used to express the fast controllability of FACTS-devices provided by the power electronics. This is one of the main differentiation factors from the conventional devices. The term 'static' means that the devices have no moving parts like mechanical switches to perform the dynamic controllability. Therefore most of the FACTS-devices can equally be static and dynamic.

The left column in Figure.1 contains the conventional devices build out of fixed or mechanically switch able components like resistance, inductance or capacitance together with transformers. The FACTS-devices contain these elements as well but use additional power electronic valves or converters to switch the elements in smaller steps or with switching patterns within a cycle of the alternating current. The left column of FACTS-devices uses Thyristor valves or converters. These valves or converters are well known since several years. They have low losses because of their low switching frequency of once a cycle in the converters or the usage of the Thyristors to simply bridge impedances in the valves.

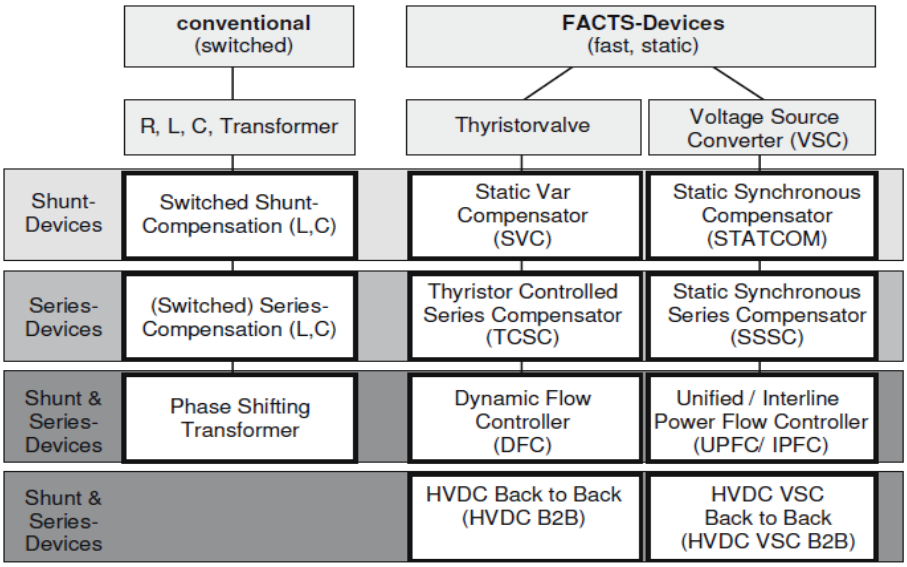

Fig.1. Overview of FACTS Devices

The right column of FACTS-devices contains more advanced technology of voltage source converters based today mainly on Insulated Gate Bipolar Transistors (IGBT) or Insulated Gate Commutated Thyristors (IGCT). Voltage Source Converters provide a free controllable voltage in magnitude and phase due to a pulse width modulation of the IGBTs or IGCTs.

High modulation frequencies allow to get low harmonics in the output signal and even to compensate disturbances coming from the network. The disadvantage is that with an increasing switching frequency, the losses are increasing as well. Therefore special designs of the converters are required to compensate this.

III. UNIFIED POWER FLOW CONTROLLER

The UPFC is a combination of a static compensator and static series compensation. It acts as a shunt compensating and a phase shifting device simultaneously.

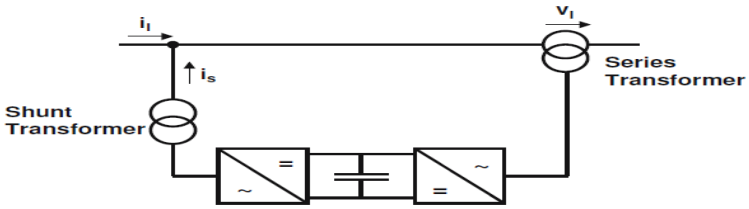

Fig.2. Principle configuration of an UPFC

The UPFC consists of a shunt and a series transformer, which are connected via two voltage source converters with a common DC-capacitor.

The DC-circuit allows the active power exchange between shunt and series transformer to control the phase shift of the series voltage. This setup, as shown in Figure 1.21, provides the full controllability for voltage and power flow.

The series converter needs to be protected with a Thyristor bridge. Due to the high efforts for the Voltage Source Converters and the protection, an UPFC is getting quite expensive, which limits the practical applications where the voltage and power flow control is required simultaneously.

Circuit Arrangement:

In the presently used practical implementation, The UPFC consists of two switching converters, which in the implementations considered are voltage source inverters using gate turn-off (GTO) thyristor valves, as illustrated in the Fig.3. These back to back converters labeled "Inverter 1 and "Inverter 2" in the figure are operated from a common dc link provided by a dc storage capacitor.

This arrangement functions as an ac to ac power converter in which the real power can freely flow in either direction between the ac terminals of the two inverters and each inverter can independently generate (or absorb) reactive power at its own ac output terminal.

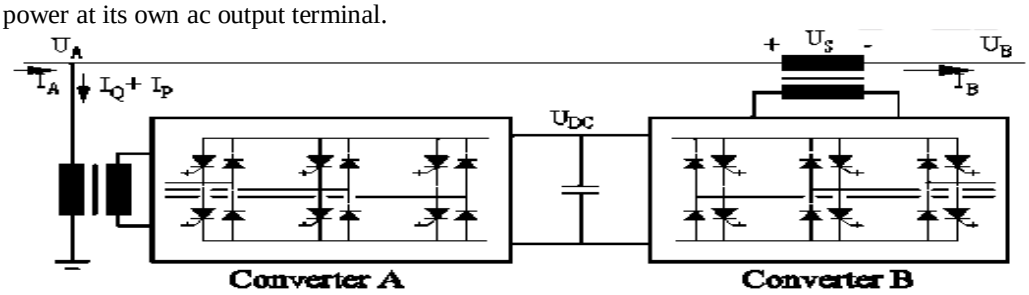

Fig.3. Basic circuit arrangement of unified power flow controller

Operation of UPFC:

Inverter 2 provides the main function of the UPFC by injecting an ac voltage Vpq with controllable magnitude V_{pq} ($0 \le V_{pq} \le V_{pqmax}$) and phase angle $\rho(0 \le \rho \le 360)$, at the power frequency, in series with the line via an insertion transformer. The injected voltage is considered essentially as a synchronous voltage source. The transmission line current flows through this voltage source resulting in real and reactive power exchange between it and the ac system. The real power exchanged at the ac terminal (i.e., at the terminal of insertion transformer) is converted by the inverter into dc power that appears at the dc link as positive or negative real power demanded. The reactive power exchanged at the ac terminal is generated internally by the inverter.

The basic function of inverter 1 is to supply or absorb the real power demanded by Inverter 2 at the common dc link. This dc link power is converted back to ac and coupled to the transmission line via a shunt-connected transformer. Inverter 1 can also generate or absorb controllable reactive power, if it is desired, and there by it can provide independent shunt reactive compensation for the line.

It is important to note that where as there is a closed "direct" path for the real power negotiated by the action of series voltage injection through Inverters 1 and 2 back to the line, the corresponding reactive power exchanged is supplied or absorbed locally by inverter 2 and therefore it does not flow through the line.

Thus, Inverter 1 can be operated at a unity power factor or be controlled to have a reactive power exchange with the line independently of the reactive power exchanged by the Inverter 2. This means there is no continuous reactive power flow through UPFC.

Basic Control Functions:

Operation of the UPFC from the standpoint of conventional power transmission based on reactive shunt compensation, series compensation, and phase shifting, the UPFC can fulfill these functions and thereby

meet multiple control objectives by adding the injected voltage V_{pq}, with appropriate amplitude. And phase angle, to the terminal voltage V_o. Using phasor representation, the basic UPFC power flow control functions are illustrated in Fig 4.

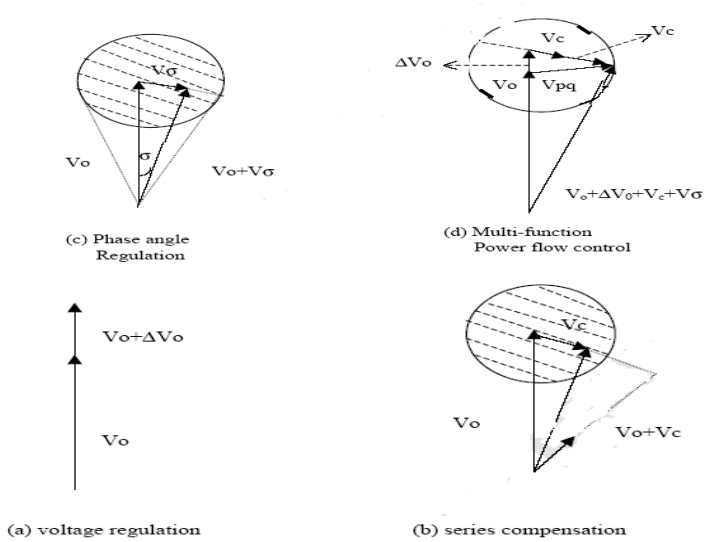

Fig.4. Basic UPFC control functions

Terminal Voltage Regulation, similar to that obtainable with a transformer tap-changer having infinitely small steps, as shown at (a) where $V_{pq}=\Delta V$ (boldface letters represent phasors) is injected in-phase (or anti-phase) with V_o.

Series capacitor compensation is shown at (b) where $V_{pq}=V_c$ is in quadrature with the line current I.

Transmission angle Regulation (phase shifting) is shown at (c) where $V_{pq}=V_o$ is injected with angular relationship with respect to V_o that achieves the desired s phase shift (advance or retard) without any change in magnitude.

Multifunctional Power Flow Control, executed by simultaneous terminal voltage regulation, series capacitive compensation, and phase shifting, is shown at (d) where $V_{pq}=\Delta V+V_c+V_o$.

Basic Principles Of P And Q Control:

Consider Fig 2.3. At (a) a simple two machine (or two bus ac inter-tie) system with sending end voltage V_s, receiving-end voltage V_r, and line (or tie) impedance X (assumed, for simplicity, inductive) is shown. At (b) the voltages of the system in the form of a phasor diagram are shown with transmission angle δ and $|V_s|=|V_r|=V$. At (c) the transmitted power P ($P=V_2/X \sin\delta$) and the reactive power $Q=Q_s=Q_r$ ($Q=V_2/X\ (1-\cos\delta)$) supplied at the ends of the line are shown plotted against angle δ. At (d) the reactive power $Q=Q_s=Q_r$ is shown plotted against the transmitted power corresponding to "stable values of δ" (i.e., $0<=\delta<=90^o$).

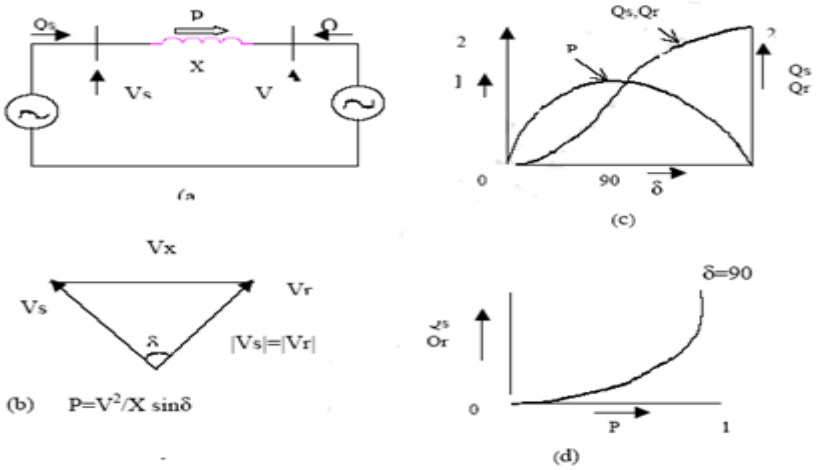

Fig.5. simple two machine system (a) related voltage phasor (b).real and reactive power verses transmission angle (c). and sending-end/receiving-end reactive power verses transmitted real power(d).

Basic power system of fig.5 with the well known transmission characteristics is introduced for the purpose of providing a vehicle to establish the capability of the UPFC to control the transmitted real power P and the reactive power demands, Q_s and Q_r, at the sending end, respectively, the receiving end of the line.
The UPFC is represented by a controllable voltage source in series with the line which, as explained in the previous section, can generate or absorb reactive power that it, or absorbed from it, bye the sending end generator.

The UPFC in series with the line is represented by the phasor V_{pq} having magnitude $V_{pq}(0 \leq V_{pq} \leq V_{pqmax})$ and angle ρ $(0 \leq \rho \leq 360)$ measured from the given phase position of phasor Vs, as illustrated in the figure. The line current represented by the phasor I, flows through the series voltage source, V_{pq} and generally results in both reactive and real power exchange. In order to represent UPFC properly, the series voltage source is stipulated to generate only the reactive power Q_{pq} it exchanges with the line. Thus the real power P_{pq} it negotiates with the line is assumed to be transferred to the sending-end generator excited.
This is in arrangement with the UPFC circuit structure in which the dc link between the two constituent inverters establish a bi-directional coupling for real power flow between the injected series voltage source and the sending end bus.

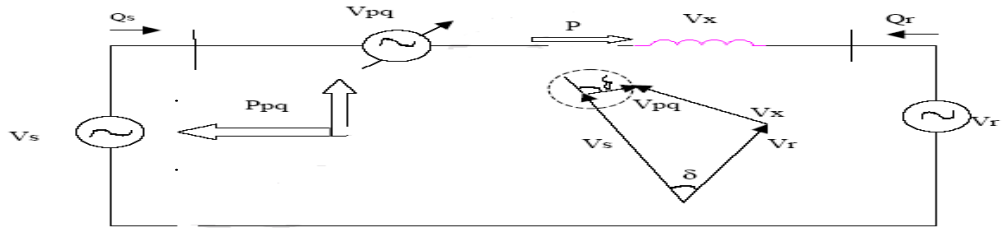

It can be observed in Fig that the transmission line "sees" V_s+V_{pq} as the effective sending end voltage. Thus it is clear that the UPFC effects the voltage (both its magnitude and angle) across the transmission line and therefore it is reasonable to expect that it is able to control, by varying the magnitude and angle of Vpq, the transmittable real power as well as the reactive power demand of the line at any given transmission angle between the sending-end and receiving-end voltages.

Independent Real And Reactive Power Flow Control:

In Fig2.5(a) through 2.5(b) the reactive power Q_s supplied by the sending-end generator, and Q_r supplied by the receiving-end generator, are shown plotted separately against the transmitted power ρ as a function of the magnitude Vpq and angle p of the injected voltage phasor V_{pq} at four transmission lines; δ=0,30,60 and 90. At V_{pq}=0 each of these plots becomes a discrete point on the basic Q-p curve as shown in Fig 2.3(d), which is included in each of the above figures for reference.
The curves showing the relationships between Q_s and P, and Q_r and P, for the transmission angle range of 0<= δ<=90, when the UPFC is operated to provide the maximum transmittable power with no reactive power control ($V_{pq}=V_{pqmax}$ and ρ= ρp=P_{max}), are also shown by a broken –line with the label "P (δ) =MAX" at the sending end and respectively, "receiving-end" plots of the figure.

Consider the first fig.5 (a), which illustrates the case when the transmission angle is zero(δ=0). With V_{pq}=0, P, Qs and Q_r are all zero, i.e., the system is standstill at the origins of the Q_s, P and Q_r, P coordinates. The circle around the origin of the {Q_s, P} and {Qr, P} planes sown the variation of Q_s and P and Q_r and P respectively. As the voltage phasor Vpq, with its maximum V_{pqmax} is rotated a full revolution (0<= ρ<=360). The area within these circles defines all P and Q values obtainable by controlling the magnitude V_{pq} and ρ of the phasor V_{pq}.

In other words, the circle in {Q_s,p} and {Q_r,p} planes define all P and Qs and respectively, P and Q_r values attainable with the UPFC of a given rating. It can be observed, for example, that the UPFC with the stipulated voltage rating of 0.5. P.u. is able to establish 0.5. P.u. power flow, in either direction, without imposing any reactive power demand on either the sending-end or the receiving-end generator.
Of course, the UPFC, as seen, can force the generator at one end to supply reactive power for the generator at the other end. (In case of inertia, one system can be forced to supply reactive power of the line.)

In general at any given transmission angle δ, the transmitted real power P, and the reactive power demands at the transmission line ends, Q_s and Q_r, can be controlled freely by the UPFC within the boundaries obtained in the {Qs,p}and {Q_r,P} planes by rotating the injected voltage phasor V_{pq} with its maximum magnitude a full revolution. The boundary in each plane is centered around the point defined by the transmission angle on the Q verses P curve that characteristic the basic power transmission at V_{pq}=0.

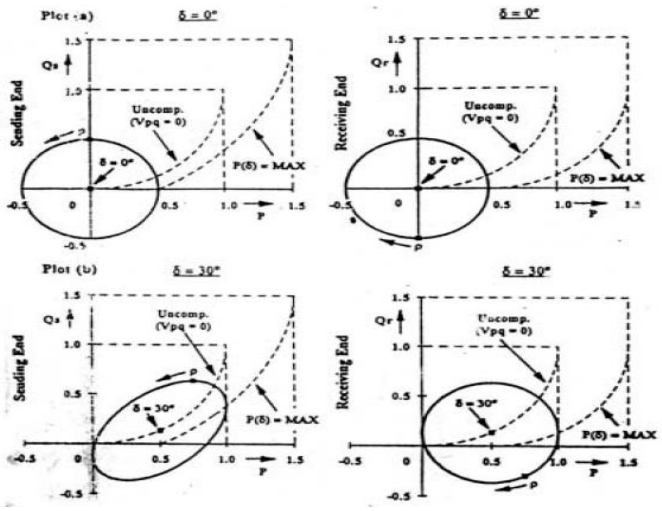

Fig.6. Attainable sending-end reactive power Vs transmitted power (left hand side plots) and receiving-end reactive power Vs transmitted power (right hand side plots) values with the UPFC at $\delta=0^o$ and $\delta=30^o$

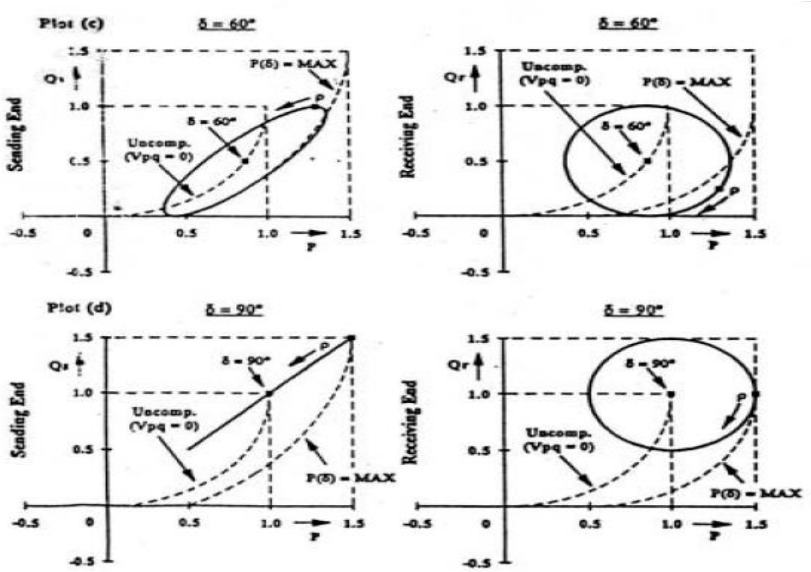

Fig .7. Attainable sending-end reactive power Vs transmitted power (left-hand side plots) and receiving-end reactive power Vs transmitted power (right hand side plots) values with the UPFC at $\delta=60^o$ and $\delta=90^o$

Consider the next case of δ=30, it is seen that the receiving-end control region boundary in the $\{Q_s, P\}$ plane become an ellipse. As the transmission angle δ is further increased, for example, to 60 , the ellipse defining the control region for P and Qs in the $\{Q_s, P\}$ plane becomes narrower and finally 90 it degerates into a straight line. By contrast, the control region boundary for p and Q_r in the $\{Q_r,P\}$ plane remains a circle at all transmission angles.

DAMPING OSCILLATIONS OF UPFC:

Problem Statement:

Figure8 shows a SMIB system equipped with a UPFC. The UPFC consists of an excitation transformer (ET), a boosting transformer (BT), two three-phase GTO based voltage source converters (VSCs), and a DC link capacitors. The four input control signals to the UPFC are m_E, m_B, δ_E, and δ_B, where

m_E is the excitation amplitude modulation ratio,

m_B is the boosting amplitude modulation ratio,

δ_E is the excitation phase angle, and

δ_B is the boosting phase angle.

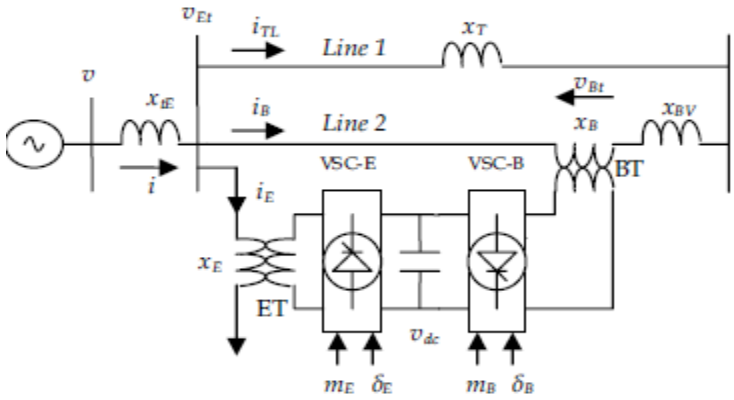

Fig.8. SMIB power system equipped with UPFC

Power System Nonlinear Model:

By applying Park's transformation and neglecting the resistance and transients of the ET and BT transformers, the UPFC can be modeled as

$$\begin{bmatrix} v_{Etd} \\ v_{Etq} \end{bmatrix} = \begin{bmatrix} 0 & -x_E \\ x_E & 0 \end{bmatrix} \begin{bmatrix} i_{Ed} \\ i_{Eq} \end{bmatrix} + \begin{bmatrix} \frac{m_E \cos\delta_E v_{dc}}{2} \\ \frac{m_E \sin\delta_E v_{dc}}{2} \end{bmatrix} \quad (1)$$

$$\begin{bmatrix} v_{Btd} \\ v_{Btq} \end{bmatrix} = \begin{bmatrix} 0 & -x_B \\ x_B & 0 \end{bmatrix} \begin{bmatrix} i_{Bd} \\ i_{Bq} \end{bmatrix} + \begin{bmatrix} \frac{m_B \cos\delta_B v_{dc}}{2} \\ \frac{m_B \sin\delta_B v_{dc}}{2} \end{bmatrix} \quad (2)$$

$$\dot{v}_{dc} = \frac{3m_E}{4C_{dc}} \begin{bmatrix} \cos\delta_E & \sin\delta_E \end{bmatrix} \begin{bmatrix} i_{Ed} \\ i_{Eq} \end{bmatrix} + \frac{3m_B}{4C_{dc}} \begin{bmatrix} \cos\delta_B & \sin\delta_B \end{bmatrix} \begin{bmatrix} i_{Bd} \\ i_{Bq} \end{bmatrix} \quad (3)$$

Where v_{Et}, i_E, v_{Bt}, and i_B are the excitation voltage, excitation current, boosting voltage, and boosting current, respectively; C_{dc} and v_{dc} are the DC link capacitance and voltage, respectively.

The ET, BT and line 2 currents can be stated as:

$$i_{TLd} = \frac{1}{x_T}(x_E i_{Ed} + \frac{m_E \sin\delta_E v_{dc}}{2} - v_b \cos\delta) \quad (4)$$

$$i_{TLq} = \frac{1}{x_T}(x_E i_{Eq} - \frac{m_E \cos\delta_E v_{dc}}{2} + v_b \sin\delta) \quad (5)$$

$$i_{Ed} = \frac{x_{BB}}{x_{d2}} E'_q + x_{d7} \frac{m_B \sin\delta_B v_{dc}}{2} + x_{d5} v_b \cos\delta + x_{d6} \frac{m_E \sin\delta_E v_{dc}}{2} \quad (6)$$

$$i_{Eq} = x_{q7} \frac{m_B \cos\delta_B v_{dc}}{2} + x_{q5} v_b \sin\delta + x_{q6} \frac{m_E \cos\delta_E v_{dc}}{2} \quad (7)$$

$$i_{Bd} = \frac{x_E}{x_{d2}} E'_q - \frac{x_{d1}}{x_{d2}} \frac{m_B \sin\delta_B v_{dc}}{2} + x_{d3} v_b \cos\delta + x_{d4} \frac{m_E \sin\delta_E v_{dc}}{2} \quad (8)$$

$$i_{Bd} = \frac{x_{q1}}{x_{q2}} \frac{m_B \cos\delta_B v_{dc}}{2} + x_{q3} v_b \sin\delta + x_{q4} \frac{m_E \cos\delta_E v_{dc}}{2} \quad (9)$$

Where x_E and x_B are the ET and BT reactance, respectively; the reactances x_{qE}, x_{dE}, x_{BB}, x_{d1}-x_{d7}, and x_{q1}- x_{q7} are as shown in

The non-linear model of the SMIB system of Figure 1 is:

$$\dot{\delta} = \omega_b(\omega - 1) \quad (10)$$

$$\dot{\omega} = (P_m - P_e - D(\omega - 1))/M \quad (11)$$

$$\dot{E}'_q = (E_{fd} - (x_d - x'_d)i_d - E'_q)/T'_{do} \quad (12)$$

$$\dot{E}_{fd} = (K_A(V_{ref} - v + u_{PSS}) - E_{fd})/T_A \quad (13)$$

Where $P_e = v_d i_d + v_q i_q, v = (v_d^2 + v_q^2)^{1/2}, v_d = x_q i_q,\ v_q = E'_q - x'_d i_d, i_d = i_{Ed} + i_{Bd}, i_q = i_{Eq} + i_{Bq}$

P_m and P_e are the input and output power, respectively; M and D the inertia constant and damping coefficient, respectively; ω_b the synchronous speed; δ and ω the rotor angle and speed, respectively; E_q', E'_{fd}, and v the generator internal, field and terminal voltages, respectively; T'_{do} the open circuit field time constant; x_d, x'_d, and x_q the d-axis reactance, d-axis transient reactance, and q-axis reactance, respectively; KA and TA the exciter gain and time constant, respectively; V_{ref} the reference voltage; and u_{PSS} the PSS control signal.

Power System Linearized Model:

The non-linear dynamic equations can be linearized around a given operating point to have the linear model given by:

$$\dot{x} = Ax + Bu \quad (14)$$

Where the state vector x, control vector u, and matrices A and B are

$$x = \begin{bmatrix} \Delta\delta & \Delta\omega & \Delta E'_q & \Delta E_{fd} & \Delta v_{dc} \end{bmatrix}^T \quad (15)$$

$$u = \begin{bmatrix} \Delta u_{pss} & \Delta m_E & \Delta\delta_E & \Delta m_b & \Delta\delta_b \end{bmatrix}^T \quad (16)$$

$$A = \begin{bmatrix} 0 & \omega_b & 0 & 0 & 0 \\ -\frac{K_1}{M} & -\frac{D}{M} & -\frac{K_2}{M} & 0 & -\frac{K_{pd}}{M} \\ -\frac{K_4}{T'_{do}} & 0 & -\frac{K_3}{T'_{do}} & \frac{1}{T'_{do}} & -\frac{K_{qd}}{T'_{do}} \\ -\frac{K_A K_5}{T_A} & 0 & -\frac{K_A K_6}{T_A} & -\frac{1}{T_A} & -\frac{K_A K_{vd}}{T_A} \\ K_7 & 0 & K_8 & 0 & -K_9 \end{bmatrix} \quad (17)$$

$$B = \begin{bmatrix} 0 & 0 & 0 & 0 & 0 \\ 0 & -\frac{K_{pe}}{M} & -\frac{K_{p\delta e}}{M} & -\frac{K_{pb}}{M} & -\frac{K_{p\delta b}}{M} \\ 0 & -\frac{K_{qe}}{T'_{do}} & -\frac{K_{q\delta e}}{T'_{do}} & -\frac{K_{qb}}{T'_{do}} & -\frac{K_{q\delta b}}{T'_{do}} \\ \frac{K_A}{T_A} & -\frac{K_A K_{ve}}{T_A} & -\frac{K_A K_{v\delta e}}{T_A} & -\frac{K_A K_{vb}}{T_A} & -\frac{K_A K_{v\delta b}}{T_A} \\ 0 & K_{ce} & K_{c\delta e} & K_{cb} & K_{c\delta b} \end{bmatrix} \quad (18)$$

Where $K_1 - K_9$, K_{pu}, K_{qu}, and K_{vu} are linearization constants.

***Model Of The Power System Including* UPFC:**

UPFC is one of the famous FACTs devices that is used to improve power system stability. Fig.1 shows a single machine-infinite-bus (SMIB) system with UPFC. It is assumed that the UPFC performance is based on pulse width modulation (PWM) converters. In figure 1 m_e, m_b and δ_e, δ_b are the amplitude modulation ratio and phase angle of the reference voltage of each voltage source converter respectively. These values are the input control signals of the UPFC.

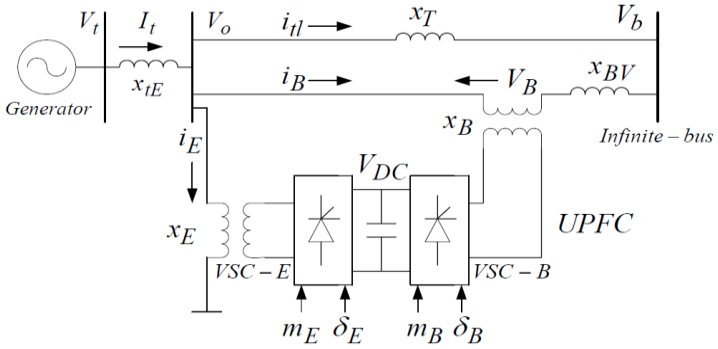

Fig.1 A single machine connected to infinite bus with UPFC

As it mentioned previously, a linearized model of the power system is used in dynamic studies of power system. In order to consider the effect of UPFC in damping of LFO, the dynamic model of the UPFC is employed; In this model the resistance and transient of the transformers of the UPFC can be ignored. The Linearized state variable equations of the power system equipped with the UPFC can be represented as

$$\begin{bmatrix} \Delta\dot{\delta} \\ \Delta\dot{\omega} \\ \Delta\dot{E}'_q \\ \Delta\dot{E}_{fd} \\ \Delta\dot{v}_{dc} \end{bmatrix} = \begin{bmatrix} 0 & \omega_0 & 0 & 0 & 0 \\ -\frac{k_1}{M} & -\frac{D}{M} & -\frac{k_2}{M} & 0 & -\frac{k_{pd}}{M} \\ -\frac{k_4}{T'_{do}} & 0 & -\frac{k_3}{T'_{do}} & \frac{1}{T'_{do}} & \frac{k_{qd}}{T'_{do}} \\ -\frac{k_A k_5}{T_A} & 0 & -\frac{k_A k_6}{T_A} & -\frac{1}{T_A} & \frac{k_A k_{vd}}{T_A} \\ k_7 & 0 & k_8 & 0 & -k_9 \end{bmatrix} \begin{bmatrix} \Delta\delta \\ \Delta\omega \\ \Delta E'_q \\ \Delta E_{fd} \\ \Delta v_{dc} \end{bmatrix} + \begin{bmatrix} 0 & 0 & 0 & 0 \\ -\frac{k_{pe}}{M} & -\frac{k_{p\delta e}}{M} & -\frac{k_{pb}}{M} & -\frac{k_{p\delta b}}{M} \\ -\frac{k_{qe}}{T'_{do}} & -\frac{k_{q\delta e}}{T'_{do}} & -\frac{k_{qb}}{T'_{do}} & -\frac{k_{q\delta b}}{T'_{do}} \\ -\frac{k_A k_{ve}}{T_A} & -\frac{k_A k_{v\delta e}}{T_A} & -\frac{k_A k_{vb}}{T_A} & -\frac{k_A k_{v\delta b}}{T_A} \\ k_{ce} & k_{c\delta e} & k_{cb} & k_{c\delta b} \end{bmatrix} \begin{bmatrix} \Delta m_E \\ \Delta\delta_E \\ \Delta m_B \\ \Delta\delta_B \end{bmatrix} \quad (19)$$

Where Δm_E, Δm_B, $\Delta\delta_E$ and $\Delta\delta_B$ are the deviation of input control signals of the UPFC. Also in this study IEEE Type- ST1A excitation system was used.

IV. CONTROLLER DESIGN

Lead-Lag Controller Design:

As mentioned before, in this study two different controllers have been used to damp LFO. The first one is conventional lead-lag controller. It consists of gain block, washout block, lead-lag compensator block. The washout block is considered as a high-pass filter, with the time constant TW. Without this block steady changes in input would modify the output. The value of TW is not critical and may be in the range of 1 to 20 seconds. In this study, the parameters obtained from lead-lag controller design were used.

Adaptive Neuro-Fuzzy Controller Design:

Another controller is adaptive neuro-fuzzy controller. In this section, we will present the procedure of designing of the adaptive neuro-fuzzy controller. In this research, the neuro fuzzy controller has 2 inputs that are $\Delta\delta$ and $\Delta\omega$ and it has 1 output that is $f \in \{ \Delta m_E, \Delta\delta_E, \Delta m_B, \Delta\delta_B \}$. For each input 20 membership functions and also 20 rules in the rules base is considered. Figure 5 demonstrates the structure of adaptive neuro-fuzzy controller for a sugeno fuzzy model with 2 inputs and 20 rules.

In Figure 9, a Sugeno type of fuzzy system has the rule base with rules such as follows:

1. If $\Delta\delta$ is A_1 and $\Delta\omega$ is B_1 then $f_1=p_1\,\Delta\delta+q_1\,\Delta\omega+r_1$.
2. If $\Delta\delta$ is A_2 and $\Delta\omega$ is B_2 then $f_2=p_2\,\Delta\delta+q_2\,\Delta\omega+r_2$.

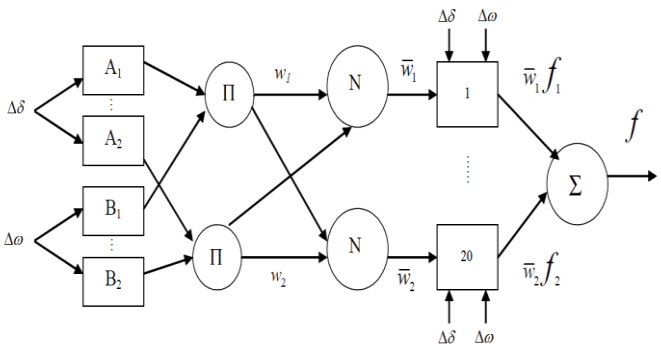

Fig.9. ANFIS architecture for a two-input Sugeno fuzzy model with 20 rules

μ_A and μ_B are the membership functions of fuzzy sets A_i and B_i for i=1,…,20. In evaluating the rules, we choose product for T-norm (logical *and*). Then controller could be designed in following steps:
1. Evaluating the rule premises:

$$w_i = \mu_{A_i}(\Delta\delta)\mu_{B_i}(\Delta\omega), \quad i = 1,\ldots,20. \tag{20}$$

2. Evaluating the implication and the rule consequences:

$$f(\Delta\delta,\Delta\omega) = \frac{w_1(\Delta\delta,\Delta\omega)f_1(\Delta\delta,\Delta\omega)+\ldots+w_{20}(\Delta\delta,\Delta\omega)f_{20}(\Delta\delta,\Delta\omega)}{w_1(\Delta\delta,\Delta\omega)+\ldots+w_{20}(\Delta\delta,\Delta\omega)} \tag{21}$$

Or leaving the arguments out

$$f = \frac{w_1 f_1+\ldots+w_{20}f_{20}}{w_1+\ldots+w_{20}} \tag{22}$$

This can be separated to phases by first defining

$$\overline{w}_i = \frac{w_i}{w_1+\ldots+w_{20}}, \quad i = 1,\ldots,20. \tag{23}$$

These are called normalized firing strengths. Then *f* can be written as

$$f = \overline{w}_1 f_1+\ldots+\overline{w}_{20}f_{20}. \tag{24}$$

The above relation is linear with respect to p_i, q_i, r_i and i=1,…,20. So parameters can be categorized into 2 sets: set of linear parameters and set of nonlinear parameters. Now Hybrid learning algorithm can be applied to obtain values of parameters. Hybrid learning algorithm is combination of linear and nonlinear parameters learning algorithm. This network is called adaptive by Jang and it is functionally equivalent to Sugeno type of a fuzzy system. It is not a unique presentation. With regard to the explanations presented and with the help of MATLAB software, adaptive neuro-fuzzy controller can be designed. The rules surface for designed controller is shown in figure10. One of the advantages of using neuro-fuzzy controller is that we can utilize one of the designed controllers for instance Δm_e controller in place of the other controllers. While if we use conventional lead-lag controller, for each controls parameters, a controller must be designed.

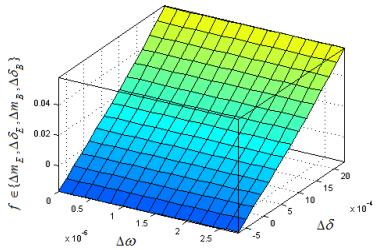

Fig.10. The rules surface

The membership functions for input variable Δω are presented in figure 11.

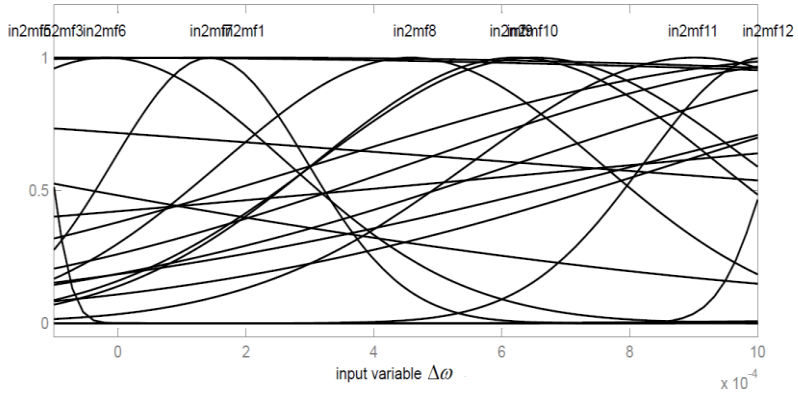

Fig.11 The membership functions for input variable Δω

V. RESULTS

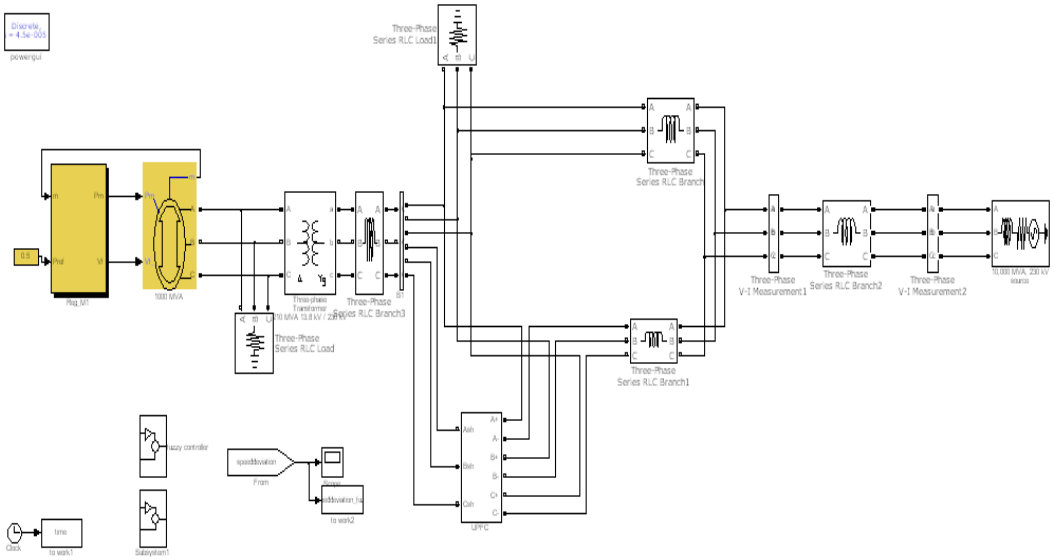

Fig.12 Matlab simulation circuit

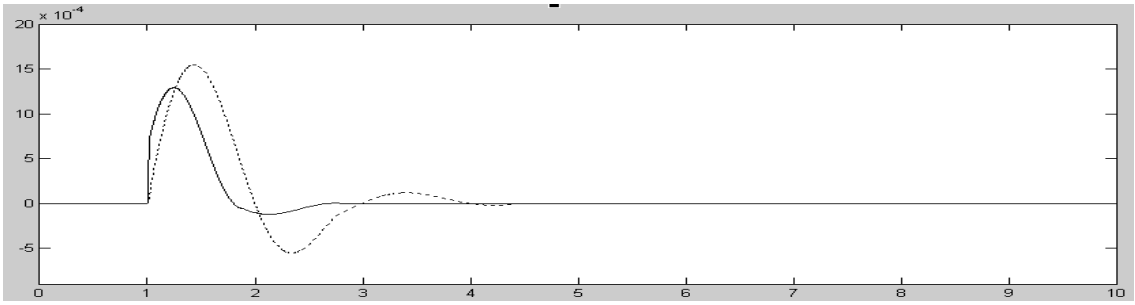

Fig.13 Angular velocity deviation during step change in mechanical input power for nominal load (me Controller)

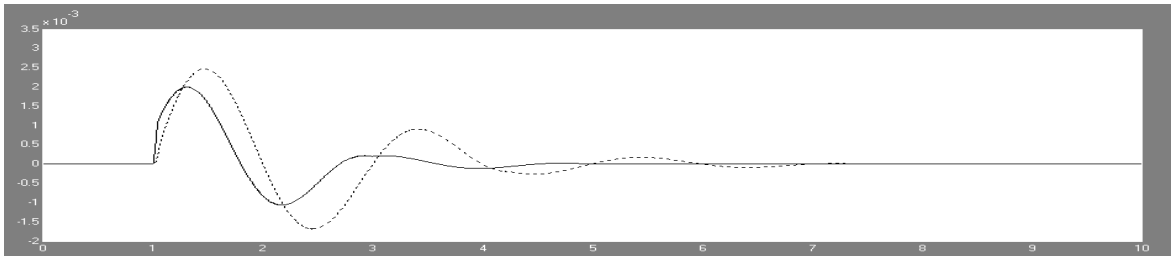

Fig.14 Angular velocity deviation during step change in mechanical input power for light load (me controller)

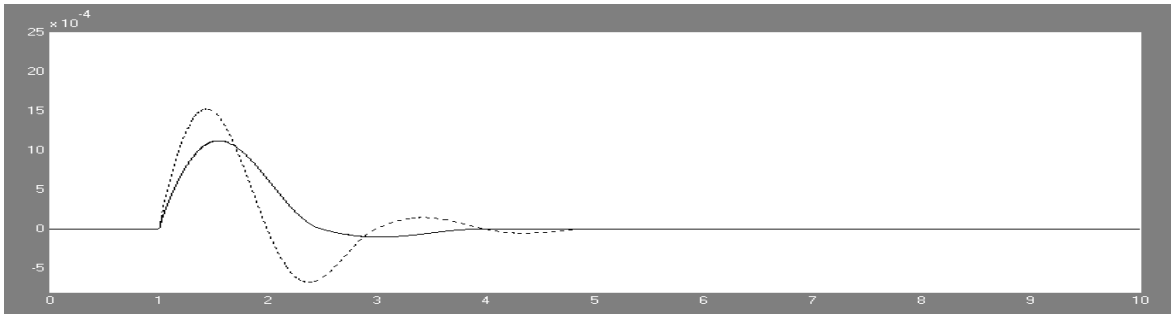

Fig.15 Angular velocity deviation during step change in mechanical input power for nominal load (δe Controller)

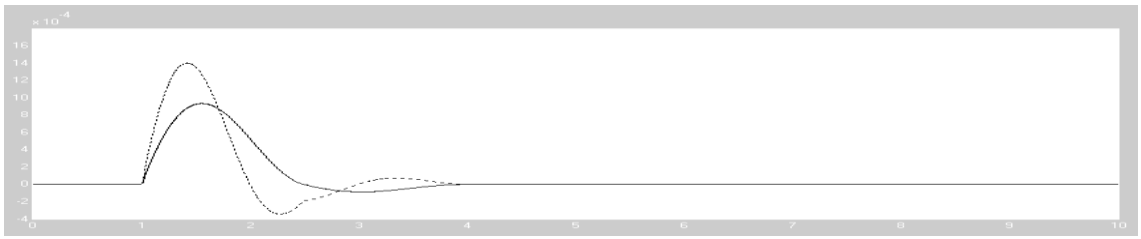

Fig.16 Angular velocity deviation during step change in mechanical input power for nominal load (mb Controller)

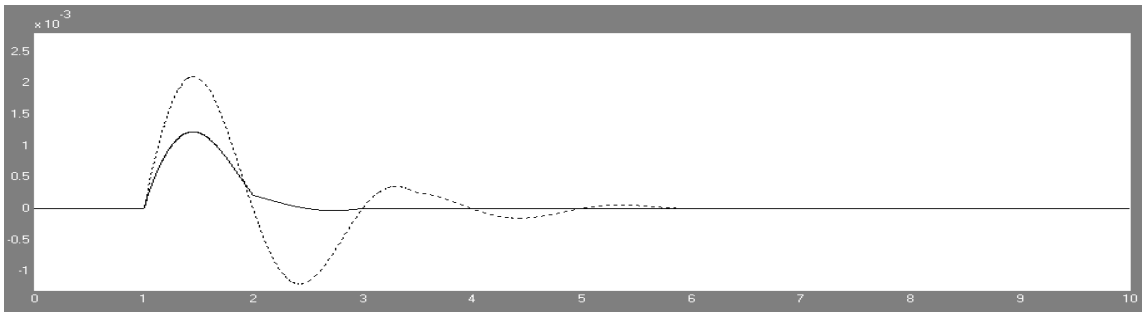

Fig.17 Angular velocity deviation during step change in mechanical input power for nominal load (δb Controller)

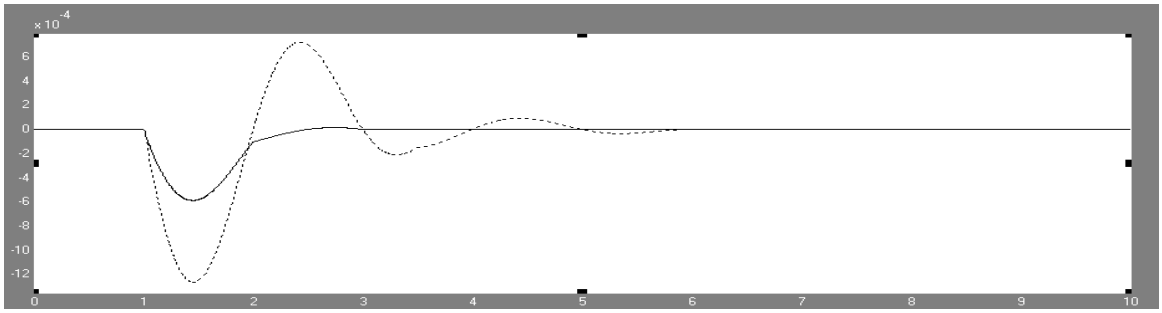

Fig. 18 Response of angular velocity for 5% step change in reference voltage in the case of nominal load (δb Controller)

VI. CONCLUSIONS

With regard to UPFC capability in transient stability improvement and damping LFO of power systems, an adaptive neuro-fuzzy controller for UPFC was presented in this paper. The controller was designed for a single machine infinite bus system. Then simulation results for the system including neuro-fuzzy controller were compared with simulation results for the system including conventional lead-lag controller. Simulations were performed for different kinds of loads. Comparison showed that the proposed adaptive neuro-fuzzy controller has good ability to reduce settling time and reduce amplitude of LFO. Also we can utilize advantages of neural networks such as the ability of adapting to changes, fault tolerance capability, recovery capability, High-speed processing because of parallel processing and ability to build a DSP chip with VLSI Technology.

REFERENCES

[1] N. G. Hingorani and L. Gyugyi, Understanding FACTS: Concepts and Technology of Flexible AC Transmission System, IEEE Press, 2000.

[2] H.F.Wang, F.J.Swift," A Unified Model for the Analysis of FACTS Devices in Damping Power System Oscillations Part I: Single-machine Infinite-bus Power Systems**",** IEEE Transactions on Power Delivery, Vol. 12, No. 2, April 1997, pp.941-946**.**

[3] L. Gyugyi, C.D. Schauder, S.L. Williams, T.R.Rietman, D.R. Torgerson, A. Edris, "The Unified Power Flow Controller: **A** New Approach to Power Transmission Control", IEEE Trans., 1995, pp. 1085-1097.

[4] Wolanki, F. D. Galiana, D. McGillis and G. Joos, "Mid-Point Sitting of FACTS Devices in Transmission Lines," IEEE Transactions on Power Delivery, vol. 12, No. 4, 1997, pp. 1717-1722.

[5] M. Noroozian, L. Angquist, M. Ghandari, and G. Anderson, "Use of UPFC for optimal power flow control", IEEE Trans. on Power Systems, vol. 12, no. 4, 1997, pp. 1629–1634.

[6] A Nabavi-Niaki and M R Iravani. 'Steady-state and Dynamic Models of Unified Power Flow Controller (UPFC) for Power System Studies.' IEEE Transactions on Power Systems, vol 11, 1996, p 1937.
[7] K S Smith, L Ran, J Penman. 'Dynamic Modeling of a Unified Power Flow Controller.' IEE Proceedings-C, vol 144, 1997, pp.7.
[8] H F Wang. 'Damping Function of Unified Power Flow Controller.' IEE Proceedings-C, vol 146, no 1, January 1999, p 81.
[9] H. F. Wang, F. J. Swift, "A Unified Model for the Analysis of FACTS Devices in Damping Power System Oscillations Part I: Single-machine Infinite-bus Power Systems," IEEE Transactions on Power Delivery, Vol. 12, No. 2, April, 1997, pp. 941-946.
[10] P. Kundur,"Power System Stability and Control", McGraw-Hill.

Mr. Gundala Srinivasa Rao[1] *is presently working as Assistant Professor in the department of Electrical & Electronics Engineering at Sri Venkateswara Engineering College, Suryapet. He has 3 years of teaching experience. He obtained master of technology in Power Electronics from Jawaharlal Nehru Technological University, Hyderabad.*

Mr. Venugopal Reddy Bodha[2] was born in India, in 1985.He received the B.Tech degree in Electrical &Electronics Engineering from J.N.T.U, Hyderabad, India, in 2007, And the M.Tech degree in Power Electronics from J.N.T.U, Hyderabad, India, in 2012.He is currently *working as Assistant Professor in the department of Electrical & Electronics Engineering at Sri Venkateswara Engineering College, Suryapet, A.P, India . He has 6 years of teaching experience.*

American Journal of Engineering Research (AJER)
e-ISSN : 2320-0847 p-ISSN : 2320-0936
Volume-02, Issue-11, pp-61-70
www.ajer.org

Research Paper Open Access

Automated Luggage Carrying System

Md. Imran Khan, Saad Bin Siddique, Nazmul Hassan, Md.Towhid Chowdhury
[1](CSE, AIUB, Bangladesh), [2](EEE, AIUB, Bangladesh), [3](EEE, AIUB, Bangladesh), [4](EEE, AIUB, Bangladesh)

Abstract: - Integument personal luggage carrying system can add comfort to the explorer inside an infrastructure possibly airport. The system consists of automated vehicles that can be borrowed and it automatically follows the borrower inside an infrastructure with luggage. These also maintain a distance from the borrower and do not follow in some of the restricted areas like restroom for comfort. After service these will automatically move to the docking station for charging and reuse. In this thesis we have identified the basic construction required for the six wheels based rigid robot body and the basic person tracking movement of the smart card holder for airport traveler's personal luggage carrier.

Keywords: - *Caring luggage , Obstacles detection, , Card tracking.*

I. INTRODUCTION

Automation is the use of machines, control systems and information technologies to optimize productivity in the production of goods and delivery of services. It is the use of control systems and information technologies to reduce the need for human work in the production of goods and services. In the scope of industrialization, automation is a step beyond mechanization. In Airport, Automated luggage loading system is introduced so many years ago which moves the luggage from the check-in to the belts servicing the flights but a passenger need to carry his/her own luggage's from the entrance of the airport till the check-in into the airport with the help of conventional luggage carrying system. Conventional luggage carrying system is both time consuming and labor intensive. At the same time it is an expensive process and slow. The proposed Automated System for luggage carrying system can provide those features needed to overcome the problems mentioned above. A real-time monitoring system using an automated system is introduced to ensure the proper movement following the Smartcard carrying passenger. For the implementation of the desired automated system, a six wheel based robot has been designed. This Smartcard is sending signal to the tower. An ultrasonic sensor is used on the automated system to sense the signal that is received by this sensor from the tower where triangular method takes place. That ultrasonic sensor detects the distance of the location of the associated Smartcard as well as the user. Then the automated system uses the person following algorithm with a view to finding out the exact position of the smart card user and follow the user. The automated system will always keep 2mitre distance from the user with a view to avoiding clashes with the user. The Smartcard will be located at the pocket of the user as well as passenger throughout the whole airport before check-in. If there two or more automated systems are devoted doing the same job for their own smartcard holder, the proper signal is received by the sensors of the each robots for their own smart-card holder and that is done with the help of triangular method. The triangular method sends the right signal to that specific ultrasonic sensor that is already waiting to getting a signal from its own Smartcard. An ultrasonic sensor is thus devoted to work with only one Smartcard. Both the Smart card and the ultrasonic sensor continuously send and receive the signal respectively. This automated system is designed in such a way so that it can sense the location of the restricted area such as wash-room; hospital and police control room inside the airport and keeps itself away from the restricted areas. In such cases there can be waiting rooms beside those kinds of rooms where the user can park their robots while using those confidential areas. This automated system is also designed in such a way so that it can sense any kind of obstacles located in front of it and easily avoid them without having any clashes with the obstacles. If there is any kind of obstacles in front of the automated system depending on the situations it is capable of taking the alternative way to follow its Smartcard holder. The proposed automated luggage carrying system is mainly designed here to walk through the airport smoothly. Airport should have one rest room and one

waiting room per each restricted area so that the automated system can gain some power while their smartcard holder is stuck. If 20% of the charge remains, the automated system can get back to the rest place and get some power to work again. When the user is done, the user will keep the smart card into the card holder located on the surface of rigid body. Then the automated proposed system will get back to the rest place.

II. OBJECTIVES

This thesis is done to find out a reliable automated system for the luggage carrying system
This thesis has following objectives:

- To identify the efficiency of convention luggage carrying system and the proposed system.
- To demonstrate the benefits of automated system over conventional system considering some important parameters such as speed, time, human labor and cost expenses.
- To identify the drawbacks of current conventional system.
- To demonstrate the scope of improving the proposed automated luggage carrying system.

III. SCOPE

Automated luggage carrying system in airport has great scope in every country in the world as well as Bangladesh. Luggage handing is always at the heart of an airport. Reducing the manpower required to distribute the baggage as required and efficiency in terms of reliability, maintainability and future flexibility are the main motivation of this automated luggage carrying system. This automated luggage carrying system is designed to arrive the luggage's to the specific smartcard user at a particular distance in the airport would be barely even touched by the human hands once they were loaded into the automated system. If the environment of the airport fully supported the demands of the automated system, it will become much more easy and effective in future to work with this automated system.

IV. WHEEL BASED RIGID BODY CONSTRUCTION

The very first challenge of the research was to implement a rigid body with six wheels. Along with these six wheels six motors are associated where each wheel is basically devoted to rotate one motor. In all robotics applications, mechanical complexity is one of the major sources of failure and considerably increases the cost. To implement this type of wheel based body, we faced mechanical complexity several times. We had to collect materials from "techs hop BD" and sometimes from many other local markets located in Dhaka. We then considered a standard size of the rigid body that is capable of carrying luggage. Then we measured the width and height carefully and constructed this.

V. SYNCHRONOUS ROTATION OF MOTORS

Then the second challenge was to make these wheels as well as motors to rotate synchronously with each other. Then after a few days we were able to rotate the motor but at first it was asynchronous. Then we had to analyze the current problem. We tried to figure out the possible solutions and we did in a short span of time. Thus our design emphasizes mechanical simplicity and promotes robustness. After the synchronous rotation of the motors, we noticed that the rigid body cannot move so fast how we desired as the battery we used was not so powerful. But the use of powerful battery will solve this problem at a glance. So, in future if anybody wants to improve the automated system there will be no inconsistency or lack of information from our documentation.

VI. SMART CARD AND ULTRA SONIC SENSOR

At our proposed automated System, we use Smart card that will be located on the pocket of the user and Ultra Sonic Sensor on the rigid robot body. This Smartcard is continuously sending signal to the tower and the Ultra Sonic Sensor is used on the rigid robot body to sense the signal that is received by this sensor from the tower where triangular method takes place. That Ultra Sonic Sensor detects the distance of the location of the associated Smartcard as well as the user. In this way, location of the user from the proposed automated system is detected but the exact position of the user cannot be determined. To know the proper use of smart card and sensors and how to make them work with user and rigid body respectively, we studied a lot of documentation of these items available on the internet and checked some of them practically and finally selected Ultra Sonic Sensor.

VII. IMPLEMENTATION OF THE PERSON TRACKING ALGORITHM

This was the challenging portion for us to implement an algorithm which results the rigid robot body to track the associated smartcard holder as well as the user. As the proper usage of Smart card and Ultra Sonic Sensor is only able to provide us with the distance of the location of the user but not

the exact position of the user. So , to implement the automated system as we desired we were needed to implement a person tracking algorithm which will not only teaches the rigid robot body to trace the person carrying associated smart card correctly but also to face the obstacles which may the proposed automated system may face while following the passengers through the airport. Thus the proposed automated system, if meets any kind of the obstacles while following the smart card holder it will easily calculate the alternative way to avoid the clash and follow its smart card holder without any kinds of hazards.

VIII. LOCOMOTION

The robot will deviate from its path automatically if it faces any hindrance in its path of movement. We have put an ultrasonic sensor at the front of robot and its function is to find what angles the robot should drive. It can be programmed on which side it should move, either front, back, left or right.

8.1 Forward

It consists of 6 wheels and the forward rotation (Fig 1) of all these wheels will cause the advancement of the robot.

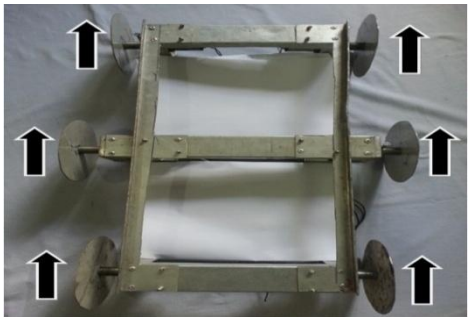

Figure 1: Forward Motion

8.2 Backward

Likewise, the backward rotation (Fig 2) of the wheels will make the robot move back.

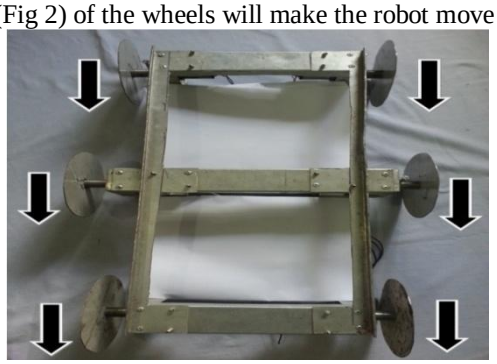

Figure 2: Backward Motion

8.3 Right

Besides, if three wheels at right rotate forward (Fig 3) and the other three wheels at left rotate backward then the robot will move towards right.

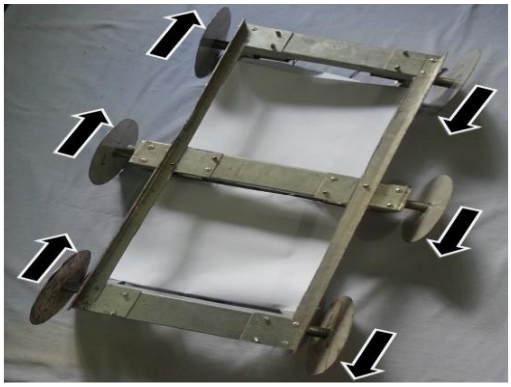

Figure 3: Towards Right Motion

8.4 Left

Again if three wheels at left rotate forward (Fig 4) and the other three at right rotate backward then the robot will move towards left.

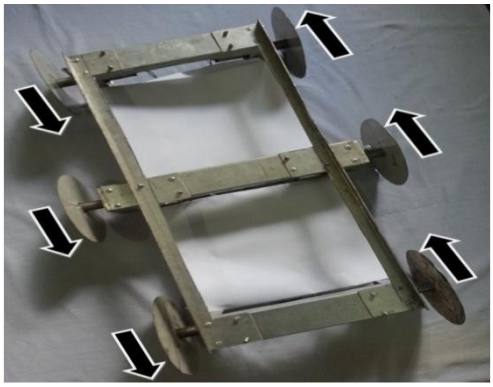

Figure 4: Towards Left Motion

IX. SMART CARD

A smart card is a wireless device that includes an embedded integrated circuit that can be either a secure microcontroller or equivalent intelligence with internal memory or a memory chip alone. The card connects to a reader with direct physical contact or with a remote contactless radio frequency interface. With an embedded microcontroller, smart cards have the unique ability to store large amounts of data, carry out their own on card functions. Smart cards are made of plastic, generally polyvinyl chloride, but sometimes polyethylene terephthalat based polyesters, acrylonitrile (Fig 5) butadiene styrene or polycarbonate.

Figure 5: Smart card.

It resembles a credit card in size and shape, but inside it is completely different. It has an inside a normal card is a simple piece of plastic. The inside of a smart card usually contains an **embedded microprocessor.** The microprocessor is under a gold contact pad on one side of the card. Smart cards can provide identification, authentication, data storage and application processing. Smart cards may provide strong security authentication for single sign-on within large organizations because the microprocessor on the smart card is there for **security. However,** the smart card functions in such a way that it sends a signal to the nearby tower and the tower in turn sends another signal to the robot. Following such method the robot can always know the place about of the user. Also as the robot finishes its work, the user then puts the smart card on its holder and the robot returns to the charging room.

X. CHARGING (REST PLACE)

The robot runs by battery. The battery is charged for reviving power. If the battery shows charge less than 20% then the robot returns to a charging room. Moreover, in case as soon as the robot finishes its function provided by the user then also it returns to the charging room. However in the charging room, the robots stay in a queue. Each of the robots consists of power connector on (Fig 6) each sides of the body.

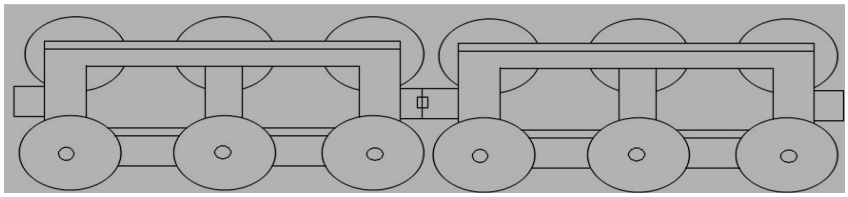

Figure 6: Charging queue.

So automatically the robots after entering the room will line up forming a joint. In this state during charging, if the user needs any robot then the one staying at the front of the queue will be appointed for the

respective job. Hence the robot next to the one that has been taken will then come forward and stand on the first position. Thus following this sequence the latter robots will take the initial position of the former robot and do its function as guided by the instructor.

XI. RESTRICTED AREA

In the places like airport, there are spaces for hospital, police control room, washroom etc. So in such cases there can be waiting rooms beside those kinds of rooms where the user can park their robots while going to those confidential areas. The user under such circumstance will use the triangulation method to find the robot. The smart card carried by the user will send a signal to the nearby tower and the tower will send another signal in return to find the actual position of the robot. The robot receiving the signal from the tower after each 2 seconds will advance towards the user and finally the user can get back his robot.

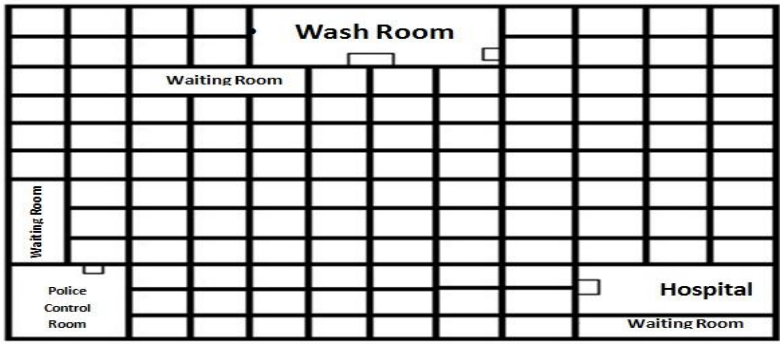

Figure 7: Operation policies while entering the restricted areas

In the cases where the rooms contain 2 doors, if the user enters through one and leaves through the other door then the robot using the same technique can get back to its user.

XII. ALGORITHM

Navigation is a major challenge in the field of artificial intelligence. There are several techniques for navigation of robot over a grid and these papers represent an approach for navigation on a grid by using breadth first algorithm. Here the entire grid of m*n is converted into a tree and with the help of these tree we apply BFS for traversing. We develop an approach for searching an object and also able to avoid an obstacle which was placed in a junction.

There are various tasks which is performed over a grid such as material handling, obstacle avoidance and object detection etc. requires a strong navigation technique which can be fulfill by using these algorithm. The major problem we faces while traversing on a grid is to maintain its current location after encounter a junction and also the path planning is required when an obstacle is detected. These problems are easily tractable with breadth first search. Here we convert the entire grid into a tree type structure. Where we apply BFS for searching the next node. The algorithm is briefly discussed in later section.

A grid is represent as the [m * n] matrix where m is the number of rows and n is the number of columns. The rows and columns are the black line which is drawn over a white surface or white line which is drawn on black surface.

To navigate over a grid we have to follow Cartesian coordinate system for finding the current location on the grid. The robot set its initial location as (0, 0) and maps the entire quadrant according to it. The left node as (-1, 0) the right node as (1, 0) and the node below the origin is taken as (0,-1) and above the origin as (0, 1) respectively. The robot has also to maintain its direction while moving forward, left or right it has to update the direction according to the turn.

The major problem that we faces in navigation is what is decision taken by the bot to find the next coordinate which can be easily achievable when a tree is constructed. Another problem we are face that is at the time of obstacle detection which can also be solve with these approach. The obstacle and object is placed on the junction. The obstacle is a cubical block; we consider the purely black or white block as an object. The decision taken by the bot after obstacle encounter is discussed in later section.

XIII. ENVIRONMENTS USED FOR ROBOT NAVIGATION

13.1Type of Grid

We can use the grid of any dimension of [m * n] as shown in figure-1.The grid may also consist of combination of multiple grid. For such situation we have to place two extra sensors in below the center of both

the wheel. These sensors are capable of to keep the robot into the grid with a condition i.e. when all the sensors in (white or black) we have to take (right or left) turn until the line is detected.

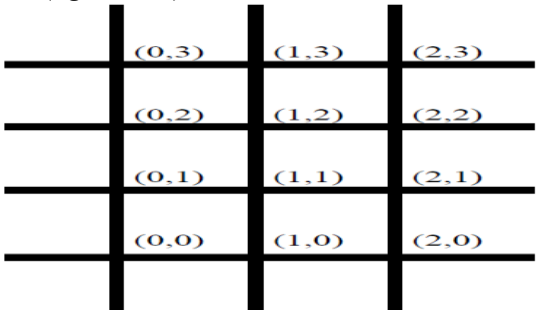

Figure 8: Grid [3*4] (shows about a black line which is drawn in a white surface or vice-versa).The junction is labeled as according to its coordinate system.

13.2 Grid Mapping

The grid is map according to Cartesian coordinate system. Robot sets the initial node as an origin and maps the entire grid according to origin and its direction which shows in (fig 8).

XIV. ALGORITHM USED

14.1 Breadth First Search

In breadth first search require five different parameter such as unexplored vertex, visited vertex, unexplored edge, discovery edge, cross edge. Firstly the node is visited which is closer to the root node or we can say the node which is at the same levels are visited and then the second level and goes to higher level accordingly.

BFS (G, s)

1. For each vertex u ϵ V[G] — {s}
2. Do color[u]←WHITE
3. D[u]← ∞
4. Π[u]←NIL
5. Color[s] ←GRAY
6. d[s] ← 0
7. Π[s] ← NIL
8. Q ← Ø
9. ENQUEUE(Q,s)
10. While Q ≠ Ø
11. Do u ← DEQUEUE(Q)
12. For each v ϵ Adj[u]
13. Do if color [v] = WHITE
14. Then color[v] ← GRAY
15. d[v] ←d[v] +1
16. Π[v] ← u
17. ENQUEUE(Q,u)
18. Color[u] ← BLACK

14.2 Transformation of Grid

While using BFS we have to construct a tree by the use of the grid. By using these transformation reduces the complexity while in navigation. Transformation to tree requires one stack such as traverse stack it keep the record of the visited node. This stack is useful to detect next node. If the coordinates of next node is matched with the traverse stack then such nodes are avoided. While constructing the node on a tree we have to move on higher level on a grid. And the junction of two adjacent node of parent node is treated as a connected node. As in Fig 1 Grid the transformation is done accordingly. The root node i.e. (0,0) consists two connected node such as (0,1) and (1,0) which is at the same level are placed as a child node of the root node and another node of (1,1) is adjacent node of (1,0) and (0,1) are also used as a connected node of (0,0).while connecting as a child node of (0,0) the connected node is checked into a traverse stack if these nodes are presents in the stack then such nodes are avoided and unvisited node are marked as a child node. So the corresponding tree of the grid is shown below is free from obstacle.

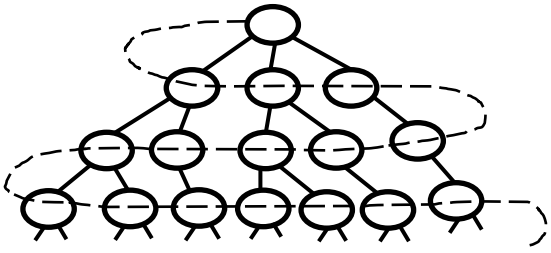

Figure 9: Grid transformation into corresponding tree.

In (fig 9) the bot start from the root node i.e. 00(due to reducing the complexity (0,0)(3,4)(6,3) etc. are written as 00,34,63) it will detect two connected node i.e. 01 ,10 and 11 as explained above. So by these properties the entire tree is formed.

14.3 Grid Transformation in presence of obstacle

The transformation is little bit clumsy when an obstacle is arrived in a junction. Such problem can also be solving by tree traversal algorithm but here we require another stack such as obstacle stack it keeps the record of obstacle. When the obstacle is detected by the bot it has to move into the next level and begin with the initial node of the next level and move up to the node it surpasses the obstacle node and again move to the previous node. For example if in a grid consists an obstacle at (1, 1) and (2, 2). So the bot has to follow the same algorithm as without obstacle but if obstacle is encounter than it has to place the value of coordinate into the obstacle stack and move to next level of starting node i.e. (0, 2) and move until the obstacle node is surpasses i.e. (3, 1) than it has to move to previous level and accordingly as shown in below graph.

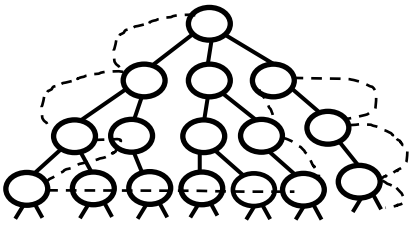

Fig 10: Bot Navigation when grid consists of an obstacle.

In (fig 3.10) grid consist of an obstacle at junction (1,1) and (2,2) whereas the dashed line shows the path i.e. 00->01->02->12->03->13->23->33->32->31->21->10->20->30. The bot navigate until the desired object is detected and give the shortest path from the root node to the object.

14.4 Calculating direction

To maintain the location of boot on any arbitrary points on a grid we have update the direction and value (x, y) which was (0, 0) initially and maintain according to its turn.

Direction	Turn	Set Direction	Set Co-ord.
North	Forward	North	Y++
North	Right	East	X++
North	Left	West	X--
East	Forward	East	X++
East	Right	South	Y--
East	Left	North	Y++
West	Forward	West	X—
West	Right	North	Y++
West	Left	South	Y--
South	Forward	South	Y--
South	Right	West	X--
South	Left	East	X++

Figure 11: Position Calculation.

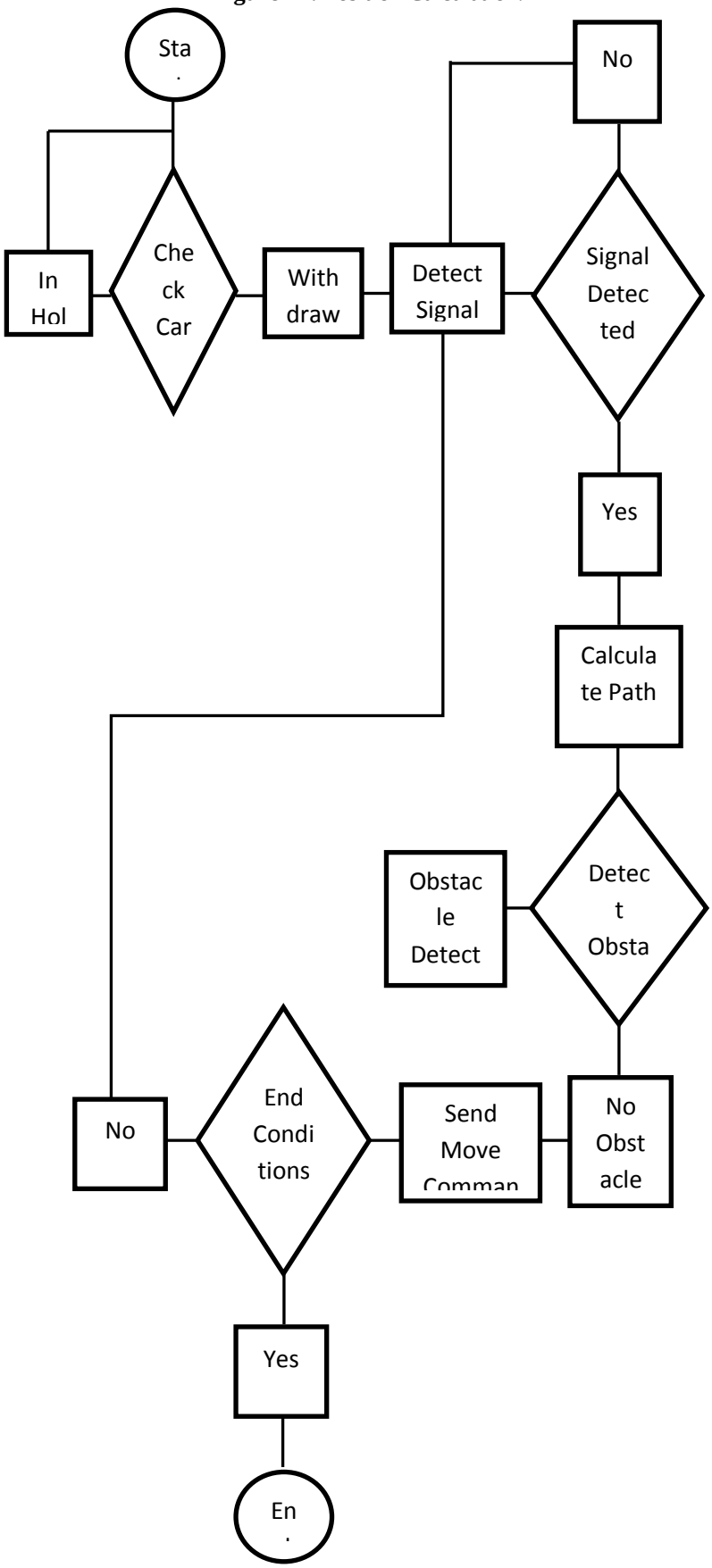

Figure 12: Flow control of overall system.

XV. HOW TO DETECT

Detection is the process of finding both position user and robot. Here we use a wire-free detection method such as triangulation with active beacons. Triangulation with active beacons is a racy, precise, pliant and widely used method of absolute detection. Many types of triangulation algorithms have been offered. These are some examples: Geometric Triangulation, Iterative Search, Newton-Raphson Iterative Search and Geometric Circle Intersection algorithm from the Imperial College Beacon Navigation System triangulation using three circle intersection triangulation using two circle intersection Position Estimator algorithm. The term absolute detection was defined by Drumheller as "the enabling of a mobile robot to determine its position and preference in a way that is independent of assumptions about previous movements".

Among them we are used here Generalized Geometric Triangulation Algorithm by João SENA ESTEVES. The Geometric Triangulation algorithm allows the self localization of a robot on a plane. However, the three beacons it uses must be "properly ordered" and the algorithm works consistently only when the robot is within the triangle formed by these beacons. Triangulation is based on the measurement of the bearings of the robot relatively to beacons placed in known positions. It differs from trilateration, which is based on the measurement of the distances between the robot and the beacons. These beacons are also called landmarks by some authors. According to the term beacon is more appropriate for triangulation methods.When navigating on a plane; three distinguishable beacons - at least - are required for the robot to localize itself (Fig. 3.12). $\lambda 12$ is the oriented angle "seen" by the robot between beacons 1 and 2. It defines an arc between these beacons, which is a set of possible positions of the robot [20]. An additional arc between beacons 1 and 3 is defined by $\lambda 31$. The robot is in the intersection of the two arcs. Usually, the use of more than three beacons results in redundancy. In, triangulation with three beacons is called three-object triangulation. Consider (Fig. 3.12) three distinguishable beacons in a Cartesian plane, arbitrarily labeled 1, 2 and 3, with known positions (x_1, y_1), (x_2, y_2) and (x_3, y_3). L_{12} is the distance between beacons 1 and 2. L_{31} is the distance between beacons 1 and 3. L_1 is the distance between the robot and beacon 1. In order to determine its position (x_R, y_R) and preference θ_R, the robot measures - in counterclockwise fashion - the angles λ_1, λ_2 and λ_3, which are the beacon preferences relative to the robot heading?

Algorithm lines 2 through 5 compute the oriented angles λ_{12} and λ_{31} "seen" by the robot between beacons 1 and 2 and beacons 3 and 1, respectively. Both λ_{12} and λ_{31} are always positive.

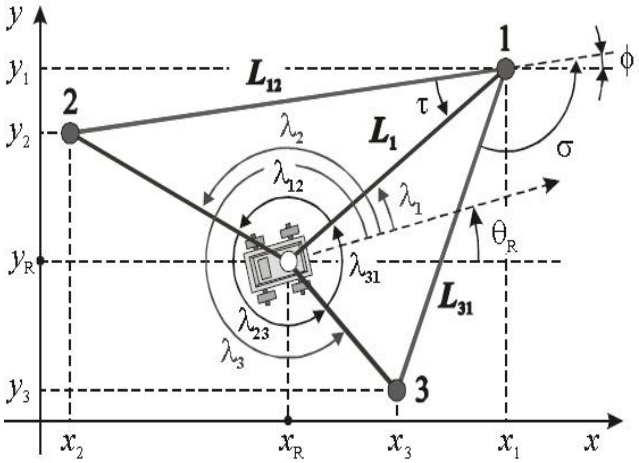

Figure 13: Simulation results for beacons labeled in counterclockwise fashion.

XVI. CONCLUSION

In this thesis we have identified the basic construction required for the six wheels based rigid robot body and the basic person tracking movement of the smart card holder. We have also identified what the proposed automated luggage carrying system would do if there are obstacles in the working route. Moreover there are many limitations left in the research due to time and lack of resources. If there are any restaurant located in the 2nd floor of the airport the proposed automated luggage carrying system cannot cross stairs. Most of the limitations in this research are created by the limitations of resources. But if there are enough resources available, the research can be done in a proper way using high powered motors and high powered battery so that the proposed automated luggage carrying system can go through any kinds of environment into airport such as stairs and unsmooth floor and carry a huge amount of loads so that the efficiency increases in an exponential way. If there are too many obstacles or hazards blocks each and every alternative way to reach the smart card user without having any clashes, the proposed automated system cannot decide quickly which path

to select to reach the user safely and thus performance decreases. In future, if those limitations are removed from the proposed automated system, the following system will have better performance to serve the user.

XVII. ACKNOWLEDGEMENT

This project is the result of our cordial effort and our supervisor's initiative and constant motivation. But first of all we would like to be grateful to the Almighty ALLAH, Who gives us the effort to work on this project for the last one/two semester(s). Special thanks go to our honourable supervisor Md. Hafizur Rahman. His excellent supervision, constant support makes this hypothesis possible. We also want to thank Mashiour Rahman, Head, Computer Science Department, for his generous support throughout the entire hypothesis. Moreover, we would like to show our immense gratitude to our Dean, Professor Dr. Tafazzal Hossain, and Vice Chancellor, Dr. Carmen Z. Lamagna, for their constant guidance and support all through our University life.

Last, but not least, we thanks to our respectable parents for giving our life in the first place, for educating us with aspect from both arts and sciences, for unconditional support and encouragement to pursue our interests, even when interests went out the boundary....

BIBLIOGRAPHY

[1] Reuleaux, F., 1876 The Kinematics of Machinery, (trans. and annotated by A. B. W. Kennedy), reprinted by Dover, New York (1963)
[2] Brady, Ian."Programmable logic controllers - benefits and applications". PLCs. Retrieved 5 December 2011.
[3] Allen, T., and M. S. Morton, eds. 1994. Information Technology and the Corporation of the 1990s. New York: Oxford University Press.
[4] http://www.gemalto.com/companyinfo/download/smartcardforum.pdf
[5] http://www.labelsensors.com/choose/labelSensorTypes.html
[6] Sreekanth Reddy Kallem,"Artificial Intelligence Algorithms"IOSR Journal of Computer Engineering (IOSRJCE).
[7] Sebastian Thrun,"Robotic Mapping:A Survey" Feb 2002, CMU-CS- 02-111, School of Computer Science, Carnegie Mellon University Pittsburgh.
[8] Robert J.Szczerba Danny Z.Chen John J. Uhran,"A Grid-Based Approach for Finding Conditional Shortest Paths inan Unknown Environment,Nov 1994.
[9] Algorithm Concept by NarasimhaKarumanchiData Structures and Algorithms Made Easy second edition.
[10] Joachim Hertzberg and Frank Kirchner. Landmark-based autonomous Navigation in sewerage pipes. In Proceedings of the First Euromicro Workshop on Advanced Mobile Robots (EUROMICRO).
[11] Hans P. Moravec. Sensor fusion in certainty grids for mobile robots. AI Magazine.
[12] Michael J.Milford Janet Wiles Gordon F.Wyeth, "Solving Navigational Uncertainty Using Grid Cells on Robots" November 2010, school of engineering systems, Queensland
[13] CarstenBuschmann Florian Muller and Stefan Fischer,"Grid- BasedNavigation for Autonomous,Mobile Robots",Institute of Operating Systems And Networks,Technical University of BraunschweigBraunschweig,Germany.
[14] http://www.atmel.com/images/doc2466.pdf
[15] Ahmedullah Aziz, Md. Shafayat Hossain and Mohammad Wahidur Rahman "Programming and construction of Ahmedullah-A Fast Grid solver robot"International Journal of Information Technology, Control and Automation (IJITCA) Vol.3, No.1, January 2013.
[16] IR Sensors reference from Robosoft System "IR Sensor Based Obstacle Detection Sensor Module".
[17] Richard T.Annoy,"Design a Line Maze Solving Robot", april2009http://www.pololu.com/file/0J195/line-maze-algorithm.pdf.
[18] Leonard, John J. and Durrant-White, Hugh F., Directed Sonar Sensing for Mobile Robot Navigation. Kluwer Academic Publishers, 1992.
[19] Borenstein, J., Everett, H. R. and Feng, L., Where am I? Sensors and Methods for Mobile Robot Positioning, Technical Report, The University of Michigan, 1996.
[20] NDC Automation Inc., Advantage Lazerway™ - Laser Guidance vs. Inertial Guidance, Technology Brief, USA (980129), 1998.
[21] Mentor AGVS, AGV Laser Guidance. 1999. http://www.mentoragvs.com/laser.html
[22] Generalized Geometric Triangulation Algorithm for Mobile Robot Absolute Self-Localization by João SENA ESTEVES1, Adriano CARVALHO2, Member, IEEE, Carlos COUTO3, Member, IEEE
[23] Everett, H.R., Sensors for Mobile Robots, A K Peters, June 1995.
[24] Fuentes, O. et al., Mobile Robotics 1994, Technical Report 588, the University of Rochester Computer Science Department, Rochester, New York 14627, June 1995.
[25] Stella, E. et al., "An Autonomous System for Indoor Structured Environment", Intelligent Autonomous Systems, U. Rembold et al. (Eds.), IOS Press, 1995.
[26] Betke, Margrit and Gurvits, Leonid, "Mobile Robot Localization Using Landmarks", IEEE Transactions on Robotics and Automation, **Vol. 13**, Nº 2, April 1997

American Journal of Engineering Research (AJER)
e-ISSN : 2320-0847 p-ISSN : 2320-0936
Volume-02, Issue-10, pp-71-79
www.ajer.org

Research Paper Open Access

Mathematical Modeling of Optimizing Power Stream Measurement Using Genetic Algorithm

Mr. K. Bhaskar, Mr. M. Vijay Albert William, Dr. Debmalya Bhattacharya
School of Electrical Engineering
Vel Tech Dr. RR & Dr. SR Technical University
Avadi, Chennai-600062, Tamil Nadu.

Abstract: - An electrical engineer always tries to generate transmit and distribute electrical energy at affordable cost while satisfying the constraints. So optimal power flow is the problem which is mathematically modeling this objective.OPF is the allocation of optimal load to each committed generators while satisfying the power flow and plant constraints. The objective is to minimize the fuel cost and reduce the total losses by maintaining the generation power in limits. In this proposed work two case studies are carried out on and IEEE-30 bus systems. The solution methodology is developed as a software tool in Matlab 7.0.1. In this project fuel cost is taken as an objective function & it is compared with the results of Matpower package. The GA tool box is utilized for these two case studies.

Keywords: - *OPF (Optimal Power Flow), GA (Genetic Algorithm), NR (Newton Raphson), PSO (Practical Swarm Optimization).*

I. INTRODUCTION

The definition of optimal power flow and solution of optimal power flow by conventional methods given in [1] and [2] will be briefly explained. Effective optimal power flow is limited by (i) the high dimensionality of power systems and (ii) the incomplete domain dependent knowledge of power system engineers. GAOPF requires two load flow to be performed per entity, per iteration because all convenient variables are included in the fitness. In this project, a simple genetic algorithm applied to the problem of optimal power flow in large power distribution systems. OPF is a tool used for both the operation and planning of a power system. It can be intuitively explained in the following way. If we are to provide a given requirement, and if we have generation units committed (participating in the dispatch), OPF gives an answer as to how much power each unit has to produce (dispatch) as well as how to adjust transformer settings in order to supply demand most economically, while respecting all the constraints imposed on the system.

II. PROBLEM FORMULATION

The standard OPF predicament can be written in the subsequent form,
Minimize $F(x)$ (the objective function) subject to :
$hi(x)=0$, $i=1,2,\ldots n$ (parity constraints) ----------(2.1)
$gi(x) \leq 0$, $j=1,2,\ldots.m$ (disparity constraints) ---------(2.2)

where x is the vector of the control variables, that is those which can be varied by a control center operator (generated active and reactive powers, cohort bus voltage magnitudes, transformers taps etc.); The essence of the optimal power flow problem resides in reducing the objective function and concurrently satisfying the load flow equations (parity constraints) without violating the dissimilarity constraints.

III. OBJECTIVE FUNCTION

The most commonly used objective in the OPF problem formulation is the minimization of the total cost of real power generation. The individual costs of each generating unit are assumed to be function, only, of

active power generation and are represented by quadratic curves of second order. The objective function for the entire power system can then be written as the sum of the quadratic cost model at each generator.

$c(p) = ap^2 + bp + c$ ----------(2.3)

Where p is in MW (or per unit) output of the generator and a, b, c are constant coefficients.

IV. CONSTRAINTS

As we stated, the OPF is a constrained optimization problem. The set of constraints can be divided into parity constraints and disparity constraints. The parity constraint set typically consists of power balance (active and reactive) at each node of the network which results from Kirchhoff's current law. Another set of constraints are disparity constraints, which are usually limits resulting from network constituent boundaries. A frequent set of disparity constraints consists of:

- Generator power constraints (P and Q)
- Line power constraints (P)
- Voltage, tap ratios, and phase shifter angle constraints

Generators are rated by maximum apparent power which they can produce. The combination of P, Q produced by a generator must obey the apparent circle equation $P2 + Q^2 \leq S_{max.}$ The maximum active power (P_{max}) produced by generator is limited by the turbine's physical limits, while maximum reactive power (Q_{max}) is often determined so that heating of the rotor is within a pre specified tolerance. Likewise, a minimum generation level is usually precise. Therefore for each and every generator in the network is subject to the following constraints:

$P_{min} \leq P \leq P_{max}$ ---------- (2.4)

$Q_{min} \leq Q \leq Q_{max}$ ---------- (2.5)

Besides generators, transformers provide an additional means of control of the flow of both active and reactive power.

There are two types of controllable transformers: tap changers and phase shifters, even though some transformers control both the magnitude and phase angle. Controllable transformers are those which provide a small adjustment of voltage magnitude, usually in the range ±10% or which shift the phase angle of the line voltages. A type of transformer considered for small adjustments of voltage rather than for changing voltage levels is called a regulating transformer.

V. TYPES OF PARITY CONSTRAINTS

While minimizing the cost function, it's necessary to make sure that the generation still supplies the load demands plus losses in transmission lines. Usually the power flow equations are used as parity constraints.

$P_i(V,\theta) - (P_{gi} - P_{di}) = 0$ ----------(2.6)

$Q_i(V,\theta) - (Q_{gi} - Q_{di}) = 0$ ----------(2.7)

Where active and reactive power injection at bus *i* are defined in the following equation:

$P_i = \sum |V_i||V_k|(G_{ik}\cos\theta_{ik} + B_{ik}\sin\theta_{ik})$ ----------(2.8)

$Q_i = \sum |V_i||V_k|(G_{ik}\sin\theta_{ik} - B_{ik}\cos\theta_{ik})$ ----------(2.9)

Where i=bus no. & k=1,2,3……n

VI. TYPES OF DISPARITY CONSTRAINTS

The disparity constraints of the OPF replicate the limits on physical devices in the power scheme as well as the limits created to ensure system protection. The most natural types of disparity constraints are advanced bus voltage limits at generations and load buses, lower bus voltage confines at load buses, var. confines at production buses, greatest active power limits corresponding to lower limits at some generators, maximum line loading limits and limits on tap setting of TCULs and phase shifter. The disparity constraints on the dilemma variables measured include:

i) Upper and lower bounds on the active generations at generator buses $P_{gi}^{min} \leq P_{gi} \leq P_{gi}^{max}$, *i = 1, ng.*\

ii) Upper and lower bounds on the reactive power generations at generator buses and reactive power injection at buses with VAR compensation $Q_{gi}^{min} \leq Q_{gi} \leq Q_{gi}^{max}$, *i = 1, npv*

iii) Upper and lower bounds on the voltage magnitude at the all buses $V_i^{min} \leq V_i \leq V_i^{max}$ *i = 1, nbus.*

iv) Upper and lower bounds on the bus voltage phase angles: $\theta_i^{min} \leq \theta_i \leq \theta_i^{max}$ i=1 to n bus.

It can be seen that the comprehensive objective function F is a non-linear, the number of the parity and disparity constraints boost with the size of the power allotment systems. Applications of a predictable optimization technique such as the gradient-based algorithms to a large power allocation system with a very non-linear objective functions and enormous quantity of constraints are not good enough to solve this problem. Because it depend on the subsistence of the first and the second derivatives of the objective function and on the well computing of these derivative in huge investigate space.

VII. EXPERIMENTAL INVESTIGATIONS

For experimental investigation the knowledge of genetic algorithm tool box is necessary. The Genetic Algorithm toolbox is a collection of functions that extend the capabilities of the Optimization Toolbox and the MATLAB numeric computing environment. The Genetic Algorithm toolbox includes routines for solving optimization problems using Genetic algorithm. This algorithm enables you to solve a variety of optimization problems that lie outside the scope of the standard Optimization Toolbox.

All the toolbox functions are MATLAB M-files, made up of MATLAB statements that implement specialized optimization algorithms. The capabilities of the Genetic Algorithm toolbox can be extended by writing own M-files, or by using the toolbox in combination with other toolboxes, or with MATLAB or Simulink.

Genetic algorithm in optimal power flow

The genetic algorithms are part of the evolutionary algorithms family, which are computational models, inspired in the Nature. Genetic algorithms are powerful stochastic search algorithms based on the mechanism of natural selection and natural genetics.

GAs works with a population of binary string, searching many peaks in parallel. By employing genetic operators, they exchange information between the peaks, hence reducing the possibility of ending at a local optimum.

GAs are more flexible than most search methods because they require only information concerning the quality of the solution produced by each parameter set (objective function values) and not lake many optimization methods which require derivative information, or worse yet, complete knowledge of the problem structure and parameters.

GA Applied to optimal power flow

A simple Genetic Algorithm is an iterative procedure, which maintains a constant size population P of candidate solutions. During each iteration step (generation) three genetic operators (reproduction, crossover, and mutation) are performing to generate new populations (offspring), and the chromosomes of the new populations are evaluated via the value of the fitness which is related to cost function. Based on these genetic operators and the evaluations, the better new populations of candidate solution are formed.

With the above description, a simple genetic algorithm is given as follow [6]:

1. Generate randomly a population of binary string
2. Calculate the fitness for each string in the population
3. Create offspring strings through reproduction, crossover and mutation operation.
4. Evaluate the new strings and calculate the fitness for each string (chromosome).
5. If the search goal is achieved, or an allowable generation is attained, return the best chromosome as the solution; otherwise go to step 3.

VIII. CROSSOVER

Crossover is the primary genetic operator, which promotes the exploration of new regions in the search space. For a pair of parents selected from the population the recombination operation divides two strings of bits into segments by setting a crossover point at random, i.e. Single Point Crossover.

The segments of bits from the parents behind the crossover point are exchanged with each other to generate their offspring. The mixture is performed by choosing a point of the strings randomly, and switching their segments to the left of this point. The new strings belong to the next generation of possible solutions. The strings to be crossed are selected according to their scores using the roulette wheel [6]. Thus, the strings with larger scores have more chances to be mixed with other strings because all the copies in the roulette have the same probability to be selected.

IX. MUTATION

Mutation is a secondary operator and prevents the premature stopping of the algorithm in a local solution. The mutation operator is defined by a random bit value change in a chosen string with a low probability of such change. The mutation adds a random search character to the genetic algorithm, and it is necessary to avoid that, after some generations, all possible solutions were very similar ones.

All strings and bits have the same probability of mutation. For example, in the string 110011101101, if the mutation affects to time bit number six, the string obtained is 110011001101.

X. REPRODUCTION

Reproduction is based on the principle of survival of the better fitness. It is an operator that obtains a fixed number of copies of solutions according to their fitness value. If the score increases, then the number of copies increases too. A score value is of associated to a given solution according to its distance of the optimal solution (closer distances to the optimal solution mean higher scores).

XI. COST FUNCTION

The cost function is defined as:

$$F(x) = \sum_i (aP_i^2+bP_i+c)\ P_i^{min} \le P_i \le P_i^{max} \quad \text{---------- (3.1)}$$

Our objective is to search the generation powers in their admissible limits to achieve the optimization problem of OPF.

Using the above components, a standard GA procedure for solving the optimal power flow problem is summarized in the diagram of the Fig 1.

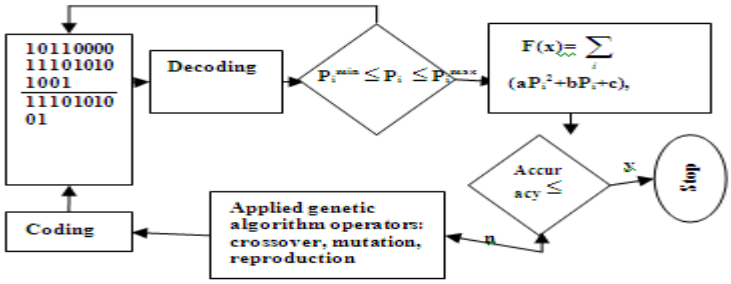

Fig 1. Simple flow chart of the GA OPF

The use of penalty functions in many OPF solutions techniques to handle generation bus reactive power limits can lead to convergence problem due to the distortion of the solution surface. In this method no penalty functions are required. Because only the active power of generators are used in the fitness. And the reactive levels are scheduled in the load flow process. Because his essence of this idea is that the constraints are partitioned in two types of constraints, active constraints are checked using the GA procedure and the reactive constraints are updating using an efficient Newton-Raphson Load flow procedure.

XII. LOAD FLOW CALCULATION

After the search goal is achieved, or an allowable generation is attained by the genetic algorithm. It's required to performing a load flow solution in order to make fine adjustments on the optimum values obtained from the GAOPF procedure. This will provide updated voltages, angles and transformer taps and points out generators having exceeded reactive limits.

- Employing the simple GA to solve the optimal power flow problem.

i) IEEE-30 BUS SYSTEM:

CHROMOSOME CODING AND DECODING:

GAs works with a population of binary string, not the parameters themselves. With the binary coding method, the active generation power set of 30 bus system(P_1,P_2,P_5,P_8,P_{11},P_{13}) would be coded as binary string of *O's* and *1'* with length B_1, B_2, B_5,B_8,B_{11} and B_{13} (may be different), respectively. Each parameter P_i have upper bound U_i and lower bound L_i .The choice of B_1, B_2, B_5,B_8,B_{11} and B_{13} for the parameters is concerned with the resolution specified by the designer in the search space. In the binary coding method, the bit length B_i and the corresponding resolution

R_i is related by

$R_i = (U_i - L_i)/(2^{Bi} - 1)$
where R_i =resolution

As result, the P_i set can be transformed into a binary string (chromosome) with cetain length and then the search space is explored. Note that each chromosome presents one possible solution to the problem. Power generation limits & generator cost parameters of IEEE-30 bus system are shown in Table 1.

Table 1: Power generation limits & generator cost parameters of IEEE-30 bus system in p.u.(Sb=100mva)

buss	Pmin	Pmax	Vmin	Vmax	a	b	c
1	0.50	2.0	0.95	1.10	200	200	0
2	0.20	0.80	0.95	1.10	175	175	0
5	0.15	0.50	0.95	1.10	625	100	0
8	0.10	0.35	0.95	1.10	83.4	325	0
11	0.10	0.30	0.95	1.10	250	300	0
13	0.10	0.40	0.95	1.10	250	300	0

a in($/MW^{2}hr), b in ($/MWhr) and c in ($/hr)
Depending on the resolution the parameter set:
(P_1,P_2,P_5,P_8,P_{11},P_{13}) can be coded according to the following Table 2.A.

Table 2 (A): Coding of pi parameter set

P_1	code	P_2	code	P_5	code
0.5	0000	0.25	0000	0.15	0000
0.6	0001	0.30	0001	0.175	0001
0.7	0010	0.35	0010	0.20	0010
0.8	0011	0.40	0011	0.225	0011
0.9	0100	0.45	0100	0.25	0100
1.0	0101	0.50	0101	0.275	0101
1.1	0110	0.55	0110	0.30	0110
1.2	0111	0.60	0111	0.325	0111
1.3	1000	0.65	1000	0.35	1000
1.4	1001	0.70	1001	0.375	1001
1.5	1010	0.75	1010	0.40	1010
1.6	1011	0.80	1011	0.425	1011
1.7	1100	0.85	1100	0.45	1100
1.8	1101	0.90	1101	0.475	1101
1.9	1110	0.95	1110	0.50	1110
2.0	1111	1.00	1111	0.525	1111

Table 2 (B): Coding of pi parameter set

P_8	code	P_{11}	code	P_{13}	code
0.10	0000	0.10	0000	0.10	0000
0.12	0001	0.12	0001	0.12	0001
0.14	0010	0.14	0010	0.14	0010
0.16	0011	0.16	0011	0.16	0011
0.18	0100	0.18	0100	0.18	0100
0.20	0101	0.20	0101	0.20	0101
0.22	0110	0.22	0110	0.22	0110
0.24	0111	0.24	0111	0.24	0111
0.26	1000	0.26	1000	0.26	1000
0.28	1001	0.28	1001	0.28	1001
0.30	1010	0.30	1010	0.30	1010
0.32	1011	0.32	1011	0.32	1011
0.34	1100	0.34	1100	0.34	1100
0.36	1101	0.36	1101	0.36	1101
0.38	1110	0.38	1110	0.38	1110
0.40	1111	0.40	1111	0.40	1111

If the candidate parameters set is (1.9, 0.80, 0.50,0.38,0.32,0.30), then the chromosome is a binary string 1110|1011|1110|1110|1011|1010. The decoding procedure is the reverse procedure.

The first step of any genetic algorithm is to generate the initial population. A binary string of length L is associated to each member (individual) of the population. The string is usually known as a chromosome and represents a solution of the problem. A sampling of this initial population creates an intermediate population. Thus, some operators (reproduction, crossover and mutation) are applied to this new intermediate population in order to obtain a new one.

Process, that starts from the present population and leads to the new population, is named as generation. When executing a genetic algorithm for IEEE -30 bus system, the results after first generation are shown in Table 3.

For this IEEE-30 bus system to apply GA we require initial population. This initial population can be obtained by using NR method. By NR method,

Results after 3rd iteration are P_1=130 MW, P_2=60.2MW, P_5=27.5MW, P_8=34MW,P_{11}=18MW, P_{13}=16MW. By substituting these values in cost function $F(x)=\sum_i (aP_i^2+bP_i+c)$,we get total generation cost=51,320 rs/hr.

Results after 4th iteration are P_1=139.9 MW, P_2=57.56MW, P_5=24.5MW, P_8=35MW, P_{11}=17.9MW, P_{13}=16.9MW. By substituting these values in cost function $F(x)=\sum_i (aP_i^2+bP_i+c)$,we get total generation cost=50,520 rs/hr.

Table 3: First generation of GA process for 30 bus system

	Chromo- some	initial population	cost(rs/hr)
3rd iteration	**1**	**1000|0111|0101|1100|0100|0011**	**51,320**
4th iteration	**2**	**1001|0110|0100|1100|0100|0011**	**50,520**
After single pt Crossover	**3** **4**	**1000|0110|0100|1100|0100|0011** **1001|0111|0101|1100|0100|0011**	**48,040** **43,600**
After Mutation	**5**	**1001|0011|0101|1100|0100|0011**	**39,200**

After 100 generations we get chromosome as 0010|1110|1010|1100|0110|0101. In decoded form P_1=71.56MW, P_2=97.63MW, P_5=41.54MW, P_8=34.8MW, P_{11}=22.06MW, P_{13}=20.02MW. For this case total generation cost=31,960 rs/hr & it is the optimal solution by using GA.

The corresponding IEEE -30 bus system is shown Fig-2

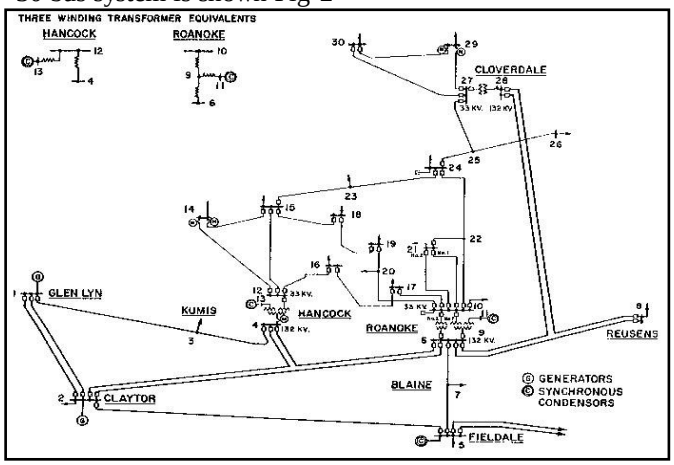

Fig 2: IEEE- 30 BUS SYSTEM

XIII. RESULTS AND ANALYSIS

Results of OPF using GA and Matpower for IEEE-30 buses will be given and they are compared.

Results

Table 4: Total cost and Losses for ieee-30 bus system using matpower:

PARAMETER	VALUE
i)TOTAL COST	32,000 (rs/hr)
ii)TOTAL LOSSES	4.34 (MW)

Description: For IEEE-30 bus system using Matpower we get,
Total generation cost =32,000 (rs/hr)
Total transmission losses =4.34(MW)

Table 4.1 Generated power for IEEE-30 bus system using matpower:

VARIABLE	VALUE (MW)
P_1	69.93
P_2	96.56
P_5	41.71
P_8	36.45
P_{11}	22.31
P_{13}	20.76

Description: Total active power generated for IEEE-30 bus system using
Matpower =$P_1+P_2+P_5+P_8+P_{11}+P_{13}$=287.74(MW)
And total load demanded =283.4 (MW)

Table 4.2 total cost and losses for ieee-30 bus system using GA:

PARAMETER	VALUE
i) TOTAL COST	31,960 (rs/hr)
ii) TOTAL LOSSES	4.23 (MW)

Description: For IEEE-30 bus system using GA we get,
Total generation cost =31,960(rs/hr)
Total transmission losses =4.23(MW)

Table 4.3 Generated power for IEEE 30 bus system with GA:

VARIABLE	VALUE (MW)
P_1	71.56
P_2	97.63
P_5	41.54
P_8	34.8
P_{11}	22.16
P_{13}	20.02

Description: Total active power generated for IEEE-30 bus system using
GA = $P_1+P_2+P_5+P_8+P_{11}+P_{13}$=287.63(MW)
And total load demanded =283.4 (MW)

XIV. COMPARISON OF RESULTS OF GA WITH MATPOWER

Table 4.4. Total cost and Losses for IEEE-30 bus system:

PARAMETER	WITH GA	WITH MATPOWER
i) TOTAL COST	31,960 (rs/hr)	32,000 (rs/hr)
ii)TOTAL LOSSES	4.23 (MW)	4.34 (MW)

Description: To meet the load demand of 283.4 MW for IEEE-30 bus system, total generated power cost using Matpower=32,000(rs/hr) & using GA =31,960(rs/hr).
Since demand is constant for both the methods, losses are less for GA compared to Matpower.

Table 4.5 Generated power for IEEE-30 bus system

VARIABLE	WITH MATPOWER	WITH GA
P_1(MW)	69.93	71.56
P_2(MW)	96.56	97.63
P_5(MW)	41.71	41.54
P_8(MW)	36.45	34.8
P_{11}(MW)	22.31	22.06
P_{13}(MW)	20.76	20.02

Description :Here P_1,P_2,P_5,P_8,P_{11} and $P_{13}$are the generated powers at buses 1,2,5,8,11 & 13 resp.To meet the demand of 283.4MW for IEEE-30 bus system ,total power generated using Matpower =287.74(MW) & using GA=287.63(MW)

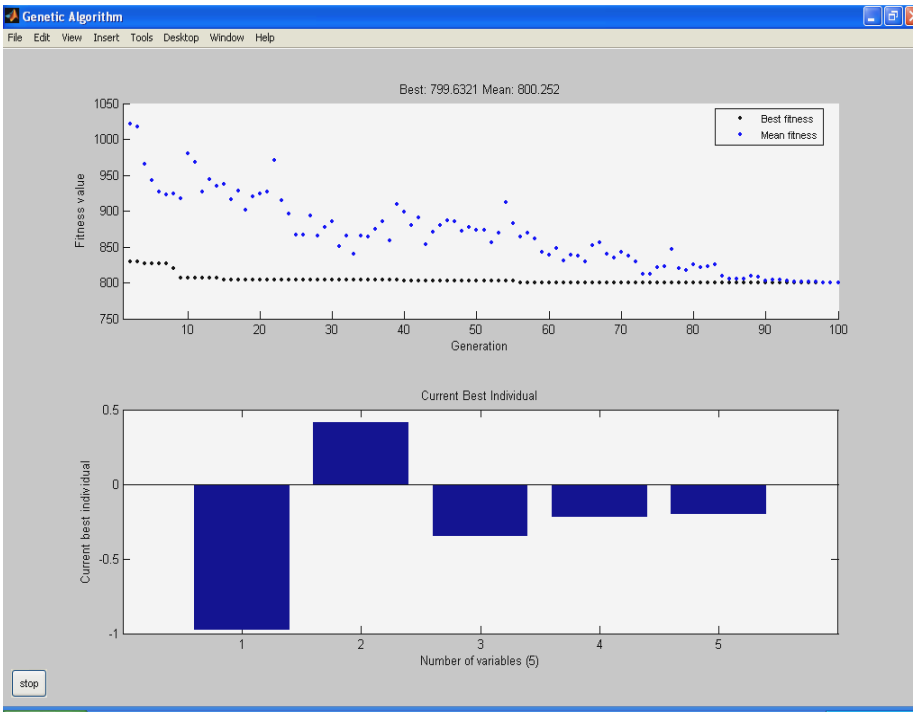

Fig 3: Total cost curve of a IEEE-30 bus system

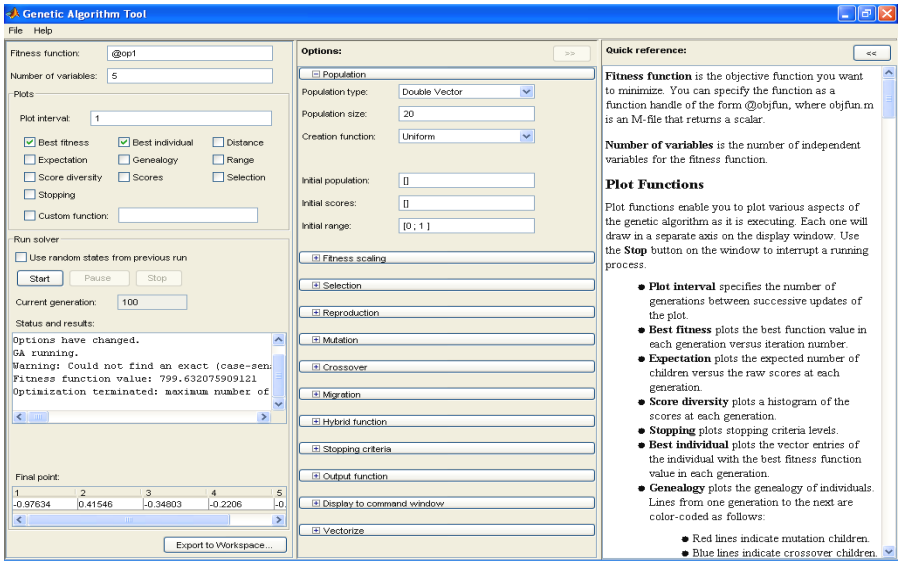

Fig 4: GA tool for IEEE -30 bus system

XV. CONCLUSION

Application of Genetic approach to Optimal Power Flow has been explored and tested. A simulation results show that a simple genetic algorithm can give a best result using only simple genetic operations such as proportionate reproduction, simple mutation, and one-point crossover in binary codes. It's recommended to indicate that in large-scale system the numbers of constraints are very large consequently the GA accomplished in a large CPU time.

To save an important CPU time, the constraints are to be decomposing in active constraints and reactive ones. The active constraints are the parameters whose enter directly in the cost function and the reactive constraints are infecting the cost function indirectly. With this approach, only the active constraints are taken to calculate the optimal solution set. And the reactive constraints are taking in an efficient load flow by recalculate active power of the slack bus. The developed system was then tested and validated on the IEEE-30 bus systems. Solutions obtained with the developed Genetic Algorithm Optimal Power Flow program has shown to be almost as fast as the solutions given by Matpower package.

XVI. FUTURE WORK

In this project OPF is solved by using GA method for IEEE-30 bus systems.OPF problem using GA in combination with the Particle Swarm Optimization technique can give better results compared to GA method alone.

REFERENCES

[1] H. W. Dommel, W. F. Tinney, Optimal Power Flow Solutions, IEEE Transactions on power apparatus and systems, Vol. PAS-87, No. 10, pp 1866-1876, October 1968.

[2] K. Y. Lee, Y.M. Park, and J.L. Ortiz, A United Approach to Optimal Real and Reactive Power Dispatch, IEEE Transactions on Power Systems, Vol. PAS-104, pp 1147-1153, May 1985.

[3] M. Sasson, Non linear Programming Solutions for load flow, minimum loss, and economic dispatching problems, IEEE Trans. on power apparatus and systems, Vol. PAS-88, No. 4, April 1969.

[4] T. Bouktir, M. Belkacemi, K. Zehar, Optimal power flow using modified gradient method, Proceeding ICEL'2000, U.S.T.Oran, Algeria, Vol. 2, pp 436-442, 13-15 November 2000.

[5] R. Fletcher, Practical Methods of Optimisation, John Willey & Sons, 1986.

[6] D. E. Goldberg Genetic Algorithms in Search, Optimization and Machine Learning, Addison Wesley Publishing Company, Ind. USA, 1989.

[7] J. Yuryevich, K. P. Wong, Evolutionary Programming Based Optimal Power Flow Algorithm, IEEE Transaction on power Systems, Vol. 14, No. 4, November 1999.

[8] L.L. Lai, J. T. Ma, R. Yokoma, M. Zhao Improved genetic algorithms for optimal power flow under both normal and contingent operation states, Electrical Power & Energy System, Vol. 19, No. 5, pp 287-292, 1997.

[9] B. S. Chen, Y. M. Cheng, C. H. Lee, A Genetic Approach to Mixed H2/H00 Optimal PID Control, IEEE Control system, pp 551-59, October 1995.

[10] Glenn W. Stagg, Ahmed H. El Abiad, Computer methods in power systems analysis, Mc Graw Hill international Book Campany, 1968.

[11] S. Kumar, R. Billinton, Low bus voltage and ill-conditioned network situation in a composite system adequacy evaluation, IEEE transactions on power systems, vol. PWRS-2, No. 3, August 1987.

[12] L. Terra, M. Short, Security constrained reactive power dispatch, IEEE transaction on power systems, Vol. 6, No. 1, February 1991.

[13] T. Bouktir , M. Belkacemi , L. Benfarhi and A. Gherbi, Oriented Object Optimal Power Flow, the UPEC 2000, 35th Universities Power Engineering Conferences Belfast, Northern Ireland, 6-8 September 2000.

American Journal of Engineering Research (AJER)
e-ISSN : 2320-0847 p-ISSN : 2320-0936
Volume-02, Issue-11, pp-80-85
www.ajer.org

Research Paper Open Access

Detection of microcalcifications in digital mammogram using wavelet analysis

Yashashri G. Garud, Neha G. Shahare
M. E. Student Department of E&TC, SITS Pune, India, Asst. Professor Department of E&TC, SITS Pune, India

Abstract: - Clusters of microcalcifications in digital mammograms are important and early sign of breast cancer. This paper presents CAD system for detection of clusters of microcalcifications in digital mammograms. Microcalcifications are tiny deposits of calcium in breast tissue. Dense nature of breast tissue and poor contrast of mammograms prohibit effectiveness in detecting microcalcifications. Thus, to detect and differentiate the microcalcifications from normal tissue, proposed system uses wavelet analysis. Proposed system also makes use of extreme learning machine which has better generalization performance at extremely fast learning speed. ELM also avoids problems like local minima, improper learning rate. In this proposed system, raw mammographic image taken from MIAS database and it is morphologically preprocessed to remove labels and noise. Then, windowing function is applied to extract sub images of 32×32. Sub images are decomposed into 4 levels and wavelet features are computed. Whole process is supported with Extreme Learning Machine which is used as classifier.

Keywords: - *Mammograms, Microcalcifications, Wavelet, Extreme Learning Machine.*

I. INTRODUCTION

Today, breast cancer is most frequent and prevalent cancer among women, especially in the western country. It is leading cause of mortality in women each year [1]. According to cancer fact sheets of World Health Organization, more than 1, 50,000 women worldwide die due to breast cancer each year. Nearly 8-13% women develop breast cancer at some point during their lives. Survival rate is directly proportional to stage at which it is detected. Clusters of microcalcifications in digital mammograms are early and important sign of breast cancer. These are considered to be best indicators for malignancy. Detection of early signs of breast cancer requires high quality images and high degree of accuracy in interpretation.

Nowadays, mammography remains most effective diagnostic technique for early breast cancer detection. Microcalcifications are tiny deposits of calcium whose general size ranges from 0.1 mm to 1 mm. And average size is 0.3 mm. When three or more than 3 deposits of calcium comes together, it forms clusters of microcalcification. Due to very small size of microcalcifications, interpretation of their presence is very difficult. They can be overlooked by radiologists. To provide confirmation to radiologists for their diagnostic decisions and to improve accuracy and sensitivity of detection, a variety of computer Aided Diagnostic (CAD) systems have been proposed, where CAD is basically computer based systems which incorporates expert knowledge of radiologists to provide second opinion in detecting abnormalities and making diagnostic decisions. But, still to detect presence of microcalcifications remains a big challenge due to fuzzy nature and poor contrast of mammograms. Microcalcifications are high frequency components with low frequency background and high frequency noise.

Thus, this paper gives a technique to detect microcalcifications in digital mammograms giving it to approach of wavelet analysis and extreme learning machine.

This paper is organized as follows: Section II gives literature review of this proposed system. Section III flow chart of the proposed system. Section IV discusses details of database collection. Section V explains complete detail methodology of proposed system. Section VI gives experimental results. Section VII provides conclusion of this proposed paper.

II. LITERATURE SURVEY

In literature, various techniques are described to detect presence of microcalcifications in digital mammograms. Bouyahia et.al. proposed wavelet based detection of microcalcifications in digitized mammograms[3]. He used undecimated wavelet transform, multi-scale product and wavelet packets transform for automatic detection of microcalcifications. M. Salmeri et.al. invented technique of mammographic image enhancement and denoising for breast cancer detection using dyadic wavelet processing [4]. He implemented a method which has its adaptability to the different nature of diagnostic relevant features in the image permitting use of same core algorithm for both microcalcifications and mass detection. Yu et.al. presented a CAD system for the automatic detection of clustered microcalcifications using neural network classifiers through two steps. In first step, microcalcification pixels are detected and in second step, individual microcalcification objects are detected [5]. Netsch et.al proposed a detection scheme for the automatic detection of clustered microcalcifications using multiscale analysis based on Laplacian-of-Gaussian filter [6]. Barman et.al. used a low pass filter to detect microcalcifications by analyzing digital mammograms [7]. Mascio et.al. developed a microcalcification detection algorithm, which operates on digital mammograms by combining morphological image processing with arithmetic processing [8]. Karssemeijer developed a statistical method for detection of microcalcifications in digital mammograms [9].

This proposed system uses extreme learning machine algorithm to train the neural network and uses Haar wavelets along with it for feature extraction to detect microcalcifications in digital mammograms.

III. FLOW CHART OF THE SYSTEM

In this section, flow of the proposed system is given as shown in figure 1. First of all stages, morphological preprocessing is done on digitized raw mammogram. Then skin lined breast image is produced and segmentation of that skin lined breast image is done by presenting it in 32×32 sub images. Then features are extracted from the mammograms using haar wavelet as it is easily decomposed. Then, selection of classifier is done and extreme learning machine is used as classifier to support wavelet based feature extraction. Thus the whole process is carried in above steps to detect micro calcified clusters in digital mammograms.

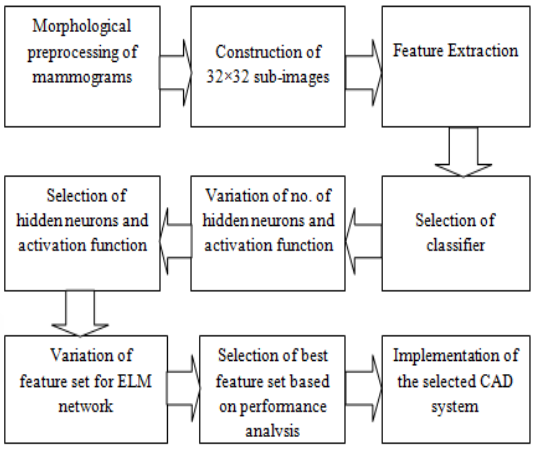

Figure 1. Block Diagram

IV. DATABASE COLLECTION

Sample images are taken from the Mammographic Image Analysis Society (MIAS) [2], an organization of research group in U.K. that are enthusiastic in the understanding in mammograms and generated a database of digital mammograms. Films in database are taken from the UK national breast screening program have been digitized to 50µm pixel edge with Joyce-Loebl scanning microdensitometer, a device linear in optical density range (0-3.2) and representing each pixel with 8 bit word. The database contains 322 digitized films and is available on 2.3 GB, 8 mm tape. It also includes radiologists truth markings, so called the ground truth on the locations of any abnormalities that may present. Database has been reduced to 200 µm pixel edge and padded so that all the images are 1024×1024.

V. METHODOLOGY

Proposed system of microcalcification detection consists of various steps, namely, Morphological preprocessing of digital mammograms, segmentation in 32×32 sub images, Texture analysis, Feature extraction

which is based on haar wavelet giving it approach of extreme learning machine. Raw mammographic image is taken of size 1024×1024.

A. Morphological Preprocessing

Mammographic images are taken from the MIAS database contains dark background and other non essential components such as labels and scribbling. The gray scale mammogram images are transformed into binary format using a global threshold T_G , having a value one tenth of the maximum intensity. The objects (connected components) present in the binary image are labeled. Area of each connected component is then calculated and all the objects having an area (number of pixels) lesser than maximum (T_A) are removed. The value of T_A for MIAS database images found to be 10000. The selected breast profile is multiplied with original image to get resultant image that is free from label and other noises. Finally, the dark background is removed by cropping rows and columns that has sum value equal to zero. Thus, the breast region alone is extracted for further processing.

B. Construction of 32×32 sub-images

After this process, sub-images (ROIs) of size 32×32 are manually cropped. The size of sub-image plays an important role in classification. A large sub-image will lead to an accurate classification in the homogenous area but a bad classification along the breast skin line areas, whereas small sub-images gives optimal classification accuracy in all the regions. The smallest possible sub-image that could contain a microcalcification cluster in a 1024×1024 image is 32×32. In the normal images, random portion of size 32×32 are taken as ROIs. In the images containing microcalcifications, ROIs are taken such that the microcalcification clusters are at different positions of the sub-images. In both, background and boundary zones are considered. The sub-images that are entirely black and those containing number of zeros more than 100 (10% of total number of pixels) are not considered.

C. Texture Analysis

Texture analysis is a potential method for studying lesions such as micro-calcifications. In this paper, texture analysis of mammograms intends to identify specific region of interest (microcalcifications). Textural features contain information about the spatial distribution of tonal variations. The scheme of tone lies on the intensity of the pixels within the defined region (gray level values in gray scale image). Thus, the texture in the sub image describes the pattern of variation in gray level values in a neighborhood. This will prove the textural features that could be used for solving classification problems on non-homogenous data such as mammograms.

D. Wavelet based feature extraction

The wavelet transformation is used to analyze different frequencies of an image using different scales. This is flexible approach than Fourier transform, enabling analysis of both local and global features present in the image. Here, orthogonal wavelet transform is used as it allows an input image to be decomposed into a set of independent coefficients, corresponding to each orthogonal basis. Orthogonal implies that there is no redundancy in the information presented by the wavelet coefficients, which results in an efficient representation of desirable features. Haar wavelet is used for decomposition as it is best suited for extracting high frequency components (microcalcifications) from mammographic image. The mammographic image is decomposed into 4 levels. The approximate and the three detailed components are extracted consecutively for 4 levels by replacing the input image for 2^{nd}-4^{th} level decomposition by the approximate component of the respective previous level. The features that are extracted for classification are the energy and infinity norm for all the 4 components at each level.

Energy, $E = \sum\sum ||M_{pq}(x, y)||^2$

Infinity norm = $\sum |x|^{p\,1/p}$

Where, P is the maximum row sum of x.

D. Extreme Learning Machine

In this proposed system, Extreme Learning Machine is selected as classifier. For selecting ELM as a classifier, ROC graph is used. Receiver Operating Characteristics (ROC) is a technique for visualizing, organizing, selecting classifier based on performance. It depicts relative tradeoffs between true positive rate and false positive rate. One point in the ROC is better than the other if it is to the northwest of the first. ELM comes under the class of SLFN (Single Layer Feed Forward Network) whose learning speed is thousand times faster than conventional feed forward network. It has better generalization as the input weights and hidden layer biases can be randomly assigned if the activation functions in the hidden layer are infinitely differentiable.

With N number of hidden neurons and activation function g(x), the ELM algorithm can be summarized as:

i. Assign input weights w_i and biases b_i.
ii. Calculate hidden layer output matrix H.
iii. Calculate the output $\beta = H^*T$ weights, where H^* the Moore-Penrose generalization inverse of the matrix H.

The Structure of ELM network is as follows:

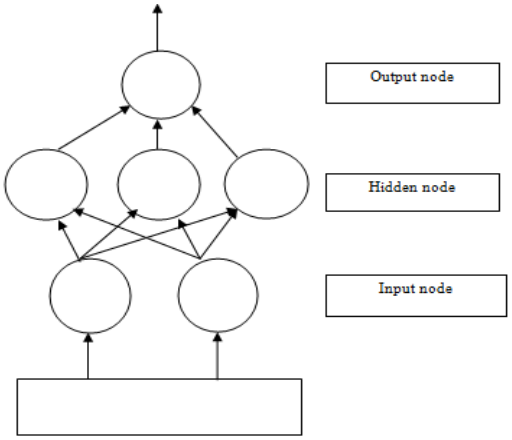

Figure 2. Structure of ELM network

The design of ELM based classification requires selection of user defined parameters namely,
i. Number of hidden neurons
ii. Activation function

Number of hidden neurons ranges from 5-80 (maximum number of input samples) for three different activation functions namely, unipolar, bipolar, and Gaussian.

VI. EXPERIMENTAL RESULTS

The combination of ELM and wavelets feature extraction is used to build CAD system that automatically locates the presence of microcalcifications in digital mammograms.

A. Morphological Preprocessing:

In this process, raw mammographic images are taken as input and morphological operations are carried out to eliminate the undesirable components from raw mammographic images.

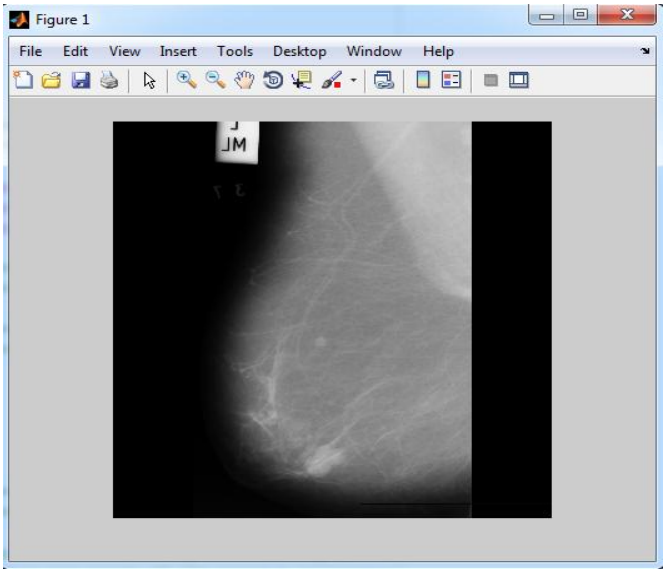

Figure 3. Original mammogram image

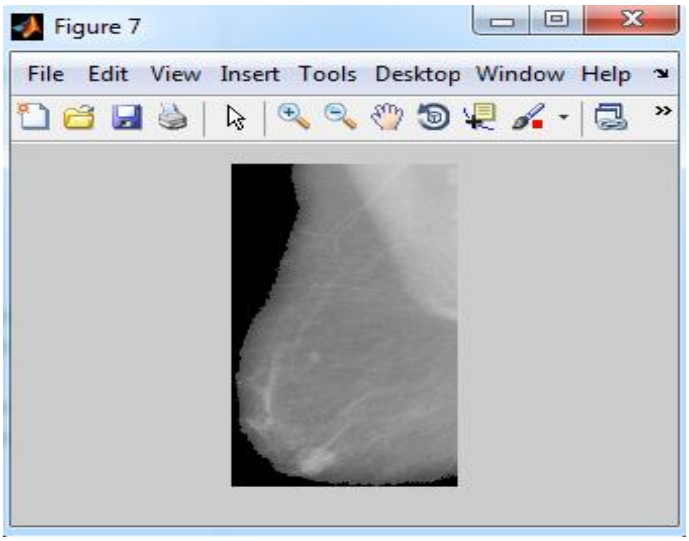

Figure 4. Image after label and background removal

B. Segmentation

A windowing function is then used after preprocessing mammographic image from top left to bottom right such that it produces sub images of size 32×32 at each instance.

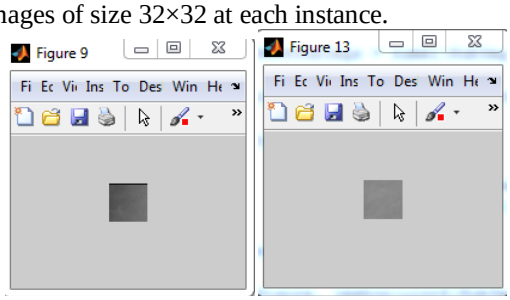

Figure 5. 32×32 sub images

C. Final Result after whole CAD implementation

After implementing CAD system for detection of clustered microcalcifications, final results for the CAD system is shown in figure 6 is as follows:

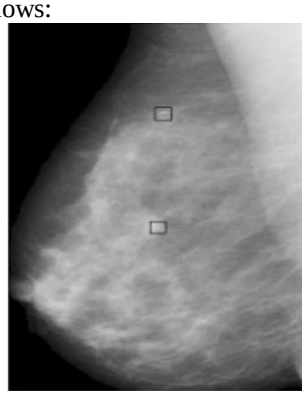

Figure 6. Microcalcifications detection

VII. CONCLUSION

Proposed method which uses wavelet feature extraction which improves sensitivity and performance of the CAD system for detection of micro calcification in digital mammograms. Original mammogram is preprocessed by morphological operations to remove the label and background and segmented in 32×32 sub images of skin lined breast images. Selected wavelet based feature extraction of sub images are used for classification and for this system extreme learning machine is used as classifier and backbone of whole system. Combination of wavelet analysis and extreme learning machine proves proposed system best in its performance.

ACKNOWLEDGEMENT

The authors gratefully acknowledge all those who have helped in making of this review paper successfully. As, this review process of this paper was carried out at Sinhgad Institute of Science & Technology,Pune. So, special thanks to Head of E&TC Department, Principal and Management of SITS, Pune.

REFERENCES

[1] WHO Cancer Fact Sheets 2009.
[2] <http://peipa.essex.ac.uk/info/mias.html>.
[3] S. Bouyahia, J. Mbainaibeye, N. Ellouze, Wavelet based microcalcifications in digitized mammograms, Icgst-Gvip J. 8 (2009) 23-31.
[4] Mencattini, M. Salmeri, R. Lojacono, Mammographic image enhancement and denoising for breast cancer detection using dyadic wavelet analysis, IEEE Trans. Med. Image, 7 (57) (2008) 1422-1431.
[5] S. Yu, L. Gaun, A CAD system for the automatic detection of clustered microcalcifications in digitized mammogram films, IEEE Trans Med. Image, 19 (2) (2000) 115-126.
[6] T. Netsch, H. Peitgen, Scale space signatures for the detection of clustered microcalcifications in digital mammograms, IEEE Trans. Med. Image, 18 (9) (1999) 774-786.
[7] H. Barman, G. Granlund, L. Haglund, Feature extraction for computer aided analysis of mammograms, in: K. W. Bower, S. Astley, State of the art of digital mammographic image analysis, 7, World Scientific, Singapore, 1994, 128-147.
[8] L. Mascio, M. Hernandez, L. Clinton, Automated analysis for microcalcifications in high resolution digital mammograms, Proc. Spie-Int Soc. Opt. Eng. 1898 (1993) 472-479.
[9] N. Karssemeijer, Stochastic model for automatic detection of calcifications in digital mammograms, in: Proceedings of 12th international conference on Information Processing in Medical Imaging, Wye, U.K., (1991).
[10] J. K. Kim, H. W. Park, Statistical texture features for detection of microcalcification in digitized mammograms, IEEE Trans. Med. Image 18 (3) (1999) 231-238.
[11] C. S. Lee, J. K. Kim, H. W. Park, Computer aided diagnostic system for breast cancer by detecting microcalcifications, Spie 3335 (1998) 615-626.
[12] G. B. Huang, Q. Y. Zhu, C. K. Siew, Extreme learning machine: theory and applications, Neurocomputing 70 (2006) 489-501.
[13] Yanpeng Qu, Qiang Shen, N. Mac Parthala, Extreme learning machine for mammographic risk analysis, in: Proceedings of UK workshop on Comp. Intel. (UKCI) (2010) 1-5.
[14] S. Suresh, S. Saraswathi, N. Sundararajan, Performance enhancement of extreme learning machine for multicategory sparse data classification problems, Eng. Appl. Artif. Intel. 23 (7) (2010) 1149-1157.

American Journal of Engineering Research (AJER)
e-ISSN : 2320-0847 p-ISSN : 2320-0936
Volume-02, Issue-11, pp-86-97
www.ajer.org

Research Paper Open Access

Design of A Room Temperature And Humidity Controller Using Fuzzy Logic

Tarun Kumar Das, Yudhajit Das
[1] *Asst. Professor, Department Of Electronics And Comm. Engineering, Future Institute Of Engg & Management, West Bengal University Of Technology, India*
[2] *Department Of Electronics And Comm Engineering, Future Institute Of Engineering & Management, India*

Abstract: - This research paper describes the design of a room temperature and humidity controller using fuzzy logic. The proposed model consists of two fuzzy logic controllers to control temperature and humidity respectively. The first controller accepts two input values- the current temperature as detected by temperature sensor and its deviation from user set-temperature, and controls the speed of heat-fan and cool-fan accordingly . When the current temperature in the room reaches set point, it serves as one of the input for second fuzzy logic controller that controls the humidity. The ideal relative humidity level for user's set temperature is preset in the system. Current humidity in % as detected by the humidity sensor in the room serves as the second input to the controller. The humidifier and exhaust fan speed is controlled accordingly to maintain the correct humidity level for that temperature. This research work will increase the capability of fuzzy logic control systems in process automation with potential benefits. MATLAB-simulation is used to achieve the designed goal.

Keywords: - *Fuzzy logic, Inference Engine, Matlab Simulation, Rule Selection*

I. INTRODUCTION

A control system is a device, or set of devices, that manages, commands, directs or regulates the behavior of other device(s) or system(s). Industrial control systems are used in industrial production for controlling an equipment or a machine. The control system design, development and implementation need the specification of plants, machines or processes to be controlled. A control system consists of controller and plant, and requires an actuator to interface the plant and controller. The behaviour and performance of a control system depend on the interaction of all the elements. **[2]**

Computational Intelligence (CI) is a field of intelligent information processing related with different branches of computer sciences and engineering. The fuzzy systems are one paradigm of CI. The contemporary technologies in the area of control and autonomous processing are benefited using fuzzy sets. One of the benefits of fuzzy control is that it can be easily implemented on a standard computer.

In contrast with traditional logic theory, where bi- nary sets have two-valued logic: true or false, fuzzy logic variables may have a truth value that ranges in degree between 0 and 1. Fuzzy logic has been extended to handle the concept of partial truth, where the truth value may range between completely true and completely false. Fuzzy logic imitates the logic of human thought, which is much less rigid than the calculations computer generally perform. Intelligent control strategies mostly involve a large number of inputs. The objective of using fuzzy logic has been to make the computer think like people. Fuzzy logic can deal with the vagueness intrinsic to human thinking and natural language and recognize its nature is different from randomness. Using fuzzy logic algorithm, we could enable machines to understand and respond to vague human concept such as hot, cold, large, small, etc. **[1] [2]**

This proposed design work of room temperature and humidity controller can be used in a processing plant to maintain comfortable atmosphere in the environment.

II. BLOCK DIAGRAM OF PROPOSED MODEL:-

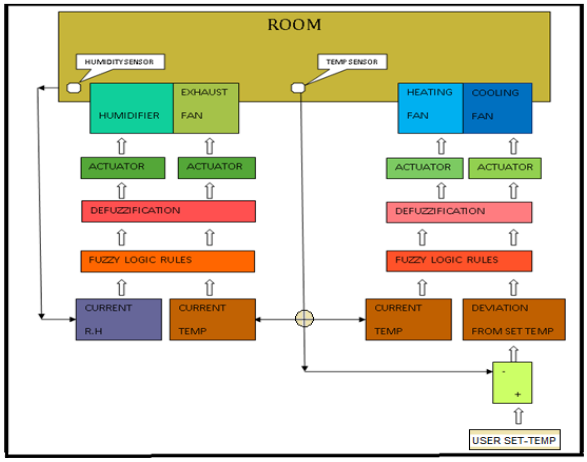

Figure 1: Block Diagram Of Room Temperature And Humidity Controller

The basic model of the proposed structure consists of room temperature and humidity controller with fuzzy logic control system. The room atmosphere controller has a heating fan, a cooling fan to heat or cool the room according to user demand ; a humidifier to release moisture in the air and a exhaust fan to dry out the air if the relative humidity is higher than the needed range. Humidity and temperature sensors used to monitor the environment of room are mounted in the room and are connected with the fuzzifiers of the two fuzzy logic control system.

2.1.Simplified Diagram For The Prposed System:-

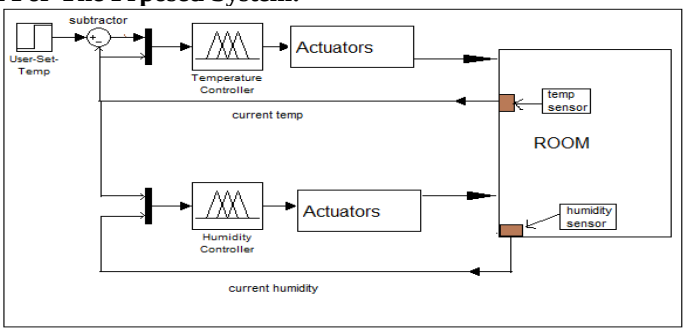

III. HOW HEATING AND COOLING IS DONE

The model basically employs the principle of ground water/air source reversible heat pumps which work in either thermal direction to provide heating or cooling to the internal space.

In cooling mode, the inside coil is the evaporator and the outside coil is condensor. The compressor takes away the low pressure vapour from the refrigerant and discharge it as high pressure vapour which thereby enters the condensor where it is cooled and condensed into liquid. After leaving the condensor as high pressure cooler liquid, the refrigerant now enters the evaporator where it changes into vapour coming in contact with low pressure atmosphere. During this evaporative cycle, heat is removed from the air which gets cooler and enters the room. The low pressure refrigerant then routes back to the compressor by suction line to repeat the cooling process.

In heating mode, the inside coil is now condensor and outside coil is evaporator. The compressor sends the high pressure vapour into the reversing valve which routes the vapour to the condenser coil where it is cooled, and condensed into liquid by passing through the coil. The heat removed from the refrigerant is expelled to the inside air by the air movement system. The refrigerant leaves the inside coil as a high pressure liquid. When this liquid enters the low pressure atmosphere of the outside coil (evaporator) it evaporates into vapor. When the evaporative process takes place, heat is removed from the air flowing through the evaporator and the air,which is now cool, is returned to the outside air (ambient). From the evaporator, the low pressure refrigerant vapour returns to the reversing valve which routes the low pressurevapour to the compressor through the suction line to start the heatingprocess again. **[2]**

A heat pump with one extra valve allows the condenser (hotcoil) and evaporator (cold coil) to reverse places in the winter. Figure 2 shows close-ups of this "reversing" valve and where it is located in the heat pump system.

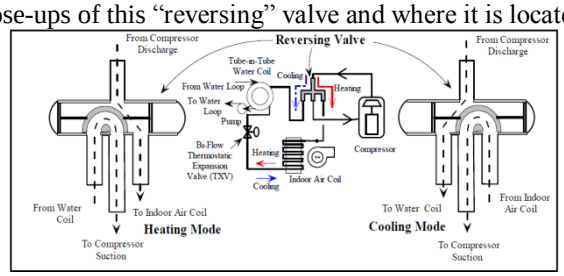

Figure 2:- Reversing Valve That Enables Both Heating And Cooling Processes

IV. DESIGN ALGORITHM OF FUZZY LOGIC FOR ROOM TEMPERATURE & HUMIDITY CONTROLLER

This simplified design algorithm is used to design the fuzzifier, inference engine, rule base and defuzzifier for the room air conditining system according to the control strategy of the processing plant to achieve the quantity and quality of the desire needs to maintain the room environment. The model can operate within 8'C to 44'C temperature range. And user can set any desired temperature from 18 to 26. For any temperature within 18 to 26 both temperature and humidity controlling part of the proposed model performs well to maintain the comfort atmosphere of the user. The humidity comfort level is pre defined and works perfectly within temperature range 18 to 26(^{o}C).

4.1.Fuzzifier:-

4.1.1.Membership Functions And Ranges For The First Fuzzy Logic Controller For Controlling The Desired Temperature

4.1.1.1.Input Variables:-

4.1.1.1.1.Current Temperature:-

It is the current temperature of the room as recorded by the temperature sensor mounted in the room. The sensor range should be wide enough to take care of climatic and regional fluctuations. The proposed model works perfectly at any temperature within range 8^{o}C-44^{o}C

Table 1: Membership Functions For Current-Temperature

MEMBERSHIP FUNCTIONS	RANGE (^{o}C)
COLD	8-14
COOL	13-19
NORMAL	18-22
WARM	21-27
HOT	26-32
VERY-HOT	31-39
EXTR-HOT	38-44

4.1.1.1.2.Deviation From Set Temperature

It gives the difference between the user preferred temperature and current temperature of the room as recorded by the temperature sensor in the room. As this model can work between temperature range 8-44'C and user can set any desired temperature from 18-26'C, so temperature difference between the current and the user preferred temperature can never go beyond -26'C (18'C – 44'C) and 18'C (26'C - 8'C). Thus (-26'C) & (+18'C) are the lower and upper limits of the input variable " deviation from set-temperature").

Table 2: Membership Functions for "Deviation from current temperature"

MEMBERSHIP FUNCTIONS	RANGE(^{o}C)
NE2	-26 to -18.5
NE1	-19.5 to -12
NL	-13 to -6
NS	-7 to 0
O	-2 to 2
PS	1 to 10.5
PL	9 to 18

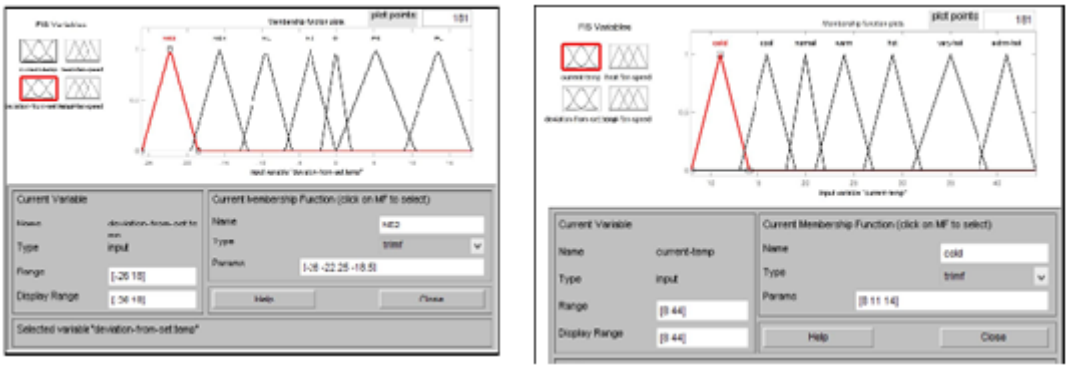

Figure 3:-Plot Of Membership Functions For " Current-Temperature" & "Deviation from current temperature"

4.1.1.2.Output Variables

4.1.1.2.1.Heat-Fan-Speed

The heat fan can either be in ON or OFF state depending on the temperature preference in the room. The heta-fan-speed is catagorised into 1. STOP 2.HEAT-SLOW 3. HEAT-MEDIUM 4. HEAT-FAST.

If the current temperature of the room is below the desired temperature then this fan automatically gets on varies speed according to temperature difference.

Table 3:-Membership Functions For "heat-fan-speed"

MEMBERSHIP FUNCTIONS	RANGE %
STOP	0-5
HEAT-SLOW	0-45
HEAT-MEDIUM	35-65
HEAT-FAST	60-100

4.1.1.2.2.Cool-Fan-Speed

The cool-fan-speed is catagorised into 1. STOP 2.COOL-SLOW 3. COOL-MEDIUM 4. COOL-FAST.

If the current temperature of the room is above the desired temperature then this fan automatically gets on varies speed according to temperature difference.

Table 4:-Membership Function For "cool-fan-speed"

MEMBERSHIP FUNCTIONS	RANGE %
STOP	0-5
COOL-SLOW	0-30
COOL-MEDIUM	25-50
COOL-FAST	45-80
COOL-V.FAST	75-100

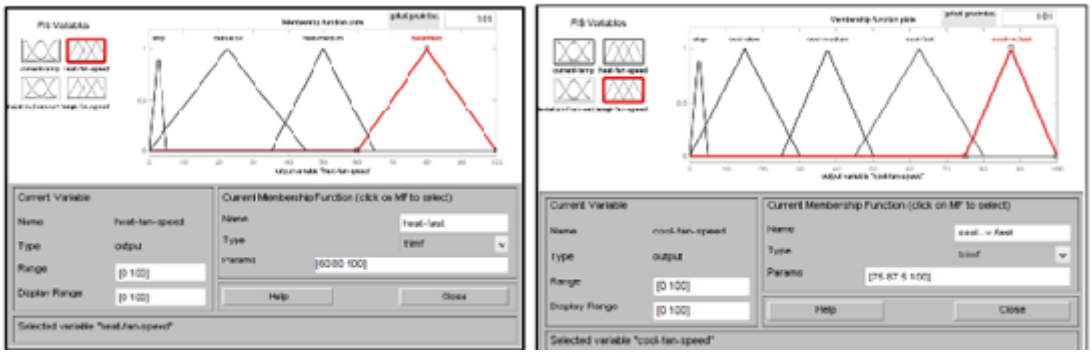

Figure.4:-. Plot Of Membership Function For "heat-fan-speed & cool-fan-speed"

4.1.2.Membership Functions And Ranges For The Second Fuzzy Logic Controller For Controlling The Relative Humidity

4.1.2.1.Input Variables

4.1.2.1.1. Current Temperature

This input variable of the second fuzzy logic controller is dependant entirely on the temperature sensor. As the user is allowed to choose the desired temperature between 18-26'C, so this temperature range is divided into two membership functions.

Table 5:- Membership Function For "current-temperature"

MEMBERSHIP FUNCTIONS	RANGES(^{o}C)
Temp-range-A	16-22.5
Temp-range-B	22-28

4.1.2.1.2.Current-Humidity

Relative Humidity is the percentage of water vapour the air is holding, in relation to the amount it is capable of holding at a given temperature.The Proper Indoor Humidity **[3]** that gives comfortable atmosphere depends on temperatures, as indicated here:

Table 6:- Proper Indoor Humidity

If Outdoor Temperature Is:	Relative Humidity That Should Be Maintained
86'F (30'C)	56%
80.5'F (27'C)	54%
77'F (25'C)	50.5%
71.5'F (22'C)	45%
68'F (20'C)	43.5%
62.5'F (17'C)	40%
59'F (15'C)	35%

The most recent advancement in humidification is a humidifier that automatically delivers the optimum RH without periodic homeowner adjustment.The humidification part is designed in this model in such a way that the user does not have to set any particular humidity. The comfort feeling humidity level within user settable temperature range (18-26C) is pre-set here . from 18(^{o}C) to 22(^{o}C) the ideal comfort RH level is taken as 45%. And from 23-26'C the ideal RH level is taken as 50-54%.

Table 7:-Membership Functions for Current-Humidity

MEMBERSHIP FUNCTIONS	RANGE (%)
DRY	0-21
NOT TOO DRY (NTD)	20-43
SUITABLE-1 (S-1)	42-48
SUITABLE-2 (S-2)	46-54
NOT TOO WET (NTW)	53-75
WET	70-100

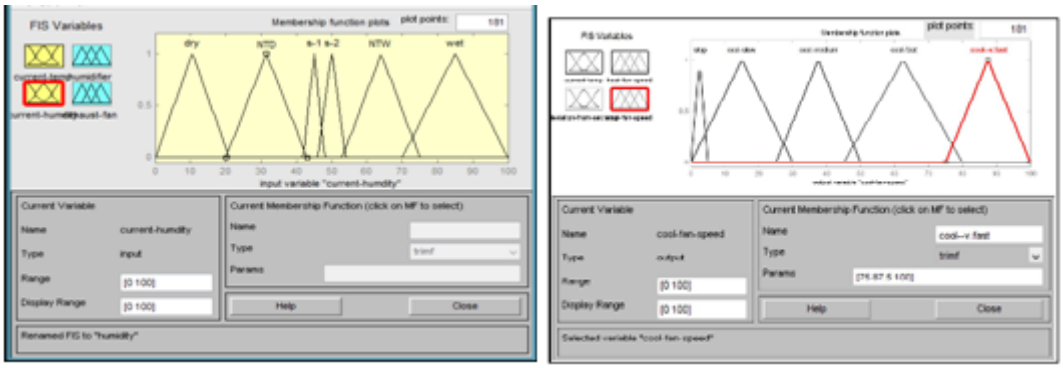

Figure 5:-Plot Of Membership Functions for "Current Temperature" & "Current Humidity"

4.1.2.2.Output Variables
4.1.2.2.1.Humidifier

Table 8:-Membership Functions for Humidifier

MEMBERSHIP FUNCTIONS	RANGE (%)
DRY	0-5
SLOW	4.5-35
MEDIUM	28-62
FAST	60-100

4.1.2.2.2.Exhaust-Fan

Table 9:-Membership Functions for Exhaust-Fan

MEMBERSHIP FUNCTIONS	RANGE(%)
STOP	0-5
SLOW	4.5-35
MEDIUM	28-62
FAST	60-100

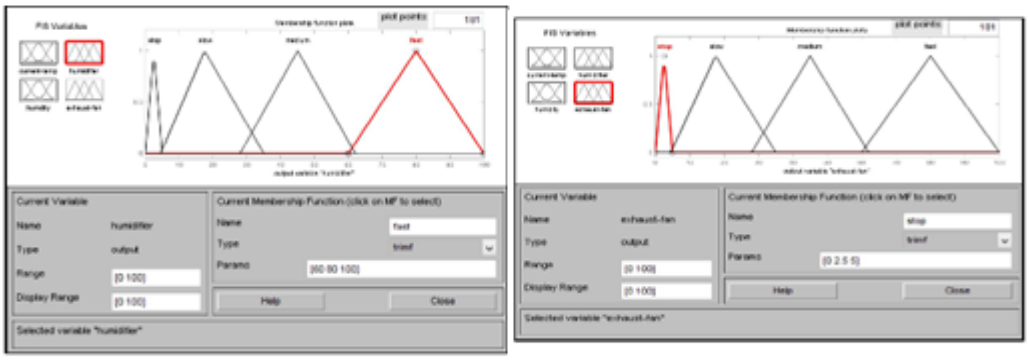

Figure 6:- Plot of Membership Functions For “Humidifier” & “Exhaust-fan-speed”

4.2.Rule Base :-

Table 10 :- Rule Base For First Fuzzy Logic Controller

RULE NO	CURRENT-TEMP	DEVIATION FROM SET-TEMP	HEAT-FAN-SPEED	COOL-FAN-SPEED
1.	Cold	PL	Heat-Fast	Stop
2.	Cold	PS	Heat-Medium	Stop
3.	Cool	PL	Heat-Medium	Stop
4.	Cool	PS	Heat-Slow	Stop
5.	Cool	O	Stop	Stop
6.	Cool	NS	Stop	Cool-Slow
7.	Normal	PS	Heat-Slow	Stop
8.	Normal	O	Stop	Stop
9.	Normal	NS	Stop	Cool-Slow
10.	Warm	PS	Heat-Slow	Stop
11.	Warm	O	Stop	Stop
12.	Warm	NS	Stop	Cool-Slow
13.	Warm	NL	Stop	Cool-Medium
14.	Hot	NS	Stop	Cool-Slow
15.	Hot	NL	Stop	Cool-Medium
16.	Hot	NE1	Stop	Cool-Fast
17.	Very-Hot	NS	Stop	Cool-Slow
18.	Very-Hot	NL	Stop	Cool-Medium
19.	Very-Hot	NE1	Stop	Cool-Fast
20.	Very-Hot	NE2	Stop	Cool-V.Fast
21.	Extrm-Hot	NE1	Stop	Cool-Fast
22.	Extrm-Hot	NE2	Stop	Cool-V.Fast

Table 11 :- Rule Base For Second Fuzzy Logic Controller

RULE NO.	CURRENT TEMPERATURE	HUMIDITY	HUMIDIFIER SPEED	EXHAUST FAN SPEED
1	Temp-Range-A	DRY	Fast	Stop
2	Temp-Range-A	NTD	Medium	Stop
3	Temp-Range-A	S-1	Stop	Stop
4	Temp-Range-A	S-2	Stop	Slow
5	Temp-Range-A	NTW	Stop	Medium
6	Temp-Range-A	WET	Stop	Fast
7	Temp-Range-B	DRY	Fast	Stop
8	Temp-Range-B	NTD	Medium	Stop
9	Temp-Range-B	S-1	Slow	Stop
10	Temp-Range-B	S-2	Stop	Stop
11	Temp-Range-B	NTW	Stop	Medium
12	Temp-Range-B	WET	Stop	Fast

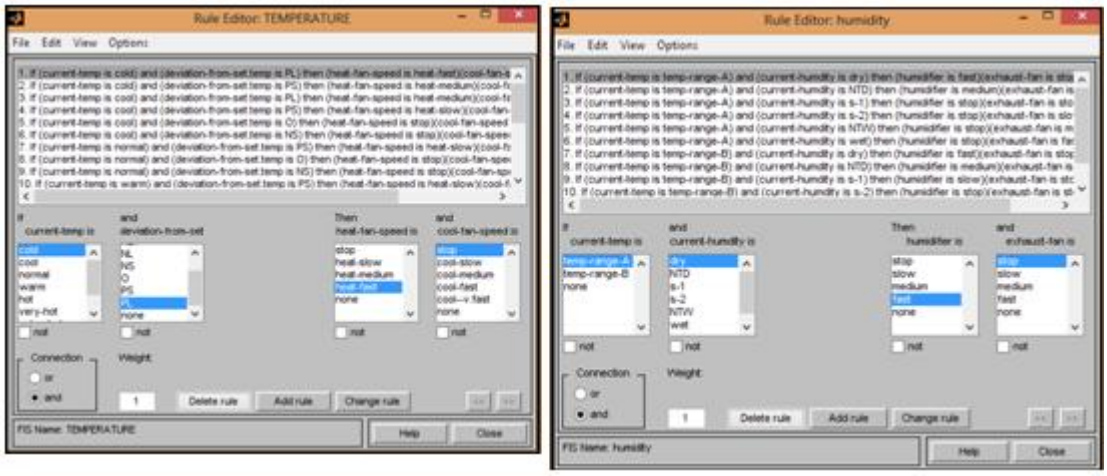

Figure 7:-Matlab Rule Editor for temperature & humidity controller

4.3.Fuzzification:-

We select two random values of input variables from first fuzzy logic controller to demonstrate how fuzzification is done in both the fuzzy logic controller used in this system.

In the first fuzzy logic controller, the signal value of current-Temperature=13C intersects with fuzzy variables "Cold" and "cool", where "cold" is taken as the first fuzzy variable f[0] and "Cool" is the second fuzzy variable, f[1]. The f[0] maps to the membership function value of 0.86 while f[l] maps to the value of 0.13. Similarly, for the input value of "deviation-from current-temperature"=+10,the corresponding intersection of fuzzy variables are "PS" as the second active fuzzy variable f[2] and "PL" as the first active fuzzy variable f[3]. The f[2] will thereby map to the membership function value of 0.04 while f[3] corresponds to 0.96.

Table 12 :- Results Of Fuzzification:-

INPUT VARIABLES	VALUES	REGION SELECTION	FUZZY SET CALCULATION
CURRENT TEMPERATURE	13	0<13<15	f1=(15-13)/15=0.13 f0=1-0.13=0.86
DEVIATION-FROM-SET-TEMPERATURE	+10	0<10<10.5	f3=(10.5-10)/10.5=0.04 f2=0.96

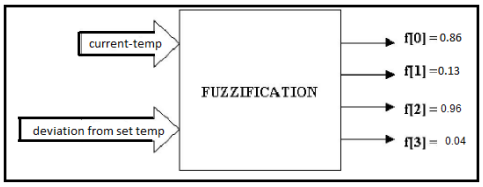

Figure 8:- Block Diagram Of Fuzzification Model

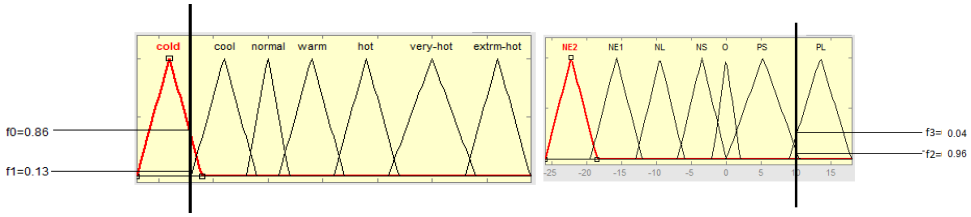

Figure 9:- Fuzzification Of Crisp Input, "Current-Temperature" = 13C. & "Deviation-From-Set-Temperature" = +10

4.4.Inference Engine:-

The inference block accepts four inputs from the Fuzzification process and the inputs of the inference would be f[O], f[l], f[2] and f[3]. The min-max inference method uses the min operator between the two inputs (rule's antecedent) resulting from rule conditions and the rules are finally combined by using OR operator and interpreted as the max operation for each possible value of the output variable. Hence four outputs RO, RI, R2, and R3 will be generated. The values of f[O], f[l], f[2] and f[3] are 0.86, 0.13, 0.96 and 0.04 respectively. Applying the max-min composition, f[O] and f[l] will perform the operation with f[2] and f[3] to output the R values as follows:

RO=f(0) ^ f(2) = f(0) AND f(2) =0.86 AND 0.96 = 0.86
R1= f(0) ^ f(3) = f(0) AND f(3) = 0.86 AND 0.04 =0.04
R2= f(1) ^ f(2) = f(1) AND f(2) = 0.13 AND 0.96 = 0.13
R3= f(1) ^ f(3) = f(1) AND f(3) = 0.13 AND 0.04 = 0.04

Note that the sign ^ indicates that a minimum value will be taken between the two membership function values. Also, in Mamdani-min, minimum is also interpreted as ANDing the two membership function values. However, it is important to note that this is not a logical ANDing. Rather, it is the comparison to obtain the minimum between the two membership functions. The inference model example of its input and outputs are shown in Fig . 10.

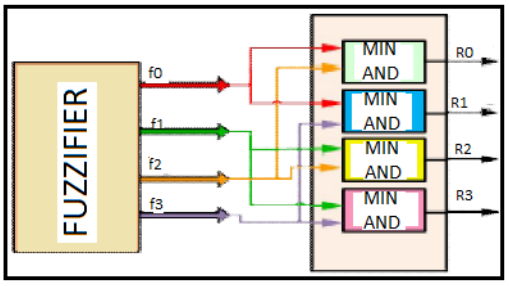

Figure 10:-Block Diagram Of Inference Engine

4.5.Rule Selector:-

The rule selector receives two crisp values of temperature and humidity. It gives singleton values of output functions under algorithm rules applied on design model. For two variables, four rules are needed to find the corresponding singleton values S1, S2, S3 and S4 for each variable according to these rules are listed in TABLE 13. The rule base accepts two crisp input values, distributes the universe of discourse into regions with each region containing two fuzzy variables, fires the rules, and gives the output singleton values corresponding to each output variable. Fig. 11 shows the main block diagram of the Rule Base.

Table 13:-Illustration Of Rules For The Applied Model

RULE NO.	INPUTS		SINGLETON VALUES OF OUTPUTS		SINGLETON VALUES
	CURRENT TEMP	DEVIATION FROM SET-TEMP	HEAT-FAN-SPEED	COOL-FAN-SPPED	
1.	COLD	PL	HEAT-FAST=0.8	STOP=0.025	S0
2.	COLD	PS	HEAT-MEDIUM=0.5	STOP=0.025	S1
3.	COOL	PL	HEAT-MEDIUM=0.5	STOP=0.025	S2
4.	COOL	PS	HEAT-SLOW=0.22	STOP=0.025	S3

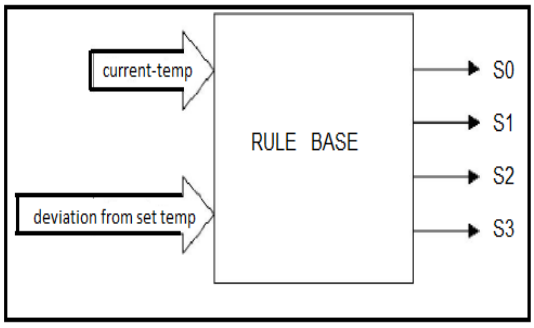

Figure 11:- Block Diagram Of Rule Base

This process is achieved by dividing the universe of discourse into six regions; with each region containing only two fuzzy variables. The illustrations of the region divisions are shown in Fig 12.

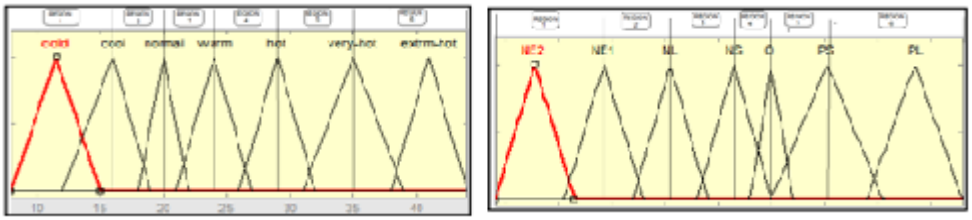

Figure 12:-Illustration of Region Deivisions

Table 14:- Division Of Regions For Current Temperature And Deviation From Set-Temperature

INPUTS	REGIONS	RANGE OF VALUES
CURRENT-TEMPERATURE	1.	8-16
	2	16-20
	3	20-24
	4	24-29
	5	29-35
	6	35-44
DEVIATION FROM SET-TEMPERATURE	1	-26 to -15.75
	2	-15.75 to -9.5
	3	-9.5 to -3.5
	4	-3.5 to 0
	5	0 to 5.25
	6	5.25 to 18

4.6.Deffuzifier:-

In this system, four defuzzifiers control the actuators; heat-fan-speed, cool-fan-speed, humidifier and exhaust-fan-speed. The defuzzification process provides the crisp value outputs after estimating its inputs **[1].** But as we are citing an example of how the defuzzification is done, we select only 2 defuzzifiers that control the heat-fan and cool-fan-speeds in correspondence to the current-temperature=+13 & deviation=+10. So 8 inputs are given to each of two defuzzifiers, four values of R0, R1, R2, R3 from the outputs of inference engine and four values S0, S1, S2, S3 from the rule selector .

Each defuzzifier estimates the crisp value output according to the center of average (C.O.A) method using the mathematical expression $\sum S[i]*R[i] / \sum R[i]$, where i = 1 to 4. Each. output variable membership function plot consists of five functions with the same range values for simplification

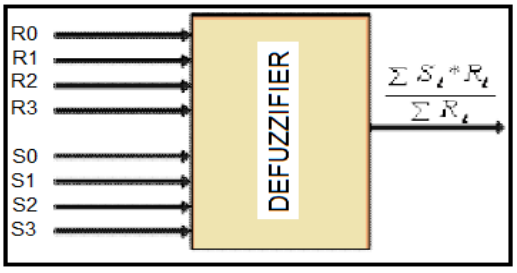

Figure 13:- Block Diagram Of Defuzzifier

V. RESULTS AND DISCUSSION

According to the results of inference engine$\sum R[i]$=R0+R1+R2+R3= 0.86+0.04+0.13+0.04=1.07

Table 15:- Designed Value For Heat-Fan-Speed

Si	Ri	Si*Ri
0.8	0.86	0.688
0.5	0.04	0.02
0.5	0.13	0.06
0.22	0.04	0.008

∑S[i]*R[i] =0.688 + 0.02 + 0.06 + 0.008 = 0.776 ; ∑R[i]=1.07 ; so ∑S[i]*R[i] / ∑R[i]= 0.776/1.07 =0.725 =72.5%

Table 16:- Designed Value For Cool-Fan-Speed

Si	Ri	Si*Ri
0.025	0.86	0.0215
0.025	0.04	0.001
0.025	0.13	0.00325
0.025	0.04	0.001

∑S[i]*R[i] =0.0215 + 0.001 + 0.003 + 0.001 =0.02675 ; ∑R[i]=1.07 =1.07.
So ∑S[i]*R[i] / ∑R[i]= 0.02675/1.07 =0.025 = 2.5%

Using the above mathematical expression the crisp values for output variables were determined and the results were found according to the MATLAB simulation as shown in Fig.14. These results are compared in TABLE 17 and found correct according to the design model. MATLAB simulation was adapted according to the arrangement of membership functions for four rules as given in TABLE 13.
In Fig. 14 the same values of input variables, Current-Temperature=13, and Deviation from set-temperature=+10 are shown. Various values of input and output variables match the dependency scheme of the system design. When the temperature reaches the set value (13+10=23'C),the humidifying controller gives the correct output as designed .

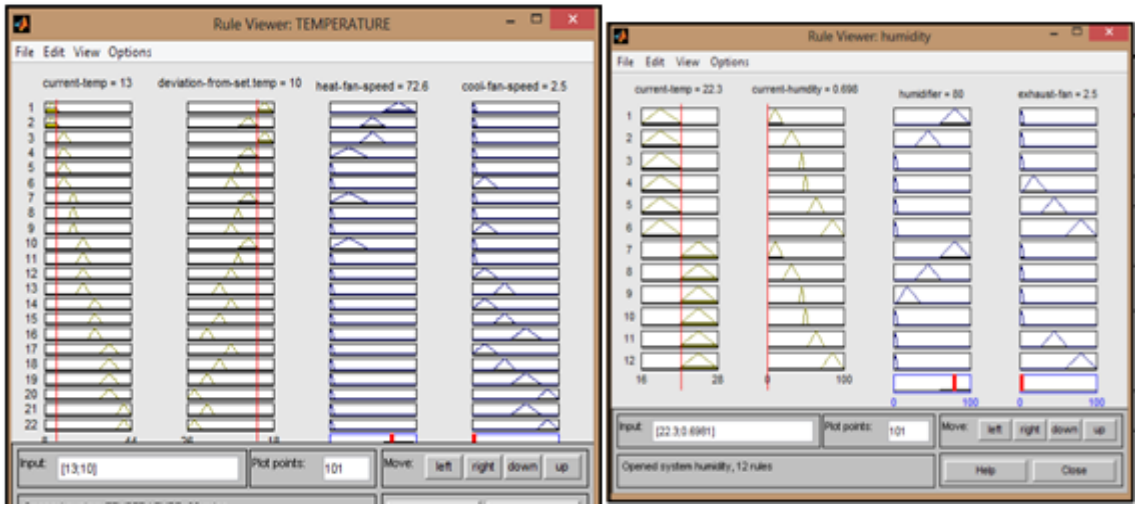

Figure 14:-Matlab Rule Viewer

The correctness of results shows the validity of the simplified design work for processing system using fuzzy control system.

5.1.Comparison Between Calculated & Simulated Result:-

Table :-17

RESULT	HEAT-FAN-SPEED	COOL-FAN-SPEED
Design values	72.6	2.5
Calculated values	72.5	2.5
% error	0.13	0

VI. SIMULATED GRAPH DISCUSSION:-

This system was simulated for the given range of input variables. In this design model, the speed of heat-fan and cool-fan depends upon the selected value of temperature sensor, whereas humidifier and exhaust fan speeds depend on the value of both humidity and temperature sensors . The simulated and calculated results are according to the reliance scheme.

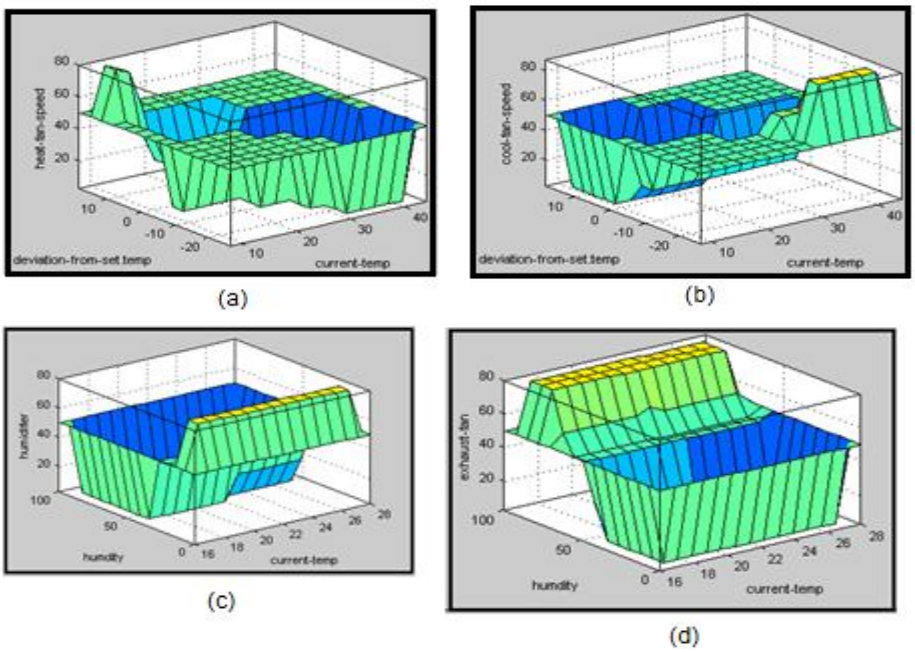

Figure 15 :- 3d Plots Between (a)Current Temperature & Deviation With Heat Fan Speed ; (b) Current Temperature & Deviation With Cool-Fan-Speed ; (c) Current Temperature & Current Humidity With Humidifier ; (d) Current Temperature & Current Humidity With Exhaust-Fan-Speed

VII. SOME SPECIAL CHARACTERISCTICS OF OUR PROPOSED MODEL

(a).The proposed room temperature and humidity controller works perfectly over a wider range of temperature 8-44 ^{0} C.

(b).There are two controllers in this system which measures temperature and humidity respectively. Both are designed using fuzzy logic. After the user sets a desired room temperature, the temperature controller starts immediately to bring back the room temperature to desired value in much shorter time. And when the current temperature is close to to desired value, the humidity controller starts working the get the ideal relative humidity for that temperature.

(c).The number of membership functions of input and output variables of both temperature and humidity controllers are more while difference between upper and lower limits of each range is reduced. This improves the accuracy and sensitivity of the controllers.

(d).The output of each of the controllers is calculation adaptive and is sensitive to small variation of temperatures.

(e).The efficiency of this model is very high as %error between calculated and measured value for a given temperature is approximately close to 0.15 only (shown in the paper).

VIII. CONCLUSION

The algorithmic design approach makes the system efficient and absolutely under control. The analysis clearly maps out advantage of fuzzy logic in dealing with problems that are difficult to study analytically yet are easy to solve intuitively in terms of linguistic variables. In case of the Air-Conditioning system, fuzzy logic helped solve a complex problem without getting involved in intricate relationships between physical variables. Intuitive knowledge about input and output parameters was enough to design an optimally performing system. The utility of the proposed system in processing plants is being carried out and in future it will help to design the advanced control system for the various industrial applications in environment monitoring and management systems.

IX. FUTURE WORK

I. Designing a powerful ground source reversible pumps using fuzzy logic controller which can handle a wider range of temperature and can heat and cool more sensitively and simultaneously.

II. Adding more intelligence to the room condition controller like occupancy, auto human detector and adjusting itself according to outdoor temperature and humidity at various times a day and all round the year.

III. In future we will come up with a device that implements the Fuzzy Logic controller in an embedded system which can be used for increasing the efficiency of Room Air Conditioners.

REFERENCES

[1]. I.J. Nagarath,M. Gopal, *Control systems engineering* (New Delhi,New age international (P) limited,2007)

[2]. Technical case studies on fuzzy logic control system from http://www.wikipedia.org, http://sciencedirect.com/, http://aptronix.com ,http://www.mastertherm.co.uk/heat-pumps-residential-use/how-does-heat-pump-work, http://www.ianrpubs.unl.edu/pages/publicationD.jsp?publicationId=1000

[3]. David P. Shelton,*Air properties: temperature and relative humidity,* University of Nebraska-Lincoln Extension, Institute of Agriculture and Natural Resources, 2008

[4]. Shabiul Islam, Shakowat, "Development of a Fuzzy Logic Controller Algorithm for Air-conditioning System", *ICSE2006Proc2006 IEEE*

[5]. M. Saleem Khan and Khaled Benkrid, "A proposed Grinding and Mixing System using Fuzzy Time Control Discrete Event Model for Industrial Application", Lecture Notes in Engineering and Computer Science vol. 2175 2009, p.p. 1231-1236, *Directory of Open Access Journals (DOAJ)*

[6]. Shakowat Zaman Sarkar, "A proposed Air–conditioning systemusing Fuzzy Algorithm for Industria Application" *ICSE IEEE Proc.* (2006) 832-834

[4] M. Spott and D. Nauck, "Towards the automation of intelligent data analysis" *Appl. Soft Comput.* 6(2006) 348-356.

[7]. Zain, Z.M. ; Kuantan ; Abdullah, N.H. ; Hanafi, A.H.M. - Microcontroller-Based Energy Saving Control for Air - Conditioning System Using Fuzzy Logic Approaching: An Overview- Research and Development, 2006. SCOReD 2006. 4th Student Conference on date 27-28 June 2006

[6]. Islam, M.S. ; Multimedia Univ., Cyberjaya ; Zaman Sarker, M.S. ; Ahmed Rafi, K.A. ; Othman, .- Development of a Fuzzy Logic Controller Algorithm for Air-conditioning System-published in Semiconductor Electronics, 2006. ICSE '06. IEEE International Conference on date Oct. 29 2006-Dec. 1 2006

[7]. Wafa Batayneh1, Omar Al-Araidah2, Khaled Bataineh1- Fuzzy logic approach to provide safe and comfortable indoor environment- International Journal of Engineering, Science and Technology Vol. 2, No. 7, 2010, pp. 65-72

[9]. sanjit kumar dash, gouravmoy mohanti, abhishek mohanti"- "Intelligent air conditioning system using fuzzy logic", International Journal of Scientific & Engineering Research Volume 3, Issue 12, December-2012 1 ISSN 2229-5518

[10]. M. Abbas, M. Saleem Khan, Fareeha Zafar- Autonomous Room Air Cooler Using Fuzzy Logic Control System, International Journal of Scientific & Engineering Research Volume 2, Issue 5, May-2011 ISSN 2229-5518.

***Tarun Kumar Das*[1]**

assistant professor in Electronics & Communication Engineering Department at Future Institute of Engineering & Management under West Bengal University of Technology. His research interest includes control system,signals and systems,Digital signal processing, microelectronics & VLSI.

Yudhajit das[2], *presently 3rd year b.tech student, future institute of engg & management (Wbut), area of interest- control system, DSP*

American Journal of Engineering Research (AJER)
e-ISSN : 2320-0847 p-ISSN : 2320-0936
Volume-02, Issue-11, pp-98-103
www.ajer.org

Research Paper Open Access

Derivation of Equations for Ground Level, Water Surface Depth and Well Depth and Determination of Flow Directions of Shallow Aquifers.

O.S. Awokola, Maku Olakunle, and O.D. Akinyemi
[1]*Department of Civil Engineering, Federal University of Agriculture, Abeokuta, Nigeria*
[2]*Department of Physics, Federal University of Agriculture, Abeokuta, Nigeria*
Awokola, O.S, Department of Civil Engineering, Federal University of Agriculture, PMB 2240, Abeokuta, Nigeria.

Abstract: - Water is essential to maintain and sustain human life, animal and water therefore is important in that it is essential for growing food, for household water uses, as a critical input into industry, for tourism and cultural purposes, and for its role in sustaining the earth's ecosystem. The study is to determine the direction of ground water flow and also establish the parametric relationship of the measured topographical and derived data for the management of exploration and exploitation of groundwater in shallow aquifers of the study area. The methods involve the selection of ten wells within the University campus. The wells were used to obtain information on ground water topographical information. Data was acquired using a Global Positioning System (GPS) Garmin 76csx which is a satellite based equipment for position determination. The data acquired were wells coordinates and the elevation of the well location above mean seal level (amsl), while the water level values of wells as measured with the aid of an Electronic Water Level Indicator was used to measure the water surface depth from the ground surface.

The relative positions of the wells were plotted using AutoCAD 2012 version and it was superimposed on the base map of the area. Suffer for window (version 8, topographical analysis software) was used to produce the contour of the Ground Level, Water surface Level and the Well Level water flow direction. Simple regression analysis was applied to the computed values according to their functional relationships, ground level-water surface level, ground level-well level and depth of well-depth of water surface. The derived equations from the measured and derived parameters were of the linear, power, exponential, logarithmic and 2nd degree polynomial types. The coefficient of determination (R^2) obtained from the various analysis ranges from 0.8485 to 0.9834. The coefficient of determination (R^2) of 0.98 is close to unity which is the highest theoretically possible thus indicating that whenever the values of the independent variables or assigned variables are known exactly, the corresponding values of the dependent or derived variables can be evaluated with a high degree of accuracy. In all the relationships the 2nd degree polynomial is consistent with higher values of the coefficient of determination. The results of the equations derived from this study indicate that there was an explanatory independent variable for ground level in predicting water surface level with a coefficient of determination r^2=98% and also the results of well level prediction of r^2 of 94% - 95% and depth of well prediction of 85% - 97% for all the five different equations considered in the study. The equations established can be a useful and essential tool in the development of sound groundwater management plans, formulation of policies for exploration and exploitation of shallow aquifers.

Keywords: *- Coefficient of determination, Shallow Aquifer, 2nd degree polynomial, Power equation, Exponential equation*

I. INTRODUCTION

Water is essential to maintain and sustain human life, animal and plant (Patil and Patil, 2010). Water therefore is important in that it is essential for growing food, for household water uses, as a critical input into industry, for tourism and cultural purposes, and for its role in sustaining the earth's ecosystem (Mark *et.al*,

2002). However, access to safe drinking water and sanitation is critical in terms of health, especially for children. For instance, unsafe drinking water contributed to numerous health problems in developing countries such as the one billion or more incidents of diarrhoea that occur annually (Mark *et al.*, 2002). According to Asonye et al. (2007), availability of safe and reliable source of water is an essential prerequisite for sustained development. The availability and purity of groundwater are affected by location, construction and operation of wells (Egbulem, 2003). Adekunle *et al*. (2007) has established the contamination of wells sited close to dumping sites in southwest, Nigeria. Of all sources of freshwater on the earth, groundwater constitutes over 90% of the world's readily available freshwater resources (Boswinkel, 2000) with remaining 10% in lakes, reservoirs, rivers and wetlands.

Groundwater differs from surface water because of the contrasting physical and chemical environment in which it occurs, although the water itself is essentially part of the same overall hydrological cycle. An increased awareness of groundwater in the hydrological cycle would result in better understanding of the resource, its susceptibility to pollution, and the need for increased efforts to protect its quality. In evaluating groundwater risk from pollution, several methods have been used that produce groundwater vulnerability maps of varying reliability (Piscopo, 2001; Rupert 2001; Radig, 1997). Groundwater moves through aquifers from areas of recharge to areas of discharge (determined by the geological structure), normally at slow rates. These slow flow rates and long residence times, consequent upon large aquifer storage volumes, are amongst the numerous distinctive features of groundwater systems. Groundwater forms the 'invisible part' of the hydrological cycle, which can lead to misconceptions amongst stakeholders. The study is to determine the direction of ground water flow and also establish the parametric relationship of the measured and derived data for the management of exploration and exploitation of groundwater in shallow aquifers of the study area. The result of the study will provide time saving and cost effective models as a tool to use for groundwater exploitation and information on how to ensure that land use activities in the recharge area will not pose a threat to the quality of the ground water.

II. STUDY AREA

The University lies on latitude 7°25´N and longitude 3°25´E and it has a landed area of 9,700 hectares which is situated northwest of Abeokuta Township. It is bounded to the west by Abeokuta- Opeji-Eruwa road and to the east by Osiele-Alabata road. The site falls within the geographical region of Odeda Local Government (UNAAB Master Plan, 1991). Ten Hand-Dug wells were selected within the University campus for study. It was ensured that the ten wells selected were best representative of the area.

III. MATERIALS AND METHODS

This involves the selection of ten wells within the University campus. The wells were used to obtain information on ground water. The geometry data was acquired using a Global Positioning System (GPS) Garmin 76csx which is a satellite based equipment for position determination. The data acquired were wells coordinates and the elevation of the well location above mean seal level (amsl) Table 1, while the water level values of wells as measured with the aid of an Electronic Water Level Indicator was used to measure the water surface depth from the ground surface Table 2, to know the depth of the well. From these three parameters, the water surface level and Well level were deduced using the following relations

(i) Well Level = Ground Level -Depth of Well
(ii) Water Surface Level = Ground Level –Water Surface Depth

The relative positions of the wells were plotted using AutoCAD 2012 version and it was superimposed on the base map of the area (i.e. FUNAAB Map) Figure 1. Suffer for window (version 8, topographical analysis software) was used to produce the contour of the Ground Level, Water surface Level and the Well Level water flow direction Figure 2. Microsoft Excel and Notepad, were used to prepare the data in the format that is acceptable to both the AutoCAD and Suffer for window software. Simple regression analysis was applied to the computed values according to their functional relationships, ground level-water surface level, ground level-well level and depth of well-depth of water surface. The computed values were subjected to scatter plot and various trend lines, the trend lines were used to graphically display trends in data to obtain appropriate models for each functional relationship (Figures 3-5).

IV. RESULTS AND DISCUSSION

The relative positions of the ten wells in are as shown in Figure 1 with reference to the longitude and latitude. The contour map of water level showing flow direction (Fig. 2) is a powerful tool for determination of appropriate location for the construction of wells, septic tank, grave, burial-ground and dumpsites. Pollution producing activities such as septic tank, grave, burial-ground and dumpsites must be sited downstream of a well.

The flow directions in Fig. 2 is in the West-East and East-West direction, pollution producing activities must be sited downstream of a well.

The derived equations from the measured parameters are of the linear, power, exponential, logarithmic and 2nd degree polynomial types. The coefficient of determination (R^2) obtained from the various analysis (Figures 3-5 and Tables 3-5) ranges from 0.8485 to 0.9834. The coefficient of determination (R^2) of 0.98 is close to unity which is the highest theoretically possible thus indicating that whenever the values of the independent variables or assigned variables are known exactly, the corresponding values of the dependent or derived variables can be evaluated with a high degree of accuracy. The coefficients of determination (R^2) can also be described as the ratio of the explained variation to the total variation that gives an indication of how well the regression line fits the observed data.

From the summary detailed in Tables 3-5 the three different relationships were summarized and the coefficient of determination was used to categorize the equations in order of higher value of coefficient of determination. In all the relationships in Tables 3-5 the 2nd degree polynomial is consistent with higher values of the coefficient of determination. The equations 5, 10 and 15 in Tables 3-5

$$y = -0.0093x^2 + 3.283x - 141.17 \cdots\cdots\cdots\cdots\cdots r^2 = 0.9834 \cdots\cdots\cdots 5(Table3)$$

$$y = -0.0093x^2 + 3.233x - 138.75 \cdots\cdots\cdots\cdots\cdots r^2 = 0.9542 \cdots\cdots\cdots 10(Table4)$$

$$y = 0.0602x^2 - 0.0043x + 0.877 \cdots\cdots\cdots\cdots\cdots r^2 = 0.9728 \cdots\cdots\cdots 15(Table5)$$

Despite the fact that the results are derived from a small sample size, the strength of the correlations provides evidence that there is a relationship between the parameters considered and their functional relationship established.

V. CONCLUSION

It can be concluded that knowledge of the direction of ground water flow can be a useful tool in the management of exploration and exploitation of shallow aquifers and in the reduction or minimization of groundwater contamination. It can be used as a guide to map out the land use of the study area and thereby take steps to ensure that land use activities in the recharge area will not pose a threat to the quality of the ground water. The flow directions in Fig. 2 is in the West-East and East-West direction, pollution producing activities must be sited downstream of a well.

The results of the equations derived from this study indicate that there was an explanatory independent variable for ground level in predicting water surface level with a coefficient of determination r^2=98% and also the results of well level prediction of r^2 of 94% - 95% and depth of well prediction of 85% - 97% for all the five different equations considered in the study. The equations established can be useful and essential in the development of sound groundwater management plans, formulation of policies for exploration and exploitation of shallow aquifers. The derived equations are time saving and cost effective models that can be used for groundwater exploration, exploitation. The groundwater study is generally site specific, the range of coefficients of correlation and determination obtained for the study area are universally acceptable.

Table 1: Coordinates and Elevations of Wells

Wells	Coordinates		Elevation Above Mean Sea Level(amsl) (m)
W_1	N7° 13′ 29.6″	E3° 25′ 26.8″	150
W_2	N7° 13′ 31.4″	E3° 25′ 27.2″	148
W_3	N7° 13′ 34.0″	E3° 25′ 27.1″	144
W_4	N7° 13′ 40.0″	E3° 25′ 29.0″	136
W_5	N7° 13′ 24.6′	E3° 25′ 54.3″	122
W_6	N7° 14′ 11.7′	E3° 26′ 12.7″	126
W_7	N7° 14′ 09.2″	E3° 26′ 11.4″	125
W_8	N7° 14′ 08.8″	E3° 26′ 11.7″	126
W_9	N7° 14′ 08.6″	E3°26′ 15.5″	127
W_{10}	N7° 13′ 58.3″	E3° 26′ 12.7″	144

Table 2: The water level values of wells as measured with the aid of an Electronic Water Level Indicator

Wells	Ground level at mean sea level(amsl)(m)	Depth of Well (m)	Average Water Surface Depth (m)	Water Surface level above mean sea level(amsl) (m)	Well level above mean sea level(amsl) (m)
W_1	150	10.87	8.81	141.19	139.13
W_2	148	10.35	6.85	141.15	137.65
W_3	144	9.92	6.16	137.84	134.08
W_4	136	4.94	2.27	133.73	131.06
W_5	122	6.13	3.86	119.73	115.87
W_6	126	2.67	1.40	124.6	123.33
W_7	125	2.02	.88	124.12	122.98
W_8	126	3.41	1.65	124.35	122.59
W_9	127	6.70	3.09	123.91	120.3
W_{10}	144	11.15	8.26	135.74	132.85

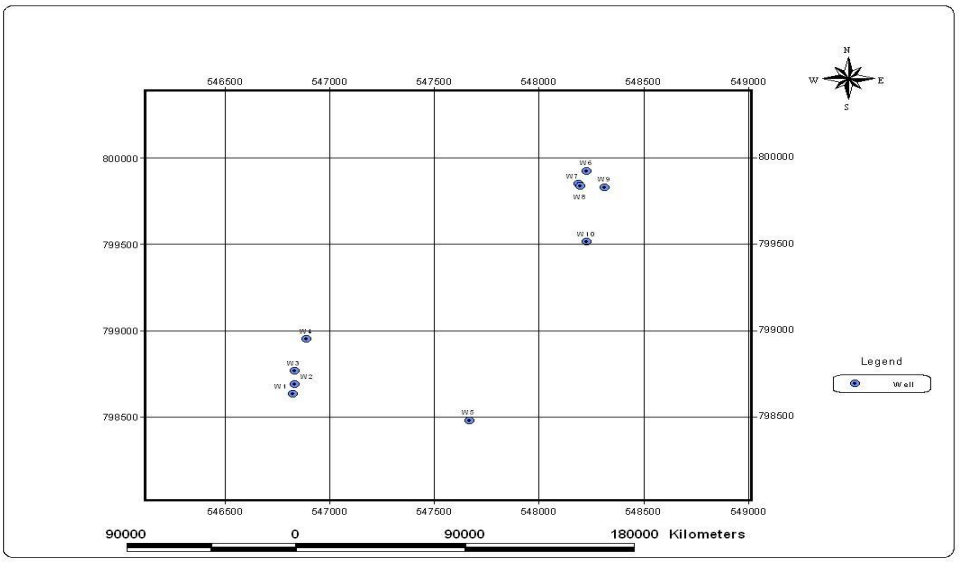

Fig. 1: Relative Positions of the Ten Wells with the Longitude and Latitude

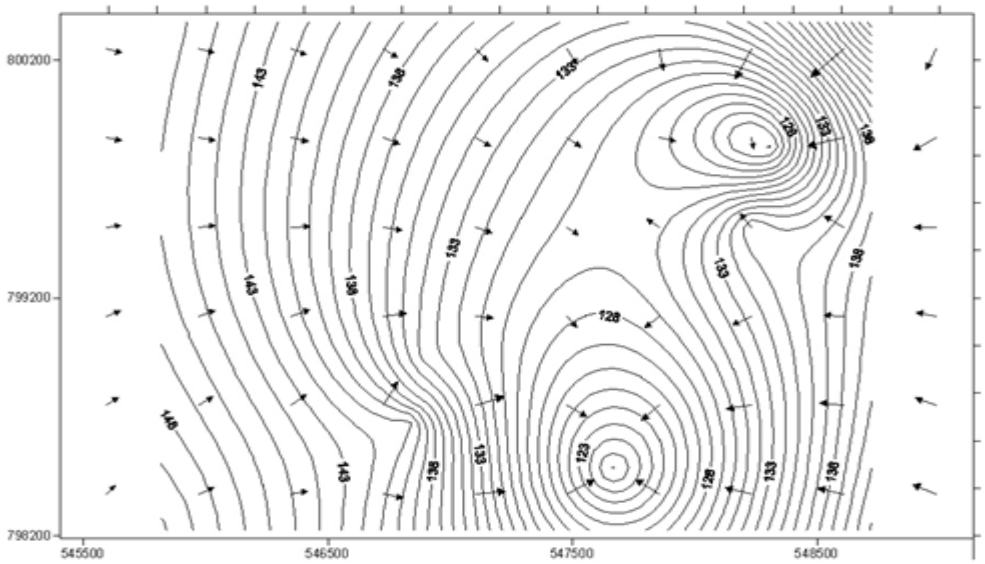

Fig. 2: Contour Map of Water Level Showing Flow Direction

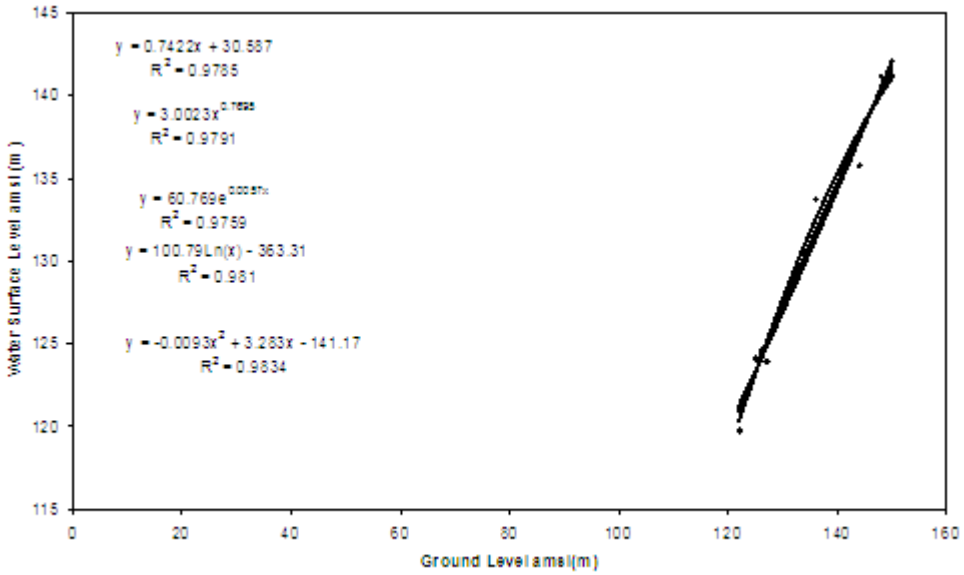

Fig 3 : Ground Level amsl and Water Surface Level amsl

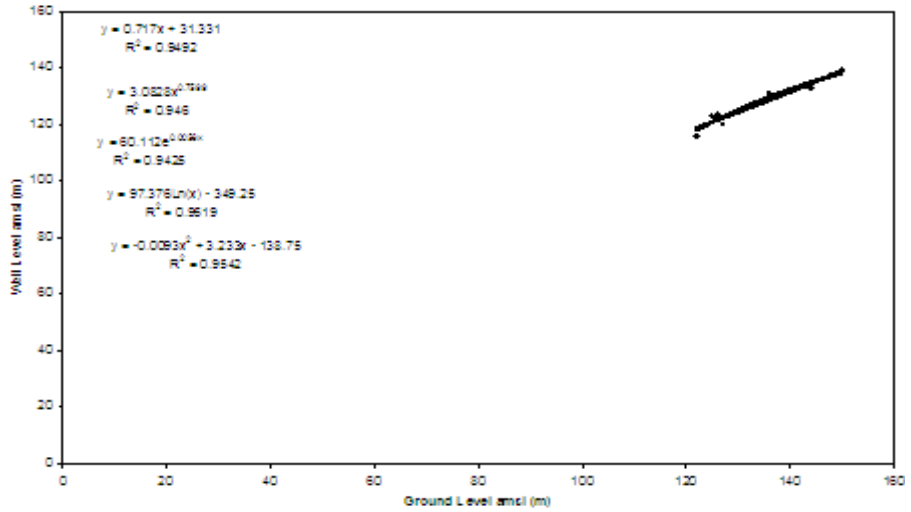

Fig. 4: Ground Level amsl and Well Level amsl (m)

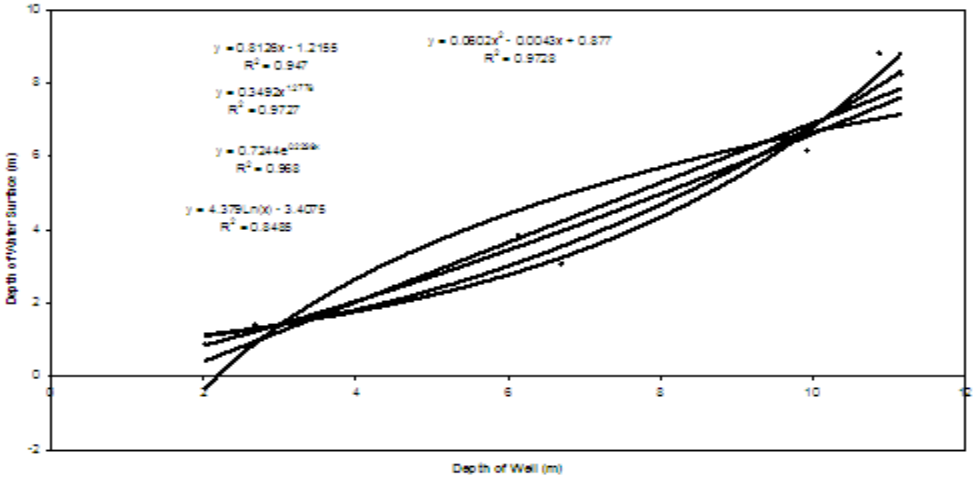

Fig 5: Depth of Well and Depth of Water Surface (m)

Table 3: Summary of various trend line equations for Ground Level (amsl) and Water Surface Level (amsl)

Equations	Equation Number	Type of Equation	Coefficient of Determination R^2
$y = 0.7422x + 30.587$	1	Linear	0.9785
$y = 3.0023\,x^{0.7695}$	2	Power	0.9791
$y = 60.769\,e^{0.0057x}$	3	Exponential	0.9759
$y = 100.79Ln(x) - 363 - 31$	4	Logarithmic	0.981
$y = -0.0093\,x^2 + 3.283\,x - 141.17$	5	2nd degree polynomial	0.9834

Table 4: Summary of various trend line equations for Ground Level (amsl) and Well Level (amsl)

Equations	Equation Number	Type of Equation	Coefficient of Determination R^2
$y = 0.717x + 31.331$	6	Linear	0.9402
$y = 3.0828\,x^{0.7599}$	7	Power	0.946
$y = 60.112\,e^{0.0056x}$	8	Exponential	0.9425
$y = 97.376Ln(x) - 349.25$	9	Logarithmic	0.9519
$y = -0.0093\,x^2 + 3.233\,x - 138.75$	10	2nd degree polynomial	0.9542

Table 5: Summary of various trend line equations for Depth of Well and Depth of Water Surface

Equations	Equation Number	Type of Equation	Coefficient of Determination R^2
$y = 0.8126x - 1.2155$	11	Linear	0.947
$y = 0.3492\,x^{1.2778}$	12	Power	0.9727
$y = 0.7244\,e^{0.2239x}$	13	Exponential	0.968
$y = 4.379Ln(x) - 3.4075$	14	Logarithmic	0.8485
$y = 0.0602\,x^2 - 0.0043\,x + 0.877$	15	2nd degree polynomial	0.9728

REFERENCES

[1] Adekunle, I.M., M.T. Adetunji, A.M. Gbadebo and O.B. Banjoko. 2007. "Assessment of Groundwater Quality in a Typical Rural Settlement in Southwest, Nigeria". *Int. J. Environ. Public Health.* 4(4): 307-318.

[2] Asonye C.C., Okolie N.P., Okenwa E.E. and Iwuanyanwu U.G. (2007) – Some physico-chemical characteristics and heavy metal profiles of Nigerian rivers, streams and waterways. African Journal of Biotechnology Vol. 6 (5), pp. 617-624

[3] Boswinkel, J. A., (2000). Information Note, International Groundwater Resources Assessment Centre (IGRAC), Netherlands Institute of Applied Geoscience, Netherlands. In: UNEP (2002), Vital Water Graphics - An Overview of the State of the World's Fresh and Marine Waters, UNEP, Nairobi, Kenya.

[4] Patil, V.T. and P.R. Patil, 2010. Physicochemical analysis of selected groundwater samples of Amalner town in Jalgaon district, Maharas htra, India. E J. Chem., &:111-116.

[5] Piscopo, G. 2001. Groundwater vulnerability map explanatory notes. MacIntyre Catchment. Published by Centre for Natural Resources. NSW Department of Land and Water Conservation. NSW Government. 13pp.

[6] Radig, S., 1997 North Dakota Geographic Targeting system for groundwater monitoring. http://www.health.state.nd.us/wq/pubs/GWT.HTM

[7] Rupert, M.G. 2001. Calibration of the DRASTIC groundwater vulnerability mapping method. Ground Water 39, 625-630

[8] Mark, W.R., Ximing Cai and Sarah A.C. 2002. World water and wood to 2025: dealing with scarcity. International Food Policy Research Institute, NW, Washington, DC, USA.

[9] Egbulem B.N. (2003) - Shallow groundwater monitoring. Proceedings of the 29th Water, Engineering and Development Centre - UK. (WEDC) International conference, held in Abuja – Nigeria. Published by WEDC, London. Pp188 – 189.

American Journal of Engineering Research (AJER)
e-ISSN : 2320-0847 p-ISSN : 2320-0936
Volume-02, Issue-11, pp-104-110
www.ajer.org

Research Paper Open Access

To assess the glaucoma diagnostic ability of Fourier Domain Optical Coherence Tomography

Dr Chandrima Paul
Affiliation : Regional Institute of Ophthalmology, Medical College, Kolkata
Address: HA 274, Saltlake, Kolkata – 700 097.
Acknowledgement: The West Bengal University of Health Sciences

***Abstract*: -** Purpose To evaluate the diagnostic accuracy of retinal nerve fibre layer thickness (RNFLT), ganglion cell complex (GCC), and optic disc measurements made with the RTVue-100 Fourier-domain optical coherence tomography (OCT) to detect glaucoma in an Indian population.
Methods One randomly selected eye of 532 Indian patients (132 healthy, 112 ocular hypertensive, 134 preperimetric glaucoma, and 154 perimetric glaucoma eyes) was evaluated.
Results Using the software-provided classification, the total population sensitivity for GCC was 82.7% , RNFLT parameters did not exceed 73.6% and for the optic nerve head 62.8. Specificity was high (92.6–100%) for most RNFLT and GCC parameters, but low (74.0–76.4%) for the optic disc parameters. Positive predictive value (PPV) varied between 96.1 and 100% for the main RNFLT parameters, 94.6 and 100% for the 16 RNFLT sectors, 96.4 and 99.0% for the GCC parameters, but did not exceed 86.3% for any of the optic disc parameters. Positive likelihood ratio (PLR) was higher than 10 for average, inferior and superior RNFLT (28.5 to infinite), 12 of the 16 RNFLT sectors (14.6 to infinite), and three of the four GCC parameters (40.0 to 48.6). No optic disc parameter had a PLR higher than 2.0.
Conclusion RNFLT and GCC parameters of the RTVue-100 Fourier-domain OCT showed high specificity, positive predictive value and PLR for detection of glaucoma as compared to the optic disc parameters.

Keywords: - *Retinal nerve fibre layer thickness; Ganglion cell complex; Optic disc; Fourier-domain optical coherence tomography; Glaucoma*

I. INTRODUCTION

Studies have consistently shown that both peripapillary retinal nerve fiber layer thickness (RNFLT) and macular volume are lower in glaucomatous eyes [1-5]. RGC bodies residing in the inner nuclear layer are known to be ten to twenty-fold thicker than their axons [1,6]. It can be speculated that improvement in the resolution of imaging technologies may increase segmentation in the macula, which can be useful for detection of glaucoma at earlier stages.

The RTVue-100 OCT (Optovue Inc., Fremont, CA, USA) is one of the new commercially available Fourier-domain OCT instruments [7-14] . Its axial resolution is approximately 5 μm and the scan speed is 26 000 A-scans per second. Thus the speed is 65 times higher than that of the Stratus OCT system, and the resolution is about twice as good as such time-domain OCT instruments. The RTVue optic nerve head map (ONH map) scan was developed for peripapillary retinal nerve fibre layer thickness (RNFLT) and two-dimension ONH measurements to detect glaucoma. As reduction of macular thickness, especially of the inner retinal layers, is an important OCT finding associated with glaucoma [15] the ganglion cell complex (GCC) scan of the RTVue system, which comprises tissue layers (the retinal nerve fibre layer, the retinal ganglion cell layer and the inner-plexiform layer) that are directly influenced by glaucomatous ganglion cell loss, may also have clinical importance. The instrument's software contains a normative database sufficient for statistical comparison for the different RNFLT, ONH and GCC parameters [16].

In this study, we investigated the diagnostic accuracy of the different RNFLT, GCC and ONH parameters of the RTVue-100 Fourier-domain OCT using the software-provided classifications for detection of glaucoma on 532 patients over a period of 18 months.

II. MATERIALS AND METHODS

One randomly selected eye of each 532 Indian individuals underwent RNFLT, GCC, and ONH measurements made with the RTVue-100 Fourier-domain OCT between 1 January 2012 and 30th June2013, was enrolled in the study. For inclusion, all participants had to have, in the study eye, sufficient central vision for optimal fixation, image quality sufficient for optimal evaluation, no macular pathology except for a small number of hard drusen, on stereoscopic evaluation. All patients underwent the same diagnostic protocol, which comprised a detailed slit-lamp evaluation, stereoscopic ONH photography and evaluation by a glaucoma specialist , stereoscopic evaluation of the macula, repeated White on white automated perimetry with the Humphrey Visual Field Analyser 750 24-2 Sita Standard visual field testing, and daytime intraocular pressure phasing made with Goldman applanation tonometry within 1 month from the RTVue-100 OCT imaging. The final clinical classification based on the results of these tests was made a Senior Consultant at the Glaucoma Service . Any image with a Signal Strength Index (SSI) of lower than 40 was discarded. The patient population comprised of 132 healthy subjects with no ONH damage, reliable and reproducible normal visual field tests with normal mean defect (MD), that is, MD less than 2 dB, and intraocular pressure consistently below 21 mm Hg, based on daytime phasing (five measurements between 0008 and 1600 hours); 112 ocular hypertensive subjects with normal ONH, visual field with MD less than 2 dB and untreated intraocular pressure consistently above 21 mm Hg; 134 preperimetric glaucoma patients characterized with definite glaucomatous neuroretinal rim loss (diffuse or localised neuroretinal rim thinning) and reliable and reproducible normal visual field with MD less than 2 dB; and 154 perimetric glaucoma patients characterized with glaucomatous neuroretinal rim loss and reliable and reproducible visual field defect typical for glaucoma (inferior and/or superior paracentral or arcuate scotomas, nasal step, hemifield defect or generalised depression with MD higher than 2 dB). Severity of glaucomatous visual field damage was classified according to the modified Bascom Palmer staging system [17]. The demographics of the participants are shown in Table I.

Table I : Demographic characteristics of the participants and eyes analysed in the study

Total number of eyes (*n*)	532 (100%)
Male/Female (*n*/*n*)	236/296
Best-corrected visual acuity (mean±SD)	0.9±0.2
Refractive error (*D*) (mean±SD, range)	−0.7±2.9 (−14.00+8.00)
Prevalence of healthy eyes	132/532 (24.8%)
Prevalence of OHT eyes	112/532(21.0%)
Prevalence of glaucoma eyes	288/532 (54.1%)
Preperimetric	114/288 (39.5%)
Perimetric	174/288 (60.4%)
Type of glaucoma	
Primary open-angle glaucoma	146/288 (51.2%)
Juvenile open-angle glaucoma	6/288 (2.0%)
Normal-pressure glaucoma	8/288 (2.7%)
Chronic angle closure glaucoma	4/288 (1.3%)
Pseudoexfoliative glaucoma	2/288 (0.69%)
Pigment glaucoma	4/288 (1.3%)
Other secondary glaucomas	4/288 (1.3%)
Mean defect (dB) (mean±SD)	
- Healthy eyes	0.4±1.4

- OHT eyes	−0.1±1.3
- Preperimetric glaucoma eyes	0.1±1.6
- Perimetric glaucoma eyes	7.8±6.9
Distribution of disease severity in the perimetric glaucoma group [a]	
Stage 1	31/288 (10.76%)
Stage 2	94/288 (32.6%)
Stage 3	81/288 (28.1%)
Stage 4	74/288 (25.6%)
Stage 5	8/288 (2.7%)
Age (years) (mean±SD)	
Healthy eyes	55.9±14.9
OHT eyes	50.5±14.5
Preperimetric glaucoma eyes	54.6±12.8
Perimetric glaucoma eyes	55.2±14.4
Untreated maximal IOP of the OHT eyes (mm Hg) (mean±SD)	27.1±7.9

III. FOURIER DOMAIN OCT

OCT was performed through undilated pupil with the RTVue-100 Fourier-domain OCT instrument (Optovue Inc.) with software version 4.0. Macular Inner retinal Layer (MIRL) thickness using the GCC scan protocol and RNFL thickness employing two scanning modes, NHM4 and RNFL 3.45, were measured. The GCC scan covered a 7 × 7-mm scan area centered on the fovea. RNFL thickness was determined by both NHM4 (RNFL1) and RNFL 3.45 modes (RNFL2).

The normative database for diagnostic classification consists of 1800 healthy eyes of Indian ethnicity subjects, with ages ranging between 18 and 80 years. RNFLT values are found to correlate significantly with age of subject, ethnicity and with optic disc size, and adjustments for these effects (using multiple linear regression equations) are implemented in the software to improve classification results. For RNFLT, GCC and ONH measurements the standard glaucoma protocol was used [8]. This includes a 3D optic disc scan for the definition of the disc margin on the basis of the computer-assisted determination of retinal pigment epithelium endpoints, an ONH scan to measure the optic disc parameters and RNFLT within an area of diameter 4 mm, centred on the pre-defined disc, and the standard GCC scan. Each ONH scan consists of 12 radial lines and six concentric rings, which are used to create an RNFLT map. The measuring circle (920 points) is derived from this map after the sample circle is adjusted to be centred on the optic disc. The measured RNFLT is automatically compared with the normative database for the total circle, the superior and inferior sectors, and each of the sixteen 22.5°-sized sectors of the measuring circle. In this investigation the following software-provided parameters were evaluated: (1) average RNFLT for the total 360° around the ONH; (2) superior quadrant RNFLT; (3) inferior quadrant RNFLT; (4) all 16 separate RNFLT sectors (abbreviations: TU; temporal upper, ST; supero-temporal, SN; supero-nasal, NU; nasal upper, NL; nasal lower, IN; infero-nasal, IT; infero-temporal, and TL; temporal lower), (5) superior GCC (thickness of all macular layers between the internal limiting membrane and the inner plexiform layer, in the area above the horizontal meridian); and (6) inferior GCC (thickness of all macular layers between the internal limiting membrane and the inner plexiform layer, in the area below the horizontal meridian); (7) average GCC; (8) GCC focal loss volume (FLV; the total sum of statistically significant GCC volume loss divided by the GCC map area, in percent); (9) cup area; (10) cup/disc area ratio; and (11) rim area. For these software calculated parameters an instrument provided classification is indicated in a colour coded manner: sectors with ‘within normal limits' classification (ie sectors for which the probability of there being no glaucomatous damage $\geqslant$5%) are printed in green, sectors with ‘borderline' classification (P<5 but $\geqslant$1%) in yellow and sectors with ‘outside normal limits' classification (P<1%) in red. In the current investigation both the retinal pigment epithelium endpoints and the ONH contour line were determined by the same trained examiner .To be included in the analysis, images had to have a signal strength index >40. Overt misalignment of the surface detection algorithm on at least 10% of consecutive A-scans or 15% of cumulative A-scans or with overt decentration of the measurement circle location (assessed

subjectively) were excluded from further analysis. Pharmacologic dilation was performed if the pupil was smaller than 3.0 mm. All images were acquired by a single well-trained operator who was masked to the diagnosis and other clinical findings, including location and severity of VF defect during the same patient visit. These RTVue-100 OCT examinations were not used for the clinical classification of the patients.

The SPSS 15.0 program package was used for statistical analysis (SPSS Inc., Chicago, IL, USA). ANOVA to compare age and the measured parameter values between the patient groups. Sensitivity, specificity, positive predictive value, negative predictive value, positive likelihood ratio (PLR) and negative likelihood ratio of the software provided classification results were determined. *P*-values of <0.05 were considered as statistically significant.

IV. RESULTS

There was no statistically significant age difference between the patients of the various groups. All images met the pre-defined signal strength criterion and were analysed. Comparison of the different RNFLT, GCC and ONH values between the patient groups is shown in Table II A, B and C .

Tables II A: Comparison of the different Ganglionic Cell Complex (GCC) parameters between the patient groups.

GCC parameters														
	Healthy **1**		OHT **2**		Preperimet-ric **3**		Perimetric **4**		p values [b]					
	Mean	SD	Mean	SD	Mean	SD	Mean	SD	1vs2	1vs3	1vs4	2vs3	2vs 4	3vs4
Average (*im*)	96.7	7.8	96.4	7.1	92.8	6.0	73.0	13.6	0.827	0.543	<0.001	0.987	<0.001	<0.001
Superior (*im*)	98.3	7.1	95.3	8.7	94.0	8.2	76.3	15.4	0.561	0.020	<0.001	0.465	<0.001	<0.001
Inferior (*im*)	97.5	7.7	98.2	7.2	91.5	6.4	70.6	14.6	0.566	0.005	<0.001	0.453	<0.001	<0.001
FLV (%)	1.0	1.4	1.8	2.6	1.6	1.6	7.4	4.6	0.364	0.812	<0.001	0.875	<0.001	<0.001

Tables II B: Comparison of the different retinal nerve fibre layer thickness (RNFLT) values between the patient groups.

RNFLT parameters (im)														
	Healthy **1**		OHT **2**		Preperimetri c **3**		Perimetric **4**		p values [b]					
	Mean	SD	Mean	SD	Mean	SD	Mean	SD	1vs2	1vs3	1vs4	2vs3	2vs 4	3vs4
Average	104.5	9.2	104.0	10.4	95.9	11.2	74.9	12.0	0.162	<0.001	<0.001	0.021	<0.001	<0.001
Temporal	76.6	9.4	74.8	10.3	67.8	9.7	53.7	13.4	0.863	0.001	<0.001	0.049	<0.001	<0.001
Superior	136.6	15.2	126.5	15.4	112.4	19.5	93.7	16.7	0.033	<0.001	<0.001	0.062	<0.001	<0.001
Nasal	82.0	10.1	76.3	13.2	72.3	11.5	61.3	11.9	0.472	0.106	<0.001	0.995	<0.001	<0.001
Inferior	138.2	15.6	132.6	17.9	122.2	18.6	92.1	14.9	0.538	<0.001	<0.001	0.034	<0.001	<0.001

Tables II C: Comparison of the different Optic Nerve Head (ONH) parameters between the patient groups.

Optic nerve Head parameters														
	Healthy **1**		OHT **2**		Preperimetric **3**		Perimetric **4**		p values [b]					
	Mean	SD	Mean	SD	Mean	SD	Mean	SD	1vs2	1vs3	1vs4	2vs3	2vs 4	3vs4
Cup area (mm2)	0.853	0.550	0.821	0.520	1.436	0.493	1.503	0.566	0.970	<0.001	<0.001	<0.001	<0.001	0.700
Cup/disc area ratio	0.425	0.243	0.517	0.224	0.696	0.121	0.839	0.167	1.000	<0.001	<0.001	<0.001	<0.001	0.005
Rim area (mm2)	1.123	0.438	0.932	0.314	0.627	0.275	0.434	0.414	0.140	<0.001	<0.001	<0.001	<0.001	<0.01

Abbreviations: FLV, focal loss volume; OHT – Ocular Hypertension
b: ANOVA<0.01 for all parameters
RNFLT, GCC and ONH parameters differed significantly between the groups, showing decreasing RNFLT, GCC thickness and rim area values, and increasing cup area and cup/disc area ratio with increasing disease severity categories.
Diagnostic performance is shown in Table III for each disease category and parameter, respectively. When borderline and outside normal limits classifications were grouped together (both considered abnormal), specificity was high (94.6–100%) for most RNFLT and GCC parameters, and low (72.0–76.3%) for the ONH parameters, in all analyses. For detection of perimetric glaucoma, GCC FLV showed the best sensitivity (92.8%).

Table III : Sensitivity, specificity, positive predictive value (PPV), negative predictive value (NPV), positive likelihood ratio (PLR) and negative likelihood ratio (NLR) of the software provided classification for detection of glaucoma in the total study population (***n***=532), for each parameter, respectively.

	Normal vs OHT, preperimetric and perimetric glaucoma					
	Sensitivity (%) (95% CI)	*Specificity (%) (95% CI)*	*PPV (%) (95% CI)*	*NPV (%) (95% CI)*	*PLR (95% CI)*	*NLR (95% CI)*
Main RNFLT parameters (µm)						
Average	82.0 (80.8–84.8)	96.0 (94.0–98.0)	94.0 (96.0–92.0)	53.4 (43.4–63.2)	Infinite	0.4 (0.3–0.5)
Superior	86.0 (85.5–87.5)	94.0 (92.0–96.0)	98.0 (96.0–100.0)	52.0 (41.9–61.8)	Infinite	0.4 (0.4–0.6)
Inferior	82.9 (80.4–.841)	97.8 (92.4–99.4)	98.1 (93.4–99.5)	51.1 (41.0–61.1)	25.5 (6.3–103.2)	0.5 (0.4–0.6)
GCC parameters						
Average (µm)	84.2 (88.3–86.2)	99.4. (99.2–99.8)	98.9 (94.2–99.8)	47.6 (37.7–57.8)	44.3 (6.2–318.3)	0.5 (0.4–0.6)
Superior (µm)	82.5 (82.4–84.2)	98.9 (94.1–100.0)	98.8 (93.6–99.8)	45.5 (35.7–55.7)	40.0 (5.6–288.6)	0.6 (0.5–0.7)
Inferior (µm)	82.8 (82.2–78.3)	99.9 (99.1–100.0)	99.0 (94.7–99.8)	50.0 (39.9–60.1)	48.6 (6.8–348.2)	0.5 (0.4–0.6)
FLV (%)	84.7 (82.8–86.8)	99.1 (98.6–100.0)	98.4 (98.2–100.0)	53.2 (42.5–63.7)	5.8 (3.1–10.9)	0.4 (0.3–0.5)
Optic nerve head parameters						
Cup area (mm 2)	70.0 (63.0–77.8)	76.3 (65.3–84.7)	86.3 (79.6–91.1)	56.8 (45.2–67.7)	3.0 (2.0–4.7)	0.4 (0.3–0.5)
Cup/disc area ratio	71.6 (64.8–79.1)	72.0 (60.3–81.4)	84.5 (77.7–89.6)	56.8 (44.9–68.0)	2.6 (4.7–3.9)	0.4 (0.3–0.5)
Rim area (mm 2)	70.0 (63.0–79.8)	76.3 (65.3–84.7)	86.3 (79.6–91.1)	56.8 (45.2–67.7)	3.0 (2.0–4.7)	0.4 (0.3–0.5)

V. DISCUSSION

Evaluation of the diagnostic accuracy of the different protocols available in current Imaging devices is of clinical importance. In such investigations, for the best performing RNFLT and GCC parameters of the RTVue-100 OCT, the area under the receiver operating characteristic curve varied between 0.900 and 0.981 [18,19]. Other authors using other Fourier-domain OCT systems reported on similar values [4, 19]. These results suggest that under pre-defined circumstances the diagnostic accuracy of Fourier-domain OCT technology is higher than that of time-domain OCT technology [4,18,19]. The significance of this approach is that disease severity may have an influence on the diagnostic capability of the Fourier-domain OCT instruments [20], thus it needs to be considered in the evaluation. To evaluate the diagnostic capability of the instrument we used the software-provided classification, which is based on comparison between the measured values and the integrated normative database. As the RTVue-100 OCT has an age and disc size adjusted separate database for Indians, which was used by us for our patients, the age-related RNFLT and GCC difference between our healthy control and ocular hypertensive subjects and the perimetric glaucoma patients was corrected for.

As shown in Table II A,B and C, in the ocular hypertensive group, the difference from the healthy group was significant only for two parameters. In contrast, for all other groups several parameters showed significant damage compared with the healthy eyes, and the measured values showed more damage for the more severe disease categories, respectively.

Specificity was consistently high (94.6–100%); sensitivity was poor for detection of ocular hypertension and preperimetric glaucoma, and moderate to good (up to 82.8%) for detection of perimetric glaucoma. For our total unselected study population, most RNFLT and GCC measurements had high specificity and positive predictive value (92.4–100%), and clinically useful PLR (>10 to infinite). No such favourable findings were obtained for the ONH parameters (cup area, cup/disc area ratio and rim area), which suggests that the Fourier-domain technology did not overcome the problems of ONH classification with the time-domain OCT technology [8,9,10].

Our results mean that in routine clinical practice a borderline or outside normal limits classification given for the main RNFLT parameters, RNFLT sectors or GCC parameters by the instrument's software, strongly suggests that the eye has lost retinal nerve fibres and macular ganglion cells. In contrast, because of the relatively low sensitivity and weak negative likelihood ratio, a within normal limits classification cannot exclude glaucoma.In conclusion, in our study population comprising healthy, ocular hypertensive, preperimetric and perimetric glaucoma patients for detection or exclusion of glaucoma, the RTVue-100 Fourier-domain OCT and its Indian normative database were found to be highly specific to detect glaucoma. Average GCC had high sensitiviy, but RNFLT parameters had highest sensitivity.

REFERENCES

[1] Greenfield DS, Bagga H, Knighton RW *Macular thickness changes in glaucomatous optic neuropathy detected using optical coherence tomography. Arch Ophthalmol. 2003;121:41–46.*

[2] Ojima T, Tanabe T, Hangai M, Yu S, Morishita S, Yoshimura N *Measurement of retinal nerve fiber layer thickness and macular volume for glaucoma detection using optical coherence tomography. Jpn J Ophthalmol. 2007;51:197–203*

[3] Leung CK, Chan WM, Yung WH, *Comparison of macular and peripapillary measurements for the detection of glaucoma: an optical coherence tomography study. Ophthalmology. 2005;112(3):391–400.*

[4] Tan O, Li G, Lu AT, . *Mapping of macular substructures with optical coherence tomography for glaucoma diagnosis. Ophthalmology. 2008;115:949–956.*

[5] Ishikawa H, Stein DM, Wollstein G, . *Macular segmentation with optical coherence tomography. Invest Ophthalmol Vis Sci. 2005;46:2012–2017.*

[6] Zeimer R, Asrani S, Zou S, . *Quantitative detection of glaucomatous damage at the posterior pole by retinal thickness mapping: a pilot study. Ophthalmology. 1998;105:224–231.*

[7] González-García AO, Vizzeri G, Bowd C, Medeiros FA, Zangwill LM, Weinreb RN. Reproducibility of RTVue retinal nerve fibre layer thickness and optic disc measurements and agreement with Stratus optical coherence tomography measurements. Am J Ophthalmol. 2009;147:1067–1074

[8] Garas A, Vargha P, Holló G. Reproducibility of retinal nerve fibre layer and macular thickness measurement with the RTVue-100 optical coherence tomograph. Ophthalmology. 2010;117:738–746.

[9] Garas A, Tóth M, Vargha P, Holló G. Comparison of repeatability of retinal nerve fibre layer thickness measurement made using the RTVue Fourier-domain optical coherence tomograph and the GDx scanning laser polarimeter with variable or enhanced corneal compensation. J Glaucoma. 2010;19 (6:412–417.

[10] Garas A, Vargha P, Holló G. Automatic, operator-adjusted, and manual disc definition for optic nerve head and retinal nerve fibre layer measurements with the RTVue-100 optical coherence tomograph J Glaucoma 2010. E-pub ahead of print 29 April 2010, doi: doi: 10.1097/IJG.0b013e3181d787fd.

[11] Mori S, Hangai M, Sakamoto A, Yoshimura N. Spectral-domain optical coherence tomography measurement of macular volume for diagnosing glaucoma J Glaucoma 2010. E-pub ahead of print 15 February 2010, doi: doi: 10.1097/IJG.0b013e3181ca7acf.
[12] Seong M, Sung KR, Choi EH, Kang SY, Cho JW, Um TW, et al. Macular and peripapillary retinal nerve fibre layer measurements by spectral domain optical coherence tomography in normal-tension glaucoma. Invest Ophthalmol Vis Sci. 2010;51:1446–1452.
[13] Tan O, Chopra V, Lu AT, Schuman JS, Ishikawa H, Wollstein G, et al. Detection of macular ganglion cell loss in glaucoma by Fourier-domain optical coherence tomography. Ophthalmology. 2009;116:2305–2314.
[14] Sehi M, Grewal DS, Sheets CW, Greenfield DS. Diagnostic ability of Fourier-domain *vs* time-domain optical coherence tomography for glaucoma detection. Am J Ophthalmol. 2009;148:597–605. Li S, Wang X, Wu G, Wang N. Evaluation of optic nerve head and retinal nerve fibre layer in early and advance glaucoma using frequency-domain optical coherence tomography. Graefes Arch Clin Exp Ophthalmol. 2010;248:429–434.
[15] Parikh RS, Parikh SR, Thomas R. Diagnostic capability of macular parameters of Stratus OCT 3 in detection of early glaucoma. Br J Ophthalmol. 2010;94:197–201.
[16] Sinai MJ, Garway-Heath DF, Fingeret M, Varma R, Liebmann JM, Greenfield S, et al. The role of ethnicity on the retinal nerve fiber layer and optic disc area measured with Fourier domain optical coherence tomography Invest Ophthalmol Vis Sci 50E-abstract 4785.
[17] Mills RP, Budenz DL, Lee PP, Noecker RJ, Walt JG, Siegartel LR, et al. Categorizing the stage of glaucoma from pre-diagnosis to end-stage disease. Am J Ophthalmol. 2006;141:24–30.
[18] Mori S, Hangai M, Sakamoto A, Yoshimura N. Spectral-domain optical coherence tomography measurement of macular volume for diagnosing glaucoma J Glaucoma 2010. E-pub ahead of print 15 February 2010, doi: doi: 10.1097/IJG.0b013e3181ca7acf.
[19] Seong M, Sung KR, Choi EH, Kang SY, Cho JW, Um TW, et al. Macular and peripapillary retinal nerve fibre layer measurements by spectral domain optical coherence tomography in normal-tension glaucoma. Invest Ophthalmol Vis Sci. 2010;51:1446–1452.
[20] Leite MT, Zangwill LM, Weinreb RN, Rao HL, Alencar LM, Sample PA, et al. Effect of disease severity on the performance of Cirrus spectral-domain OCT for glaucoma diagnosis. Invest Ophthalmol Vis Sci. 2010;51:4104–4109.

American Journal of Engineering Research (AJER)
e-ISSN : 2320-0847 p-ISSN : 2320-0936
Volume-02, Issue-11, pp-111-114
www.ajer.org

Research Paper Open Access

Accurate Design of A Corner Fed Square Slot Patch Antenna For Circular Polarization

Monika Bhatnagar, Dr. A.k.Gautam
I.T.S Engg College/ Greater Noida /G.B.Pant Engg College /Pauri-Garhwal

Abstract: **-** New fast form analytic expressions to determine the impedance elements of the desegmentation matrix have been obtained. These results, using the Green's function approach, enable an accurate determination of the dimensions of the slot at the centre of a corner fed square patch antenna to produce circular polarisation.

INTRODUCTION

The desegmentation technique [1] applied to the antenna with a slot (Fig. 1) is outlined in [2], Perturbation analysis, together with the determination of the initial estimates of the overall patch dimensions, is given in [3], In this Letter new fast form expressions have been obtained to determine the impedance elements of the desegmentation matrix. These expressions, used in the desegmentation technique together with the procedure reported in [3], enable the geometric design to be fully and accurately determined.

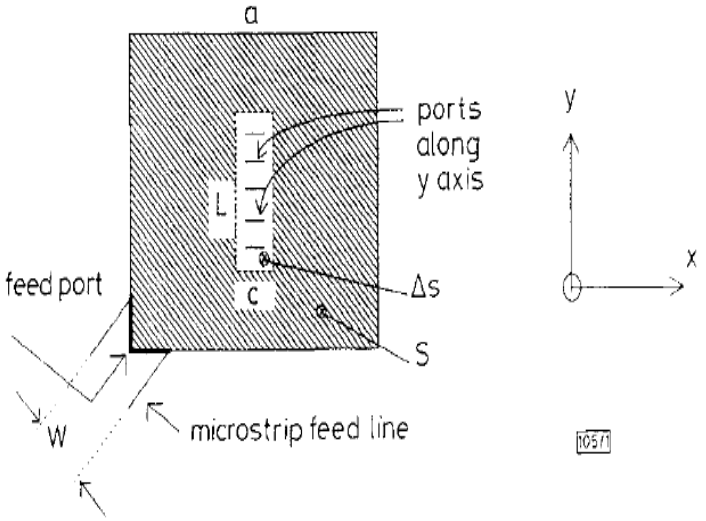

Fig. 1 *Corner microstrip fed square patch antenna with slot at centre*

$W = 1.25\text{mm}$, $h = 1.575\text{mm}$, $\delta = 0.0012$, $\varepsilon_r = 2.33$, $s = a^2$, $\Delta_s = L \times C$

I. ANALYSIS

The submatrix elements Z_{pp}, Z_{pq}, Z_{qp} and Z_{qq} of the Zmatrix, for both lower and higher excitations, are determined bythe procedure described in [2], and evaluated with the aid of thenew closed form expressions given below. In these expressions thevalues of z_p, z_q, $z_>$ and $z_<$ are assigned according to the given selec-tion rules, eqn. 1 has been reported in [3].

$$Z_{pp} = -\frac{j\omega\mu_o h}{4\sqrt{2}a}\frac{1}{k\sin(ka)}\left[1+\cos\left(k\frac{W}{2\sqrt{2}}\right)\sin c\left(k\frac{W}{2\sqrt{2}}\right)\right] \times\left[\cos(ka)+\cos\left[k\left(\frac{W}{2\sqrt{2}}-a\right)\right]\sin c\left(k\frac{W}{2\sqrt{2}}\right)\right] \quad (1)$$

$$Z_{pq} = -\frac{j\omega\mu_o h}{2a}\frac{1}{k\sin(ka)}\left[\cos[k(z_q-a)]\sin c\left(k\frac{W_q}{2}\right)\right] \times\left[1+\cos\left(k\frac{W}{2\sqrt{2}}\right)\sin c\left(k\frac{W}{2\sqrt{2}}\right)\right] \quad (2)$$

$$Z_{qp} = -\frac{j\omega\mu_o h}{2\sqrt{2}a}\frac{1}{k\sin(ka)}\left[\cos[k(z_q-a)]\sin c\left(k\frac{W_q}{2}\right)\right] \times\left[1+\cos\left(k\frac{W}{2\sqrt{2}}\right)\sin c\left(k\frac{W}{2\sqrt{2}}\right)\right] \quad (3)$$

$$Z_{qq} = -\frac{j\omega\mu h}{a}\frac{1}{k\sin(ka)}\cos[k(z_> - a)]\cos(kz_<) \times\sin c\left(k\frac{W_p}{2}\right)\sin c\left(k\frac{W_q}{2}\right) \quad (4)$$

where h = substrate thickness, k = effective wave number, sine(x) = sin(x)/x.

The closed form of the above equations is obtained by removing the summation in the Green's function using the formula in[4].The centre co-ordinates z_p and z_q of the desegmentation ports, widths w_p, w_q, take the values x_p, x_q, y_p or y_q according to the port orientation.

II. THEORETICAL AND PRACTICAL RESULTS

The area of the patch S and the area of the slot (perturbation element, As) of dimension L x c, were first estimated by following the procedure described in [3], The submatrixelements $z_p = x_p$, $z_a - x_a$, and, for the higher modes $z_p = y_p$, $z_a = y_a$. In eqn. 4, z, = max(z_p, z_q) and z< = min(z_p, z_q). The desegmentation technique is then applied to determine the modal impedances.

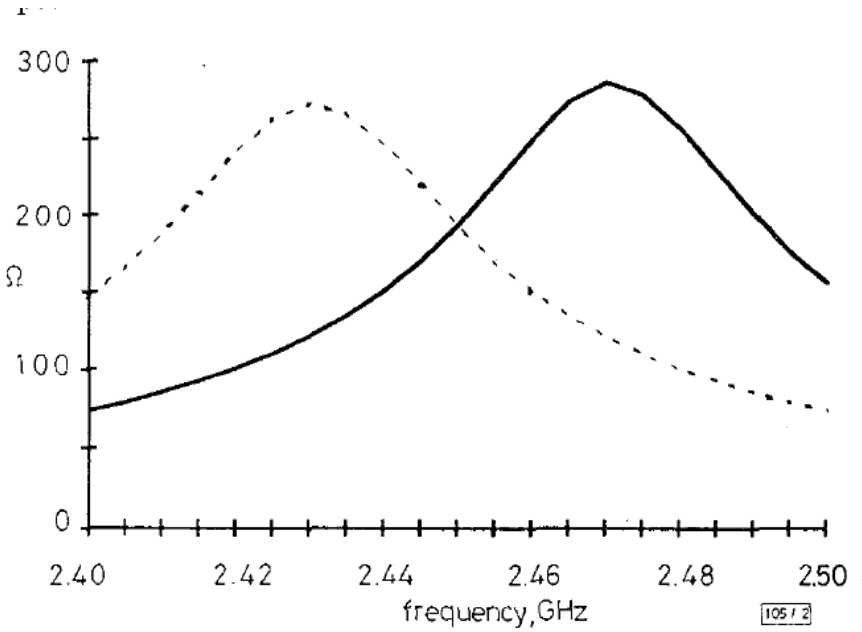

Fig. 2 Theoretical magnitude of modal impedances
mag. of higher mode
mag. of lower mode

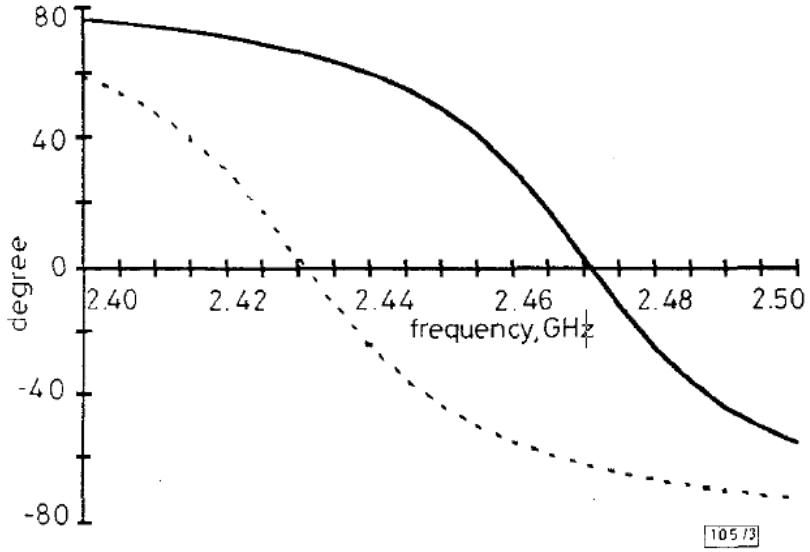

Fig. *3 Theoretical phase of modal impedances*
----------phase of higher mode
----------phase of lower mode

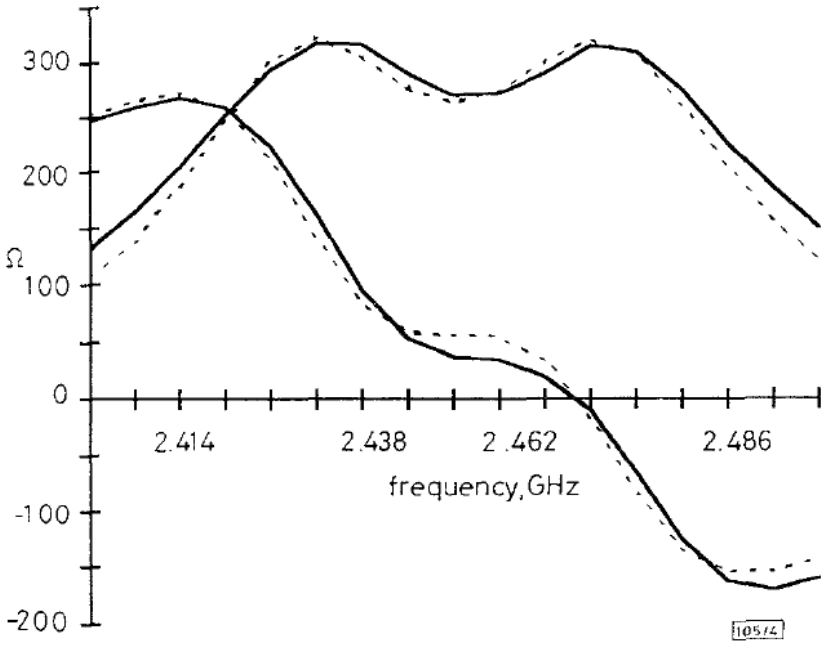

Fig. 4 *Theoretical and practical input impedance*
Re(Zin), practical
Im(Zin), practical
-~~~ Re(Zin), theory
~~~~ Im(Zin), theory

III. THEORETICAL AND PRACTICAL RESULTS

The area of the patch *S* and thearea of the slot (perturbation element, *A$* of dimension *L* x c,were first estimated by following the procedure described in *[3]*.The submatrix elements of the *Z* matrix used in the desegmentation technique were evaluated using eqns. 1 ~ 4 for the lower and higher modes. Graphs of the magnitude and phase of the modalimpedances against the frequency were then plotted. The outward extensions of the patch caused by the flinging fields are includedin the model, but the fringing fields in the slot are not taken into account. By altering the dimensions of the patch and slot the magnitudeand phase modal responses were adjusted to satisfy the necessary conditions for circular polarisation, i.e. the equal magnitude and phase quadrature requirement. At the design frequency of2.45GHz, the optimised dimensions were a = 37.9mm, L = 8.5mmand c = 2.5mm . The theoretical values of the magnitude and the phase of the modal impedances against
~~~~

frequency are shown inFigs. 2 and 3, respectively. In the desegmentation procedure,excellent convergence was obtained using 20 interconnection ports.The computed values of the impedances caused by the orthogonal higher and lower modes are obtained and combined. In Fig. **4** the graphs of the real and imaginary parts of the combined impedance values are compared with graphs of measured values, and are in good agreement.

IV. CONCLUSION

New fast form analytic expressions for the detenninationof the submatrices *Zpq*,*Z* <,*n*a nd *Zqq*b, ased on the Green'sfunction approach, have been obtained. These sub matrices were then used in the deseg mentation technique to determine the modal impedances of a square patch antenna with a slot. The optim umdimension of the antenna was then found by adjusting these responses in order to satisfy the two conditions for circular polarization .The theoretical and practical results are in very good aggreement.This procedure can be used to optimise the dimensions of any corner fed patch antenna with rectangular perturbation segments designed to produce circular polarisation. This type of antenna can be used as a microwave tag in a moving vehicle for a variety of traffic applications.

REFERENCES

[1] SHARMA**,** P.c., and GUPTA, K.c.: 'Desegmentation method foranalysis of two-dimensional microwave circuit', IEEE Trans.Micvow. Theory Tech., 1981, MTT-29, (lo), pp. 10941098

[2] LIM, B.w., KOROLKIEWICZ, E., and SCOTT, s.: 'Input impedance ofcorner-fed patch antenna for circular polarisation usingdesegmentation techniques', Electron. Lett., 1995, **31,** (20), pp.1708-1709

[3] LIM, B.w., KOROLKIEWICZ, E., and SCOTT, s.: 'Optimised design ofcorner microstrip fed nearly square patch antenna for circularpolarisation', Electron. Lett., 1996, **32,** (7), pp. 610-612

[4] GRADSHTEYN, **I** s., and RYZHJK, **I.M** : 'Table of integrals, series andproducts' (Academic Press Inc., 1994), p.48 (1.445/6)

American Journal of Engineering Research (AJER)
e-ISSN : 2320-0847 p-ISSN : 2320-0936
Volume-02, Issue-11, pp-115-121
www.ajer.org

Research Paper Open Access

Performance Evaluation of the HEC-HMS Hydrologic Model for Lumped and Semi-distributed Stormflow Simulation (Study Area:Delibajak Basin)

Arash Asadi, Fardin Boustani
Islamic Azad University, Dehdasht branch, Iran
Department of Water Engineering, Science and Research Branch, Islamic Azad University, Fars, Iran

***Abstract*: -** Rainfall-runoff processes in small Delibajak basin(16.3 km^2) in kohgilouye and boyerahmad , iran was examined.At first, In this study, Delibajak basin was considered as Lumped and then basin divided into a number of sub- basins where the hydrologic parameters may vary from one sub-basin to another. In such case, lumped models may be labeled as "semi-distributed." The hydrologic model HEC-HMS (Hydrologic Engineering Center, Hydrologic Modeling System), used in combination with the Geospatial Hydrologic Modeling Extension, HEC-GeoHMS. The SCS curve number method (Soil conservation Service, 1972) was considered for the Rainfall-runoff modelling and in both cases The model was carefully calibrated and verified in basin using historical observed data. The determination coefficients and coefficients of agreement for all the flood events were above 0.9, and the percent errors in peak flow and volume were all within the acceptable range. Then,a local sensitivity analysis was adopted for evaluating the event model. There are three parameters(curve number,initial abstraction and lag time) of the event model that were subject to the sensitivity analysis.In the Delibajak basin. In both lumped and distributed model,The highest differences between the generated peak hydrographs and the baseline peak hydrograph was caused by initial abstraction,I_a. The results indicated that Semi-distributed model captured the peak runoff discharges and total runoff volume better than Lumped model. However, overall, the performance of both models was quite reasonable.

***Keywords:* -** *Semi-distributed model, Delibajak basin, HEC-HMS, Sensitivity analysis, Rainfall-runoff modelling, HEC-GeoHMS,SCS , kohgilouye and boyerahmad.*

INTRODUCTIOEN

Currently available watershed models range from simple conceptual lumped models to comprehensive physically based distributed models. Conceptual lumped models use an integrated description of parameters representing an average value over the entire basin. A watershed can be divided into a number of sub- basins where the hydrologic parameters may vary from one sub-basin to another. In such case, lumped models may be labeled as "semi-distributed." They remain non-physically based, however, as they use synthetic methods of transforming rainfall to runoff. This study used the HEC-HMS Version 3.2. The HEC model is designed to simulate the surface runoff response of a basin to precipitation by representing the basin with interconnected hydrologic and hydraulic components. It is primarily applicable to flood simulations. In HEC-HMS, the basin model comprises three vital processes; the loss, the transform and the base flow. Each element in the model performs different functions of the precipitation-runoff process within a portion of the basin or basin known as a sub-basin. An element may depict a surface runoff, a stream channel, or a reservoir. Each of the elements is assigned a variable which defines the particular attribute of the element and mathematical relations that describe its physical processes. The result of the modeling process is the computation of stream flow hydrographs at the basin outlet. The design, construction and operation of many hydraulic projects require an adequate knowledge of the variation of the basin's runoff, and for most of these problems it would be ideal to know the exact magnitude and the actual time of occurrence of all stream flow events during the construction period and economic life of the project. If this information was available at the project planning and design stages, it would be possible to select from amongst all alternatives a design, construction program, and operational procedure

that would produce a project output with an optimized objective function. Unfortunately, such ideal and precise information is never available because it is impossible to have advance knowledge of the project hydrology for water resources development projects; it is necessary to develop plans, designs, and management techniques using a hypothetical set of future hydrologic conditions. It is the determination of these future hydrologic conditions that has long occupied the attention of engineering hydrologists who have attempted to identify acceptable simplifications of complex hydrologic phenomena and to develop adequate models for the prediction of the responses of basins to various natural and anthropogenic hydrologic and hydraulic phenomena. In view of these, a number of hydrologic models have been developed for flood forecasting and the study of rainfall-runoff processes (Yusop and Chan, 2007; Yener and orman,2008; Li and Jia, 2008; Stisen and Jensen,2008; Khakbaz and et al,2009; Salerno and Tartari, 2009; Amir and Emad,2010; Jang and Kim, 2010; James and Zhi,2010;).In recent times, GIS (geographic information systems) has become an integral part of hydrologic studies because of the spatial character of the parameters and precipitation controlling hydrologic processes. GIS plays a major role in distributed hydrologic model parameterization. This is to overcome gross simplifications made through representation by lumping of parameters at the river basin scale. The extraction of hydrologic information, such as flow direction, flow accumulation, watershed boundaries and stream networks, from a DEM (digital elevation model) is accomplished through GIS applications(Asadi and porhemat,2012). This study combined GIS with HEC-HMS, and analyzed the model's suitability for the studied basins. The Delibajak basin are selected as the study areas in this research and basin parameters(curve number and initial abstraction) were calibrated using the rainfall-runoff data of the basin that are collected by 2 rainfall and one runoff stations for 2008-2011 period.
The present study has two main objectives: (1) calibration ,verification and sensivity analysis of the HEC-HMS hydrologic model in Delibajak basin, in both cases, lumped and distributed, and (2) Model Performance Evaluation by statistical measures.

MATERIALS AND METHODS

The Study Area

The Delibajak basin are located in the west of Yasooj City,kohgilouye and boyerahmad Province in Southwest iran. The basin is in between 30º 29′ - 30º 32′ northern latitudes and 51º 26′ - 51º 31′ eastern longitudes. This basin is one of the subbasins of Delibajak river. Delibajak basin has a total basin area of 16.3 km^2 with an elevation ranging from 2100 near the outlet to 2750m at the basin divide with an average channel slope of 0.07.Average annual precipitation is about 1020 mm of which over 90% occurs between November to April in the form of frontal rainfall induced flood. It has a humid and cold climate, an average annual temperature of about 11 *ċ*. (Fig 1.)

Data used

In the Delibajak basin ,streamflow and precipitation have been monitored since 2008 by the gricultural research center. Precipitation data was collected by two raingauges located in the middle and upper parts of the basin. Stream flow data were collected at the outlet of the basin (Delibajak hydrometric station) at one hour interval. meteorological data were acquired from the local climatological station. All the hydrologic model simulations are performed on an hourly time step basis.

Software used

Hec-GeoHMS 5.0

It is a geospatial hydrology toolkit for engineers with limited GIS experience. It is an extension package used in ArcMap software. In this study, Hec-GeoHMS is used to derive river network of the basins and to delineate subbasins of the basins from the digital elevation model (DEM) of the basins. In the subbasins delineation process streamflow gages Delibajak is used for Delibajak basin.

HEC-HMS 3.2

It is a hydrologic modeling software developed by US Army Corps of Engineers Hydrologic Engineering Center. It includes many of the well-known and well applicable hydrologic methods to be used to simulate rainfall-runoff processes in river basins.

MODEL APPLICATION AND CALIBRATION

In this study, 3 flood events that occurred during the three-year period of 2009-2011 in the Delibajak Basin was used for model testing. HMS uses a project name as an identifier for a hydrologic model. An HMS project must have the following components before it can be run: a basin model, a meteorological model, and control specifications. The basin model and basin features were created in the form of a background map file imported to HMS from the data derived through HEC-GeoHMS for model simulation (Fig. 2 and Fig. 3). The observed precipitation and discharge data were used to create the meteorological model using the user gauge

weighting method and, subsequently, the control specification model was created. The control specifications determine the time pattern for the simulation; its features are: a starting date and time, an ending date and time, and a computation time step. To run the system, the basin model, the meteorological model, and the control specifications were combined. The observed historical data of two raingauge stations representing each sub-basin and one stream gauge station in the Delibajak Basin, were used for model calibration and verification. An hourly time step was used for the simulation based on the time interval of the available observed data.
The SCS curve number method was employed to model infiltration loss. The SCS (Soil Conservation Service) unit hydrograph method was used to model the transformation of precipitation excess into direct surface runoff. The constant monthly method was employed to model baseflow. The Muskingum routing model was used to model the reaches.

Each method in HEC-HMS has parameters and the values of these parameters should be entered as input to the model to obtain the simulated runoff hydrographs.Some of the parameters may be estimated by observation and measurements of stream and basin characteristics, but some of them cannot be estimated. When the required parameters cannot be estimated accurately, the model parameters are calibrated, i.e. in the presence of rainfall and runoff data the optimum parameters are found as a result of a systematic search process that yield the best fit between the observed runoff and the computed runoff. This systematic search process is called as optimization. Optimization begins from initial parameter estimates and adjusts them so that the simulated results match the observed streamflow as closely as possible.

The trial and error method, in which the hydrologist makes a subjective adjustment of parameter values in between simulations in order to arrive at the minimum values of parameters that give the best fit between the observed and simulated hydrograph, was employed to calibrate the model. Although the model was calibrated manually, the HEC-HMS built-in automatic optimization procedure was used to authenticate the acceptability and suitability of the parameter values and their ranges as applicable to their uses in HEC-HMS. The choice of the objective function depends upon the need. The SCS Curve Number method, which is used to handle the infiltration loss in the subbasins, has three parameters such as: curve number, initial abstraction and percent impervious area in the basin. Percent impervious area is taken as “0 %”, since no urban settlements are present inside the subbasin. Therefore, the remaining two parameters (curve number, initial abstraction) of SCS curve number method were calibrated. The SCS unit hydrograph method, which is used to model the transformation of precipitation excess into direct surface runoff, has lag time parameter. This parameter was calibrated,as well.

MODEL PERFORMANCE EVALUATION METHODS

The criteria used to evaluate the performance of the models are the overall agreement between predicted and measured runoff discharges, and the models' ability to predict time and magnitude of hydrograph peaks, and runoff volume. The following statistical measures were used to quantify the performance accuracy of both models during each simulation periods, and combined over all periods:

- Percent error in peak flow (*PEPF*). The *PEPF* measure only considers the magnitude of computed peak flow and does not account for total volume or timing of the peak:

$$PEPF = 100\left|\frac{Q_O(peak) - Q_S(peak)}{Q_Q(peak)}\right| \quad (1)$$

where $Q_O(Q_S)$ is the the observed (simulated) flow.

- Percent error in volume (*PEV*). The *PEV* function only considers the computed volume and does not account for the magnitude or timing of the peak flow:

$$PEV = 100\left|\frac{V_O - V_S}{V_O}\right| \quad (2)$$

where $V_O(V_S)$is the volume of the observed (simulated) hydrograph

- Coefficient of correlation (R) . The lag-0 cross correlation coefficient was calculated as:

$$R = \frac{\sum_{t=1}^{N}(O_t - \bar{O}) \times (S_t - \bar{S})}{\sqrt{[\sum_{t=1}^{N}(O_t - \bar{O})^2 \times \sum_{t=1}^{N}(S_t - \bar{S})^2]}} \quad (3)$$

Where O_t (S_t) is the observed (simulated) flow at time *t*, and $\bar{O}$($\bar{S}$)is the average observed (simulated) flow during the calibration period.

- The relative root mean squared error, *RRMSE*, were calculated as:

$$RRMSE = 100 \times \sqrt{\frac{1}{N}\sum_{t=1}^{N}(\frac{S_t - O_t}{O_t})^2} \quad (4)$$

where *N* is the number of streamflow ordinates and the meaning of the remaining symbols is the same as in Equation (3).

SENSIVITY ANALYSIS

Sensitivity analysis is a method to determine which parameters of the model have the greatest impact on the model results. It ranks model parameters based on their contribution to overall error in model predictions. Sensitivity analysis can be local and global. In this study, a local sensitivity analysis was adopted for evaluating the event model. There are three parameters(curve number, initial abstraction and Lag Time) of the event model that were subject to the sensitivity analysis. The final set of the parameters of the calibrated model was deemed as baseline/nominal parameter set. Then, the model was run repeatedly with the starting baseline value for each parameter multiplied, in turn, by 0.7, 0.8, 0.9, 1.1, 1.2 and 1.3, while keeping all other parameters constant at their nominal starting values. The hydrographs resulting from the scenarios of adjusted model parameters were then compared with the baseline model hydrograph.

RESULTS AND DISCUSSION

As described in the introduction, each component of HEC-HMS models an aspect of the precipitation-runoff process within a portion of the basin, commonly referred to as a sub-basin. Representation of a component requires a set of parameters that specify the particular characteristics of the component and mathematical relations that describe the physical processes. Tables 1 and 2 show the calibrated parameter values in the Lumped and Semi-distributed Delibajak basin,respectively. Apart from the sub-areas, which are fixed, parameters were calibrated simultaneously through adjustment of their values until a good agreement between the observed and simulated hydrographs was achieved.

The calibration and validation graphs of basin, in both cases, are shown below. Figs. 4 through 7 show good agreement between observed and simulated graphs. Also, Tables 3 and 4 show observed and simulated values for both calibration and validation basin, in both cases. Table 5 show a summary of the models performance. It can be seen in the above graphs that the simulated and observed peak discharges occurred on the same day, and their maximum time difference was one hour, which is acceptable for flood forecasting.

Also, Figures 8 and 9 summarize the absolute differences obtained from the -30% scenarios for each parameter of the event model. In both cases, The highest differences were generated by the change in initial abstraction parameter, I_a.

CONCLUSIONS

As shown in the results above, the model predicted peak discharge accurately based on the available historical flood data. Both the flood volume and timing were fairly accurate. This shows that HEC-HMS is suitable for the studied basin. From the results, we can conclude that the complexity of the model structure does not determine its suitability and efficiency. Though the structure of HEC-HMS is simple, it is a powerful tool for flood forecasting. A further application of HEC-HMS should be encouraged to confirm its suitability for the iran basins. The results indicated that Semi-distributed model captured the peak runoff discharges and total runoff volume better than Lumped model. However, overall, the performance of both models was quite reasonable.As well, three parameters(curve number,initial abstraction and lag time) of the event model that were subject to the sensitivity analysis. In both cases, lumped and semi-distributed basin, The highest differences were generated by the change in initial abstraction parameter, I_a. Also, the optimmized hydrologic parameters, curve number and initial abstraction were compared in both cases. In the lumped case, curve number , initial abstraction and Lag Time Were 53 , 49mm, and 92 min, respectively. In the semi-distributed case, curve number and initial abstraction, ranges from 51 to 52, and 47 mm to 51 mm, respectively. This variationes is due to differences in basin slope, geologic formations,vegetation cover and land use in subbasins.

REFERENCES

[1] Amir. A, Emad. H,2010,Application of a Conceptual Hydrologic Model in Teaching Hydrologic Processes, Int. J. Engng Ed. Vol. 26, No. 4, pp. 1–11

[2] Asadi.A,Boustani.F, 2013, Application of HEC-HMS for Flood Forecasting in Kabkian Basin and Delibajak Subbasin in Iran, Vol. 3, Issue 9 ,PP 10-16

[3] Asadi.A,Porhemat.J, 2012, Calibration, verification and sensitivity analysis of the HEC-HMS hydrologic model (study area: Kabkian basin and Delibajak subbasin), Iran, Journal of ECOLOGY, ENVIRONMENT AND CONSERVATION, 18 (4) ,805-812.
[4] James .O,Zhi-j. L ,2010,Application of HEC-HMS for flood forecasting in Misai and Wan'an catchments in China, Water Science and Engineering, 2010, 3(1): 14-22
[5] Jang, T. I. and Kim, H. K., 2010.Estimation of storm hydrographs in a mixed – land use watershed using a modified TR-20 model.
[6] Khakbaz, B., et al,2009. From lumped to distributed via semi-distributed: Calibration strategies for semi-distributed hydrologic models. J. Hydrol. doi:10.1016
[7] Li, S. Y., Qi, R. Z., and Jia, W. W. 2008. Calibration of the conceptual rainfall-runoff model's parameters. Proceeding of 16th IAHR-APD Congress and 3rd Symposium of IAHR-ISHS, 55-59. Beijing: Tsinghua University Press.
[8] Parajka J,Blosch G,2010,The value of MODIS snow cover data in Validating and calibrating conceptual hydrologic model, Journal of Hydrology, vol 358,240-258.
[9] Salerno, F., and Tartari, G., 2009, "A coupled approach of surface hydrological modelling and Wavelet Analysis for understanding the baseflow components of river discharge in karst environments", Journal of Hydrology, Volume 376, Issues 1-2, Pages 295-306.
[10] Stisen.S,Jensen.K,2008, A Remote Sensing driven distributed hydrological model of the Senegal river basin,journal of hydrology 354:131-148.
[11] U. S. Army Corps of Engineers (USACE), 2009b, Hydrologic Modeling System: Technical Reference Manual, Davis, CA: U.S. Army Corps of Engineers, Hydrologic Engineering Center.
[12] U. S. Army Corps of Engineers (USACE), 2000a,Geospatial modeling extension. HEC-GeoHMS, User's Manual, Davis, CA: U.S. Army Corps of Engineers, Hydrologic Engineering Center.
[13] Yener, M.K. orman, A.Ü.2008. Modeling Studies With Hec-Hms and Runoff Scenariosin Yuvacik Basin, Turkiye. Department of Civil Engineering, Middle East Technical University, 06531 Ankara/Türkiye.
[14] Z. Yusop, C.H. Chan and A, 2007,Katimon,Runoff characteristics and application of HEC-HMS for modelling stormflow hydrograph in an oil palm catchment, Water Science & Technology Vol 56 No 8 pp 41–48

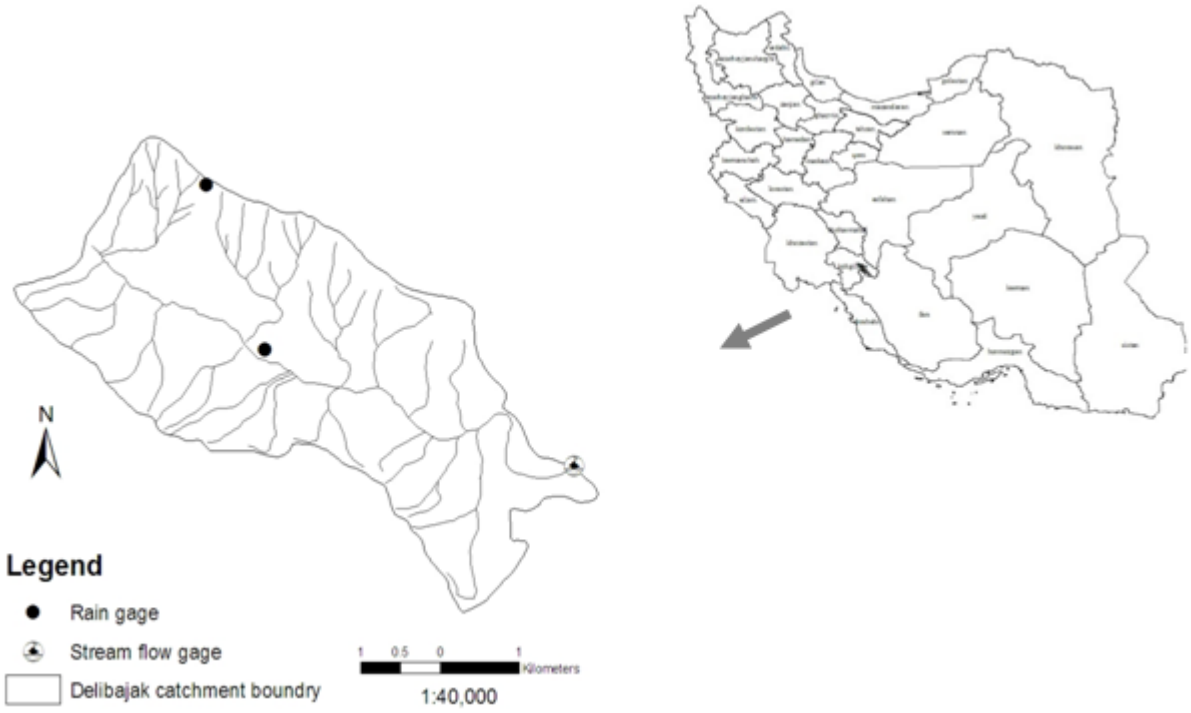

Fig 1. Regional map of Iran , location of study basin and monitoring stations

Fig 2. Processed results for Lumped Delibajak basin imported to HEC- HMS for simulation

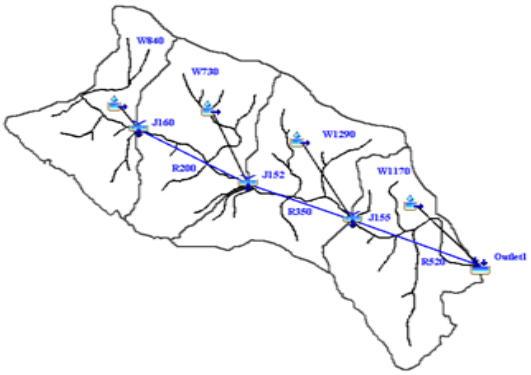

Fig 3. Processed results for Semi- Distributed Delibajak basin imported to HEC- HMS for simulation

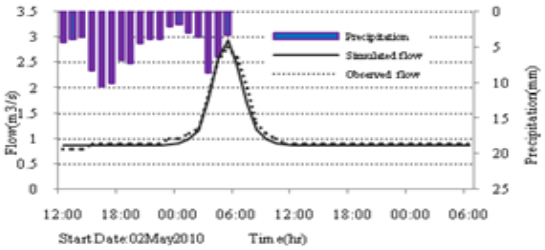

Fig 4. Observed vs. simulated flow in May 2010 for Lumped Delibajak basin calibration

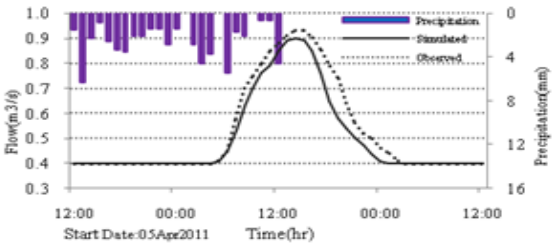

Fig 5. Observed vs. simulated flow in Apr 2011 for Lumped Delibajak basin validation

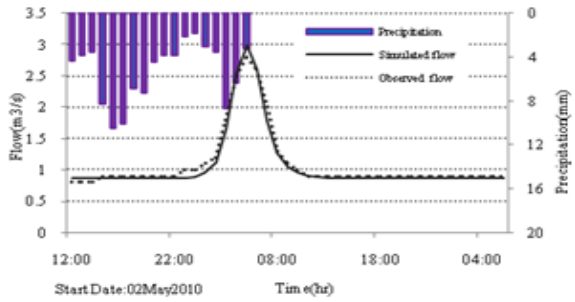

Fig 6. Observed vs. simulated flow in May 2010 for Semi-distributed Delibajak basin calibration

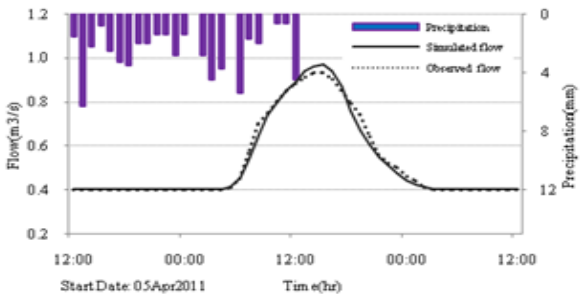

Fig 7. Observed vs. simulated flow in Apr 2011 for Semi-distributed Delibajak basin validation

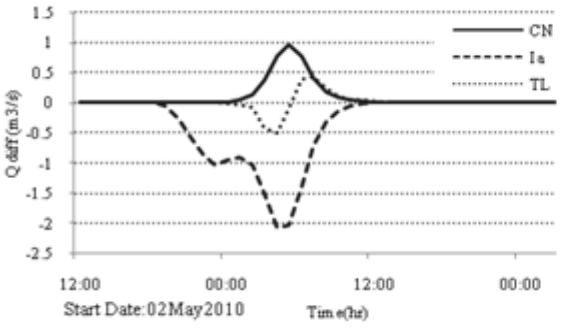

Fig 8. Sensivity analysis of the parameters in the Delibajak Lumped basin.

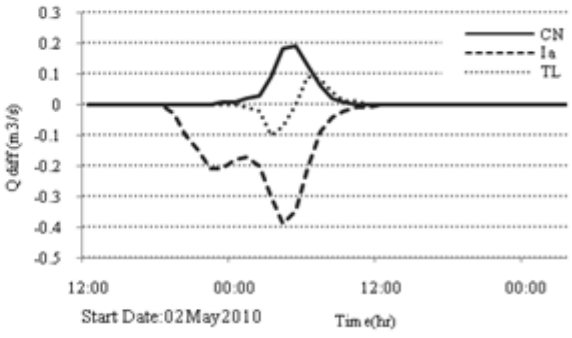

Fig 9. Sensivity analysis of the parameters in the W840 sub- basin.

Table 1. values of calibrated parameters in Lumped Delibajak Basin

Sub-basin	Area(km^2)	Curve Number (CN)	Initial Abstraction (mm)	SCS Lag (min)
Delibajak	16.3	53	49	92

Table 2. values of calibrated parameters in Semi-Distributed Delibajak Basin

Sub-basin	Area(km^2)	Curve Number (CN)	Initial Abstraction (mm)	SCS Lag (min)	Muskingum coefficient	
					X	*K*(hr)
W840	4.3	51.1	47.2	42.2	-	-
W730	4.4	51.7	50.5	84.3	.2	.28
W1290	4.3	52.5	48.6	49.9	.2	.25
W1170	3.3	51.5	47.1	78.1	.2	.39

Table 3. Calibration and validation results for Lumped Delibajak Basin

Period	Date	Simulated			Observed		
		$Q_s(m^3/s)$	$V_s(1000\,m^3)$	Time to peak	$Q_s(m^3/s)$	$V_s(1000\,m^3)$	Time to peak
Calibration	02May2010	2.9	159.4	03May2010,05:00	2.8	166.1	03May2010,05:00
	09Mar2011	9.8	1494.5	12Mar2011,18:00	9	1515	12Mar2011,17:00
Validation	05Apr2011	.9	95.8	06Apr2011,14:00	.93	100.1	06Apr2011,14:00

Table 4. Calibration and validation results for Semi-Distributed Delibajak Basin

Period	Date	Simulated			Observed		
		$Q_s(m^3/s)$	$V_s(1000\,m^3)$	Time to peak	$Q_s(m^3/s)$	$V_s(1000\,m^3)$	Time to peak
Calibration	02May2010	3	161.3	03May2010,05:00	2.8	166.1	03May2010,05:00
	09Mar2011	9.6	1539.3	12Mar2011,18:00	9	1515	12Mar2011,17:00
Validation	05Apr2011	.97	90.87	06Apr2011,15:00	.93	100.1	06Apr2011,14:00

Table 5. Model performance evaluation for selected storm events

Basin	Period	Date	Evaluation criteria			
			PEPF(%)	PEV (%)	R(-)	RRMSE (%)
Delibajak (Semi-distributed)	Calibration	02May2010	.6	6.8	.99	16.7
		09Mar2011	.17	5.4	.99	13.5
	Validation	05Apr2011	1.6	3.3	.99	7.9
Delibajak(Lumped)	Calibration	02May2010	8.8	1.4	.99	6.1
		09Mar2011	6.6	1.6	.98	12.7
	Validation	05Apr2011	3.2	4.3	.98	6.5

American Journal of Engineering Research (AJER)
e-ISSN : 2320-0847 p-ISSN : 2320-0936
Volume-02, Issue-11, pp-122-128
www.ajer.org

Research Paper Open Access

Steganography: A Review of Information Security Research and Development in Muslim World

Yunura Azura Yunus, Salwa Ab Rahman, Jamaludin Ibrahim
Kuliyyah of Information and Communication Technology International Islamic University Malaysia
Kuliyyah of Information and Communication Technology International Islamic University Malaysia
Kuliyyah of Information and Communication Technology International Islamic University Malaysia

Abstract: - Conveying secret information and establishing hidden relationship has been a great interest since long time ago. Therefore, there are a lot of methods that have been widely used since long past. This paper reviewed one of the methods for establishing hidden communication in information security and has gained attraction in recent years that is Steganography. Steganography is the art and science of hiding a secret message in a cover media such as image, text, signals or sound in such a way that no one, except the intended recipient knows the existence of the data. In this paper, the research and development of steganography from three years back starting from 2010 until recently, 2013 in Muslim world are reviewed. The future research in the field of Steganography is briefly discussed.

Keywords: - *Cover Image, Stego Image, Cryptography, Steganography, Information Hiding, Information Security, Muslim World*

a. INTRODUCTION

In today's information technology era, the internet has played a vital part in the communication and information sharing. Due to the rapid development in Information Technology and Communication and the Internet, the security of the data and the information has raise concerned. Every day, confidential data has been compromised and unauthorized access of data has crossed the limits. Great measures should be taken to protect the data and information [1,2]. Steganography combined with encryption will be a powerful and efficient tool that provides high level of security [3].

A review on steganography research and development throughout the year will be discussed in part 2 of this paper. The review will be focusing on Muslim world and narrowing it down to Middle East countries. The review includes past, current and future research on steganography and the possible future research on the latest algorithm and technologies in steganography.

II. MUSLIM WORLD TERMINOLOGIES

The term Muslim World is also known as the Ummah and Islamosphere [4]. There are different meanings referring to the term. In a religious sense, the Islamic Ummah is referring to those who follow the teachings of Islam referring to as a Muslim. In a cultural sense, the Muslim Ummah is referring to the Islamic civilization, this inclusive of non-Muslims living in the civilization. In a modern geopolitical sense, the term Muslim World is referring to collectively to Muslim-majority countries. As of 2010, over 1.6 billion or about or about 23.4% of the world population is Muslims [5]. 62% of Muslims live in Asia-Pacific [6], 20% in the Middle East-North Africa [7], 15% in Sub-Saharan African [8], around 3% in Europe [9] and only 0.3% in the Americas [10][11][12][13]. This paper focuses on steganography research and development in Muslim World narrowing it down to Middle East countries. The majority of the population in Middle East countries are Muslim [14].

III. STEGANOGRAPHY HISTORY

The word Steganography comes from the Greek origin that means "concealed (covered) writing". The word 'steganos' means "covered or protected" and 'graphie' means "writing" [15]. Steganography thus not only emphasize on the art of hiding information but also the art and science of hiding the communication that take place [16]. First applications of Steganography were documented by Herodotus, a Greek historian. Steganography can be traced back to ancient Greek centuries when the message is tattooed on the messengers shaved heads. The hair then grows to hide the message. Their head will be shaved when they reach the recipient of the message [17,18,19].Another steganography method that was used during those days is tablet wax. In order to hide the message, the tablet was erased by wax and text was etched on and then again covered it by wax and appeared blank upon inspections [18,20].

During the century, the methods of using invisible inks were extremely popular [18]. During the World War II where people used ink for writing hidden messages, this was true [17]. The mixture will turn darker and the written message becomes visible upon heating. After some time, the Germans introduced the microdot technique where microdots are considered as photographs as small as a printed period, but with a clear format of a typewritten page [17, 21]. They were included in a letter or an envelope, and because of their tiny sizes, they could be indiscernible. Microdots were also hidden in body parts including nostrils, ears, or under fingernails [18].The military and several governmental agencies are looking into steganography for their own secrettransmissions of information. They are also desirous of discerning secret information communicated by criminals, terrorists, and other aggressive forces. Following investigations into the Al-Qaeda attack, steganography was suspected to be made use of in their attack of the World Trade Centre [22].

3.1 STEGANOGRAPHY FEATURES AND APPLICATIONS

Steganography can be used in a lot of useful applications. For example copyright control of materials, to enhance the robustness of an image search engines and smart identity cards where the details of individuals are embedded in their photographs. Other applications include video-audio synchronization, TV broadcasting, TCP/IP packets where a unique ID is embedded in an image to analyse the network traffic of particular users [20]. Medical Imaging Systems is one of the modern applications that use Steganography where a separation is recommended between patients' image data or DNA sequences and their captions for security or confidentiality reasons. Thus, embedding the patient's information in the image could be a security measure to help solving security issues [23].Digital technologies have swept the confidence in the integrity of visual imagery [24]; a matter that motivated researchers to conduct research on digital document forensics. In 2009, Cheddad and his colleagues propose a steganographic scheme which protects scanned documents from forgery using self-embedding techniques. It also allows legal or forensics experts to access the original document though it is manipulated [25].

3.2 THE DIFFERENCE BETWEEN CRYPTOGRAPHY AND STEGANOGRAPHY

Users on the internet have to send, share or receive confidential data most of the time [26]. With the increasing number of users and the increasing number of unauthorized access of confidential data, information security played an important role. Therefore, the main issue now is to mitigate and to lessen the impact of the chances of the information being detected during transmission. Cryptography deals message encryption but the communication is easily aroused suspicious but on the other hand, steganography deals with secret message hiding but the communication is invisible. This is the major differences between cryptography and steganography.

It is often thought that by encrypting the traffic, the communications will be secured but this has not been adequate in real live situation [27]. In cryptography method, people become aware of the existence of information by observing coded information, although they are unable to comprehend the information. Steganography hides the existence of the message so that intruders can't detect the communication and thus provides a higher level of security than cryptography. Both steganographic and cryptographic systems provide secret communications but different in terms of system breaking. If the intruder can read the message in cryptographic then it is broken but steganographic is considered broken once the intruders detect the existence of the secret message [28]. Steganography system is more fragile than cryptography systems in terms of system failure. This is because if the communication is detected even without decoding the message, a steganographic system is considered a failure [29].

3.3 A REVIEW OF STEGANOGRAPHY RESEARCH AND DEVELOPMENT IN MUSLIM WORLD

Table 1 : A review of steganography research and development

No	Title	Year	Country	Keyword	Summary
1.	A modified high capacity image steganography technique based on wavelet transform [30]	2010	Iraq and United Kingdom	Steganography, security, wavelets, cryptography, and information hiding	This paper proposed a modified high-capacity image steganography technique that uses wavelet transform. The wavelet transform must be at acceptable levels of imperceptibility and distortion in the cover image.
2.	Arabic/Persian text steganography utilizing similar letters with different codes [31]	2010	Iran	information hiding, Persian/Arabic text, text steganography, Unicode	This paper proposeda new method in hiding information by using Persian (Farsi) and Arabic texts. In the Unicode Standard, "Ya" and "Kaf" are two different characters having the same shape. The two characters used different codes at the beginning or in the middle of the words. Thus, the information can be hidden in texts using one of these two characters. The method has been used by Java Programming Language.
3.	Using contourlet transform and cover selection For secure steganography [32]	2010	Iran	Contourlet transform, Steganography,Steganalysis,Cover selection, Image complexity	This paper proposed a new adaptive contourlet-based steganography method. The method decomposes the cover image by contourlet transform. The authors also investigate the effect of cover selection on steganography embedding and steganalysis results.
4.	An arabic text steganography technique using zwj and zwnj regular expressions [33]	2011	Jordan	Arabic text, Unicode, cryptography, hiding information, text steganography	This paper proposed a text steganography technique for Arabic Unicode texts. Arabic Unicode text uses two special characters that arethe zero width joiner character (JWZ) to join two letters and the zero width non joiner character (JWNZ) to prevent two letters from joining. The authors use two regular expressions to generate a sequence of special characters that consists of JWZ and JWNZ characters for information hiding.
5.	Steganography In Programming [34]	2011	Iran	Steganography, Trithemius, Methods, Microdot	This paper reviewed different steganography methods that are text, photo or sound. There are three methods studied in text steganography that are life shift coding, word shift coding and feature coding. In photo steganography the authors observed filtering and masking methods. While in sound steganography, the methods are bit insertion, phase coding, spread spectrum coding and echo hiding. Steganalysis or the science of finding hidden information is also discussed.
6.	Blind Colour Image Steganography in Spatial Domain [35]	2011	Iraq	information hiding, colour image steganography, spread spectrum	This paper proposed a blind colour image steganography method that embeds secret message by spraying theme on the blocks in the high order bits in colour channel such as blue. However it also depends on the constant sequence spread spectrum method to survive loss compression image like JPG.

7.	Microdots DNA Steganography [36]	2011	Iraq	Steganography, DNA, DNA computing. Microdots, DNA steganography	This paper reviewed the use of DNA computing in steganography and the fundamentals of DNA. DNA computing in steganography has been recognized as a future technology that can help in unbreakable algorithms. The authors then proposed new ideas to enhance the established method.
8.	Steganography in Digital Images: Common Approaches and Tools [37]	2013	Saudi Arabia and Malaysia	Digital image steganography, Frequency domain, Spatial domain, Steganalysis.	This paper presents common approaches and tools that are used in digital image steganography. It is shown mathematically and graphically. The differences between steganography, cryptography and watermarking technique are discussed. The authors also highlighted the current steganography tools and demonstrate how the secret information is embedded into image through the tools.
9.	Optimal Image Steganography Content Destruction Techniques [38]	2013	Iraq	Steganography, stego-destruction, DCT, LSB, Denoising and Filtering, overwriting	The paper presents two methods for destroying steganography content in an image that are the overwriting and the denoising method. The overwriting method is a random data that can be written again over steganographic images while the denoising method uses two kinds of destruction techniques that are filtering and discrete wavelet techniques.These two methods have been simulated and evaluated over two types of hiding techniques that are Least Significant Bit LSB technique and Discrete CosineTransform DCT technique.
10.	Steganography in image files: A survey [39]	2013	Iraq and Malaysia	Image files, Spatial Domain, Steganography, Survey, Taxonomy, Transform Domain	This paper presents the use of an image file as a carrier and the taxonomy of current steganographic techniques. The authors analysed and discussed steganography techniques for their ability in information hiding and the robustness to different image processing attacks. They also briefly discussed steganalysis which is the science of attacking steganography.

Table 1: Illustrates a review of Steganography research and development in the Muslim world from the year 2010 until 2013. In 2010, there are three researches being reviewed.

3.3.1 The first research proposed a modified high capacity image steganography technique that uses wavelet transform. The second research proposed a new method in hiding information by using Persian (Farsi) and Arabic texts while the third research proposed a new adaptive contourlet-based steganography method. The similarities of all these three researches are they are proposing a new method or technique in the field of steganography. The first and the third research are focusing on image steganography while the second research is focusing on text steganography.

3.3.2 In 2011, there are four researches being reviewed. The first research proposed a text steganography technique for Arabic Unicode texts. Arabic Unicode text uses two special characters that are the zero width joiner character (JWZ) to join two letters and the zero width non joiner character (JWNZ) to prevent two letters from joining. Two regular expressions are used to generate a sequence of special characters that consists of JWZ and JWNZ characters for information hiding. The second research reviewed different steganography methods that are text, photo or sound. There are three methods studied in text steganography that are life shift coding, word shift coding and feature coding. In photo steganography, filtering and masking methods are observed. While in sound steganography, the methods are bit insertion, phase coding, spread spectrum coding and echo

hiding. The third research proposed a blind colour image steganography method that embeds secret message by spraying theme on the blocks in the high order bits in colour channel such as blue while the fourth research reviewed the use of DNA computing in steganography. The fundamentals of DNA are discussed and new ideas are proposed to enhance the established method.

3.3.3 In 2013, there are three researches being reviewed. The first research presents common approaches and tools that are used in digital image steganography. It is shown mathematically and graphically. The differences between steganography, cryptography and watermarking technique are discussedand the current steganography toolsused are also highlighted. The second research presents two methods for destroyingsteganography content in an image that are the overwriting and the denoising method. The overwriting method is a random data that can be written again over steganographic images while the denoising method uses two kinds of destruction techniques that are filtering and discrete wavelet techniques. While the third research presents the use of an image file as a carrier and the taxonomy of current steganographic techniques. Steganography techniques are analysed and discussed for their ability in information hiding and the robustness to different image processing attacks.

3.3.4 From the three consecutive years from 2010 to 2013, the image steganography is the most popular choice of researchers. There are four main categories that used in steganography that are image, audio, sound and protocol [1]. Out of the ten researches, five is proposing new techniques or methods in image steganography. Nearly all digital file formats can be used for steganography but the formats that are more compatible are those with high degree of redundancy. The terms redundancy means the bits of an object that provide accuracy far greater than necessary for the object's use and display [40]. The redundant bits of an object then can be altered without the alteration being detected easily [22]. Image files usually comply with this main requirement even though research has also uncovered other types of file formats that also can be used for hiding information.

IV. FUTURE RESEARCH

As steganography continue on its evolutionary path, the world of information security looks forward in the future research regarding the field of steganography as modern encryption algorithms are broken. Some of the future researches include:

1. Steganalysis that is defined as a process to crack the cover object in order to get the hidden information.
2. Combining the technology of cryptography with steganography to achieve a higher level of security that even the intruder detects the hidden message, the message cannot be decoded.
3. Researchers continue to discover new platforms that could potentially use to hide information apart from the traditional platforms such as audio, video and images.
4. The concept of using DNA computing in the fields of cryptography and steganography has been identified as a possible technology for unbreakable algorithms.

V. CONCLUSION

As per conclusion, this paper discussed an overview of Steganography, the features and applications, history and how it's differs from cryptography. This paper also highlighted a review of research and development of Steganography in Muslim world from the year 2010 to 2013. This paper suggested a few for future research like Steganalysis, technology combined, discover new platform and possible unbreakable algorithms.

REFERENCES

[1] T. Morkel , J.H.P. Eloff and M.S. Olivier "An Overview of Image Steganography".
[2] Amanpreet Kaur, Renu Dhir, and Geeta Sikka "A New Image Steganography Based On First Component Alteration Technique" (IJCSIS) International Journal of Computer Science and Information Security,Vol. 6, No. 3, 2009.
[3] Nagham Hamid, Abid Yahya, R. Badlishah Ahmad and Osamah M. Al-Qershi "ImageSteganography Techniques: An Overview" International Journal of Computer Science and Security (IJCSS), Volume (6): Issue (3): 2013.
[4] Amir Ahmad Nasr. My Isl@m: How Fundamentalism Stole My Mind --- and Doubt Freed My Soul. Page 147. 2013.
[5] "Executive Summary". The Future of the Global Muslim Population. Pew Research Center. 27 January 2011. Retrieved 1 November 2013.

[6] "Region: Asia-Pacific". The Future of the Global Muslim Population. Pew Research Center. Retrieved 1 November 2013.
[7] "Region: Middle East-North Africa". The Future of the Global Muslim Population. Pew Research Center. Retrieved 1 November 2013.
[8] "Region: Sub-Saharan Africa". The Future of the Global Muslim Population. Pew Research Center. Retrieved 1 November 2013.
[9] "Region: Europe". The Future of the Global Muslim Population. Pew Research Center. Retrieved 1 November 2013.
[10] "Region: Americas". The Future of the Global Muslim Population. Pew Research Center. Retrieved 1 November 2013.
[11] Tom Kington (31 March 2008). "Number of Muslims ahead of Catholics, says Vatican". The Guardian. Retrieved 1 November 2013.
[12] "Muslim Population". IslamicPopulation.com. Retrieved 1 November 2013.
[13] "Field Listing - Religions". Retrieved 1 November 2013.
[14] "Muslim Population by Country". The Future of the Global Muslim Population. Pew Research Center. Retrieved 1 November 2013.
[15] Rajkumar Yadav "Study of Information Hiding Techniques and their Counterattacks: A Review Article" , International Journal of Computer Science & Communication Networks, Vol 1(2), 142-164, Oct-Nov 2011.
[16] Angela D. Orebaugh " Steganalysis: A Steganography Intrusion Detection System" , George Mason University
[17] R. Krenn, "Steganography and steganalysis," An Article, Santa Barbara, California, January 2004, available from: http://www.krenn.nl/univ/cry/steg/article.pdf [Last accessed on 1 November 2013]
[18] J.C. Ingemar, M.L. Miller, J.A. Bloom, J. Fridrich, and T. Kalker, "Digital watermarking and steganography", Burlington: Morgan Kaufmann; 2008.
[19] J. Fridrich, "Steganography in Digital Media: Principles",Algorithms, and Applications, Cambridge, England: Cambridge University Press; 2009.
[20] N.F. Johnson, and S. Jajodia, "Exploring steganography: Seeing the unseen," Computer, IEEE, Vol. 31, pp. 26-34, 1998.
[21] T. Morkel, J.H.P. Eloff, and M.S. Olivier, "An overview of image steganography" in Proceedings of the Fifth Annual Information Security South Africa Conference (ISSA2005), Sandton, South Africa, pp. 1-12, 29 Jun.-1 Jul. 2005.
[22] M. Bachrach, and F.Y. Shih, "Image steganography and steganalysis,"Wiley Interdisciplinary Reviews: Computational Statistics, Vol. 3, pp. 251-9, 2011.
[23] Petitcolas, F.A.P." Introduction to information hiding". In S. Katzenbeisser & F. A. P. Petitcolas (Eds.), Information hiding techniques for steganography and digital watermarking (pp. 1-12). Boston, London: Artech House,2000.
[24] Farid, H. "Image forgery detection". Signal Processing Magazine, IEEE, 26(2): 16-25. doi: 10.1109/msp.2008.931079, 2009.
[25] Cheddad, A., J. Condell, K. Curran, & P. Mc Kevitt. "A skin tone detection algorithm for an adaptive approach to steganography". Signal Processing, 89(12): 2465-2478. doi: 10.1016/j.sigpro.2009.04.022, 2009.
[26] Arvind Kumar and Km. Pooja "Steganography- A Data Hiding Technique", International Journal of Computer Applications (0975 – 8887) Volume 9– No.7, November 2010.
[27] Fabien A. P. Petitcolas, Ross J. Anderson and Markus G. Kuhn "Information Hiding A Survey"Proceedings of the IEEE, special issue on protection of multimedia content, 87(7):1062{1078, July 1999.
[28] Banasthali Vidyapith, Rjasthan "Image Steganography Techniques: A Review Article", Bulletin of Engineering, Faculty of Engineering, Hunedoara, Romania, July-September,2013.
[29] Adel Almohammad "Steganography-Based Secret and Reliable Communications: Improving Steganographic Capacity and Imperceptibility" A thesis submitted for the degree of Doctor of Philosophy, Department of Information Systems and Computing, Brunel University, August,2010.
[30] Ali Al-Ataby, Fawzi Al-Naima, "A Modified High Capacity Image Steganography Technique Based on Wavelet Transform,"The International Arab Journal of Information Technology, Vol. 7, No. 4, October 2010.
[31] M. Hassan Shirali-Shahreza, Mohammad Shirali-Shahreza, "Arabic/Persian Text Steganography Utilizing Similar Letters With Different Codes," The Arabian Journal for Science and Engineering, Volume 35, Number 1B, April 2010.

[32] Hedieh Sajedi, Mansour Jamzad, "Using contourlet transform and cover selection for secure steganography," Springer, Int. J. Inf. Secur. (2010) 9:337–352, August 2010.
[33] A.F. Al Azawi, M.A. Fadhil, "An Arabic Text SteganographyTechnique Using Zwj And Zwnj Regular Expressions," International Journal Of Academic Research Vol. 3. No. 3. May 2011.
[34] Mahmoud Vaziri Nasab , Behzad Mahjour Shafiei, "Steganography In Programming," Australian Journal of Basic and Applied S ciences, 5(12): 1496-1499, 2011.
[35] F. A. Abdullatif, W. A.Shukur," Blind Color Image Steganography in Spatial Domain," Ibn Al- Haitham J. For Pure & Appl. Sci. Vol.24 (1) 2011.
[36] Wissam Makki Alwash, "Microdots DNA Steganography," Journal of Babylon University/Pure and Applied Sciences/ No.(3)/ Vol.(19): 2011.
[37] Samer Atawneh, Ammar Almomani1 and Putra Sumari, "Steganography in Digital Images: Common Approaches and Tools,"IETE Technical Review, Vol 30, Issue 4, Jul-Aug 2013.
[38] Siddeeq Y. Ameen, Muthana R. Al-Badrany, "Optimal Image Steganography Content Destruction Techniques," Proceedings of the 2013 International Conference on Systems, Control, Signal Processing and Informatics, 2013.
[39] Nagham Hamid, Abid Yahya, R. Badlishah Ahmad, Dheiaa Najim, Lubna Kanaan, "Steganography in image files: A survey," Australian Journal of Basic and Applied Sciences, 7(1): 35-55, 2013.
[40] W Bender, D. Gruhl, N. Morimoto, and A. Lu, "Techniques for data hiding," IBM Systems Journal, Vol. 35, No. 3 and 4, pp. 313-336,1996.
[41] Mehdi Kharrazi, Husrev T. Sencar and Nasir Memon "Image Steganography : Concepts and Practices "Polytechnic University, Brooklyn, NY 11201, USA.

American Journal of Engineering Research (AJER)
e-ISSN : 2320-0847 p-ISSN : 2320-0936
Volume-02, Issue-11, pp-129-150
www.ajer.org

Research Paper Open Access

Control of Biped Robot with Stable Walking

Tran Dinh Huy, Ngo Cao Cuong, and Nguyen Thanh Phuong
HUTECH High Technology Research Instituite

Abstract: - This paper presents the development results of the 10 DOF biped robot with stable and human-like walking using the simple hardware configuration. Kinematics model of the 10 DOF biped robot and its dynamic model based on the 3D inverted pendulum are presented. Under assumption that the COM of the biped robot moves on the horizontal constraint plane, ZMP equations of the biped robot depending on the coordinate of the center of the pelvis link obtained from the dynamic model of the biped robot are given based on the D'Alembert's principle. A ZMP servo control system is constructed to track the ZMP of the biped robot to ZMP reference input which is decided by the footprint of the biped robot. A discrete time optimal controller is designed to control ZMP of the biped robot to track trajectories reference inputs based on discrete time systems. When ZMP of biped robot is controlled to track trajectory reference input decided inside stable region, a trajectory of COM is generated as stable walking pattern of the biped robot. Based on the stable walking pattern of the biped robot, a stable walking control method of the biped robot is proposed. From the trajectory of COM of the biped robot and trajectory reference input of the swinging leg, inverse kinematics solved by solid geometry method is used to compute the angle of joints of the biped robot. Because joint's angles reference of the biped robot are computed from the stable walking pattern of the biped robot, the walking of the biped robot is stable if the joint's angles of the biped robot are controlled to track those references. The stable walking control method of the biped robot is implemented by simple hardware using PIC18F4431 and dsPIC30F6014. The simulation and experimental results show the effectiveness of this control method.

Keywords: - *Discrete Time Optimal Control, ZMP Servo Control System, Biped Robot.*

I. INTRODUCTION

Research on humanoid robots and biped locomotion is currently one of the most exciting topics in the field of robotics and there exist many ongoing projects. Although some of those works have already demonstrated very reliable dynamic biped walking [12], it is still important to understand the theoretical background of the biped robot. The biped robot performs its locomotion relatively to ground while it is keeping its balance and not falling down. Since there is no base link fixed on the ground or the base, the gait planning and control of the biped robot is very important but difficult. Up so far, numerous approaches have been proposed. The common method of these numerous approaches is to restrict zero moment point (ZMP) within stable region to protect biped robot from falling down [8].

In the recent years, a great amount of scientific and engineering research has been devoted to the development of legged robots able to attain gait patterns more or less similar to human beings. Towards this objective, many scientific papers have been published, focusing on different aspects of the problem. Sunil, Agrawal and Abbas [3] proposed motion control of a novel planar biped with nearly linear dynamics. They introduced a biped robot that the model was nearly linear. The motion control for trajectory following used nonlinear control method. Jong Hyeon Park [4] proposed impedance control for biped robot locomotion so that both legs of the biped robot were controlled by the impedance control, where the desired impedance at the hip and the swing foot was specified. Qiang Huang and Yoshihiko [5] introduced sensory reflex control for humanoid walking so that the walking control consisted of a feedforward dynamic pattern and a feedback sensory reflex. In these papers, the moving of the body of the robot was assumed to be only on the sagittal plane. The biped robot was controlled based on the dynamic model. The ZMP of the biped robot was measured by sensor so that the structure of the biped robot was complex and required high speed controller hardware system. This paper presents a stable walking control of biped robot by using inverse kinematics with simple hardware configuration based on the walking pattern which is generated by ZMP servo system. The robot's body can

move on sagittal and lateral plane. Furthermore, the walking pattern is generated based on the ZMP of the biped robot so that the stable of the biped robot during walking or running is guaranteed without the sensor system to measure ZMP of biped robot. In addition, a simple inverse kinematics using solid geometry is used to obtain angle of joints of the biped robot based on the stable walking pattern. The biped robot is modeled as 3D inverted pendulum [1]. A ZMP servo system is constructed based on the ZMP equation to generate trajectory of center of mass (COM). A discrete time optimal tracking controller is also designed to control ZMP servo system. From the trajectory of COM, inverse kinematics of the biped robot is solved by solid geometry method to obtain angle joints of the biped robot. It is used to control walking of the biped robot.

II. MATHEMATIC MODEL OF THE BIPED ROBOT

2.1 Kinematics Model of Biped Robot

A 10 DOF biped robot developed in this thesis is considered as shown in Fig. 1. It is assumed that the biped robot is supported by right leg and swung by left leg.

In Fig. 1, l_1 and l_5 are length of the lower links of the right leg and left leg, l_2 and l_4 are length of the upper links of the right leg and left leg, l_3 is length of the pelvis link, (x_b, y_b, z_b) and (x_e, y_e, z_e) are coordinates of the ankle joints B_2 and E, and (x_c, y_c, z_c) is coordinate of the center of pelvis link C.

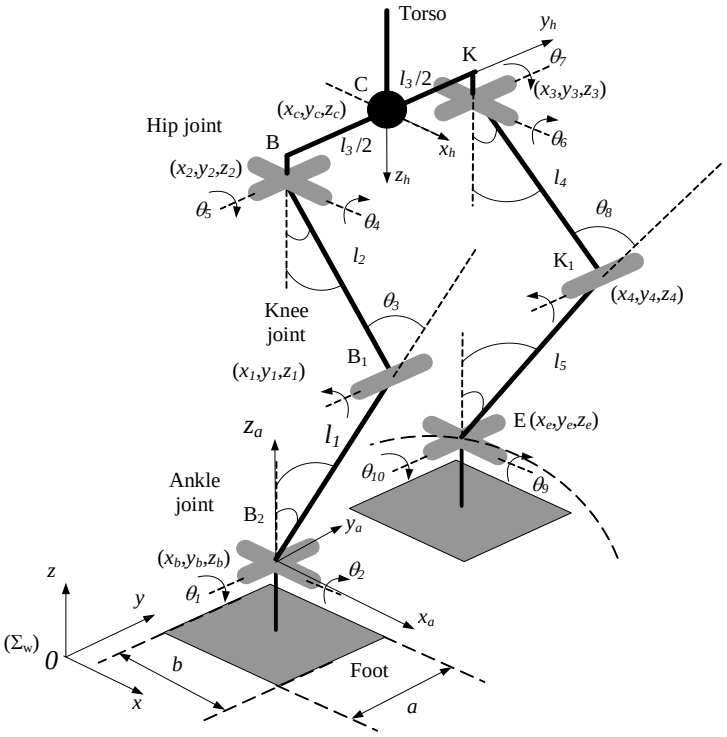

Fig. 1: Configuration of 10 DOF biped robot model.

The biped robot consists of five links that are one torso, two links in each leg with upper link and lower link, and two feet. The two legs of the biped robot are connected with torso via two DOF rotating hip joints. Hip joints can rotate the legs in the angles θ_5 for left leg and θ_7 for right leg on sagittal plane, and in the angles θ_4 for left leg and θ_6 for right leg on frontal plane. The upper links are connected with the lower links via one DOF rotating knee joints which can rotate only on sagittal plane. Right knee joint can rotate lower link and upper link of the right leg in angle θ_3, and left knee joint can rotate lower link and upper link of the left leg in angle θ_8. The lower links are connected with feet via two DOF ankle joints. The ankle joints can rotate the feet in angle θ_1 (for left leg) and θ_{10} (for right leg) on the sigattal plane, and in angle θ_2 for left leg and θ_9 for right leg on the in frontal plane. All the rotating joints are considered to be friction free and each one is driven by one DC motor.

In choosing Cartesian coordinate Σ_a whose origin is taken on the ankle joint, position of the center of the pelvis link is expressed as follows:

$$x_{ca} = l_1 \sin\theta_1 - l_2 \sin(\theta_3 - \theta_1) \quad (1)$$

$$y_{ca} = l_1 \sin\theta_2 + l_2 \cos(\theta_3 - \theta_1)\sin\theta_2 + \frac{l_3}{2}\cos(\theta_2 + \theta_4) \quad (2)$$

$$z_{ca} = l_1 \cos\theta_1 \cos\theta_2 + l_2 \cos(\theta_3 - \theta_1)\cos\theta_2 - \frac{l_3}{2}\sin(\theta_2 + \theta_4) \quad (3)$$

where x_{ca}, y_{ca} and z_{ca} are position of the center of the pelvis link in the coordinate system Σ_a.
Similarly, position of the ankle joint of swinging leg is expressed in the coordinate system Σ_h as:

$$x_{eh} = l_4 \sin\theta_7 - l_5 \sin(\theta_8 - \theta_7) \quad (4)$$

$$y_{eh} = \frac{l_3}{2} + l_4 \sin\theta_6 - l_5 \cos(\theta_8 - \theta_7)\sin\theta_6 \quad (5)$$

$$z_{eh} = l_4 \cos\theta_6 \cos\theta_7 + l_5 \cos(\theta_8 - \theta_7)\cos\theta_6 \quad (6)$$

It is assumed that the center of mass of each link is concentrated at the tip of the link.
The center of mass of the robot can be obtained as follows:

$$x_{com} = \frac{m_b x_b + m_1 x_1 + m_2 x_2 + m_c x_c + m_3 x_3 + m_4 x_4 + m_e x_e}{m_b + m_1 + m_2 + m_c + m_3 + m_4 + m_e} \quad (7)$$

$$y_{com} = \frac{m_b y_b + m_1 y_1 + m_2 y_2 + m_c y_c + m_3 y_3 + m_4 y_4 + m_e y_e}{m_b + m_1 + m_2 + m_c + m_3 + m_4 + m_e} \quad (8)$$

$$z_{com} = \frac{m_b z_b + m_1 z_1 + m_2 z_2 + m_c z_c + m_3 z_3 + m_4 z_4 + m_e z_e}{m_b + m_1 + m_2 + m_c + m_3 + m_4 + m_e} \quad (9)$$

where
m_b, m_1, m_2, m_c, m_3, m_4 and m_e are mass of the ankle joint of the right leg B_2, knee joint of the right leg B_1, hip joint of the right leg B, center of the pelvis link C, hip joint of the left leg K, knee joint of the left leg K_1 and ankle joint of the left leg E.
(x_b, y_b, z_b), (x_e, y_e, z_e), (x_1, y_1, z_1), (x_4, y_4, z_4), (x_2, y_2, z_2), (x_3, y_3, z_3) and (x_c, y_c, z_c) are coordinates of the ankle joints B_2, E, knee joints B_1, K_1, hip joints B, K, and center of pelvis link C.
It is assumed that the mass of links of legs is negligible compared with mass of the trunk. Eqs. (7)~(9) can be rewritten as follows:

$$x_{com} = x_c, \; y_{com} = y_c \text{ and } z_{com} = z_c \quad (10)$$

This means that the center of mass (COM) is concentrated at the center of the pelvis link.

2.2 Dynamic Model of Biped Robot

When the biped robot is supported by one leg, the dynamics of the robot can be approximated by a simple 3D inverted pendulum whose base is the foot of biped robot and head is COM of biped robot as shown in Fig. 2. The length of inverted pendulum r is able to be expanded or contracted. The position of the COM of the inverted pendulum C(x_{ca}, y_{ca}, z_{ca}) in the Cartesian coordinate can be uniquely specified by $\boldsymbol{q} = [\theta_r, \theta_p, r]^T$ in the polar coordinate as follows [1]:

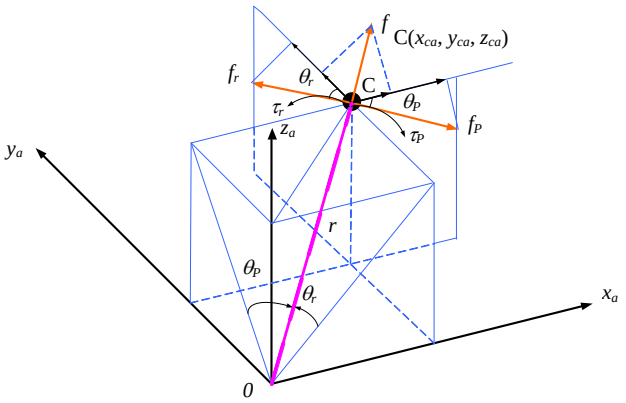

Fig. 2: Three dimension (3D) inverted pendulum.

$$x_{ca} = r \sin\theta_p \equiv rS_p \quad (11)$$

$$y_{ca} = -r \sin\theta_r \equiv -rS_r \quad (12)$$

$$z_{ca} = r\sqrt{1 - \sin^2\theta_r - \sin^2\theta_p} \equiv rD \quad (13)$$

where $S_r \equiv \sin\theta_r$, $S_p \equiv \sin\theta_p$, $C_p \equiv \cos\theta_p$, $C_r \equiv \cos\theta_r$, and $D \equiv \sqrt{1 - \sin^2\theta_p - \sin^2\theta_r}$.

$[\tau_r, \tau_p, f]^T$ are defined as the actuator torques and force associated with the variables $[\theta_r, \theta_p, r]^T$. The Lagrangian of the 3D inverted pendulum is

$$L = \frac{1}{2} m(\dot{x}_{ca}^2 + \dot{y}_{ca}^2 + \dot{z}_{ca}^2) - mgz_{ca} \quad (14)$$

where m is the total mass of the biped robot, and g is the gravitational acceleration.
Based on the Largange's equation, the dynamics of 3D inverted pendulum can be obtained in the Cartesian coordinate as follows:

$$m\begin{bmatrix} \ddot{x}_{ca} \\ \ddot{y}_{ca} \\ \ddot{z}_{ca} \end{bmatrix} = \left(\boldsymbol{J}^T\right)^{-1} \begin{bmatrix} \tau_r \\ \tau_p \\ f \end{bmatrix} + \begin{bmatrix} 0 \\ 0 \\ -mg \end{bmatrix}. \quad (15)$$

where $\boldsymbol{J}$ is Jacobian matrix which is expressed as

$$\boldsymbol{J} = \frac{\partial \boldsymbol{p}}{\partial \boldsymbol{q}} = \begin{bmatrix} 0 & rC_p & S_p \\ -rC_r & 0 & -S_r \\ -\frac{rC_rS_r}{D} & -\frac{rC_pS_p}{D} & D \end{bmatrix}. \quad (16)$$

The dynamics equation of inverted pendulum along y_a axis can be obtained as

$$m\left(-z_{ca}\ddot{y}_{ca} + y_{ca}\ddot{z}_{ca}\right) = \tau_x - mgy_{ca}. \quad (17)$$

where $\tau_x \equiv \frac{D}{C_r}\tau_r$ is the torque around x_a axis.

Using similar procedure, the dynamics equation of inverted pendulum along x_a axis can be derived as

$$m\left(z_{ca}\ddot{x}_{ca} - x_{ca}\ddot{z}_{ca}\right) = \tau_y + mgx_{ca} \quad (18)$$

where $\tau_y \equiv \frac{D}{C_p}\tau_p$ is the torque around y_a axis.

There are many classes of moving pattern of inverted pendulum. For selecting one of them, a constraint is applied to limit the motion of the inverted pendulum. That is, the motions of the COM of inverted pendulum are constrained on the plane whose normal vector $\boldsymbol{v_{cp}}$ is $[k_x,k_y,-1]^T$ and z_a intersection is z_{cd} as shown in Fig. 3.

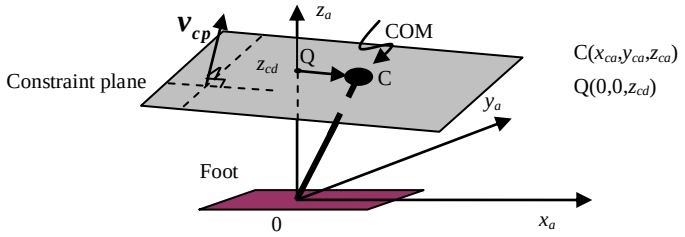

Fig. 3: Motion of inverted pendulum on constraint plane.

It is assumed that the constraint plane intersects the z_a axis at $Q(0,0,z_{cd})$ as shown in Fig. 3. Because $C(x_{ca},y_{ca},z_{ca})$ is located on the constraint plane, vector $\boldsymbol{v_{cp}}$ is perpendicular to vector $\overrightarrow{QC}$. The constraint condition of the motion of the COM of inverted pendulum is expressed as

$$z_{ca} = k_x x_{ca} + k_y y_{ca} + z_{cd} \quad (19)$$

where k_x, k_y and z_{cd} are constants.
When the biped robot walks on a rugged terrain, the normal vector of the constraint plane should be perpendicular to the slope of the ground, and z_a intersection z_{cd} in the coordinate system Σ_a is set as distance between COM and the ground.
The second order derivative of Eq. (19) is

$$\ddot{z}_{ca} = k_x \ddot{x}_{ca} + k_y \ddot{y}_{ca}. \quad (20)$$

Substituting Eqs. (19)~(20) into Eqs. (17)~(18), the equation of motion of 3D inverted pendulum under constraint can be expressed as

$$\ddot{y}_{ca} = \frac{g}{z_{cd}} y_{ca} - \frac{k_x}{z_{cd}}\left(x_{ca}\ddot{y}_{ca} - \ddot{x}_{ca}y_{ca}\right) - \frac{1}{mz_{cd}}\tau_x \quad (21)$$

$$\ddot{x}_{ca} = \frac{g}{z_{cd}} x_{ca} + \frac{k_y}{z_{cd}}\left(x_{ca}\ddot{y}_{ca} - \ddot{x}_{ca}y_{ca}\right) + \frac{1}{mz_{cd}}\tau_y. \quad (22)$$

It is assumed that the biped robot walks on the flat floor and horizontal plane. In this case, k_x and k_y are set to

zero. It means that the COM of inverted pendulum moves on a horizontal plane which has height $z_{ca} = z_{cd}$ as shown in Fig. 3.
Eqs. (21)~(22) can be rewritten as:

$$\ddot{y}_{ca} = \frac{g}{z_{cd}} y_{ca} - \frac{1}{mz_{cd}} \tau_x \quad (23)$$

$$\ddot{x}_{ca} = \frac{g}{z_{cd}} x_{ca} + \frac{1}{mz_{cd}} \tau_y . \quad (24)$$

When the inverted pendulum moves on the horizontal plane, the dynamic equations along the x_a axis and y_a axis are independent each other and can be rewritten as linear differential equations.
(x_{zmp}, y_{zmp}) is defined as location of ZMP on the floor as shown in Fig. 4.

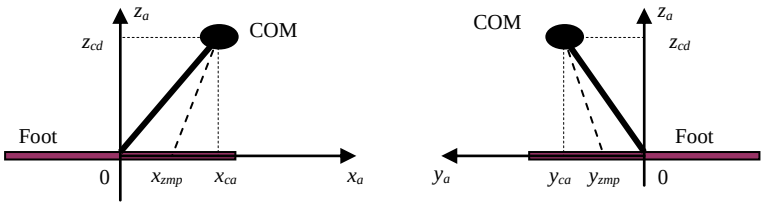

Fig. 4: ZMP of inverted pendulum.

(x_{ca}, y_{ca}, z_{ca}) is projection of COM in the coordinate system Σ_a.
ZMP is a point where the net support torques from floor about x_a axis and y_a axis are zero. From D'Alembert's principle, ZMP of inverted pendulum under constraint can be expressed as

$$x_{zmp} = x_{ca} - \frac{z_{cd}}{g} \ddot{x}_{ca} \quad (25)$$

$$y_{zmp} = y_{ca} - \frac{z_{cd}}{g} \ddot{y}_{ca} . \quad (26)$$

Eq. (25) shows that position of ZMP along x_a axis depends only on the position and acceleration of COM along x_a axis. Similarly, position of ZMP along y_a axis does not depend on the position of COM along x_a axis, but it depends only on the position and acceleration of COM along y_a axis.
When the biped robot moves with slow speed, Eqs. (25)~(26) can be approximated as Eqs. (27). It is shown that coordinate of the ZMP is projection of COM.

$$x_{zmp} = x_{ca} \text{ and } y_{zmp} = y_{ca} \quad (27)$$

Since there are no actions torques that cause robot to fall down at ZMP, ZMP is very important for walking robot and generally used as dynamic criterion for gait planning and control. During the walking of robot, ZMP is located inside of the footprint of supported foot or inside the supported polygon.

III. WALKING PATTERN GENERATION

The objective of controlling the biped robot is to realize a stable walking or running. The stable walking or running of the biped robot depends on walking pattern. Walking pattern generation is used to generate a trajectory for COM of the biped robot. For the stable walking or running of the biped robot, the walking pattern should satisfy the condition that the ZMP of the biped robot always exists inside the stable region. Since position of COM of the biped robot has the close relationship with position of ZMP as shown in Eqs. (25)~(26), trajectory of COM can be obtained from the trajectory of ZMP. Based on a sequence of desired footprint and period time of each step of the biped robot, a reference trajectory of ZMP can be specified. Fig. 5 illustrates footprint and reference trajectory of ZMP to guarantee stable gait.

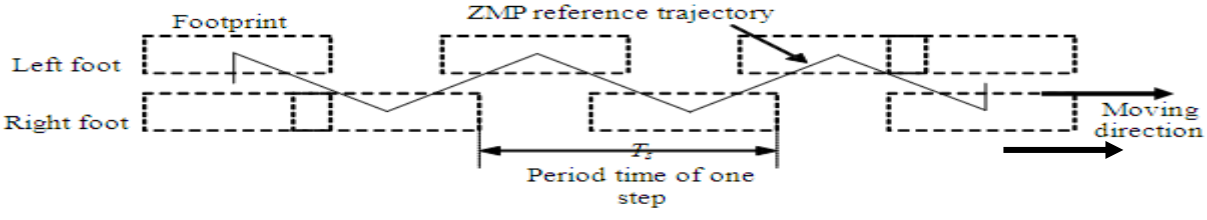

Fig. 5: Footprint and reference trajectory of ZMP.

3.1 Walking Pattern Generation Based on Servo Control of ZMP

When a biped robot is modeled as 3D inverted pendulum which is moved on horizontal plane, the ZMP's position of the biped robot is expressed by linear independent equations along x_a and y_a directions which are shown as Eqs. (25)~(26).

$u_x = \frac{d}{dt}\ddot{x}_{ca} = \dddot{x}_{ca}$ and $u_y = \frac{d}{dt}\ddot{y}_{ca} = \dddot{y}_{ca}$ are defined as the time derivative of the horizontal acceleration along x_a and y_a directions of the COM, u_x and u_y are introduced as inputs. Eqs. (25)~(26) can be rewritten in strictly proper form as follows:

$$\underbrace{\begin{bmatrix}\dot{x}_{ca}\\ \ddot{x}_{ca}\\ \dddot{x}_{ca}\end{bmatrix}}_{\dot{x}_x(t)} = \underbrace{\begin{bmatrix}0 & 1 & 0\\ 0 & 0 & 1\\ 0 & 0 & 0\end{bmatrix}}_{A}\underbrace{\begin{bmatrix}x_{ca}\\ \dot{x}_{ca}\\ \ddot{x}_{ca}\end{bmatrix}}_{x_x(t)} + \underbrace{\begin{bmatrix}0\\ 0\\ 1\end{bmatrix}}_{B}u_x, \quad (28)$$

$$x_{zmp} = \underbrace{\begin{bmatrix}1 & 0 & -\frac{z_{cd}}{g}\end{bmatrix}}_{C}\underbrace{\begin{bmatrix}x_{ca}\\ \dot{x}_{ca}\\ \ddot{x}_{ca}\end{bmatrix}}_{x_x(t)},$$

$$\underbrace{\begin{bmatrix}\dot{y}_{ca}\\ \ddot{y}_{ca}\\ \dddot{y}_{ca}\end{bmatrix}}_{\dot{x}_y(t)} = \underbrace{\begin{bmatrix}0 & 1 & 0\\ 0 & 0 & 1\\ 0 & 0 & 0\end{bmatrix}}_{A}\underbrace{\begin{bmatrix}y_{ca}\\ \dot{y}_{ca}\\ \ddot{y}_{ca}\end{bmatrix}}_{x_y(t)} + \underbrace{\begin{bmatrix}0\\ 0\\ 1\end{bmatrix}}_{B}u_y, \quad (29)$$

$$y_{zmp} = \underbrace{\begin{bmatrix}1 & 0 & -\frac{z_{cd}}{g}\end{bmatrix}}_{C}\underbrace{\begin{bmatrix}y_{ca}\\ \dot{y}_{ca}\\ \ddot{y}_{ca}\end{bmatrix}}_{x_y(t)}.$$

where position of ZMP along x_a axis, x_{zmp}, is output of system (28), position of ZMP along y_a axis, y_{zmp}, is output of system (29), x_{ca} and y_{ca} are position of COM with respect to x_a and y_a axes, and $\dot{x}_{ca}$, $\ddot{x}_{ca}$, $\dot{y}_{ca}$, $\ddot{y}_{ca}$ are horizontal velocity and acceleration with respect to x_a and y_a directions, respectively.

Instead of solving differential Eqs. (25)~(26), position of COM can be obtained by constructing a controller to track the ZMP as output of Eqs. (28)~(29). When x_{zmp} and y_{zmp} are controlled to track reference trajectory of ZMP, COM trajectory can be obtained from state variables x_{ca} and y_{ca}. According to this pattern, the walking or running of the biped robot are stable.

By constructing ZMP tracking control systems, walking pattern generation problem turns into designing tracking controller to track ZMP's reference trajectory.

To control output of the systems with Eqs. (28)~(29), There are many type of controllers can be applied. In this paper, a discrete time optimal control theory is chosen to design tracking controller.

The systems (28) and (29) can be discretized with sampling time T as follows [6]:

$$\boldsymbol{x}_x[(k+1)] = \boldsymbol{\Phi}(T)\boldsymbol{x}_x(k) + \boldsymbol{\theta}(T)u_x(k) \quad (30)$$
$$x_{zmp}(k) = \boldsymbol{C}\boldsymbol{x}_x(k)$$
$$\boldsymbol{x}_y[(k+1)] = \boldsymbol{\Phi}(T)\boldsymbol{x}_y(k) + \boldsymbol{\theta}(T)u_y(k) \quad (31)$$
$$y_{zmp}(k) = \boldsymbol{C}\boldsymbol{x}_y(k)$$

where $\boldsymbol{x}_x(k) \equiv [x(kT) \quad \dot{x}(kT) \quad \ddot{x}(kT)]^T$ and $\boldsymbol{x}_y(k) \equiv [y(kT) \quad \dot{y}(kT) \quad \ddot{y}(kT)]^T$ are states vectors, $u_x(k) \equiv u_x(kT)$ and $u_y(k) \equiv u_y(kT)$ are input signals, and $x_{zmp}(k) \equiv x_{zmp}(kT)$ and $y_{zmp}(k) \equiv y_{zmp}(kT)$ are outputs, $\boldsymbol{\Phi}(T) = \begin{bmatrix}1 & T & T^2/2\\ 0 & 1 & T\\ 0 & 0 & 1\end{bmatrix}$ and $\boldsymbol{\theta}(T) = \begin{bmatrix}T^3/6\\ T^2/2\\ T\end{bmatrix}$.

The controllability matrix of systems (30) and (31) has full rank. The system is controllable and stabilizable [6]. Similarly, observability matrix $\boldsymbol{O}_d$ of them has full rank.

3.2 Controller Design for ZMP Tracking Control

In this section, discrete time optimal tracking controller utilizing the future values of reference input is designed to control the systems (30) and (31) to track ZMP reference input.

A time invariant discrete time system is considered as follows:

$$\begin{aligned} \boldsymbol{x}[(k+1)] &= \boldsymbol{A}_d \boldsymbol{x}(k) + \boldsymbol{B}_d u(k) \\ y(k) &= \boldsymbol{C}_d \boldsymbol{x}(k) \end{aligned} \quad (32)$$

where $\boldsymbol{x}(k) \in \Re^{n\times 1}$ is $n\times 1$ state vector, $y(k) \in \Re$ is output, $u(k) \in \Re$ is control input, and $\boldsymbol{A}_d \in \Re^{n\times n}$, $\boldsymbol{B}_d \in \Re^{n\times 1}$, $\boldsymbol{C}_d \in \Re^{1\times n}$ are matrices with corresponding dimensions.

An error signal $e(k) \in \Re$ is defined as the difference between reference input $r(k)$ and output of the system $y(k)$ as follows:

$$e(k) = r(k) - y(k) \quad (33)$$

It is denoted that the incremental control input is $\Delta u(k) = u(k) - u(k-1)$ and the incremental state is $\Delta \boldsymbol{x}(k) = \boldsymbol{x}(k) - \boldsymbol{x}(k-1)$. If the system (32) is controllable and observable, it can be rewritten in the increment as follows:

$$\begin{aligned} \Delta \boldsymbol{x}[(k+1)] &= \boldsymbol{A}_d \Delta \boldsymbol{x}(k) + \boldsymbol{B}_d \Delta u(k) \\ y(k) &= \boldsymbol{C}_d \boldsymbol{x}(k) \end{aligned} \quad (34)$$

The error at the $k+1^{th}$ sample time can be obtained from Eq. (33) as

$$e(k+1) = r(k+1) - y(k+1). \quad (35)$$

Substituting Eq. (34) into result of subtracting Eq. (33) from Eq. (35) yields

$$e(k+1) = e(k) + \Delta r(k+1) - \boldsymbol{C}_d \boldsymbol{A}_d \Delta \boldsymbol{x}(k) - \boldsymbol{C}_d \boldsymbol{B}_d \Delta u(k). \quad (36)$$

where $\Delta r(k+1) = r(k+1) - r(k) \in \Re$

From the first row of Eq. (34) and Eq. (36), the error system can be obtained as

$$\underbrace{\begin{bmatrix} e(k+1) \\ \Delta \boldsymbol{x}(k+1) \end{bmatrix}}_{\boldsymbol{X}(k+1)} = \underbrace{\begin{bmatrix} 1 & -\boldsymbol{C}_d \boldsymbol{A}_d \\ \boldsymbol{0}_{n\times 1} & \boldsymbol{A}_d \end{bmatrix}}_{\boldsymbol{A}_E} \underbrace{\begin{bmatrix} e(k) \\ \Delta \boldsymbol{x}(k) \end{bmatrix}}_{\boldsymbol{X}(k)} + \underbrace{\begin{bmatrix} 1 \\ \boldsymbol{0}_{n\times 1} \end{bmatrix}}_{\boldsymbol{G}_R} \Delta r(k+1) + \underbrace{\begin{bmatrix} -\boldsymbol{C}_d \boldsymbol{B}_d \\ \boldsymbol{B}_d \end{bmatrix}}_{\boldsymbol{G}} \Delta u(k) \quad (37)$$

where $\boldsymbol{X}(k) \in \Re^{(1+n)\times 1}$, $\boldsymbol{A}_E \in \Re^{(1+n)\times(1+n)}$, $\boldsymbol{G}_R \in \Re^{(1+n)\times 1}$ and $\boldsymbol{G} \in \Re^{(1+n)\times 1}$.

It is assumed that at each time k, the reference inputs of the error system (37) can be known for N future values as well as the present and the past values are available.

A scalar cost function of the quadratic form is chosen as

$$J = \sum_{k=0}^{\infty} \left[\boldsymbol{X}^T(k) \boldsymbol{Q} \boldsymbol{X}(k) + R \Delta u^2(k) \right] \quad (38)$$

where $\boldsymbol{Q} = \begin{bmatrix} Q_e & \boldsymbol{0}_{1\times n} \\ \boldsymbol{0}_{n\times 1} & \boldsymbol{0}_{n\times n} \end{bmatrix} \in \Re^{(1+n)\times(1+n)}$ is semi-positive definite matrix, $Q_e \in \Re$, and $R \in \Re$ are positive scalar.

An optimal problem is solved by minimizing the cost function (38).

It is assumed that N future values of the reference input $r(k+1), r(k+2), \cdots, r(k+N)$ can be utilized. The future values of reference beyond time $(k+N)$ are approximated by $r(k+N)$. It means that the following is satisfied.

$$\Delta r(k+i) = 0 \qquad (i = N+1, N+2, \ldots). \quad (39)$$

$\boldsymbol{X}_R(k) = \left[\Delta r(k+1) \quad \Delta r(k+2) \quad \cdots \quad \Delta r(k+N) \right]^T \in \Re^{N\times 1}$ is defined as a future reference input incremental vector depending on N incremental future values of the reference input.

The augmented error system with future values of reference input is obtained as

$$\begin{bmatrix} \boldsymbol{X}(k+1) \\ \boldsymbol{X}_R(k+1) \end{bmatrix} = \begin{bmatrix} \boldsymbol{A}_E & \boldsymbol{G}_{PR} \\ \boldsymbol{0}_{N\times(n+1)} & \boldsymbol{A}_R \end{bmatrix} \begin{bmatrix} \boldsymbol{X}(k) \\ \boldsymbol{X}_R(k) \end{bmatrix} + \begin{bmatrix} \boldsymbol{G} \\ \boldsymbol{0}_{(Nm)\times r} \end{bmatrix} \Delta \boldsymbol{u}(k). \quad (40)$$

where $\boldsymbol{G}_{PR} = \begin{bmatrix} \boldsymbol{G}_R & \boldsymbol{0}_{(1+n)\times 1} & \cdots & \boldsymbol{0}_{(1+n)\times 1} \end{bmatrix} \in \Re^{(1+n)\times N}$, and

$$\boldsymbol{A}_R = \begin{bmatrix} 0 & 1 & 0 & \cdots & 0 \\ \vdots & & \ddots & \ddots & \vdots \\ \vdots & & & \ddots & 0 \\ \vdots & & & & 1 \\ 0 & \cdots & \cdots & \cdots & 0 \end{bmatrix} \in \Re^{N\times N}$$

The cost function (38) can be rewritten as

$$J=\sum_{k=0}^{\infty}\left\{\begin{bmatrix}\boldsymbol{X}^T(k) & \boldsymbol{X}_R^T(k)\end{bmatrix}\begin{bmatrix}\boldsymbol{Q} & \boldsymbol{0}_{(n+1)\times N}\\ \boldsymbol{0}_{N\times(n+1)} & \boldsymbol{0}_{N\times N}\end{bmatrix}\begin{bmatrix}\boldsymbol{X}(k)\\ \boldsymbol{X}_R(k)\end{bmatrix}+R\Delta u^2(k)\right\} \quad (41)$$

The optimal control signal $\Delta u(k)$ that minimizes cost function (41) of system (40) can be obtained as [6]

$$\Delta u(k)=-\left[\boldsymbol{R}+\begin{bmatrix}\boldsymbol{G}^T & \boldsymbol{0}_{N\times 1}\end{bmatrix}\boldsymbol{P}\begin{bmatrix}\boldsymbol{G}\\ \boldsymbol{0}_{N\times 1}\end{bmatrix}\right]^{-1}\begin{bmatrix}\boldsymbol{G}^T & \boldsymbol{0}_{N\times 1}\end{bmatrix}\boldsymbol{P}\begin{bmatrix}\boldsymbol{A}_E & \boldsymbol{G}_{PR}\\ \boldsymbol{0}_{N\times(n+1)} & \boldsymbol{A}_R\end{bmatrix}\begin{bmatrix}\boldsymbol{X}(k)\\ \boldsymbol{X}_R(k)\end{bmatrix} \quad (42)$$

where $\boldsymbol{P}$ is semi-positive definite matrix that is a solution of the algebraic Ricatti equation corresponding to Eq. (40) [6].

$\boldsymbol{P}$ can be partitioned as follows:

$$\boldsymbol{P}=\begin{bmatrix}\boldsymbol{P}_1 & \boldsymbol{W}\\ \boldsymbol{W}^T & \boldsymbol{P}_2\end{bmatrix}\in\Re^{(1+n+N)\times(1+n+N)}. \quad (43)$$

where $\boldsymbol{P}_1\in\Re^{(n+1)\times(n+1)}$, $\boldsymbol{P}_2\in\Re^{N\times N}$ and $\boldsymbol{W}\in\Re^{(n+1)\times N}$

$$\boldsymbol{P}_1=\boldsymbol{Q}+\boldsymbol{A}_E^T\boldsymbol{P}_1\boldsymbol{A}_E-\boldsymbol{A}_E^T\boldsymbol{P}_1\boldsymbol{G}\left[\boldsymbol{R}+\boldsymbol{G}^T\boldsymbol{P}_1\boldsymbol{G}\right]^{-1}\boldsymbol{G}^T\boldsymbol{P}_1\boldsymbol{A}_E \quad (44)$$

$$\boldsymbol{W}=\boldsymbol{A}_E^T\left(\boldsymbol{I}-\boldsymbol{P}_1\boldsymbol{G}\left(\boldsymbol{R}+\boldsymbol{G}^T\boldsymbol{P}_1\boldsymbol{G}\right)^{-1}\boldsymbol{G}^T\right)\left(\boldsymbol{P}_1\boldsymbol{G}_{PR}+\boldsymbol{W}\boldsymbol{A}_R\right) \quad (45)$$

The optimal control signal $\Delta u(k)$ becomes

$$\Delta u(k)=\begin{bmatrix}\boldsymbol{K}_1 & \boldsymbol{K}_2\end{bmatrix}\begin{bmatrix}\boldsymbol{X}(k)\\ \boldsymbol{X}_R(k)\end{bmatrix}=\boldsymbol{K}_1\boldsymbol{X}(k)+\boldsymbol{K}_2\boldsymbol{X}_R(k) \quad (45)$$

Where $\boldsymbol{K}_1=\begin{bmatrix}\boldsymbol{K}_{1e} & \boldsymbol{K}_{1x}\end{bmatrix}=-\left[\boldsymbol{R}+\boldsymbol{G}^T\boldsymbol{P}_1\boldsymbol{G}\right]^{-1}\boldsymbol{G}^T\boldsymbol{P}_1\boldsymbol{A}_E\in\Re^{1\times(1+n)}$ is defined as feedback gain matrix and $\boldsymbol{K}_2=-\left[\boldsymbol{R}+\boldsymbol{G}^T\boldsymbol{P}_1\boldsymbol{G}\right]^{-1}\boldsymbol{G}^T\left(\boldsymbol{P}_1\boldsymbol{G}_{PR}+\boldsymbol{W}\boldsymbol{A}_R\right)\in\Re^{1\times N}$ is defined as feed forward matrix.

Corresponding with *N* future values of reference input, feed forward matrix $\boldsymbol{K}_2$ and $\boldsymbol{W}$ can be rewritten as

$$\boldsymbol{W}=\begin{bmatrix}\boldsymbol{W}(1) & \boldsymbol{W}(2) & \cdots & \boldsymbol{W}(N)\end{bmatrix} \quad (47)$$

$$\boldsymbol{K}_2=\begin{bmatrix}\boldsymbol{K}_2(1) & \boldsymbol{K}_2(2) & \cdots & \boldsymbol{K}_2(N)\end{bmatrix} \quad (48)$$

where $\boldsymbol{W}(i)\in\Re^{(n+1)\times 1}, i=1,2\ldots,N$; $\boldsymbol{K}_2(i)\in\Re, i=1,2\ldots,N$

Using Eq. (40) and Eq. (47), Eq. (48) is re-expressed as

$$\boldsymbol{K}_2=-\left[\boldsymbol{R}+\boldsymbol{G}^T\boldsymbol{P}_1\boldsymbol{G}\right]^{-1}\boldsymbol{G}^T\times\left\{\boldsymbol{P}_1\begin{bmatrix}\boldsymbol{G}_R & \boldsymbol{0}_{(n+1)\times 1} & \cdots & \boldsymbol{0}_{(n+1)\times 1}\end{bmatrix}+\begin{bmatrix}\boldsymbol{0} & \boldsymbol{W}(1) & \cdots & \boldsymbol{W}(N-1)\end{bmatrix}\right\} \quad (49)$$

From Eq. (40) and Eq. (47), Eq. (44) becomes

$$\begin{bmatrix}\boldsymbol{W}(1) & \boldsymbol{W}(2) & \cdots & \boldsymbol{W}(N)\end{bmatrix}=\boldsymbol{A}_E^T\left[\boldsymbol{I}-\boldsymbol{P}_1\boldsymbol{G}\left(\boldsymbol{R}+\boldsymbol{G}^T\boldsymbol{P}_1\boldsymbol{G}\right)^{-1}\boldsymbol{G}^T\right]\times\left\{\boldsymbol{P}_1\begin{bmatrix}\boldsymbol{G}_R & \boldsymbol{0}_{(n+1)\times 1} & \cdots & \boldsymbol{0}_{(n+1)\times 1}\end{bmatrix}+\begin{bmatrix}\boldsymbol{0}_{(n+1)\times 1} & \boldsymbol{W}(1) & \cdots & \boldsymbol{W}(N-1)\end{bmatrix}\right\} \quad (50)$$

It is defined that $\boldsymbol{F}=\boldsymbol{A}_E^T\left(\boldsymbol{I}-\boldsymbol{P}_1\boldsymbol{G}\left(\boldsymbol{R}+\boldsymbol{G}^T\boldsymbol{P}_1\boldsymbol{G}\right)^{-1}\boldsymbol{G}^T\right)$.

Eq. (50) yields

$$\boldsymbol{W}(i)=\boldsymbol{F}^i\boldsymbol{P}_1\boldsymbol{G}_R \qquad i=1,2,..,N \quad (51)$$

From Eq. (49), $\boldsymbol{K}_2(i),\ i=1,2,\ldots,N$, can be obtained as

$$\boldsymbol{K}_2(i)=-\left[\boldsymbol{R}+\boldsymbol{G}^T\boldsymbol{P}_1\boldsymbol{G}\right]^{-1}\boldsymbol{G}^T\boldsymbol{F}^{i-1}\boldsymbol{P}_1\boldsymbol{G}_R. \quad (52)$$

Eq. (45) can be rewritten as

$$\Delta u(k)=K_{1e}e(k)+\boldsymbol{K}_{1x}\Delta\boldsymbol{x}(k)+\sum_{i=1}^{N}K_2(i)\Delta r(k+i) \quad (53)$$

By taking the initial values as zero and integrating both side of Eq. (53), the control law $u(k)$ can be obtained as

$$u(k)=K_{1e}\frac{z}{z-1}e(k)+\boldsymbol{K}_{1x}\boldsymbol{x}(k)+\sum_{i=1}^{N}K_2(i)\,r(k+i) \quad (54)$$

The block diagram of the closed loop ZMP tracking control system using discrete time optimal tracking controller utilizing the future values of reference input is shown in Fig. 6.

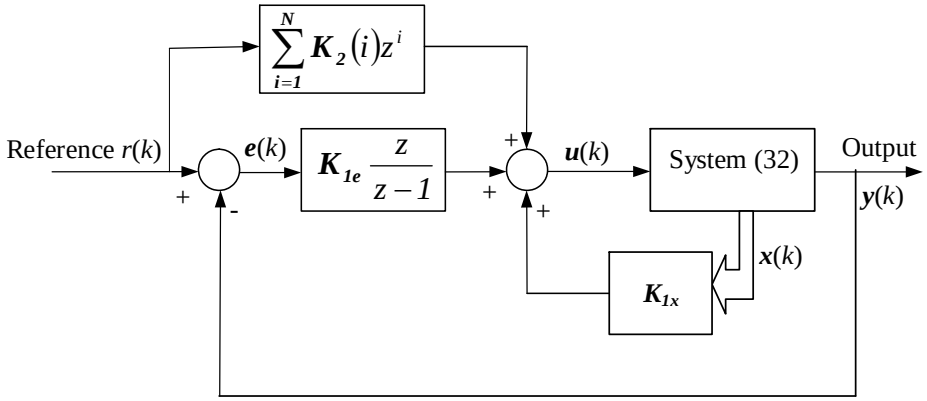

Fig. 6: Closed loop ZMP control system with discrete time optimal tracking controller.

IV. WALKING CONTROL OF THE BIPED ROBOT

Based on the walking pattern generation discussed in previous sections, a trajectory of COM of the biped robot is generated by ZMP servo control system. The ZMP reference input trajectory of the ZMP servo system is chosen to satisfy the stable condition of the biped robot. The control objective for the stable walking of the biped robot is to track the center of pelvis link to the COM trajectory. The inverse kinematics of the biped robot is solved to obtain the angle of each joint of the biped robot. The walking control of the biped robot is performed based on the solutions of the inverse kinematics which is solved by solid geometry method.

4.1 Inverse Kinematics of the Biped Robot

The configuration of a 10 DOF biped robot is shown in Fig. 1. The relationship between biped robot and 3D inverted pendulum is shown in Fig. 7. Solving the inverse kinematics problems directly from kinematics models is complex. An inverse kinematics based on the solid geometry method is presented in this section.

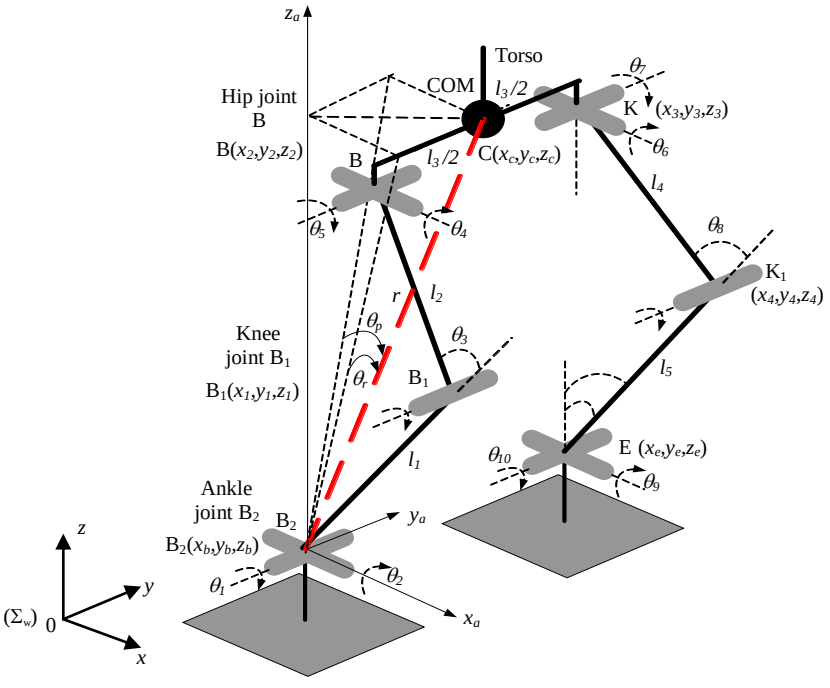

Fig. 7: Biped robot and 3D inverted pendulum.

During the walking of the biped robot, the following assumptions are supposed

- Trunk of robot is always located on the sagittal and lateral plane: when the trunk of robot is located on the sagittal and lateral plane, from the geometric structure of the biped robot, it is easy to obtain $\theta_2 = -\theta_4$ and $\theta_9 = -\theta_6$.

- The feet of robot are always parallel with floor: when the trunk of robot is on the sagittal plane, the feet of robot are parallel with floor if following conditions are satisfied

$$\theta_3 = \theta_1 + \theta_5, \quad \theta_8 = \theta_7 + \theta_{10}. \quad (55)$$

- The walking of the biped robot is divided into three phases: Two-legs supported, right-leg supported and left-leg supported. When the robot is supported by one leg, another leg swings.

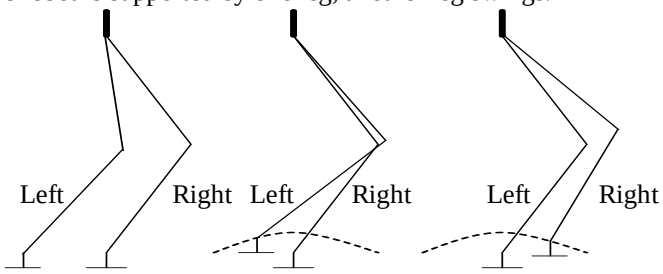

(a) Two-leg supported phase

(b) Right-leg supported and left-leg swinging phase

(c) Left-leg supported and right leg swinging phase

Fig. 8: Three walking phases of the biped robot.

- The origin of the 3D inverted pendulum is located at the center of the ankle joint of supported leg.

4.1.1 Inverse kinematics of biped robot in one-leg supported phase

It is supposed that biped robot is with the right-leg supported and left-leg swinging. The coordinate of the COM in coordinate system Σ_a whose origin is taken at the center of the ankle joint of supported leg can be obtained as

$$x_{ca} = x - x_b, \; y_{ca} = y - y_b \text{ and } z_{ca} = z - z_b \quad (56)$$

where (x,y,z) and (x_b,y_b,z_b) are coordinate of the COM and center of the ankle joint of supported leg in the world coordinate and (x_{ca},y_{ca},z_{ca}) is Coordinate of the COM in the coordinate Σ_a.
Solving Eqs. (11)~(13) at k^{th} sample time with $z_{ca} = z_{cd}$ yields

$$r(k) = \sqrt{z_{cd}^2(k) + x_{ca}^2(k) + y_{ca}^2(k)} \quad (57)$$

Since the trunk of robot is always located on the sagittal plane, the pelvis link is always on the horizontal plane $\square CBDC_1$ as shown in Fig. 9. The BC line is perpendicular to the line 0A at A, and it yields $\angle 0CB = \frac{\pi}{2} - \theta_r$.
Using the cosine's law, the length of 0B side of the triangle 0BC at the k^{th} sample time is obtained as follows:

$$h(k) = \sqrt{x_{ca}^2 + \left(y_{ca} - \frac{l_3}{2}\right)^2 + z_c^2} = \sqrt{\frac{l_3^2}{4} + r^2(k) - l_3 y_{ca}(k)} \quad (58)$$

The angle $\alpha(k)$ between l_2 and l_1 sides of the triangle $0BB_1$ is calculated by the cosine's law as follows:

$$\alpha(k) = \arccos\left(\frac{l_1^2 + l_2^2 - h^2(k)}{2 l_1 l_2}\right). \quad (59)$$

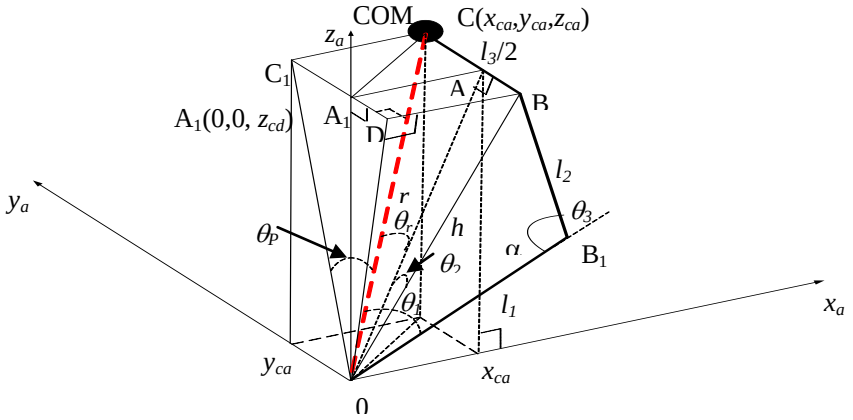

Fig. 9: Inverted pendulum and supported leg.

From $\alpha(k)$ in Eq. (59), the knee joint angle of the biped robot is gotten as Eq. (60).

$$\theta_3(k) = \pi - \alpha(k) \quad (60)$$

In Fig. 9, the BC line is perpendicular to the line 0A at A. From the right-triangle 0AB, the ankle joint angle $\theta_2(k)$ can be obtained as

$$\theta_2(k) = \angle \mathrm{A0B} = arcsin\left(\frac{y_{ca}(k) - \frac{l_3}{2}}{h(k)}\right). \quad (61)$$

Since height of COM of the biped robot is always kept equal to constant z_{cd} and COM is on sagittal plane during walking of biped robot, the BD line is perpendicular to $0y_a z_a$ plane. It means that the BD line is perpendicular to 0D line. The triangles OBB_1 and ODB lie on the same plane which contains the links l_1 and l_2 of the biped robot as shown in Fig. 9. The angle $\theta_1(k)$ can be obtained as follows

$$\theta_1(k) = \angle \mathrm{D0B} + \angle \mathrm{B0B}_1 = arcsin\left(\frac{x_{ca}(k)}{h(k)}\right) + arccos\left(\frac{h^2(k) + l_1^2 - l_2^2}{2h(k)l_1}\right). \quad (62)$$

4.1.2 Inverse kinematics of swinging leg

It is assumed that the biped robot is supported by right leg and is swung by left leg as shown in Fig. 10.

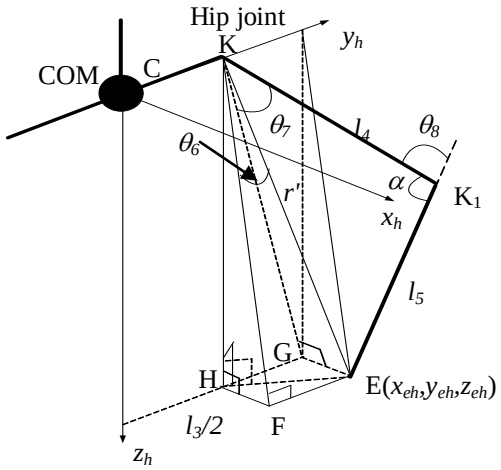

Fig. 10: Swinging leg of biped robot.

A coordinate system Σ_h with the origin taken at the middle of pelvis link is defined as shown in Fig. 10. During the swing of this leg, the coordinate y_{eh} of the foot of swinging leg is constant.

$r'(k)$ is defined as the distance between ankle joint and hip joint of swinging leg at the k^{th} sample time. It is expressed in the coordinate system Σ_h as follows:

$$r'(k)^2 = x_{eh}^2(k) + \left(y_{eh}(k) - \frac{l_3}{2}\right)^2 + z_{eh}^2(k) \quad (63)$$

where $(x_{eh}(k), y_{eh}(k), z_{eh}(k))$ is coordinate of the ankle joint of swinging leg in the coordinate Σ_h at the k^{th} sample time.

Since *EF* line is perpendicular to the line KF at F, the hip angle $\theta_6(k)$ of the swinging leg is obtained based on the right-triangle KEF as

$$\theta_6(k) = -arcsin\left(\frac{y_{eh}(k) - l_3/2}{r'(k)}\right) \quad (64)$$

The minus sign in (64) means counterclockwise.

The links l_4 and l_5 lie on the plane which contains right-triangle KGE. The hip angle $\theta_7(k)$ is equal to the angle between link l_4 and Cy_hz_h plane. It is can be expressed as

$$\theta_7(k) = \angle\text{GKE} + \angle\text{EKK}_1 = arcsin\left(\frac{x_{eh}(k)}{r'(k)}\right) + arccos\left(\frac{r'^2(k) + l_4^2 - l_5^2}{2r'(k)l_4}\right) \quad (65)$$

Using the cosine's law, the angle of knee of swinging leg can be obtained as

$$\theta_8(k) = \pi - \alpha_1 = \pi - arccos\left(\frac{l_5^2 + l_4^2 - r'^2(k)}{2l_5l_4}\right). \quad (66)$$

Similarly, when the biped robot is supported by left leg and is swung by right leg. The angles of right leg are calculated from Eqs. (64)~(66).

4.1.3 Inverse kinematics of biped robot in two-leg supported phase

It is assumed that the swinging leg of the biped robot contacts the ground after swinging phase as shown in Fig. 11. The biped robot is supported by two legs.

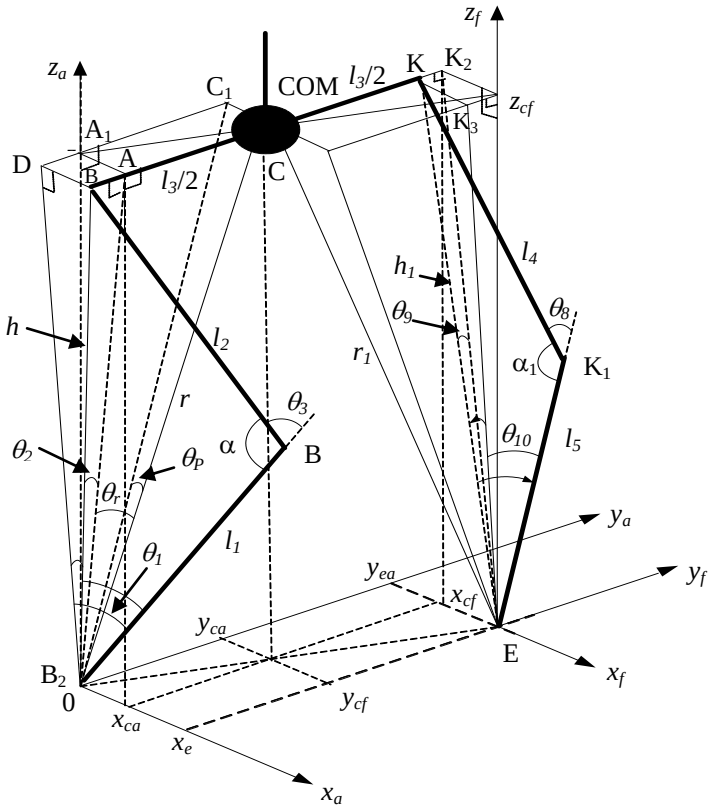

Fig. 11: Biped robot with two legs supported.

The coordinate of COM is expressed in coordinate system Σ_f whose origin is taken at the ankle joint of new supported leg as

$$x_{cf}(k) = x_{ca}(k) - x_{ea}(k) \quad (67)$$

$$y_{cf}(k) = y_{ca}(k) - y_{ea}(k) \quad (68)$$

$$z_{cf}(k) = z_{ca}(k) \quad (69)$$

where (x_{ea}, y_{ea}, z_{ea}) is coordinate of the ankle joint of the new supported leg in coordinate system Σ_a, (x_{ca}, y_{ca}, z_{ca}) is coordinate of the COM in coordinate system Σ_a and (x_{cf}, y_{cf}, z_{cf}) is coordinate of the COM in coordinate system Σ_f.

$r_1(k)$ is defined as distance between COM and ankle joint of the left leg. It is calculated based on the

coordinate of COM in coordinate system Σ_f as

$$r_1^2(k) = x_{cf}^2(k) + y_{cf}^2(k) + z_{cf}^2(k) \quad (70)$$

Similarly to the procedure in one-leg supported phase, the inverse kinematics of the biped robot in two-leg supported phase can be obtained. It can be expressed as following equations.

$$h(k) = \sqrt{\frac{l_3^2}{4} + r^2(k) - l_3 y_{ca}(k)} \quad (71)$$

$$\alpha(k) = \angle BB_1B_2 = arccos\left(\frac{l_1^2 + l_2^2 - h^2(k)}{2l_1 l_2}\right) \quad (72)$$

$$\theta_3(k) = \pi - \alpha(k) \quad (73)$$

$$\theta_2(k) = \angle BB_2A = arcsin\left(\frac{y_{ca}(k) - \frac{l_3}{2}}{h(k)}\right) \quad (74)$$

$$\theta_1(k) = \angle DB_2B + \angle BB_2B_1 = arcsin\left(\frac{x_{ca}(k)}{h(k)}\right) + arccos\left(\frac{h^2(k) + l_1^2 - l_2^2}{2h(k)l_1}\right) \quad (75)$$

$$h_1(k) = \sqrt{\frac{l_3^2}{4} + r_1^2(k) - l_3 |y_{cf}(k)|} \quad (76)$$

$$\alpha_1(k) = \angle KK_1E = arccos\left(\frac{l_5^2 + l_4^2 - h_1^2(k)}{2l_5 l_4}\right) \quad (77)$$

$$\theta_8(k) = \pi - \alpha_1(k) \quad (78)$$

$$\theta_9(k) = \angle KEK_2 = arcsin\left(\frac{y_{cf}(k) + \frac{l_3}{2}}{h_1(k)}\right) \quad (79)$$

$$\theta_{10}(k) = \angle KEK_1 + \angle KEK_3 = arccos\left(\frac{h_1^2(k) + l_5^2 - l_4^2}{2h_1(k)l_5}\right) + arcsin\left(\frac{x_{cf}(k)}{h_1(k)}\right) \quad (80)$$

where h and h_1 are distance between right hip joint and ankle of right and left legs.

4.2 Control of the biped robot

Considering one step walking of the biped robot is illustrated by consequent movement as shown in Fig. 12. At the beginning of walking step, the left leg leaves the ground to start swinging. This leg swings with following a reference trajectory. During the swing of the left leg, the ZMP of the biped robot exists at the geometry center of the right foot. At the end of swinging, the left leg is contacted on the ground, and the biped robot is supported by two legs.

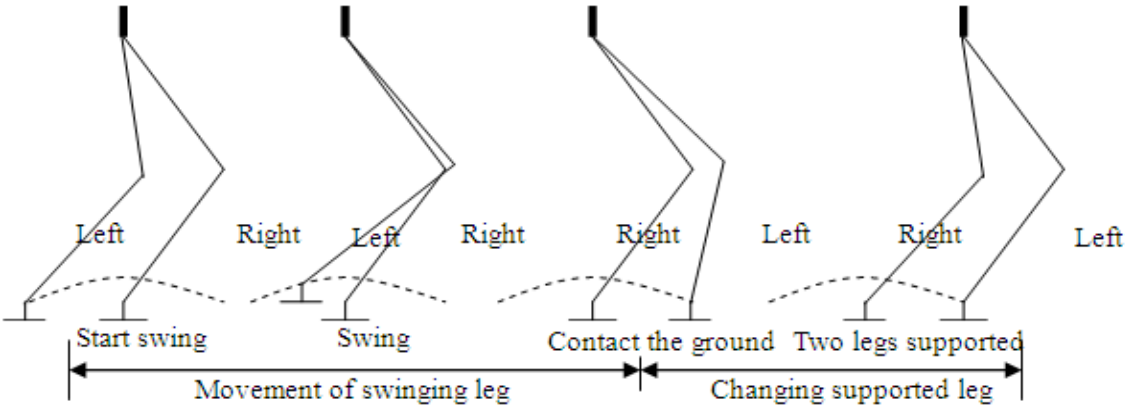

Fig. 12: One step walking of biped robot.

During two-leg supported phase, the ZMP of the biped robot moves from geometry center of the right foot to that of left foot. The left leg becomes new supported leg and the right leg becomes swinging leg for next step. Based on the reference trajectory of swinging leg and the trajectory of COM which is generated by ZMP servo system, the inverse kinematics is solved to obtain the angle of each joint of the biped robot. The control problem of biped robot becomes tracking control problem of DC motors of joints. The block diagram of the biped robot control system is shown in Fig. 13.

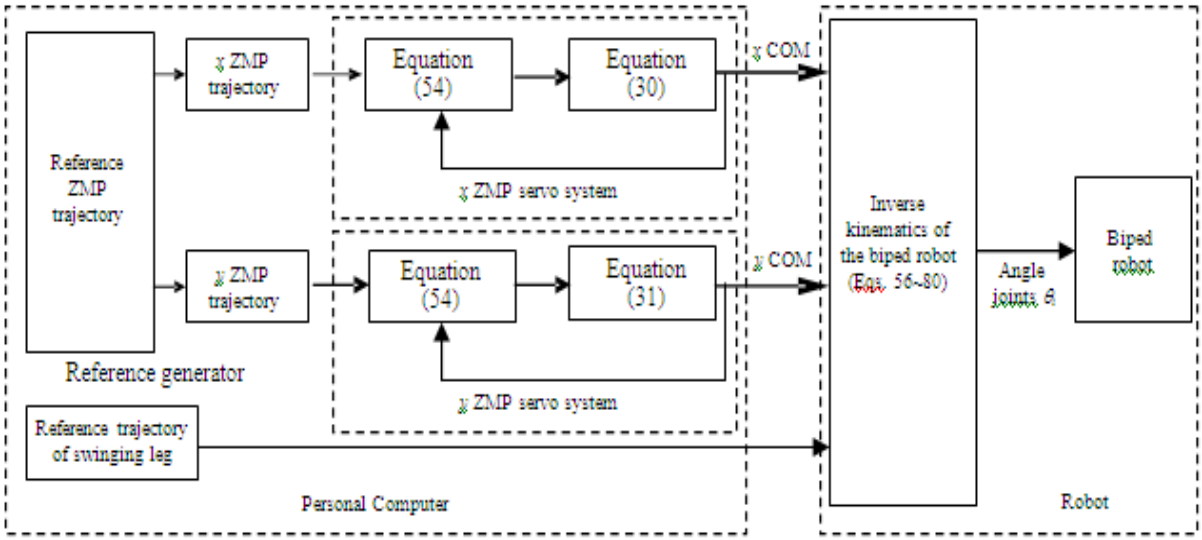

Fig. 13: Block diagram of the biped control system.

V. SIMULATION AND EXPERIMENTAL RESULTS

5.1 Hardware of the Biped Robot

The walking control method proposed in previous sections is implemented in CIMEC-1 developed for this paper as shown in Fig. 14.

Fig. 14: CIMEC-1 biped robot.

A simple hardware configuration using three PIC18F4431 and one dsPIC30F6014 for CIMEC-1 is shown in Fig. 15.

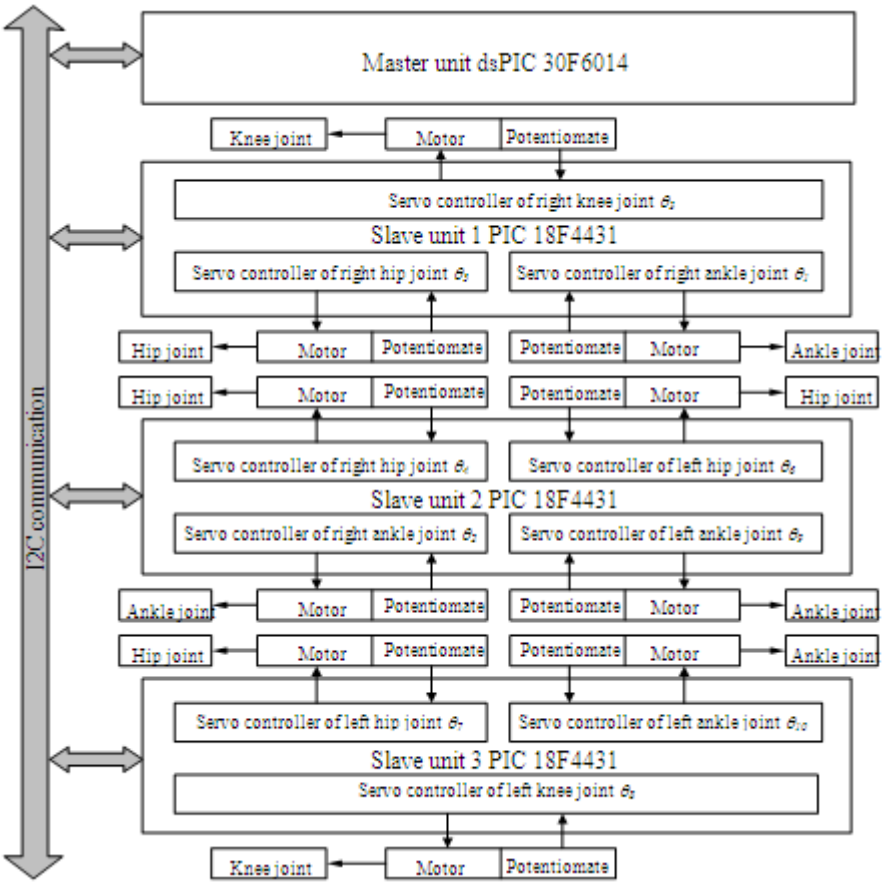

Fig. 15: Hardware configuration of the CIMEC-1.

dsPIC30F6014 is used as master unit, and PIC18F4431 is used as slave unit. The master unit and slave units communicate each other via I2C communication. The master unit is used to solve the inverse kinematics problem based on the trajectory of the center of the pelvis of the biped robot and trajectory of the ankle of swinging leg which are contained in its memory. It can also communicate personal computer via RS-232 communication. The angles at the k^{th} sample time obtained from inverse kinematics are sent to slave units as reference signals.

5.2 Simulation and experimental results

To demonstrate the performance of the biped walking based on the ZMP walking pattern generation combined with the inverse kinematics, the simulation results for walking on the flat floor of the biped robot using Matlab are shown. The period of step is 10 seconds: changing supported leg time is 5 seconds and swinging leg time is 5 seconds. The length of step is 20 cm. During the moving of the biped robot, the height of the center of pelvis link is constant. In the one-leg supported phase, ZMP is located at the center of the supported foot. When two legs of the biped robot are contacted on the ground, the ZMP moves from center of foot of current supported leg to the center of foot of the new supported leg.
The parameters values of the biped robot used in the simulation and experiment are given in Table 4.1.

Table 4.1 Numerical values of the biped robot' parameters used in simulation and experiment

Parameters	Description	Values	Units
$l_1 = l_5$	Length of lower leg links	0.28	[m]
$l_2 = l_4$	Length of upper leg links	0.28	[m]
l_3	Length of pelvis link	0.2	[m]
a	Width of foot	0.18	[m]
b	Length of foot	0.24	[m]
z_{cd}	Height of center of pelvis link	0.5	[m]

θ_{01}	Initial value of θ_1	26.75	[deg]
θ_{02}	Initial value of θ_2	0	[deg]
θ_{03}	Initial value of θ_3	53.5	[deg]
θ_{04}	Initial value of θ_4	0	[deg]
θ_{05}	Initial value of θ_5	26.75	[deg]
θ_{06}	Initial value of θ_6	0	[deg]
θ_{07}	Initial value of θ_7	26.75	[deg]
θ_{08}	Initial value of θ_8	53.5	[deg]
θ_{09}	Initial value of θ_9	0	[deg]
θ_{010}	Initial value of θ_{10}	26.75	[deg]

The footprint and the Zigzag reference trajectory of ZMP are shown in Fig. 16.

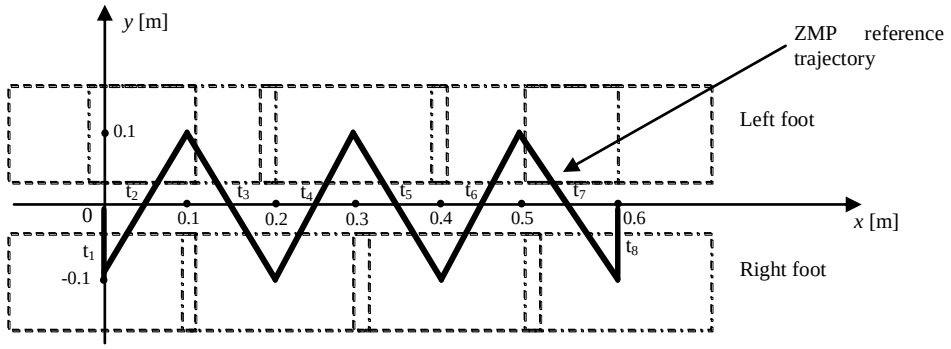

Fig. 16: Footprint and zigzag reference trajectory of ZMP.

The *x* and *y* ZMP trajectories versus times corresponding to the zigzag reference trajectory of ZMP in Fig. 16 can be obtained as shown in Fig. 17.

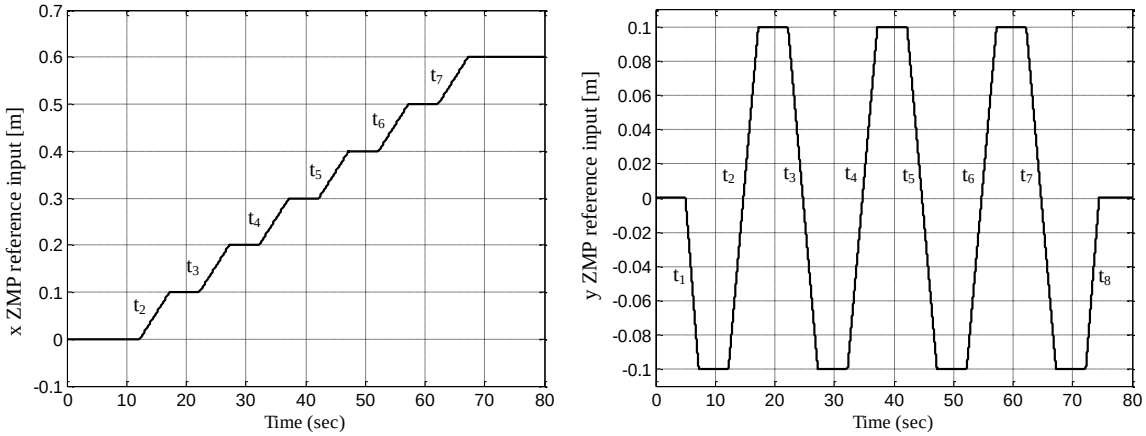

(a) *x* ZMP reference input versus time. (b) *y* ZMP reference input versus time.

Fig. 17: Zigzag ZMP reference input trajectory versus time.

The reference input trajectory of the ankle joint of swinging leg is an arc which has radius equal to 0.1 [m]. The reference input trajectory equations of arc are expressed as Eq. (81) for left leg and Eq. (82) for right leg.

$$\begin{cases} x_{aa}^2 + z_{aa}^2 = 0.01 \\ y_{aa} = l_3 \end{cases} \quad for \quad -0.1 \le x_{aa} \le 0.1 \quad (81)$$

$$\begin{cases} x_{af}^2 + z_{af}^2 = 0.01 \\ y_{af} = l_3 \end{cases} \quad for \quad -0.1 \le x_{af} \le 0.1 \quad (82)$$

where (x_{aa}, y_{aa}, z_{aa}) is coordinate of the point on the arc in the coordinate system Σ_a, and (x_{af}, y_{af}, z_{af}) is coordinate of the point on the arc in the coordinate system Σ_f.

The *x*, *y* ZMP servo control systems (30) and (31) are sampled with sampling time T = 1 [ms] and controlled by discrete time optimal tracking controller with $R = 1$, $Q = \left[\begin{array}{c|c} 0.12 & \boldsymbol{0} \\ \hline \boldsymbol{0} & \boldsymbol{0} \end{array}\right]$ and number of sample time in future of reference input $N = 1200$. The simulation and experimental results are shown in Figs. 18~27. Fig. 18 and Fig. 20 show the ZMP reference inputs, outputs and positions of the COM in *x* and *y* directions with respect to time. Fig. 19 and Fig. 21 show that the tracking errors of *x* and *y* ZMP servo systems converge to zeros and the errors at the transition points of reference inputs are very small. Figs. 22~26 show angles of each joint of the biped robot. In these figures, the sharp points occur at the transition states of the biped robot where joints of the biped robot change its direction of rotation. The movement of the COM of the biped robot is shown in Fig. 27.

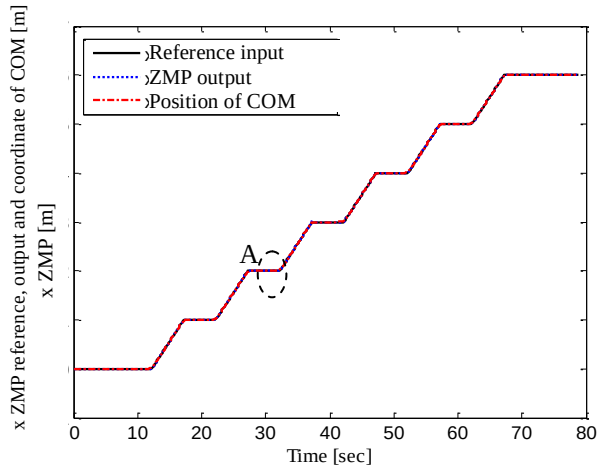

(a)

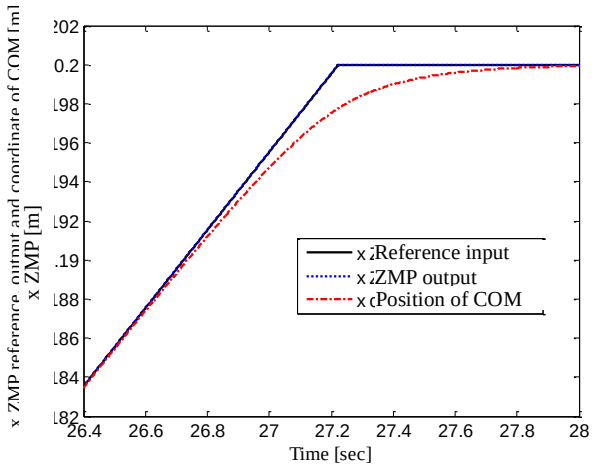

(b) A region.

Fig. 18: *x* ZMP reference input, *x* ZMP output and position of COM.

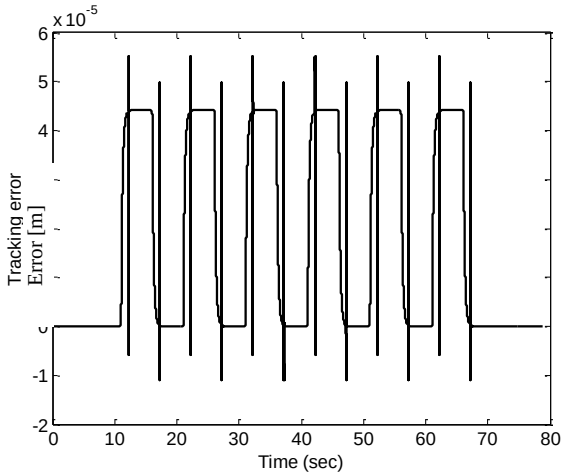

Fig. 19: *x* ZMP position error.

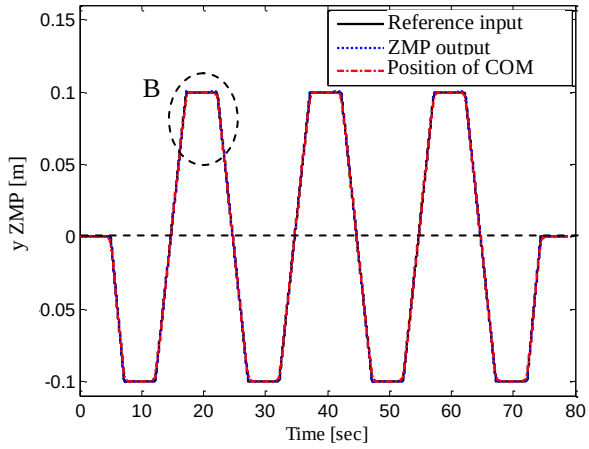

(a)

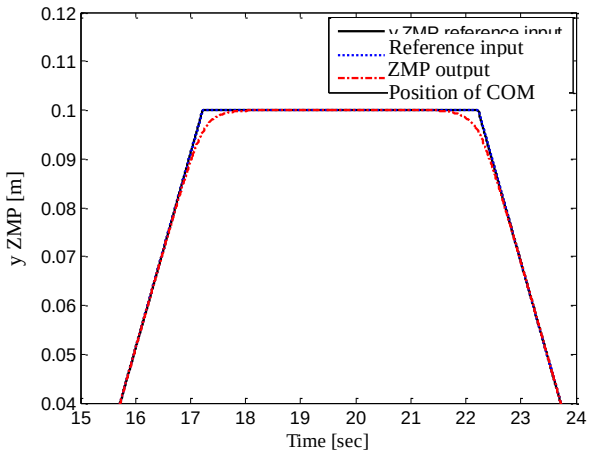

(b) B region.

Fig. 20: *y* ZMP reference input, *y* ZMP output and position of COM.

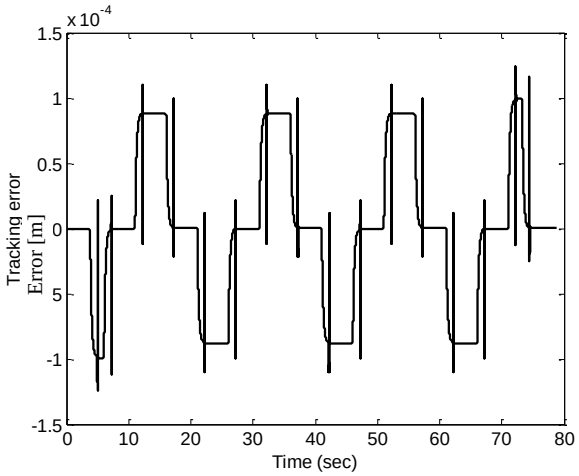

Fig. 21: *y* ZMP position error.

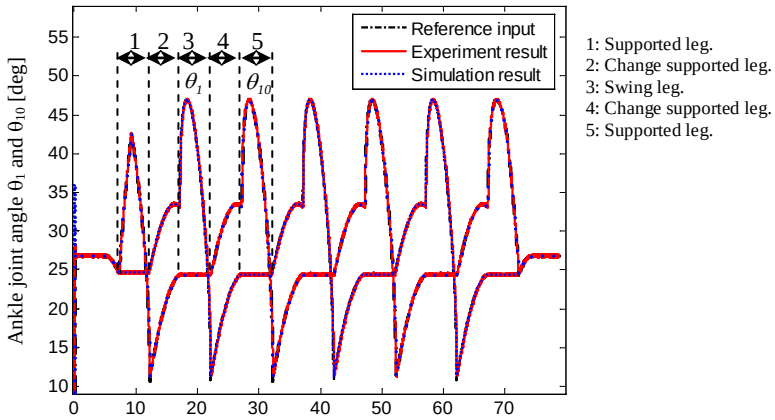

Fig. 22: Simulation and experimental results of ankle joints angle θ_1 and θ_{10}.

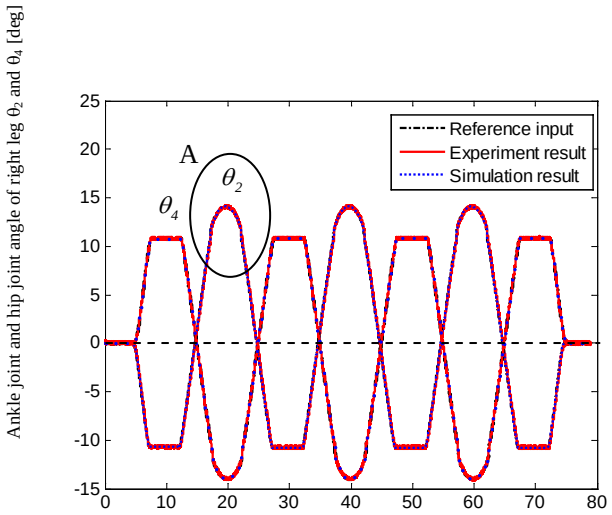

a)

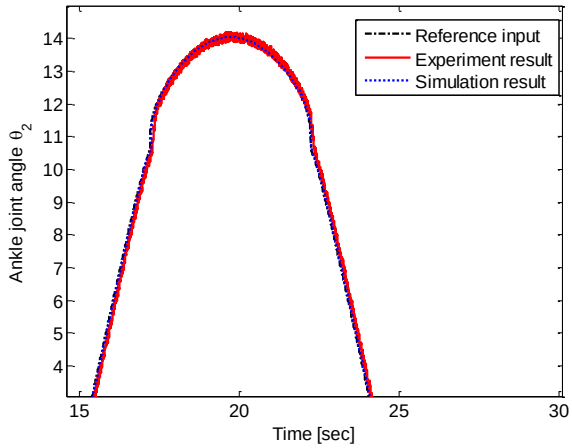

b) A region.

Fig. 23: Simulation and experimental results of ankle and hip joints angle θ_2 and θ_4.

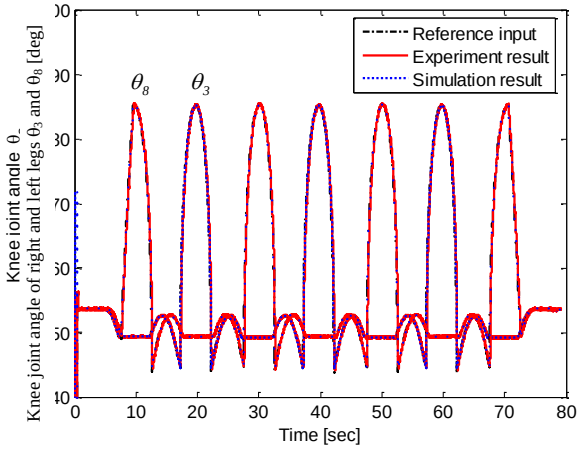

Fig. 24: Simulation and experimental results of knee joints angle θ_3 and θ_8.

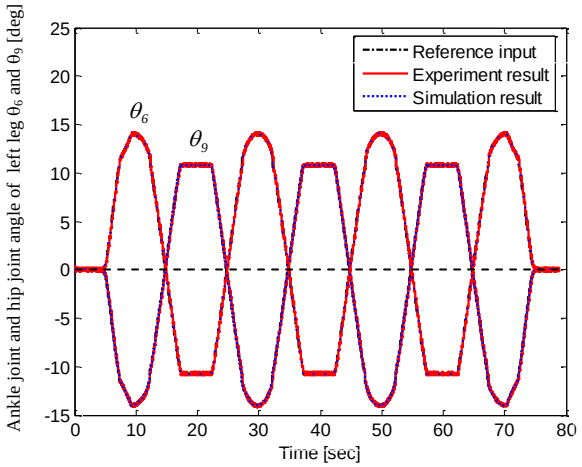

Fig. 25: Simulation and experimental results of hip and ankle joints angle θ_6 and θ_9.

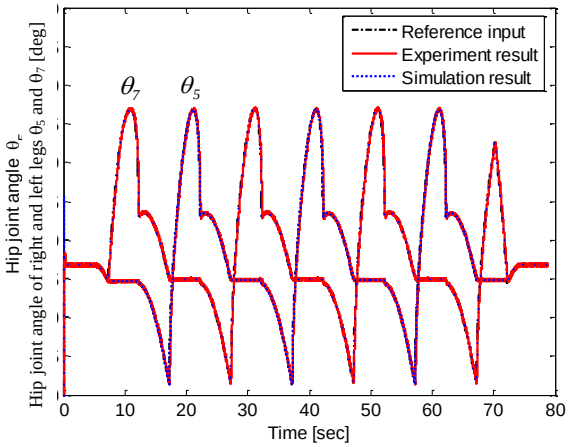

Fig. 26: Simulation and experimental results of hip joints angle θ_5 and θ_7.

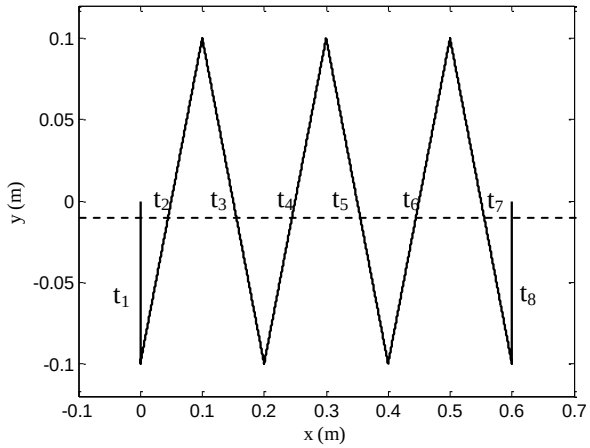

Fig. 27: Movement of the center of pelvis link.

VI. CONCLUSIONS

In this paper, a 10 DOF biped robot is developed. The kinematics and dynamic model of the biped robot are presented. For the stable walking, a controller using the discrete time optimal theory is designed to generate the trajectory of COM. The walking control of biped robot is performed based on the solutions of the inverse kinematics which is solved by solid geometry method. A simple hardware configuration is constructed to control for biped robot. The simulation and experimental results are shown to prove effectiveness of proposed controller.

REFERENCES

[1] S. Kajita, F. Kanehiro, K. Kaneko, K, Yokoi and H. Hirukawa, 2001, "The 3D Linear Inverted Pendulum Mode: A simple modeling for a biped walking pattern generation", Proc. of IEEE/RSJ International conference on Intelligent Robots and Systems, pp. 239~246.

[2] C. Zhu and A. Kawamara, 2003, "Walking Principle Analysis for Biped Robot with ZMP Concept, Friction Constraint, and Inverted Pendulum Model", Proc. of IEEE/RSJ International conference on Intelligent Robots and Systems, pp. 364~369.

[3] S. K. Agrawal, and A. Fattah, 2006, "Motion Control of a Novel Planar Biped with Nearly Linear Dynamics", IEEE/ASME Trans. Mechatronics, Vol. 11, No. 2, pp. 162~168.

[4] J. H. Part, 2001, "Impedance Control for Biped Robot Locomotion", IEEE Trans. Robotics and Automation, Vol. 17, No. 3, pp. 870~882.

[5] Q. Huang and Y. Nakamura, 2005, "Sensor Reflex Control for Humanoid Walking", IEEE Trans. Robotics, Vol. 21, No. 5, pp. 977~984.

[6] B. C. Kou, 1992, "Digital Control Systems", International Edition.

[7] D. Li, D. Zhou, Z. Hu, and H. Hu, 2001, "Optimal Priview Control Applied to Terrain Following Flight", Proc. of IEEE Conference on Decision and Control, pp. 211~216.

[8] C. Zhu and A. Kawamara, 2003, "Walking Principle Analysis for Biped Robot with ZMP Concept,

Friction Constraint, and Inverted Pendulum Model", Proc. of IEEE/RSJ International conference on Intelligent Robots and Systems, pp. 364~369.
[9] D. Plestan, J. W. Grizzle, E. R. Westervelt and G. Abba, 2003, "Stable Walking of A 7-DOF Biped Robot", IEEE Trans. on Robotics and Automation, Vol. 19, No. 4, pp. 653-668.
[10] F. L. Lewis, C. T. Abdallah and D.M. Dawson, 1993, "Control of Robot Manipulator", Prentice Hall International Edition.
[11] G. F. Franklin, J. D. Powell and A. E. Naeini, "Feedback Control of Dynamic System", Prentice Hall Upper Saddle River, New Jersey 07458.
[12] G. A. Bekey, 2005, "Autonomous Robots From Biological Inspiration to Implementation and Control", The MIT Press.
[13] H. K. Lum, M. Zribi and Y. C. Soh, 1999, "Planning and Control of a Biped Robot", Int. Journal of Engineering Science ELSEVIER, Vol. 37, pp. 1319~1349.
[14] H. Hirukawa, S. Kajita, F. Kanehiro, K. Kaneko and T. Isozumi, 2005, "The Human-size Humanoid Robot That Can Walk, Lie Down and Get Up", International Journal of Robotics Research, Vol. 24, No. 9, pp. 755~769.
[15] K. Mitobe, G. Capi and Y. Nasu, 2004, "A New Control Method for Walking Robots Based on Angular Momentum", Journal of Mechatronics ELSEVIER, Vol. 14, pp. 164~165.
[16] K. Harada, S. Kajita, K. Kaneko and H. Hirukawa, 2004, "Walking Motion for Pushing Manipulation by a Humanoid Robot", Journal of the Robotics Society of Japan, Vol. 22, No. 3, pp. 392–399.

American Journal of Engineering Research (AJER)
e-ISSN : 2320-0847 p-ISSN : 2320-0936
Volume-02, Issue-11, pp-151-162
www.ajer.org

Research Paper Open Access

Analysis of Pavement Deterioration Using three-dimensional Finite Elements Technique

Ahmed Mohamady, Abu-Bakr M. Elhady, and Mohamed S. Eisa
[1] *Assoc. Prof. of Highways and Airports Engineering, Faculty of Engineering, Zagazig University, Egypt*
[2] *Egyptian Space Program*
[3] *PhD candidate, Faculty of Engineering, Zagazig University, Egypt*

Abstract: - Three-dimensional Finite elements models have been used to describe stress and strain response parameters for steel wire grid reinforced flexible pavement sections. In this study three paving sections were analyzed. The first section represents one of the commonly sections used in the paving of local roads, the second section is commonly used in expressways and the third section is used in freeways. Study was conducted using Finite element computer package ADINA. The reinforcement was arranged at different depths. Steel wire grid reinforced sections results are compared to geosynthetics grid reinforced sections as well as typical rigid pavement section commonly used in Egypt. The analysis showed that the best location of reinforcement is at bottom of base layer. Comparisons show that steel mesh reinforced sections characteristics improved than geosynthetics grids reinforced sections and are almost close to rigid section.

Keywords: - *3-D finite elements, paving sections, geosynthetics grids, rigid pavement, steel wire grid*

I. INTRODUCTION

Increasing truck loads on Egyptian road network Also several locations of low speeds were introduced due to high traffic volumes. All of these may cause several pavement distresses. The most common distress types occurring in the Egyptian roads are rutting and cracking, sags, corrugations, etc. Pavement distresses cause many troubles to the vehicles and users [1,2]. The maintenance of such distresses may need high budget and time consuming and hence cause traffic trouble during maintenance and repair processes. The design of flexible pavements is largely based on empirical methods. However, there is currently a shift underway towards more mechanistic design techniques. Finite element (FE) methods have generally been used to determine stresses, strains and displacements in flexible pavement [3-5].

II. OBJECTIVES AND METHODOLOGY

This paper investigate the paving sections used in places that have vehicles to reduce speed as a result of traffic and the presence of some speed sedatives like railway crossing and town entrances also at places of U-turns to opposite directions. This study also aims to strengthen the pavement layers of these sections with steel wire grid or geosynthetics grids at different depths and effect of this strengthen to reduce the stresses on the pavement sections and hence increasing the pavement life. Three paving sections were studied; local road section, expressway section and freeway section. The proposed layers thicknesses and the associated properties for the investigated sections are shown in Tables (1) to (3) [10,11]. These sections rested on infinite subgrade soil and its modulus of elasticity is 50 MPa and value of passion's ratio is 0.25. The reinforcement materials are steel wire grid or geosynthetics grids with wire diameter 4mm and square cell side length 10cm and its properties were given in Table (4)[6,7]. In local road section, the locations of strengthening were chosen at bottom of wearing surface, middle of base and bottom of base, while in expressway section the locations of strengthening were chosen at bottom of wearing surface, bottom of binder layer, middle of base and bottom of base, finally the locations of strengthening in freeway section were chosen at bottom of wearing surface, bottom of binder layer, bottom of bituminous base, middle of base and bottom of base. The reinforced sections were

compared with typical rigid pavement section commonly used in Egypt to evaluate the proposed strengthening technique.

III. FINITE ELEMENTS MODELING (FEM)

Considering the studied sections are modeled as multilayer semi finite elements. All materials are treated as homogeneous and isotropic. Deformations are considered very small relative to the dimensions so the equation of liner elasticity is valid [12].

3.1 ADINA computer program

The multi-purpose finite element program ADINA version 8.7 [9] was used to model 3-D finite element analysis. All materials was modeled as 3D-solid elements as 8- node. This type of node gives a high level of accuracy in combination with an acceptable computing time demand.

3.2 Boundary conditions and loading

The boundary conditions and loading of static analysis for selected sections are shown in Fig (1). It can be observed that the bottom of the pavement is fixed at X, Y and Z translations while the sides of pavement are restricted with Z translation only.

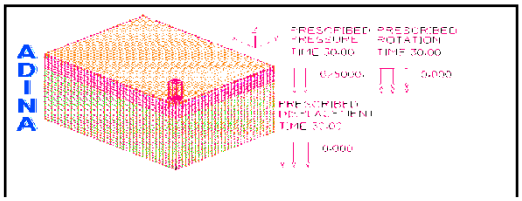

Fig.1. FEM model for freeway section

IV. NUMERICAL RESULTS

In pavement design the most important parameter is the stress distribution as vertical compressive stress and lateral tensile strain shown in fig (2).The investigated cases were modeled with ADINA program and the results were presented and discussed here in after.

4.1 Results of sections affected by vertical loads

4.1.1 Vertical stress

The variation of vertical stress σ_Z at bottom of base layer in studied sections due to vertical pressure of wheel is presented in figures (3) to (8). Figures illustrate the effect of adding reinforcement with different locations.Figures (3) and(4)for local road section display that the vertical stress σ_Z in without reinforcement case decrease gradually from -5.54E+04 Pa under the middle of the wheel load to vanished at the surface, and shows that there is no change in cases reinforcement at bottom of wearing surface. Figures also show that there is a noticeable change when steel reinforcement was arranged at middle of base layer , the vertical stress σ_Z under the center line of the wheel load decreased to -5.32+04 Pa i.e.19% from without reinforcement case, while for case of reinforcement with geosythetic there is no change. Figures illustrate that there is a drastic change in vertical stress σ_Z values when the steel reinforcement was added at bottom of base layer, the vertical stress σ_Z under the center line of the wheel load decreased to -2.89+04 Pa i.e.48% from without reinforcement case, while in case of reinforcement with geosythetic arrived to-3.57+04Pa i.e.35.6% from without reinforcement case.

Table 1. Layers thickness and the associated properties for local road section

Layer	Modulus of elasticity (MPa)	Possion's ratio	Density (KN/m^3)	Thickness (mm)
Wearing surface	2757.91	0.30	22	50
Base	275.791	0.20	20	300
Subgrade	50	0.25	17	Infinite

Table 2. Layers thickness and the associated properties for expressway section

Layer	Modulus of elasticity (MPa)	Possion's ratio	Density (KN/m^3)	Thickness (mm)
Wearing surface	2757.91	0.30	22	50
Binder	2757.91	0.30	22	50
Base	275.791	0.20	20	400
Subgrade	50	0.25	17	Infinite

Table 3. Layers thickness and the associated properties for freeway section

Layer	Modulus of elasticity (MPa)	Possion's ratio	Density (KN/m^3)	Thickness (mm)
Wearing surface	2757.91	0.30	22	50
Binder	2757.91	0.30	22	50
Bit. base	2413.16	0.35	21	70
Base	275.791	0.20	20	400
Subgrade	50	0.25	17	Infinite

Table 4. Properties of reinforcing materials

Material	Modulus of elasticity (MPa)	Possion's ratio	Density (KN/m^3)
Steel	210000	0.25	78.50
Geosythetics	4230	0.35	18.00

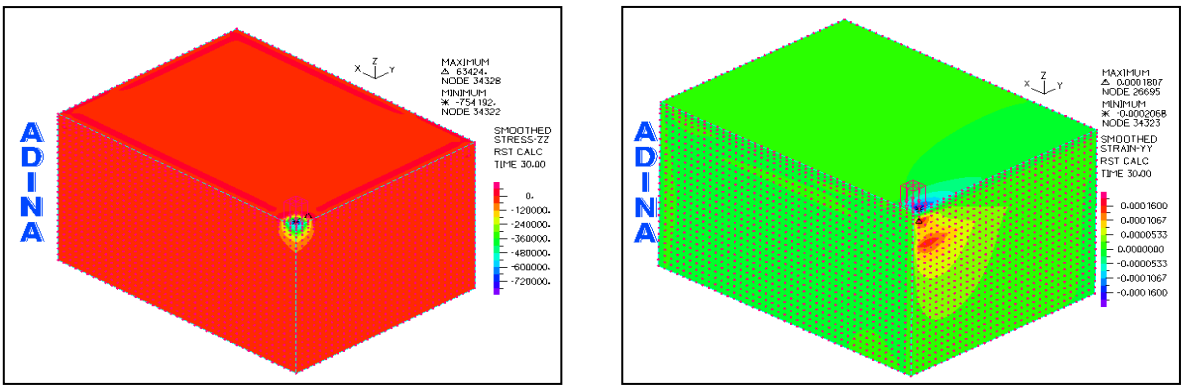

(a) (b)

Fig.2. (a) Vertical stress σ_Z (b) Lateral strain ε_Y

Figures (5) and (6) for expressway section illustrate that the vertical stress σ_Z in without reinforcement case start decrease from -3.94E+04Pa under the middle of the wheel load to decay at the surface, and show that there is no change in cases reinforcement at bottom of wearing surface, at bottom of binder layer. Figures also show that there is a noticeable change when the steel reinforcement was arranged at middle of base layer, in this location the vertical stress σ_Z under the center line of the wheel load decreased to -3.74+04 Pa i.e.18% from without reinforcement case, while for case of reinforcement with geosythetic there is no change. Figures also illustrate that there is a drastic change in vertical stress σ_Z values when the steel reinforcement was added at bottom of base layer. The vertical stress σ_Z under the center line of the wheel load decreased to -2.05+04 Pa i.e.48% from without reinforcement case. In case of reinforcement with geosythetic arrived to-2.55+04Pa i.e.35.50% from without reinforcement case.

Figures (7) and (8) for freeway section show the vertical stress σ_Z in without reinforcement case start decrease from -3.27E+04Pa under the middle of the wheel load to zero Pa at the surface. Figures show that there is no change in cases reinforcement at bottom of wearing surface, bottom of binder layer and bottom of bituminous base layer. Figures also show that there is a noticeable change when we add the steel reinforcement at middle of base layer, in this location vertical stress σ_Z under the center line of the wheel load decreased to -3.00+04 Pa i.e. 8% from without reinforcement case while for case of reinforcement with geosythetic there is no change. Figures illustrate that there is a drastic change in vertical stress σ_Z values when the reinforcement was at bottom of base layer, vertical stress σ_Z under the center line of the wheel load decreased to -1.70+04 Pa i.e.48% from without reinforcement case, while in case of reinforcement with geosythetic arrived to -2.13+04Pa i.e.35% from without reinforcement case.

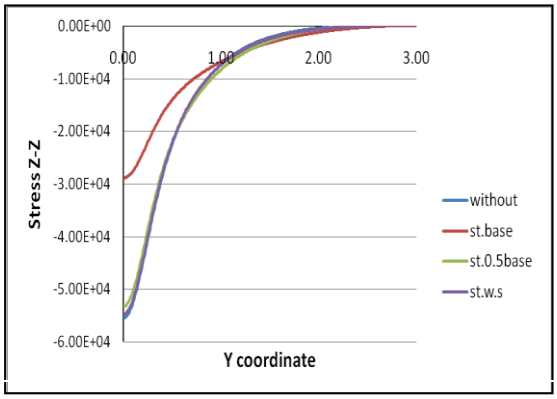

Fig. 3. Vertical stress σ_Z due to vertical pressure of wheel at bottom of base layer for local road section with and without steel reinforcement

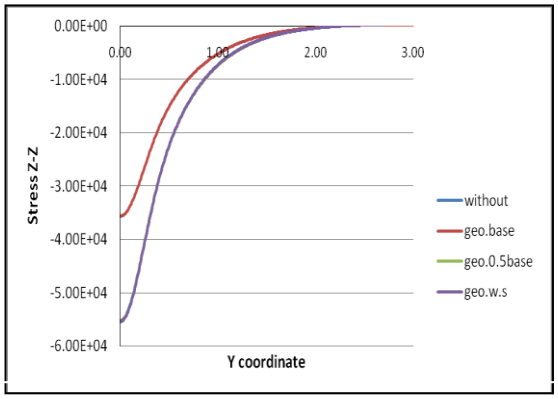

Fig. 4. Vertical stress σ_Z due to vertical pressure of wheel at bottom of base layer for local road section with and without geosynthetics reinforcement

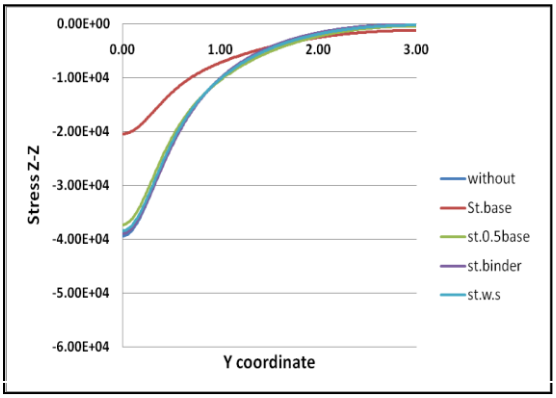

Fig. 5. Vertical stress σ_Z due to vertical pressure of wheel at bottom of base layer for expressway section with and without steel reinforcement

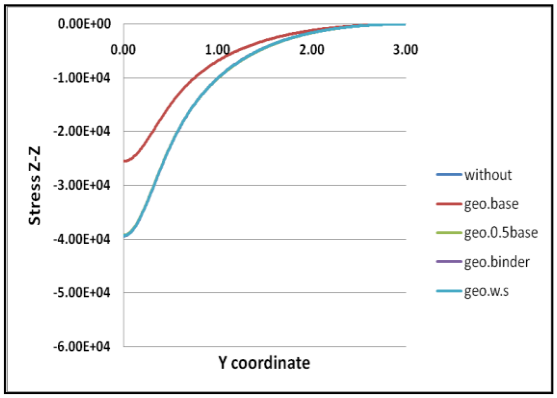

Fig. 6. Vertical stress σ_Z due to vertical pressure of wheel at bottom of base layer for expressway section with and without geosynthetics reinforcement

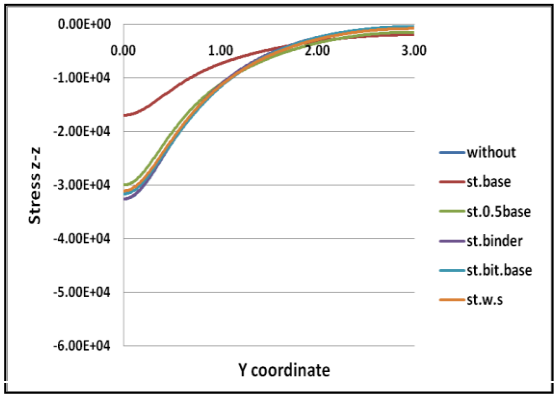

Fig. 7. Vertical stress σ_Z due to vertical pressure of wheel at bottom of base layer for freeway section with and without steel reinforcement

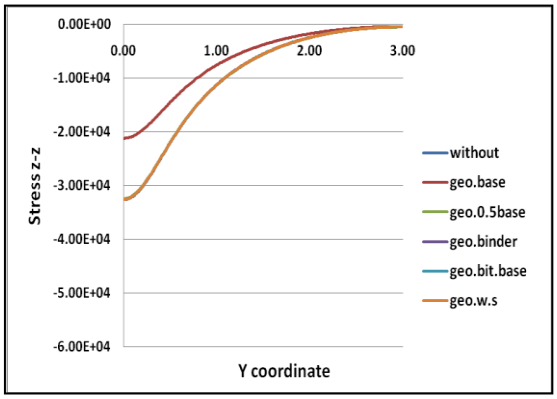

Fig. 8. Vertical stress σ_Z due to vertical pressure of wheel at bottom of base layer for freeway section with and without geosynthetics reinforcement

4.1.2 Lateral strain

For studied sections the lateral strain ε_Y variation versus section depth under center of wheel pressure are presented in figures (9) to (14). Figures present comparison of lateral strain variation in sections without and with reinforcement at different depths. It is depicted that for the case without reinforcement the lateral strain starts with negative value at top of wearing surface layer and rapidly increases to zero approximately at middle of wearing surface layer then continue increases to the maximum value at bottom of base layer and vanished at

the end of section. The maximum lateral strain ε_Y values at bottom of base layers in sections A, B and C are 4.91E-04, 3.59E-04 and2.92E-04 respectively. For reinforced section the lateral strain behavior the same as unreinforced sections but it is confined at the reinforcement location.

Figures (9) and (10) for local road section show when we add the steel reinforcement at the middle of base layer the lateral strain ε_Y is decreased to 4.44E-05 i.e. decreasing percent is 80.35% from without reinforcement case (1.92E-04)then arrived to 3.73E-04 at bottom of base layer i.e. 24.12% decreasing percent from the strain in original case. Figures also illustrate that there is a drastic change the lateral strain ε_Y values when the steel reinforcement at bottom of base layer, lateral strain ε_Y in this location was 6.52E-05 i.e. decreasing percent is 86.70% from its value in without reinforcement case. While in case of reinforcement with geosythetic at same location the lateral strain ε_Y was 4.12E-04 i.e. decreasing percent is 16.00% from its value in without reinforcement case. Also show there are no change in lateral strain ε_Y distribution for others cases and case without reinforcement.

Figures (11) and (12) for expressway section show that there is no change in the strain values in cases of steel or geosynthetic reinforcement at bottom of wearing surface , at bottom of binder layer and geosynthetic reinforcement at middle of base layer , shows that there is a noticeable change in case steel reinforcement at middle of base layer In this location the lateral strain ε_Y is decreased to 3.16E-05 i.e. decreasing percent is 75.5% from without reinforcement case then arrived to 2.65E-04 at bottom of base layer i.e.26.6%decresing percent from the lateral strain ε_Y in ordinary case. Figures also illustrate that there is a drastic change in the lateral strain ε_Y values when the steel reinforcement at bottom of base layer, lateral strain εY in this location was 5.90E-05 i.e. decreasing percent is 83.60% from its value in without reinforcement case. While in case of reinforcement with geosythetic at same location lateral strain ε_Y was 3.15E-04 i.e. decreasing percent is 12.55% from its value in without reinforcement case.

Figures (13) and (14) for freeway section show that there is a noticeable change when we add the steel reinforcement at middle of base layer, the lateral strain ε_Y is decreased to 4.96E-05 i.e. 72.01% decreasing percent from without reinforcement case (1.77E-04) then arrived to 1.94E-04 at bottom of base layer i.e. 33.30% decreasing percent from the strain in ordinary case. And illustrate that there is a drastic change in lateral strain ε_Y values when the steel reinforcement was at bottom of base layer. The lateral strain ε_Y arrived in this location to 5.39E-05 i.e. decreasing percent is 81.50% from its value in without reinforcement case. While for case of reinforcement with geosythetic the lateral strain ε_Y arrived in this location to 2.61E-04i.e. decreasing percent is 10.62% from its value in without reinforcement case. Figures show that there is no change in lateral strain ε_Y distribution in others cases and case without reinforcement.

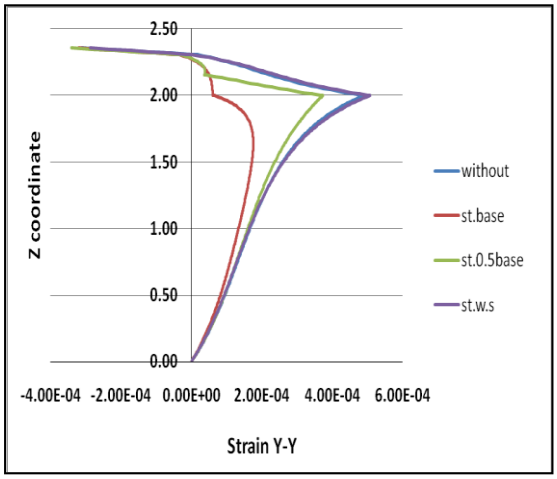

Fig. 9. Lateral strain ε_Y due to vertical pressure of wheel versus section depth for local road section with and without steel reinforcement

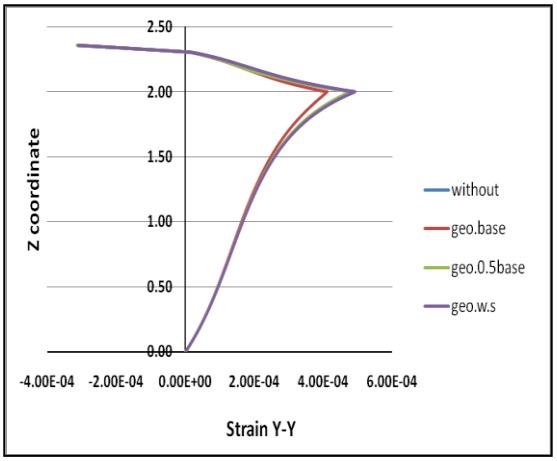

Fig. 10. Lateral strain ε_Y due to vertical pressure of wheel versus section depth for local road section with and without geosynthetics reinforcement

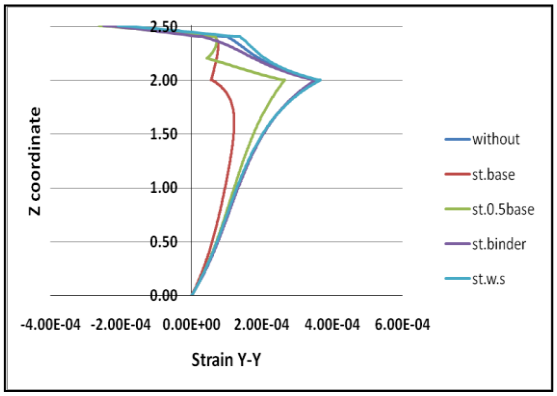

Fig. 11. Lateral strain ε_Y due to vertical pressure of wheel versus section depth for expressway section with and without steel reinforcement

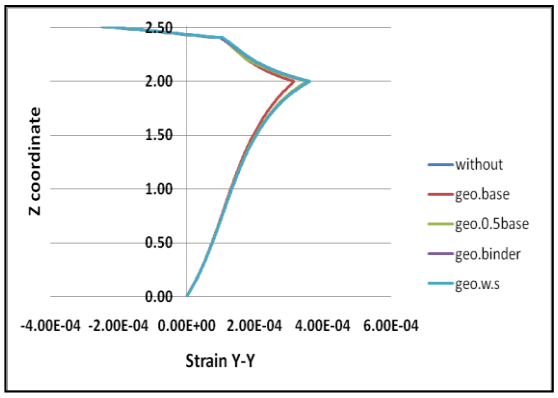

Fig. 12. Lateral strain ε_Y due to vertical pressure of wheel versus section depth for expressway section with and without geosynthetics reinforcement

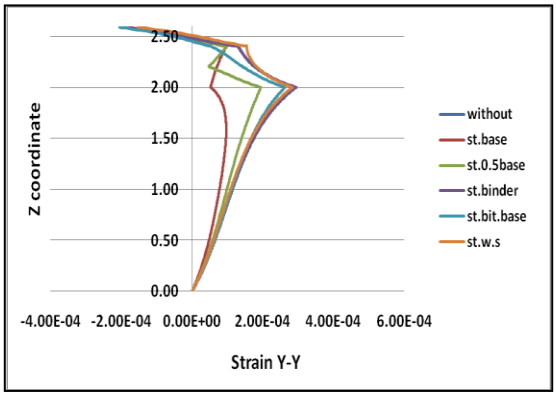

Fig. 13. Lateral strain ε_Y due to vertical pressure of wheel versus section depth for freeway section with and without steel reinforcement

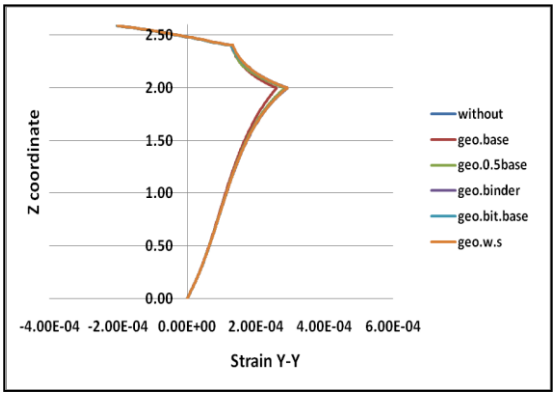

Fig. 14. Lateral strain ε_Y due to vertical pressure of wheel versus section depth for freeway section with and without geosynthetics reinforcement

4.2 Results of sections affected by vertical loads and friction force

4.2.1Vertical stress

Figures (15) to (20) present the variation of vertical stress σ_Z at bottom of base layer in studied sections vertical pressure of wheel and horizontal force due to friction and illustrate the effect of adding reinforcement with different locations. Figures (15) and (16) for local road section show that the vertical stress σ_Z in without reinforcement case start increase from -4.00E+04Pa under the center line of the wheel load to -4.15E+04 Pa at 0.17 m from center line of the wheel load and then decreases to decay at the end of section width. Figures also show that there is no change in cases reinforcement at bottom of wearing surface. Figures also show that there is a noticeable change after adding the steel reinforcement at middle of base layer the steel reinforcement at middle of base layer, the vertical stress σ_Z start increase from -3.64E+04 Pa i.e. decrease percent is 8.9% under the center line of the wheel load to -3.88E+04 Pa i.e. decrease percent is 12.29% at 0.17 m from center line of the wheel load and then decreases to decay at the end of section width, while for case of reinforcement with geosythetic there is no change.

Figures illustrate that there is a drastic change in vertical stress σ_Z values when the steel reinforcement was added at bottom of base layer, The vertical stress σ_Z start increase from -2.04E+04Pa i.e. decrease percent is 48.75% under the center line of the wheel load to -2.14E+04Pa i.e. decrease percent is 48.47% at 0.17 m from center line of the wheel load and then decreases to decay at the end of section width, while in case of reinforcement with geosythetic ,the vertical stress σ_Z start increase from -2.56E+04Pa i.e. decrease percent is 35.91% under the center line of the wheel load to -2.68E+04Pa i.e. decrease percent is 35.45% at 0.17 m from center line of the wheel load and then decreases to decay at the end of section width.

Figures (17) and (18) for expressway section show that the vertical stress σ_Z in without reinforcement case start increase from -3.13+04Pa under the center line of the wheel load to -3.14E+04Pa at 0.17 m from center line of the wheel load and then decreases to decay at the end of section width. Figures also show that there is a noticeable change when we add the steel reinforcement at middle of base layer, the vertical stress σ_Z start increase from -2.86E+04 Pa i.e. decrease percent is 8.5% under the center line of the wheel load to -

2.88E+04 Pa i.e. decrease percent is 8.29% at 0.20 m from center line of the wheel load and then decreases to decay at the end of section width.. Figures also illustrate that there is a drastic change in vertical stress σ_Z values when the steel reinforcement was added at bottom of base layer, The vertical stress σ_Z start from -1.62E+04 Pa i.e. decrease percent is 48.5% under the center line of the wheel load and still at same value to 0.17 m from center line of the wheel load and then decreases to decay at the end of section width, while in case of reinforcement with geosythetic The vertical stress σ_Z start from -2.00E+04 Pa i.e. decrease percent is 36% under the center line of the wheel load and still at same value to 0.17 m from center line of the wheel load and then decreases to decay at the end of section width. Figures show that there is no change in vertical stress σ_Z distribution in others cases and the case without reinforcement.

Figures (19) and (20) for freeway section display that the vertical stress σ_Z in without reinforcement case start from -2.67E+04 Pa under the center line of the wheel load and still at same value to 0.17 m from center line of the wheel load and then decreases to decay at the end of section width. Figures also show that there is no change in cases reinforcement at bottom of wearing surface and at bottom of binder layer. Figures also show that there is a noticeable change when we add the steel reinforcement at the end of bituminous base layer, the vertical stress σ_Z start from -2.55E+04 Pa i.e. decrease percent is 4.31% under the center line of the wheel load and still at same value to 0.17 m from center line of the wheel load and then decreases to decay at the end of section width, while there is no change in geosynthetic reinforcement at same location. Figures also show that there is a noticeable change when we add the steel reinforcement at middle of base layer, the vertical stress σ_Z start from -2.38E+04 Pa i.e. decrease percent is 10.77% under the center line of the wheel load and still at same value to 0.17 m from center line of the wheel load and then decreases to decay at end of section width. Figures also show that there is a drastic change in vertical stress σ_Z values when the reinforcement was added at bottom of base layer. The vertical stress σ_Z start from -1.39E+04 Pa i.e. decrease percent is 48% under the center line of the wheel load and still at same value to 0.17m from center line of the wheel load and then decreases to decay at end of section width, while in case of reinforcement with geosythetic, the vertical stress σ_Z start from -1.70E+04pa i.e. decrease percent is 35.9% under the center line of the wheel load and still at same value to 0.17 m from center line of the wheel load and then decreases to decay at end of section width.

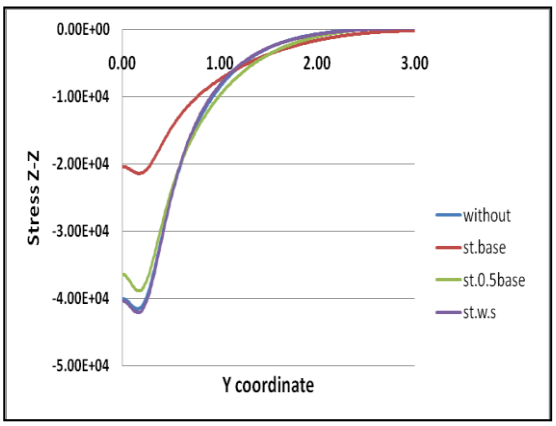

Fig. 15. Vertical stress σ_Z due to vertical pressure of wheel and friction force at bottom of base layer for local road section with and without steel reinforcement

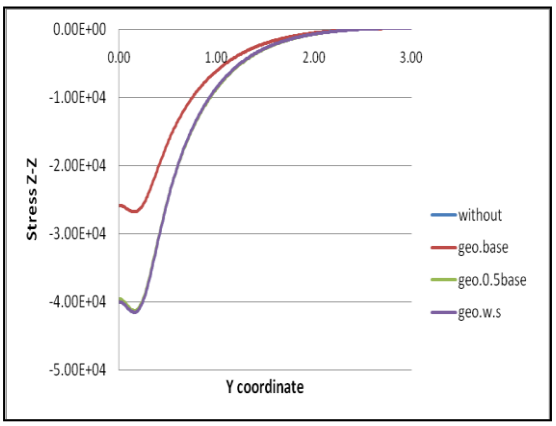

Fig. 16. Vertical stress σ_Z due to vertical pressure of wheel and friction force at bottom of base layer for local road section section with and without geosynthetics reinforcement

4.2.2 Lateral strain

Figures (21) to (26) present the variation of lateral strain under the center line of the wheel through the depth of the studied sections due to vertical pressure of wheel and horizontal friction force. Figures (21) and (22) for local road section exhibit that the lateral strain ε_Y start increase from 2.22E-04 at surface to 3.45E-04 at bottom of wearing surface layer then decrease to 2.15E-04 at 160mm from surface layer then increase to 3.61E-04 at bottom of base layer and then decreases to decay. But for steel reinforcement at middle of base layer the lateral strain ε_Y start increase from 1.73E-04 at surface to 2.81E-04 at 60mm from surface thendecrease to 5.12E-05 at middle of base then increase to 2.08E-04 i.e. 42.35% of ordinary value at bottom of base layer then decreases to decay.

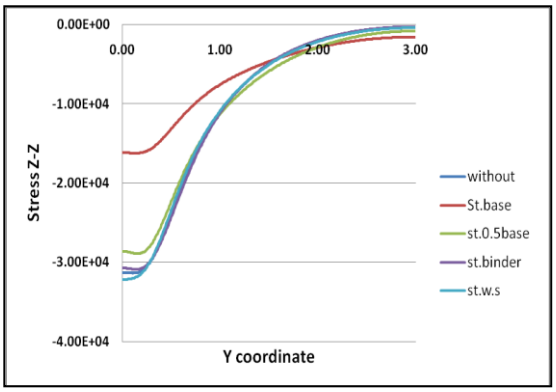

Fig. 17. Vertical stress σ_Z due to vertical pressure of wheel and friction force at bottom of base layer for expressway section with and without steel reinforcement

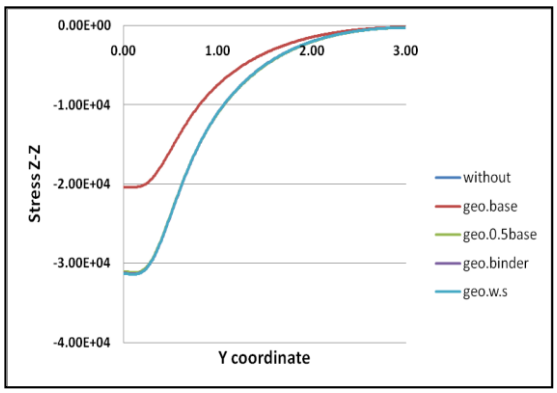

Fig. 18. Vertical stress σ_Z due to vertical pressure of wheel and friction force at bottom of base layer for expressway section with and without geosynthetics reinforcement

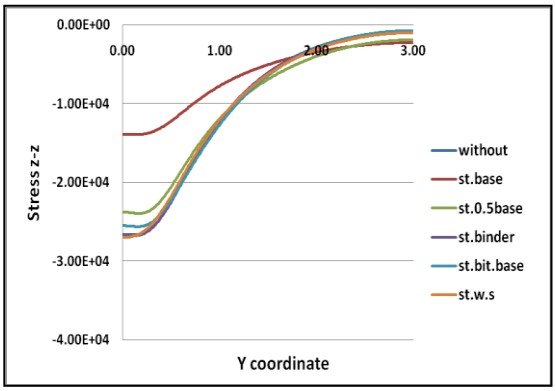

Fig. 19. Vertical stress σ_Z due to vertical pressure of wheel and friction force at bottom of base layer for freeway section with and without steel reinforcement

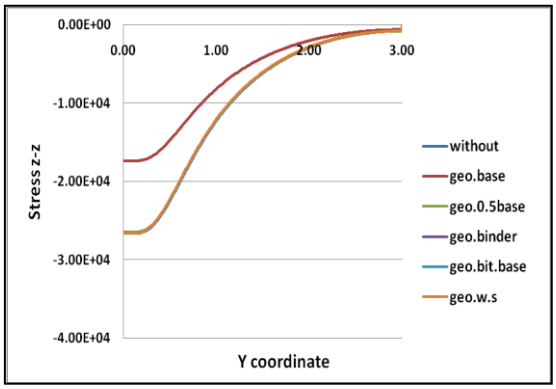

Fig. 20. Vertical stress σ_Z due to vertical pressure of wheel and friction force at bottom of base layer for freeway section with and without geosynthetics reinforcement

Figures also show the lateral strain ε_Y in geosynthetic reinforcement at bottom of base layer decreased by 10.8% from values in without reinforcement case. And for steel reinforcement the lateral strain ε_Y start increase from 1.97E-04 at surface to 2.90E-04 at 60mm from surface then decrease 6.06E-05 at bottom of base layer i.e. decreasing percent is 83.60% from its value in without reinforcement case and then decreases to decay.

Figures (23) and (24) for expressway section show that the horizontal lateral strain ε_Y start increase from 1.84E-04 at surface to 1.91E-04 at 20mm from surface layer then decrease to 1.11E-04 at 180mm from surface layer then increase to 2.32E-04 at bottom of base layer then decreases to decay. Figures show in case steel reinforcement at bottom of wearing surface layer the lateral strain ε_Y start increase from 9.85E-05 at surface to 1.04E-04 at 10mm from surface then decrease to 6.18E-05 at 50mm from surface layer then increase to 2.79E-04 at surface of sub grade and then decreases to decay. Figures also show in case of steel reinforcement at bottom of binder layer the lateral strain ε_Y start increase from 1.41E-04 at surface to 1.46E-04 at 10mm from surface then decrease to 4.96E-05 at 160mm from surface layer then increase to 2.40E-04 i.e. 10% of original case at surface of sub grade and then decreases to decay. Figures also show in case of steel reinforcement at middle of base layer the lateral strain ε_Y start increase from 1.66E-04 at surface to 1.71E-04 at 10mm from surface then decrease to 4.00E-05 at 250mm from surface layer then increase to 1.66E-04 i.e. 37.9% of ordinary value at surface of sub grade and then decreases to decay. Figures also illustrates that no change in the lateral strain ε_Y values between adding the geosynthetic reinforcement at bottom of base layer and the case without reinforcement from surface to subgrade but the lateral strain ε_Y at surface of subgrade decreased by 10.8% from the lateral strain ε_Y in without reinforcement case. And for steel reinforcement the lateral strain ε_Y start increase from 1.85E-04 at surface to 1.89E-04 at 10mm from surface then decrease to4.44E-05 at 290 mm from surface layer then increased to to5.11E-05 i.e. 80.75% of ordinary value at bottom of base layer and then decreases to decay. Figures show that there is no change in lateral strain ε_Y distribution in others cases and the case without reinforcement.

Figures (25) and (26) for freeway section clarify that the lateral strain ε_Y start increase from 1.48E-04at surface to 1.55E-04 at 20mm from surface layer then decrease to 6.98E-05 at 190mm from surface layer then increase to 2.13E-04 at bottom of base layer and then decreases to decay. For steel reinforcement at bottom of wearing surface the lateral strain ε_Y start increase from 8.00E-05 at surface to 8.65E-05 at 10mm from surface then decrease to 4.63E-05 at 50mm from surface layer then increase to 2.27-04 at bottom of base layer and then decreases to decay. In case of steel r at bottom of binder layer the lateral strain ε_Y start increase from 1.29E-04 at surface to 1.35E-04 at 10mm from surface then decrease to 4.96E-05 at 110mm from surface layer then increase to 2.10E-04at bottom of base layer and then decreases to decay. Figures show in case steel reinforcement at bottom of bituminous base layer the lateral strain ε_Y start increase from 1.27E-04 at surface to 1.32E-04 at 20mm from surface then decrease to 4.14E-05 at 190mm from surface layer then increase to 1.79E-04 i.e. 16% of ordinary value at bottom of base layer and then decreases to decay.

Figures also present that no change in the lateral strain ε_Y values between adding the geosynthetic reinforcement at the middle of base layer and the case without reinforcement from surface to subgrade but the lateral strain ε_Y at surface of subgrade decreased by 10.8% from the lateral strain ε_Y in without reinforcement case, while for steel reinforcement at the same location the lateral strain ε_Y start increase from 1.44E-04 at surface to 1.48E-04 at 10mm from surface then decrease to 3.59E-05 at 250mm from surface layer then increase to 1.23E-04 i.e. 42.16%of ordinary value at bottom of base layer and then decreases to decay. Figures also illustrate that no change in the lateral strain ε_Y values between adding the geosynthetic reinforcement at bottom of base layer and the case without reinforcement from surface to subgrade. But the lateral strain ε_Y at surface of subgrade decreased by 8% from the lateral strain ε_Y in without reinforcement case, while for steel reinforcement the lateral strain ε_Y start increase from 1.59E-04 at surface to 1.63E-04 at 10mm from surface then decrease to4.44E-05 at 170 mm from surface layer then increased to to4.63E-05 i.e. 78.30% of ordinary value at bottom of base layer then decreases to decay. Figures show that there is no change in lateral strain ε_Y distribution in others cases and the case without reinforcement.

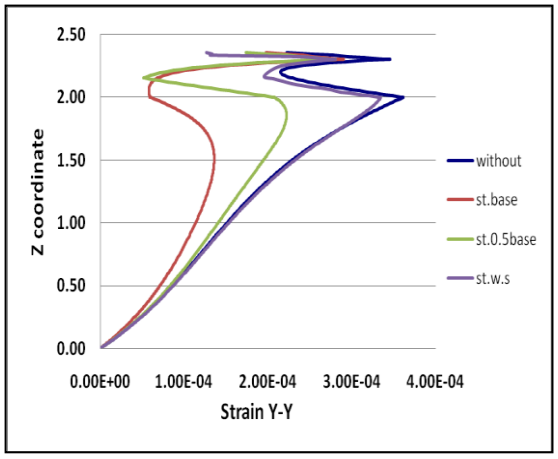

Fig. 21. Lateral strain ε_Y due to vertical pressure of wheel and friction force versus section depth for local road with and without steel reinforcement

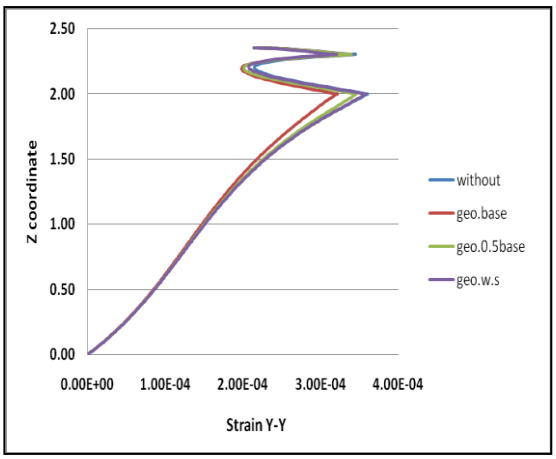

Fig. 22. Lateral strain ε_Y due to vertical pressure of wheel and friction force versus section depth for local road section with and without geosynthetics reinforcement

4.3 Comparison between the reinforced flexible pavements sections and rigid pavement section

4.3.1 Vertical stress

The variation of vertical stress σ_Z at top of subgrade for studied paving sections with steel or geosynthetic reinforcement and selected rigid pavement section 20cm reinforced concrete slab with steel diameter is 8 mm and rested on 15cm sub base layer is shown in figures (27) and (28). From figure (27) it is clear that the values of vertical stress σ_Z in section reinforced with steel mesh are lower than the values in section reinforced with geosynthetic. Figure (28) show that the value of vertical stress σ_Z under the wheel in rigid pavement section is lower with15.93% than value in local road section reinforced with steel, but it is greater with 15.64% than values in expressway section reinforced with steel and greater with 29.85% than the stress in freeway section reinforced with steel.

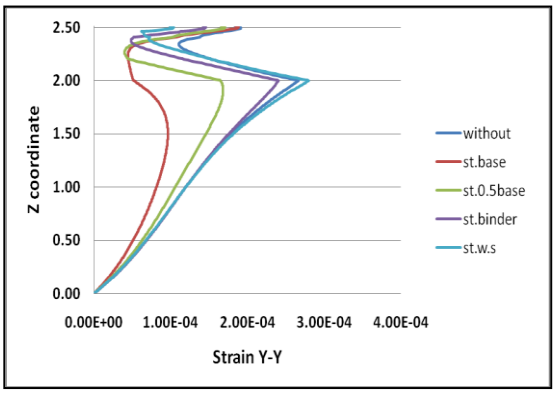

Fig. 23. Lateral strain ε_Y due to vertical pressure of wheel and friction force versus section depth for expressway section with and without steel reinforcement

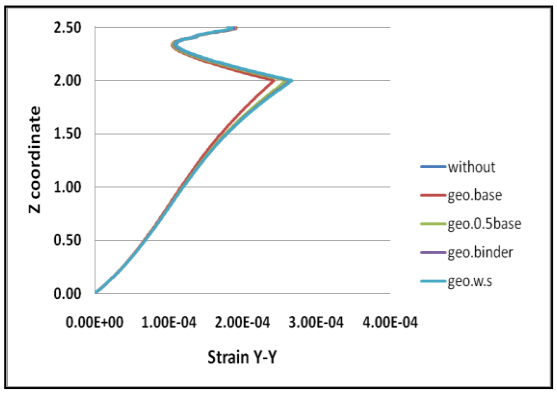

Fig. 24. Lateral strain ε_Y due to vertical pressure of wheel and friction force versus section depth for expressway section with and without geosynthetics reinforcement

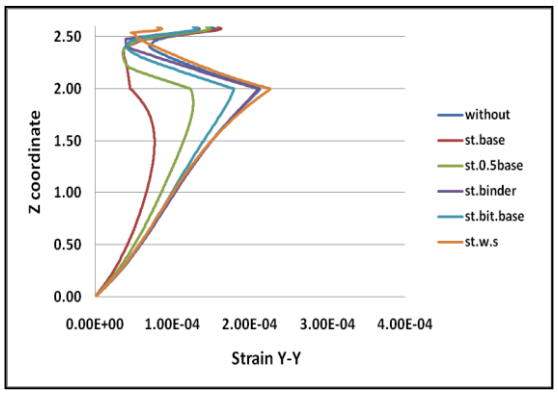

Fig. 25. Lateral strain ε_Y due to vertical pressure of wheel and friction force versus section depth for freeway section with and without steel reinforcement

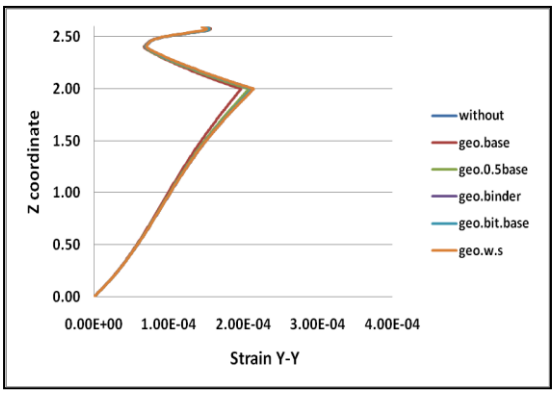

Fig. 26. Lateral strain ε_Y due to vertical pressure of wheel and friction force versus section depth for freeway section with and without geosynthetics reinforcement

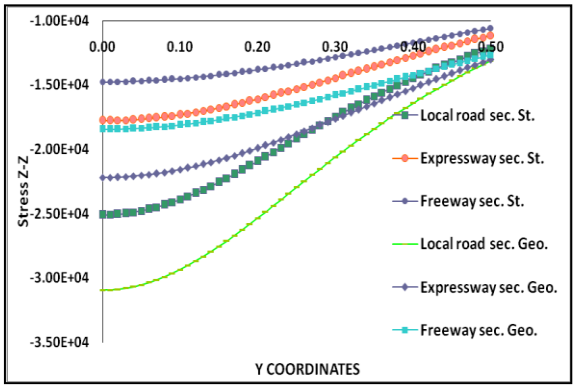

Fig. 27. Vertical stress σ_Z due to vertical pressure of wheel at bottom of base layer for investigated sections with steel reinforcement or geosynthetics reinforcement

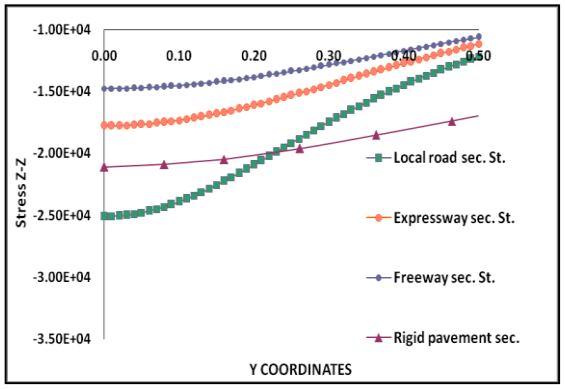

Fig. 28. Vertical stress σ_Z due to vertical pressure of wheel at bottom of base layer for investigated sections with steel reinforcement or rigid pavement

4.3.2 Lateral strain

Lateral strain ε_Y values under the centerline of the wheel load at top of subgrade for studied sections with steel or geosynthetic reinforcement and selected rigid pavement section (20cm reinforced concrete slab with steel diameter is 8 mm and rested on 15cm sub base layer) are shown in Table (5). From this table it is clear that the values of lateral strain ε_Y in steel reinforced sections are decreased than its values in geosynthetic reinforced sections. Table also shows that the values of lateral strain ε_Y in rigid pavement section are lower with 7% than value in local road section reinforced with steel but it is greater with 1.1% than values in expressway section reinforced with steel and greater with 12.50% than the stress in freeway section reinforced with steel.

Table 5. Lateral strain ε_Y at top of subgrade due to vertical pressure of wheel for studied sections with steel reinforcement or geosynthetics reinforcement and rigid pavement section

Reinforcement Type	Section	Lateral Strain
Geosythetics Reinforcement	Local Road	4.12E-04
	Expressway	3.15E-04
	Freeway	2.61E-04
Steel Reinforcement	Local Road	6.52E-05
	Expressway	5.90E-05
	Freeway	5.39E-05
Rigid Pavement Section		5.80E-05

V. CONCLUSION

Based on the previous analysis the following conclusions are given:

1. Bottom of base layer was found to be the most suitable location of reinforcing where the maximum reduction in vertical stress and lateral stain is occurred in all investigated sections.
2. Vertical stress σ_Z under middle of wheel at bottom of base layer in steel wire grid reinforced paving sections subjected to vertical load due to wheel pressure only is decreased with about 48% from without reinforcement cases in the investigated three sections, while in geosynthetic reinforcement cases the decreasing percent is about 35% from without reinforcement cases.
3. In cases paving sections subjected to vertical load due to wheel pressure and horizontal friction force, the vertical stress σ_Z under center line of wheel at bottom of base layer in steel wire grid reinforced cases is decreased with about 48.75% from without reinforcement cases in the investigated three sections, while in geosynthetic reinforcement cases the decreasing percent is about 36% from without reinforcement cases.
4. Lateral strain ε_Y under the centerline of the wheel load at the bottom of base layer in steel wire grid reinforced paving sections subjected to vertical load due to wheel pressure only is decreased from without reinforcement sections, with 86.70% in local road section, 83.60% in expressway section and81.50%in freeway section, while in geosynthetic reinforcement cases the decreasing percents are 16%, 12.55% and 10.62% respectively.
5. In cases paving sections subjected to vertical load due to wheel pressure and horizontal friction force, lateral strain ε_Y under the centerline of the wheel load at the bottom of base layer in steel wire grid reinforced cases is decreased from without reinforcement sections with 83.60% in local road section, 80.75%in expressway section and78.30%in freeway section, while in geosynthetic reinforcement cases the decreasing percents are 10.8% in sections local road section and expressway section while 8% for freeway section.
6. Lateral strain ε_Y under the centerline of the wheel load at top of subgrade in selected rigid pavement section is lower with 7% than value in local road section reinforced with steel but it is greater with 1.1% than values in expressway section reinforced with steel and greater with 12.50% than the stress in freeway section reinforced with steel.
7. Vertical stress σ_Z at top of subgrade in selected rigid pavement section is lower with15.93% than value in local road section reinforced with steel, but it is greater with 15.64% than values in expressway section reinforced with steel and greater with 29.85% than the stress in freeway section reinforced with steel.
8. Investigators recommend in future work:
   - An economic study to assess the benefit of using proposed strengthening technique.
   - Enhance the analysis to include the environmental effects on the reinforced paving sections.
   - Investigate the effect of dynamic loading on the reinforced paving sections.

REFERENCES

[1] Al-Qadi, I.L., Elseifi, M. and Leonard D., 2007. Development of an overlay design model for reflective cracking with and without steel reinforcing netting. AAPT Conference.

[2] Choi, S.K., 2009. FLOWMEC – A 3-dimensional finite element code for the modelling of multiphysics problems.

[3] Nods, M., 2000. Effectiveness of asphalt reinforcement with geogrids. Huesker Synthetic.

[4] Vuong, B.T., 2005. Initial development of models to predict pavement wear under heavy vehicles. Austroads Project No: T+E.P.N.537. Austroads Report. ARRB Group Ltd.

[5] Hadi MNS, Bodhinayake BC. Non linear finite element analysis of flexible pavements. Adv Eng Soft 2003; 34(3):657–62.

[6] Bassam Saad, Hani Mitri and Hormoz Poorooshasb. 3D FE Analysis of Flexible Pavement with Geosynthetic Reinforcement. Journal of transportation engineering © ASCE / MAY 2006.

[7] Vuong, B.T. and Choi, X., 2009. Modelling of responses of road pavements containing reinforced materials. Contract Report for RTA-NSW. ARRB Group Ltd. (Unpublished).
[8] H. Akbulut, K. Aslatas. Finite element analysis of stress distribution on bituminous pavement and failure mechanism. Materials and design 26(2005)383-387.
[9] ADINA 8.7.3 Manuals (2005) ADINA R&D, Inc. Watertown, MA, USA.
[10] Egyptian Code for roads, part (4) Road construction materials and tests, Egypt 2008.
[11] Specifications of General Authority for Roads and Bridges, Egypt 1990
[12] Finite element modelling of flexible pavements on soft soil subgrades R.M. Mulungye, P.M.O. Owende, K. Mellon. Materials and Design 28 (2007) 739–756.

American Journal of Engineering Research (AJER)
e-ISSN : 2320-0847 p-ISSN : 2320-0936
Volume-02, Issue-11, pp-163-173
www.ajer.org

Research Paper Open Access

Pressure Sensed Fast Response Anti-Collision System for Automated Railway Gate Control

Subrata Biswas, Rafiul Hoque Bhuiyan, Samiul Hoque, Robiul Hasan, Tanzila Nusrat Khan

[1, 2, 3, 4, 5] *(Department of Electrical and Electronic Engineering, American International University-Bangladesh, Dhaka, Bangladesh)*

Abstract: **-** This paper presents an innovative project design of a pressure sensor based swift response anti-collision system for an automatic railway gate control. By replacing the manual system of railway gate control at the level crossing it has been develop an automatic system in which the arrival and departure of the train will be sensed automatically to control the gate. The novelty of this project based paper is the use of pressure switch which has been integrated in this anti-collision system for the railway. By chance if a vehicle gets stuck at the level crossing of the rail-line, the pressure sensor will detect the object and will take necessary action by following the developed algorithm. The whole operation of this project has been controlled by a Microcontroller PIC16F84A. Two IR sensors have been used to detect the arrival and departure of the train. IR sensor will give the signal to the Microcontroller and the Microcontroller will pass this signal to the DC motor and it will rotate as its requirement. This noble project is very much reliable, safe and cost effective.

Keywords: **-** *Anti-collision, Automatic, Microcontroller, MPLAB IDE, Proteus, Receiver, Sensor, Transmitter.*

I. INTRODUCTION

Now a days in Bangladesh numerous number of railways are running on track every day. A railway has its way of running that is straight and it is risky and dangerous as per as public and traffic concern. Every year many people died at the level crossing of the rail-line due to the carelessness of the gate keeper. Also some major collisions occur when any vehicle gets stuck at the level crossing. The rate of these accidents is increasing day by day. That's why our concept is to make an automatic system to avoid the collisions at the level crossing of the rail-line.

An automatic railway gate control system is an arrangement of physical components which sense the arrival of the train and make the gate pull up and pull down automatically. As a train approaches at the railway crossing from either side, the sensors placed at a certain distance from the gate detect the approaching train and accordingly controls the operation of the gate. Also an indicator light has been provided to alert the driver of the train if any vehicle or living object gets stuck at the level crossing of the rail-line. [1]

By employing the automatic gate control at the railway level crossing the arrival of the trains are detected by the IR sensors placed on either side of the gate. Once the arrival is sensed, the sensed signal is sent to the microcontroller and it checks the possible presence of any vehicle between the gates, again using sensor. Once no vehicle is sensed in between the railway gate then the motor is activated and the gates are closed. But if any obstacle is sensed it is indicated to the train drivers and necessary steps are taken according to solve the emergency problems. When the train is passed through using the same process gate is opened.

Earlier, railway gate is controlled manually all over the world. Now a day's many countries of the world are practicing automatic railway gate control system. But it was not the scenario in the late past. Walkie-talkie sets were provided to drivers and guards of all the trains for communication in static mode or at low speeds. VHF

sets was also used at stations on board gauge double line or multiple line sections so that train crew can communicate with the nearest station masters in the case of emergencies. In early age, guards used conventional kerosene lit tail lamps to pass the signals to the driver after closing the gates at the railway level crossing. But this system has less reliability. Due the carelessness of the gate keepers and the guards many accidents took place in the past. [2]

Now a days, a system has been designed to reduce the complexity and tried to make a reliable system. In this system when a train is about to its arrival at the railway crossing which is shown in Fig. 1, the station master informs the gate keeper who stands at the side of the railway gate by calling him through telephone and then he closes the gate so that the traffic cannot pass through the rail-line. Sooner he passes this information to the station master using same process and the station master gives signal to the train to pass through. When the train passes through the level crossing completely gate keeper gives this information to the station master and the station master gives him the right to open the gate.

Sometimes vehicles get stuck at the level crossing of the rail-line; at that time there is huge chance of occurrence of accident. In fact, such situation triggered many accidents in the past. The ordinary system of railway gate control has no safety purpose as it is operated manually. In manual system, road users have to suffer many hours at the level crossing due to the laziness of the gatekeeper. And the more important thing there is no anti-collision system in manual operated railway gate control system.

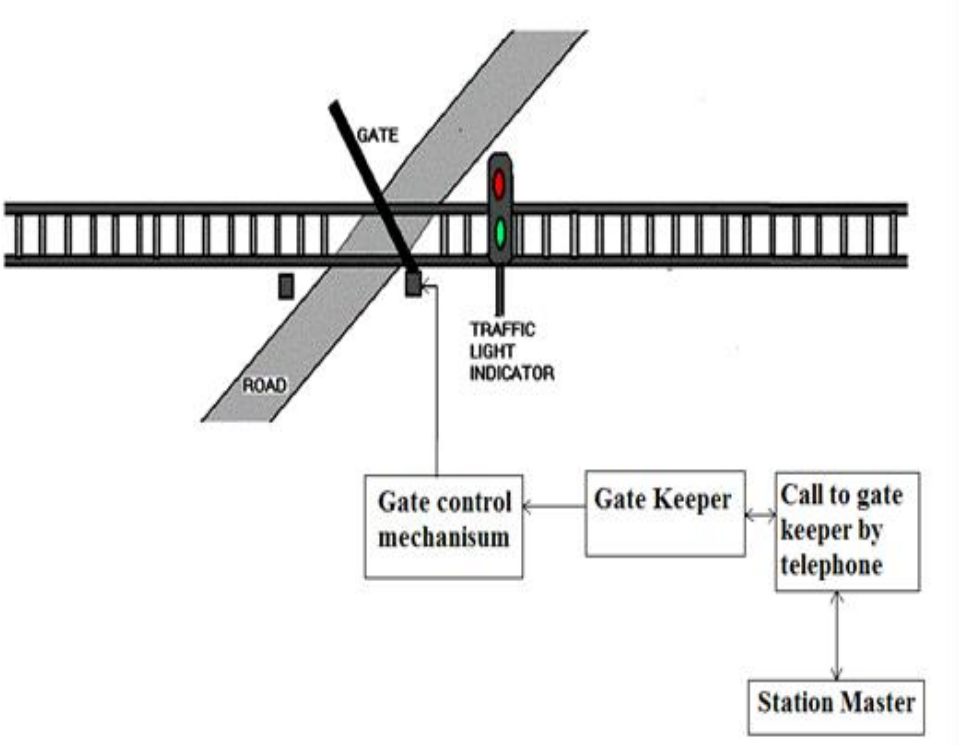

Fig. 1. Oldest technique of gate control [3]

II. OVERVIEW OF THE PROJECT

2.1 Block Diagram of the Project

We can describe the whole operation of the circuit briefly by using some block diagrams. A block diagram is a graphical method used to explain the concept of a system without the need to understand the individual components within that system. This type of diagram might be used in a variety of industries to illustrate and educate individuals about how a system operates, either in part or in its entirety. Block diagrams usually will have a logical, methodical flow from beginning to end. [4]

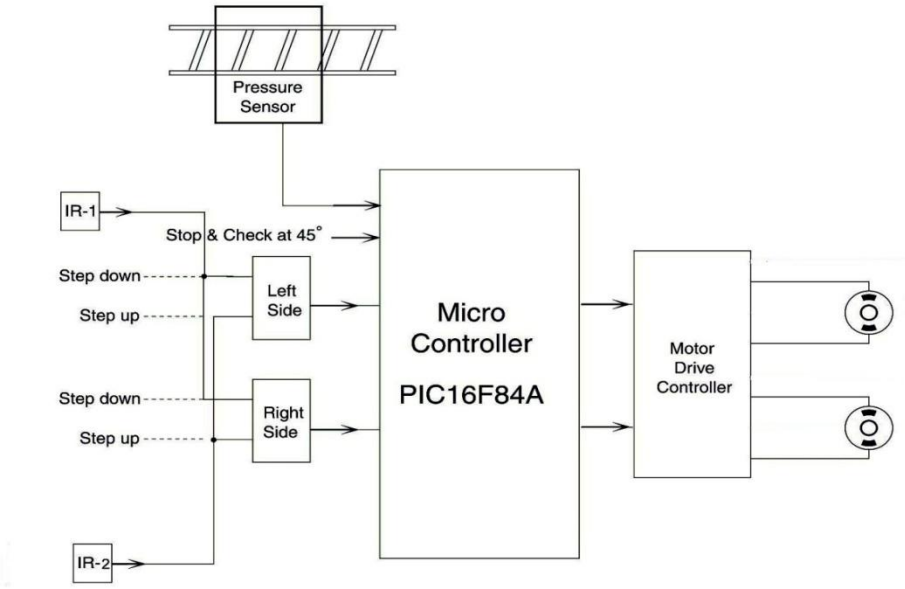

Fig. 2. Proposed technical block diagram

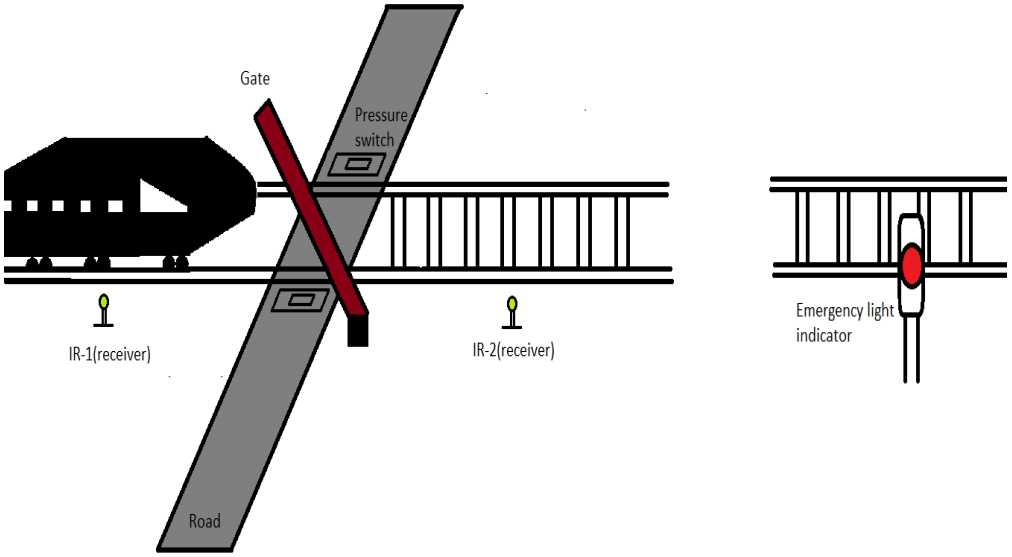

Fig. 3. Proposed implementation planning

To describe the whole operation of the project, we need to explain the two block diagrams in Fig. 2 and Fig. 3. We are placing the IR transmitter in the train so that it would only be activated when it would be closer to the receiver. We need to select the side from which the train is coming. If we consider the train is coming from the left side of the track (Fig. 3) then if the train touches the IR-1 (Receiver) it will send the signal to the Microcontroller and the microcontroller pass this signal to the motor driver controller. It will drive the motor in its way. In our project it will rotate at anti-clock wise position if it gets signal from the IR-1 in Fig. 2.

When the gate is closing down it will stop and check at 45° for any presence of the vehicle from the pressure sensor. If no vehicle gets stuck at the level crossing, then our Microcontroller will allow the gate to be closed at 90°.If the microcontroller could sense any presence of the vehicle at the level crossing it will send signal to the motor and it will stop at 45°. It will also give an emergency signal to train driver so that the driver of the train could take necessary actions to avoid the collision in Fig. 2 and Fig. 3. At the time of departure of the train, it will touch the sensor IR-2 and it will send signal to the Microcontroller and our Microcontroller will

allow the gate to rotate at clock wise direction. And that's how the gate could come in its initial position.
In practical case, the IR receiver will be placed 1 km away from the level crossing and so that the train could reduce its speed when an object gets stuck at the level crossing.

2.2 Flow Chart

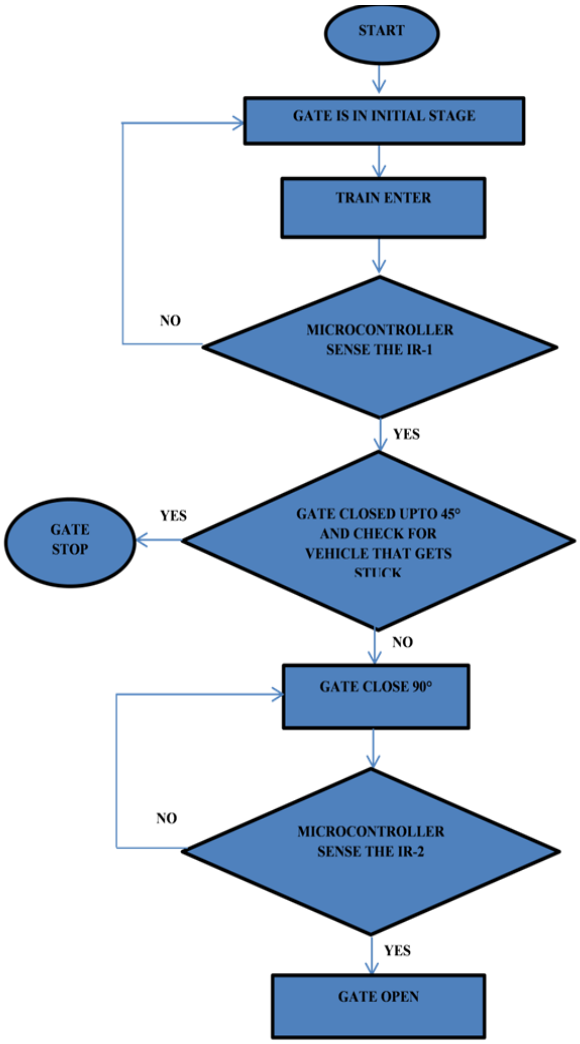

Fig. 4. Flow Chart

2.3 Algorithm

The algorithms used in the flow chart in Fig. 4 are described in steps.

⇒ Start.
⇒ Set the variables.
⇒ Make initial settings for the signal of the train.
⇒ Check the arrivals of the train in either direction by the IR-1 sensor. If train is sensed then go step-5 otherwise go the step-2.
⇒ If the arrival of the train is sensed then the gate is closed up to 45° and check for the vehicle that gets stuck. If any vehicle gets stuck it would be Stop otherwise go to Step- 6.
⇒ Close the gate.
⇒ The departures of the train are sensed then go to Step-8 otherwise goes to Step-6.
⇒ Open the gate.

III. SOFTWARE INTERFACING

Compiling the code for microcontroller, MPLAB IDE is the best solution. For burning the code to the microcontroller PICkit2 is very efficient. For showing the circuits and simulation virtually Proteus is perfect for this job.

3.1 MPLAB Integrated Development Environment

MPLAB Integrated Development Environment (IDE) is a full-featured compiler for PIC devices from Microchip. It is called an Integrated Development Environment, or IDE, because it provides a single integrated environment to develop code for embedded microcontrollers. It is the best solution for developing code for PIC devices. It includes a host of free software components for fast application development and supercharged debugging. MPLAB IDE also serves as a single, unified graphical user interface. [5]

3.2 Working with MPLAB IDE

Starting with MPLAB at first we need to create a project from project wizard. From there a language tool needs to select which is shown in Fig. 5. Then have to create a project with a valid name. After that others file or work can be included from there. Then new file should be created for writing the code. For assembly language file name should be "filename.asm" format. From source that assembly file should be include.

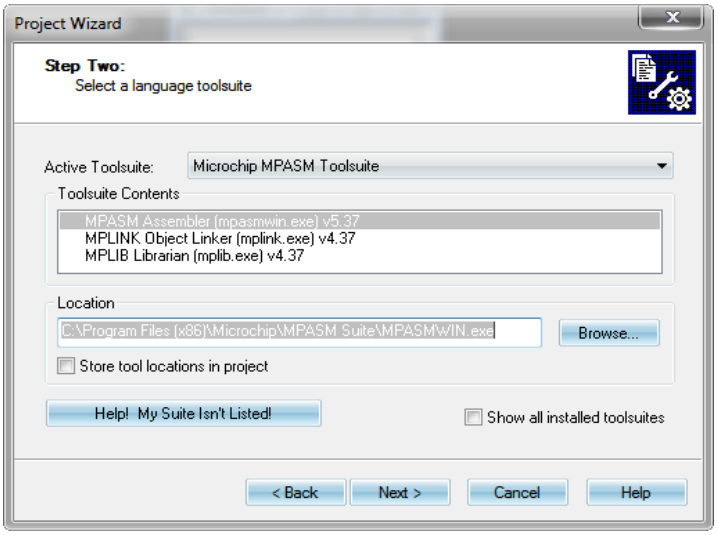

Fig. 5. Selecting compiler language

3.3 Features of MPLAB IDE

Some features of MPLAB IDE is given below:

⇒ It assembles, compile and link the source code.
⇒ It debugs the executable logic by watching program flow with the built-in.
⇒ Simulator or in real time with in-circuit emulators or in-circuit debuggers.
⇒ It makes timing measurements with the simulator or emulator.
⇒ It views variables in watch windows.
⇒ Program firmware into devices with device programmers.
⇒ These are the features of MPLAB IDE. [5]

3.4 Proteus

Proteus software is renowned to all for software simulation. Proteus is the software of "LABCENTER" Electronics. It is even possible to connect Proteus VSM with third party software debugger, and watch animated schematic diagram at work as if it was real hardware. [6] This software has a library. From this library any components can be include in the circuit for simulation. It has thousands of components that use in real life

which is shown in Fig. 6 and for a certain period of time library can be updated by internet. It is the professional software for embedded designers. It helps a designer to complete the work.

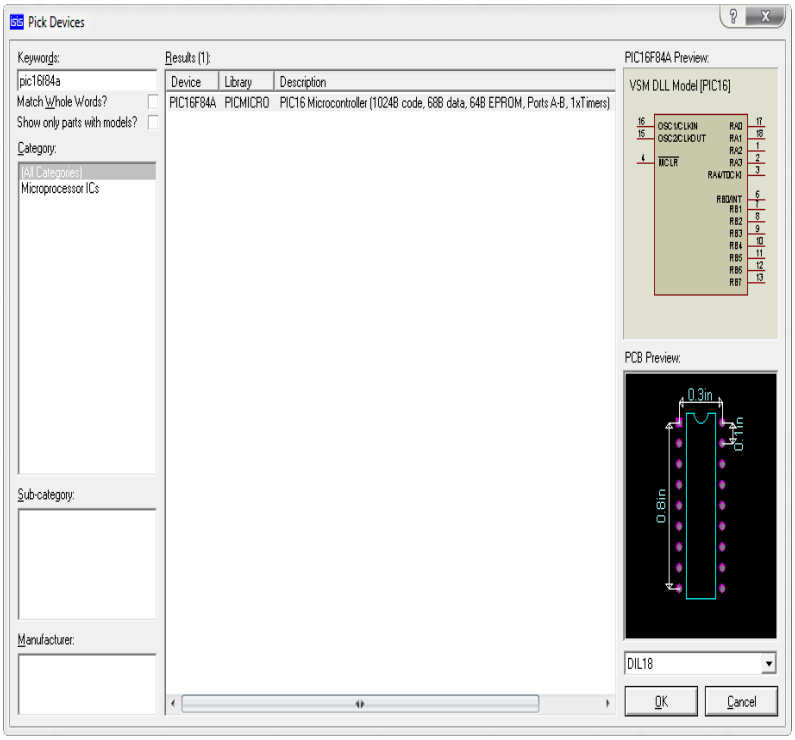

Fig. 6. Picking up devices from Proteus Library

3.5 Working with Proteus

The Proteus is the simple and most essential software with latest technology for circuit implementation and simulation. It has ISIS which is for circuit design and simulation and ARES which is for PCB designing. Starting the software there is a library for including the components. Including necessary components it can be simulate after building the circuit. It is necessary to give corresponding information to the components and microcontroller needs to include the hex file for its necessary work.

3.6 Applications of Proteus software

Microcontrollers are widely applied in the field of industry to solve engineering control problems. A new simulation software package for microcontroller, Proteus virtual system modeling (VSM), is introduced for industrial and educational use. Proteus combines circuit simulation, animated components and microprocessor models to facilitate co-simulation of complete microcontroller based designs. Proteus makes it possible to develop and test designs before a physical prototype is constructed. Proteus is very suited for teaching students about the design and operation of microcontroller-based systems. [7] – [8].

IV. SIMULATION AND RESULT ANALYSIS

This project is about the implementation of a smart anti-collision system as well as to control the railway gate automatically. By studying the rate of accidents in our country we are trying to reduce or minimize the accidents by using an automatic system. This is a system which is designed using Microcontroller 16F84A.

4.1 Proposed Circuit Design

We have built the circuit to simulate our project using Proteus v7.8 which is shown in Fig. 7. We are using this software because this is very much user friendly to design and simulate any circuits instead of using other software's. The design of the circuit in Proteus is given below.

As IR sensor is not available in Proteus we are using push button here. Here two push buttons are used to instead of using IR-1 and IR-2 and that stands for closing and opening the gate. Another button is used for checking at 45° and other stands for giving the presence of vehicle if that gets stuck. We are using four more push buttons directly connected with the motors as we are using DC motor. It will work as a trip switch. LED D1 is used to give signal to the train if any vehicle or living object gets stuck at the level crossing of rail-line. We can explain the whole operation and its results using the following figure.

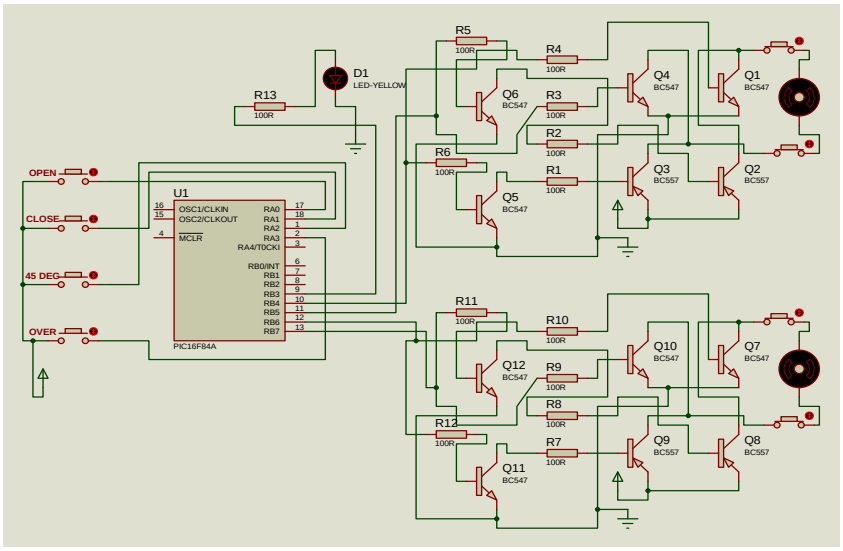

Fig. 7. Circuit design using Proteus

4.2 Results in Three Different Cases

Result part presents three important cases here. Those are:

⇒ When the train arrives

⇒ When the train leaves

⇒ When any vehicle gets stuck

4.2.1 Train Arrival Detections

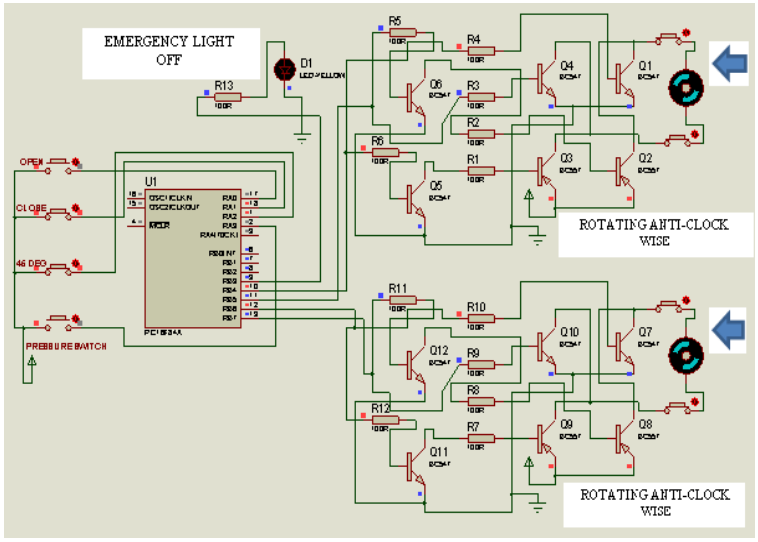

Fig. 8. Arrival of the train detections

As the gate will always check at 45° it would always be closed as we can see from the figure. When the train is coming we need to close the push button named as Close. So the gate will be closing down and at 45° it will check for the presence of any vehicle that gets stuck. If any object is not found then the gate it is closed properly. That's why it is rotating in anti-clock wise direction shown in Fig. 8.
As it is not sensing any living object at the level crossing so the emergency light D1 will remain off.

4.2.2 Departure of the Train Detections

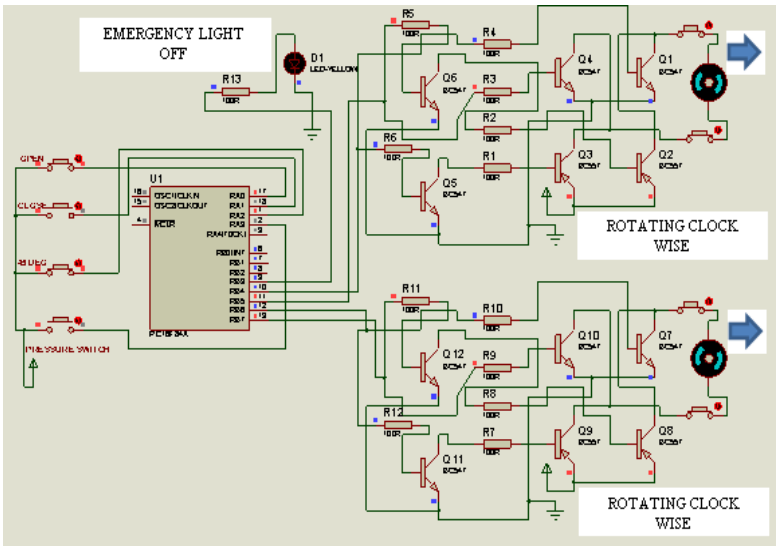

Fig. 9. Departure of the train detections

Fig. 10.

To show the departure of the train from the level crossing shown in Fig. 9 we need to open the CLOSE button and close the OPEN button. As soon as we close this button, it will send signal to the Microcontroller and motor will rotate in clock wise position so that the gate can open and allow the vehicle to pass through the level crossing.
As our Microcontroller is not getting any signal from the pressure switch emergency light indicator D1 will remain off.

4.2.3 When a Vehicle Gets Stuck

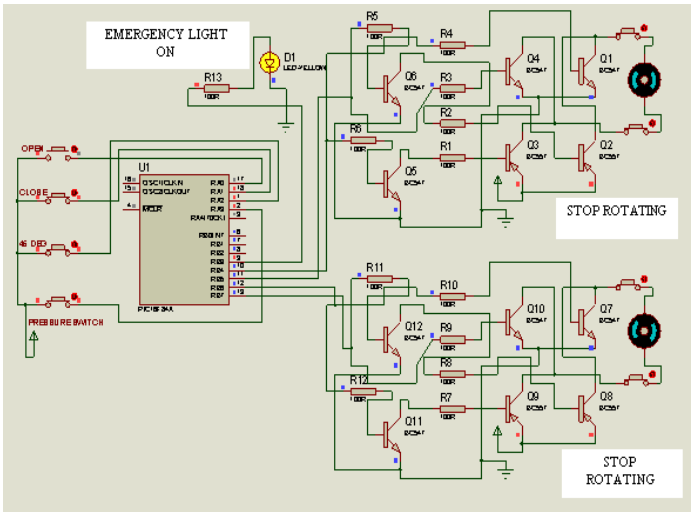

Fig. 11. Pressure switch is activated

For this operation in Fig. 10 we need to activate the pressure switch as well as to CLOSE button. So the gate is closing down it will check at 45° and it will get a signal of any living object that gets stuck at the level crossing of the rail-line. So our Microcontroller will give signal to the motor to Stop and send this emergency signal to the train driver making the emergency light ON. As we can see from the figure D1 is activated and that's how train driver will take necessary actions to reduce the accident.

V. DESIGN PROTOTYPE

We have designed the PCB layout after implementing the whole circuit on the bread board to check whether it works properly or not.

5.1 PCB Design (Front and Back)

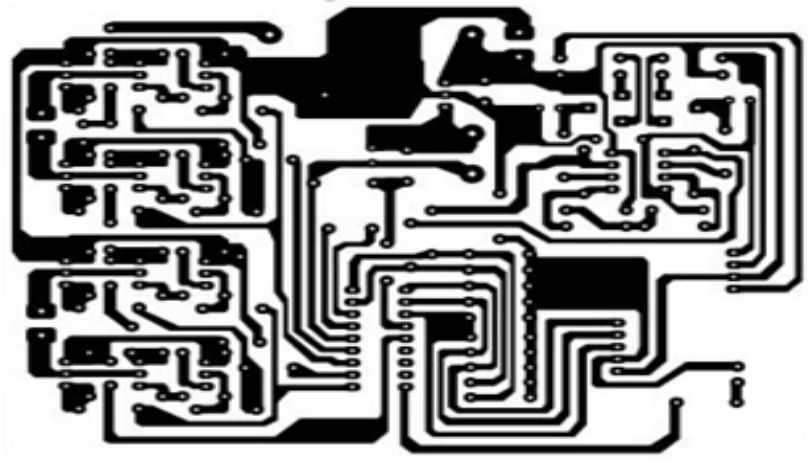

Fig. 12. Back part of the PCB layout

As we are making a model of the whole project, it would not be possible to test its functionality with the practical railway system. That's why using a demo train we had observe its functionality. When every function of the project runs properly then the PCB layout has been designed which is shown is Fig. 11 and Fig. 12 and implemented the circuit on the PCB.

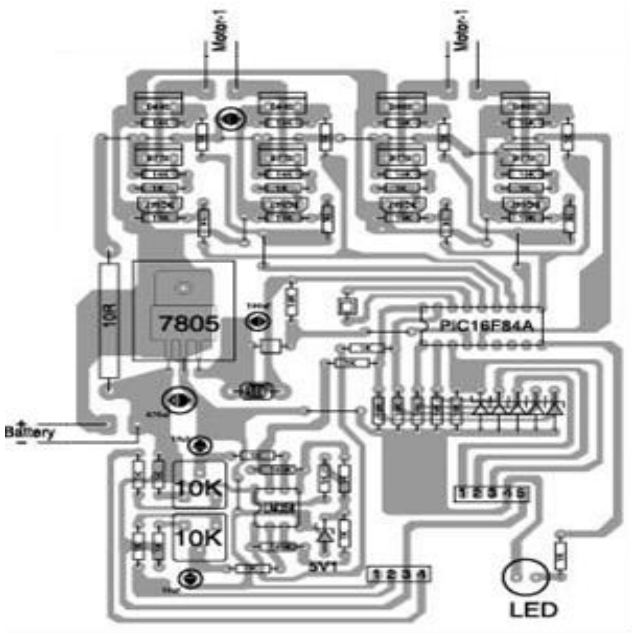

Fig. 13. Front part of the PCB layout

5.2 Physical Construction

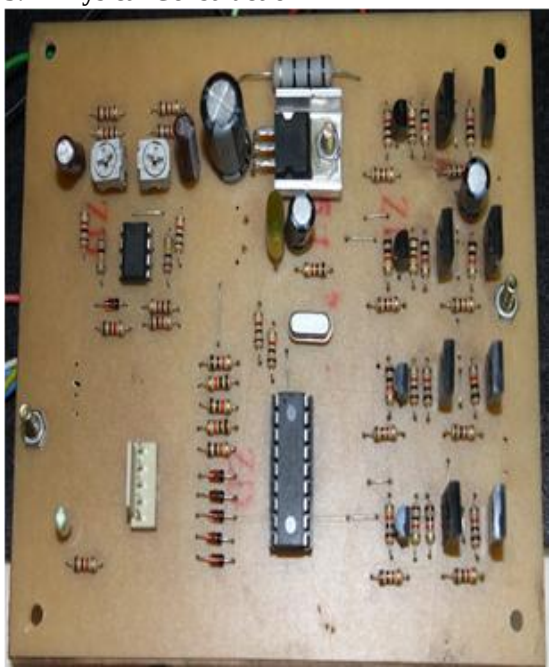

Fig. 14. Physical construction

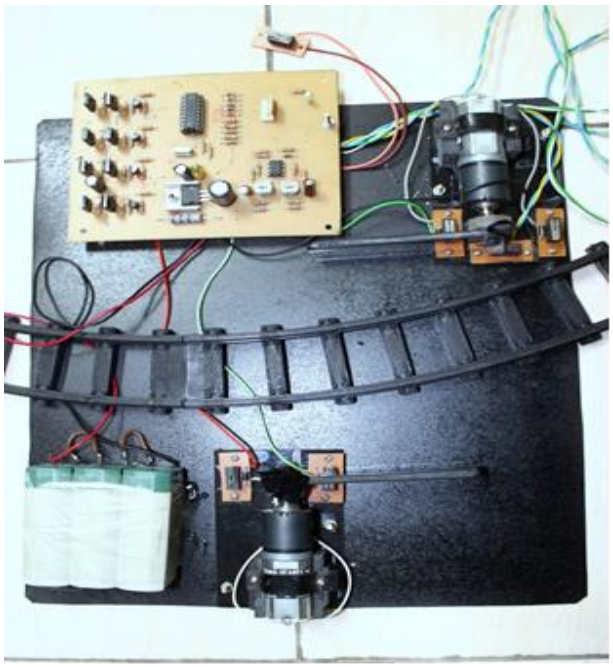

Fig. 15. Physical construction

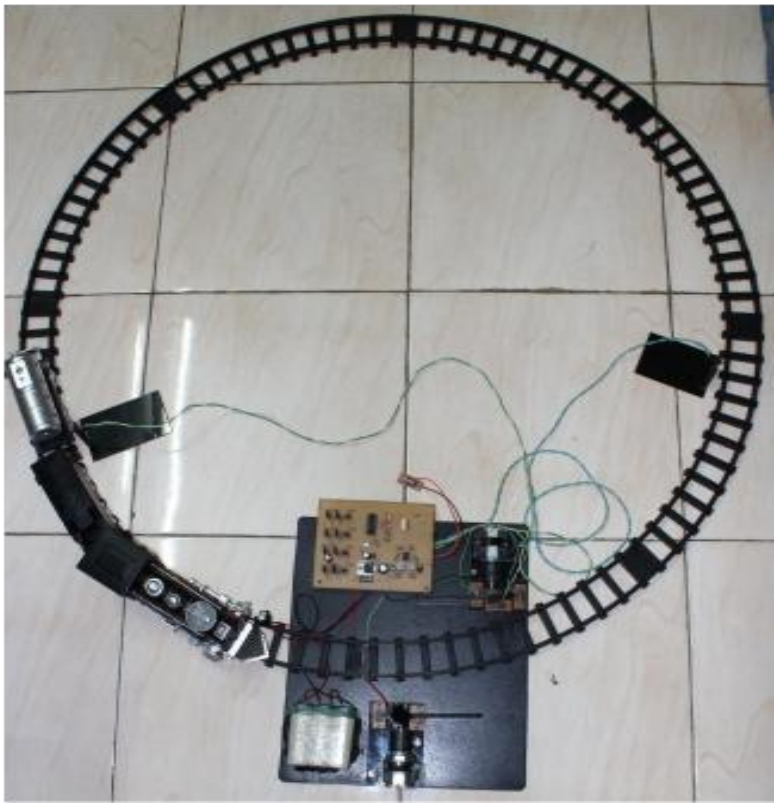

Fig. 15. An automatic railway gate control

The above Fig. 13 and Fig.14 present the physical of the actual implemented hardware. Fig. 15 is the total design prototype and it also shows how the pressure sensed automatic gate control system will be placed.

VI. CONCLUSION

The pressure sensed anti-collision system for an automatic railway gate control is developed to reduce the loss of death and injuries for the human at the level crossing of the rail-line. An automatic system is more reliable than a manual system. That's why this project is very much effective and efficient considering the safety of the human life. In this project, all the apparatus were handled safely to avoid unexpected short circuit. The novelty of this project is the safety of the human life at the level crossing of the railway.

VII. FUTURE WORK

There are many scopes to improve this project in future. If we overlook the whole project we can get the idea of using RF module instead of using wire for the transmission of signal. Another improvement of this project could be the sector of pressure switch. Instead of using this, a high-tech load sensor could be used so that it could give the actual rating of the vehicle that gets stuck at the level crossing. So, it is expected that more works will be done on relevant project in near future.

VIII. ACKNOWLEDGEMENTS

The authors acknowledge the department of Electrical and Electronic Engineering, American International University – Bangladesh for giving permission to access equipment's and work in Microprocessor and I/O System Lab, Control System Lab and Analog Electronics Lab and also express their special thanks to the authorities of Bangladesh Railway (BR) for preparing the proposed model.

APPENDIX

```
:020000040000FA
:1000000083161F3085000030860083128501860128
:10001000051C0B280E28851C08281128A0308600F6
:1000200008285030860005 1D0828851D082808303E
:0C00300086008519192850308600082829
:00000001FF
```

REFERENCES

[1] Atul Kumar Dewangan, Meenu Gupta, Pratibha Patel, "Automation of Railway Gate Control Using Microcontroller", International Journal of Engineering Research & Technology (IJERT), ISSN: 2278-0181, Vol. 1 Issue 3, May – 2012

[2] Santosh B. Patil, Rupal M. Walli, "Design and Development of Fully Automatic AT89C52 Based Low Cost Embedded System for Rail Tracking", International Journal of Electronics, Communication & Soft Computing Science and Engineering (IJECSCSE), Volume 1, Issue 1, February 2012.

[3] Ahmed Salih Mahdi, Al-Zuhairi, "Automatic Railway Gate and Crossing Control based Sensors & Microcontroller", International Journal of Computer Trends and Technology (IJCTT), Volume 4, Issue 7, July 2013

[4] Daniel D. Frey, Assistant Professor, Kevin N. Otto, Associate Professor, Stan Taketani, "Manufacturing Block Diagrams and Optimal Adjustment Procedures", Journal of Manufacturing Science and Engineering, Volume 123, Issue 1, October 1999.

[5] Sanchez, G.A.; Carlos, G.O., "A low-cost control system for hydraulic applications," ANDESCON, 2010 IEEE , vol., no., pp.1,5, 15-17 Sept. 2010. doi: 10.1109/ANDESCON.2010.5631888

[6] Ćika, D.; Grundler, D., "Proteus Virtual System Modelling used for microcontroller education," MIPRO, 2010 Proceedings of the 33rd International Convention , vol., no., pp.1034,1038, 24-28 May 2010.

[7] Bo Su, Li Wang, "Application of Proteus virtual system modelling (VSM) in teaching of microcontroller", IEEE 2010 International Conference on E-Health Networking, Digital Ecosystems and Technologies (EDT), (Volume:2), ISBN- 978-1-4244-5514-0, 375 – 378.

[8] Ahmed M. A. Haidar, Chellali Benachaiba, Mohamad Zahir, "Software Interfacing of Servo Motor with Microcontroller", Journal of Electrical Systems, Volume 9, Issue 1, September 2013, 84 – 99.

American Journal of Engineering Research (AJER)
e-ISSN : 2320-0847 p-ISSN : 2320-0936
Volume-02, Issue-11, pp-174-184
www.ajer.org

Research Paper Open Access

Modeling, Simulation and Optimization of Hybrid Renewable Power System for Daily Load demand of Metropolitan Cities in India

Balachander Kalappan, Dr. Vijayakumar Ponnudsamy
[1](Research Scholar, Karpagam University, Coimbatore, India)
[2](Department of Electrical and Electronics Engineering, Kathir College of Engineering, Coimbatore, India)

Abstract: **-** Demand for energy is increasing day by day because of increasing the residents and industrialization. In this critical stage of energy crisis, renewable energy is one of the most important substitute energy sources. Electricity consumption in India has more than doubled in the last decade, outpacing economic growth. The paper presents a study and design of a complete hybrid renewable power system model for day to day load demand of Metropolitan cities in India. The optimized renewable energy power systems for four different locations are presented. The possible sources of powers are photovoltaic and wind turbine system and two possible storage systems are a battery bank and a hydrogen storage fuel cell system. The proposed power system is photovoltaic-wind system. The sizing, optimization and economic estimation of the systems were performed using HOMER software. HOMER solves the optimization problem to minimize the total cost and provides the optimum photovoltaic, wind turbine, battery and fuel cell ratings. In addition, a comparison between the three different suggested power system configurations is illustrated in details.

Keywords: **-** *Optimization, Modeling, Simulation, Net present cost, Homer, Sizing*

I. INTRODUCTION

India's significant and sustained economic growth is placing enormous demand on its energy resources. However, there is a pervasive demand-supply imbalance that necessitates serious efforts by the government of India to augment energy supplies. The country imports about 80 percent of its oil. With the threat of a further increase in oil prices, serious problems with regard to energy security is anticipated. India also runs the substantial risk of lesser thermal capacity being installed. While dependence on imported coal is increasing, supply of indigenous coal is likely to decrease in the coming years because of production and logistic constraints [1]. Economic growth, increasing prosperity and urbanization, rise in per capita consumption, and spread of energy access are the key factors that would be responsible for substantially increasing the total demand for electricity. Thus there is an emerging energy supply-demand imbalance. According to a Central Electricity Authority report, the anticipated energy and peaking shortage in the country is estimated to be 10.3 percent and 12.9 percent, respectively, in 2011 and 2012.

Renewable energy can make a substantial contribution in each of the above mentioned areas. It is in this context that the role of renewable energy needs to be seen. It is no longer "alternate energy", but is increasingly becoming a vital part of the solution to the nation's energy needs. In terms of all renewable energy categories, India is currently ranked fifth in the world with 15,691.4 MW grid connected and 367.9 MW off-grid renewable-energy based power capacity [1].

This paper proposes three different renewable energy system models for four different locations in India.

II. SYSTEM SPECIFICATIONS

2.1 Homer

HOMER (Hybrid optimization model for electric renewable) Simulation simulates the operation of a system by making energy balance calculations for each of the 8,760 hours in a year. For each hour, HOMER

compares the electric and thermal load in the hour to the energy that the system can supply in that hour. For systems that include batteries or fuel-powered generators, HOMER also decides for each hour how to operate the generators and whether to charge or discharge the batteries. If the system meets the loads for the entire year, HOMER estimates the lifecycle cost of the system, accounting for the capital, replacement, operation and maintenance, fuel and interest costs [2].

2.2 Study Locations

An Indian metropolitan cities was taken for the study.

Chennai (Latitude 13° 04' N, Longitude 80° 17' E) is the capital city of Tamil Nadu. Located on the Coromandel Coast of the Bay of Bengal. As of the 2011 census, the city had 4.68 million residents making it the sixth most populous city in India, the urban agglomeration, which comprises the city and its suburbs, was home to approximately 8.9 million, making it the fourth most populous metropolitan area in the country [4].

Kolkata (Latitude 22° 57' N, Longitude 88° 36' E) is the capital of West Bengal. Located on the east bank of the Hooghly river. As of 2011, the city had 4.5 million residents; the urban agglomeration, which comprises the city and its suburbs, was home to approximately 14.1 million, making it the third-most populous metropolitan area in India. Kolkata confronts substantial urban pollution, traffic congestion, poverty, overpopulation, and other logistic and socioeconomic problems [4].

Mumbai (Latitude 19° 07' N, Longitude 72° 87' E) is the capital of Maharashtra. It is the most populous city in India, and the fourth most populous city in the world, with a total metropolitan area population of approximately 20.5 million. Mumbai lies on the west coast of India and has a deep natural harbor [4].

Delhi (Latitude 28° 63' N, Longitude 77° 22' E), officially the National Capital Territory of Delhi (NCT) that includes the Indian capital is the largest metropolis of India. With the population of 16.7 million in 2011. There are nearly 22.2 million residents in the greater NCR urban area, which includes the neighboring cities of Baghpat, Gurgaon, Sonepat, Faridabad, Ghaziabad, Noida and Greater Noida along with other smaller nearby towns [4].

2.3 Load Profile

A typical electrical load system shown in Table I for single residence has been considered for load analysis. For a particular residence we consider a fluorescent light, fan, television, compact disc player, computer, water heater and other small loads. In HOMER made a 24 hours load profile for a single home [2]. If we consider an average load demand of all locations are same. The total electrical load demand for the residence is 2kWh / day, 350W peak. Fig. 1 Shows the daily load profile a small base load of 100W

TABLE 1 LOAD DETAILS OF SINGLE HOME USER

Appliances	**Number**	**Wattage**
Florescence light	2	20
Fan	1	80
TV	1	100
CD Players	1	80
Computer	1	150
Water Heater	1	150
Others	2	50
Total capacity		630

occurs throughout the day and night. Small peaks of 300W occur at morning and at night, while the majority of the load occurs in the evening.

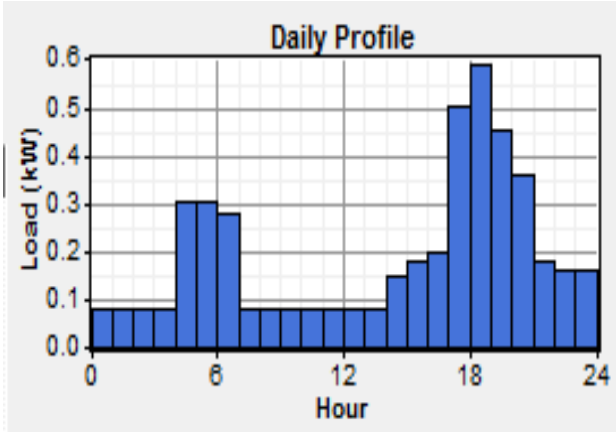

FIG. 1.DAILY LOAD PROFILE

The evening load, with a peak load of 600 W, would likely include fluorescent lighting, television load, fan, computer and audio system.

2.4 System Components

2.4.1 Photovoltaic (PV)

Solar energy is the most promising of the renewable energy sources in view of its apparent unlimited potential. The sun radiates its energy at the rate of about 3.8 x 1023 kW per second. Most of this energy is transmitted radially as electromagnetic radiation which comes to about 1.5kW/m2 at the boundary of the atmosphere. After traversing the atmosphere, a square meter of the earth's surface can receive as much as 1kW of solar power, averaging to about 0.5 over all hours of daylight. Solar radiation data for the study regions was obtained from Synergy Environmental Engineers (India) Private Limited web site. The Synergy Environmental Engineers (India) Private Limited has been monitoring solar radiation data in India at for the last many years. Monthly clearness index and radiation data is shown in table II [5].

TABLE 2 MONTHLY CLEARNESS INDEX AND RADIATION DATA

City / Month	Chennai		Kolcutta		Mumbai		Delhi	
	A*	B**	A*	B**	A*	B**	A*	B**
Jan	0.581	4.93	0.663	4.67	0.698	5.32	0.602	3.66
Feb	0.636	5.89	0.604	4.9	0.728	6.25	0.638	4.65
Mar	0.659	6.64	0.589	5.54	0.726	7.05	0.66	5.85
Apr	0.637	6.72	0.527	5.51	0.701	7.38	0.659	6.76
May	0.577	6.12	0.5	5.5	0.674	7.33	0.638	7.08
Jun	0.498	5.24	0.315	3.51	0.516	5.64	0.58	6.6
Jul	0.45	4.73	0.323	3.56	0.46	5	0.512	5.74
Aug	0.457	4.8	0.351	3.73	0.483	5.12	0.513	5.4
Sep	0.492	5.01	0.352	3.43	0.568	5.65	0.564	5.25
Oct	0.467	4.42	0.477	4.04	0.644	5.72	0.685	5.3
Nov	0.471	4.06	0.62	4.5	0.689	5.38	0.68	4.31
Dec	0.539	4.42	0.663	4.43	0.686	5	0.623	3.55
Ave	0.539	5.248	0.499	4.443	0.631	5.903	0.613	5.346

*Clearness index **Radiation

2.4.2 Wind turbine system

The energy available in the wind depends on the density and air velocity. The density, as any other gas, changes with the temperature and pressure which varies with the high level of the sea. The energy of a mass of air which is displaced is determined by the Kinetic Energy (K.E) flux [2]. The hub height of the wind turbine system is 10m. Wind speed details of study areas are shown in table III [5].

TABLE 3 MONTHLY WIND SPEED DATA

City / Month	Chennai	Kolcutta	Mumbai	Delhi
Jan	4.87	1.63	3.84	2.77
Feb	4.46	2.00	4.66	3.13
Mar	4.45	2.27	5.10	3.46
Apr	4.49	3.10	5.62	3.87
May	4.86	3.15	5.67	4.02
Jun	5.52	2.87	5.64	4.11
Jul	5.30	2.56	6.46	3.39
Aug	5.24	2.19	5.84	2.91
Sep	3.83	2.01	4.05	2.85
Oct	3.56	1.43	3.48	2.16
Nov	4.56	1.57	3.41	1.83
Dec	5.28	1.54	3.45	2.40
Ave	4.702	2.193	4.768	3.075

2.4.3 Fuel cell

Hydrogen storage Fuel Cell (FC) is available in different configurations, power ranges, type of electrodes and operating characteristics. Proton Exchange Membrane (PEM) FC has a good start up and shut down characteristics. The basic structure of PEM fuel cell has two electrodes (anode and cathode) separated by a solid membrane. In the hydrogen storage system, surplus renewable power goes to an electrolyzer which produces hydrogen. Hydrogen goes into a storage tank to be consumed by the fuel cell when required. Hydrogen fuel is fed continuously to the anode and air is fed to the cathode [3].

2.4.4 Electrolyzer and Hydrogen Tank

Hydrogen can be produced by the decomposition of water into its elementary components by passing the electric current. An electrolyzer consists of several cells connected in series. Two electrodes of the electrolyzer are separated by an aqueous electrolyte or solid polymer electrolyte. Electrical current through the electrolyzer enables the decomposition of water into hydrogen and oxygen. The hydrogen tank stores hydrogen produced by the electrolyzer for later use in a hydrogen-fueled generator. Homer assumes that the process of adding hydrogen to the tank requires no electricity, and that the tank experiences no leakage [3].

2.4.5 Battery

Battery bank is a conventional approach to store electrical energy with high efficiency. Its discharging level cannot exceed a minimum limit defined as depth of discharge. The capacity of the battery is so designed so as to supply the ultimate load during the non-wind hours.

2.5 System Control

Homer model, the system control inputs define the operation of the battery bank and generators and dispatch strategy determines how the system charges the battery bank Fig. 2). The control strategies have been selected to see which is more suitable in the given constraints of the system. The simulation time step is 60 minutes and set point charge for the batteries is at 80% [2].

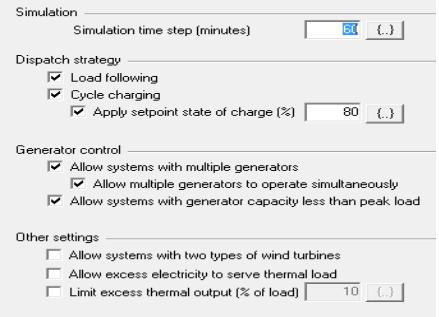

Fig. 2 System control inputs

2.6 Economics

Our plan is to minimize the total net present cost (NPC) and the optimal system configuration. Homer applies the economic inputs (Figure 3) to each system it simulates to calculate system's net present cost.

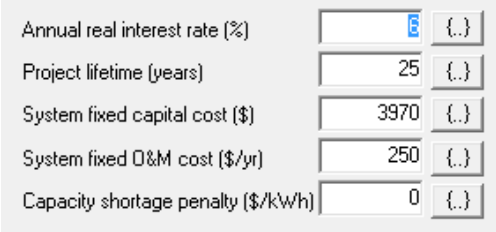

Fig. 3 System economic inputs

2.7 System constrains

The constraints (Figure. 4) are conditions that system meet to be feasible. Infeasibility systems do not include operating in the sensitivity and optimization analysis [2].

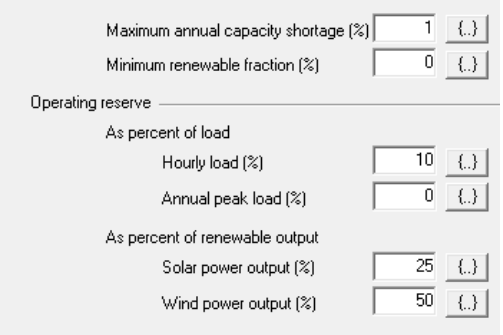

Fig. 4 System constraints

III. METHODOLOGY

The proposed hybrid renewable system (Fig. 5) consists of a photovoltaic and wind turbine system. Hydrogen storage fuel cell, electrolzer and battery are back-up and storage system. The project lifetime is estimated at 25 years. The annual interest rate is fixed at 6%.

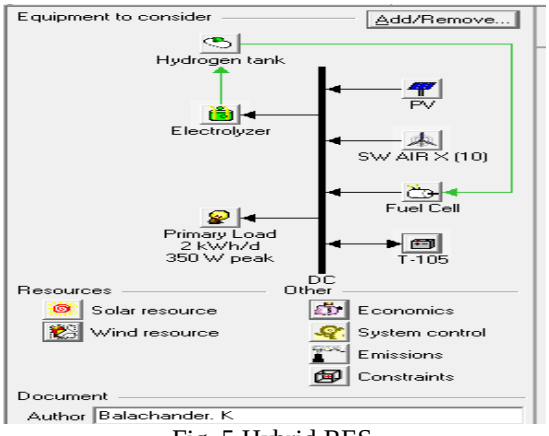

Fig. 5 Hybrid RES

IV. SIMULATION

In this paper we consider four metropolitan cities in India i.e. Chennai, Kolkata, Mumbai, New Delhi and load condition is 2KWh/day 350W peak for simulation. Components to be considered for stand-alone Photovoltaic Wind Hybrid Power System and storage medias are a Battery bank and a Hydrogen storage Fuel Cell system is shown in table IV.

TABLE 4 COMPONENTS ASSESSMENT

Component	Parameter	
PV Array	Rated power	1KW DC
	Derating factor	90%
	Slope	23°
	Life time	20Years
Wind turbine	***SW AIR X***	
	Rated power	0.55kW DC
	Hub height	15m
	Life time	15Years
Electrolyzer	Rated power	1KW DC
	Life time	15Years
	Efficiency	76%
Hydrogen tank	Size	1Kg
	Life time	25Years
Fuel cell	Rated power	1KW DC
	Life time	40000 operating hrs
	Fuel	Stored Hydrogen
Battery	***Trojan T-105***	
	Nominal capacity	225Ah
	Nominal voltage	6V
	Batteries per string	1 (6V Bus)
	Float life	10Years
Load	***Primary Load***	
	Type of Load	2kWh/Day 350W peak DC

HOMER performs the simulation for a number of prospective designed configurations. After examining every design, it selects the one that meets the load with the system constraints at the least life cycle cost. HOMER performs its optimization and sensitivity analysis across all mentioned components and their resources, technical, cost parameters, system constraints and sensitivity data over a range of exogenous variables [2]. Table V and VI shows the cost summary of the overall system and cost analysis of the three different Renewable Energy System (RES) options are compared regarding the least-cost scenario.

TABLE 5 COST SUMMARY

Component	Rating	Cost (INR)
PV Panel	1kW	306000
Wind Turbine	0.55kW	76500
Electrolyzer	1kW	102000
Hydrogen Tank	1Kg	66300
Fuel Cell	2kW	153000
Battery	6V, 225Ah	6120

Table 6 Cost Analysis of 3 RES and 3 different locations

Cost / Location	Chennai		
	RES 1	RES 2	RES 3
System Combination	Pv, Bat	Pv, wind, Bat	Pv, Fc, Bat, Ele
Initial Capital (Rs.)	435,030	425,850	537,030
Operating Cost (Rs./yr)	17,901	18,972	17,544
Total Net Present Cost (Rs.)	663,714	668,610	761,022

Cost of energy (Rs./kWh)	71.15	71.96	81.60
Cost / Location	**Calcutta**		
	RES 1	***RES 2***	***RES 3***
System Combination	Pv, Bat	Pv, wind, Bat	Pv, Fc, Bat, Ele
Initial Capital (Rs.)	496,230	511,530	598,230
Operating Cost (Rs./yr)	18,411	20,910	18,054
Total Net Present Cost (Rs.)	731,901	779,025	829,209
Cost of energy (Rs./kWh)	78.44	83.49	88.84
Cost / Location	**Mumbai**		
	RES 1	***RES 2***	***RES 3***
System Combination	Pv, Bat	Pv, wind, Bat	Pv, Fc, Bat
Initial Capital (Rs.)	410,550	450,330	512,550
Operating Cost (Rs./yr)	17,799	20,400	17,442
Total Net Present Cost (Rs.)	638,265	710,838	735,573
Cost of energy (Rs./kWh)	68.90	76.30	79.41
Cost / Location	**New Delhi**		
	RES 1	***RES 2***	***RES 3***
System Combination	Pv, Bat	Pv, wind, Bat	Pv, Fc
Initial Capital (Rs.)	435,030	450,330	537,030
Operating Cost (Rs./yr)	17,901	20,400	17,544
Total Net Present Cost (Rs.)	663,714	710,838	761,022
Cost of energy (Rs./kWh)	71.25	76.25	81.70

Pv – Photovoltaic array Wind - Wind turbine System
Bat – Battery Fc – Fuel Cell

Table 7 Electrical Production

Components	**Chennai**		
	RES 1 **(**Pv,Bat**)**	***RES 2*** (Pv, wind, Bat)	***RES 3*** **(**Pv, Fc**)**
PV(kWh/Yr)	1,055	703	1,055
Wind(kWh/Yr)	-	538	-
Total	1,055	1,241	1,055
Components	**Calcutta**		

	RES 1 (Pv,Bat)	***RES 2*** (Pv, wind, Bat)	***RES 3*** (Pv, Fc)
PV(kWh/Yr)	1,511	1,133	1,511
Wind(kWh/Yr)	-	149	-
Total	1,511	1,282	1,511
Components	**New Delhi**		
	RES 1 (Pv,Bat)	***RES 2*** (Pv, wind, Bat)	***RES 3*** (Pv, Fc)
PV(kWh/Yr)	1,175	783	1,175
Wind(kWh/Yr)	-	147	-
Total	1,175	930	1,175
Components	**Mumbai**		
	RES 1 (Pv,Bat)	***RES 2*** (Pv, wind, Bat)	***RES 3*** (Pv, Fc)
PV(kWh/Yr)	1,114	743	1,114
Wind(kWh/Yr)	-	152	-
Total	1,114	895	1,114

V. OPTIMIZATION

For the single residential load demand of metropolitan cities in India, various combinations have been obtained of hybrid systems with photovoltaic, wind turbines, fuel cell, batteries and converters from the HOMER Optimization. Sensitivity analysis eliminates all infeasible combinations and ranks the feasible combinations taking into account uncertainty parameters [2].

HOMER allows taking into account future developments, such as increasing or decreasing load demand as well as changes regarding the resources, for example fluctuations in the river's water flow rate, wind speed variations or the biodiesel prices. In this model the various sensitive variables are considered to select the best suited combination for the hybrid system to serve the load demand [2].

	PV (kW)	AIR	FC (kW)	T-105	Elec. (kW)	H2 Tank (kg)	Disp. Strgy	Initial Capital	Operating Cost ($/yr)	Total NPC	COE ($/kWh)	Ren. Frac.	Capacity Shortage	FC (hrs)
	0.6			8			CC	$ 8,530	351	$ 13,014	1.395	1.00	0.00	
	0.4	1		4			CC	$ 8,350	372	$ 13,110	1.411	1.00	0.01	
	0.6		0.4	8	0.4		CC	$ 10,530	344	$ 14,922	1.600	1.00	0.00	0
	0.4	1	0.4	4	0.4		CC	$ 10,350	365	$ 15,018	1.616	1.00	0.01	0
		3		12			CC	$ 9,910	532	$ 16,704	1.795	1.00	0.00	
		2	0.4	4	0.4	2	LF	$ 12,050	430	$ 17,552	1.886	1.00	0.00	724
	0.6	1	0.4		0.6	2	CC	$ 14,070	506	$ 20,537	2.201	1.00	0.00	4,900
		3	0.4		0.6	3	CC	$ 14,770	626	$ 22,767	2.452	1.00	0.01	5,523
	1.5		0.4		0.6	2	CC	$ 17,970	505	$ 24,428	2.618	1.00	0.00	5,187

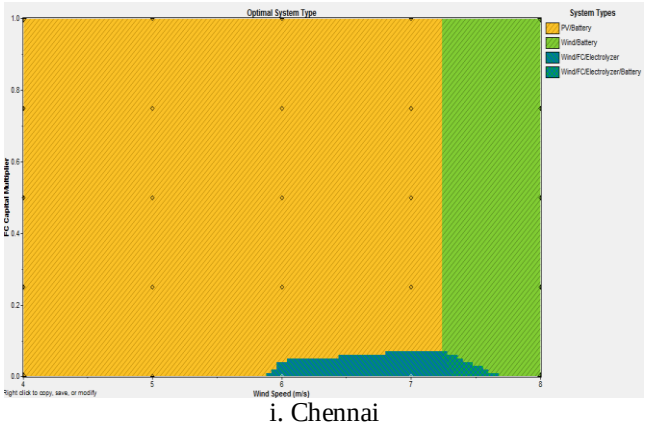

i. Chennai

Figure 6 shows the sensitivity analysis and optimal system type for four metropolitan cities in India. It can be observed that with change in the sensitive variables, the configuration of the system changes. Even in this analysis, HOMER ranks the configurations in descending order of

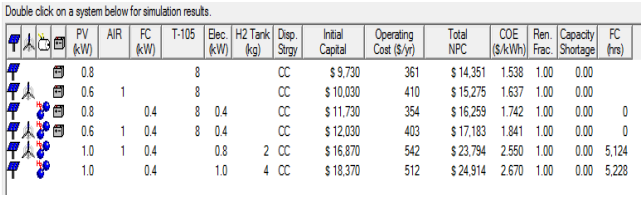
Double click on a system below for simulation results.

PV (kW)	AIR	FC (kW)	T-105	Elec. (kW)	H2 Tank (kg)	Disp. Strgy	Initial Capital	Operating Cost ($/yr)	Total NPC	COE ($/kWh)	Ren. Frac.	Capacity Shortage	FC (hrs)
0.8			8			CC	$ 9,730	361	$ 14,351	1.538	1.00	0.00	
0.6	1		8			CC	$ 10,030	410	$ 15,275	1.637	1.00	0.00	
0.8		0.4	8	0.4		CC	$ 11,730	354	$ 16,259	1.742	1.00	0.00	0
0.6	1	0.4	8	0.4		CC	$ 12,030	403	$ 17,183	1.841	1.00	0.00	0
1.0	1	0.4		0.8	2	CC	$ 16,870	542	$ 23,794	2.550	1.00	0.00	5,124
1.0		0.4		1.0	4	CC	$ 18,370	512	$ 24,914	2.670	1.00	0.00	5,228

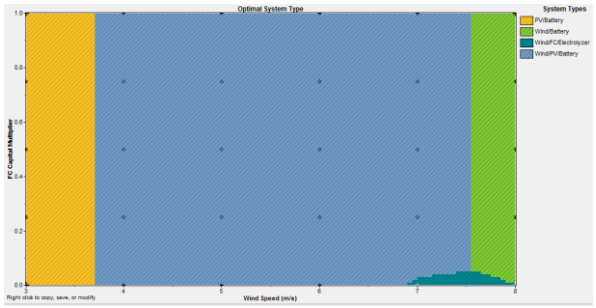

ii. Calcutta

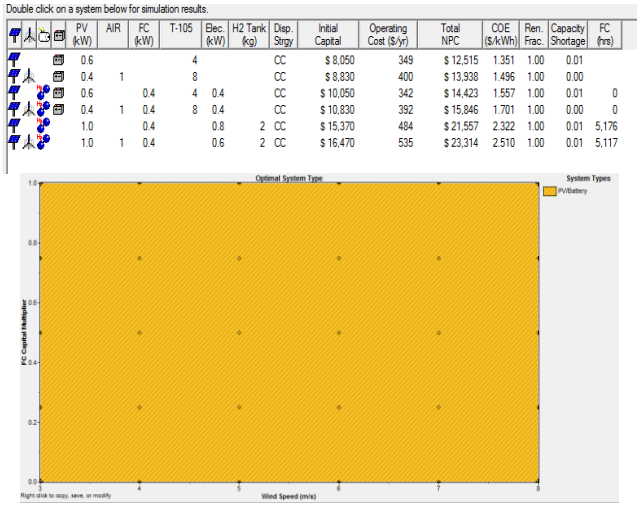
Double click on a system below for simulation results.

PV (kW)	AIR	FC (kW)	T-105	Elec. (kW)	H2 Tank (kg)	Disp. Strgy	Initial Capital	Operating Cost ($/yr)	Total NPC	COE ($/kWh)	Ren. Frac.	Capacity Shortage	FC (hrs)
0.6			4			CC	$ 8,050	349	$ 12,515	1.351	1.00	0.01	
0.4	1		8			CC	$ 8,830	400	$ 13,938	1.496	1.00	0.00	
0.6		0.4	4	0.4		CC	$ 10,050	342	$ 14,423	1.557	1.00	0.01	0
0.4	1	0.4	8	0.4		CC	$ 10,830	392	$ 15,846	1.701	1.00	0.00	0
1.0		0.4		0.8	2	CC	$ 15,370	484	$ 21,557	2.322	1.00	0.01	5,176
1.0	1	0.4		0.6	2	CC	$ 16,470	535	$ 23,314	2.510	1.00	0.01	5,117

iii. New Delhi

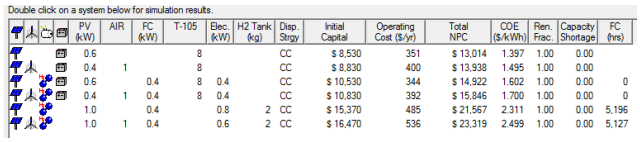
Double click on a system below for simulation results.

PV (kW)	AIR	FC (kW)	T-105	Elec. (kW)	H2 Tank (kg)	Disp. Strgy	Initial Capital	Operating Cost ($/yr)	Total NPC	COE ($/kWh)	Ren. Frac.	Capacity Shortage	FC (hrs)
0.6			8			CC	$ 8,530	351	$ 13,014	1.397	1.00	0.00	
0.4	1		8			CC	$ 8,830	400	$ 13,938	1.495	1.00	0.00	
0.6		0.4	8	0.4		CC	$ 10,530	344	$ 14,922	1.602	1.00	0.00	0
0.4	1	0.4	8	0.4		CC	$ 10,830	392	$ 15,846	1.700	1.00	0.00	0
1.0		0.4		0.8	2	CC	$ 15,370	485	$ 21,567	2.311	1.00	0.00	5,196
1.0	1	0.4		0.6	2	CC	$ 16,470	536	$ 23,319	2.499	1.00	0.00	5,127

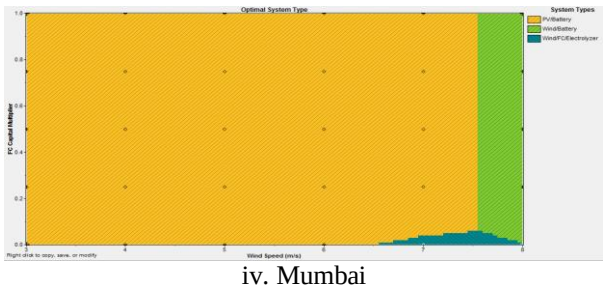

iv. Mumbai

Fig. 6 I, ii, iii and iv Sensitivity analysis and Optimal system solution of Metropolitan Cites in India

their total net present cost. The feasible system and economical details of all the configurations of the hybrid systems from the optimization process are shown (Fig. 6). The above optimum results confirmed that the proposed stand alone hybrid system will be able to provide for the power to the DC load of 2KWh/day 350W Peak, constantly right through the year.

VI. RESULTS AND CONCLUSION

After analyzing the simulation, one can suggest that for higher loading stand-alone PV-Battery System is most suitable, for supplying the power to the DC load. The simulation result suggests that this Hybrid system is most suitable for all locations and result suggests that from the different possible configuration, one can choose the better

Table 8 Cost of Energy

Locations	Cost of Energy (INR)
Chennai	71.15
Mumbai	68.90
Kolcutta	78.44
New Delhi	71.25

optimal solution and the cost of energy production is calculated for Chennai, Mumbai, Kolcutta and New Delhi (Table. 8). It can be concluded that for loading condition of 2KWh/day, 350W Peak.

REFERENCES

[1] The Potential for Renewable Energy in India – 2012, Gyan Research and Analytics Pvt. Ltd., 2012 pp.1-7

[2] Lambert, T., Gilman, P., Lilienthal, P. (2005) 'Micro-power System modelling with Homer', in Farret, F.A., Godoy Simões, M. (eds), *Integration of alternative sources of energy*, pp. 379 - 417

[3] Munuswamy, S., Nakamura, K., Katta, A. (2011) 'Comparing the cost of electricity sourced from a fuel cell-based renewable energy system and the national grid to electrify a rural health centre in India: A case study', *Renewable Energy* 36, pp. 2978 - 2983 hhtp//. Wikipedia.com Synergy India website

[4] Givler, T., Lilienthal, P., (2005) 'Using HOMER® Software, NREL's Micropower Optimization Model, To Explore the Role of Gen-sets in Small Solar Power Systems Case Study: Sri Lanka', Technical Report NREL/TP-710-36774, available from http://www.osti.gov/bridge

[5] Kaundinya, D.P., Balachandra, P., Ravindranath, N.H. (2009) 'Grid-connected versus stand-alone energy systems for decentralized power—A review of literature', Renewable and Sustainable Energy Reviews 13, pp. 2041–2050

[6] Integrated Energy Policy: Report of the Expert Committee, Government of India, Planning Commission, New Delhi, August 2006

[7] Bossi, C., Del Corono, A., Scagliotti, M., and Valli, C. 2007. Characterization of a 3 kW PEFC Power System coupled with a metal Hybrid H2 Storage Science direct, pp. 122-129.

[8] Ajao K.R and Adegun I.K (2009). Development and Power Performance Test of a Small Three-Blade Horizontal-Axis Wind Turbine. Heat Transfer Research, Vol. 40, No. 8, pp.777-792

[9] Markvart. T, "Sizing of Hybrid Photovoltaic-Wind Energy systems," Solar Energy vol. 57 (4), pp. 277-281, 1996.

[10] McGowan J.G., Manwell J.F., Avelar C., Warner C.L., "Hybrid wind/PV/Diesel Hybrid power systems modeling and South American applications" , WREC 1996,

[11] Borowy, B.S. & Salameh, Z.M., Optimum Photovoltaic Array Size for a Hybrid Wind/PV System, IEEE

[12] http://www.synergyenviron.com/

[13] Antoni Dmowski., Piotor Biczel., and Bartlomiej Kras. 2001. Hybrid solar panel fuel cell power plant. 11 2001, pp. 22-23.

[14] Nelson, D. B., Nehrir, M. H., and Wang, C. 2006. Unit Sizing of Stand-Alone Hybrid Wind/PV/Fuel power Generation systems. Renewable energy 31:1641-1656.

[15] E. G. Potamianakis, C. D. Vournas, "Modeling and Simulation of Small Hybrid Power Systems", to appear in IEEE Power Tech, Bologna Italy, June 2003.

[16] K. Akella, M. P. Sharma, R. P. Saini, Optimum utilization of renewable energy sources in remote area, Renewable and Sustainable Energy Reviews vol. 11, pp. 894–908, 2007.

[17] Katti, P.K., Khedkar, M.K. (2007) 'Alternative energy facilities based on site matching and generation unit sizing for remote area power supply', Renewable Energy 32, pp. 1346–62

[18] Lagorse, J., Paire, D., Miraoui, A. (2009) 'Sizing optimization of a stand-alone street lighting system powered by a hybrid system using fuel cell, PV and battery', Renewable Energy 34, pp. 683–91
[19] http://www.windenergysolutions.nl/
[20] Hellenic ministry of evelopment (http://www.ypeka.gr).
[21] Demiroren and U. Yilmaz, Analysis of change in electric energy cost with using renewable energy sources in Gökceada, Turkey: An island example, Renewable and Sustainable Energy Reviews vol. 14, pp. 323–333, 2010.
[22] Rajoriya and E. Fernandez, Sustainable energy generation using hybrid energy system for remote hilly rural area in India, International Journal of Sustainable Engineering vol. 3, pp. 219–227, May 2010.
[23] B.E. Türkay and A. Y.Telli, Economic analysis of standalone and grid connected hybrid energy systems, Renewable Energy vol. 36, pp. 1931–1943, 2011.
[24] Photovoltaic Geographical Information System (PVGIS), 2008. Available from http://re.jc.ec.europa.eu/pvgis/.
[25] GNTO Greek National Tourism Organisation (http://www.visitgreece.gr/portal/site/eot)
[26] E.D. Giannoulis and D. A. Haralambopoulos, Distributed generation in an isolated grid: Methodology of case study for Lesvos – Greece, Applied Energy vol. 88, pp. 2530–2540, 2011.
[27] G. N. Prodromidis and F. A. Coutelieris, A comparative feasibility study of stand-alone and grid connected RESbased systems in several Greek Islands, Renewable Energy vol. 36, pp. 1957–1963, 2011.
[28] J. K. Kaldellis, D. Zafirakis, E. Kondili, Optimum sizing of photovoltaic-energy storage systems for autonomous small islands, Electrical Power and Energy Systems vol. 32, pp. 24–36, 2010.

Balachander Kalappan[1] received the B.E. degree in Electrical and Electronics Engineering from Coimbatore Institute of Technology, Barathiyar University, Coimbatore, in 2001, the M.E. degree in VLSI Design from Anna University of Technology, Coimbatore, in 2009 and he is currently pursuing the Ph.D. degree in Electrical and electronics from the Karpagam University, Coimbatore. His research interests include Renewable Energy, Smart Grid and Micro Grid. He is having 10 years of Industrial Experience in Erection and Commissioning of Textile machineries .

Dr. Vijayakumar Ponnusamy[2] obtained his Masters Degree ME (Applied Electronics) from PSG College Technology in 2002. He is currently with Kathir College of Engineering, Coimbatore, India. He had totally around 11 years of teaching experience. He was working in industry for about 7 years between 1992 and 1999. He has published around 10 National and International Journal papers besides 20 papers in Conference proceedings. His areas of interests are Low Power VLSI and Virtual Instrumentation.

American Journal of Engineering Research (AJER)
e-ISSN : 2320-0847 p-ISSN : 2320-0936
Volume-02, Issue-11, pp-185-194
www.ajer.org

Research Paper Open Access

Integrated Traffic Management in Banani

Azharul Islam, Md. Rokib Hasan, Ashikuzzaman
*1*Junior Engineer, City Region Development Project, MDSC,LGED*
2 Lecturer, Department of Civil Engineering, World University of Bangladesh, Dhaka
3 Junior Engineer, City Region Development Project, MDSC, LGED

***Abstract*: -** *In its traditional sense, traffic management is the science of extracting maximum capacity from existing roads. Roads and streets, particularly in the urban areas, suffer from numerous inhibiting factors that constrain their efficiency as traffic routes. Hence, the imposition of measures such as stopping and parking restrictions, junction-signalization and prohibition of particular traffic movements can increase traffic capacity and improve efficiency. Faster and more fluid traffic movements also save the cost. The study provides a technical assessment of integrated traffic management in Banani area of Dhaka Ward no. 19 which expressed support for better traffic management across the city, to help alleviate traffic congestion, provide safer pedestrian condition and better vehicle parking so that inhabitants of Banani get special benefits as well as nearby adjacent area.*

***Keywords:* -** *Existing Scenario, Traffic Management, Parking, Pedestrian, Road width*

I. INTRODUCTION

Integrated traffic management comprises the application of various techniques to make the best use of any given network of roads and streets in terms of balancing the needs of traffic flow [1] pedestrian activity and the environmental needs people living, working or playing alongside streets-or otherwise exposed to traffic in them. But the concept of integrated traffic management should not be confined to vehicular and pedestrian movement. Recent decades have witnessed increasing recognition of traffic environment impact: just ass roads have a theoretical traffic capacity, so too do they have an environmental capacity. This may be quantified in terms of acceptable maximum levels of pedestrian delay, noise, traffic vibration and local pollution. Managing demand can be a cost effective alternative to increasing capacity [2]. Certainly, an integrated traffic management scheme can improve economic efficiency by eliminating or reducing time lost in traffic, but it can make urban places safer and more liveable, which are surely measures of efficiency in any civilized society. Despite their logic, these ideas may seem inapplicable in a city such as Dhaka- where many people resignedly accept that motor traffic must inevitably move noisily and incoherently from one snarl to the next. Whereas it is easy to criticize the pro-road in Dhaka, it is regrettably an opinion that is still widely held, even in advanced economics [3]. Usually traditional philosophy of predict (more traffic) and provide (more road space) is giving way to alternative methods of dealing without movement. A question that may be asked is whether it is actually possible to upgrade Banani into a well-ordered community. Whereas the precedents are not encouraging, there is one that can be found within a short walk of Banani itself. Dhaka Cantonment area is a model of well ordered community, sidewalks, road markings, traffic signs and other representative of the type of proposal made in this report.

II. LITERATURE REVIEW AND BACKGROUND

Several researches had been conducted on the integrated traffic management system. The World Bank has conducted a range of traffic movement management improvements with Dhaka City Corporation (DCC), including strategic junction improvement and comprehensive traffic management at district level [4]. Intermodal surface Transportation Efficiency has conducted post modal transportation act in 1991[5]. International Integrated Systems, Inc has conducted Advanced Urban Traffic Management System (AUTMS) is traffic control platform that aims to improve comprehensive urban traffic network [6]. Gary Hui investigated on Urban

Traffic Management and Control strategies [7]. An integrated traffic management system will soon be introduced in Chennai city on a BOT (build, operate and transfer) basis under the annuity model [10]. A critical integration point of IBM Intelligent Transportation is the gathering of traffic and event data from other traffic center systems and field devices based on the increasingly popular Traffic Management Data Dictionary (TMDD) standard [11]. Integrated Traffic Management Systems (ITMS) need reliable, accurate, and real-time data [12].

2.1 Background: The Sub-Project is focused on central Banani, comprising streets within an area Defined by New Airport Road to the west, Banani Lake to the east, Kamal Ataturk Avenue to the north and Banani Road 11 to the south (Figure 1 refers).

Figure 1: The Banani Study Area

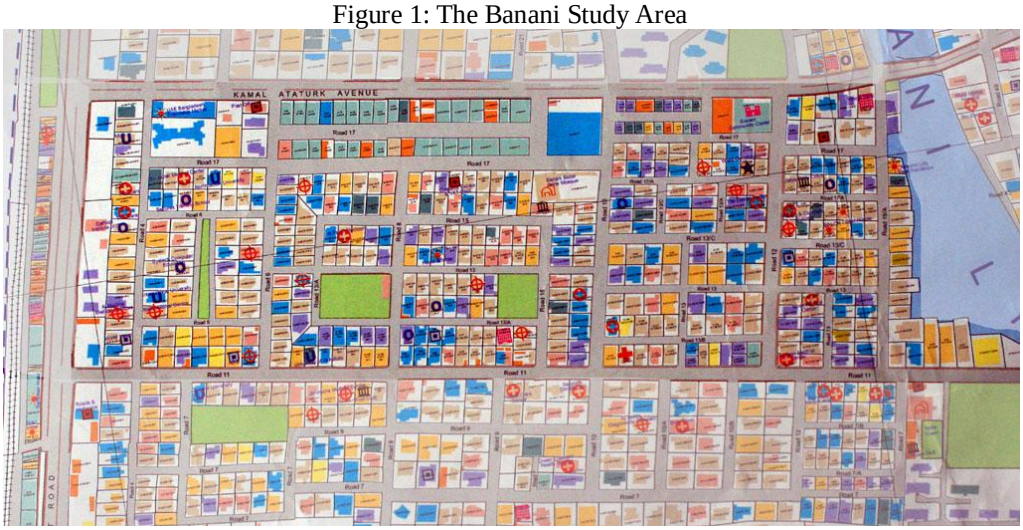

The Study Area is highlighted on this map, as a part of Dhaka's Ward19.

Selection of central Banani for a "pilot" District Traffic Management scheme (from the four areas listed above) responds to a number of factors/problems which can be ameliorated as a result of comprehensive and integrated planning and investment: They are:

• Serious and increasing levels of traffic congestion in a largely uncontrolled environment;
• Largely uncontrolled road junctions and cross roads, resulting in significant traffic delays and occasional grid-locking;
• Degraded road surfaces restricting road traffic flows;
• Uncontrolled and haphazard vehicular parking, adding to traffic congestion and pedestrian hazards;
• Arrogant and uncontrolled driver behavior adding to levels of traffic congestion and pedestrian hazards, particularly at road junctions;
• The lack of a pedestrian footpaths and facilities (eg pedestrian crossings) resulting in very uncomfortable and hazardous pedestrian environment;
• Largely uncontrolled use of the area by through traffic adding to the levels of traffic congestion and resulting in the deterioration of the predominantly residential environment;
• Increasing building densities and largely uncontrolled commercial uses are exacerbating unsustainable levels of traffic congestion in the area; and
• Significant deterioration of the landscaped residential environment

. The character of the land uses and the traffic in central Banani are representative of the rest of the Banani area, the whole of the Gulshan 1 and 2 areas and Dhanmondi. To this extent the pilot scheme proposals can be applied in a District Traffic Management scheme within central Banani will be readily transferable across all four areas and in other similar districts elsewhere in the Dhaka City Region, such as Uttara. In selecting central Banani, the close links between the area and the rest of Gulshan are such that the Banani scheme could be the first part of a Traffic Management Master Plan for whole Gulshan (1 and 2) and Banani. This would not only benefit residents and businesses over a wide area, it would also facilitate an approach to transport planning and traffic management, which would facilitate the wider application of the principles for multi-modal contained in the Dhaka Strategic Transport Plan. For instance the medium-long term potential to introduce mass-transit systems into the area will facilitate better local public transport feeding into mass transit hubs, and the opportunity to reduce the scale of private transport in residential streets, thus leading to a more sustainable environment. To this extent the adaptability and flexibility in the detailed design of the "pilot" scheme for central Banani is important. Many of the principles to be used in a District Traffic Management scheme for central Banani would

also be capable of being adapted in areas, which may have different land use and traffic characteristics, be they in the Dhaka City Region or elsewhere. For instance the need for transport planning measures to prevent unnecessary through traffic and the need to provide better pedestrian segregation will be constants in most districts. Of particular interest in the September 2005 *Urban Transport Policy* is the 'Pedestrians
First, policy that sought to construct properly designed and continuous footpaths and to launch a pedestrian awareness program within a road safety program [8]. In summary, every plan and policy for transport in Dhaka within the last decade has referred to the need to apply traffic management techniques, to improve the pedestrian environment and to manage travel demand.

2.2 Situation Analysis:

Banani is a mainly residential area of north Dhaka, clearly bounded to its west by the busy dual-four lane New Airport Road. Banani Lake defines its eastern border, whilst the area itself is bisected by two east-west roads that effectively split it into three 'character areas'. The most capacious of these roads is Kamal Ataturk Avenue, a divided highway that connects New Airport Road with the district centre of Gulshan 2 Circle. Banani Road 11 provides the other east-west route. Until quite recently this road terminated eastwards at the edge of Banani Lake, but the construction of the Gulshan-Banani Bridge and its link roads on the Gulshan side have transformed Banani Road 11 into a heavily-trafficked thoroughfare. The 'Study' comprises the centremost, busiest and densest of Banani's three character areas, situated between Kamal Ataturk Avenue and Road 11. On first acquaintance, this locality (the 'Study Area') gives a favourable impression of tree-lined avenues. The main development type is residential flats, typically rising to the maximum permitted six storeys (although this limit now appears to have been relaxed to eight storey). Commercial premises now dominate Road 11, whilst along the Study Area's northern edge several buildings reach as high as 20 storeys –, lining the southern side of Kamal Ataturk Avenue and two parallel streets, both known as Road 17. Of these, Road 17(2) is flanked by high-rise buildings to either side. These premises accommodate several universities, corporate offices and one substantial hotel. The overall width of Road 17(2) is generous, but much is lost to such functions as right angled car parking, construction material dumps and food stalls. Other roads in the north also serve commercial functions, including the whole southern side of Kamal Ataturk Avenue.

Thorough inspection reveals barely-concealed vices all over the Study Area. Everywhere, it is apparent that redevelopment is advancing vigorously. Flats have almost entirely replaced single-family houses, whilst apartment blocks are themselves being demolished to make way for alternatives with greater earning-potential (typically by making replacements taller, increasing their plot ratio or changing their use to commercial or mixed developments). Indeed, non-residential uses are scattered everywhere, with educational and medical premises being particularly commonplace. Shops, boutiques, and guest houses are also spread throughout the area.

In the south of the Study Area, Road 11 is largely commercialised, with shops, banks, restaurants and a hotel. Traffic is particular intense along this road, not only because it is used as a through-route but also because of numerous parking and 'un-parking' activities and a tendency for vehicles to make three-point turns in the road. The road must once have been a quiet local distributor, but it was transformed into a major through-route when the Gulshan-Banani Bridge was opened. The result of this (doubtlessly well-intentioned) innovation is an overwhelming traffic environment where pedestrians cross the road at great peril and where the cacophony of horns and rickshaw bells persists throughout day and late into the night. Impenetrable vehicular congestion often blights the road as through-traffic contests its right of passage with cars trying to reverse from angle-parked positions on shop and restaurant forecourts. The road is a source of stress to its users, signified by the eruption of unpleasant episodes amongst drivers, rickshaw pullers and pedestrians.

The Study Area is no haven for the urban poor, although there is a noteworthy slum on the west bank of Banani Lake, near the Gulshan-Banani Bridge. Even so, many poor people throng Banani's streets, and there is an undeniable fusion of private affluence and public squalor. The superficially-attractive tree-lined avenues are thronged with cars, vans and rickshaws, whilst their surfaces are often rutted. Every street was once *pucca* (metalled) but incessant traffic and erosion by monsoon rains have stripped several sections of their black-top layer. Hence some street-sections are *semi-pucca* (with crushed brick surfaces) and others are merely *katcha* (earth surfaced). There are few sidewalks, and where they survive, most are unusable because of uneven surfaces and such obstacles as hawker stalls, heaps of construction materials and discarded refuse and vegetation. At the time of writing Road 11 revealed the impact of sewer works, with open gullies and innumerable holes puncturing its residual sidewalks. Pedestrian conditions are very bad: most access roads within the Study Area lack any form of sidewalk. Indeed, the most common form of street comprises a narrow central strip of *pucca* road bordered to either side by *katcha* 'sidewalks' that suffer from numerous obstructions. Walking in the Study Area reveals that the pedestrian is regarded with contempt by every type of mechanised road user, leading at best to prolonged delays and at worst to an omnipresent risk of injury. Additional perils emerge after sunset: street lighting is variously inadequate, switched off, or absent altogether. Traffic conditions

vary by street and time of day. Some streets are thronged by rickshaws, both moving and congregated by the dozen in the hope of winning customers. Rickshaws are permitted on all streets except Kamal Ataturk Avenue, although this stricture does not necessarily mean that they cannot be found there. Motor vehicles are commonplace, and the Study Area's general income level indicates that car ownership may be several times greater than in Dhaka generally. The only road in the Study Area that carries recognizable public buses is Kamal Ataturk Avenue, although the service is infrequent compared with that on New Airport Road and some other bus corridors. There is a general absence of the traffic signs, road markings and street furniture that could otherwise guide, warn or control traffic. Apart from traffic signals at the junction of Kamal Ataturk Avenue and New Airport Road, there are no traffic signals within the Study Area. Likewise, there are no Give Way lines or lane-divider markings. One junction, namely at roads 10 and 11, regularly benefits from a traffic policeman, whilst elsewhere doormen (who are employed by hotels and businesses) venture into the traffic to assist pedestrians and customers trying to park or un park their cars. Other than a few businesses and apartment blocks that benefit from dedicated car parks, there is no formal parking provision within the Study Area. Cars may be parked randomly at the roadside, but the most common arrangement is right-angle parking, which both reduces the available road width for traffic and impedes pedestrian movement.

III. METHODOLOGY

The Study area covers the Central Banani area. Every road is listed in Table 1, which includes basic information on its characteristics. The traffic and pedestrian conditions in Central Banani are shown in Figure 2 The Study Area covers 32 ha and contains 8.76 km of roads (including the bordering roads of Kamal Ataturk Avenue and Road 11). Roads were originally set out in a hierarchical fashion. Kamal Ataturk Avenue is a district distributor, whilst Road 11 has assumed a similar role, despite being totally unsuited to such a function.8 Several north south roads serve as local distributors, even though the available carriageway widths are quite inadequate for the task. All east-west roads (other than Kamal Ataturk Avenue and Road 11) are local access roads: some are very narrow and several lack metal surfaces.

Traffic mainly comprises cycle-rickshaws, pedal-cycles, saloon cars and 4WD vehicles. Private vehicles are numerous because many local residents and visitors can afford to own and use them. Buses, personnel carriers and motor cycles are rare and lorries only appear at night (unless they are employed on construction projects). Pedestrian activity is quite intense, and comprises residents, workers, shoppers, students, pedlars, beggars and the homeless.

Figure 2: Traffic and Pedestrian Conditions in the Banani Study Area

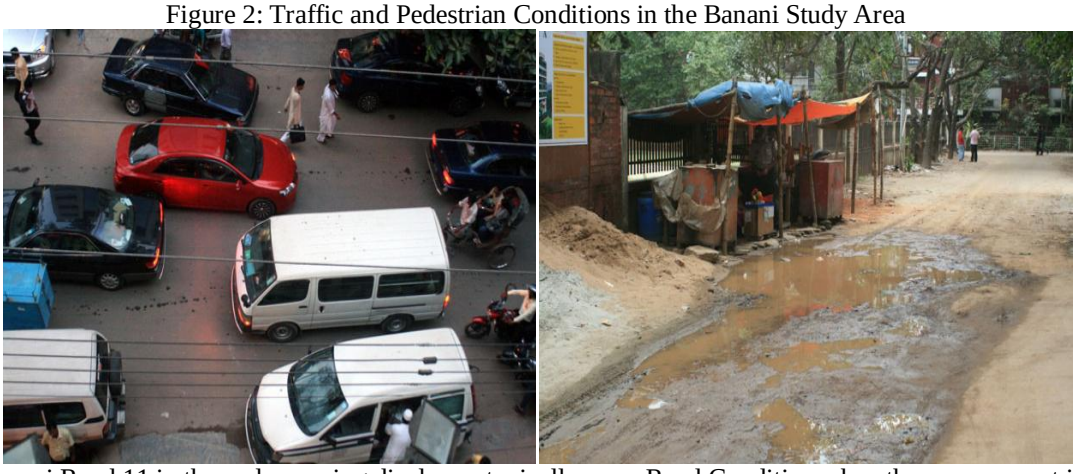

Banani Road 11 in the early evening displays a typically anarchic mixture of vehicles and pedestrians jostling for supremacy.

Road Condition when the monsoon set in.

3.1: Data Collection

- Information on representative traffic flows
- Interview data on travel origins and destinations
- Inventories of vehicles based within the Study Area
- An appraisal of street lengths, widths and conditions,
- Surface and sub-surface drainage arrangements, and
- An assessment of utilities equipment (mains, sewers, gas supply and power cables and telecommunications wires);

The Table 1 is given below for the road information of Banani Area

Road	Length (m)	Width (m)	Remarks
KAA	933	2 x (12/14)	District distributor, dual carriageway, commercial frontages.
4	322	4.5/7.5	Narrow road used as N-S local distributor, commercial frontages. Some *katcha* surface.
6(0)	322	6/15	Relatively narrow road used as N-S local distributor. Some *katcha* surface.
6(1)	144	6/12	Residential E-W access road.
6(12)	122	5.5/7.5	Residential minor N-S access road, residential.
6(2)	144	5.5/8.5	Residential E-W access road.
6(21)	122	5.5/7.5	Residential minor N-S access road, residential. Some *katcha* surface.
8	233	7.5/15	N-S local distributor, commercial frontages.
10	322	6/15	N-S local distributor, mixed (shop house) frontages. *Katcha* surface at southern end
11	1172	9/21	E-W local distributor used as district distributor. Worst pedestrian and traffic conditions of any road in Banani.
12	322	6/18	N-S local distributor, commercial frontages.
13(0)	389	4.5/9	Residential E-W access road, narrow usable carriageway.
13(1)	194	4.5/7.5	Residential E-W access road, narrow usable carriageway.
13(2)	128	5.5/12	Residential E-W access road, narrow usable carriageway.
13(3)	161	5.5/14	Residential N-S access road, narrow usable carriageway
13(4)	100	5.5/14	Residential N-S access road, narrow usable carriageway
13/A(1)	266	4.5/10.5	Residential E-W access road, narrow usable carriageway. Some *katcha* surface.
13/A(2)	128	4.5/7.5	Residential N-S access road, narrow usable carriageway.
13/A(3)	67	7.5/10.5	Residential N-S access road, reasonably wide carriageway.
13/B	194	4.5/12	Residential E-W access road, narrow usable carriageway, *semi-pacca* and *katcha* surface.
13/C(1)	200	6/20	Residential E-W access road, reasonably wide carriageway.
13/C(2)	122	5.5/12	Residential E-W access road, reasonably wide carriageway.
13/C(3)	61	3.5/10.5	Residential N-S access road, very narrow usable carriageway.
15(1)	266	7.5/18	Residential E-W access road, reasonably wide carriageway.
15(2)	233	9/18	Residential N-S access road, wide carriageway.
17(1)	144	10.5/17	E-W access road, educational activity, many pedestrians, wide carriageway.
17(2)	305	12/24.5	E-W access road, canyon-like street between tall buildings (commercial, educational, hotel). Seriously degraded street.
17(3)	389	7.5/21	E-W access road, tall buildings to north (commercial, educational, hotel). Seriously degraded street: just over a third of its width is available for traffic.
17(4)	200	7.5/15	E-W access road, mainly commercial to north side.
17(5)	111	4.5/17	Residential E-W access road, narrow usable carriageway.
17/A(1)	194	7.5/18	Residential E-W access road, reasonably wide carriageway.
17/A(2)	117	3/7.5	Residential E-W access road, very narrow carriageway.
19/A	339	6/14	Residential N-S access road, narrow usable carriageway. Blockaded during site visit because of construction works.
UNR(1)	83	15/24.5	Short, relatively wide N-S commercial connector.
UNR(2)	111	12/17	Shopping street with tall frontages to both sides; heavily trafficked.
UNR(3)	56	12/17	Very wide N-S connector alongside open air car park.
UNR(4)	44	7.5/9	Short, relatively wide N-S residential connector.
Notes: KAA= Kamal Ataturk Avenue, UNR=Un-named road, N-S= North South, E-W= East-West			

3.2 Way of Traffic Management

1) Developing a *Traffic Management Master Plan*;
2) Designing requisite infrastructure to incorporate all relevant proposals for subsurface drainage and utility provisions, surface drainage, sidewalks, road reconstruction and surfacing, car parking provision, and any other appropriate requirements;
3) Devising suitable traffic management measures to improve traffic flow by the use of one-way streets, junction improvements, parking restrictions, road markings, traffic signs, traffic signals and other relevant techniques;
4) Giving particular consideration to the present incompatible 'vehicle mix' to identify dedicated routes for rickshaws and the best role that thelas might play in freight distribution within the traffic management task. This exercise should also review the contribution made by public buses and determine the scope for better services on Kamal Ataturk Avenue, plus a possible new service of small buses along Road 11 after its refurbishment;
5) Developing solutions that would give particular help to pedestrians, such as the provision of decent sidewalks, the identification of preferred pedestrian routes, pedestrian crossings along roads and at intersections, and pedestrian-only streets and shared surfaces;
6) Identifying the scope for travel demand management (TDM) to reduce vehicular travel within the Study Area, with special regard to discouraging the use of local roads as 'rat runs' and to reduce the traffic overload on Road 11;
7) Examining development controls within town planning practice to establish whether they are sufficiently robust or suitably applied to prevent the over development' of streets within the Study Area. Given the potential for a surfeit of traffic to be generated by 'overheated' development, developers in future should be required to submit traffic impact assessments (TIAs) from reputable and authorized traffic consultants;
8) Seeking the views of local residents and business people about the proposed integrated traffic management scheme, and incorporating their opinions as appropriate; and
9) Developing a participatory environment to enable local residents and business people to be active in the implementation and ongoing monitoring and enforcement of the proposed District Traffic Management scheme.

3.3 Upgrading the Public Realm

When the integrated traffic management scheme is implemented, the public realm will be primarily affected. Activities will necessarily include:

1) Preparing a *Landscape Master Plan* to support improvements to the public realm, including the provision of identity and visual quality, and specifying locations for hard and soft landscaping;
2) Designing a 'toolbox' of measures to assist pedestrians including: (i) discrete pedestrian footpaths and other areas, physically separated and protected from road vehicles; (ii) traffic calming in support of pedestrian comfort; and (iii) landscape and shade in the pedestrian environment;
3) Specifying that road openings for the reconstruction and relocation of utility services must include replacement (subsurface) drains and connections to properties, plus (ideally) the 'undergrounding' of telecom wires and power cables that currently sag into the public realm;
4) Fully rehabilitating the streets within the Study Area, using materials appropriate to the intended function of the street (black-top asphalt would not be appropriate– for example – in a pedestrian zone); and
5) Providing traffic signs, road markings and other traffic management aids, together with street lighting and other street furniture and landscaping, both hard and soft.

IV. RESULTS AND DISCUSSIONS

The Traffic Management scheme for central Banani is may be noted that all but two of the major and minor roads have been made into one-way streets. All but three of the local distributors have also been made one-way, the exceptions being Roads 8, 10 and11. However, Road 11 has a one-way eastbound section towards its western end to discourage through traffic, in combination with the prohibition of the right-turn northbound from New Airport Road. Vehicular access has been maintained in Road 11 for the benefit of frontage traders, but consideration could be given to pedestrianising the central section of Road 11 between its junctions with Roads 6(0) and 10. However, it is proposed to wholly pedestrianise one street (Road 17(1)), which serves university premises and which is heavily thronged with pedestrians at most times. The internal one-way system has been proposed because it will make the roads safer for vehicles and pedestrians and it will also lengthen journey times within the Study Area, thereby discouraging drivers seeking short-cuts and rat-runs. Consideration was given to converting some streets into *culs de sac*. However, this would require them to be wide enough to carry two-way traffic and to accommodate turning circles or hammer heads at their sealed ends. Whereas such possibilities could be considered if this Project Component is advanced to detailed design, they have not been

defined here. Careful attention has been given to road and footway widths. Reference was made to contemporary British standards for local distributors and major and minor access roads. However, whilst the British terminology has been retained in Tables 2 and 3, compromises have been made with the dimensions. It should be appreciated that the British standards are relatively generous, and apply to 'new build' roads in residential areas [9]. In the case of the Study Area, the roads already exist, and it was considered essential to accommodate the reconstruction works within the existing boundary lines set by building frontages. Bearing this stricture in mind, road widths were developed on the assumption that a one-way lane should be able to accommodate a lorry 2.8 meters wide (over rear-view mirrors) plus a rickshaw with a width of about 1.2 metres: thus the minimum width for a lane designed to cope with both lorries and rickshaws would be 4.0 metres, which is wider than the international standard of 3.5 meters (or 3.0 meters in constricted situations). However, the Consultant recognizes that in some situations there would not be space to accommodate 4.0-metre lanes, and that in any case the widest vehicles (lorries) are time-restricted, whilst few rickshaws would be running during lorry-operating hours. Bearing such considerations in mind, the width requirements shown in TABLE 2 were developed for guidance purposes.

Table 2: Proposed road footway widths

Road Classification	Width	Remarks
Local distributor (two-way)	8.5m	May be reduced to 7.0 m if wide vehicles or rickshaws are prohibited.
Local distributor (one-way)	4.5m	May be reduced to 4.0 m where frontage constraints apply.
Major access road (two-way)	7.0 m	Scope for reduction not recommended.
Major access road (one-way)	4.0 m	May be reduced to 3.5 m in extreme situations.
Minor access road (two-way)	7.0 m	Possible scope for reduction to 6.0 m in constrained situations.
Minor access road (one-way)	3.5 m	May be reduced to 3.0 m in extreme situations.
Sidewalk (commercial and other high-activity streets)	3.0 m each side	May be expanded to 4.0 m or more where activity levels are high or where frontage positions allow.
Sidewalk (other streets)	2.0 m each side	May be reduced to 1.5 m where necessary or a single 3.0 m sidewalk may be provided on one side of the road only.
Car parking bay (parallel to the carriageway)	3.0 m	May be reduced to 2.5 m in constrained situations.
Rickshaw 'station'	3.0 m	Depending on space available, may be considered on north-south local distributor or major access roads at junction approaches with KAA and Road11.

Table 3 shows that most local access roads in the Study Area would be narrower than they are now. However, much potential space is currently lost to side friction and unused space. A narrower, safer road with proper sidewalks, planned on-street parking would greatly improve the character and operations in the Study Area. Redundant space could be properly landscaped, rather than becoming a dump for refuse and construction materials. Obviously, it will be important to enlist the co-operation of residents and business tenants to ensure that standards are maintained.

Table 3: Banani Study Area Traffic Management Proposals:

Road	Length (m)	Width (m)	Remarks
KAA	933	2 x (12/14)	As now, but with rebuilt sidewalks
4	322	4.5/7.5	Minor access road, one-way northbound. Sidewalk to one side only.
6(0)	322	4.5/8.5	Local distributor, one-way southbound.
6(1)	144	4.0/7.5	Major access road, one-way westbound.
6(12)	122	3.0/7.5	Minor access road, one-way northbound.
6(2)	144	4.0/7.5	Major access road, one-way eastbound.
6(21)	122	3.0/7.5	Minor access road, one-way southbound.
8	233	8.5/14.5	Local distributor, two-way, signals at junction with Road 11. Parallel parking can be permitted in bays 2.5 m wide.

10	322	8.5/14.5	Local distributor, two-way, signals at junction with Road 11 and KAA. Parallel parking can be permitted in bays 2.5 m wide.
11	1172	8.5/14.5	Local distributor, two-way, signals at junctions with Roads 8 and 10 and New Airport Road. One-way eastbound between Roads 6 and 10.
12	322	4.5/10.5	Local distributor, one-way, signals at junction with KAA, no right turn from Road 11 westbound. Parallel parking can be permitted in bays 2.5 m wide.
13(0)	389	4.5/9	Major access road, one-way eastbound.
13(1)	194	3.5/7.5	Minor access road, one-way westbound.
13(2)	128	3.5/7.5	Minor access road, one-way westbound.
13(3)	161	3.5/7.5	Minor access road, one-way eastbound.
13(4)	100	3.5/7.5	Minor access road, one-way southbound.
13/A(1)	266	3.5/7.5	Minor access road, one-way westbound.
13/A(2)	128	3.5/7.5	Minor access road, one-way northbound.
13/A(3)	67	3.5/7.5	Minor access road, one-way southbound.
13/B	194	3.5/7.5	Minor access road, one-way eastbound.
13/C(1)	200	3.5/7.5	Minor access road, one-way westbound.
13/C(2)	122	3.5/7.5	Minor access road, one-way westbound.
13/C(3)	61	3.5/7.5	Minor access road, one-way northbound.
15(1)	266	3.5/7.5	Minor access road, one-way eastbound.
15(2)	233	3.5/7.5	Minor access road, one-way southbound.
17(1)	144	15/15	Pedestrian street, shared surface type with block or sett surface dressing, residents' access only.
17(2)	305	4.0/24	Major access road, one-way eastbound, parallel parking can be permitted in bays 2.5 m wide. Remaining width to be pedestrianised.
17(3)	389	4.0/20	Major access road, one-way westbound, parallel parking can be permitted in bays 2.5 m wide. Remaining width to be pedestrianised.
17(4)	200	4.0/8.0	Major access road, one-way westbound.
17(5)	111	4.5/17	Minor access road, one-way westbound.
17/A(1)	194	7.5/18	Minor access road, one-way eastbound.
17/A(2)	117	3.5/7.5	Minor access road, one-way eastbound
19/A	339	4.0/8.0	Major access road, one-way southbound, no right turn at Road 11.
UNR(1)	83	7.0/13.0	Major access road, two-way.
UNR(2)	111	4.0/7.5	Major access road, one-way eastbound.
UNR(3)	56	7.0/13.0	Major access road, two-way.
UNR(4)	44	3.5/7.5	Minor access road, one-way southbound.
Notes: KAA= Kamal Ataturk Avenue, UNR=Un-named road, N-S= North South, E-W= East-West			

Figure 3: Traffic Management Diagram for the Banani Study Area

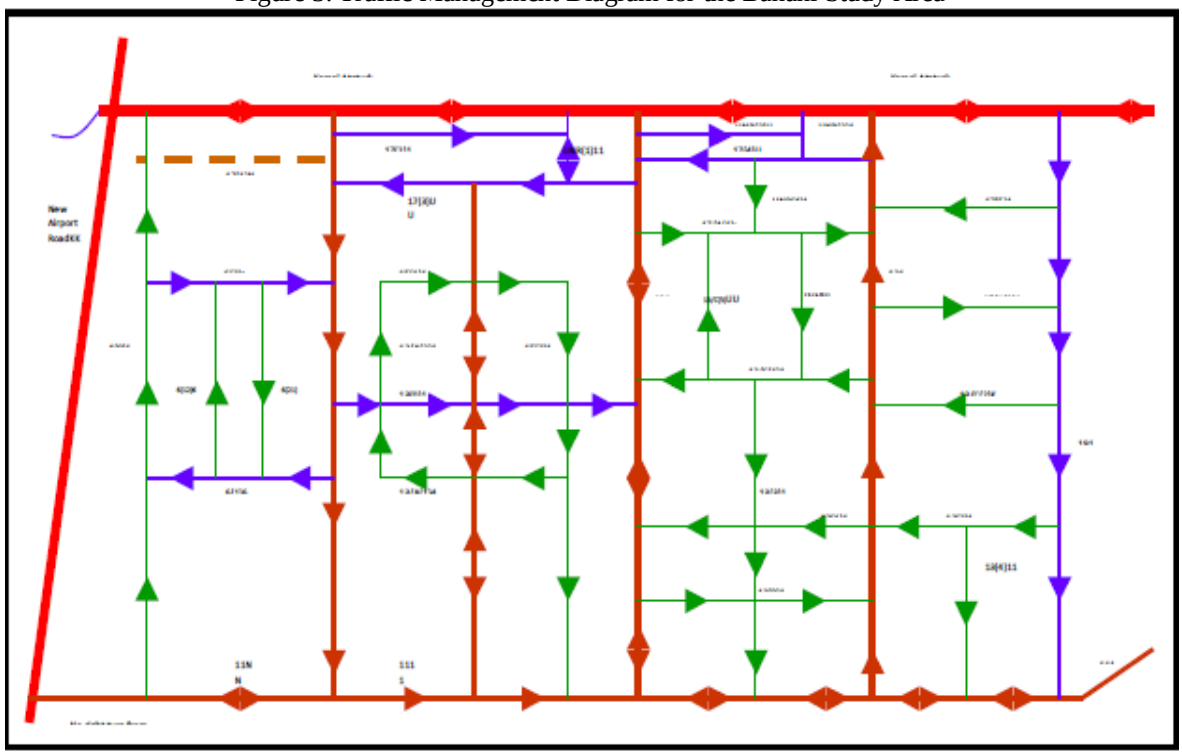

Figure 4: Conceptual Future Residential Road Cross- Section in Banani

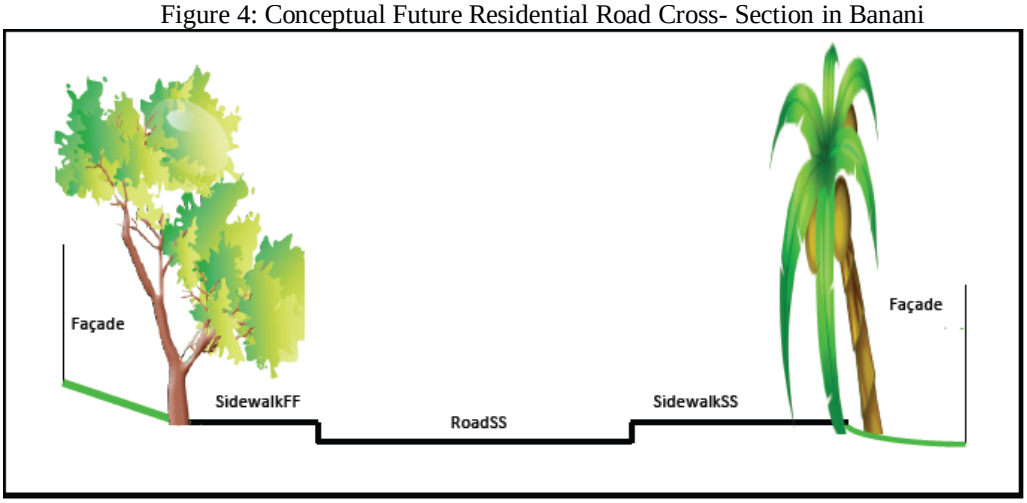

A cross section of a typical residential street in Banani as it might appear after upgrading as part of the integrated traffic management component.

V. CONCLUSIONS

The findings of this research can be an effective tool for Banani integrated traffic management system. The inhabitants of Banani would get the highest facilities as well as it might reduce the traffic congestion of surrounding area. As a result of this study traffic conflicts in the area of Banani will resolved and random parking will come in disciplined area. People will drive smoothly without traffic congestion. As a result of proper management system people will be attractive in this area, so economic benefits will be in good phase. Of course there has some limitations and difficulties for this study. For example the data collection was difficult due to non co- operative attitude of the respondents and the response rate of the people was low. More modern techniques to attract respondents to the surveys can be explored in future research. Further, the model created in this project is based on the survey, and it can be improved by studying other kind of models which might have better options.

VI. ACKNOWLEDGEMENT

The authors would also like to thank the people and driver of that area for their kind cooperation.

REFERNCES

[1] B. K. Banik, "Evaluation of Traffic Congestion in Sylhet City and Development of a Mathematical Model" *B.Sc. Engineering Thesis*, Department of Civil and Environmental Engineering, Shahjalal University of Science and Technology, Sylhet, Bangladesh, 2005.
[2] Travel Demand management (TDM)
[3] "Balanced transportation in Wisconsin is half concrete, half asphalt" John Norquist, Mayor of Milwaukee
[4] The World Bank Case Project will promote improvements to strategic road junctions in the DCC area.
[5] Intermodal Surface Transportation Efficiency Act (ISTEA) 1991
[6] International Integrated System, Inc
[7] Gary Hui "Intelligent Urban Traffic Management and Control Strategies
[8] Dhaka Transport Co-ordination Board (2005). Urban Transport Policy Final Report Dhaka, The Louis Berger Group,Inc, and Bangladesh Consultants Ltd.
[9] The Traditional British Terminology which has been adapted and updated in Bangladesh roads as Primary Secondary, Connector, Local and Narrow.
[10] "City to soon get integrated traffic management system" Times of India
[11] Build intelligent transportation systems with the Traffic Management Data Dictionary standard (TMDD).
[12] Ardeshir Faghri, Khaled Hamad Application of GIS in Transportation Management Systems in Springer link January 2002, Volume 5, Issue-3 pp 52-60, January 2002

American Journal of Engineering Research (AJER)
e-ISSN : 2320-0847 p-ISSN : 2320-0936
Volume-02, Issue-11, pp-195-203
www.ajer.org

Research Paper Open Access

Experimental Study on the Performance of a PCM-Based Solar Energy Storage System

Oluwaseun S. Alajo, Victor C. Ibekwe, Emmanuel C. Nsofor
[1]Graduate Research Assistant, [2]Undergraduate Research Assistant, [3]Associate Professor
Department of Mechanical Engineering & Energy Processes, Southern Illinois University, Carbondale, IL, USA

Abstract: - A vegetable-based PCM-based solar energy storage system capable of simultaneous energy utilization and energy storage was developed. The PCM is non-toxic, renewable, non-flammable and biodegradable. The system consists of a solar collector that transfers thermal energy to water circulated by a pump. The water flows through a heat exchanger in the PCM in a storage tank. Energy is thus transferred to the PCM which changes phase and stores thermal energy. Another pump circulates water through a secondary heat exchanger also enclosed in the PCM tank to recover energy. The system is designed to divert heated water to a liquid-to-air heat exchanger by means of a three-way valve. A fan blows air through one of the heat exchangers so that hot air for building heating can be obtained. Experimental studies performed show that more than half of the energy collected at the solar collector can be stored by the system irrespective of the season. Also, despite maximum energy losses to the surroundings, in the summer, the efficiency of energy storage by the system based on actual energy collected was found to be highest during this period. The types of fluid flow rates for best energy storage and recovery were identified.

Keywords: *– Solar energy storage, Experimental studies, Phase Change Material (PCM), System performance*

I. INTRODUCTION

Environmental problems, electricity deregulation, and anxiety over energy security are contributing to growing attention being paid to more solar energy utilization. However, because of intermittent supply and low concentration of solar energy which varies, depending on geographical location, the need for more research such as this continues to exist. Phase change materials (PCMs) have been found to be very useful in solar energy storage applications [1-4]. They can be classified as organic, inorganic or eutectic compounds and can store a lot of energy as latent heat compared to sensible heat storage materials.

Studies related to this one include an experimental study by Vikram et al. [5] on the feasibility and thermal behavior of solar water heating systems using encapsulated PCM as thermal energy storage medium. It concluded that the system was able to effectively store sufficient amount of water to meet the needs of a family of four. Ibanez et al. [6] studied the monetization of a new technology in which PCM modules were implemented in domestic hot water (DHW) tanks to reduce their sizes without reducing the energy stored. This was after demonstrating that the use of PCM in DHW tanks was feasible. The studies concluded that the PCM used in the study is powerful for evaluating the performance of PCM modules in water tanks. Al-Hinti et al. [7] used paraffin wax contained in small cylindrical aluminum containers packed inside a storage tank on two levels to study the use of water-phase change material storage in conventional solar water heating systems. The results from the study showed a 13°C to 14°C advantage in the stored hot water temperature over extended periods compared to a setup without PCM. The study also showed that the use of short periods of forced circulation had little effect on the system performance.

Haillot et al [8] investigated the effect of using a PCM medium in the solar collector of a DHW system. The results showed that the ratio of the amount of energy contributed by a solar energy system to the total energy required (solar fraction), decreases by PCM addition in the solar collector during the simulated winter months but increases during summer months if PCM is added to the collector of the system for the case of a solar tank volume. The conclusion was based on the limits of the tank volume used in the study.

In this present study, an experimental system was designed, constructed and used to investigate the performance (charging and discharging) of vegetable-based PCM applied to a solar energy storage system for air and water heating. Solar energy was applied in the system to power all the electrical components to ensure applicability of the system in parts of the world where electricity is not readily available. Energy storage is essential in solar energy utilization to cater for its intermittence. For residential buildings that depend on relatively big hot water tanks to keep up with demand, the application of PCM energy storage helps to reduce the size of the tank. Experimental studies performed, investigated the performance of the system leading to useful results and new design strategies for high-efficiency building energy utilization.

II. BASIC EQUATIONS USED IN THE SYSTEM DEVELOPMENT

The energy balance equation on the solar collector side [9] is:

$$\dot{Q}_{coll} = \eta G A_{coll} \quad (1)$$

where: $\eta = \eta_o - a\frac{(T_{avg} - T_a)}{G} - b\frac{(T_{avg} - T_a)^2}{G}$ (2)

In these equations, $\dot{Q}_{coll}$ = heat energy collected per unit time, η = efficiency of the solar collector, G= incident solar radiation on the collector, A_{coll} = solar collector absorber surface area η_o =collector efficiency constant, a, b = solar collector efficiency constant, T_{avg} = average temperature of water in the solar collector, T_a = ambient temperature.

Thermal properties of a PCM changes rapidly during a phase change. The enthalpy approach was used to analyze the heat transfer in the tank. The energy balance expression is:

$$(MC)_{pcm}\frac{dT_{pcm}}{dt} = \dot{Q}_{hx} - \dot{Q}_{losses} \quad (3)$$

where: $\dot{Q}_{hx} = \frac{1}{R_{hx}}(T_{co} - T_{pcm})$, $R_{hx} = \frac{ln\left(\frac{d_o}{d_i}\right)}{2\pi k_{hx} L_{hx}}$

$$\dot{Q}_{losses} = \frac{1}{R_{tot}}(T_{pcm} - T_a)$$

$$R_{tot} = \frac{ln\left(\frac{r_{to}}{r_{ti}}\right)}{2\pi k_t L_t} + \frac{ln\left(\frac{r_{ins}}{r_{to}}\right)}{2\pi k_{ins} L_t} + \frac{1}{2\pi r_{ins} L_t h_{air}}$$

The total energy stored in the PCM tank over a finite temperature difference is given as:

$$Q_{pcm} = (MC)_{pcm}\Delta T_{pcm} + m_{pcm} L \quad (4)$$

Using Euler integration method, the temperature derivative can be written as:

$$\frac{(T'_{pcm} - T_{pcm})}{\Delta t} \quad (5)$$

Solving for the PCM temperature at the end of a time increment gives:

$$T'_{pcm} = T_{pcm} + \frac{\Delta t}{(MC)_{pcm}}[Q_{hx} - Q_{losses}] \quad (6)$$

The expression for the energy recovery process is:

$$(MC)_{pcm}\frac{dT_{pcm}}{dt} = -\dot{Q}_{load} - \dot{Q}_{losses} \quad (7)$$

where $\dot{Q}_{load} = \dot{m}_{tank} C_{p,w}(T_{pcm} - T_{w,avg})$

The efficiency of the solar energy storage system can be obtained by the relation: $\eta_{sys} = \frac{Q_{pcm}}{Q_{coll}}$ (8)

The volumetric storage capacity is given by the equation:

$$volumetric\ storage\ capacity = C_p \times \rho \times \Delta T \times volume \quad (9)$$

In equation (9), C_p is the specific heat capacity of the liquid PCM, ρ is the density and ΔT is the temperature difference. These equations can be solved to obtain the hourly temperatures of the PCM and water in the hot water tank.

Figure 1 is a picture of the experimental system (view from the back of the solar collector). Different PCMs are available for use in latent heat storage applications. Some examples are salt hydrate, paraffin waxes, fatty acids and sugar alcohols [10]. The PCMs can be classified as organic compounds, inorganic compounds and eutectics. Important properties of PCMs that enhance thermal energy storage include high latent heat of fusion per unit mass and high specific heat. Disadvantages of PCMs include, low thermal conductivity, high

Figure 1. System setup (View from the back of the Solar Collector)

cost, being toxic and possessing flammability risks. Desired advantages include being chemically stable, non-toxic, and non-corrosive. Since sustainability is one of the focal points of this project, there was the need to select a PCM that is stable, non-toxic, non-flammable, renewable and biodegradable. The PCM used is a patented natural vegetable-based phase change material derived from 100% renewable resources [11]. It is stable, non-toxic, non-flammable and biodegradable. The relevant thermal properties are shown in Table 1. The three major subsystems in the experimental set-up shown in figure 1 are the thermal energy intake (evacuated tube solar collector), PCM storage (tank containing the PCM) and output (water and air with the

Table 1. Some Thermal Properties of the PCM

Melting temperature		56^{o}C
Latent heat		237 kJ/kg
Density		810 kg/m^3
Specific heat capacity	Solid	2.47 kJ/kg^{o}C
	Liquid	2.71 kJ/kg^{o}C

water storage tank). The other parts of the system include piping, check valve, the water pump, thermocouples, cables, probes, heat exchangers, insulation, fittings, battery with the wiring system and the data acquisition system. The complete system is set on wheels so that it was easy to be wheeled out of the laboratory to the outside to enable experiments to be performed. Solar energy conversion was applied in the system to power all the electrical components to ensure applicability of the system everywhere including places where electricity is not readily available.

III. EXPERIMENTAL SETUP AND PROCEDURE

Figure 2 shows a line diagram illustrating the experimental setup. The storage tanks (3) and (6) are well insulated with tank (3) containing the PCM and two heat exchangers while tank (6) stores the hot water for other purposes, including air heating. The evacuated tube solar collector (1) is used to transfer thermal energy to water circulated by a solar energy-operated pump (2.1). This water flows through one of the two heat exchangers embedded in the PCM contained in the storage tank, thus transferring energy to the PCM. The PCM

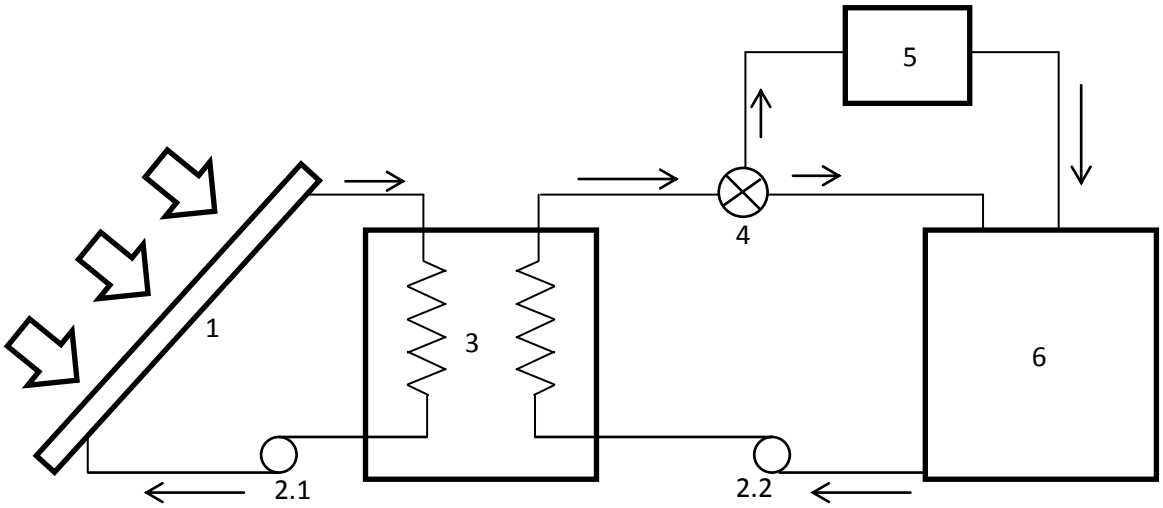

Figure 2. Schematic diagram showing the system setup

increases in temperature and eventually changes phase as it stores thermal energy. Another solar energy-operated pump (2.2) functions to circulate water through the second heat exchanger contained in the PCM storage tank to recover energy from the PCM. The heated water which can be diverted to a liquid-to-air heat exchanger by means of a three-way valve (4) is stored in tank (6). In order to obtain hot water for other purposes, a solar-powered heat exchanger fan (5) is installed to blow air through the heat exchanger so that hot air for example, building heating can be obtained from the system.

The experiments were conducted in Carbondale, Illinois, a city located at 37.7^{o}N, 89.2^{o}W with an elevation of 126 m above sea level. It can be seen from figure 2 that the system set-up has two heat transfer loops. One of the loops transfers thermal energy from the solar collector to the PCM while the other loop transfers thermal energy from the PCM to the water in the hot water tank. Before starting the experiment for investigating the storage performance at various flow rates, one of the loops was shut so that no heat transfer takes place between the PCM and the hot water tank. The required heat transfer flow rate was set and verified by the flow meter.

For the purpose of gaining heat from the solar collector and transferring the heat gained to the PCM, only the solar-powered battery pump for one of the loops was switched on to circulate the heat transfer fluid (HTF) across the loop. The data acquisition system was switched on so that temperatures of the HTF at the solar collector inlet, outlet and the PCM could be read and recorded at regular intervals. The experiments were each conducted for a period of at least six hours from morning to afternoon to ensure that adequate data were obtained for the period when the sun was shining. The experiments were repeated for a number of days during the summer, fall, winter and spring periods for each HTF flow rate. This was to ensure repeatability. The HTF flow rates used in the experiments were classified as high, medium and low. These are given respectively as:

(a) 10 LPM (0.16 kg/s).
(b) 5 LPM (0.083 kg/s).
(c) 3 LPM (0.05 kg/s).

The thermal energy available for storage compared to that which was stored for each of these operating HTF flow rates was investigated. These energy amounts were determined hourly. The basis used for the timing is such that, hour 0 is the time between 12 midnight and 1:00 a.m. while hour 1 is the time between 1:00 a.m. and 2:00 a.m. and so on. The performance of the system during energy recovery was also investigated.

IV. SUMMARY OF THE RESULTS AND DISCUSSION

Typical results for energy storage performance for the relatively high flow rate of 10 LPM (0.16 kg/s) of the HTF are shown in figure 3. Ambient temperature during these experiments ranged from 24°C to 32°C. From the figure it can be seen that the PCM temperature increased until about 56°C when it started to melt or undergo phase change. After melting, it gained heat sensibly and the temperature started to rise again. The

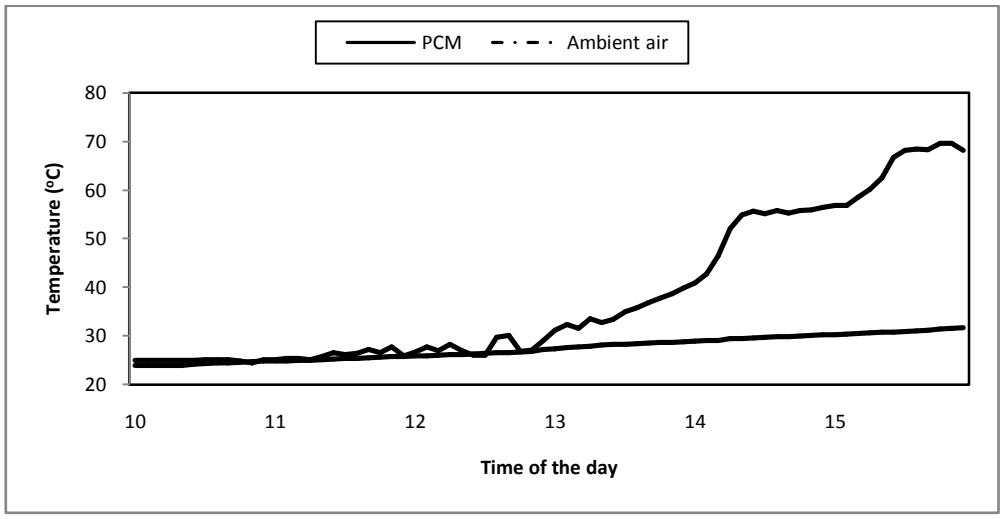

Figure 3. Thermal energy storage performance at the flow rate of 10 liters/minute

experiments show the behavior of the PCM as it maintained an almost constant temperature near its melting temperature and then gained heat sensibly after melting. Figure 4 shows the results for the performance at medium HTF. It can be seen from the figure that the temperature of the PCM increased steadily with time even though the ambient temperature for the day was on the low side (about 21°C average temperature). The results for the storage performance for a relatively low HTF flow rate of 3 LPM (0.05kg/s) are shown in figure 5. It can be seen from the figure that the PCM temperature was steady for a long duration at an average temperature of about 56°C. When compared to the case for the high HTF, it can be seen that the beginning of the phase change and the end are more precisely defined. The figure shows that the performance of the system for the

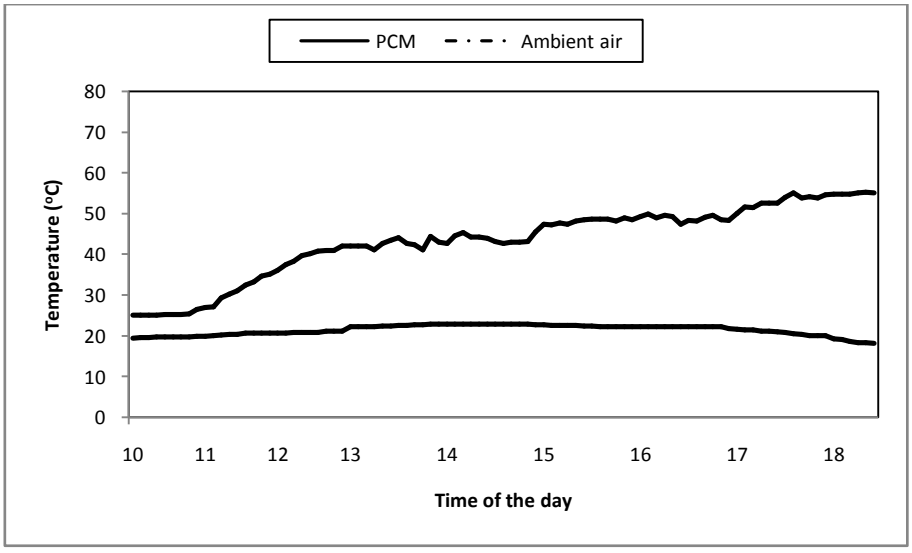

Figure 4. Thermal energy storage performance at the flow rate of 5 liters/minute

case of the low HTF allows the PCM to gain thermal energy much more steadily and without shocks. Thus the solid phase, the melting phase and the period of increase in temperature after melting are more clearly defined when the low HTF flow rate is used.

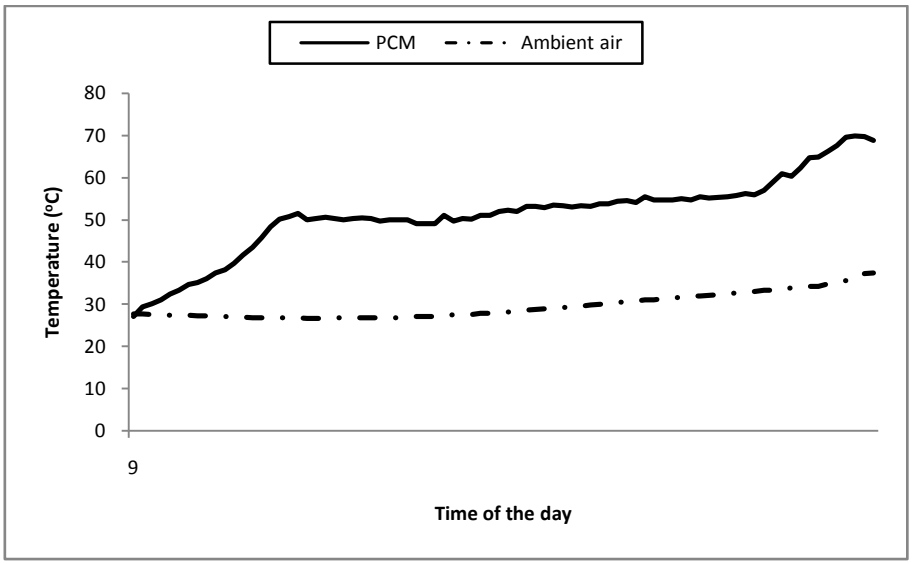

Figure 5. Thermal energy storage performance at the flow rate of 3 liters/minute

Figures 6 - 8 show the amounts of thermal energy stored hourly for the different operating HTF flowrates. The results for the thermal energy available at the collector and the amounts actually stored for the different flowrates are shown in Table 2. Evidence from the table shows that although large amounts of thermal energy were available for storage for the cases with high HTF flow rate, comparatively small fractions of the energy were stored. When compared to the cases with low HTF flow rate it is seen that a higher percentage of the available thermal energy was stored by the PCM. This can be explained by the fact that when the flow rate is low, more time was available for the PCM to extract the thermal energy from the HTF as it flowed through the PCM tank.

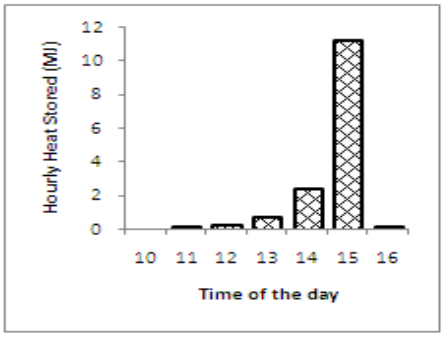

Figure 6. Energy Stored at 10 L/m flow rate

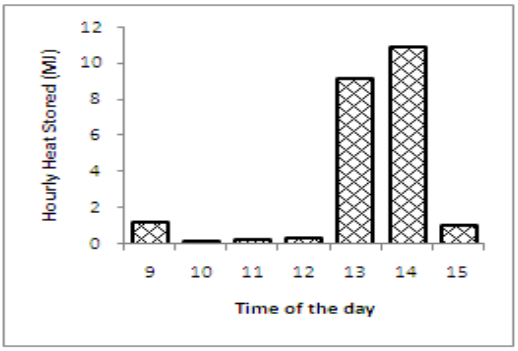

Figure 7. Energy Stored at 5 L/m flow rate

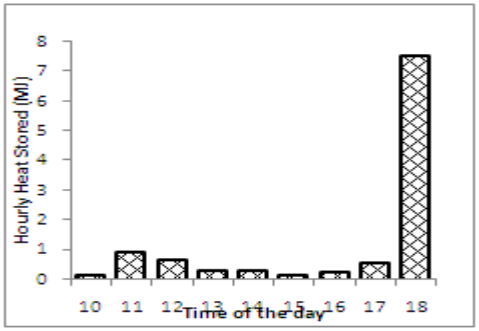

Figure 8. Heat Stored at 3 L/m flow rate

Table 2. Thermal energy availability and storage with varying flowrates

HTF Flow rate	Heat available (MJ)	Heat stored (MJ)	Percentage (%)
High (10 L/min)	98.4	14.9	15
Medium (5 L/min)	76	14.2	19
Low (3 L/min)	48.6	24.2	50

Table 3 shows typical results for the average thermal energy stored by the PCM during the seasons of the year. The table shows that as expected, the largest amount of daily thermal energy that could be stored by

Table 3. Average daily thermal energy stored by season of the year

Season	Thermal Energy Stored (MJ)
Summer	19.57
Fall	14.13
Winter	2.44
Spring	14.49
TOTAL	50.63

the system occurred during the summer season. The lowest amount occurred during the winter period. The results for the typical daily thermal energy losses from the system during various seasons of the year are shown in Table 4. The losses can be seen to be least during the summer period. This could be due to the fact that the average ambient temperature was relatively high (37.3^{o}C). The temperature difference between the PCM and ambient air was about 14^{o}C which is the least compared to the other seasons. This could be the main reason for the least thermal energy loss from the system.

Table 4. Typical thermal energy losses from the energy storage system

Season	Heat loss (MJ)	Average PCM Temp. (^{o}C)	Average Ambient Temp. (^{o}C)
Summer	0.2	51.3	37.3
Fall	0.44	44.1	21.9
Winter	0.5	40.5	11.8
Spring	0.55	44.5	14.9

Table 5 shows the efficiency of the solar energy storage system obtained using equation (8). The values of the efficiency are seen to vary with season with the highest value occurring in the summer and the lowest occurring in the spring. It is noted that these average values are for the combination of the different HTF flow rates. Experiments were also performed to study thermal energy recovery from the system. These were to

Table 5. Solar energy storage system efficiency for the seasons

Season	Q_{solar} (MJ)	Q_{pcm} (MJ)	Efficiency (%)
Summer	30.8	19.6	63.6
Fall	25.1	14.1	56.2
Winter	4.0	2.4	60
Spring	27.2	14.5	53.3

evaluate how much thermal energy that could be recovered from that stored in the PCM. Two types of HTF flowrates were used in these experiments. Typical results from these experiments are shown in figures 9 and 10. The results for the first flow rate of 5 L/min are shown in figure 9. It can be seen that the hot water temperature rose from about 28^{o}C to about 35^{o}C in the first hour and then the temperature increment started to decrease.

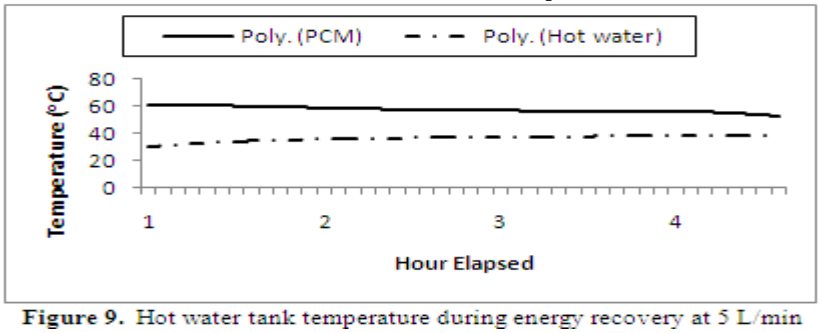

Figure 9. Hot water tank temperature during energy recovery at 5 L/min

Only a small rise in temperature was noticed for the rest of the recovery period. This is explained by the clogging which was noticed to occur around the heat exchanger coils in the PCM tank. The PCM was found to solidify around the coils causing an insulating effect. This reduced further heat transfer to the coils. It was found that the maximum temperature of water in the tank after the experiment was about 38.5°C. A conclusion from this is that an auxiliary heater would be needed to bring the temperature of the hot water to about 40°C, which is the temperature required for most usage in homes.

It was this inability of the hot water to reach the desired temperature of 40°C and above that prompted the idea of a reduction in flow rate to 2 L/min. Figure 10 shows the results obtained for running the experiments using this reduced HTF flow rate. Compared to the case of HTF flow rate of 5 L/min, the hot water temperature rose at a very fast rate from 28°C to about 40°C within the first hour and then it quickly approached steady state. The maximum temperature achieved was about 44.3°C which is some degrees higher than the required hot water

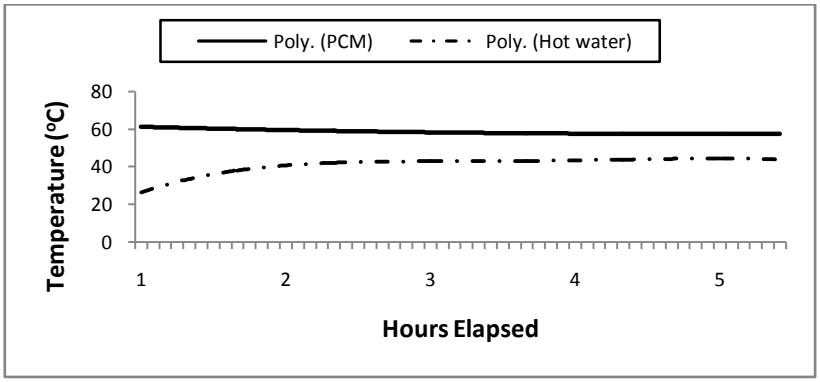

Figure 10: Hot water tank temperature during energy recovery at 2 L/min

temperature of about 40°C. Thus, a low heat transfer fluid flow rate of 2 L/min (0.033 kg/s) produced the best thermal energy recovery process from the system.

V. CONCLUSION

Solar energy storage system based on a vegetable-based, non-toxic, non-flammable, renewable and biodegradable phase change material (PCM) was developed. The system involves the two storage tank system, one for the PCM and the other for the hot water storage. The system used was designed such that the heated water can be diverted to a heat exchanger by means of a 3-way valve such that a fan can be made to blow air through one of the heat exchangers so that hot air for other purposes such as air heating can also be achieved through the system. Solar energy was applied in the system to power all the electrical components to ensure applicability of the system in parts of the world where electricity is not readily available.

An experimental study on the performance of this system was done leading to a number of useful results. Based on the scale of this system, projections show that it can be extended to home building and commercial building applications. One of the results from this study shows that using the best or optimum low flow rate for the HTF for energy storage and energy recovery process gives the best performance by the system. The highest system efficiency of 63.6% was recorded for the summer period. However, results show that more than half of the energy absorbed at the solar collector was stored by the system irrespective of the season. A low heat transfer fluid flowrates of 3 L/min (0.05 kg/s) and 2 L/min (0.033 kg/s) produced the best heat storage and heat recovery processes respectively.

VI. ACKNOWLEDGEMENTS

The authors are very grateful to the American Society of Heating, Refrigerating and Air-Conditioning Engineers (ASHRAE) for funding received, Tim Attig, Sewa Pokhrel, Jacob Rutger, Madhav Soti, Evan Yaworsky and Adam Young for valuable contributions during the development and construction of the experimental system.

NOMENCLATURE

a 1st order heat loss coefficient of the collector
A_{coll} solar collector absorber surface area
b 2nd order heat loss coefficient of the collector
C specific heat capacity
$C_{p,w}$ specific heat capacity of water
d_i inside diameter of the heat exchanger tube
d_o outer diameter of the heat exchanger tube
DHW Domestic Hot Water
f solar fraction
G incident solar radiation

h	enthalpy of the PCM
h_{air}	heat transfer coefficient of air
HTF	Heat Transfer Fluid
k_{ins}	thermal conductivity of insulation material
k_{hx}	thermal conductivity of the heat exchanger material
k_t	thermal conductivity of the tank material
L	latent heat of fusion of PCM
L_{hx}	length of the heat exchanger material
L_t	height of the tanks
$\dot{m}_{coll}$	flow rate of water in the solar collector
$\dot{m}_{tank}$	mass flow rate of water in the PCM tank
M	mass
M_{pcm}	mass of the PCM in the tank
PCM	Phase Change Material
Q_{aux}	auxiliary heat energy
$\dot{Q}_{coll}$	useful heat supplied by the solar collector
Q_{coll}	energy gained by the solar collector in a time interval
$\dot{Q}_{hx}$	rate of heat exchange from the copper coils to the PCM
$\dot{Q}_{load}$	heat supplied to the load
$\dot{Q}_{losses}$	rate of heat loss from the PCM tank
Q_{losses}	energy lost by the PCM tank in a time interval
Q_{pcm}	energy stored in PCM tank in a time interval
r_{ins}	radius of insulation material
r_{ti}	inside radius of the tanks
r_{to}	outer radius of the tanks
R_{hx}	thermal resistance on the coils of the heat exchanger
R_{tot}	total thermal resistance of the PCM tank
t	time
T	temperature
T_a	surrounding ambient temperature
T_{avg}	average water temperature in the solar collector
T_{ci}	water temperature at the solar collector inlet
T_{co}	water temperature at the solar collector outlet
T_{pcm}	PCM temperature
T'_{pcm}	PCM temperature after a time interval
T_w	required water temperature for user
$T_{w,avg}$	Average water temperature in the hot water tank

Greek Letters

Δt	time increment
ΔT_{pcm}	temperature difference of the PCM
η	solar collector efficiency
η_o	solar collector optical efficiency
η_{sys}	solar energy storage system efficiency

REFERENCES

[1] S. Mekhilef, R. Saidur, and A. Safari 2011, A review on solar energy use in industries, *Renewable & Sustainable Energy Reviews*, ***15*** *(4), 2011, 1777-1790.*

[2] A. Sharma, V. V. Tyagi, C. R. Chen, and D. Buddhi, Review on thermal energy storage with phase change materials and applications: *Renewable and Sustainable Energy Reviews*, ***13****, 2009,318–345.*

[3] M. Kenisarin, and K. Mahkamov, Solar energy storage using phase change materials: *Renewable and Sustainable Energy Reviews*, ***11****, 2007, 1913-1965.*

[4] M. Farid, A. Khudhair, S. Razack and S. Al-Hallaj, A review on phase change energy storage: materials and applications, *Energy Conversion and Management*, ***45****, 2004, 1597–1615.*

[5] D. Vikram, S. Kaushik, V. Prashanth, and N. Nallusamy, An improvement in the solar water heating systems using phase change materials, *Proceedings of the international conference on renewable energy for developing countries – 2006.*

[6] M. Ibanez, L. F. Cabeza, C. Sole, J. Roca, and N. Miguel, Modelization of a water tank including a PCM module, *Applied Thermal Engineering*, ***26****, 2006, 1328-1333.*

[7] I. Al-Hinti, A. Al-Ghandoor, A. Maaly, I. Abu Naqeera, Z. Al-Khateeb and O. Al-Sheikh, Experimental investigation on the use of water-phase change material storage in conventional solar water heating systems, *Energy Conversion and Management,* ***51****, 2010, 1735-1740.*

[8] D. Haillot, F. Nepveu, V. Goetz, X. Py and M. Benabdelkarim, Numerical model of a solar DHW including PCM media in the solar collector, *Proc., Energy Studies – Effstock 2009.*

[9] J. Duffle, and W. Beckman, Solar Engineering of Thermal Processes, (John Wiley and Sons, New York 3rd Edition, 2006)

[10] A. F. Regin, S. C. Solanki and J. S. Saini, J. S., An analysis of a packed bed latent heat thermal energy storage system using PCM capsules: Numerical investigation, *Renewable Energy*, ***34****, 2009, 1765-1773.*

[11] Pure Temp, "Pure Temp". http://www.puretemp.com/technology.html

American Journal of Engineering Research (AJER)
e-ISSN : 2320-0847 p-ISSN : 2320-0936
Volume-02, Issue-11, pp-204-215
www.ajer.org

Research Paper Open Access

Structural and Stratigraphic Mapping of Delta Field, Agbada Formation, Offshore Niger Delta, Nigeria

E.K. Nyantakyi*[1,2], W.S. Hu[2], J.K. Borkloe[1,2], Gong Qin[2], M. Cheng Han[2]
[1]*Department of Civil Engineering, Kumasi Polytechnic, Kumasi, 00233, Ghana.*
[2]*School of Earth Sciences, Yangtze University, Wuhan, Hubei 430100, China*
***Corresponding author:emmanuelkwesinyantakyi@yahoo.com**

Abstract: - The Niger Delta is ranked among the world's major hydrocarbon provinces in the world. Oil and gas in the Niger Delta are mainly trapped in sandstones and unconsolidated sands in the Agbada formation. The traps, structure and stratigraphy are not easy to map precisely because they are very slight, not obvious and very complicated. The degree of reliability and precision of the mapping can be greatly enhanced by integrating seismic data with well logs commonly used independently in hydrocarbon exploration and exploitation studies. Seismic data were integrated with well logs to define the subsurface geometry, stratigraphy and hydrocarbon trapping potential of Delta field, off shore Niger Delta. Lithologic units were identified on the logs and correlated across the wells. The stratigraphic cross-sections produced show a general lateral continuity of the lithologic units across the field. Five (5) sequence boundaries namely SB1, SB2, SB3, SB4 and SB5 were mapped and structure contour maps drawn for each of the sequence boundaries. Fault closures of high quality hydrocarbon prospects were identified and delineated. Stratigraphic plays such as pinch-outs, unconformities, sand lenses and channels are also suspected. The integration of seismic data with well logs greatly improved the extent of accuracy and exactness of structural and stratigraphic mapping in predicting lateral and vertical variations, hydrocarbon prospects and its development in Delta Field.

Key words: *- Delta Field, Niger Delta, Integration, Stratigraphic mapping, Structural interpretation, well logs.*

I. INTRODUCTION

The Niger Delta is ranked among the world's major hydrocarbon provinces in the world. It is the most important in the West African continental margin. Oil and gas in the Niger Delta are primarily produced from sandstones and unconsolidated sands mainly in the Agbada formation. The 12 km thick Niger Delta clastic wedge spans a 75, 000 km^2 area in southern Nigeria and the Gulf of Guinea offshore Nigeria. This clastic wedge contains the 12th largest known accumulation of recoverable hydrocarbons, with reserves exceeding 34 billion barrels of oil and 93 trillion cubic feet of gas (Tuttle et al., 1999). These deposits have been divided into three large-scale lithostratigraphic units: (1) the basal Paleocene to Recent pro-delta facies of the Akata Formation, (2) Eocene to Recent, paralic facies of the Agbada Formation, and (3) Oligocene-Recent, fluvial facies of the Benin Formation (Evamy et al., 1978; Short and Stauble, 1967; Whiteman, 1982). These formations become progressively younger farther into the basin, recording the long-term progradation of depositional environments of the Niger Delta onto the Atlantic Ocean passive margin. Stratigraphy of Niger Delta is complicated by the syndepositional collapse of the clastic wedge as shale of the Akata Formation mobilized under the load of prograding deltaic Agbada and fluvial Benin Formation deposits. A series of large scale, basinward-dipping listric normal faults formed as underlying shales diapered upward. Blocks down dropped across these faults filled with growth strata, changed local depositional slopes, and complicated sediment transport paths into the basin.

The goal of oil and gas exploration is to identify and delineate structural traps suitable for profitably exploitable accumulations and delineate the extent of discoveries in field appraisals and development. These traps are very slight, not obvious and very complicated and are therefore not easy to map precisely. Major improvements in seismic and well logs have made it possible to map such structural and stratigraphic arrangements with high degree of accuracy and exactness. Seismic profiles provide almost a continuous lateral

view of the subsurface by defining its geometry and providing an estimate of the acoustic impedance which is related to the formation densities and velocities.

However, vertical details are limited due to lengthy duration of the individual seismic wavelets and the occurrence of overlapping wavelets from closely spaced reflectors. Well logs are limited in their definition of lateral variation of subsurface parameters. Thus, the extent of accuracy in mapping complicated structural plays would be improved greatly by combining seismic data with well logs (Adejobi and Olayinka, 1997; Barde et al. (2000 and 2002). In addition, the risk associated with finding oil and gas in very slight, not obvious and complicated structural/stratigraphic places will be reduced tremendously since such integration will help to discriminate between poor and rich reservoirs and also greatly improve the extent of accuracy and exactness of the structural maps in hydrocarbon prospects and its development.

In the present work, 3-D seismic reflection data were integrated with well logs so as to define the subsurface geometry, stratigraphy and hydrocarbon potential of Delta field, offshore Niger Delta. The aims of the study include characterization of the subsurface geometry and stratigraphy, determination of hydrocarbon trapping potential of the field and identification and delineation of possible hydrocarbon prospects in the field.

1.1 Geological Setting of the Field

Delta field is located in 12 feet of water on Oil Mining Leases (OML) 49/95 in the Southwestern part of the Niger Delta (Figure 1). The field was discovered in 1965 after completion of Delta 1 well, and targeting a structural prospect; the field was opened for production in 1968. The field is divided into 2 major fault blocks (Figure 1C). The western block 1 is down dropped relative to the eastern block 2 along a major normal fault. A third fault block in the northeastern part of the field, defined by a minor horst, does not contain commercial oil reserves. Wells in Delta field were generally drilled to lower parts of the Agbada Formation, and targeted structural prospect in the middle of the formation. Only a few wells were logged through the Benin Formation, which contains fresh-water saturated sands. Of the 37 wells drilled in the field, 14 are vertical and 23 are deviated (5 of these deviated wells become horizontal at depth). Twelve of the wells are located in fault block 2 (Figure 1C). One well in fault block 2 is a water injector well used to provide pressure support (DE-34I). Additional horizontal wells were recently drilled to address a water-coning problem in producing wells and to optimize production based on results of a reservoir simulation study. Fifty-three distinct reservoirs have been discovered within the field to date. The Niger Delta, situated at the apex of the Gulf of Guinea on the west coast of Africa, covers an area of about 75 000 km^2. The geology of the tertiary Niger Delta province has been described by several workers Short and Stauble (1967); Weber (1971); Weber and Daukoru (1975); Weber et al., (1978); Evamy et al., (1978); Doust and Omatsola (1990); Haack et al., (2000).

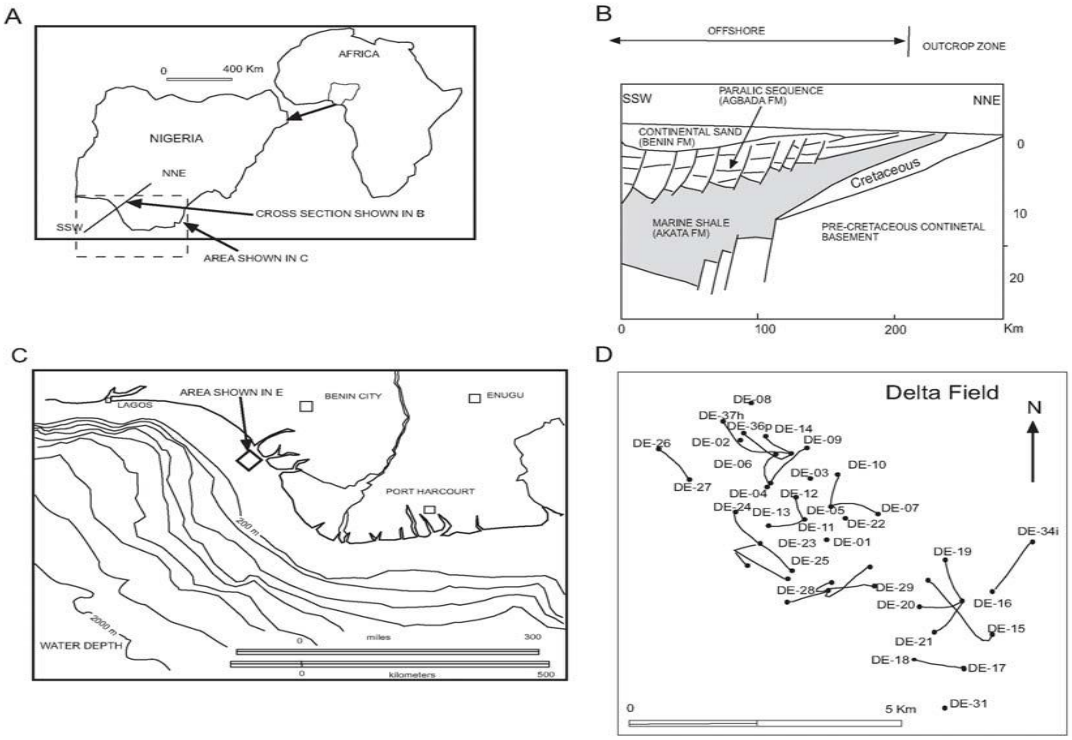

Figure 1: Location map of study area. (A) Position of Nigeria in Africa and Niger Delta Basin. (B) Cross section from NNE to SSW across Niger Delta Modified from Stacher (1995). See location of cross section in

(A). (C) Delta field well locations. (D) Delta field location map. (E) Seismic survey area. Dash line enclosed area with seismic data provided by Chevron Nigeria Ltd. Area studied is enclosed in the bold line. (F) Area shown in horizontal seismic slices.

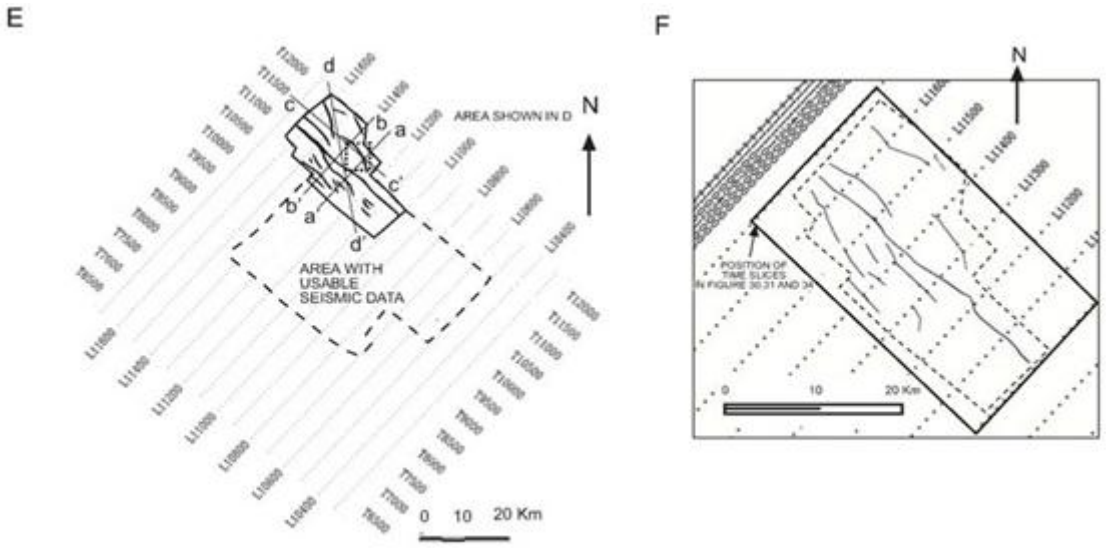

Figure 1: Continued.

Basement tectonics related to crucial divergence and translation during the late Jurassic and Cretaceous continental rifting probably determined the original site of the main rivers that controlled the early development of the Delta. The Cenozoic development of the delta is also believed to have taken place under approximate isostatic equilibrium. The main depocenter is thought to have been at the triple junction between the continental and oceanic crust where the delta reached a main zone of crustal instability.

The Niger Delta basin is located on the continental margin of the Gulf of Guinea in equatorial West Africa and lies between latitudes 4^{o} and 7^{o}N and longitudes 3^{o} and 9^{o}E (Whiteman, 1982). It ranks among the world's most prolific petroleum producing Tertiary deltas that together account for about 5% of the world's oil and gas reserves. It is one of the economically prominent sedimentary basins in West Africa and the largest in Africa (Reijers, 1996). Detailed studies on tectonics, stratigraphy, depositional environment, petrophysics, sedimentology and hydrocarbon potential are well documented in the literature (Short and Stauble (1967); Weber and Daukoru (1975); Evamy et al., (1978); Knox and Omatsola (1989); Doust and Omatsola (1990), Nton and Adebambo (2009); Nton and Adesina (2009)) among others.

The Niger Delta is a large arcuate delta of the destructive, wave-dominated type and is composed of an overall regressive clastic sequence which reaches a maximum thickness of about 12 km in the basin centre.
The Delta's sediments show an upward transition from marine pro-delta shales (Akata Formation) through a paralic interval (Agbada Formation) to a continental sequence (Benin Formation). These three sedimentary environments, typical of most deltaic environments, extend across the whole delta and ranges in age from early tertiary to recent. A separate member, the Afam clay member, of the Benin formation is recognized in the eastern part of the delta and is considered as an ancient valley fill formed in Miocene sediments. The formations are strongly diachronous (Murat, 1970) and cut across the time stratigraphic units which are characteristically S-shaped in cross-section. Most economically exploitable hydrocarbon in the delta is believed to be trapped within the Agbada formation.

Structurally, the Niger Delta shelf developed as a prograding extensional complex overlying a ductile substrate which probably composed largely of over pressure marine shales. The onshore growth fault systems have been described by (Doust and Omatsola, 1990) as a series of major growth fault bounded depobelts or mega-structures thought to be transient basinal areas succeeding one another in space and time as the delta progrades southward. The extensional system is dominated by "tepee" structure in which landward-dipping growth faults intersects seaward dipping in complex interlocking fault networks (Figure 2).

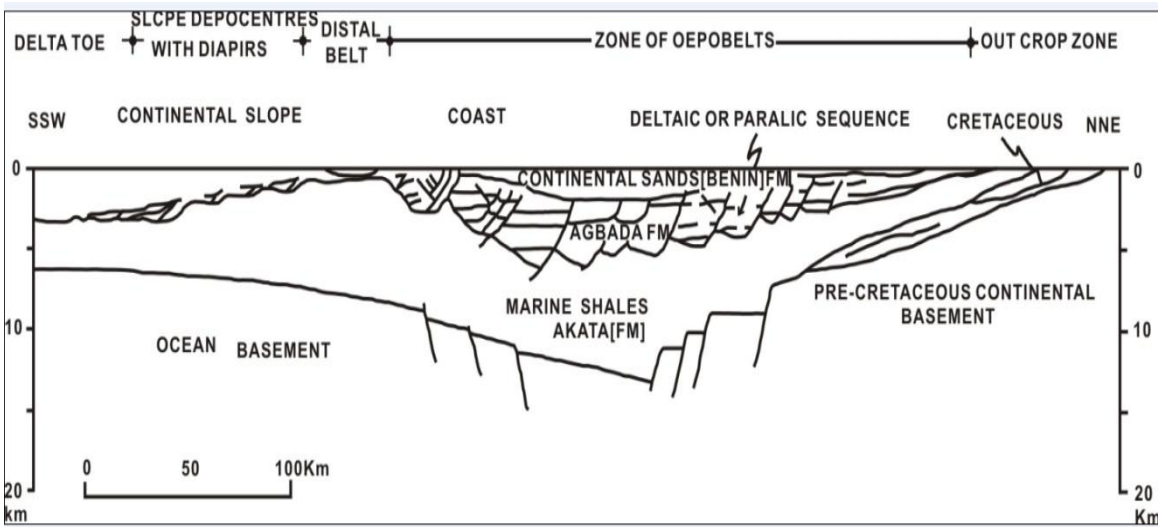

Figure 2: Schematic section through the axial potion of the Niger Delta showing the relationships of the tripartite division of the tertiary sequence to basement. Modified from Doust and Omatsola (1990).

The most striking structural features of the Cenozoic Niger Delta complex are the syn-sedimentary structures which deform the delta largely beneath the Benin sand facies. These structures, regarded as the product of gravity sliding during the course of deltaic sedimentation, are polygenic in origin and their complexity increases generally in down delta direction (Merki, 1972). The syn-sedimentary structures, called growth faults, are predominantly trending northeast to southwest and northwest to southeast (Hosper, 1971). Associated with these growth faults are rollover anticlines, shale ridges and shale diapers which are caused by shale upheaval ridges. Mud diapers are the most common and occur on the landward side of the growth faults restricting sedimentation on the up-thrown side of the faults and enhancing sedimentation on the down-thrown side. Most of the faults are listric normal; others include structure building growth faults, crestal faults, flank faults, counter-regional faults and antithetic faults.

In general, the offshore Niger Delta has the characteristic shelf slope break of growth fault modified ramp margins. The present day shelf is dominated by long counter regional faults. Further offshore, there exist a back-to-back fault trend along the shelf edge and upper slope. Down the slope, there are examples gentle folds, with thrust and diapers sometimes cutting the sea bed (Figure 3).

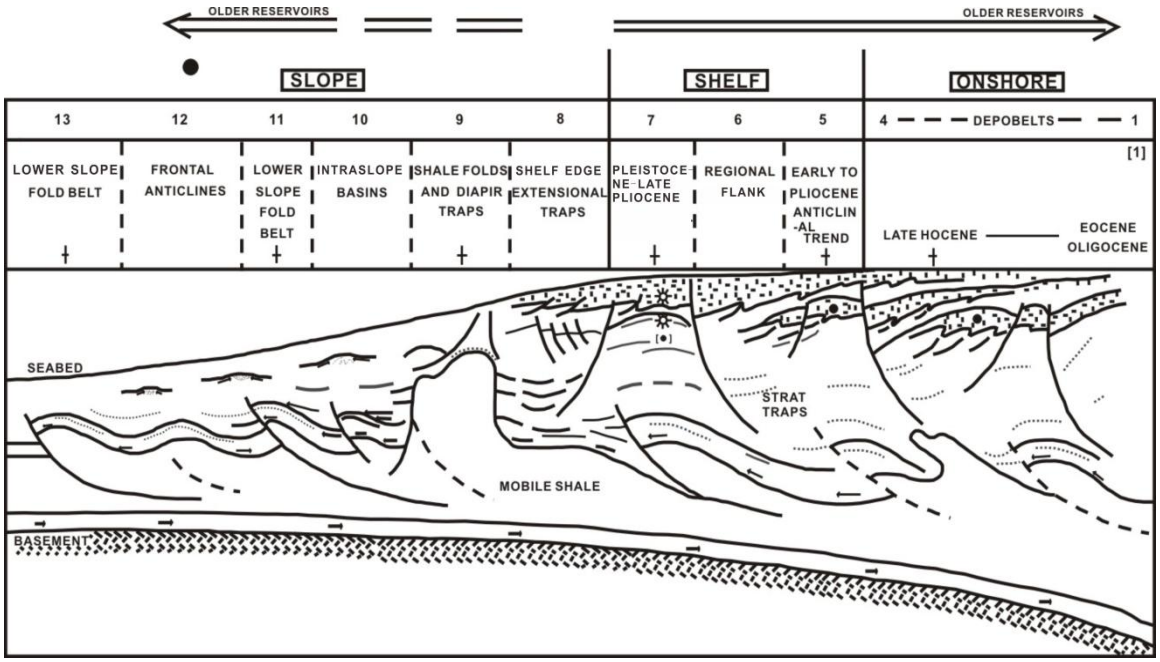

Figure 3: Niger Delta schematic structural profile of the deep water area characterized by listric extension faults gentle folds thrusts and diapirs. Modified from Ojo (1996)).

Oil and gas are mainly trapped by rollover anticlines and fault closures. Hydrocarbon distribution in the Niger Delta is complex with gas-to-oil ratio generally increasing southward away from the depocentre within a depobelts (Evamy et al., 1978) and is primarily controlled by thermal history of the source rocks, source rocks quality, migration and sealing quality. In addition, the timing of traps formation could be a factor that controls the distribution of hydrocarbon (Chukwueke, 1997).

Trap arrangement in the deep water Nigeria is controlled by gravity driven system of linked extensional growth faults and compressional toe thrusts initiated during the Paleogene, when the modern Niger delta was formed (Haack et al., 2000). Most of the reservoir facies in the offshore Niger Delta are related to an aggrading lowstand complex where a slow relative rise in the sea levels allows sediment input to keep pace with the creation of accommodation space over a long period of time. A thick expanding edge of coarse clastics is trapped on the shelf behind the counter regional faults and most of the sediments are therefore, deposited on the shelf, indicating that the sand content and gross sediment input reduces dramatically with increasing distance from provenance.

Normal faults triggered by the movement of deep-seated, overpressured, ductile, marine shale have deformed much of the Niger Delta clastic wedge (Doust and Omatsola, 1989). Many of these faults formed during delta progradation and were syndepositional, affecting sediment dispersal. Fault growth was also accompanied by slope instability along the continental margin. Faults flatten with depth onto a master detachment plane near the top of the overpressured marine shales at the base of the Niger Delta succession.

II. METHODOLOGY

2.1 Seismic and well logs data

The different datasets employed in this research were provided by Chevron Nigeria Ltd (a division of ChevronTexaco Overseas) which includes 36 well logs and a 3-D seismic cube of the area around Delta field (Figure 1E). The seismic data, with 1501 lines and 6001 traces, has been obscured from view in areas away from delta field to protect proprietary area prospects. A biostratigraphic report of Delta-2 well is also available. The research focuses on the determination of structural and stratigraphic mapping within the Niger Delta using well logs and seismic data from Delta field. Well log data for the 36 wells and the seismic volume were loaded into Landmark Stratworks™ and Seisworks™, respectively. Stratal discontinuities and regionally parallel reflections in the seismic cube were related to vertical patterns in well logs. Well logs were hung on the shale marker near the top of the Agbada Formation and well log correlations were loop tied to ensure consistency. Stratigraphic surfaces observed in the seismic volume and correlated between well logs were mapped across a 400km^2 area. Ten stratigraphic surfaces and major faults were mapped. Five of the stratigraphic surfaces were major erosion surfaces and the rest five were nearly horizontal surfaces between these erosional surfaces. Five of the surfaces within lower parts of the stratigraphic succession were mapped across a smaller area than the rest due to poor seismic data quality or severe structural distortion of strata above underlying mobile shales. Locations of major faults were interpreted from the seismic data to define structural discontinuities. Vertical patterns in seismic reflections were used to relate strata across faults. Well log patterns were also used to correlate strata across faults where wells cut deposits on both upthrown and downthrown fault blocks. Mapped stratigraphic surfaces and faults observed in the seismic data were converted to depth using Lankmark's TDQ™ and loaded in to GOCAD™ to model the geometry and spatial relationships between stratal surfaces and faults in the area of Delta field. Well logs were also loaded into GOCAD™ and stratigraphic surfaces and faults were adjusted to well logs to define stratigraphic surface positions.

2.2 Sequence Boundary Selection and Fault Identification

Stratigraphic surfaces observed in the seismic volume and correlated between well logs were mapped across a 400km^2 area. Sequence boundaries within the well logs that showed hydrocarbon prospects were selected for mapping. Five Sequence boundaries namely SB1, SB2, SB3, SB4 and SB5 were chosen and correlated through all the seismic sections. Major faults were identified mainly on abrupt termination of reflection events and marked on the cross-lines. Fault traces at all levels was consistent. The sequence boundaries were then tied at their intersection points in order to ensure consistency in all the lines of intersections and in all the seismic sections which covered the entire survey area. The analysis was rechecked in areas where there were misties and the misties corrected.

2.3 Structural Maps of Sequence Boundaries

The chosen sequence boundaries were digitized using a scale appropriate to the seismic sections and structural maps were then produced for each of the sequence boundaries. During contouring, the variable nature of the seismic signals as well as the varying structural features of rock deformation was taken into consideration. The fault traces were posted to the structural maps produced. The fault throws and directions obtained from the seismic sections were correlated with well logs.

III. RESULTS AND DISCUSSION

3.1 Seismic interpretations and stratigraphic cross-sections

The seismic record is characterized by a series of nearly parallel reflections offset by listric normal faults dipping to the southwest. Most wells in Delta field pass into a hanging wall anticline within a relatively large coherent fault block. Offshore of the field, normal faults are more closely spaced and antithetic faults occur, hindering correlation of stratigraphic surfaces. Seismic reflections also become more chaotic deeper within the seismic record (below 3.0 seconds), where diapiric movement of underlying mobile shale has complicated reflector geometry. Truncation of reflectors against an irregular high relief overlying reflector indicates an allostratigraphic discontinuity or an erosional "sequence boundary". Five sequence boundaries are observed within the Agbada Formation in Delta field. Successive erosion surfaces are generally more closely spaced higher within the stratigraphic section. Parallel to paleoflow, the relief along these surfaces is more subdued, but can show up to 200 meters of local relief. Incisions along sequence boundaries 1 and 2 have up to 300 feet of relief. Locally there is a 3 km wide, 300 foot deep channel along sequence boundary 1, and a 1 km wide, 100 foot deep channel along sequence boundary 2. The relief along sequence boundary 3 is more subdued, and is expressed in Delta field only by low-angle truncation of reflectors down dip. Relief along sequence boundaries 4 and 5 is substantially greater, with steep margined channels 5 km wide and 600 feet deep along boundary 4, and 5 km wide, 900 feet deep along boundary 5.

In most locations reflector patterns within sequences can be divided into two parts: 1) a lower part with chaotic patterns and or a set of inclined reflectors, and an upper part where reflectors are generally parallel and more closely spaced. In some locations the deposits directly above sequence boundaries comprise a 50 to nearly 500 feet thick set of inclined reflectors dipping at a fraction of a degree basinward. These sets of inclined beds are thickest directly above the most deeply incised areas along sequence boundaries. In other locations strata directly above these erosion surfaces have chaotic or mounded reflection patterns. In the area of greatest incision along sequence boundary 5, inclined reflectors downlap onto underlying chaotic reflectors.

Seismic reflectors significantly above each sequence bounding erosion surface are parallel, generally continuous across the field, and are generally more closely spaced, unlike thicker intervals with chaotic or inclined reflectors directly overlying sequence boundaries. These parallel reflectors are interpreted to image nearly horizontal strata across the 5-10 km span of Delta field, even though they may dip at regional-scales as very low angle basinward dipping strata. A practically continuous reflector traced within each sequence was correlated through the seismic volume to provide datum's for mapping changes in stratigraphic thickness across the study area and across specific faults. In some cases, these intra-sequence reflectors appear to correspond to the finest grained parts of sequences, but this is not true in all cases. Intra-sequence reflectors within sequences 1 and 2 could not be traced across the major fault south of Delta field, because of deformation and abundant faults produced by diapiring shales under the down thrown blocks at these depths. Intra-sequence reflectors mapped within sequences 3 and 4 are locally cut out where overlying sequence boundaries incise deepest into underlying deposits.

Stratigraphic differences in the Agbada Formation of Delta field show the regression of depositional environments within the Niger Delta Basin. This broadly changes from finer-grained deposits deeper in wells directly above underlying Akata Formation shales (higher gamma-ray log values) to progressively coarser-grained deposits shallower in wells below the overlying Benin Formation (lower gamma-ray log values). The top of the Agbada Formation is defined as the base of fresh water sands at about 3000 feet below sea level. The base of the formation, not penetrated by the wells, lies greater than 8000 feet below sea level. The Agbada Formation is thus somewhat over 5000 feet thick under Delta field. Gamma-ray logs show tens to a few hundred feet vertical differences superimposed on this formation scale trend, which record alternation between sandier and muddier successions e.g., (Delta 2 Well gamma-ray log, Figure 4). Following standard interpretations of the Agbada Formation, log successions that gradually decrease in gamma-ray value and then rapidly increase (gradually coarsen and then abruptly fine) are interpreted to be prograding delta deposits. Those that abruptly decrease in gamma ray value and have "blocky" or gradually increasing trends (abruptly coarsen and remain sandy or gradually fine) are interpreted to be channel deposits (Figure 4).

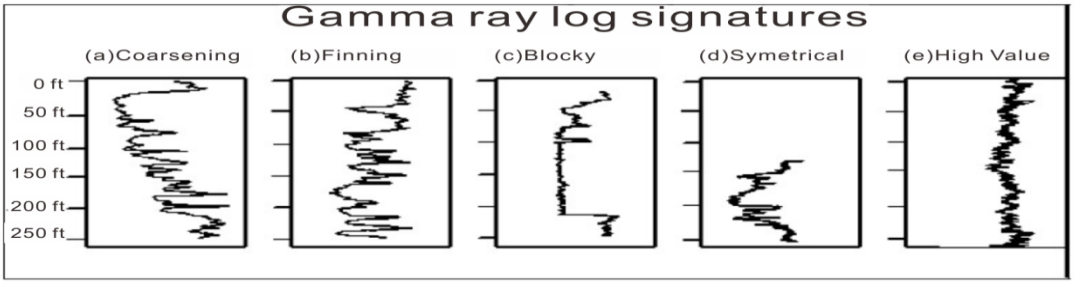

Figure 4: Types of well log patterns observed in Delta field. (a) Upward-coarsening, progradation log pattern. (b) Upward-fining, retrogradational log pattern. (c) Sharp-based, blocky log pattern. (d) Symmetrical log pattern. (e) High gamma- ray value log pattern.

Serrated high value gamma ray intervals are dominated by mudstone with varying amounts of thin sandstone beds. It should be acknowledged, however, that different log trends related to prograding shorelines are not always fundamentally distinct from those of prograding deeper water mass flow fans, and that no cores from Delta field are available. Biostratigraphic studies commissioned by Chevron conducted on material from Delta 2 Well place broad constraints on the age of the Agbada Formation (Figure 5). The first down hole occurrence of *Sphenolitus heteromorphis* at 7700 feet and *Praeorbulina glomerosa* at 8090 feet corresponds to N9 planktonic foraminifera zone of Bolli and Saunders (1985), indicating an early Middle Miocene age. The first down hole occurrence of *Discoaster deflandrei* at 7640 feet corresponds to the NN5 nannozone of Perh-Neilsen (1985), also indicating an early Middle Miocene age. The last down hole occurrence of *Sphenolithus abies* at 3500 feet and first down hole occurrence of *Sphenolithus moriformis* at 2840 feet indicate a Late Miocene age. These data suggest that Agbada Formation in Delta field was deposited over about 6-7 million years during the Middle to Late Miocene, at average deposition rates of about 1000 feet per million years. The stratigraphy of the Agbada Formation is significantly complicated by faulting, formation of growth strata over down thrown blocks, and structural deformation associated with upward movement of underlying Akata Formation shales.

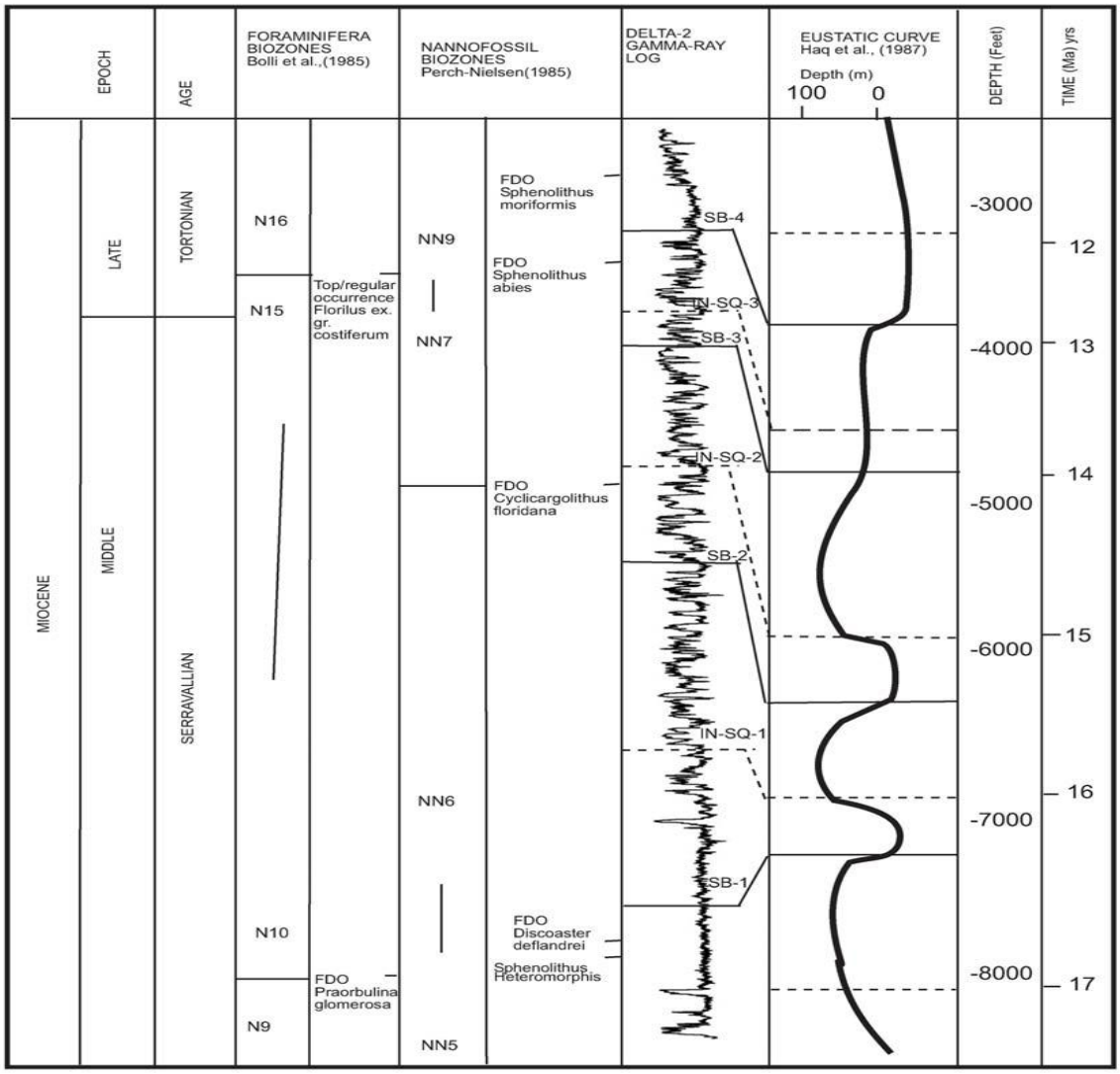

Figure 5: Biostratigraphic zonation within Delta-2 Well. Well log variations are also related to sea level curve of Haq (1987). The age of intra-sequence surfaces in this well estimated from biostrigraphic divisions appear to generally match the date of maximum flooding surfaces on the Haq curve.

3.2 Structural contour maps

The sequence boundaries mapped were laterally continuous on the seismic records and formed a closed loop along the tie lines. Figures 6 to 10 displayed the structural maps of the sequence boundaries SB1, SB2, SB3, SB4 and SB5 mapped respectively.

Structure-contour maps of sequence boundaries provide a record of the timing of structural offset across major faults and patterns of deformation within fault blocks. Stratigraphic surfaces are abruptly lower on western sides of faults relative to east sides and are consistent with displacement observed in the seismic cross sections. Older surfaces show significantly greater offset across faults than younger surfaces, demonstrating syndepositional movement of faults. The difference in offset of successive surfaces across faults also progressively decreases up-section. Areas of greatest listric normal fault movement may have shifted to the west with progradation of the clastic wedge; loading Akata Formation shales most rapidly in progressively more distal areas of the basin over time.

Given the magnitude of lateral thickness changes between individual horizons mapped through the seismic volume (more than 500 feet over a few km laterally in older deposits), thickness trends between faults probably reflect structural deformation of fault blocks, rather than changes in delta bathymetry. The syndepositional down drop of fault blocks across faults is likely to have produced bathymetric lows that accumulated sediment more rapidly and influenced sediment dispersal patterns farther basinward. Deposits in hanging wall blocks tend to be thicker directly basinward of areas showing the greatest stratigraphic offset across faults and are relatively thinner down basin from areas with lesser fault displacement. Deposits on downthrown blocks generally thin for a few hundred meters away from major faults and then progressively thicken basinward across the remainder of the fault block. These patterns record the syndepositional development of rollover anticlines within the hanging wall. Strata in the hanging wall block are deformed to dip toward the upthrown block directly adjacent to the fault, and thus rise in elevation toward the anticline crest. Beyond the crest, strata are rotated to dip more steeply in the direction of fault displacement, increasing in depth with greater distance away from the fault.

Although patterns of sediment accumulation reflecting growth strata deposition over deforming anticlinal fault blocks is observed within all stratigraphic intervals, it is more pronounced within sequence boundaries 1 and 2, than for later sequences which show less offset across faults.

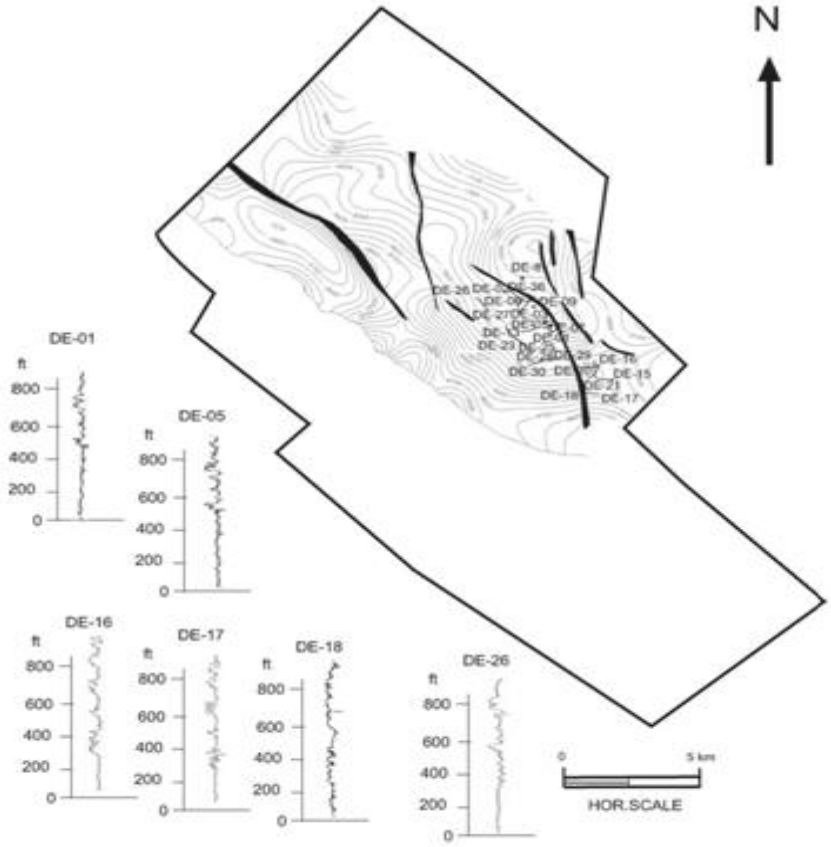

Figure 6**:** Structure map of sequence boundary, SB1. Gamma-ray logs show typical log pattern above the surface to the intra-sequence surface. General upward-coarsening trend from fine-grained basal section above sequence boundary.

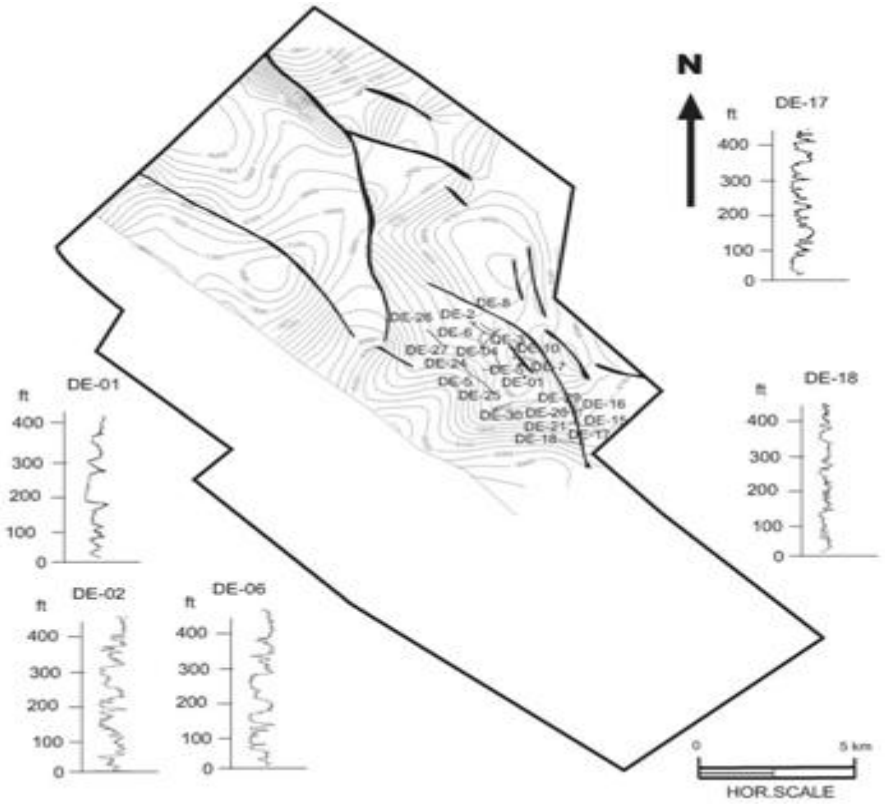

Figure 7: Structure map of sequence boundary, SB2. Gamma-ray log pattern above the sequence boundary ranges from blocky to fine. The pattern either coarses or fines upward.

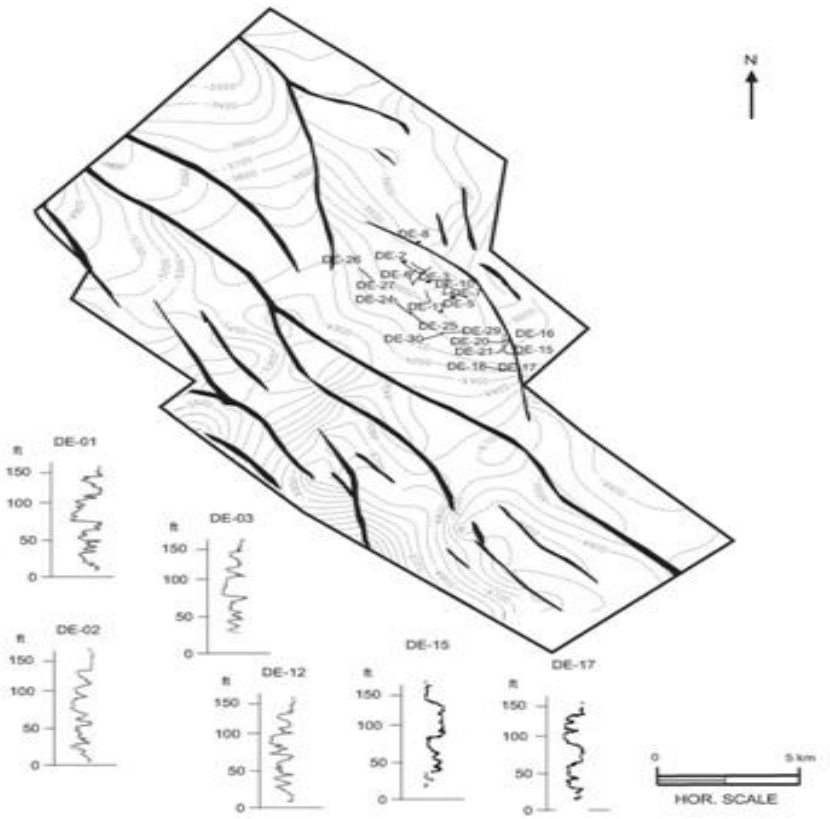

Figure 8: Structure map of sequence boundary, SB3. Gamma-ray log pattern above the surface ranges from upward coarsen upward to upward-fining.

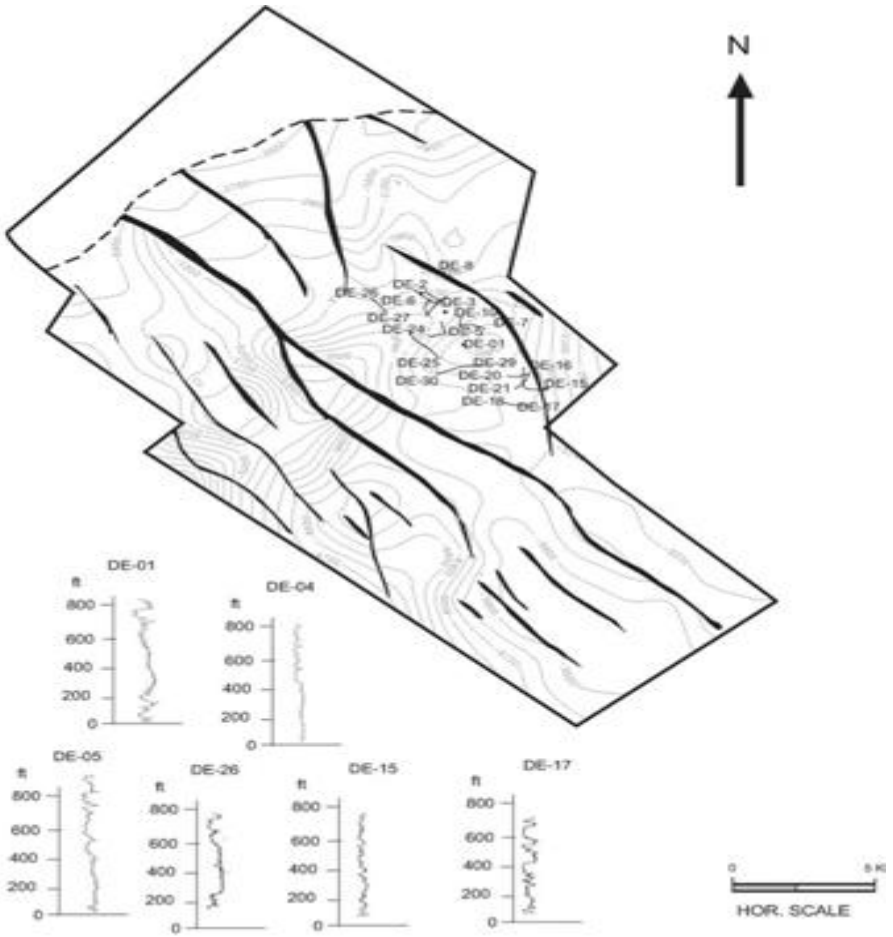

Figure 9: Structure map of sequence boundary, SB4. Gamma-ray log pattern coarsen upward from fine-grained deposits above the horizon. Delta-1 Well located at the trough of the structure the log show a coarser base.

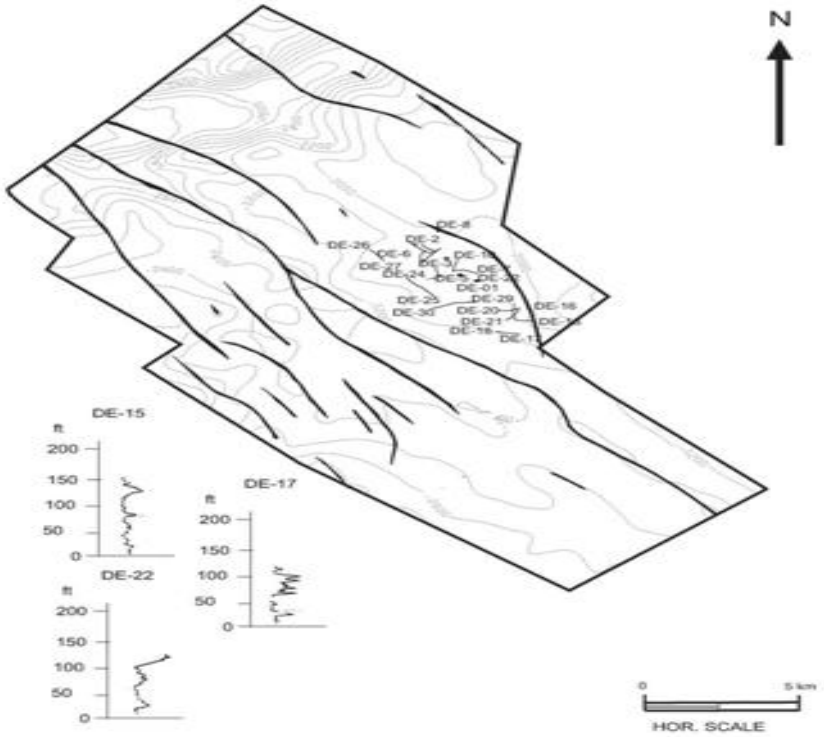

Figure 10: Structure map of sequence boundary, SB5. There is no well that penetrated the trough axis, but sediments above the surface are coarse-grained in Delta field.

IV. CONCLUSIONS

Five sequence boundaries (major erosion surfaces) divide the Agbada Formation, each formed during an episode of structural collapse of the basin prograding clastic wedge along basinward dipping listric normal faults. Sequence boundaries were carved by submarine mass flows across basin gradients steepened over a succession of down-dropped fault blocks. The five (5) sequence boundaries mapped were all within the Agbada formation since most of the hydrocarbon was believed to be trapped in the Niger Delta. Anticlinal closures and fault assisted closures regarded as good hydrocarbon prospect areas were delineated in the structural maps. The integration of seismic data and well logs proved to be a useful and important technique in structural mapping and was successful in defining the subsurface geometry, and determining the structure and hydrocarbon trapping potential of Delta field. The technique proved to be very useful in structural mapping. Hydrocarbon prospect areas were delineated in the structural maps produced. The growth faults acted as conduits for hydrocarbon from the underlying Akata formation. Thus, it is necessary to integrate all exploration and evaluation tools so as to effectively explore the study area and optimize well locations. Amplitude variation with offset (AVO), seismic attributes analysis and seismic inversion should be carried out in the study area to better discriminate the lithology, characterize the reservoirs and define the hydrocarbon types.

V. ACKNOWLEDGEMENT

The authors would like to acknowledge the management of Kumasi Polytechnic, Kumasi headed by the Rector Prof. N.N.N. Nsowah-Nuamah, for providing financial assistance and also the management and staff of Chevron Nigeria Ltd. (a division of ChevronTexaco Overseas), for providing 3-D seismic data and well logging data for the research.

REFERENCES

[1]. Adejobi AR, Olayinka AI (1997). Stratigraphy and hydrocarbon potential of the Opuama channel complex area, western Niger delta. Nig. Ass. of petrol. Expl. (NAPE) Bull., 12: 1-10

[2]. Barde JP, Chambertain P, Gralla P, Harwijanto J, Marsky J, Schroeter T (2000). Explaining a complex hydrocarbon system in the Permo- Triassic of the precaspian basin by integration of independent models. Abstracts, 62nd European Association of Geoscientists and Engineers Conference and Technical Exhibition, 2: (P.021), P. 4

[3]. Barde JP, Gralla P, Harwijanto J, Marsky J (2002). Exploration at the eastern edge of the prescapian basin impact of data integration on Upper Permian and Trasic prospectivity. Am. Assoc. Petrol. Geol. Bull., 86: 399-415.

[4]. Chukwueke C.C. (1997). Factors controlling hydrocarbon distribution in the central swamp deposit of the Niger Delta. Nig. Assoc. Petrol. Explorat. Bull., 12: 41-45.

[5]. Doust, H. and E. Omatsola, (1989). Niger delta: AAPG Memoir 48 p. 201-238.

[6]. Doust H, Omatsola E (1990). Niger Delta in divergent/passive margin basins, *in* J. D. Edwards and P. A. Santogrossied, eds., Am. Assoc. Petrol. Geol. Memoir, 48: 201-238.

[7]. Evamy, B.O., Herembourne, J., Kameline, P., Knap, W.A., Molloy, F.A. and Rowlands, P.H. (1978). Hydrocarbon habitat of Tertiary Niger Delta, American Association of Petroleum Geologists Bulletin, 62, p.1-39

[8]. Haack RC, Sundararaman P, Diedjomahor JO, Xiao H, Gant NJ, May ED, Kelsch K (2000). Niger Delta petroleum systems, Nigeria, *in* M. R. Mello and B. J. Katz, eds., Petroleum systems of South Atlantic margins: Am. Assoc. Petrol. Geol. Memoir, *73*: 213-231.

[9]. Haq, B.U., J. Hardenbol and P.R., Vail, 1987, Chronology of fluctuating sea-levels since the Triassic: Science, v. 235, p. 1153-1165.

[10]. Hosper J (1971). The geology of the Niger Delta area, in the Geology of the East Atlantic continental margin, Great Britain, Institute of Geological Science, Report, 70(16): 121-141

[11]. Knox, G. J. & Omatsola, M. E. (1989). Development of the Cenozoic Niger Delta in terms of the escalator regression model and impact on hydrocarbon distribution, in W. J. M. van der Linden et al., eds, 1987, Proceedings, KNGMG Symposium on Coastal Lowlands, Geology, and Geotechnology: Dordrecht, Klumer Academic Publishers, p. 181-202.

[12]. Merki PJ (1972). Structural geology of the Cenozoic Niger Delta: 1st Conference on African Geology Proceedings, Ibadan University Press, pp. 635-646.

[13]. Murat RC (1970). Stratigraphy and Paleogeography of the Cretaceous and Lower Tertiary in Southern Nigerian. 1st Conference on African Geology Proceedings, Ibadan University Press, pp. 251-266.

[14]. Nton, M.E. and Adebambo, B.A., (2009). Petrophysical evaluation and depositional environments of reservoir sands of X- field, offshore Niger delta ., Mineral Wealth Vol. 150 pp 1-12

[15]. Nton, M.E. and Adesina, A. D., (2009). Aspects of structures and depositional environment of sand bodies within tomboy field, offshore western Niger Delta, Nigeria RMZ – Materials and Geoenvironment, Vol. 56, No. 3, pp. 284–303
[16]. Ojo A.O. (1996). Pre-drill prospect evaluation in deep water Nigeria. Nig. Assoc. Petrol. Explo. Bull., 11: 11-22.
[17]. Reijers, T.J.F., (1996). Selected Chapters on Geology, SPDC of Nigeria, Copporate Reprographic Services, Warri, 197p
[18]. Short, K.C. and Stauble, A. J. (1967). Outline of the geology of Niger Delta, American Association of Petrroleum Geologists Bulletin, 51 p. 761-779
[19]. Tuttle, M. L. W., R. R. Charpentier and M. E. Brownfield, (1999). The Niger delta petroleum system: Niger delta province, Nigeria, Cameroon, and Equatorial Guinea, Africa: USGS Open-file report 99-50-H.
[20]. Weber KJ (1971). Sedimentological aspect of oil fielding the Niger Delta. Geol. Minjbouw, 50: 559-576.
[21]. Weber, K.J. and Daukoro, E.M. (1975). Petroleum geological aspects of the Niger Delta. Tokyo, 9th world Petroleum Congress Proceedings, 5 (2), p. 209-221
[22]. Weber KJ, Mandi J, Pilaar WF, Lehner E, Precious RG (1978). The role of faults in hydrocarbon migration and trapping in Nigeria growth fault structures. 10th Annual Offshore Technology Conference Proceedings, 4: 2643-2653.
[23]. Whiteman, A., (1982). Nigeria: Its Petroleum Geology, Resources and Potential: London, Graham and Trotman, 394 p.

American Journal of Engineering Research (AJER)
e-ISSN : 2320-0847 p-ISSN : 2320-0936
Volume-02, Issue-11, pp-216-222
www.ajer.org

Research Paper Open Access

Land use planning for sustained utilization of resources using Remote Sensing & GIS techniques: A case study in Mamit District, Mizoram, India

R.K. Lallianthanga, Robert Lalchhanhima Sailo
[1,2]*Mizoram Remote Sensing Application Centre, Science & Technology, Aizawl, Mizoram*

Abstract: **-** Proper land use planning for sustained and productive yields is the immediate need in north-east India, especially in states like Mizoram where the practice of shifting cultivation have rendered considerable destruction to both land resources and environment. It is imperative to develop land use plans which can counteract the detrimental effects on environment, and at the same time improve productivity of land. The present study deals with the application of remote sensing and GIS for land use planning in Mamit district of Mizoram. Indian Remote Sensing satellite data (LISS-III and Cartosat-I) had been used for generating various thematic layers like land use, slope, soil, drainage, etc. They were then integrated in conjunction with the ground and socio-economic data to evolve a comprehensive land use plan. The analysis in a GIS system helped in bringing out maps and statistics with constructive options for alternate land use plans which are expected to be both productive and sustainable.

Keywords: **-** *GIS, land use plan, Mamit, remote sensing*

I. INTRODUCTION

Land use planning in the context of this study, refers to the assessment of physical land resources and associated socio-economic factors in such a way that it can assist the farmers and planners in selecting options that not only increase land productivity but also are sustainable to meet the long term needs of the society. The present land use pattern of the district is unproductive and ecologically destructive due to the inherent system of shifting cultivation. The utilization of land resources had its impact on the biodiversity and environment of the region as much of the land use changes depended on how it was used in time and space. With a decadal growth rate of 36.59% in the population of the study area [1], there is need for proper methods of utilization, conservation and planning of land resource to keep pace with the basic requirements of the study area. Sustained utilization of available resources requires a scientifically approached land use planning process. There is, thus, an urgent need for research and evolution of proper strategical plans and policies based on reliable and sound technologies to find new land use alternatives.

Several plans and policies have been formulated and implemented to eradicate the age old land use system of shifting cultivation in the state by providing the farmers with alternative solutions and amenities. These policies had basic objectives for improving the rural economy and the socio-economic condition of population. A policy with a coherent approach for balancing productivity and conservation practices through constant monitoring and identification of problem areas [2] will go a long way in ensuring sustained utilization of natural resources.

Information on land use / land cover and possibilities for their optimal use is essential for the selection, planning and implementation of land use schemes to meet the increasing dynamics of land use [3]. Previous studies done to map the pattern of spatial distribution of various land use/land cover categories and area coverage in Serchhip rural development block highlighted the need for natural resource based planning for proper utilization and conservation of natural resources [4]. Similar studies based on satellite Remote Sensing techniques has also formulated strategic land and water resource development plans for Mat watershed, Aizawl district and has proven the effectiveness of IRS data for micro-level planning of rugged hilly terrain [5].

Geographic Information System (GIS), which has a strong capacity in data integration, analysis and visualization has become an important tool to support land use planning approaches [6]. The system's capacity to manage large amount of spatial data and derive additional information has also been proven [7]. In the context of land use planning, geospatial techniques and models have been researched and developed for its effective use in sustainable development of natural resources by integration of various GIS layers, which further demonstrates that geospatial techniques help in generation of a reliable spatial and non-spatial information database [8]. Geospatial modeling techniques used for locating various levels of biological richness has also been envisaged to be useful in land-use zonation and planning for sustainable use of natural resources [9].

Mapping of spatial patterns of land use, slope, drainage and other related natural landforms and features based on fine resolution Indian satellite data provides relevant, reliable and timely information as shown during the course of this study. Besides facilitating the creation of a comprehensive geo-database, spatial analysis in GIS has enabled the generation of an environmentally and economically sound land use plan for implementation in the study area.

II. STUDY AREA

The study area - Mamit District, is located in the north-western part of Mizoram, India between 23° 15' 21.25" and 24° 15' 16.80" N latitudes and 92° 15' 44.54" and 92° 40' 39.63" E longitudes [10]. It is bounded on the north by Assam and Kolasib District, on the south by Lunglei District, on the east by Aizawl District and on the west by Tripura and Bangladesh (Fig. 1). The total geographical area of the district is 3025 sq. km.

The study area experiences moderate climate conditions owing to its sub-tropical location. It is observed that the average mean summer temperature is (April to June) 24.20°C and average mean winter temperature (November to February) is 18.85°C [11]. The area also receives heavy rainfall as it is under the direct influence of south-west monsoon. The average annual rainfall is 3067 mm [11].

According to the 2011 census, the total population of the study area is 85,757 [1]. There are 3 notified towns [12] in the study area. The District headquarter- Mamit is well connected by road, and distance from the state capital, Aizawl is 112 km [13].

Although shifting cultivation still dominates the agriculture farming system, the study area is well known for its agricultural/horticultural plantations, forest plantations and vast areas of bamboo forest. The well-known "Dampa Tiger Reserve" is located to the western fringe of the study area and accounts for a larger percent of dense forest cover. Owing to flat plains to the north-western edge, these areas are dotted with ponds and lakes, both naturally and artificially formed

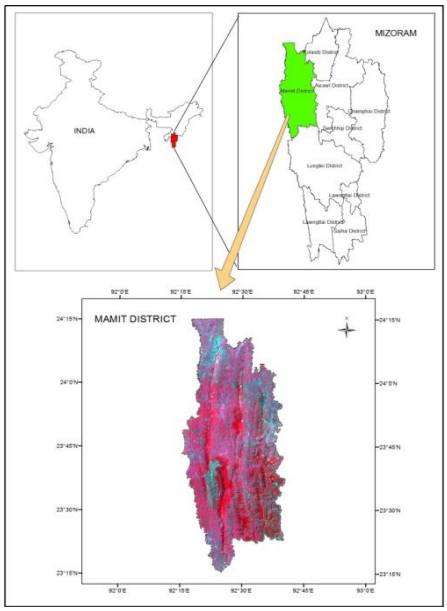

Figure 1. Location map of study area

. The forest type is mainly tropical evergreen forest mixed with semi evergreen forests. Among the forest resources, bamboo forests occupy a vast stretch and constitutes a larger fraction of tropical moist deciduous forests. The study area represents a monotonous sequence of argillaceous and arenaceous rocks. Apart from several minor ridge lines, the area is also characterized by three main ridgelines, intervening valleys and less prominent ridges [10].

III. MATERIALS AND METHOD

3.1. Data used

IRS P6 LISS III and Cartosat I (stereo pair ortho kit) satellite data were used to prepare thematic maps, and the ancillary data including past records/reports/maps collected from various sources were used for reference. Survey of India Toposheets were also referred for preparing base maps and obtaining physiographic information.

3.2. Method

The study incorporates standard techniques of remote sensing and geographic information system (GIS) for mapping of the land use/ land cover features. Image processing was carried out using Image Processing system (Erdas Imagine) and Geographic Information System (Arc Info) to increase the visual perceptibility of land use features. Visual interpretation and on-screen digitization techniques were used for classifying and delineating the various land use / land cover classes from the satellite data. Cartosat I data was utilized to derive and generate other information (eg. roads, drainage) and also used for generation of slope map.

Table 1. Guidelines for generation of Proposed Land use systems

S.No.	Present Land Use	Slope	Soil	Proposed Land Use
1	Single cropped agricultural land, current jhum, abandoned jhum, Scrubland	0 – 25%	Fine Loamy Fluventic Dystro-chrepts and Fine Loamy Fluvaquentic Dystrochrepts, very deep, good moisture.	Wet Rice Cultivation (WRC)/ Pisciculture.
2	Single cropped agricultural land, current jhum, abandoned jhum	25 – 35%	Fine Loamy Fluventic Dystro-chrepts and Fine Loamy Fluvaquentic Dystrochrepts, deep, good moisture.	Terrace cultivation
3	Current jhum, abandoned jhum	35 – 50%	Fine Loamy Typic Dystro-chrepts. Loamy Skeletal Umbric Dystrochrepts and clayey, Typic Haplohumults, very deep, good moisture.	Agro-Horticulture
4	Existing plantation. Bamboo, current jhum & abandoned jhum adjacent to road.	25 – 50%	Fine Loamy Typic Dystro-chrepts. Loamy Skeletal Typic Hapludults and clayey, Typic Haplohumults, very deep, good moisture.	Agri/Horti plantations
5	Scrub lands, hill top/crest	25 – 50%	Loamy Skeletal Typic Dystro-chrepts, deep, moderate moisture	Silvi-pasture
6	Current jhum, abandoned jhum, open forest, Scrubland	> 50%	Loamy Skeletal Typic Dystro-chrepts and Loamy Skeletal Typic Hapludults, deep, moderate moisture	Afforestation
7	Forest (dense & open), Forest plantations and bamboo	-	-	To be conserved as forest and bamboo reserves

A land use plan was generated on the basis of various parameters of the present land use, slope percent and soil conditions in the study area. There are various criteria adopted for this purpose as given in Table 1 and the process of generating these proposed land use systems was done in a GIS environment.

Ground truthing forms the core activity of the study. Pre-field interpretations and plans prepared in map forms were, therefore, subjected to evaluation on-site. Various field information necessary for assessing and validating the accuracy of the maps prepared were collected during ground truth surveys. Data from these surveys were then incorporated during the final stages of land use plan preparation.

IV. RESULTS AND DISCUSSION

4.1. Land Use / Land Cover

The major land use/land cover classes in the study area were broadly classified into built-up land, agricultural land/horticultural land, forests (dense and open), bamboo forest, forest plantation, jhum land (current and abandoned jhum/shifting cultivation), scrubland and water body. The land use / land cover statistics is given in Table 2 and the map shown in Fig. 2.

Table 2. Land Use/Land Cover statistics of Mamit District

Land Use / Land Cover categories	Sq.km	%
Built-up	16.74	0.55
Wet Rice cultivation (WRC)	7.09	0.23
Agri/horti plantation	8.93	0.30
Dense Forest	406.32	13.43
Open Forest	727.45	24.05
Bamboo	1563.06	51.67
Forest plantation	13.01	0.43
Current Jhum	72.92	2.41
Abandoned Jhum	170.33	5.63
Scrubland	21.43	0.71
Water Body	17.72	0.59
Total	**3025.00**	**100.00**

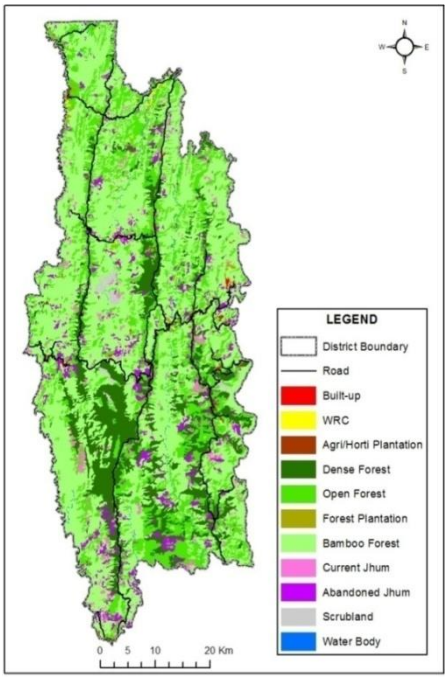

Figure 2. Land use/Land cover Map of Mamit District

4.2. Soil

The soils found in the study area were mostly of red and yellow loamy. They contained high amount of organic carbon and were high in available nitrogen, low in phosphorus and potassium content [10]. The soil is also acidic in nature as the study areas experiences heavy rainfall. On the basis of their physico-chemical and morphological properties, the soils found at order level are: - Entisols, Inceptisols and Ultisols [14]. The classification of soil in the study area upto Family level was referred to as per previous project work done by MIRSAC.

4.3. Slope

The study area is characterized by few prominent hill ridges running parallel to each other. The western part constitutes narrow river valley plains which ascend gradually to the east. The southeastern part consists of rather rugged hilly ridges with steep slope, narrow valleys and small streams. The hillside slopes are mostly gentle to steep, and escarpments are also visible in many places of the study area. It can be summarized that the eastern part of the study area has steeper slopes as compared with the western part. For the purpose of this study, the district area has been classified into four slope facets (Fig. 3) to be incorporated during land use plan preparation in a GIS environment.

4.4. Land Use Planning

Various sustainable land use practices (as discussed below) were modeled using the layers generated in GIS environment and considerations were also given to the socio-feasibility and implementation by incorporating data from ground surveys. The area statistics is given in Table 3 and the map showing areas for various proposed land use activities are shown in Fig. 4.

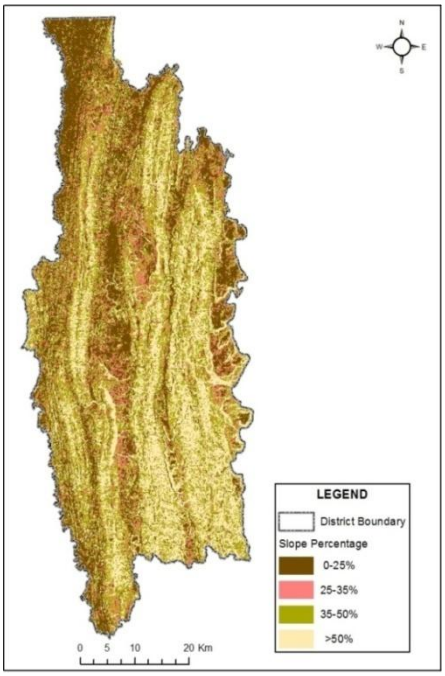

Figure 3. Slope Map of Mamit District

***4.4.1. Wet Rice Cultivation / Pisciculture* :**

The study area has potential wet rice cultivation areas scattered along river banks and valley plains. These areas can be further brought under cultivation of other crops along with the practice of pisciculture. The existing farms and cultivation areas can also be extended The main components of the system are composite fish culture with paddy or vegetables. The area proposed for this land use system is 74.33 sq.km, which is 2.46% of the total study area. *Oryza sativa* (rice) is recommended as the main crop during the kharif season. The Rabi crops recommended are legumes and vegetables.

4.4.2. Terrace farming :

Terrace farming proposed in the study area can meet the additional cropping needs of the farmers on sloping lands as well as ensure soil and water conservation. This system of land use requires good irrigation facilities. Paddy as well as other crops can be cultivated in rotation on these terraces. The analysis has shown that terrace farming can be carried out in several places and most of the jhum lands can also be converted to terrace farms. The proposed area for this form of farming occupies 25.85 sq.km or 0.85% of the district.

4.4.3. Agro-horticultural system :

This system refers to a farming practice where both fruit bearing trees and field crops can be grown together in many variations. Perennial crops, seasonal crops and nitrogen fixing plants may be grown in rotations. The recommended crops for this system include Betelnut (*Areca catechu*), Tea (*Camellia sinensis*), Banana (*Musa paradisiacal*), Orange (*Citrus reticulate*), Red oil palm (*Elaies guinensis*), etc. with vegetables and other root crops. The proposed area for this system is 73.22 sq.km which is 2.42% of the district.

4.4.4. Agricultural/Horticultural Plantation :

The study area has several places suitable for agriculture and horticulture plantations. Existing land use and slope plays an important factor for selecting plantation sites. Some plantations have to be confined to specific locations keeping in mind the socio-economic value of such plantations. The species identified as suitable crops for plantation under this system includes Coffee (C*offea spp*), Broomgrass (*Thysanolaena maxima*), Ginger (*Zingiber officinale*), Hatkora (*Citrus macroptera*), Pineapple (*Ananus comosus*), etc. The area proposed for taking up these plantations covers 709.33 sqkm or 23.45% of the district.

***4.4.5. Silvi-pastoral system* :**

This system refers to cultivation of fodder crops along with trees. The tree component in this system can assist in conservation of forest resources. Besides providing fuel and fodder, the system helps in maintaining a good vegetative cover. Species having fodder, firewood and fruit bearing values as well as adaptable to the

sites may be selected. Degraded scrublands and forests can be utilized for this system. Other agroforestry systems such as Agri-silvicultural systems, Agri-horti-pastural systems, Horti-sericultural system, etc. can also be practiced depending upon the terrain and the local needs. The area proposed for this system of land use is 29.42 sq.km which covers 0.97% of the district.

***4.4.6. Afforestation* :**

Degradation of forest lands and its adjoining areas have necessitated taking up of afforestation programmes in the study area. Various afforestation programmes in which commercial tree species are planted as Government or private plantations like Teak (*Tectona grandis)*, Michelia (*Michelia champaca*), Gamari *(Gmelina arborea),* Toona (*Cedrela toona*) plantations have been taken up. The wastelands can also be reclaimed through afforestation programmes. The additional recommended species for this system are –*Albizia procera, Ficus spp., Grevelia robusta, Gmelina oblongifolia,* etc and other native tree species found in the area may also be planted under such programmes. The area proposed for afforestation is 319.32 sq km of land or 10.55% of the district.

Table 3. Proposed Land Use Plan - Mamit District

Proposed Land Use Plan	SqKm	%
WRC/Pisciculture	74.33	2.46
Terrace Cultivation	25.85	0.85
Agro-Horticultural system	73.22	2.42
Agri/Horti Plantation	709.33	23.45
Silvi-pastoral system	29.42	0.97
Afforestation	319.32	10.55
Forest	904.35	29.90
Bamboo forest	854.72	28.26
Non-Planned area		
Water body	17.72	0.59
Built-up	16.74	0.55
Total	**3025.00**	**100.00**

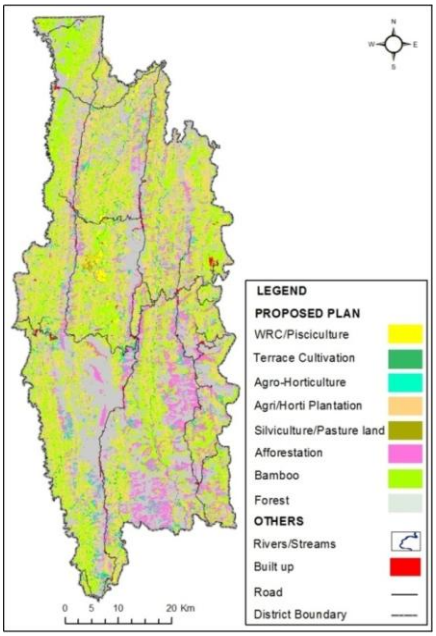

Figure 4. Land Use Plan Map for Mamit District

***4.4.7. Forest* :**

Forests of the study area comprises dense and open forests, as well as forest plantations (Govt. owned and private). Open forests generally refer to successive secondary successions of fallow lands (7 years and above), once used for shifting cultivation, but have remained unused for a long period of time [15]. It is proposed that the existing forest cover and the supply/community reserves be preserved, and additional conservation techniques may be adopted to prevent encroachment and exploitation of forests for unsolicited commercial purposes. Voluntary organizations / NGOs can be entrusted the task of forest conservation as well as extension of the forests in the form of parks, etc. The proposed area under tree forest is estimated to be 904.35 sq km, constituting 29.90 % of district.

4.4.8. Bamboo Forest :

The study area abounds with bamboo forests and they constitute a larger percentage of forest resources. They are confined to lower altitudes and are generally found between 80-1400 m MSL [16]. Although rich in this forest resources, there are certain areas that require conservation from over exploitation as well as from shifting cultivation. Projects under the state and central government can assist in ensuring the conservation and rehabilitation of stocks. Initiative taken up by the village communities in the form of bamboo reserves can be encourage by providing proper incentives. An estimated proposed area of 854.72 sq km or 28.26% of the total study area has been demarcated for conservation of bamboo forest.

V. CONCLUSION

Land use planning in hilly terrains has always been a challenge for planners as there are many bio-physical and socio-economic factors to be considered. This is where remote sensing and GIS can play an

important role with its ability to incorporate both spatial and non-spatial data to generate realistic and effective land use plan. The inherent system of land use in the study area has produced a lot of changes in the present land use / land cover pattern. The present land use shows that only a fraction of the total land (0.30%) is used as permanent agricultural/horticultural lands for food and cash crop production. This aspect could be improved as the study indicates that there is good potential for Agricultural / Horticultural system and Agriculture /Horticulture plantations. In addition, the available flat lands could provide extensions for taking up other allied agricultural activities such as WRC, Pisciculture and terrace cultivations. The land use plan prepared in the study has also considered the conservation of the existing forests including bamboo forests to maintain ecological balance while taking up improved and alternate farming practices. The sustained utilization of forest resources has to be considered while planning for any development that uses these resources.

REFERENCES

[1] Directorate of Census Operations, Census of India 2011. Provisional Population Totals, Paper 2, Volume 1 of 2011. Mizoram series 1(Directorate of Census Operations, Mizoram., 2011). pp: 2.

[2] Lallianthanga RK, Satellite Remote Sensing for Sustainable Development of Mizoram in the 21st Century. Proc. of Symposium on Science & Technology for Mizoram in the 21st Century, Aizawl, 17-18 June, 1999, 155.

[3] Archana & Sandeep Kumar Kaushik, Land use / Land cover mapping of IGNP Command area in Bikaner District of Rajasthan. Int. J. of Engineering Science & Research Technology, 2(2), 2013, 209.

[4] Lallianthanga RK & Goswami DC, Land Use satellite mapping of land cover patterns in Mizoram, India : A case study of Serchhip rural development block, Aizawl district. Indian Journal of Landscape Sys. & Eco. studies, 20, 1997, 64-68.

[5] Lallianthanga RK & Goswami DC, Satellite Mapping of Shifting cultivation in Mat Watershed, Aizawl District, Mizoram : An Agro-Environmental perspective. Proc. of NAGI's (En.Region) National Conference on Environment & Sustainable Development, Guwahati, Vol.1, 13th & 14th Oct. 1998.

[6] Trung NH, Le Quang Tri, Mensvoort MEF van & Bregt AK, Application of GIS in land-use planning, a case study in the coastal Mekong Delta of Vietnam. In: Proc. International Symposium on Geoinformatics for Spatial Infrastructure Development in Earth and Allied Sciences, Ho Chi Minh, Vietnam, 01-11 November 2006.

[7] F.C. Dai, C.F. Lee & X.H. Zhang, GIS-based geo-environmental evaluation for urban land-use planning: A case study, Engineering Geology, 61(4), 2001, 257-271.

[8] Kushwaha SPS, Suchismita Mukhopadhyay, Hari Prasad V & Suresh Kumar, Sustainable development planning in Pathri Rao sub-watershed using geospatial techniques. Current Science, 98, 2010, 1486.

[9] Chandrashekhar MB, Sarnam Singh & Roy PS, Geospatial modeling techniques for rapid assessment of phytodiversity at landscape level in western Himalayas, Himachal Pradesh. Current Science, 84, 2003, 669.

[10] MIRSAC, *Natural Resources Mapping of Mizoram using Remote Sensing and GIS, Mamit District (A Project Report),* (Mizoram Remote Sensing Application Centre, Science Technology & Environment, Aizawl, 2005), pp. 2, 8, 23, 37, 44.

[11] MIRSAC, *Meteorological data of Mizoram* (Mizoram Remote Sensing Application Centre, Science & Technology, Aizawl, 2012). pp. 7. 9.

[12] Economics & Statistics, *Statistical Handbook, Mizoram*, (Directorate of Economics & Statistics, Govt. of Mizoram, 2010), pp. 152.

[13] NIC, Mizoram - More information - Distances by Routes. http://mizoram.nic.in/more/rkanhmun.htm (Accessed : 11 Nov. 2013).

[14] USDA, *Soil taxonomy. A Basic system of soil classification for interpreting soil surveys. US Department of Agriculture, Soil Conservation Service.* (Robert E. Krieger Publishing Company Inc, Krieger drive, Malabar, Florida 32950, 1988), pp. 179, 227, 349.

[15] Lallianthanga RK, Goswami DC & Sarma CM, Satellite Monitoring of Secondary Succession subsequent to Shifting Cultivation : A Case Study of Kolasib District, Mizoram. *J. of Ecology, Environment & Conservation*, 5(1), 1999, 32.

[16] Lallianthanga RK & Sailo RL, Monitoring of bamboo flowering using satellite remote sensing and GIS techniques in Mizoram, India. *Science Vision*, 12(4), 2012, 147.

American Journal of Engineering Research (AJER)
e-ISSN : 2320-0847 p-ISSN : 2320-0936
Volume-02, Issue-11, pp-223-229
www.ajer.org

Research Paper Open Access

Effect of Channel Condition on the Performance of LTE in various Transmission Mode

Rashedul Haque Chowdhury, Mostarina Zinnat-Ara,Ammar A.R. Khan,Tanjima Neherin,Md. Jakaria Rahimi
(Dept. of EEE, Ahsanullah University of Science & Technology, Bangladesh)

Abstract: - *Long Term* Evaluation (LTE) is an emerging 4G wireless technology. Multiple-Input Multiple-Output (MIMO) systems are a primary enabler of the high data rate to be achieved by LTE . According to LTE Release 9 there are 7 MIMO configurations from mode 2 to 8. An LTE base station is expected to select and switch among these transmission modes based on channel quality feedback like Channel Quality Indicator (CQI) . In this paper we have investigated the effect of different channel conditions at different SNR levels on the performance achieved through transmission mode 1 to 4. The simulation output shows that the mode 3 and 4 which are open loop and close loop spatial multiplexing respectively using 4 transmitting antenna outperforms all other mode in terms of high throughput at very reasonable BLER.

Keywords: - *LTE, Transmit Diversity, Open Loop Spatial Multiplexing, Close Loop Spatial Multiplexing, Throughput*

I. INTRODUCTION

In This Paper we have investigated the effect of channels as CQI on the performance of LTE Release 9 through LTE link level simulator developed by the Institute of Communications and Radio Frequency Engineering, Vienna University of Technology[1]. This paper is made for the developing countries, who are migrating towards 4G LTE Technology, so that they can use this as a helping manual.That's why transmission mode 1-4 are simulated in high multipath fading environment and the superiority of the open loop and close loop spatial multiplexing were demonstrated.

The paper is organized in following section. In section two we have presented the brief over view of LTE transmission modes. In Release 8 , Long Term Evaluation(LTE) [2] was standardized by 3GPP as the successor of the Universal Mobile Telecommunication System (UMTS). The targets for downlink and uplink peak data rate requirements were set to 100Mbits/sec and 50Mbits/sec, respectively when operating in a 20MHz spectrum allocation [3].

First performance evaluations show that the throughput of the LTE physical layer and MIMO enhanced WCDMA [4] is approximately the same [5-9] . However, LTE has several other benefits of which the most important are explained in the following.

The LTE downlink transmission scheme is based on Orthogonal Frequency Division Multiple Access (OFDMA) which converts the wide-band frequency selective channel into a set of many flat fading sub-channels. The flat fading sub-channels have the advantage that even in the case of MIMO transmission – optimum receivers can be implemented with reasonable complexity , in contrast to WCDMA systems .OFDMA additionally allows for frequency domain scheduling , typically trying to assign only "good" sub-channels to the individual users . This offers large throughput gains in the downlink due to multi-user diversity [10,11].

II. TRANSMISSION MODE DOWNLINK IN LTE

In the downlink, LTE uses technologies such as MIMO, transmit diversity or SISO, Beamforming etc are used to achieve high data rates. In the Release 9 specification [12], up to four antennas are defined in the base station and up to four antennas in the UE[13].

Table 1: Transmission Modes in LTE Release 9		
Transmission Mode (TM)	**Description**	**Comment**
1	Single transmit antenna	Single antenna port; port0
2	Transmit diversity	2/4 antennas
3	Open loop spatial multiplexing with cyclic delay diversity(CDD)	2/4 antennas
4	Close loop spatial multiplexing	2/4 antennas
5	Multi-user MIMO	2/4 antennas
6	Close loop spatial multiplexing using a single transmission layer	1 layer (rank 1), 2/4 antennas
7	Beamforming	Single antenna port; port 5
8	Dule-layer beamforming	Dule-layer transmission, antenna ports 7 or 8

Here we discussed about Transmission Mode 1,2,3,4.
Transmission Mode 1 is Single transmit antenna[13].

Transmission Mode 2 is Transmit diversity which sends the same information via various antennas, whereby each antenna stream uses different coding and different frequency resources. This improves the signal-to-noise ratio and makes transmission more robust. For two antennas, a frequency-based version of the Alamouti codes (space frequency block code, SFBC) is used, while for four antennas, a combination of SFBC and frequency switched transmit diversity (FSTD) is used [13] .

Transmission Mode 3 is Open loop spatial multiplexing with CDDwhich supports spatial multiplexing of two to four layers that are multiplexed to two to four antennas, respectively, in order to achieve higher data rates. It requires less UE feedback regarding the channel situation (no precoding matrix indicator is included), and is used when channel information is missing or when the channel rapidly changes, e.g. for UEs moving with high velocity[13].

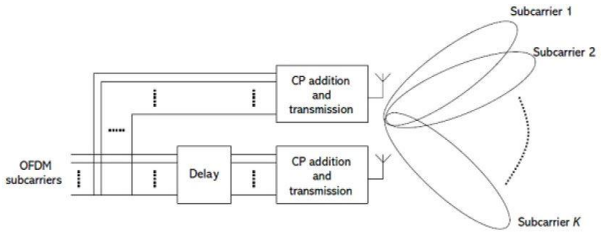

figure 1: TM 3, Spatial multiplexing with CDD

Transmission Mode 4 is Closed loop spatial multiplexing with up to four layers that are multiplexed to up to four antennas, respectively, in order to achieve higher data rates. To permit channel estimation at the receiver, the base station transmits cell-specific reference signals (RS), distributed over various resource elements (RE) and over various timeslots[13].

Table 2 : Codebook indices for spatial multiplexing with two antennas [12]

Spatial multiplexing LTE		
Codebook index	Number of layers υ	
	1	2
0	$\frac{1}{\sqrt{2}}\begin{bmatrix}1\\1\end{bmatrix}$	$\frac{1}{\sqrt{2}}\begin{bmatrix}1 & 0\\0 & 1\end{bmatrix}$
1	$\frac{1}{\sqrt{2}}\begin{bmatrix}1\\-1\end{bmatrix}$	$\frac{1}{2}\begin{bmatrix}1 & 1\\1 & -1\end{bmatrix}$
2	$\frac{1}{\sqrt{2}}\begin{bmatrix}1\\j\end{bmatrix}$	$\frac{1}{2}\begin{bmatrix}1 & 1\\j & -j\end{bmatrix}$
3	$\frac{1}{\sqrt{2}}\begin{bmatrix}1\\-j\end{bmatrix}$	-

III. SIMULATION RESULT

In LTE we have seen the variation in Throughput & BER with the change of Transmission mode & CQI. Ideally it seems like the picture below :

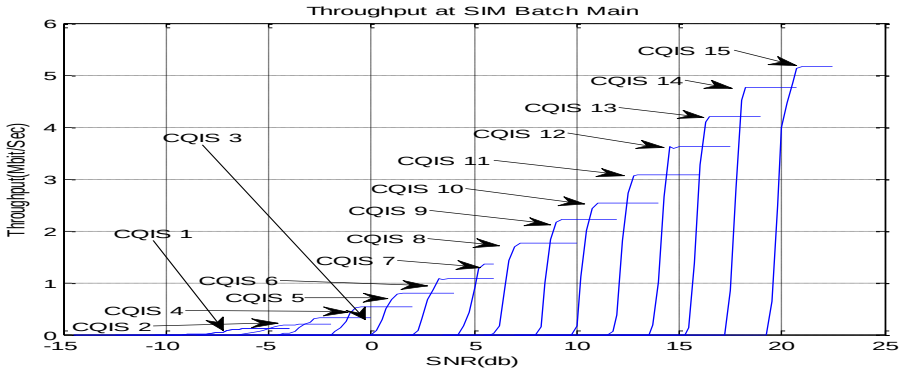

figure 2:Ideal variation in throughput with the change of CQI

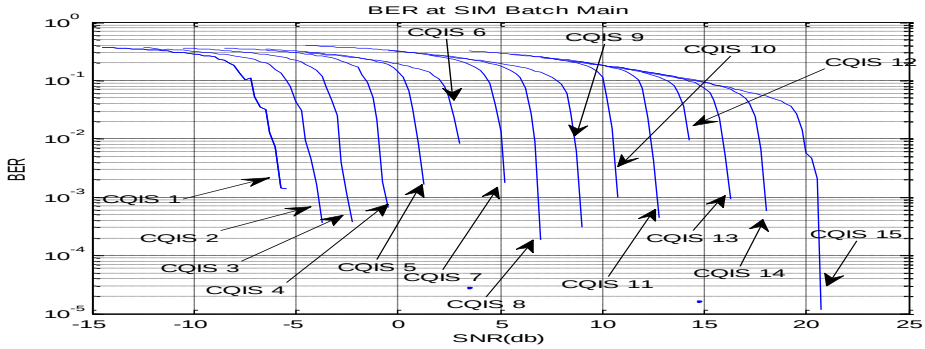

figure 3:Ideal variation in SNR with the change of CQI

Here SUMIMO (Single User Multiple Input Multiple Output),MUMIMO(Multiple User Multiple Input Multiple Output),SUSISO(Single User Single Input Single Output) are used as parameters.

But practically, the variation doesn't happen in this way. The throughput & BER varies differently for each types of transmission mode. Every transmission mode follows a definite rate to vary the parameter (Throughput & BER). We can observe the variation rate through the table below:

Table 3 : Variation Rate of Transmission Mode with the change of CQI

CQI	Transmission Mode (Transmission mode,nTx,nRx)	Peak throughput (Mbit/Sec)
1	1	0.1
	221	0.1
	242	0.1
	342	0.2
	442	0.2

2	1	0.25
	221	0.25
	242	0.2
	342	0.35
	442	0.35
3	1	0.35
	221	0.35
	242	0.35
	342	0.75
	442	0.75
4	1	0.55
	221	0.5
	242	0.5
	342	1
	442	1
5	1	0.8
	221	0.75
	242	0.7
	342	1.4
	442	1.5
6	1	1.1
	221	1.01
	242	1
	342	2
	442	2
7	1	1.4
	221	1.3
	242	1.4
	342	2.4
	442	2.4
8	1	1.8
	221	1.8
	242	1.6
	342	3.2
	442	3.2
9	1	2.2
	221	2.1
	242	2
	342	4
	442	4
10	1	2.6
	221	2.4
	242	2.3
	342	4.6
	442	4.6
11	1	3.1
	221	2.9
	242	2.8
	342	5.6
	442	5.6
12	1	3.6
	221	3.4
	242	3.3
	342	6.5
	442	6.5
13	1	4
	221	4
	242	3.8
	342	7.6
	442	7.6
14	1	4.8
	221	4.5

	242	3.5
	342	8.9
	442	8.9
15	1	4.1
	221	4.8
	242	2.4
	342	8.8
	442	8.8

The variation rate & characteristics' can also be determined graphically at a fixed value of SNR.

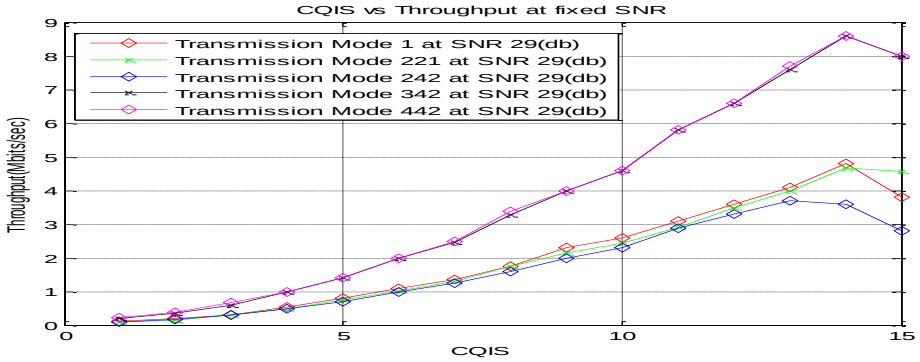

figure 4: Variation Rate of Transmission Mode

IV. SIMULATION COMPARISON

From the graph we have seen that, Transmission Mode 3 & 4 have highest throughput rate.At the same time we have observed that each transmission mode has a peak value for a fixed CQIS.After that it tends to decrease . we can compare all the four transmission modes (1,2,3,4) by taking graphs showing all transmission mode for some CQI.

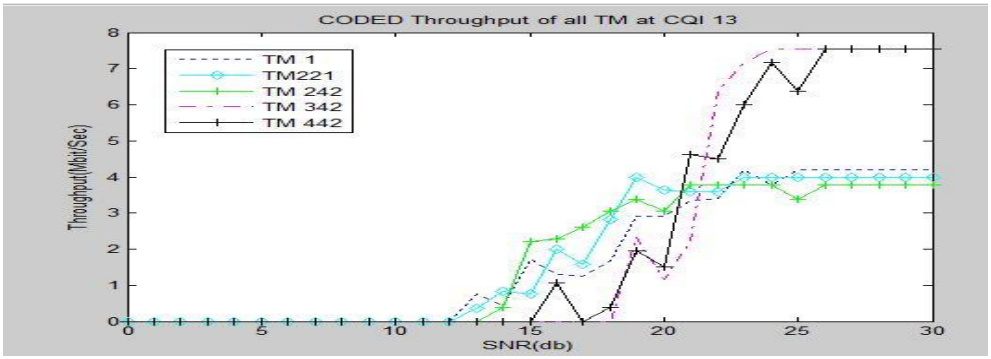

figure 5 : Coded Throughput for all Transmission Mode at CQI 13

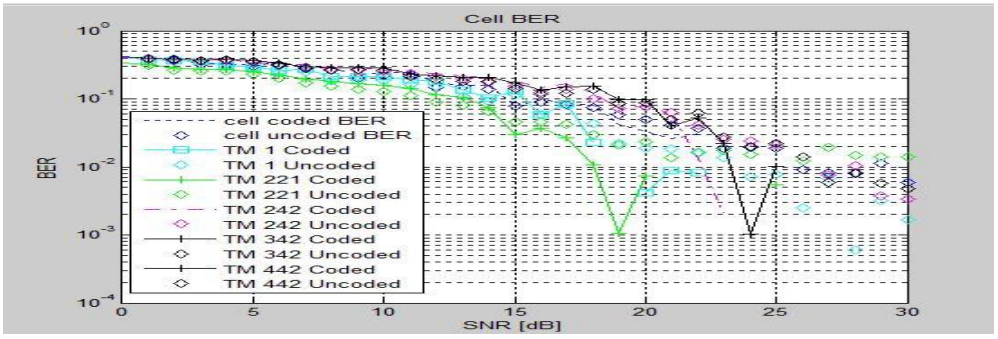

figure 6: SNR for all Transmission Mode at CQI 13

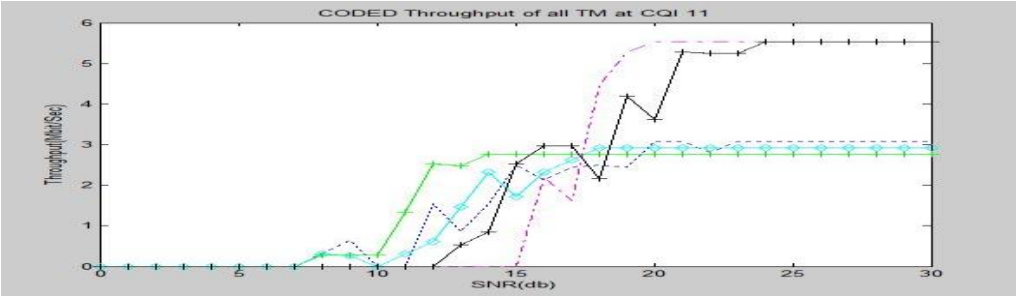

figure 7 : Coded Throughput for all Transmission Mode at CQI 11

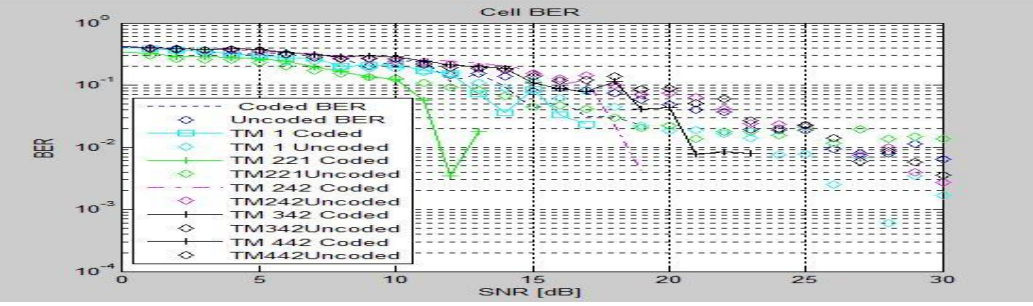

figure 8: Snr for all Transmission Mode at CQI 11

From the comparison we can easily say that transmission mode 3 & 4 (Open loop & close loop spatial multiplexing) has large throughput than transmission mode 2 (transmit diversity).

V. CONCLUSION

For transmit diversity[14], Space Time Block Codes (STBC) are used to provide improvement against the channel deteriorating effects. Alamouti STBC are considered to be the simplest space time block codes. It is well known that Alamouti codes [15] can achieve full diversity and full code rate simultaneously. For this reason it is used in noisy channel.

Spatial Multiplexing[16] provides extra gain as compared to TxD Independent data streams are transmitted from the NT transmit antennas in spatial multiplexing. Two classes of spatial multiplexing, open and closed loop spatial multiplexing Figures 3 and 4, are discussed. OLSM transmits the independent data streams without deploying any feedback algorithm. In CLSM essential amount of CSI is used as feedback which enables us to achieve high throughput. That's why in noiseless channel Spatial Multiplexing (Transmission Mode 3 & 4) is used for getting high throughput.

VI. ACKNOWLEDGEMENTS

We would like to thank the whole LTE research group for continuous support and lively discussions. We would also like to thank our supervisor Md. Jakaria Rahimi for his continuous help. Without his help it would be impossible to complete the work.

REFERENCES

[1] Christian Mehlführer, Martin Wrulich, Josep Colom Ikuno, Dagmar Bosansk and Markus Rupp, Simulating the long term evolution physical layer , *Proc. of the 17th European Signal Processing Conference (EUSIPCO 2009)*, Glasgow, Scotland, 2009/8,1471-1478

[2] 3GPP, *Technical speci_cation group radio access network; (E-UTRA) and (E-UTRAN)*, stage 2,Sep. 2008. [Online]. Available: http://www.3gpp.org/ftp/Specs/html-info/36300.htm

[3] 3G Evo-lution ,in E. Dahlman, S. Parkvall, J. Skold, and P. Beming, HSPA and LTE for Mobile Broadband, 1st ed. (Academic Press, 2007).

[4] H. Holma, A. Toskala, K. Ranta-aho, and J. Pirskanen, High-speed packet access evolution in 3GPP release 7,*Proc. IEEE Communications Magazine, 45(12)*, Dec. 2007, 29-35,.

[5] E. Dahlman, H. Ekstrom, A. Furuskar, Y. Jading,J. Karlsson, M. Lundevall, and S. Parkvall, The 3G longterm evolution - radio interface concepts and performance evaluation, *in Proc. 63rd IEEE Vehicular Technology Conference 2006 (VTC2006-Spring), vol. 1*, May 2006, 137-141.

[6] H. Ekstrom, A. Furuskar, J. Karlsson, M. Meyer, S. Parkvall,J. Torsner, and M. Wahlqvist, Technical solutions for the 3G long-term evolution, *IEEE Communications Magazine, 44(3)*, Mar. 2006, 38-45,.

[7] S. Parkvall, E. Dahlman, A. Furuskar, Y. Jading, M. Olsson, S. Wanstedt, and K. Zangi, LTE-advanced – evolving LTE towards IMT-advanced, *in Proc. 68th IEEE Vehicular Technology Conference 2008 (VTC2008-Fall)*, Sep. 2008.
[8] M. Tanno, Y. Kishiyama, N. Miki, K. Higuchi, and M. Sawahashi, Evolved UTRA - physical layer overview, *in Proc. IEEE 8th Workshop on Signal Processing Advances in Wireless Communications 2007 (SPAWC 2007)*, Jun.2007.
[9] J. J. S_anchez, D. Morales-Jim_enez, G. G_omez, and J. T. Enbrambasaguas, Physical layer performance of long term evolution cellular technology, *in Proc. 16th IST Mobile and Wireless Communications Summit 2007*, Jul. 2007.
[10] T. Tang and R. Heath, Opportunistic feedback for downlink multiuser diversity, *IEEE Communications Letters, 9(10)*, Oct. 2005, 948-950.
[11] A. Gyasi-Agyei, Multiuser diversity based opportunistic scheduling for wireless data networks, *IEEE Communications Letters, 9(7)*, Jul. 2005, 670-672.
[12] Technical Specification Group Radio Access Network, *Physical Channels and Modulation, Release 9; 3GPP TS 36.211 V 9.1.0*, March 2010.
[13] Rohde and Schwarz,LTE Transmission Modes and Beamforming (Bernhard Schulz, 1MA186_0e, October 2011).
[14] Syed Ali Irtaza, Aamir Habib and Qamar-ul-Islam, Performance Comparison of LTE Transmission Modes in High Speed Channels using Soft Sphere Decoder .
[15] J. Guan, X. Ye, and P. Tian, A robust scheme for transmit diversity and spatial multiplexing based on channel spatial correlation, *in International Conference on MultiMedia and Information Technology*, 2008
[16] G. Wetzker, Definition of spatial multiplexing gain, *in Electronic Letters*.

American Journal of Engineering Research (AJER)
e-ISSN : 2320-0847 p-ISSN : 2320-0936
Volume-02, Issue-11, pp-230-241
www.ajer.org

Research Paper Open Access

Lignocellulosic-Based Rheological Modifier for High Temperature Oilfield Drilling Operations

Mohamed Rashid Ahmed-Haras[1], Mohamad Nasir Mohamad Ibrahim[1], Abdussalam Salhin Mohamed Ali[1], Coswald Stephen Sipaut[2], Ashraf Ahmed Ali Abdalsalam[3]

[1]*School of Chemical Sciences, Universiti Sains Malaysia, 11800 Penang, Malaysia*
Email: chemoscientific@gmail.com, mnm@usm.my
[2]*School of Engineering and Information Technology, Universiti Malaysia Sabah, UMS Road, 88400 Kota Kinabalu Sabah, Malaysia*
[3]*School of Pharmaceutical Sciences, Universiti Sains Malaysia, 11800 Penang, Malaysia*

Abstract: - In this study, a rheological modifier for water-based drilling mud is prepared by exploiting the Kraft pulping residual of oil palm empty fruit bunch (OPEFB) fibers. From an experimental point of view, readily combination between water-based drilling mud and Lignin Graft Copolymer (LGC) provided an optimum rheological performance and gelling effect for the water-based drilling mud. This new water-based drilling mud additive demonstrated competitive characteristics to other existing commercial additives. The rheological performances of LGC are studied and the findings show that LGC gives good gelling, viscosity building, and pH controlling abilities at low concentration of 0.5% w/w. It is also illustrates excellent thermal stability at high temperature up to 200°C.

Keywords: - *Rheological modifier; Drilling mud; OPEFB fibers; Lignin Graft Copolymer; Thermal stability*.

I. INTRODUCTION

The selection of proper drilling mud during the rotary drilling process is vital for the success of any drilling operation. In fact, most of drilling problems are a direct or indirect consequence of improper mud selection. Within this context, there are many types of drilling mud used in the petroleum industry. Generally all of these types are classified into three main categories: (1) air and foam-based mud (ABM); there are drilling conditions under which a liquid drilling fluid is not the most desirable circulating medium. In such a case, air or foam is used as drilling mud to accommodate these special conditions. Moreover, this is the most advantageous and effective type of drilling mud in consolidated rock formations, (2) oil-based mud (OBM); this drilling mud is made up of oil as the continuous phase. Diesel oil is widely used to provide the oil phase. In addition, this type of drilling mud is more expensive, as it requires stringent pollution control measurement and is also difficult to dispose, and (3) water-based mud (WBM); this type is the mud in which water is the continuous phase. This is the most common drilling mud used in oil drilling and it consists mainly of water, clay, and specialized chemical additives. Besides that, this type is mixed friendly with water and allows drilling mud additives to perform efficiently. Beyond that; it is inexpensive and presented less environmental problems compared to oil-based mud [1]. Owing to that fact, the type of drilling mud used in this study is a water-based mud.

Nevertheless and during the course of drilling an oil or gas well, the drilling mud without any additives is unable to provide satisfactory rheological properties required for optimum performance in well drilling [2]. Thus, a number of additives are used to alter the mud properties to fulfill all of the requirements of drilling mud. In addition, different types of additives, either chemicals or polymers, are used in designing a drilling mud to meet some functional requirements, such as appropriate mud rheology, density, mud activity, fluid loss control, etc [3]. It is noteworthy to mention that when drilling in deep wells for oil, gas, or geothermal reservoirs; high temperatures are usually encountered which adversely influence the performance of drilling muds [4]. Also, a

major difficulty in formulating high-temperature drilling muds is that mud is negatively affected by elevated temperatures, first gelling excessively and then becoming inert at extreme temperatures [3]. For that reason, there is always a need for drilling mud additives which can stabilize drilling mud suspensions at high temperatures. This need can be fulfilled by developing new additives (polymers) that have better resistance to the high temperature drilling operations. Accordingly, both naturally occurring and synthetic polymers have been widely used. Among them, chemically modified biopolymer is probably one of the most extensively studied due to its low cost, lack of toxicity, and biodegradability characteristics [5]. In the same way, this study is designed to produce chemically modified lignin by means of graft copolymerization technique. Such technique could offer new type of drilling mud additives, i.e. thermally stable rheological modifier.

Traditionally, lignin has been viewed as a waste material or a low value by-product of pulping and paper industry with its utilization predominantly limited to its use as a fuel to fire the pulping boilers [6]. Almost all lignins extracted from lignocellulosic materials from the pulp and paper industry are burnt to generate energy and considered as an excellent fuel, since lignin yields more energy when burnt than cellulose. Nevertheless, the possible development in the lignin industrial utilization is limited to very low growth because until now only a small amount (2%) of lignin is commercially used [7]. This includes the manufacturing of wide range of products. In fact, due to the lack of appropriate industrial processes, lignin is considered as a mostly non-commercialized product.

On the other hand, lignins have many specifications (chemical and biophysical properties) which can advantageously be exploited to develop new and environmentally friendly products. In this regard, lignins are non toxic, potentially of high value, inexpensive, and available in large amounts. They possess highly reactive locations that can be surprisingly modified through a selection of chemical, physical and/or enzymatic reactions, which give them a great potential for their exploitation as industrial raw materials [8]. In agreement with that, this study is an effort to investigate the potentiality of using modified lignin as a drilling mud additive in oilfield drilling operations especially in high temperature and high pressure conditions.

II. EXPERIMENTAL STUDY

2.1 Materials

The raw material used in this study was oil palm empty fruit bunch (OPEFB) long fiber supplied by Sabutek (M) Sdn. Bhd, a Malaysian company that specializes in the recycling of OPEFB.

The catalyst p-toluenesulfonic acid (PTS) was used as received from Merck (Merck, Germany). Acrylic acid (AA) with 99% purity was purchased from Aldrich® (Sigma-Aldrich, USA). AA was purified under vacuum distillation process to remove phenolic inhibitors, stored in the refrigerator, and brought to room temperature before being used. The commercial viscosifying and gelling agents, High Viscosity Sodium Carboxy Methyl Cellulose (CMC-HV), Guar Gum (GG), and Xanthane Gum (XG) were supplied by Kota Mineral Chemical (M) Sdn. Bhd, Sim Company and Aldrich® (Sigma-Aldrich, USA).

2.2 Methods

2.2.1 Isolation of Kraft Lignin (KL)

This technique includes different laboratory procedures. In addition, these procedures have been applied subsequently in order to produce pure KL. Apart from these, they consist of three experimental processes as explained in the following subsections.

2.2.1.1 Kraft pulping of OPEFB

The Kraft pulping process involves digesting of OPEFB fibers at elevated temperature and pressure in cooking liquor, which is an aqueous solution of sodium sulfide (Na_2S) and sodium hydroxide (NaOH). The cooking liquor chemically dissolves the lignin that binds the cellulose fibers together.

Prior to the pulping process, 1000 g of OPEFB fibers was soaked in water for two days to remove non-fibrous materials. In the pulping process, the soaked OPEFB fibers were mixed with 41.8 g of Na_2S, 128.7 g of NaOH, and 5.6 L of distilled water in a 20 L stainless steel rotary digester. After which, the mixture was heated from approximately 70°C to a maximum cooking temperature 170°C, followed by 3 hr cooking period. Once the cooking period was completed, the contents of the digester were transferred to a container and washed in the pulp washer, where the spent cooking liquor (black liquor) was separated from the pulp.

2.2.1.2 Extraction of KL

The extraction of KL from the black liquor was accomplished by employing an acidification method. In this direction, the high alkali pH black liquor which was collected after the completion of the pulping process was then acidified using sulphuric acid in order to recover KL as precipitate. In particular, 800 mL of black liquor in 1000 mL beaker was acidified with 20% v/v sulphuric acid until pH 2; thereby a precipitation of KL was formed. The precipitate was filtered and washed with pH 2 water, which was prepared using the same acid

in the previous step. KL was then dried in a vacuum oven at 45°C for 72 hr. In order to avoid the moisture in the KL particles, it was grinded to a powder form and dried again in a vacuum oven at 45°C for 72 hr.

2.2.1.3 Purification of K L

In general, lignins are rarely isolated as pure materials, and are always associated with carbohydrate linkages (cellulose and hemicellulose) to varying extent depending on their isolation procedure [9].
The purification of KL was conducted by extracting KL in the soxhlet apparatus for 6 hr with n-pentane to remove lipophilic, non-lignin matters such as wax and lipids [10]. The precipitate was filtered and washed twice with pH 2 water to remove the excess n-pentane and non-lignin phenolic compounds which may still remain after the pulping process. The purified KL was then dried further in the vacuum oven at 45°C for another 48 hr.

2.2.2 Preparation of Lignin Graft Copolymer (LGC)

A grafting reaction was achieved in small test tubes equipped with magnetic stirrers. In details, about 0.75 g of PTS was introduced into test tube with appropriate amounts of Kraft lignin (KL) and acrylic acid (AA). The tube was deoxygenated by flushing it with nitrogen gas for 10 min, sealed with aluminum foil and then placed in a water bath at 80^{o}C for 18 hr with vigorous stirring. After a specific reaction time, the tube was immersed in an ice bath at 0^{o}C for one hour with incessant stirring. The result was a highly turbid black liquid that was decanted into 0.1 M zinc sulfate aqueous solution at a ratio of 1:10 v/v with agitation and was allowed to stand at room temperature overnight. After this period, unreacted KL was precipitated and removed by filtration. The light brown liquid was evaporated to remove the aqueous solution and unreacted AA. The lignin graft copolymer (LGC) was obtained as light brown fine particles. These particles were collected and dried in an oven at 100^{o}C for 72 hr to remove moisture from the LGC [11].

2.2.3 Application of LGC

In this study, LGC, which is a chemically modified biopolymer, was used as a drilling mud additive, i.e. viscosity building (viscosifying) agent, gelling agent, and pH controlling agent. In addition, LGC was subjected to the simulated hydrocarbon drilling conditions in order to evaluate its ability as a drilling mud additive.

2.2.3.1 Preparation of water-based mud

In the present study, in all the experiments related to mud property tests, the basic water-based mud was prepared by adding 80 g of bentonite and 4 g of sodium carbonate into 1000 mL of water that was previously heated in a large beaker at 80°C. The ingredients of water-based mud were mixed with pre-heated water gradually with vigorous stirring using mixer which was set at high speed of 2000 revolution per minute. This process was conducted for half an hour, after which, the beaker was sealed with aluminum foil and allowed to stand for 24 hours at room temperature [12-18].

2.2.3.2 Effect LGC as a rheological modifier

The rheological properties of the water-based mud samples in this study were measured using a direct-indicating rheometer (Fann Rheometer model 286). The Fann rheometer constants had been adjusted so that the apparent viscosity, plastic viscosity, and yield point could be obtained using readings from rotor sleeve speeds of 300 rpm and 600 rpm. Rotor speeds of 300 or 600 were obtained by setting the position of the speed control lever. Measurements were read directly from the deflection scale. Accordingly, these parameters could be calculated using the following formulae from API Recommended Practice of Standard Procedure for Field Testing Drilling Fluids [19-20].

$$\text{Apparent viscosity } (\mu_a) = \theta_{600} / 2 \text{ (cp)}$$
$$\text{Plastic viscosity } (\mu_p) = \theta_{600} - \theta_{300} \text{ (cp)}$$
$$\text{Yield point } (\tau_y) = 0.511(\theta_{300} - \mu_p) \text{ (lb/100 ft}^2\text{)}$$

Additionally, gel strength (θ) measurements were read directly from the deflection scale. When making gel strength measurements, force was applied manually by turning the gel knob and observing the maximum reading on the deflection scale before the gel broke. In order to estimate the effect of different aging temperatures on the drilling mud rheological parameters, the API drilling mud aging experiments were carried out using a Fann Roller Oven Series 2500 and a 500 mL Fann stainless steel aging cell.

In this study, two sets of experiments were performed according to the American Petroleum Institute standard procedures [12-13]. In the first experiment, the basic drilling mud samples were treated with different concentrations of LGC in order to optimize its efficiency as a drilling mud viscosifier and gelling agent. Furthermore, two values of temperature were chosen to study the performance of LGC at room temperature and

high temperature. In details, LGC were added with different concentrations of 0.3, 0.5, and 0.7% w/w into the basic mud samples, after which, the rheological parameters were measured before and after heating and vigorous agitation at 25°C and 90°C for half an hour. The second experiment was designed to evaluate the performance of LGC as a drilling mud viscosifier and gelling agent at high temperature (200°C). Moreover, the viscosity building and gelling abilities of LGC were tested and compared to the commercial viscosity building and gelling agents that are available in the market, such as sodium carboxy methyl cellulose (CMC), guar gum (GG), and xanthane gum (XG). In this experiment, the basic drilling mud samples were treated with either 0.5% w/w of LGC, CMC, GG, or XG simultaneously with vigorous stirring in order to homogenize the mud samples with the additives. This concentration (0.5%) was chosen since LGC acts optimally as a viscosity building and gelling agent at this level (based on the first experiment result). The rheological parameters were measured before and after the heating and aging process at 200°C for 16 hr.

2.3 Characterizations

2.3.1 Differential Scanning Calorimetry (DSC) analysis

In this study, glass transition temperature (T_g) values of KL and LGC were estimated using Perkin Elmer model Pyres 1 DSC. Approximately 10 mg of sample was heated from -50°C to 180°C at the heating rate of 20 °C/min in a nitrogen atmosphere at the flow rate of 30 mL/min.

2.3.2 Fourier Transform Infrared (FTIR) spectroscopy

FTIR spectroscopy was used as an analytical technique for the estimation of the functional groups presented in lignin [21].

In this study, FTIR spectroscopy was able to differentiate the chemical bonds in the molecular structure of KL and LGC. The ungrafted KL and LGC samples were analyzed using KBr pellet technique. In this technique, the KBr thin pellet was prepared by grinding 1% of sample into potassium bromide (KBr). It was then scanned by the Perkin Elmer system 2000 FT-IR spectrometer in the range from 4000 cm^{-1} – 400 cm^{-1}.

III. RESULTS AND DISCUSSION

3.1 Extraction of KL

During the Kraft pulping process, the lignin that dissolved from the raw material (OPEFB) is separated in the form of a liquor, rich in phenolic compounds, that represents the process effluent [22]. This effluent is dark brown or black in color; hence is called black liquor. The black liquor contains, in addition to the main fraction, lignin, sugars from degraded hemicellulose and cellulose, hereafter grouped as hemicellulose and salts [23].

Conventionally, lignin can be separated from other black liquor components using acid precipitation method. In addition, the acid precipitation method is the most common method to recover the lignin from the black liquor [24]. From an experimental point of view, the reduction in the pH of this liquor which is proportioned by the sulphuric acid addition caused the precipitation of the solubilized lignin, such that the lower the pH the higher the recovered lignin mass [25]. In this study, Kraft lignin (KL) was extracted from the black liquor by means of minimizing its alkali pH (11.52) to acidic pH (2) using acid precipitation method via diluted (20%) sulphuric acid (H_2SO_4); thereby KL was precipitated as a brown powder.

3.2 KL graft copolymerization reaction

The main chemical functional groups in KL are the hydroxyl, methoxyl, carbonyl, and carboxylic groups [26]. These functional groups present prospective positions on lignin structure to associate with other monomers and induce the graft copolymerization reaction. Therefore, acrylic acid may possibly polymerize with KL and the reaction takes place by the formation of the ester bond which linked AA with KL. A possible reaction mechanism of grafting the AA chain onto the KL structure might comprise two reaction steps, as shown in Figure 3.1. The suggested mechanism involved in the attachment of polyacrylic acid (PAA) chain onto the KL backbone via polycondensation process produced LGC and eliminated water. An ester bond was formed by the interaction, i.e. the esterification between hydroxyl group in KL and carbonyl group of AA homopolymer chain. Furthermore, the ester bridge linked PAA as a pendant chain onto the KL main chain {Figure 3.1(a)}. The PAA homopolymer chain was formed using a PTS inducement of AA monomers, as shown in Figure 3.1(b).

Figure 3.1 Suggested reaction mechanism of grafting AA chain onto KL main chain

3.3 Thermal properties of KL and LGC

The thermal properties of ungrafted KL and LGC were studied using the DSC analysis. The KL is an amorphous compound with T_g at 58.03°C, as illustrated by DSC thermogram in Figure 3.2. The amourphousity of the KL may be due to the complication in its structure which somewhat impedes the occurrence of an arrangement in its composition. Therefore, no melting temperature T_m or crystallization temperature T_c has been recorded in the DSC thermogram.

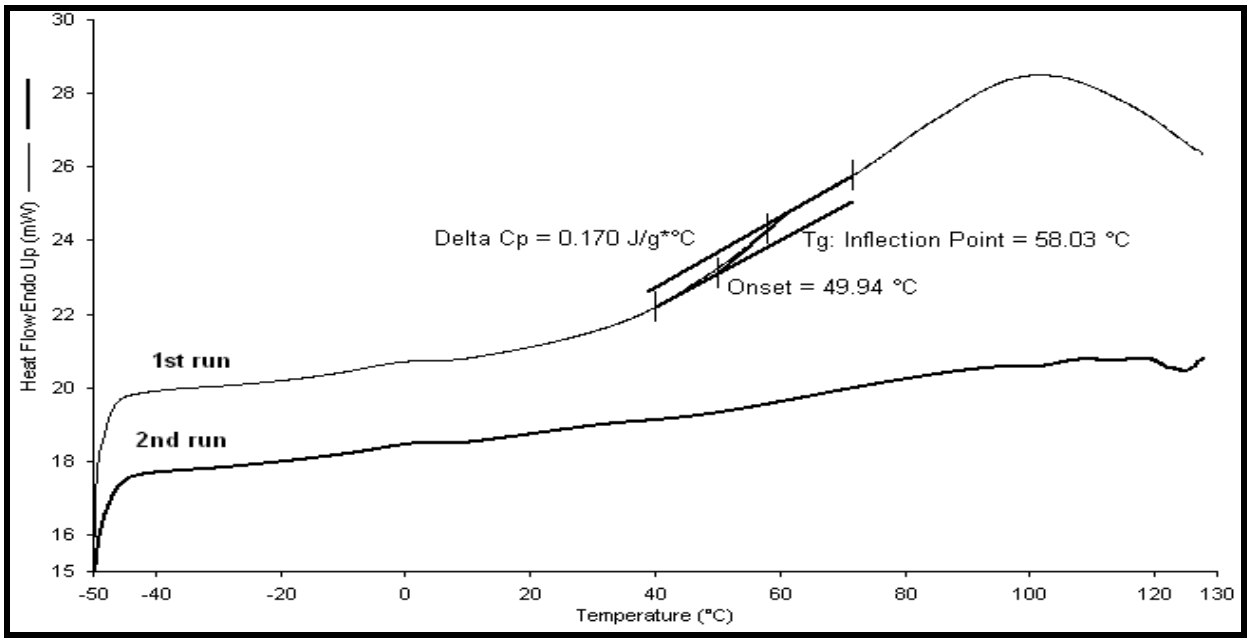

Figure 3.2 DSC thermogram of KL

After the grafting reaction had been achieved, it was observed that the resulting LGC also occurred in an amorphous phase, verifying that the grafting reaction had not strongly adapted the complexity of KL starting material. LGC has two T_g values at 73.85°C and 121.84°C respectively, as shown in the DSC thermogram in Figure 3.3. This illustrates the incompatibility in the LGC structure. The possible explanation of occurrence of these two T_g values is based on the free volume concept, which attributed a low T_g value to the large free volume in the graft copolymer chain while the highest T_g value refers to the chain with less free volume [27].
As free volume increases, the T_g temperature tends to decrease [28]. The above-mentioned explanation investigated the correlation between free volume property and LGC chemical structure that was suggested in Figure 3.1. Therefore, the lower T_g value corresponds to AA homopolymer branched chain which is a hydrocarbon chain without bulky groups that gives PAA molecules enough space to move. This means, the mobility of PAA molecules tends to be more flexible, which may increase the free volume and decrease the T_g. On the contrary, the phenyl groups in KL may increase the bulkiness in KL main chain and decrease its molecules mobility as well as its chain flexibility; thus, the free volume decreases and high T_g value obtained. Furthermore, the grafting reaction has enhanced the thermal properties of KL, whereas the two T_g temperatures of LGC are both more than the T_g temperature of KL.

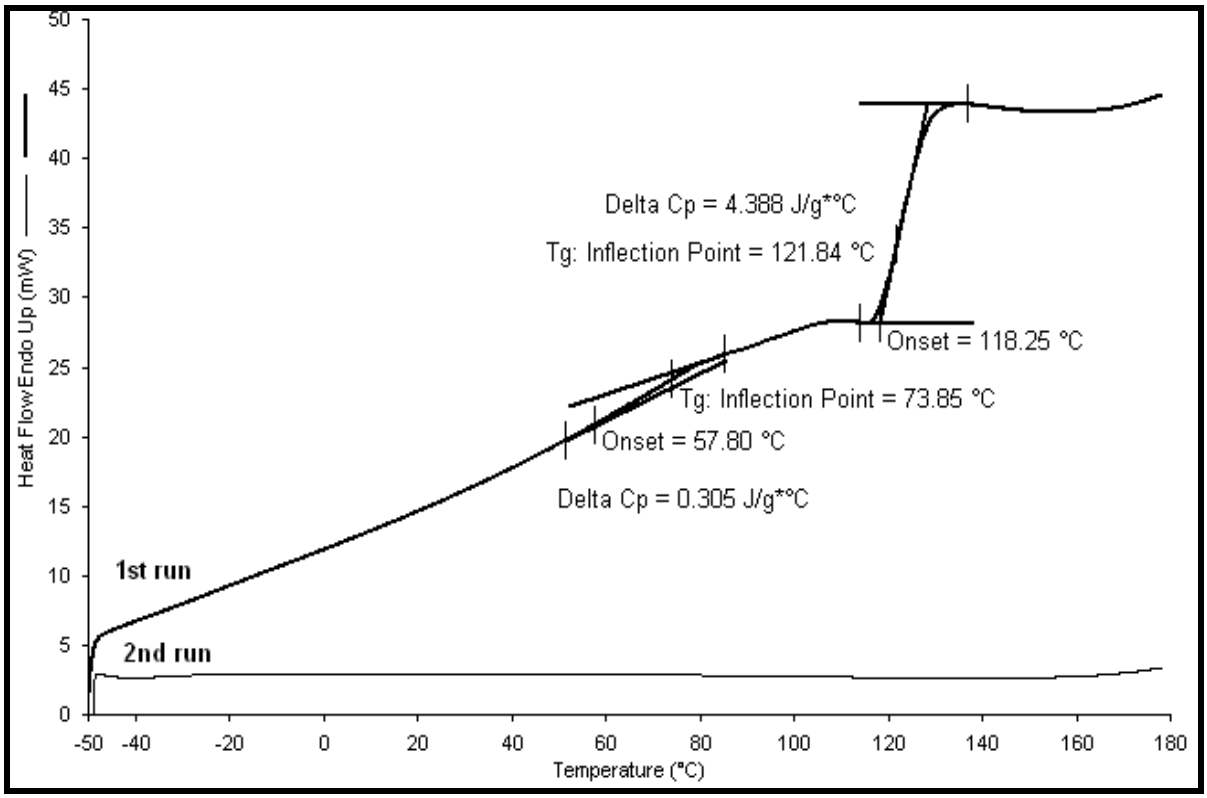

DSC thermogram of LGC

3.4 FTIR spectroscopy

Figure 3.4 illustrates the FTIR spectra of KL and LGC. The KL spectrum shows absorption at 3415.52 cm^{-1} assigned to (OH) broaden band of either hydrogen bonded or hydroxyl group in the phenolic and aliphatic compounds. The absorption peak at 2935.29 cm^{-1} was due to (C-H) stretch band of methyl group [29]. The vibration at 1712.69 cm^{-1} exhibited (C=O) stretch band of carbonyl group [30]. The stretching of (C=C) and (C-C) bands in the aromatic range were recorded at 1616.20 cm^{-1} and 1462.98 cm^{-1} respectively [31]. The peak at 1143.11 cm^{-1} could be attributed to (C-O) bond in ethers.

In the LGC spectrum, the presence of peak at 3419.04 cm^{-1} was assigned to (OH) stretch bonds of hydroxyl group [32]. The frequency at 2920.86 cm^{-1} was due to the stretching of (C-H) band of methyl group in lignin [33]. Peaks at 2489.21 cm^{-1} and 1919.17 cm^{-1} were considered aromatic overtones. The absorption at 1723.07 cm^{-1} was due to (C=O) the stretch band in α and β-unsaturated esters which verified the placement of ester bonds between aromatic rings in the KL structure and unsaturated polymeric chain of PAA and supported the expected grafting reaction mechanism in Figure 3.1. The characteristic ester group in the spectrum

substantiated that the LGC was formed by ester bonding between the KL and PAA. 1601.55 cm^{-1} and 1497.10 cm^{-1} wave numbers were distinguished as (C-C) stretching bonds in aromatic rings in lignin components [34]. Further evidence to the occurrence of the ester groups among LGC structure was provided by the absorption at 1189.59 cm^{-1} which was assigned as an expanding (C-O) bond in the ester groups.

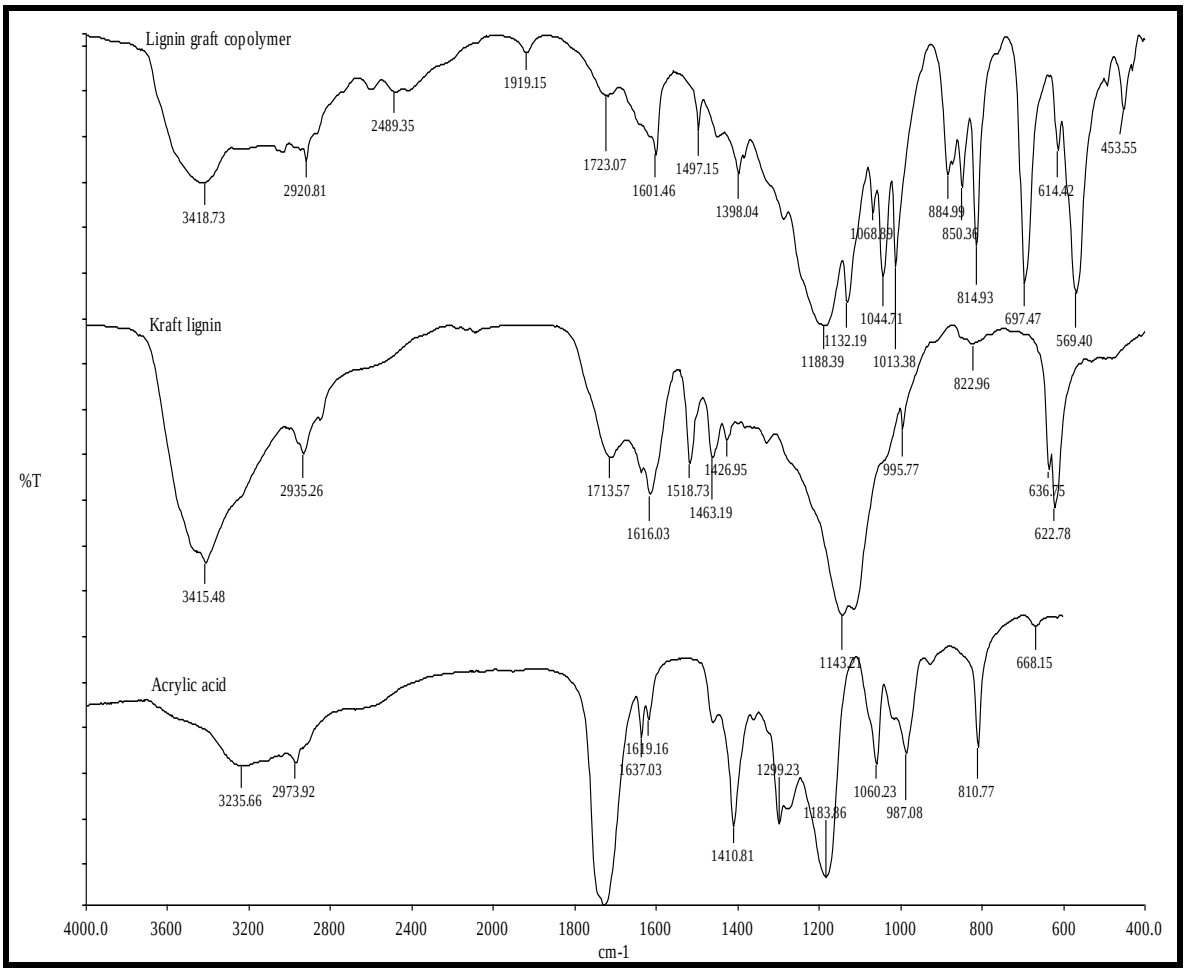

Figure 3.4 FTIR spectra of LGC, KL, and AA

3.5 Effect of LGC on drilling mud properties

The study was conducted to explore the use of this water-soluble LGC as a potential drilling mud multi-functional additive.

3.5.1 LGC Rheological effect

The mud rheological tests were performed according to the American Petroleum Institute (API) standard specifications by means of a direct-indicating viscometer with other equipment which specifically designed to simulate the hydrocarbon drilling well conditions.

Table 3.1 shows the rheological experimental data of water-based mud and different concentrations of LGC-based mud under different aging temperatures. In this regard, the rheological properties of water-based drilling mud without any additives (i.e. as the basic mud sample) was tested before and after the aging process at two temperatures; ambient temperature of 25°C (room temperature) and high temperature of 90°C. These two values of temperature were chosen in order to investigate the effect of temperature on the rheological behavior of the drilling mud. Regarding to that, the rheological parameters such as apparent viscosity, plastic viscosity, and gel strength of water-based mud were increased as the aging temperature elevated to 90°C. These phenomena could be related to the decrease of the mud pH value, which simultaneously decreased with the increase in the aging temperature. The pH of the mud was slightly decreased after experiencing high temperature rolling process. In conformity with the elevated temperature, the decrease of the pH value facilitates

the occurrence of the interlayer dehydration reaction [35]. In addition, the dehydration at high temperature may release a small amount of water present between the layers. Thus, the loss of water causes the aggregation of the mud interlayers or plates. As a consequence, this aggregation generated the increase of drilling mud viscosity and gel strength due to the corresponding increase of the aging temperature.
Nevertheless, lignin graft copolymer was introduced into the basic water-based mud samples at different concentrations (i.e. 0.3, 0.5, and 0.7% w/w) in order to optimize its ability to enhance the rheological properties of the drilling mud. Apart from that, the batches of the drilling mud with different LGC concentrations were subjected to the aging process to explore its thermal stability at low and high temperatures. However, an acceptable thermal stability of the drilling mud additives significantly enhanced the drilling mud transporting properties, e.g. viscosity and gel strength [36]. Within this context, the rheological data reveals that the drilling

Types of Mud	T (^{o}C)	μ_a (cp)	μ_p (cp)	τ_y (lb/100ft^2)	θ (lb/100ft^2)	pH
Water-based mud	27	28.00	12.00	34.15	48.04	11.91
0.3% w/w LGC + based mud	27	32.50	11.00	45.89	156.67	10.49
0.5% w/w LGC + based mud	27	40.00	14.00	55.50	152.49	9.63
0.7% w/w LGC + based mud	27	45.00	15.00	64.04	139.96	7.45
Water-based mud	90	30.50	15.00	33.08	64.75	11.82
0.3% w/w LGC + based mud	90	41.50	11.00	65.11	189.45	10.15
0.5% w/w LGC + based mud	90	40.50	11.00	62.96	158.76	9.20
0.7% w/w LGC + based mud	90	43.00	11.00	68.31	125.34	7.22

mud mixed with 0.5% w/w is much thermally stable at high temperature than 0.3%, and 0.7 % w/w LGC-drilling mud. Apart from that, it is also illustrated the optimum concentration of LGC is 0.5% which gives moderate viscosity, gel strength, and yield point compared to others at both temperatures.

Table 3.1 Rheological experimental data of water-based mud and different concentrations of LGC-based mud with different aging temperatures

It was observed that LGC with low concentrations developed the viscosity and gel strength required for water-based mud. This revealed the viscosity-building and gelling abilities of LGC despite experiencing the temperature changes and the dynamic agitation. Moreover, this phenomenon may attribute to two causes. First, the carboxylate group in the LGC structure {Figure 3.1(a)} provides a negative charge that may absorb effectively onto the positive mud (bentonite) edges via electrostatic attraction force that may develop the rheological properties of the drilling mud. Second, the methoxy group in the LGC structure {Figure 3.1(a)} could be a good proton acceptor during the formation of the hydrogen bond [37]. Within same direction, the hydroxyl group in the LGC structure (LGC FTIR spectrum) eases the progress of the intermolecular hydrogen bonding formation [38]. Consequently, the formation of the hydrogen bond increases the inter-particle attraction forces between the LGC particles and the mud edges which lead to the flocculation in the mud system. Due to the aforementioned results and discussions, LGC has revealed its capability to be a potential rheological controlling agent in terms of viscosifying and gelling the water-based drilling mud.

3.5.2 Effect of LGC concentration on the drilling mud pH

Besides the study of the rheological behavior of the water-based mud with and without LGC addition, the effect of the LGC concentration on the pH of drilling mud samples was also investigated at room temperature and high temperature. In general, it is well known that the pH of the water-based mud is an alkaline pH medium [39]. In agreement with that, the pH of the water-based drilling mud was strong alkali pH value and then it was deviated slightly after the heating and the agitation at 90^{o}C. On the other hand, the LGC addition has an acidic affect on the water-based mud. As the LGC concentration increases in the drilling mud samples, the pH value decreases. This acidification affect of the LGC could be results from two causes. First, the acidification effect might be due to the use of sulphuric acid during the separation process of the Kraft lignin from the other wood components [40]. The sulphuric acid might have affected the structure of Kraft lignin used in the LGC preparation reaction. The other cause might possibly be corresponding to the branched acrylic monomer in the LGC structure {Figure 3.1(a)}. That might give the acidic character to LGC when it was used as

a drilling mud additive. However, the acidic character of the LGC offered advantageously another application to the LGC as a water-based drilling mud additive, i.e. pH controlling agent. Since it is efficiently reduced the pH of the drilling mud without further additives that were normally used in the drilling field. Those additives were employed to control the pH of the drilling mud in order to avoid the corrosivity of the drilling tools. Generally, the corrosion rates are lower at the mildly alkaline pH and higher in the mildly acidic pH range [41]. Within this context, the desired pH value for the drilling operation indicated to be within the range 10 to 8. Regarding to this study, among all LGC concentrations which have been evaluated, only 0.5% w/w of LGC maintained the pH of the water-based mud within the desired pH range.

3.5.3 Effect of high temperature on drilling mud additives

In recent years, there have been a number of challenges for drilling muds to keep pace with the advancing operational drilling mud technologies [42]. Among these challenges is the thermal stability of the drilling mud and the drilling mud additives. In general, the thermal stability of the drilling mud is described as its ability to withstand progressively increasing temperature while flowing downhole and decreasing temperature on flowing back to the surface [41]. The indicator to determine the drilling mud thermal stability is the mud's rheological properties. In relation to this study, the thermal stability of LGC and commercial additives, e.g. CMC, GG, and XG were investigated using the aging process at 200^{o}C for 16 hr. Apart from that, 0.5% w/w of each of them was chosen to be treated with the drilling mud batches. This percentage was chosen since the LGC acted optimally as a drilling mud multi-functional additive at this level.

Table 3.2 Rheological experimental data of water-based mud with 0.5% w/w of LGC, CMC, GG, and XG before and after the aging process at 200^{o}C for 16 hr

Types of mud	μ_a (cp)		μ_p (cp)		τ_y (lb/100ft^2)	
	Before	After	Before	After	Before	After
0.5% w/w LGC + based mud	38.00	58.50	13.00	37.00	53.37	45.74
0.5% w/w CMC+ based mud	97.50	25.00	19.00	18.00	129.10	14,93
0.5% w/w GG + based mud	105.00	23.50	35.00	18.00	149.36	11.74
0.5% w/w XG + based mud	82.50	21.00	64.00	16.00	58.70	10.67

3.5.3.1 Lignin Graft Copolymer (LGC)

The rheological parameters of LGC were listed in Tables 3.2 and 3.3; these parameters were measured before and after the aging process at 200^{o}C for 16 hr. It was found that the LGC rheological parameters slightly changed after the LGC-drilling mud was exposed to high temperature of 200^{o}C. Accordingly, this change did not affect the miscibility and the consistency of the mud, i.e. inertness was not observed on the drilling mud after the aging process. Interestingly, in spite of the high temperature aging process, the LGC maintained the pH of the drilling mud within the desired drilling pH range. The pH value was slightly deviated after the aging at high temperature. This also reveals the thermal stability of the LGC up to 200 ^{o}C. The thermal stability may ascribe to the chemical structure of LGC which comprised different functional groups. These functional groups such as hydroxyl, carboxylate, and methoxy groups may activate the interconnection between the LGC and the mud plates. For that reason, the rheological properties of the drilling mud were developed as explained in the previous section.

3.5.3.2 Carboxy Methyl Cellulose (CMC)

The rheological performance of CMC was investigated under simulated hydrocarbon drilling well conditions, at 200^{o}C with the aging process of 16 hr. The CMC rheological parameters and the pH values were tabulated in Tables 3.2 and 3.3. It was observed that the CMC rheological parameters were drastically decreased after the aging process. Besides and regarding the CMC pH study, the pH value tends to moderate alkali medium after the highly temperature aging process. It was deduced that the CMC illustrated weaker viscosifying and gelling abilities at high temperature 200^{o}C. This could be due to the thermal degradation of the CMC at higher temperature. The poor rheological properties of the CMC at high temperatures are in good agreement with the previous study [43].

3.5.3.3 Guar Gum (GG)

The rheological properties of GG were examined and its rheological parameters were tabulated in Tables 3.2 and 3.3. As shown in these tables, the rheological parameters decreased extensively after the high temperature aging process at 200°C for 16 hr. Accordingly, the pH value deviated from strong alkali medium to weak alkali medium after the exposure to high temperature. The above mentioned results illustrated the insufficiency of the GG as a drilling mud viscosifying and gelling agent at high temperature of 200°C. Besides that, the high temperature drilling simulation was negatively reduced the ability of the GG to control the drilling mud rheological properties. This was resulted from the pronounced effect of the temperature on the degradability of GG. From previous report and this study, high temperature obviously accelerates the GG degradation process [44].

Table 3.3 Gel strength (θ) and pH values of water-based mud with 0.5% w/w of LGC, CMC, GG, and XG before and after the aging process at 200°C for 16 hr

Types of mud	θ (lb/100ft^2)		pH	
	Before	After	Before	After
0.5% w/w LGC + based mud	152.49	154.58	9.65	9.25
0.5% w/w CMC+ based mud	200.54	29.24	11.62	9.30
0.5% w/w GG + based mud	582.83	14.62	11.53	8.73
0.5% w/w XG + based mud	139.96	8.35	11.62	8.64

3.5.3.4 Xanthane Gum (XG)

Likewise other commercial drilling mud additives, the XG rheological parameters severely decreased after the high temperature hydrocarbon drilling simulation at 200°C for 16 hr as observed in Tables 3.2 and 3.3. Furthermore, the pH value was also decreased after the aging process. As a consequence, these results indicated the deficiency of the XG to develop the drilling mud rheological properties at high temperatures. This could be due to the effect of the high temperature on the XG chemical structure. In this regard, the high temperature caused the thermal degradation of XG and therefore influenced its rheological properties [45].

IV. CONCLUSIONS

In this study, the Kraft lignin (KL) was extracted from the Kraft black liquor which is an effluent from the Kraft pulping process of the oil palm empty fruit bunch (OPEFB) fiber. As indicated in the FTIR spectrum, the extracted product has wide diversity of functional groups which chemically considered as active centers. Such functional groups could open newer possibilities to expand the chemically modification process of lignin. Within this sight, this process will enhance the applicability of lignin in many industrial aspects. In this direction, the water soluble LGC was successfully prepared by the means of bulk copolymerization reaction using p-toluenesulfonic acid (PTS) as a catalyst. Apart from that, the reaction mechanism involves an esterification process that facilitates the grafting reaction.

In the application part and unlike other drilling mud additives, the LGC demonstrated an excellence thermal stability regardless the high temperature hydrocarbon drilling well simulation. This becomes an advantage when it is combined with its abilities as a drilling mud viscosifying and gelling agent. Thus, LGC has a remarkable potential to be used as a drilling mud additive.

V. ACKNOWLEDGMENTS

The authors are deeply grateful to the financial support from Universiti Sains Malaysia (USM) under the research grant (304/PKIMIA/6310038).

REFERENCES

[1] Hamida, T.; Kuru, E.; Pickard, M. Rheological Characteristics of Aqueous Waxy Hull-Less Barley (WHB) Solutions. J. Pet. Sci. Technol. 2009, 69, 163-173.

[2] Mahto, V.; Sharma, V.P. Rheological Study of a Water Based Oil Well Drilling Fluid. J. Pet. Sci. Technol. 2004, 45, 123-128.

[3] Caenn, R.; Chillingar, G. V. Drilling Fluids: State of The Art. J. Pet. Sci. Technol. 1996, 14, 221-230.
[4] Kelessidis, V. C.; Tsamantaki, C.; Michalakis, A.; Christidis, G. E.; Makri, P.; Papanicolaou, K.; Foscolos, A. Greek Lignites as Additives for Controlling Filtration Properties of Water-Bentonite Suspensions at High Temperatures. Fuel. 2007, 86, 1112-1121.
[5] Zhang, L. M.; Tan, Y. B.; Li, Z. M. New Water-Soluble Ampholytic Polysaccharides for Oilfield Drilling Treatment: A Preliminary Study. Carbohydr. Polym. 2001, 44, 255-260.
[6] Stewart, D. Lignin as a Base Material for Materials Applications: Chemistry, Application and Economics. Ind. Crop. Prod. 2008, 27, 202-207.
[7] Gosselink, R.J.A.; de Jong, E.; Guran, B.; Abächerli, A. Co-ordination Network for Lignin--Standardisation, Production and Applications Adapted to Market Requirements (EUROLIGNIN). Ind. Crop. Prod. 2004, 20, 121-129.
[8] Sena-Martins, G.; Almeida-Vara, E.; Duarte, J.C. Eco-Friendly New Products from Enzymatically Modified Industrial Lignins. Ind. Crop. Prod. 2008, 27, 189-195.
[9] Singh, R.; Singh, S.; Trimukhe, K. D.; Pandare, K. V.; Bastawade, K. B.; Gokhale, D. V.; Varma, A. J. Lignin-Carbohydrate Complexes from Sugarcane Bagasse: Preparation, Purification, and Characterization. Carbohydr. Polym. 2005, 62, 57-66.
[10] Sun, R.; Tomkinson, J. Fractional Separation and Physico-Chemical Analysis of Lignins from The Black Liquor of Oil Palm Trunk Fibre Pulping. Sep. Purif. Technol. 2001, 24(3), 529–539.
[11] Mohamad Ibrahim, M.N.; Ahmed-Haras, M.R.; Sipaut, C.S.; Aboul-Enein, H.Y.; Mohamed, A.A. Preparation and Characterization of a Newly Water Soluble Lignin Graft Copolymer from Oil Palm Lignocellulosic Waste. Carbohydr. Polym. 2010, 80, 1102-1110.
[12] American Petroleum Institute. Recommended Practice Standard Procedure for Field Testing Water-Based Drilling Fluid. API Recommended Practice. 2008, 13 B-1, 2nd Ed. Washington, DC.
[13] American Petroleum Institute. Recommended Practice Standard Procedure for Laboratory Testing Drilling Fluid. API Recommended Practice. 2008, 131, 8th Ed. Washington, DC.
[14] Mohamad Ibrahim, M.N.; Nazlina, M.N.; Fauzana, A.D.; Chuah, S.B. Recycling Black Liquor of Oil Palm EFB into Drilling Mud Thinner. J. Phys. Sci. 2003, 24, 114-115.
[15] Roland, M.; A. Rejmann. Fractionation of Kraft Lignin by Successive Extraction with Organic Solvents. Holzfotschung. 2000, 42, 111-116.
[16] Zhang, L.M.; Yin, D.Y. Novel Modified Lignosulfonate as Drilling Mud Thinner Without Environmental Concern. J. Appl. Polym. Sci. 1999, 74, 1662-1668.
[17] Bourgoyne, Jr. A. T.; K. K. Millheim.; M. E. Chenever.; F. S. Young Jr. Applied Drilling Engineering Texas. Society of Petroleum Engineers Textbook Series. 1991, 42-47.
[18] Van Olphen, H. An Introduction to Clay Colloid Chemistry. New York. John Wiley and Sons. 1963, 57-82.
[19] Zhang, L.-M.; Yin, D.-Y. Preparation of A New Lignosulfonate-Based Thinner: Introduction of Ferrous Ions. Colloids. Surf., A. 2002, 210, 13-21.
[20] American Petroleum Institute. Recommended Practice Standard Procedure for Field Testing Oil-Based Drilling Fluid. API Recommended Practice. 2005, 13 B-2, 3rd Ed. Washington, DC.
[21] Boeriu, C. G.; Bravo, D.; Gosselink, R. J. A.; Van Dam, J. E. G. Characterisation of Structure-Dependent Functional Properties of Lignin with Infrared Spectroscopy. Ind. Crop. Prod. 2004, 20, 205-218.
[22] Fengel, D.; Wegener, G.; Greune, A. Studies on The Delignification of Spruce Wood by Organosolv Pulping Using SEM-EDXA and TEM. Wood. Sci. Technol. 1989, 23, 123-130.
[23] Nadif, A.; Hunkeler, D.; Käuper, P. Sulfur-Free Lignins from Alkaline Pulping Tested in Mortar for Use as Mortar Additives. Bioresour. Technol. 2002, 84, 49-55.
[24] Ghatak, H.R. Spectroscopic Comparison of Lignin Separated by Electrolysis and Acid Precipitation of Wheat Straw Soda Black Liquor. Ind. Crop. Prod. 2008, 28, 206-212.
[25] Mussatto, S.I.; Fernandes, M.; Roberto, I.C. Lignin Recovery from Brewer's Spent Grain Black Liquor. Carbohydr. Polym. 2007, 70, 218-223.
[26] El Mansouri, N.-E.; Salvadó, J. Analytical Methods for Determining Functional Groups in Various Technical Lignins. Ind. Crop. Prod. 2007, 26, 116-124.
[27] Li, Y.; Zhang, R.; Chen, H.; Zhang, J.; Suzuki, R.; Ohdaira, T.; Feldstein, M.M.; Jean, Y.C. Depth Profile of Free Volume in a Mixture and Copolymers of Poly(N-vinyl-pyrrolidone) and Poly(ethylene glycol) Studied by Positron Annihilation Spectroscopy. Biomacromolecules. 2003, 4, 1856-1864.

[28] Pticek, A.; Hrnjak-Murgic, Z.; Jelencic, J.; Kovacic, T. Study of The Effect of Structure of Ethylene-Propylene-Diene-Graft-Polystyrene Copolymers on their Physical Properties. Polym. Degrad. Stabil. 2005, 90, 319-325.
[29] Jin, X.-j.; Pu, J.-w.; Xie, Y.-m.; Takeshi, F.; Liu, X.-y. Lignin Characterization of Triploid Clones of Populus Tomentosa Carr. Forestry Studies in China. 2005, 7, 52-56.
[30] Ishimaru, K.; Hata, T.; Bronsveld, P.; Meier, D.; Imamura, Y. Spectroscopic Analysis of Carbonization Behavior of Wood, Cellulose and Lignin. J. Mater. Sci. 2007, 42, 122-129.
[31] Trinsoutrot, I.; Jocteur Monrozier, L.; Cellier, J.; Waton, H.; Alamercery, S.; Nicolardot, B. Assessment of The Biochemical Composition of Oilseed Rape (Brassica Napus L.) 13C-Labelled Residues by Global Methods, FTIR and 13C NMR CP/MAS. Plant. Soil. 2001, 234, 61-72.
[32] Milstein, O.; Gersonde, R.; Huttermann, A.; Frund, R.; Feine, H.J.; Ludermann, H.D.; Chen, M.J.; Meister, J.J. Infrared and Nuclear Magnetic Resonance Evidence of Degradation in Thermoplastics Based on Forest Products. J. Polym. Environ. 1994, 2, 137-152.
[33] Bonini, C.; D'Auria, M.; Mauriello, G.; Pucciariello, R.; Teghil, R.; Tofani, D.; Viggiani, L.; Viggiano, D.; Zimbardi, F. Graft Copolymers of Lignin from Straw with 1-Ethenylbenzene: Synthesis and Characterization. J. Appl. Polym. Sci. 2001, 79, 72-79.
[34] Sreekala, M.S.; Kumaran, M.G.; Joseph, S.; Jacob, M.; Thomas, S. Oil Palm Fibre Reinforced Phenol Formaldehyde Composites: Influence of Fibre Surface Modifications on the Mechanical Performance. Appl. Compos. Mater. 2000, 7, 295-329.
[35] Hunter, S.E.; Ehrenberger, C.E.; Savage, P.E. Kinetics and Mechanism of Tetrahydrofuran Synthesis via 1,4-Butanediol Dehydration in High-Temperature Water. J. Org. Chem. 2006, 71, 6229-6239.
[36] Santoyo, E.; Santoyo-Gutierrez, S.; Garcia, A.; Espinosa, G.; Moya, S. L. Rheological Property Measurement of Drilling Fluids Used in Geothermal Wells. Appl. Therm. Eng. 2001, 21, 283-302.
[37] Palusiak, M.; Grabowski, S.J. Methoxy Group as An Acceptor of Proton in Hydrogen Bonds. J. Mol. Struct. 2002, 642, 97-104.
[38] Lee, J.; Jang, J. IR Study on The Character of Hydrogen Bonding in Novel Liquid Crystalline Epoxy Resin. Polym. Bull. 1997, 38, 447-454.
[39] Thakare, M.R.; Wharton, J.A.; Wood, R.J.K.; Menger, C. Exposure Effects of Alkaline Drilling Fluid on The Microscale Abrasion-Corrosion of WC-Based Hardmetals. Wear. 2007, 263, 125-136.
[40] Domburg, G.E.; Sergeeva, V.N. Thermal Degradation of Sulphuric Acid Lignins of Hard Wood. J. Therm. Anal. Calorim. 1969, 1, 53-62.
[41] Shokoya, O.S.; Al-Marhoun, M.A.; Ashiru, O.A. The Rheology and Corrosivity of Water-Base Drilling Fluid under Simulated Downhole Conditions. Mater. Corros. 1996, 47, 307-316.
[42] Wu, Y.M.; Zhang, B.Q.; Wu, T.; Zhang, C.G. Properties of The Forpolymer of N-Vinylpyrrolidone with Itaconic Acid, Acrylamide and 2-Acrylamido-2-Methyl-1-Propane Sulfonic Acid as A Fluid-Loss Reducer for Drilling Fluid at High Temperatures. Colloid. Polym. Sci. 2001, 279, 836-842.
[43] Bazarnova, N.G.; Chubik, P.S.; Khmel'nitskii, A.G.; Galochkin, A.I.; Markin, V.I. Carboxymethylated Wood as a Chemical Reagent for Preparation of Drilling Fluids. Russ. J. Appl. Chem. 2001, 74, 681-686.
[44] Wang, Q.; Ellis, P.R.; Ross-Murphy, S.B. The Stability of Guar Gum in An Aqueous System under Acidic Conditions. Food Hydrocolloids. 2000, 14, 129-134.
[45] Borges, C.D.; de Paula, R.C.M.; Feitosa, J.P.A.; Vendruscolo, C.T. The Influence of Thermal Treatment and Operational Conditions on Xanthan Produced by X. Arboricola PV Pruni Strain 106. Carbohydr. Polym. 2009, 75, 262-268.

American Journal of Engineering Research (AJER)
e-ISSN : 2320-0847 p-ISSN : 2320-0936
Volume-02, Issue-11, pp-242-251
www.ajer.org

Research Paper Open Access

Modeling for strength assessment of backfill materials associated with the reduction of surface subsidence at the Barapukuria coalmine area, NW Bangladesh

Dr. Md. Rafiqul Islam[1*], Mohammed Omar Faruque[1], Md. Abid Hasan[1], Md. Ashraf Hussain[1], Shamim Ahammod[2]

[1]Department of Petroleum & Mining Engineering, Shahjalal University of Science & Technology, Sylhet-3114 Bangladesh

[2]Department of Earth & Environmental Sciences, Wright State University, Dayton, OH 45435, USA

Abstract: The Barapukuria coal mine, which is the first underground multi-slice longwall coal mine of the country, is located in northwest part of Bangladesh. The southern part of the Barapukuria coalmine area is a vulnerable zone because of the present underground coal mining activities. Land subsidence due to underground coal mining activities has great potential impacts on the surface and near surface structures. After extraction of the first slice of the Barapukuria coalmine, a massive surface subsidence has been occurred throughout the high productive agricultural landscapes and some public houses were damaged that were very close to the mine plan. This study uses numerical modeling techniques to calculate the mining-induced stress characterization and displacement values around an excavation mine panel. The modeling results were emphasized on the two mechanical parameters- (i) mean stress, and (ii) total displacement values. Calculated values of these two parameters have been used to predict the required strength of backfill materials. The values were estimated before and after the surface subsidence. Modeling results reveal that before backfilling the values of mean stress was ranging from 3.3 to 5.7 MPa, and the value of total displacement (surface subsidence) was about 1.23 m. Subsequent to backfilling, the values of mean stress was ranging from 8.1 to 10.50 MPa, which coincides with the value of the natural stress state. After backfilling, the calculated total displacement or surface subsidence value was about 0.136 m. Four samples of sand and silty sands were collected from Phulchari Gat, Sharishabari Gat, Vhanderbari, Pukuria area of the Jamuna riverbed. Strength of backfill materials (cement: fly ash: sand) was detected by using unconfined compressive strength (UCS) test associated with a curing period of 7, 14, and 28 days.

Keywords: - Mean Stress, Surface Subsidence, Unconfined Compressive Strength (UCS), Backfill Materials

I. INTRODUCTION

Surface subsidence is a very common phenomenon in many underground coal mining areas of the world. Surface subsidence is one of the significant mining-induced visible features of a coalmine that produced after a longwall panel has been extracted [1, 2, 3, 4]. Extraction of coal from underground mines generally leads to subsidence of the overlaying land within a period of days to years. Land subsidence can give important clues as to the extent of a mine and its impact on the land [5, 6, 7]. Subsequent to the extraction of first-slice of the Barapukuria coalmine in northwest Bangladesh (Fig.1a), it causes mining-induced surface subsidence (Fig.1b) that eventually causes environmental threats to the agricultural landscapes and its associated structures.

Backfill is one of the modern technologies that are being used to minimize the mining-induced surface subsidence in many countries of the world. Backfill is the term for material that is used to fill voids created by mining activity [8]. Backfill is used for the purposes of some mining engineering functions like- (i) control of ground pressure, (ii) manage of deformation of surrounding rock strata of a mine panel, and (iii) prevention of the ground movement and fracturing of overburden strata. It leads to less deterioration in ground conditions in the mine, improving economic operations and safety. The purpose of the backfill is not to transmit the rock stresses, but to reduce the relaxation of the rock mass so that the rock itself will retain a load carrying capacity

and will improve load shedding to crown pillars and abutments [9, 10]. Therefore, it is reasonable to mention that surface subsidence can be reduced and production of a coal mine can be enhanced by using backfill technology [11].

In the past decades, several methods have been used to predict surface subsidence parameters, including- (i) Graphical Methods, such as the National Coal Board Method used in the U.K, (ii) Profile Function Methods, (iii) Influence Function Methods, (iv) Numerical Modeling Methods, and (v) Empirical Methods [12]. The Permian age Gondwana coal has been mined since 2005 at the Barapukuria area [13, 14, 15, 16], which is located within a high-productive agricultural landscapes associated with densely populated areas in northwest Bangladesh. Mining operation without any backfill technology in the Barapukuria coalmine area causes a massive surface subsidence that damages high-productive agricultural landscapes associated with some public houses. So, the most important query regarding the key point of the present study would be focused on that, is it possible to minimize the surface subsidence by using the backfill technology in Barapukuria? To resolve query, the present study uses finite element numerical modeling method to predict the strength of backfill materials that would be required to minimize the surface subsidence at the Barapukuria coalmine area. The modeling result would be useful to enhance the production optimization and safe operation of the mine. Two major objectives of the present study are-

- to compute the mean stress distribution around a mine excavation panel of the Barapukuria coalmine by using finite element numerical modeling, and
- to predict the unconfined compressive strength (UCS) values of backfill materials that were collected from the different locations of the Jamuna riverbed

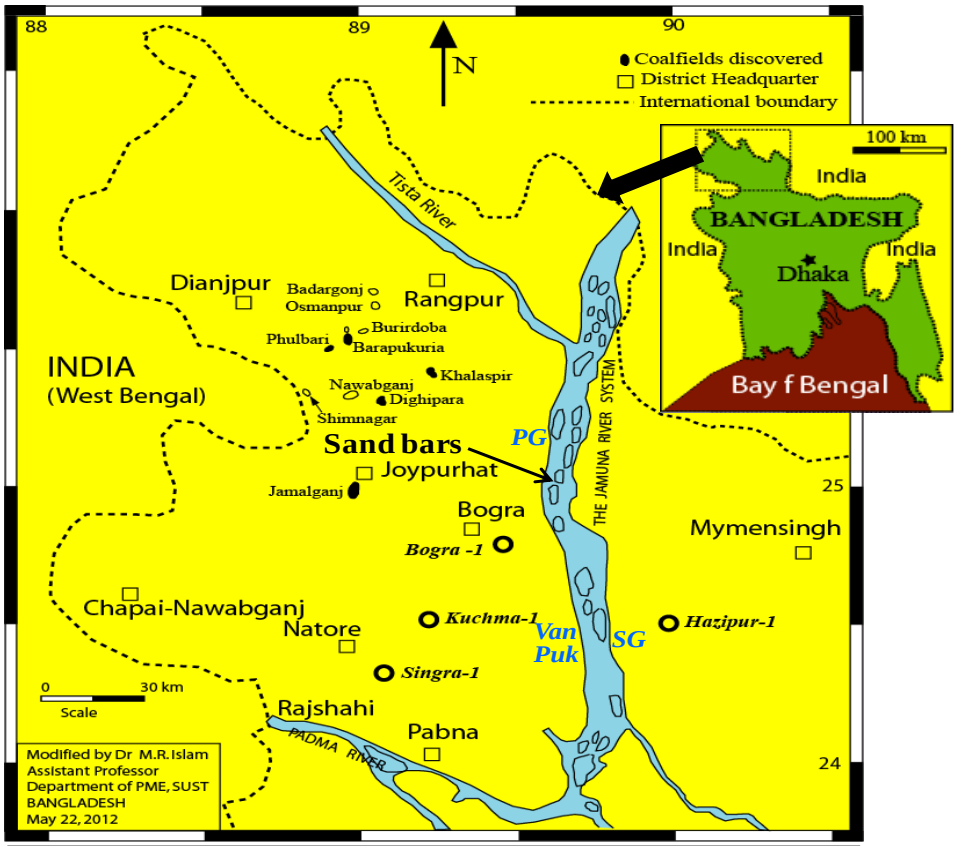

PG = Phulchari Ghat of Gaibandha District,;SG = Sharishabari Ghat of Jamalpur District; Van = Vhanderbari area of Dhunut, Bogra District; Puk = Pukuria area of Dhunut, Bogra District, Bangladesh

Figure 1a. Location of the the Permian age Gondwana coal basins in Bangladesh. Sources of sands and silts at the numerous sand bars on the Jamuna riverbed. Four locations of collected samples are shown in Figure.

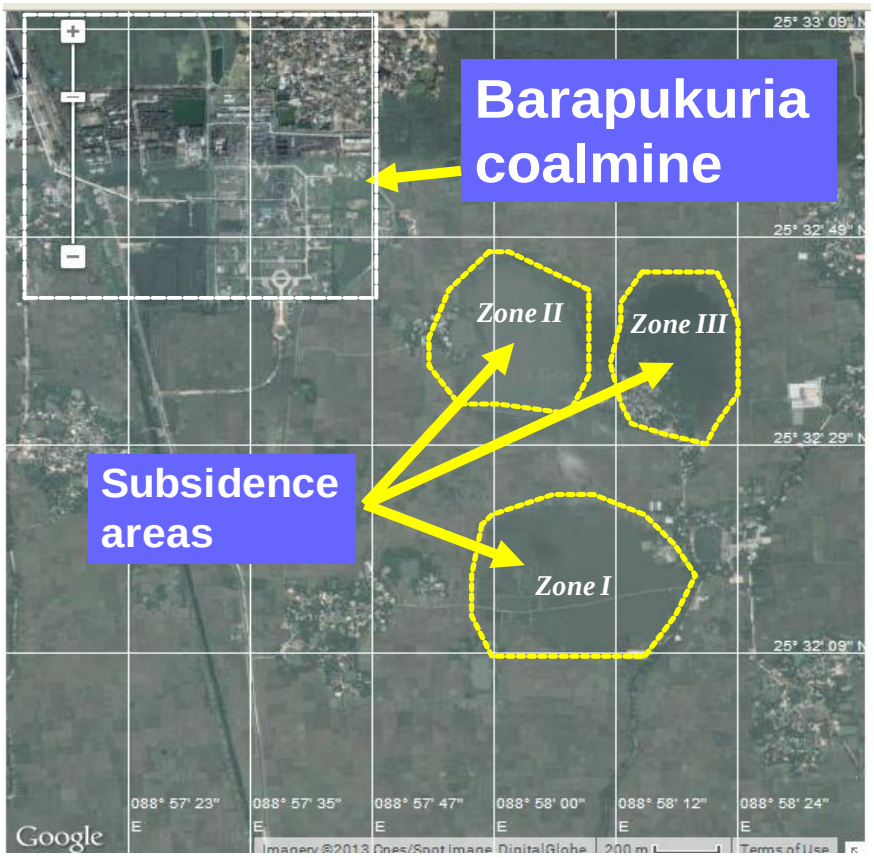

Figure 1b. Area of surface subsidence (about 0.9 to 1.3 m) caused by multi-slice longwall mining method after first slice extraction of coal in the Barapukuria coalmine area, Bangladesh.

II. METHODS AND MATERIALS

2.1. Numerical Modeling

In the present study, a finite element numerical modeling method has been applied to determine the mean stress and total displacement values around an excavation mine panel of the Barapukuria coalmine. Two stages of calculations were carried out. In the first stage, mean stress and displacement values were calculated just before backfilling of the mine goaf area, whereas in the second stage, mean stress and displacement values were computed subsequent to backfilling of the goaf area. The calculated values of mean stress were applied to predict the required strength of backfill materials. Model configuration and boundary conditions are shown in Fig.2. Rock mechanical properties of different geological layers (MCF, UDT, LDT, GUSS, GMSS, Coal seam VI, GLSS) as mentioned in the model are shown in Table 1. For details about the geological and hydrogeological conditions of the Barapukuria coal basin, interested readers are requested to go through the article of Islam and Hayashi, 2008 [13]. The upper surface of the model is free. X axis at the right and left sides of the model is restrained. Y axis is restrained at the bottom of the model.

Table 1: Rock mechanical properties of different geological layers

Material properties	MCF	UDT	LDT	GUSS	GMSS	Seam VI	GLSS	Backfill material
Unit weight (MN/m^3)	0.018	0.022	0.020	0.025	0.025	0.014	0.025	0.015
Young's modulus (MPa)	10000	12650	13500	6500	7555	3239	7860	10
Poisson's ratio	0.15	0.2527	0.20	0.2876	0.3861	0.1929	0.3732	0.21
Tensile strength (MPa)	0.028	0.96	0.47	1.28	1.32	0.007	1.74	0.09
Peak friction angle (deg.)	12	28	15	35	32	15	25	12
Peak cohesion (MPa)	0.085	0.280	0.190	0.440	0.445	0.20	0.440	0.25

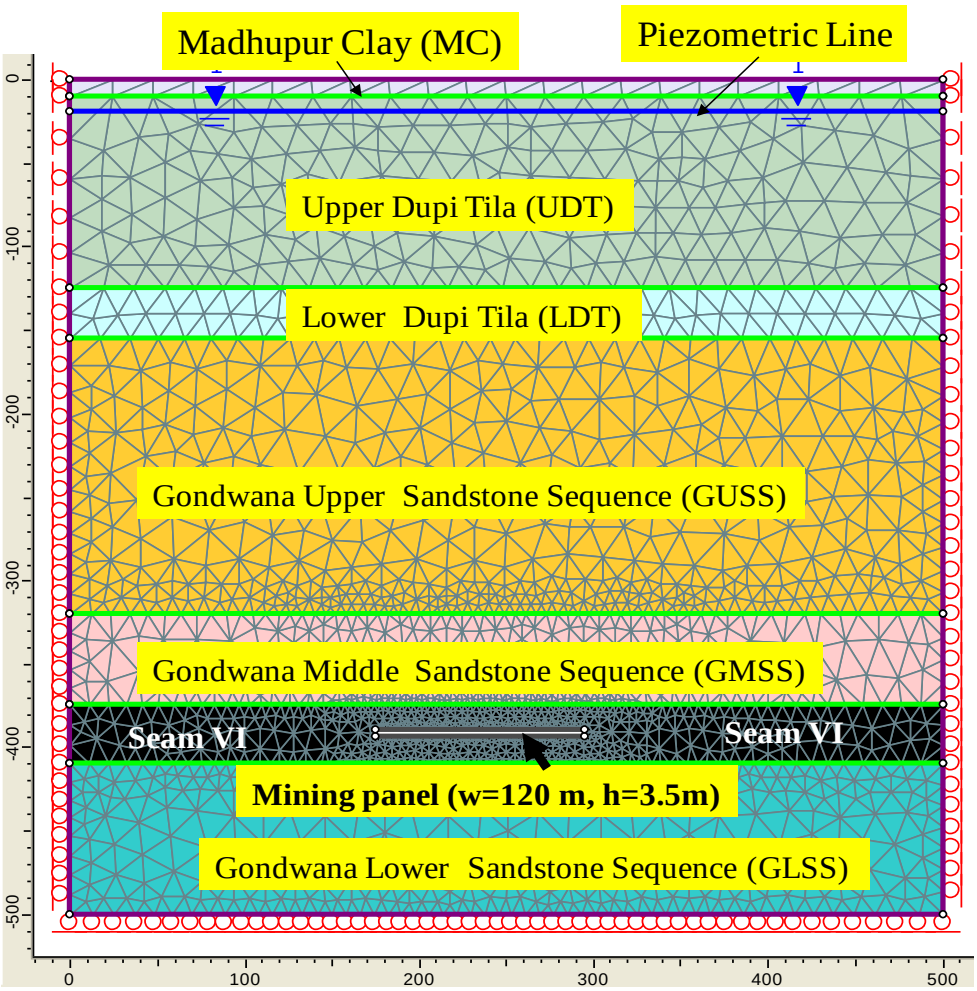

Figure 2. FE numerical model mesh and boundary conditions.

2.2. Modeling Results

Results of the numerical modeling are illustrated in Figs.3 and 4. The modeling results are presented in terms of two mechanical parameters as follows.

- distribution contours of mean stress (MPa) before backfilling (Fig.3a)
- distribution contours of mean stress (MPa) after backfilling (Fig.3b)
- distribution contours of total displacement (m) or subsidence before backfilling (Fig.4a)
- distribution contours of total displacement (m) or subsidence after backfilling (Fig.4b)

Before backfilling, the mean stress at the upper and lower part of the mine excavation panel was about 3.3 MPa. The value increased gradually up to 5.7 MPa towards the upper part of the model up to about 250 m depth (Fig.3a). Then the value decreased gradually towards the upper surface of the model. However, at the upper left and right sides of the excavation panel, the mean stress was ranging from 8.1 to 10.50 MPa. After backfilling, the mean stress around the excavation zone was about 8.5 MPa. However, at the upper left and right sides of the excavation panel, the mean stress was ranging from 8.4 to 9.4 MPa (Fig.3b). This means, the strength of backfill materials almost coincide with the natural strength of rock strata.

Before backfilling, total displacement or computed surface subsidence was about 1.23 m (Fig.4a). It is reasonable to mention that the computed result in the present study almost coincides with the measured field data at the Barapukuria coalmine area. The measured data was ranging from 0.90 to 1.3 m, approximately. The computed result shows that subsequent to backfilling, total displacement or surface subsidence would be about 0.136 m (Fig.4b).

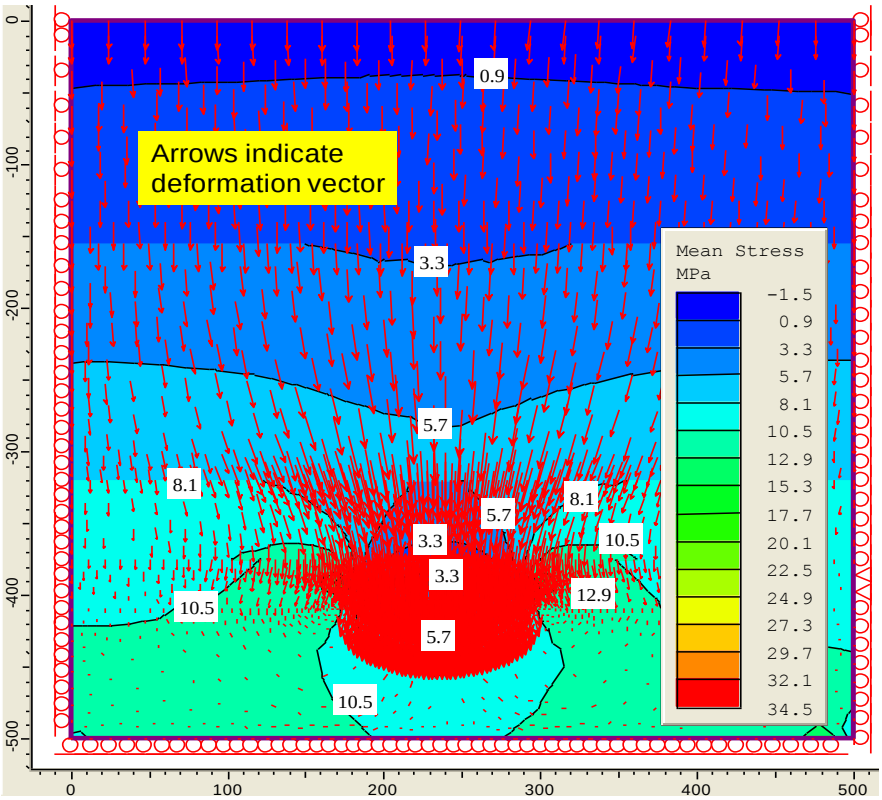

Figure 3a. Distribution contours of mean stress (MPa) before backfilling.

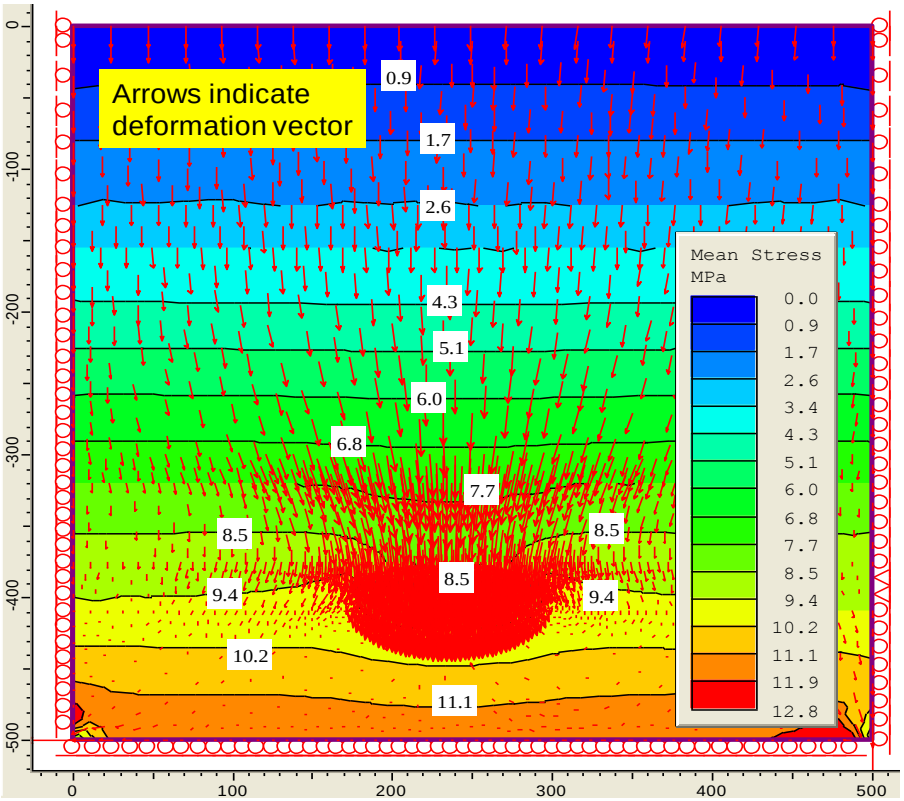

Figure 3b. Distribution contours of mean stress (MPa) after backfilling

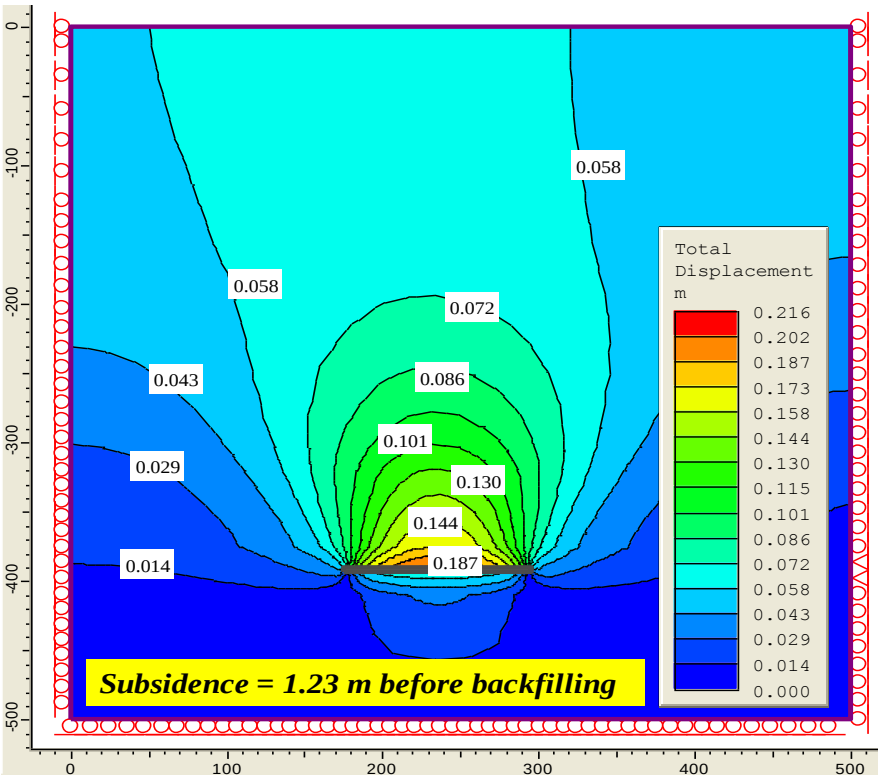

Figure 4a. Distribution contours of total displacement (m) before backfilling

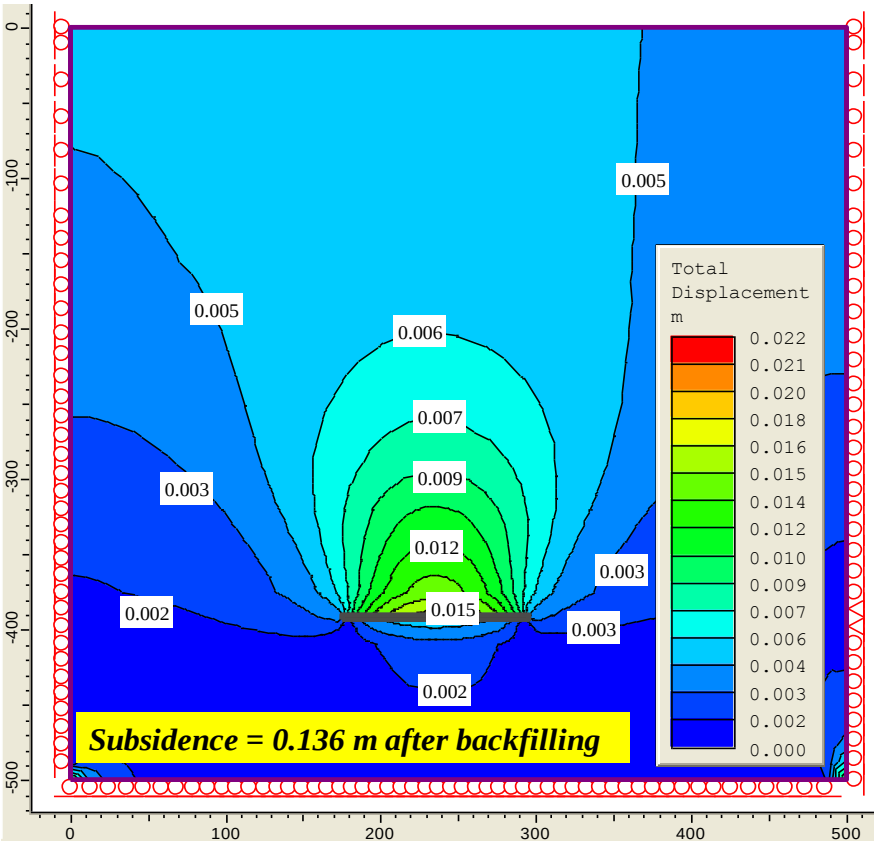

Figure 4b. Distribution contours of total displacement (m) after backfilling

2.3. Test of strength of behavior of backfill materials

Four samples of backfill material, like sands and silty sands were collected from the different parts of the Jamuna riverbed, which is the widest riverbed of the country having numerous sand bars (as shown in Fig.1a) with huge amounts of deposits. The following laboratory procedures were carried out to verify the strength behaviors of backfill materials.

- Collected samples were dried in the air and sunlight first and then the sieving analyses were carried out by using ASTM standard sieves. The grain size distributions curves are presented in Fig.5, which was prepared by using semi-log graphical plots.
- Some cubes with a size of 25mm×25mm×25mm (Fig.6) were made using the riverbed sands, fly-ash and Portland cement with different ratio.
- Unconfined compressive strength (UCS) test of cubes with different ratio of materials were carried out to determine the required strength of backfill material with a curing period of 7, 14 and 28 days. The test results are shown in Table 2.

2.3.1. Grain size distribution curves

The grain size distribution curves of collected samples are shown in Fig.5. Distribution curves show that the values of co-efficient of uniformity were ranging from 1.15 to 1.76, which indicates a poorly graded uniform soil. Usually, a poorly graded soil having a coefficient of uniformity of 2 or less [17].

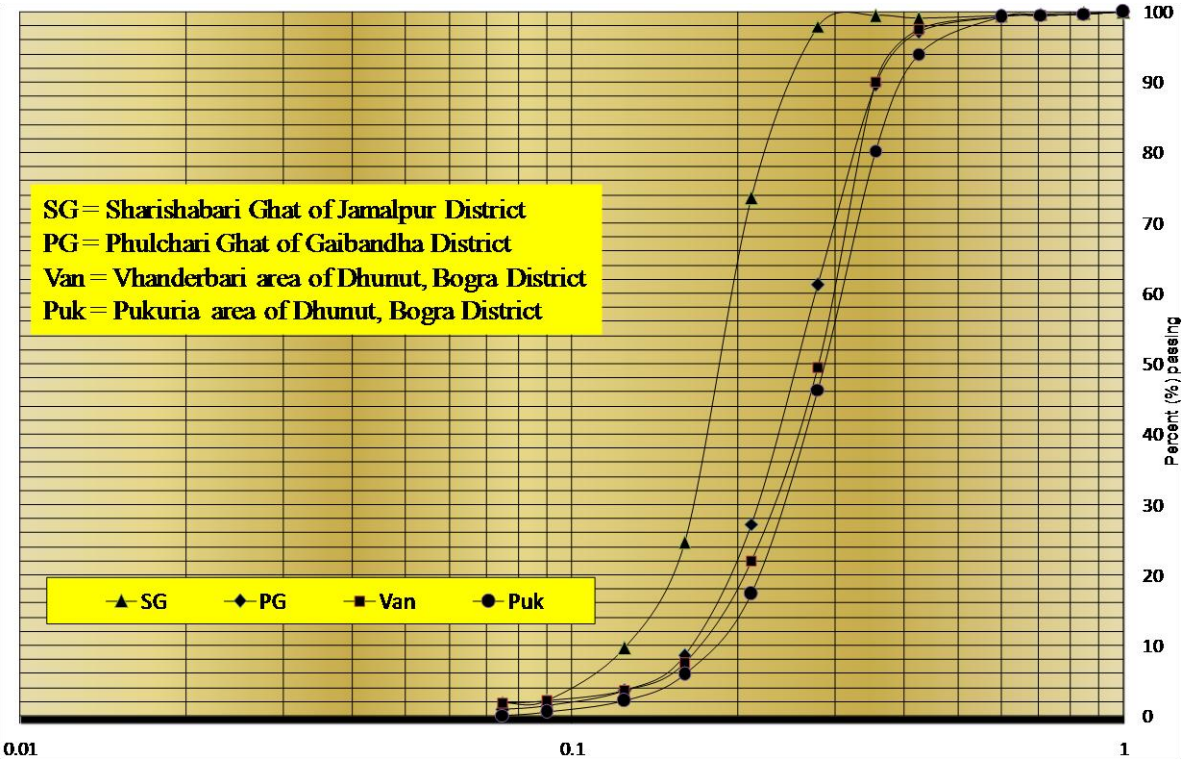

Figure 5. The grain size distribution curves of collected samples

2.3.2. UCS test results

The UCS test were carried out by taking into consideration of four samples of sands and silts that were collected from Phulchari Gat, Sharishabari Gat, Vhanderbari, and Pukuria area of the Jamuna riverbed (Fig. 1a). For the case of Phulchari Gat sample, the material ratio of 3:2:6 (cement: fly ash: sand), respectively, provided a result 3.30, 3.85, 5.0 MPa, respectively after a curing period of 7, 14, 28 days. If the considerable material ratio was 3:2:8 (cement: fly ash: sand), the strength values were 2.92, 3.50 and 4.38 MPa, respectively; after a curing period of 7, 14, 28 days. For the case of Vhanderbari sample, the ratio of 3:2:6 (cement: fly ash: sand) provides a series of strength values of about 3.64, 4.40, 5.50 MPa, respectively, after a curing period of 7, 14, 28 days. If the considerable material ratio was 3:2:8 (cement: fly ash: sand), the strength values were 4.10, 4.96 and 6.20 MPa respectively, after a curing period of 7, 14, 28 days. For the case of Sharishabari Gat sample, the ratio of 3:2:6 (cement: fly ash: sand) provided a series of strength values of 3.06, 3.68, 4.60 MPa respectively, after a curing period of 7, 14, 28 days. If the considerable material ratio is 3:2:8 (cement: fly ash: sand), the tested strength values were 2.72, 3.20 and 3.96 MPa, respectively, after a curing period of 7, 14, 28 days. For the case of Pukuria sample with a ratio of 3:2:6 (cement: fly ash: sand) provided a series of strength of 4.67, 5.60, 7.00

MPa respectively, after a curing period of 7, 14, 28 days. If the considerable material ratio was 3:2:8 (cement: fly ash: sand), the tested strength were 4.45, 5.34 and 6.67 MPa, respectively, after a curing period of 7, 14, 28 days. Unconfined compressive strength (UCS) test values with a curing period of different samples are shown in Table 2.

Table 2: Unconfined compressive strength (UCS) test values with a curing period of 7, 14 and 28 days.

Samples collected from the Jamuna Riverbed (Fig.1)		Cement: Fly ash: Sand	Curing period and Unconfined Compressive Strength (MPa)		
Sample No	**Locations**		***7 days***	***14 days***	***28 days***
Sample-1	Phulchari Gat	1:0:8	0.38	0.48	1.03
Sample-2	Vhanderbari	1:0:8	0.53	0.43	1.06
Sample-3	Sharishabari Gat	1:0:8	0.32	0.40	0.87
Sample-4	Pukuria	1:0:8	0.46	0.58	1.00
Sample-1	Phulchari Gat	1:2:8	0.66	0.80	1.00
Sample-2	Vhanderbari	1:2:8	0.64	0.78	0.99
Sample-3	Sharishabari Gat	1:2:8	0.64	0.78	0.98
Sample-4	Pukuria	1:2:8	1.34	1.60	2.00
Sample-1	Phulchari Gat	1:2:6	1.30	1.56	1.96
Sample-2	Vhanderbari	1:2:6	1.32	1.59	1.98
Sample-3	Sharishabari Gat	1:2:6	1.34	1.58	1.97
Sample-4	Pukuria	1:2:6	1.37	1.65	2.06
Sample-1	Phulchari Gat	3:2:8	2.92	3.51	4.38
Sample-2	Vhanderbari	3:2:8	3.10	4.96	6.20
Sample-3	Sharishabari Gat	3:2:8	2.72	3.20	3.96
Sample-4	Pukuria	3:2:8	4.45	5.34	6.67
Sample-1	Phulchari Gat	3:2:6	3.30	3.85	5.00
Sample-2	Vhanderbari	3:2:6	3.64	4.40	5.50
Sample-3	Sharishabari Gat	3:2:6	3.06	3.68	4.60
Sample-4	Pukuria	3:2:6	4.67	5.60	7.00

Figure 6. Some samples of backfill material with different ratio of cement: fly ash: sand

2.3.3. Cost analysis of backfill materials

The cost analysis of backfill materials includes cost of samples, transport and labor costs. Bangladesh Railway (BR) wagon and/or Truck would be required to transport sands from the dumping grounds that should be located at the western bank of Jamuna River. The cost analysis of backfill material is shown in Table 3.

Table 3: Cost analysis of backfill materials

Material Ratio	Bangladesh Railway wagon		Truck	
Cement:Fly ash:Sand	Cost per $(1)^3$	Cost per $(m)^3$	Cost per $(1)^3$	Cost per $(m)^3$
1:0:8	0.20	$19.2	0.33	$32
1:2:6	0.32	$31.2	0.54	$52
1:2:8	0.27	$26.4	0.45	$44
3:2:6	0.51	$49.2	0.85	$82

III. DISCUSSION

Subsidence is a very common phenomenon in many coal mining areas of the world. Most of the subsidence problems are reported to have occurred suddenly and those often remain as serious threats to the subsequent development [18]. From the beginning of commercial production at the Barapukuria coalmine in 2005, the first subsidence was recorded in 2006 in Kalupara and Balarampur villages, which is located above the coal faces 1101 [14]. Subsequently, further subsidence was recorded in other areas during 2008, 2009, 2011 and by the end of 2012. At present, the total affected area of surface subsidence is almost 6.825 hectares that includes 300000 m^2 in zone-I, 213750 m^2 in zone-II, and 168750 m^2 in zone-III (please see in Fig. 1b). High productive agricultural landscapes are affected by surface subsidence that also includes 8 villages in and around the coalmine. Subsidence height was ranging from 0.9 to 1.3 m in respond to extraction of about 3 m coal in the underground. The surface areas affected by water logging for a long period of the year.

Hydraulic sand stowing or backfilling can be a remedial measure to reduce land subsidence. This practice is well developed in many underground mines around the world. However, there has not been taken any backfilling or stowing procedures adopted in Barapukuria mine [15].

The present study emphasizes the strength assessment of backfill material that would be used in the Barapukuria coalmine to reduce the surface subsidence. Numerical modeling of a mine panel geometry associated with two stages of calculation for mean stress and total displacement around- (i) mining-induced goaf area, and (ii) backfilling conditions of that goaf, have been considered here. Subsequent to the extraction of the mine panel, the calculated mean stress and total displacement values around the mine goaf were 3.3 to 5.7 MPa, and 1.23 m, respectively. Subsequent to the backfilling of the goaf area, the computed mean stress and total displacement (subsidence) values around the mine panel were 8.1 to 10.50 MPa, and 0.136 m, respectively.

IV. CONCLUSIONS

The following grounds should be considered for the sustainable development of coalmines Bangladesh in the near future.

- Applied numerical modeling results associated with mean stress and total displacement values in the present study emphasize that the surface subsidence at the Barapukuria coalmine area would be reduced up to 90%, if backfilling technology is applied.
- Unconfined Compressive Strength (UCS) test values (Table 2) and cost analysis (Table 3) of backfill materials reveal that the Jamuna riverbed sands and silts could be used as a cost-effective backfill material for the development of coalmines in Bangladesh.
- Backfilling could be enhanced the production optimization of the Barapukuria coalmine up to 70-80% of the total coal resources (377 Mt).

REFERENCES

[1] Reddish D. J. (1984). Study of Ground Strain in Relation to Mining Subsidence, PhD Thesis, University of Nottingham, UK.

[2] Yao X. L., (1992) Modelling of Mining Subsidence with Reference to Surface Structure Behaviour, Ph.D. Thesis, University of Nottingham.

[3] Benbia A., (1996). Ground Movement Associated with Longwall Mining Extraction, Ph.D. Thesis, University of Nottingham, UK.

[4] Lloyd, P. W., Mohammad, N., and Reddish, D. J., (1997). Surface subsidence prediction techniques for UK coalfields- an innovative numerical modeling approach. Mining Congress of Turkey, Guyaguler, Ersayýn,Býlgen(eds), 1997, ISBN 975-395-216-3, p.111-124

[5] Zbigniew, P. (2000). The interpretation of ers-1 and ers-2 InSAR data for the mining subsidence monitoring in upper Silesian coal basin, Poland, Int'l Arch. Photogramm. Remote Sens. 33, pp. 1137–1141,
[6] G. Liu, H. Guo, R. Hanssen, P. Zbigniew, et al., (2008). The application of InSAR technology to mining area subsidence monitoring, Remote Sens. Land Resources 2, pp. 51–55.
[7] Yue, H., Liu, G., Perski, Z., and Guo, H., (2011). Satellite radar reveals land subsidence over coal mines. SPIE, p.1-3. DOI: 10.1117/2.1201110.003898
[8] Grice, T, (1998). Underground Mining with Backfill. The 2nd Annual Summit – Mine Tailings Disposal Systems, Brisbane, 1998; 24-25 November, pp. 1-14.
[9] Barrett J. R., Coulthard, M. A., Dight, P.M., (1978). Determination of Fill Stability, Mining with Backfill, 12th Canadian Rock Mechanics Symposium, CIM Special v. 19: 23-25.
[10] Donovan, J. G., and Karfakis, M. G., (2004). Design of backfilled thin-seam coal pillars using earth pressure theory. Geotechnical and Geological Engineering v. 22(4): 627–642.
[11] Islam, M. R., Faruque, M.O., Ahammod, S., Shimada, H., and Matsui, K., (2013). Numerical Modeling of Mine Backfilling Associated with Production Enhancement at the Barapukuria Coalmine in Bangladesh. Electronic Journal of Geotechnical Engineering, v. 18/T, p. 4313-4334.
[12] General Discussion on Systematic and Non Systematic Mine Subsidence Ground Movements. Mine Subsidence Engineering Consultants Mine Subsidence Engineering Consultants, August 2007, NSW 2068, Australia
[13] Islam, M. R., Hayashi, D., (2008). Geology and coal bed methane resource potential of the Gondwana Barapukuria coal basin, Dinajpur, Bangladesh. International Journal of Coal Geology. V. 75(3): 127–143.
[14] Islam, M. R., Hayashi, D., Kamruzzaman A.B.M (2009). Finite element modeling of stress distributions and problems for multi-slice longwall mining in Bangladesh, with special reference to the Barapukuria coal mine. International Journal of Coal Geology. v. 78(2); 91–109.
[15] Islam, M. R, Shinjo, R., (2009a). Numerical simulation of stress distributions and displacements around an entry roadway with igneous intrusion and potential sources of seam gas emission of the Barapukuria coal mine, NW Bangladesh. International Journal of Coal Geology.v. 78(4): 249–262.
[16] Islam, M. R, Shinjo, R., (2009b). Mining-induced fault reactivation associated with the main conveyor belt roadway and safety of the Barapukuria Coal Mine in Bangladesh: Constraints from BEM simulations. International Journal of Coal Geology 2009b; 79(4): 115–130.
[17] Earth Manual, Part-1, Third Edition Earth Sciences and Research Laboratory Geotechnical Research Technical Service Center, Denver, Colorado, 1998, p.8.
[18] Liu, W. Y., Sun, H. H., et al. (1999). Solidifying tailings slurry with new binder at Meishan iron mine.Proceedings of the 99th International Symposium on Mining Science and Technology, 571-574 (in Chinese).

About the principal author: Dr. Md. Rafiqul Islam is the pioneer Mining Geoscientist of Bangladesh. He has

authored with 17 scientific articles in different scientific international journals that have been published in Elsevier, Springer and other national and international journals. He has also authored more than 20 popular articles associated with national and international events in the daily newspapers of Bangladesh. He has three years (2001-2004) practical experiences in underground coalmine development in Bangladesh. By means of successive combination of (i) practical experiences in coalmine field, (ii) high ranking research activities in Japan and (iii) teaching experiences, Dr. Islam is the topmost coalmining expert of the country, who has also worked with some renowned experts of the International Mining Consultants of United Kingdom and China University of Mining and Technology (CUMT). The Japanese Government awarded him as a ***Monbukagakusho Scholar*** since October 2004 to September 2009. Dr. Islam has aquired PhD in coalmining field with a specialization on numerical modeling associated with rock mechanics. He had been nomnaiated for the ***'President's Honorary Award-2009'*** by the President of the University of the Ryukyus, Okinawa, Japan for his scholarly achievements and contribution to the university and others scientific community. Recently, Dr. Islam has been nominated for the '***Young Scientist Award-2013'*** which is organized by ***The World Academy of Sciences (TWAS)*** of Italy. At present, he is a faculty member in the department of Petroleum and Mining Engineering, Shahjalal University of Science and Technology, Sylhet-3114, Bangladesh.

American Journal of Engineering Research (AJER)
e-ISSN : 2320-0847 p-ISSN : 2320-0936
Volume-02, Issue-11, pp-252-259
www.ajer.org

Research Paper Open Access

Performance Analysis of A Driver Cricuit and An Input Amplifier for BCC

Abdulah Korishe, Md Hasan Maruf
Department of Electrical Engineering Linköping University Linköping, Sweden
Department of Electrical Engineering Linköping University Linköping, Sweden

Abstract: - Body-Coupled Communication (BCC) is based on the principle of electrical field data transmission attributable to capacitive coupling through the human body. In this paper, we have newly proposed a voltage mode driver circuit in the transmitter (Tx) part and an input amplifier in the receiver (Rx) part to construct a transceiver for (BCC). The entire work is designed in ST65 nm CMOS technology. The driver circuit is cascaded of two single-stage inverter and an identical inverter with drain resistor. The cycle to cycle jitter is 0.87% which is well below to the maximum point and the power supply rejection ratio (PSRR) is 65 dB indicating the good emission of supply noise. A flipped voltage follower (FVF) topology is used for designing the input amplifier to support the low supply voltage. The open loop gain is 24.01 dB and the close loop gain is 19.43 dB for this amplifier. The performance analysis is evaluated on the basis of corner analysis, noise analysis and eye diagram to find out the best possible results. The total system is maintained with very low supply voltage of 1-1.2V.

Keywords: - *BCC, FVF, driver cirtuit, amplifier, corner analysis, eye diagram*

I. INTRODUCTION

Body-Coupled Communication (BCC) is one of the most interesting topics in the recent years. Communication through the body is attractive to the researchers due to its low power operation. BCC is clearly defined by Body Area Network (BAN). BAN is formally defined by IEEE 802.15 as "A communication standard optimized for low power devices and operation on, in or around the human body (but not limited to humans) to serve a variety of applications, including medical, consumer electronics, personal entertainment and other" [1].

The strongest motivation of using human body as a communication channel is its speed, less interference, low power consumption and inherent security system compared with the existing wireless communication systems like Bluetooth, Zigbee and WiFi. The low power transceiver for BAN is mainly focused on developing an architecture of transceiver using human body as a communication channel that is capable of higher data rate (10 Mbs) operating at 10 MHz frequency range. This application of near field communication (NFC) with BAN is going to increase the number of application as well as solves the problem with cell based communication system depending upon the frequency allocation. So the inductive or capacitive coupling technique by using a human body as a communication channel could be a solution for the wireless or mobile communication system. Moreover, a low power transceiver for BAN would be given in favor of capacitive coupling as viable means of next generation touch-and-go communication.

BCC can operate at MHz frequencies without large couplings because the signals transmit between the conductive human tissues of the body coupled transceiver and the floated ground with a capacitive return path [2]. Basically, Low impedance capacitive coupling consumes most of the power. So, it is possible to reduce the power consumption by using a low impedance capacitive coupling. This communication system has different applications such as human health monitoring system, cardiac monitoring, blood pressure measuring, business card handshake and door code unlock.

This paper presents a driver circuit for the transmitter (Tx) and an input amplifier for receiver (Rx) to support the BCC. In figure 1, the overall idea behind the entire work is illustrated. It is a half duplex communication system that the digital data is delivered by the digital transceiver (TxRx) Baseband and first

Analog Front End (AFE) TxRx receives the data. The data are transmitted by the first TxRx and it is passed through the human body with high attenuation due to high impedance provided by the human body. The attenuated signal is amplified as well as provides the digital data by the second TxRx and finally it goes back to digital TxRx baseband. The human body acts as a communication channel and it provides almost 60 dB attenuation.

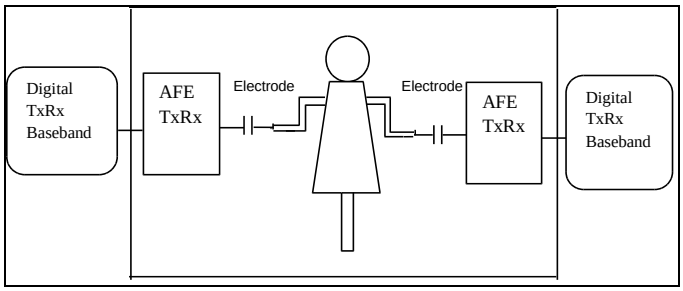

Figure 1: System description of BCC

The transmitter of the analog front end (AFE) is mainly focused on the output driver which provides ones and zeros to one side of the capacitor. It is important to maintain the shape of the signal on the other side of the capacitor by controlling the rising and falling edge of the signal. However, the attenuation factor due to high impedance provided by the human channel, the filter is not mandatory as the amplitude of the signal is very low and very minor change to get mixed with noise. On the other hand, an input amplifier of the receiver is considered to be a most complex and challenging part of the entire work. Weak signals from the transmitter need to be stronger and also need to be free from noise. Therefore, it requires an amplifier that can amplify the signal to the desired level. In this paper, a differential amplifier is designed based on the FVF topology that can give higher gain as well as low noise and low power consumption. By cascading the amplifier it is possible to obtain the higher gain. At the analog or digital interface, a Schmitt trigger is used to detect the correct information as well as low noise.

II. CHANNEL DESCRIPTION

The capacitive coupling approach is chosen for BAN because of the some physical and application advantages. Nowadays the communication demands more flexibility, security, high data rate, low power consumption, small chip area and so on. The capacitive coupling approach is the new generation touch- and-go communication system where the modeling of the human body is a challenge to characterize the channel. In figure 2, it shows the top view of the capacitively coupled human body with two electrodes.

The top view of the body model for BAN clearly shows there is no need of direct contact between the electrodes and the person. On the other hand, it is important to consider the distance as the movement of the body affects the signal on the receiver side. As the body distance is considered 2 meter or less than that so the transmitted signal should be strong enough to recover when it detects from the receiver electrodes.

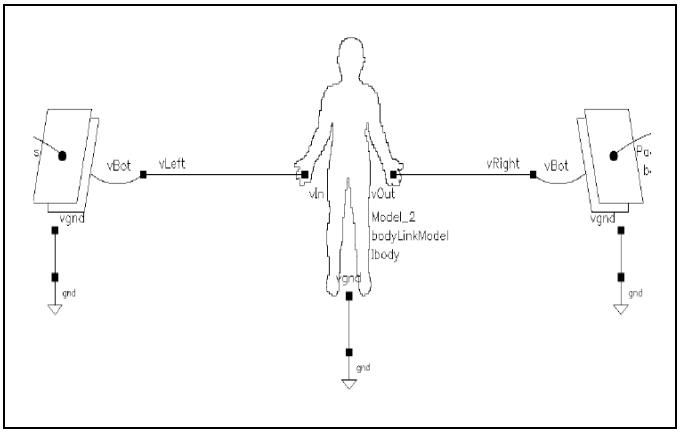

Figure 2: Body model with capacitive coupling

The receiver needs to be very sensitive enough to detect the transmitted signal as the signal is attenuated by human body. The transmission behavior of the human channel is fully depended upon the body resistance and coupling capacitor.

III. DRIVER CIRCUIT

A good driver circuit is characterized by an optimized output impedance, a controlled falling and rising edges of the signal in order to shape the pulses and of course the offset error free clean signal levels. The basic requirements of designing a strong driver circuit for BCC is to produce a significant amount of current due to high attenuation of the human body at the same time low capacitance (small plates) at the transmitter side. On the other hand, the receiver might not detect the weak signal so that the driver circuit need to maintain the voltage level. Basically, there is no filter block for this design because of very well noise reduction by the body channel which is a great advantage of BCC. In this paper, the driver circuit is designed in such a way that it can maintain the signal quality which depends on the pulse distortion, skew and systematic jitter.

In the Body-Coupled Communication project, the Manchester coded signals is chosen as it is a promising and simple modulation technique. In general, the Manchester encoding is applied to a simple transmitter consisting of only driver (inverter) driving a capacitive plate connected to the human body. Another advantage of Manchester encoding is that it is easier to integrate in hardware. However, depending on transmission modes the driver circuit divided into two basic types such as voltage mode driver and current mode driver. In this work a three stage voltage mode driver is used for measuring the leakage power consumption when the circuit is off state [3]. This architecture has very low output impedance that allows resistive region by using the CMOS technology. So it is essential to understand the basic properties of the COMS inverter. The static CMOS inverter has some important design matrix such as cost in respect to the area, integrity and robustness on the basis of static behaviour, performance analysis with the help of dynamic behaviour and the energy efficiency measured by the energy and power consumption [4].

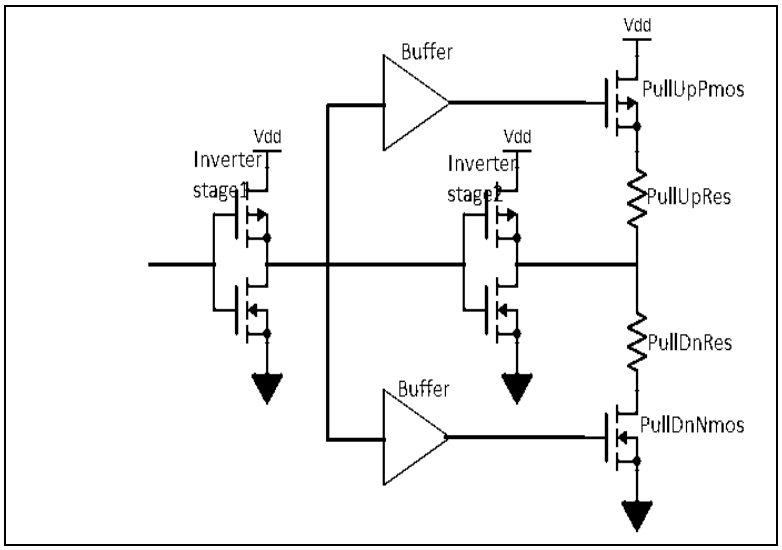

Figure 3: Basic architecture of the tri-state voltage mode driver

Table 1: Sizing technique of the transistors in the driver chain

Inverter stage	Width (NMOS)	Value (µm)	Width (PMOS)	Value (µm)
Stage 1	$W_{nStage1}$	119	3* $W_{nStage1}$	357
Stage 2	2* $W_{nStage1}$	238	3*2* $W_{nStage1}$	714
Stage 3	3* $W_{nStage1}$	476	3*2*2*$W_{nStage1}$	1428

The driver circuit demands big transistor size as the design requires high current. It is obvious that increasing the size of the transistor also increases the power consumption. It is cascaded in three stage inverters as shown in the figure 3. In table 1, it is shown that the width of the PMOS is three times with the NMOS of the same inverter. On the other hand, the width of the NMOS is two times with the preceding stage NMOS. Apart from, 195 nm length of the transistor provides proper pulses at the transmitter.

Finally, the power consumption is determined 7.398 mW for transistor level which is quite high as it is inversely proportional to the transistor width. In table 2, the power supply rejection is found 65 dB which

indicates a good emission of supply noise. The cycle to cycle jitter is lower than 1%. In addition, it consumes only 1.954 µW leakage power when the driver is in high impedance state.

Table 2: The performance of the entire driver circuit

Parameters	Value
Supply Voltage	1.2 V
Operating frequency	10 MHz
Power Consumption	7.398 mW
Propagation delay	6.14 ns
Jitter	0.87%
PSRR	65dB
Leakage power	1.954 µW

IV. AN INPUT AMPLIFIER

Depending upon the reduction of the supply power, different techniques are proposed to meet the requirement in analog and mixed signal circuits like folding, triode-mode and subthreshold operation of metal oxide semiconductor (MOS) transistors, floating gate techniques and current mode processing [5]. To maintain the requirement of the integrated circuit design, flipped voltage follower (FVF) is chosen in this work. It is a kind of basic cell, which is suitable for low power and low voltage operation. Compare to other topologies, FVF gives a wide range of frequency band and lower output impedance, which is the main advantage of this topology. It is one kind of voltage follower but the main difference of the traditional voltage follower and FVF is that FVF has low output resistance. In traditional voltage follower for improving its high output resistance, there needs to increase the transconductance gain, g_m which requires large current biasing and also the large W/L ratio.

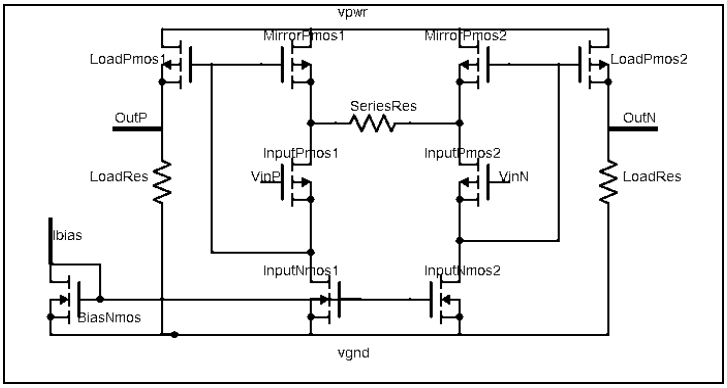

Figure 4: The transistor level implementation of an amplifier

In figure 4, the transistor level implementation of preamplifier is mentioned. The circuit is developed with the concept of flipped voltage follower. Two cascaded flipped voltage follower stages connect with a series resistance ($R_{SeriesRes}$). This resistance is mainly a degeneration resistance. The advantage of using this degeneration resistance is that when the input signal is weak, small $R_{SeriesRes}$ gives high gain and low noise. Neglecting the short-channel effect and body effect, and assuming $R_{SeriesRes} \gg 2/(g_{m1}r_{o1}r_{o2})$ [6], the equivalent input transconductance is $1/R_{SeriesRes}$ [6]. The gain of the circuit is approximately,

$$A_v \approx R_{LoadRes} / R_{SeriesRes} \qquad (1)$$

The important thing is that the gain does not depend on the transistor but they depend on the resistance. For this, it gives good linearity and high accuracy performance. The circuit is also suitable for low power like 1 V or less. In Figure 5 and 6, the open and close loop gain of the input amplifier is shown. In table 3, the overall performance of the input amplifier is mentioned.

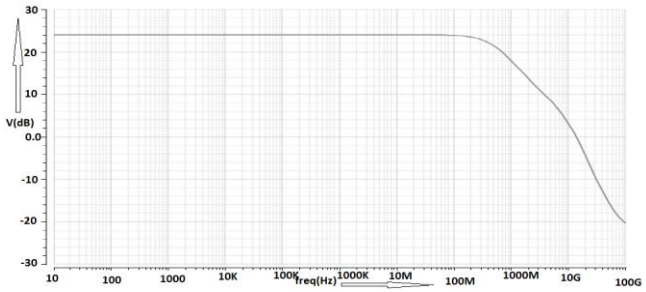

Figure 5: Open loop gain of the amplifier

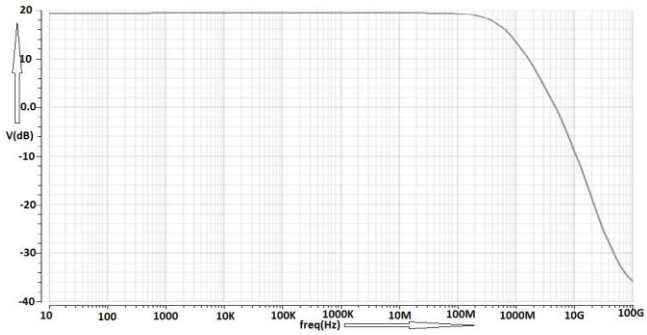

Figure 6: Close loop gain of the amplifier

Table 3: Performance analysis of the amplifier

Parameters	Value
Supply voltage	1 V
Open loop gain	24.01 dB
Close loop gain	19.63 dB
Unity-gain frequency	474 MHz
Input referred noise PSD @ 10 MHz	8.69 nV/ sqrt(Hz)
Phase margin	59.87
Power consumption	2.3 mW
Biasing current	83.931 µA

V. SIMULATION RESULTS

A. *Corner Analysis*

The corner analysis is nothing but the variation of different process nodes with different supply voltages and temperatures. For finding the worst-case performance in the integrated circuit, corner analysis gives a better view of the variations. For example, when the transistors changes their states from one logic state to another at the same time speed may change.

Figure 7 & 8 describe the corner analysis of the Tx and Rx. For Tx, the supply voltage varies from 1 V to 1.4 V but for Rx, it varies only from 0.9 V to 1.1 V. Temperature varies for the both from -40°C to 120°C. The simulation is run for 9 process corners. So the corner analysis is run for in total 9*3*3=81 points where 3 for supply voltage variation and another 3 for temperature variation.

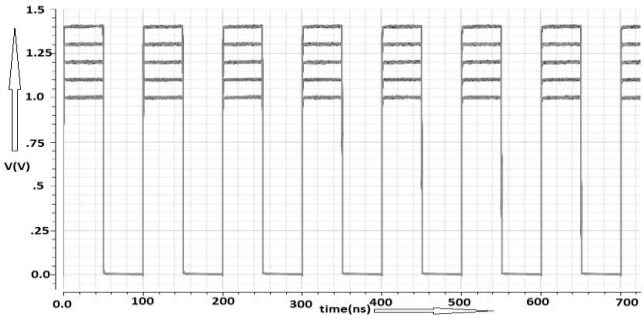

Figure 7: Corner analysis of the driver circuit

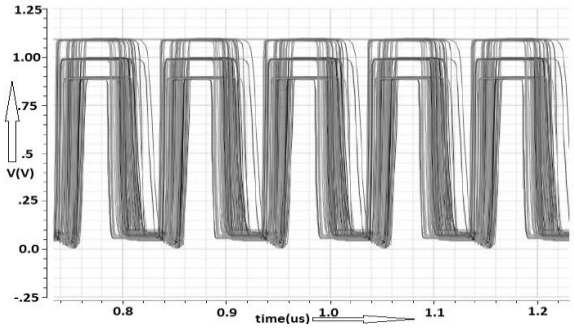

Figure 8: Corner analysis of the receive chain by using the suggested amplifier

The ones or zeros are decoded in the baseband by sampling the obtained data from the AFE. The sampling frequency is eight times of the clock frequency. From this, it is clear that one can detect when the length is more than 0.0125 µs. The length of ones and zeros are respectively 0.05 µs and 0.05 µs. From the corner analysis, it is clear that the minimum length of ones is 0.049 µs in Tx and 0.025 µs in Rx, which can be easily detected by the digital baseband.

*B. **Eye Diagram***

The eye diagram is a kind of graphical representation that can give a set of information about the high speed digital data transmission. In addition, it can give information about the noise, jitter, rise time and fall time.

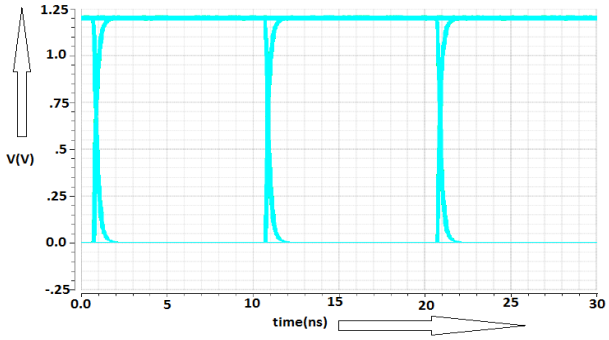

Figure 9: Eye diagram for the driver circuit performing in a Tx

In figure 9, the eye diagram for transmitted signal is presented where the simulation run for 30 ns with 10 mV supply noise. In table 4, the two basic characteristics of the eye diagram are determined that one is horizontal eye opening at 2.5 ns and another is vertical eye opening at 1.1 V. The timing variation at zero crossing indicates the amount of noise where the zero crossing occurs. The timing variation at zero crossing is measured as 0.55 ns. The cycle to cycle jitter with respect to the data clock is 0.87%.

Table 4: The results show the performance of the eye diagram in Tx

Vertical eye opening	1.1 V
Horizontal eye opening	2.5 ns
Noise margin	0.25 V
Timing variation at zero crossing	0.55 ns
Eye level zero	5 mV
Eye level one	10 mV
Rise time	1.2 ns
Fall time	1.5 ns
Jitter	0.87%

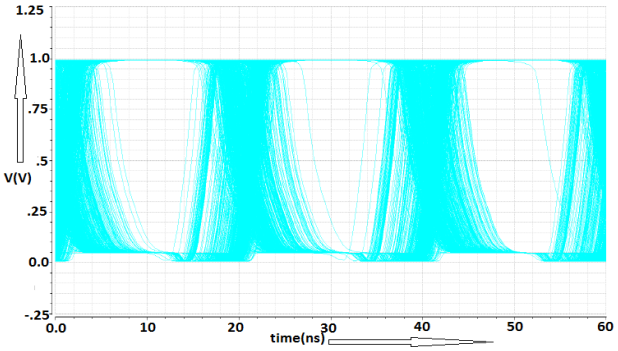

Figure 10: Eye diagram for the receiver chain

In figure 10, the eye diagram is run for 60 ns period. From the table 5, the value of horizontal eye opening is 19.5 ns and the vertical eye opening is 0.94 V. The value of timing variation of zero crossing measures at 4 ns. Noise margin is the minimum tolerance level of the proper operation of the circuit which is 0.47 V.

Table 5: Measurement table for eye diagram in Rx

Vertical eye opening	0.94 V
Horizontal eye opening	19.5 ns
Noise margin	0.47 V
Timing variation at zero crossing	4 ns
Eye level zero	7 mV
Eye level one	1 mV
Rise time	3 ns
Fall time	4.5 ns

C. Noise Analysis

Noise is an important consideration of designing any integrated circuit because it distorts the original signal so that the detection is hampered at the receiver. Figure 11 shows the results of transmitter after adding 3 mV noise to the supply voltage. Figure 12 shows the noise performance after adding 1 mV noise to the supply. Signal is recovered successfully by passing it through the input amplifier. It is not possible to recover the original signal if the noise is more than 2 mV in the Rx.

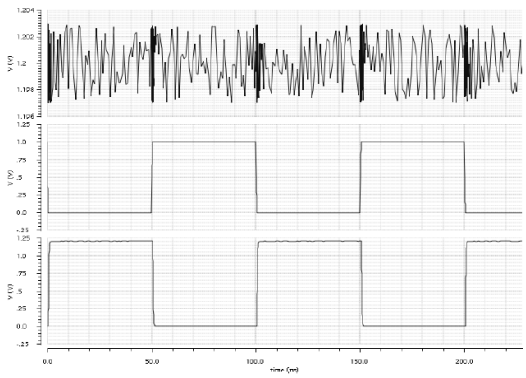

Figure 11: The waveform of the input data and the transmitter output by adding 3 mV noise

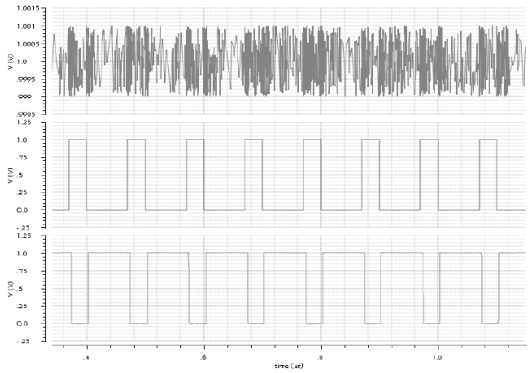

Figure 12: Adding 1mV noise to the supply voltage and showing output signal of Tx, Rx

VI. CONCLUSION

In BCC application, the proposed driver circuit gives progressive value in terms of jitter calculation, power leakage and also in PSRR compare to other circuit. The proposed input amplifier for Rx has provided some noteworthy results in gain performance, noise and power consumption. It is very difficult to maintain a low noise and low power consumption in low supply voltage but this architecture provides the improvement value of 8.69 nV/sqrt(Hz) and 2.3 mW respectively. We also highlighted the construction and function of the human body channel. Finally, this work can be considered as a new gateway for future improvement of BCC.

VII. ACKNOWLEDGMENT

It was very challenging for us at the beginning to adopt the overall system but we are very thankful to our teachers, seniors and friends to make a successful completion of this work.

REFERENCES

[1] Erik Karulf, eak2@cec.wustl.edu "Body Area Network (BAN)" (A survey paper written under guidance of Prof. Raj Jain).

[2] Hoi-Jun Yoo, and N. Cho, " Body Channel Communication for Low Energy BSN/BAN," in IEEE Asia Pacific Conference on Circuits and Systems, 2008, pp. 7-11.

[3] S. Song, N. Cho, H. Yoo, "A 0.2-mW 2-Mb/s Digital Transceiver Based on Wideband Signaling for Human Body Communications,"Solid-State Circuits, IEEE Journal of, vol.42, no.9, pp.2021,2033, Sept. 2007.

[4] J.M. Rabaey, A.P. Chandrakasan and B. Nikolic, "Digital integrated circuits : a design perspective," Upper Saddle River, N.J.: Pearson Education,2003.

[5] R.G. Carvajal, J. Ramirez-Angulo, A.J. Lopez-Martin, A. Torralba, J.A.G. Galan, A. Carlosena, and F.M. Chavero, " The Flipped Voltage Follower: A Useful Cell for Low-Voltage Low-Power Circuit Design," in IEEE Transaction on Circuits and Systems—I:Regular Paper,Vol. 52, No. 7, July 2005, pp. 1276-1291.

[6] H. Libin, L. Zhiqun, " A Low-Voltage CMOS Programmable Gain Amplifier for WSN Applification," Wireless Communications and Signal Processing (WCSP), 2011, pp. 1- 4.

American Journal of Engineering Research (AJER)
e-ISSN : 2320-0847 p-ISSN : 2320-0936
Volume-02, Issue-11, pp-260-266
www.ajer.org

Research Paper Open Access

Optimization Of The Operating policy Of The Multipurpose Hirakud Reservoir By Genetic Algorithm

S.N.Pradhan, Prof U.K.Tripathy
[1( ] *Department of Mathematics, Sundargarh Engg College, INDIA)*
[2( ] *Department of Mathematics, KIIT University, INDIA)*

***Abstract*: -** Genetic Algorithms is an optimization technique , based on the principle of natural selection, derived from the theory of evolution , are popular for solving parameter optimization problem. The main aim of this study is to develop a policy for optimizing the total release of water for irrigation, power generation and industry purpose in different months with different constraints during lean period of the multipurpose Hirakud reservoir of Odisha state in India by Genetic algorithms. The policy thus developed is compared with the current policy used by the department water resources, Government of Odisha to release the water for irrigation, power generation and industry use. The result thus found out is depicted through tables and graphs. It can be concluded that Genetic Algorithms model has the capability to perform efficiently.

Key wards: - *Genetic Algorithm, Optimization, Hirakud Reservoir*.

I. INTRODUCTION

The optimal reservoir operation policy for multipurpose reservoir should specify how the total demand of water could meet the available water in the reservoir. The operating policies are generally defined by a set of rules that specify either the reservoir target storage volume or the target release. In many practical situations, It is observed that the operating policies are established at the planning stage of reservoir to meet the planned demand like irrigation, power generation. But now a days, industrialization is one of the most important factor to improve the economic growth of a country. So the supply of water to the industries cannot be over ruled. Hence the demand and release of water for industrial purpose should be another parameter for the specific multipurpose reservoir operating model .

To obtain optimal operating rules, a large number of optimization and simulation models have been developed and applied over the past two decades. Genetic Algorithm is a robust search and optimization technique for solving complex problem. It was developed from the work done by Holland [1]. A large number of works has been reported on the application of GA for various complex reservoir problems .East and Hall [2] has applied GA to a reservoir problem with the objective of maximizing the power generation and irrigation. The optimal operating policies and release rules were also derived using GA by Olivera and Loucks [3].Wardlaw and Sharif [4] developed a GA model for a multi-reservoir system and reported that GA can be satisfactorily used in real time operations and extended the applicability to complex reservoir problem. Sharif and Wardlaw [5] developed a GA model for optimization of a multi-reservoir system in Indonesia by considering different scenarios. GA models were also successfully applied by Chen [6], Kuo et al. [7]; Ahmed and Sharma [8]; Chang et al. [9]; Anon-dominated sorting Genetic Algorithm (NSGA-II) was developed by Chang and Chang [10], to derive the operational strategies for the operations of a multi-reservoir system. Mathur and Nikam [11] optimized the operation of an existing multipurpose reservoir in India using GA, and derived reservoir operating rules for optimal reservoir operations. Hakimi-Asiabar M et al. [12] developed a self learning GA model for deriving operational policies for multi-objective reservoir system. Jothiprakash V. et al [13] derived a multi reservoir optimal operating policies using GA model and results of the GA model were then compared with conventional stochastic dynamic programming model. Recently Tripathy U.K. and Pradhan S.N. [14] developed a GA model for deriving optimal operating policy for Hirakud reservoir in India. The results obtained by GA model are compared with the current policy used by the Government of Odisha and observed that GA gives a better policy. From the above study, It is found that most of the works deal with

release of water only for irrigation and power generation in reservoir system till date. In the present study an attempt has been made to derive an optimal operating policy using GA model by taking another parameter i.e. release of water for industrial purpose. The results of the GA model were then compared with the current policy used by the Government of Odisha.

II. STUDY AREA

The reservoir consider in this study is the Hirakud Dam ,Multi-purpose reservoir located in the river Mahanadi at latidute 21^0 - 32' N, and longitude 83^0 - 52' E . The reservoir is constructed in the year 1956 . The reservoir required to meet irrigation demand, hydro power demand and flood control , which are different in different months. The reservoir is irrigating 1,55,635 hectors of kharif,1,08,385 hectors of rabi in Sambalpur ,Bargarh, Balangir and Subarnapur district of orissa .The water released by the power plant irrigates another 4560 km^2 of the CCA area in the Mahanadi delta. Again it generates 307 MW hydro electricity through two hydro electric controlling the river flow of 9500 power plant ie. Burla and Chiplima .The dam is also km^2 of the delta area in Cuttack and Puri district through the drainage system.

The multipurpose Hirakud dam across the river Mahanadi was constructed for flood control, irrigation and power generation. Hirakud dam is a composite structure of earth, concrete and masonry. The main dam having an overall length of 4.8 km spans between hills Lamdunguri on left and Chandli dunguri on the right sides to close the low saddles beyond the abutment hills. It has the distinction of being one time this longest dam in the world, being 25.8 km long with dams and dykes taken together.

It also has the rare distinction of forming the biggest artificial lake in Asia with reservoir spread of 743 square kilometers at full reservoir level. The reservoir has life storage of 5818 million cubic meters with gross storage of 8136 million cubic meters (mcm). Spilling can be affected by the operation of sluice gates incorporated in the concrete dam .The crest level of the spill way is at reservoir level 185.928 meter (610ft.) Both the split way contain 64 number under sluices, out of which 40 numbers are in the left and 24 number are in the right with floor at reservoir level 154.43 meters(510 ft) Each sluice has width of 3.658m(12ft) and height of 6.08m(20.34ft) .The sluices can discharge up to 0.95 million cubic meter per second .Free board is to be controlled during the filling season by the expected input capacity of the power channel and the discharge capacity of the spilling system subject to the flood control restraint.

III. MODEL DEVELOPMENT

Genetic Algorithm is a search and optimization technique based on the principle of natural selection and genetics. This is efficient, adaptive and robust search process, producing near optimal solution. Genetic Algorithm are heuristic technique for searching over the solution space of a given problem in an attempt to find the best solution or set of solution. The basic elements of natural genetics –reproduction, cross over, mutation are used in the genetic search procedure. Genetic algorithm differs from conventional optimization techniques in following ways:

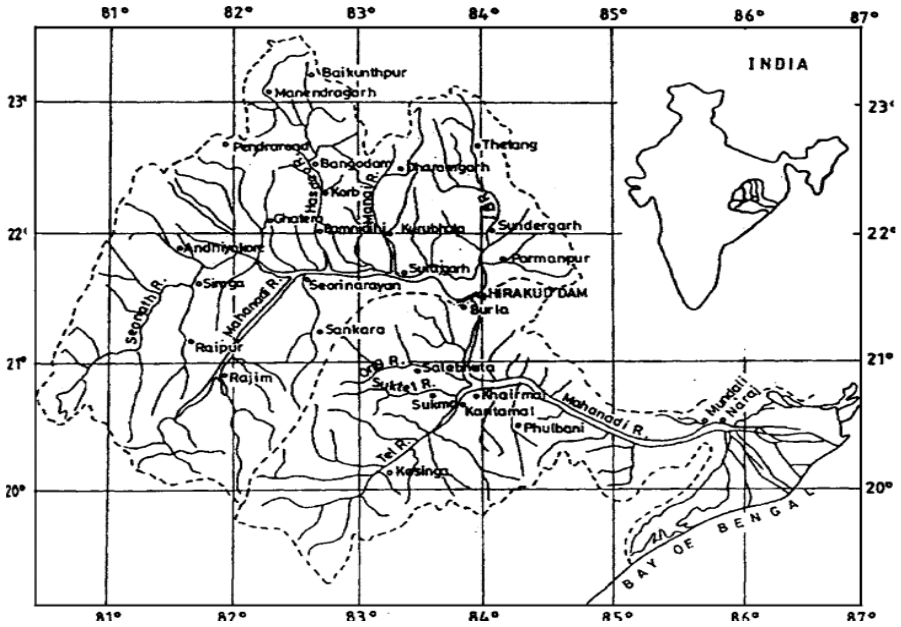

(Fig-1, catchment area of Hirakud dam ,India)

1. GAs operate with coded versions of the problem parameters rather than parameters themselves .
2. Almost all conventional optimization techniques search from a single point but GAs always operate on a whole population of points(strings) .
3. GA uses fitness function for evaluation rather than derivatives. As a result, they can be applied to any kind of continuous or discrete optimization problem. The key point to be performed here is to identify and specify a meaningful decoding function.

These are the major differences that exist between Genetic Algorithm and conventional optimization techniques. The basic genetic algorithm is as follows:

• [start] Genetic random population of n chromosomes (suitable solutions for the problem)
• [Fitness] Evaluate the fitness f(x) of each chromosome x in the population
• New population] Create a new population by repeating following steps until the New population is complete
- [selection] select two parent chromosomes from a population according to their fitness (the better fitness, the bigger chance to get selected).
- [crossover] With a crossover probability, cross over the parents to form new offspring (children). If no crossover was performed, offspring is the exact copy of parents.
- [Mutation] with a mutation probability, mutate new offspring at each locus (position in chromosome)
- [Accepting] Place new offspring in the new population.

A Simple Genetic Algorithm

• [Replace] Use new generated population for a further sum of the algorithm.
• [Test] If the end condition is satisfied, stop, and return the best solution in current population.
• [Loop] Go to step2 for fitness evaluation.

In the present study, the fitness function of the GA model is minimizing the squared deviation of monthly irrigation demand, power generation demand, industrial demand and squared deviation in mass balance equation for the lean period(Jan-June). The objective function is given by the equation

$$\mathbf{Z= Minimize}\sum_{t=1}^{6}(RI_t - DI_t)^2 + \sum_{t=1}^{6}(RP_t - DP_t)^2 + \sum_{t=1}^{6}(RF_t - DF_t)^2 + \sum_{t=1}^{6}(AS_t + I_t - RI_t - RP_t - RF_t - Et2$$

Where RI_t= Monthly irrigation release for month 't'
DI_t= Monthly downstream irrigation demand for the month 't'
RP_t= Monthly power generation release for month 't'
DP_t= Monthly power generation demand for month 't'
RF_t= Monthly release for industry purpose for month 't'
DF_t= Monthly demand for industry purpose for month 't'
$AS_t = \frac{1}{2}(S_t + S_{t+1})$= Average storage in the month 't'
S_t = initial storage in the beginning of the month 't'
S_{t+1} =Final storage in the end of the month 't'
I_t= Monthly inflow during the period 't'
E_t= Monthly evaporation loss from the reservoir during the month 't'
The above fitness function of GA model is subjected to the following constraints and bounds.

A. Release constraint

The irrigation and power generation release during the month t should be less than or equal to the irrigation and power generation demand in that month and are represented by

$RI_t \leq DI_t$ t=1,2,3,4,5,6.

$RP_t \leq DP_t$ t=1,2,3,4,5,6.

B. Storage constraint

The reservoir storage in any month should not be more than the capacity of the reservoir, and should not be less than the dead storage capacity and is represented by

$$S_{min} \leq S_t \leq S_{max}$$

Where
S_{min} = Dead storage of the reservoir = 1814.976 mcm
S_{max} = Maximum capacity of the reservoir = 7190.856 mcm

IV. SENSITIVE ANALYSIS

Sensitivity analysis has been carried out to evaluate the effect of population size on the GA performance. All other parameters and run controls were set constant. Fig (2) shows that the best fitness value

42475 is achieved at the population size 400 and is not might be good from 500 to 1000. Now by taking population size 400, sensitive analysis has been done to evaluate the effect of crossover fraction and from Fig (3) , It can be observed that the best fitness value 42676 is achieved for the crossover fraction of 0.8 . If too less values of crossover fraction are used, then the performance of GA is not so good. Again by taking population size 400 and crossover fraction .08 , sensitivity analysis has been carried out to evaluate the effect of mutation rate on the performance of GA . In this case we are getting the best fitness value as 42204 at the mutation rate 0.01.The reasonable solutions are obtained when the rate of mutation has risen except at 0.05.

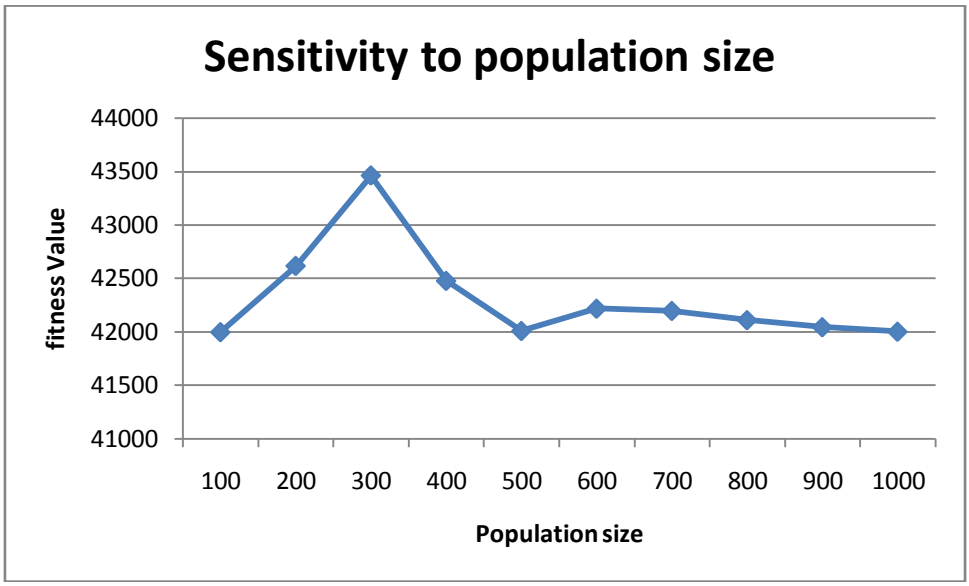

(Fig-2 , Sensitivity to population size)

Table - 1, fitness values on different population size

Population size	100	200	300	400	500	600	700	800	900	1000
Fitness value	41996	42615	43460	42475	42007	42215	42194	42108	42043	42000

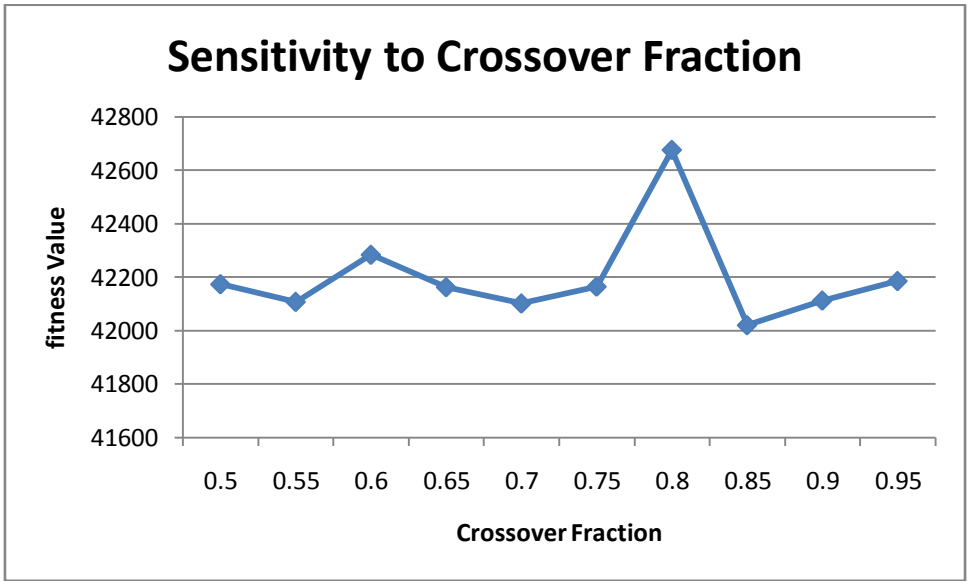

(Fig-3 , Sensitivity to crossover fraction)

Table - 2, Fitness values on different crossover fraction

Crossover fraction	0.50	0.55	0.60	0.65	0.70	0.75	0.80	0.85	0.90	0.95
Fitness value	42174	42108	42284	42163	42102	42165	42676	42021	42113	42186

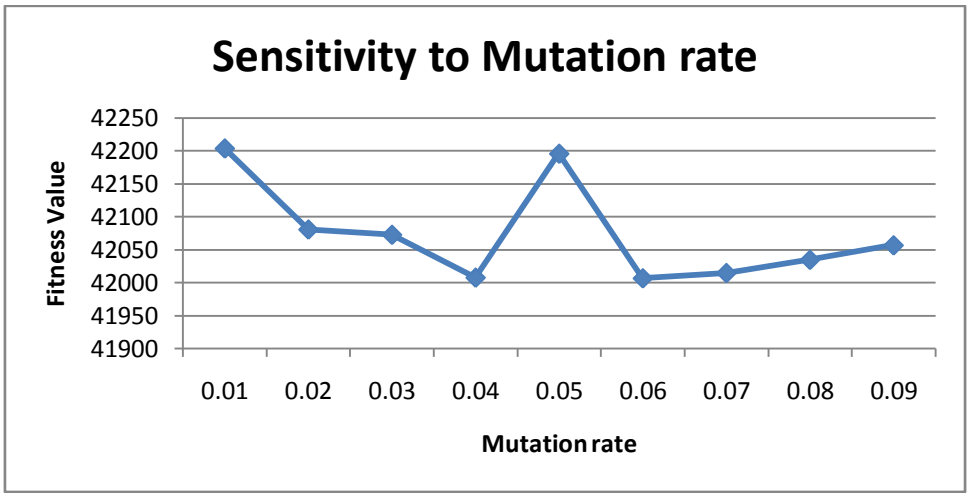

(Fig-4 , Sensitivity to mutation rate)

Table - 3, Fitness values on different mutation rate

Mutation rate	0.01	0.02	0.03	0.04	0.05	0.06	0.07	0.08	0.09
Fitness value	42204	42081	42073	42008	42196	42007	42015	42035	42057

V. IV. MODEL APPLICATION AND DISCUSSION

GA has been applied to the above formulated model . We have encoded at MATLAB software for optimizing the above multipurpose reservoir. The use of efficiency of data are taken from the sensitive analysis and the average inflow data has been taken from the data base of water resources department of Government of Odisha in India. The important input variables in the present GA model study are the monthly irrigation demand, monthly power generation demand , monthly industrial demand and the mean storage in the reservoir. The objective of the study is to compute the quantity of water that should be released for irrigation, power generation and industrial purpose, keeping in view the minimum storage in the reservoir in that particular month. Thus 24 decision variables are considered for the lean period (Jan-June). The fitness function evaluation gives the measure of goodness of the fit of the string. After fitness function evaluation ,strings are selected based on the percentage contribution of the population fitness for mating and mutation to form the next generation by the Roulette Wheel method.

The population size in GA is one of the important parameters. It is very important for obtaining optimum population. The size of the population ranges from 64 to 300 and even up to 1000 in water resources applications. A large population helps to maintain greater diversity but it involves considerable computational cost when the full model is being used to generate performance predictions. The policy thus derived shows the irrigation, power generation and industrial purpose deficit.

VI. WATER RELEASE FOR IRRIGATION

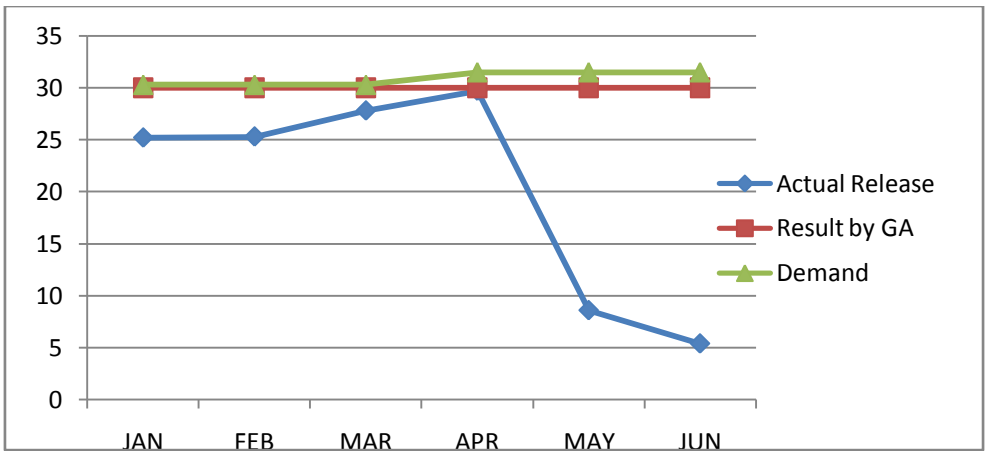

(figure-5, Water release for irrigation)

Table-4 (Release of water for irrigation)

All figures are in MAcF * 10^2

Month	January	February	March	April	May	June
Actual Release	25.2	25.3	27.8	29.7	8.6	5.4
Result by GA	29.978	29.996	29.984	29.987	29.995	29.995
Demand	30.29	30.29	30.29	31.5	31.5	31.5

WATER RELEASE FOR POWER GENERATION

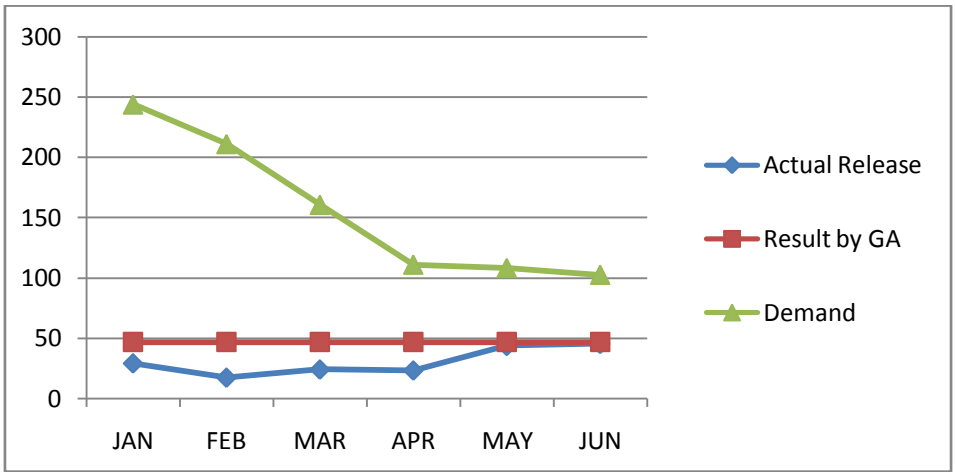

(figure-6, Water release for power generation)

Table-5 (Release of water for Power Generation)

All figures are in MAcF * 10^2

Month	January	February	March	April	May	June
Actual Release	29.4	17.6	24.3	23.5	43.8	45.5
Result by GA	47	46.995	46.987	46.99	46.99	46.99
Demand	244.14	211.24	160.71	111.0	108.2	102.6

Table-6 (Release of water for Industry Use)

All figures are in MAcF * 10^3

Month	January	February	March	April	May	June
Actual Release	6.925	5.938	7.783	6.438	7.254	7.621
Result by GA	7.72	7.59	7.88	7.82	7.8	7.87
Demand	9.0	7.719	10.11	8.369	9.43	9.907

WATER RELEASE FOR INDUSTRIAL PURPOSE

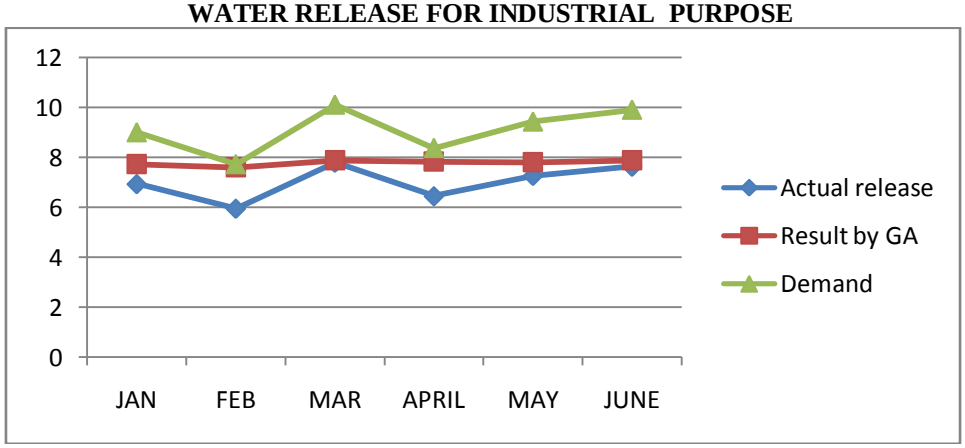

(figure-7, Water release for industry purpose)

VII. CONCLUSION

An optimal policy has been developed for release of water from the reservoir for irrigation, power generation and industrial purpose with average storage of the reservoir for a particular month t. Our policy developed through GA shows that the release of water for irrigation, power generation and industrial purpose is more than that of the release by the department of water resources, Government of Odisha, keeping strict vigil on dead storage of the reservoir. Table-4 shows the release of water for irrigation. It is observed that the result obtained by the GA fulfils 99% of the demand in the month of February which is the maximum and 95% is the minimum in the month of April. The table-5 shows the release of water for power generation. The result obtained by GA fulfils 46% of the demand in the month of April which is the maximum and 19% is the minimum in the month of January. Similarly table- 6 shows the release of water for industrial purpose . The result obtained by GA fulfils 98% of the demand in the month of February which is maximum and 79% is the minimum in the month of April. Thus the policy developed by Genetic Algorithm is far better than the policy being used by the water resources department of Government of Odisha in India.

VIII. REFERENCES

[1] J H Holland , Adaptation in natural and artificial systems. MIT press, Cambridge Mass,1975

[2] V. East,MJ Hall, Water resources system optimization using genetic algorithms. Proc.1st int. conf. on Hydroniformatics, Balkema,Rotterdam, The Netherlands, 1994,pp 225-231

[3] R.Oliveira, DP Loucks ,Operating rules for multi reservoir system. Water Resour Res 33(4),1997,839-852

[4] R.Wardlaw, M Sharif , Evaluation of genetic algorithms for optimal reservoir system operation.J water Resour Plan Manage ASCE 125(1),1999,25-33

[5] M. Sharif,R. Wardlaw , Multi reservoir system optimization using genetic algorithms case study. J comput Civ Eng ASCE 14(4),2000,255-263

[6] L. Chen L , Real coded genetic algorithm optimization of long term reservoir operation. JAWRA, J Am Water Resour Assoc 39(5),2003, 1157-1165

[7] JT Kuo, WC Cheng, L.Chen L , multi objective water resources systems analysis using genetic algorithms – application to Chou-shui river basin, Taiwan. Water Sci Technol 48(10),2003,71-77

[8] J.A.Ahmed ,A.K. Sharma, Genetic algorithm for optimal operating policy of a multipurpose reservoir. Water Resour Manag 19(2),2005, 145-161

[9] F. Chang , L. Chen, L. Chang, Optimizing the reservoir operating rule curves by genetic algorithms. Hydrol process 19(11),2005, 2277-2289

[10] L. Chang, F. Chang, Multi-objective evolutionary algorithm for operating parallel reservoir system. J Hydrol 377(1-2),2009, 12-20

[11] Y. Mathur ,S. Nikam , Optimal reservoir operation policies using genetic algorithm. Int J Eng Technol 1(2),2009, 184-187

[12] M.Hakimi-Asiabar , SHGhodsypour, R Kerachian, Deriving operating policies for multiobjective reservoir systems: applition of self-learning genetic algorithm. Appl soft comput 10(4),2010, 1151-1163

[13] V.Jothiprakash.,S. Shanthi, R. Arunkumar , Development of operational policy for a multi-reservoir System in India Using Genetic algorithms, Water resource management,2011

[14] U.K.Tripathy , S.N Pradhan , Application of Genetic Algorithm for optimal operating policy of the multi purpose Hirakud reservoir of IWWA 44(4),2012, 315-320

American Journal of Engineering Research (AJER)
e-ISSN : 2320-0847 p-ISSN : 2320-0936
Volume-02, Issue-11, pp-267-271
www.ajer.org

Research Paper Open Access

Analysis Of Mass Transfer During Microwave Drying Of Yam Slabs

Dagde, Kenneth Kekpugile, Goodhead, ThankGod Oweifa.
Department of Chemical/ Petrochemical Engineering,
Rivers State University of Science and Technology, Port Harcourt, Nigeria

Abstract: - This paper presents an experimental approach to the drying of yam slabs using microwave. The reduction in the mass of the yam slab with time at medium low conditions was investigated. A theoretical model to describe the drying of the yam slab in microwave was developed and validated using the experimental data. The effective diffusivity of water molecules in yam slab in medium low power condition of the microwave oven was estimated to be 5.83 x 10^{-8} m^2/s. Simulations of the model reveals that the microwave drying of yam slabs is very sensitive to the thickness of the yam slab and is independent of the moisture content and initial mass of the yam slab. As the thickness of the yam slab increases the rate of drying decreases and therefore the time for complete drying increases.

Keywords: - *Effective diffusivity, Microwave Drying, Model Development, Moisture content.*

I. INTRODUCTION

Drying of food products is essential for the preservation of the food product for long periods of time due to the fact that micro-organisms and food enzymes need moisture to function effectively causing food spoilage. Drying processes for food products include sun drying, hot air drying, freeze-drying, flash freezing and microwave drying.

Microwaves are short high frequency radio waves lying between infrared and conventional radio waves. Microwave drying is a rapid dehydration technique that can be applied to specific foods. The microwaves agitate the water molecules in the food causing them to vibrate and produce heat which drives the drying process. Microwave drying is rapid, uniform, energy efficient and space saving [1, 2, 3, 4

Zogzas *et al*. [5], presented a review of reported experimental moisture diffusivity data in food materials. Krokida *et al*. [6], investigated the effects of the drying methods on the colour of the obtained products and found that the colour characteristics were significantly affected by the drying methods employed. Sharma and Prasad [7] determined the effective moisture diffusivity of garlic cloves during a microwave convective drying process. They also investigated its dependence on factors such as microwave power, air temperature and air velocity. McMinn *et al*. [8] investigated the mass transfer characteristics for potato slabs and cylinders subjected to natural convective and microwave convective drying by adopting the analytical model proposed by Dincer and Dost [9,10]. They showed that the model accurately described the drying process of Potato slabs and that the power of the microwave has the main effect in drying. The model developed by Dincer and Dost [9, 10] was not developed from experimental data for microwave drying of food products although when applied to the drying of Potato slabs by McMinn *et al*. [8] it was accurate. Sharma and Prasad [7], investigation was limited to drying of garlic cloves using microwave convective drying process. In this paper, experimental data from a microwave drying system are used to determine the mass transfer characteristic for slab yam samples. An accurate theoretical model for the microwave drying of yam slabs is developed and validated using the experimental data. The effective diffusivity of water molecules in yam slab in medium low power condition of the microwave oven was estimated to be 5.83 x 10^{-8} m^2/s. Simulations of the model reveals that the microwave drying of yam slabs is very sensitive to the thickness of the yam slab and is independent of the moisture content and initial mass of the yam slab. As the thickness of the yam slab increases the rate of drying decreases and therefore the time for complete drying increases.

II. EXPERIMENTATION AND THEORETICAL FORMULATION.

The key Apparatus used for the experiment includes; Microwave oven, Weighing balance, Knife, crucible and scale rule. The materials used for the experiment are the yam tubers and water.

1.1 Experimental Procedure

Wash the yam tubers with water. Peel the yam tubers using knife. Cut the yam to the required thickness (1 cm) using knife and scale rule. Weigh the yam slab to obtain the initial weight using weighing balance. Switch on the microwave oven at medium low operating condition for 5 minutes. Put the yam slab on the crucible into the microwave oven and allow for 2 minutes. Weigh the yam slab from the microwave oven using the weighing balance. Repeat steps 6 and 7 until there is no significant change in weight of the yam slab or burning is observed.

1.2 Model Development

The model for microwave drying of yam was done based on the following assumptions:
Initially there is uniform distribution of moisture in the yam.
There is zero concentration of moisture on the surface of the yam.
Drying occurs only from the upper surface of the yam slab on the crucible.
No reaction or burning of the yam slab takes place during the drying process.
Transfer of water molecules from the yam slab occurs in the vertical direction only.

A … of conse… s:

Rate of Accumulation of water within the yam slab	Rate of Input of water in yam slab	Rate of Output of water from yam slab	Rate of Generation of water within the yam slab

S … ne yam …

$$\frac{\partial}{\partial} \qquad 2$$

where, C_w is moisture content, t is time, D is effective diffusivity and y is distance in the vertical direction within the yam slab.
The moisture content is given by

$$C_w = \frac{w - w_e}{w_e} \qquad 3$$

where, w is mass of yam slab and w_e is the mass of yam slab when drying is complete.
The following boundary conditions are applied to solve equation (2)

$$C_w(0,t) = 0 \text{ for } 0 < t < \infty \qquad 4$$

$$C_w(l,t) = 0 \text{ for } 0 < t < \infty \qquad 5$$

$$C_w(y,0) = \varphi \text{ for } 0 < y < l \qquad 6$$

where, l is the thickness of the yam slab and φ is the initial moisture content which is given by

$$\varphi = \frac{w_1 - w_e}{w_e} \qquad 7$$

where, w_1 is the initial mass of the yam slab.
Equation 2 is solved with the boundary conditions of Eqs (4, 5 and 6) to yield

$$w = w_e + \frac{4}{\pi}(w_1 - w_e)\left[e^{-Dt\left(\frac{\pi}{l}\right)^2} - \frac{1}{3}e^{-9Dt\left(\frac{\pi}{l}\right)^2} + \frac{1}{5}e^{-25Dt\left(\frac{\pi}{l}\right)^2} - \frac{1}{7}e^{-49Dt\left(\frac{\pi}{l}\right)^2} \ldots\right] 8$$

Taking the first 4 terms and writing equation (8) in terms of wet moisture content (ϑ)
where,

$$\vartheta = \frac{w_1 - w_e}{w_1} \qquad 9$$

$$w = w_1(1 - \vartheta) + \frac{4}{\pi}w_1\vartheta\left[e^{-Dt\left(\frac{\pi}{l}\right)^2} - \frac{1}{3}e^{-9Dt\left(\frac{\pi}{l}\right)^2} + \frac{1}{5}e^{-25Dt\left(\frac{\pi}{l}\right)^2} - \frac{1}{7}e^{-49Dt\left(\frac{\pi}{l}\right)^2}\right] \qquad 10$$

Equation (10) is the model equation describing the microwave drying of yam slab.

III. RESULTS AND DISCUSSION

Table 1 shows the comparison of the experimental data to the model results as described by equation (10). Table 1 shows a representative result of 10 yam slabs of 1 cm thickness with which the model results were compared with.

Table 1. **Comparison of experimental data and model result**

Time (mins)	*Experiment mass (g)*	*Model mass (g)*	*% Deviation*
0	9.8470	9.3435	-5.113
2	7.6000	7.5192	-1.063
4	5.7130	5.4808	-4.064
6	4.1960	4.4562	6.200
8	3.8980	3.9425	1.140
10	3.6000	3.6849	2.359
12	3.4370	3.5558	3.457
14	3.4260	3.4911	1.899
Effective Diffusivity		5.83×10^{-8} m^2/s	
Wet Moisture Content		0.6521	

% deviation = (model – experiment)/experiment

It was observed during the experiment that at the 16th minute all yam slabs were burned and therefore any loss in weight after the 14th minute was attributed to burning. Maximum % deviation is 6.2%. The deviation can be attributed to the assumptions made and random error during the experiment. The effective diffusivity of water molecules from the yam at medium low power conditions of the microwave was calculated to be $5.83 \times 10^{-8} m^2/s$ and the wet moisture content of the yam is 0.6521.

Figure 1 shows the graphical representation of the experimental data and the model results. From Figure 1 it is seen that the model accurately predicts the experimental data. This indicates that the model developed is very accurate.

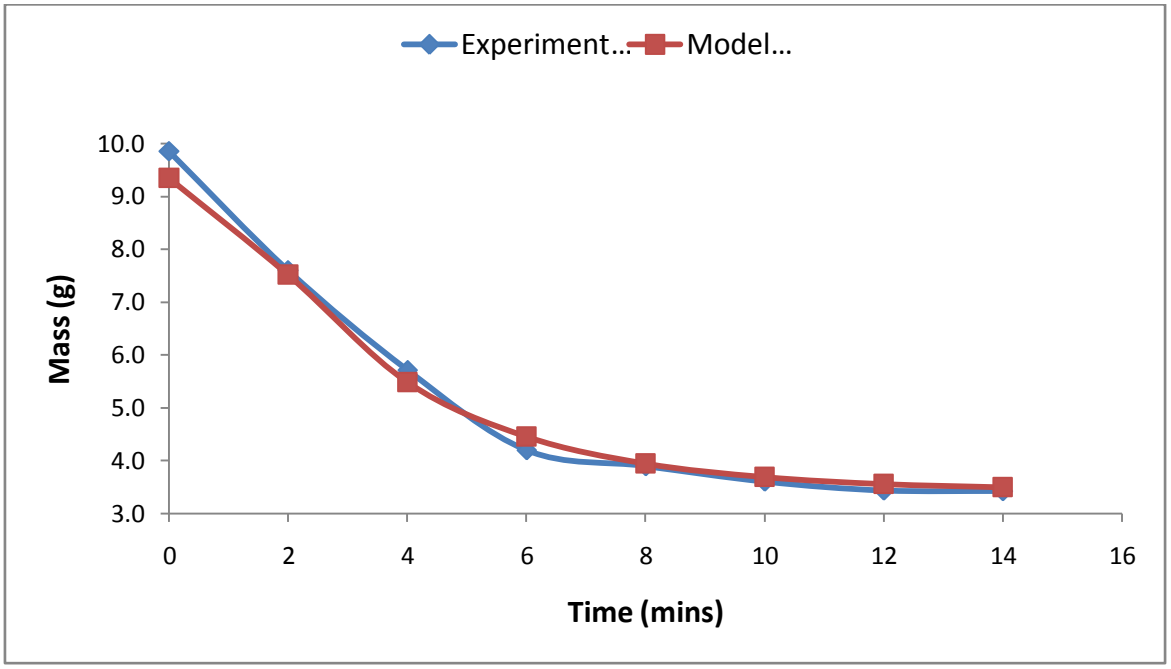

Figure 1. Graph of mass of yam slab against drying time.

The result of the simulation of the model for different thickness of the yam slabs assuming constant initial weight of 9.847g and moisture content of o.6521 is shown in Figure 2. From Figure 2 it can be observed that as the thickness increases, the rate of decrease of the mass (drying) of the yam slab with drying time decreases.

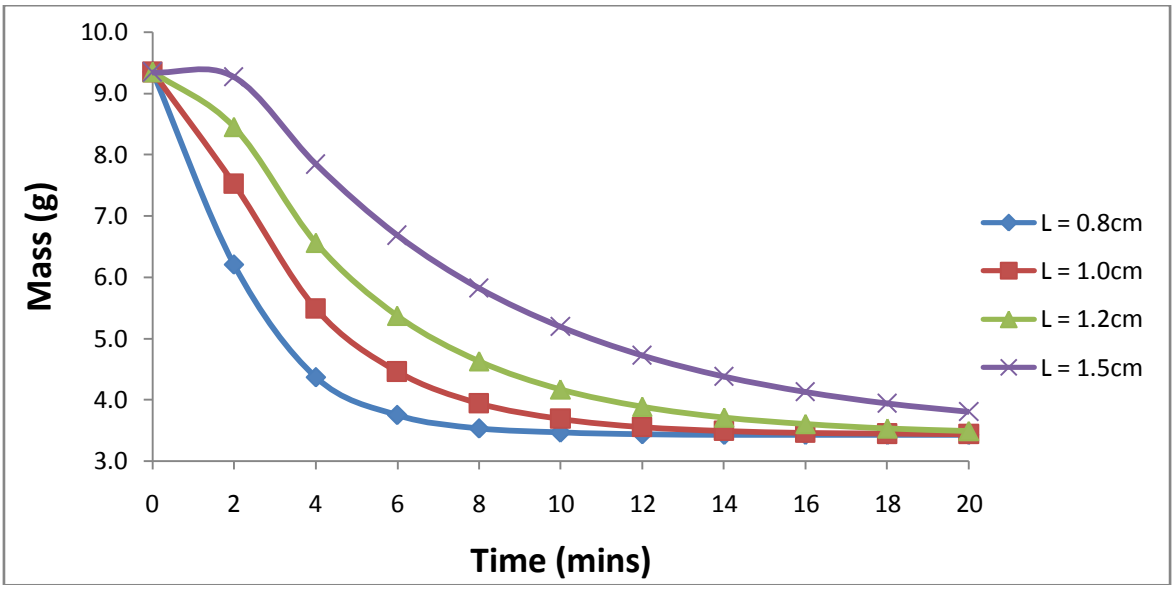

Figure 2. Graph of mass of yam slab against time for different thickness.

This can be attributed to the increase in the distance travelled by the water molecules from the interior of the yam before it is expelled and the corresponding lesser surface (cross section) area available for transfer of water molecules from the yam slab since its initial mass is constant. This indicates that for microwave drying of yam, a thinner thickness of the yam makes for rapid drying of the yam (lesser time for complete drying).
The result of the simulation of the model for different wet moisture content of the yam slabs assuming constant initial weight of 9.847g and thickness of 1cm is shown in Figure 3.

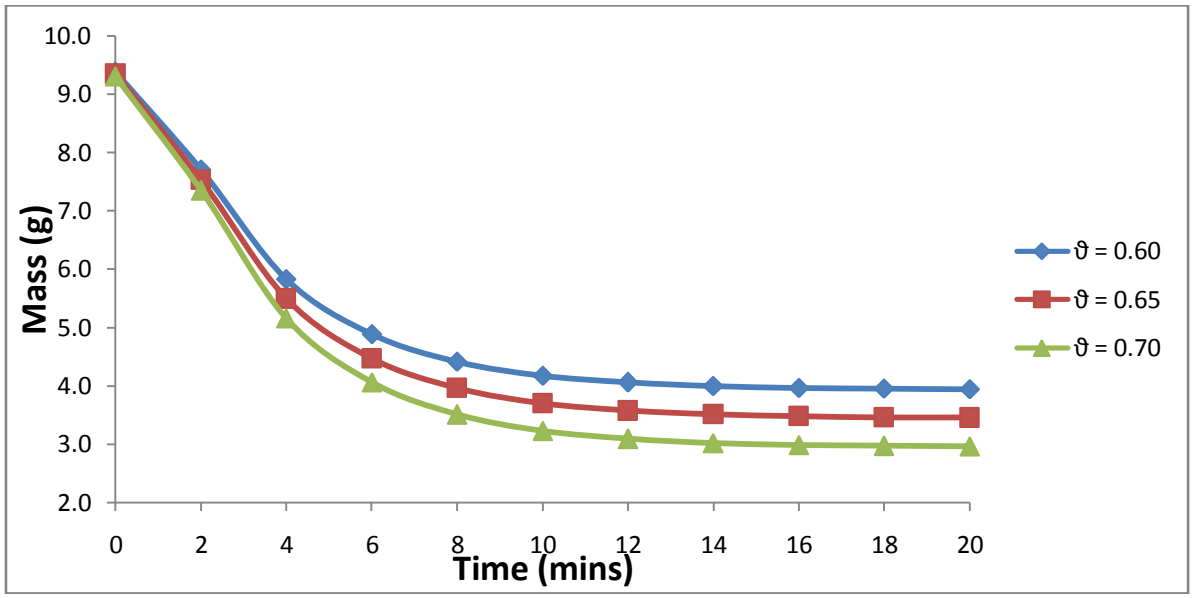

Figure 3. Graph of mass of yam slab against drying time for different wet moisture content.

From Figure 3, it is observed that as the wet moisture content increases the mass of the yam slab when drying is complete decreases. However the mass of yam slab tends to this limiting value following the same trend. This can be attributed to the nature of microwave. The microwave agitates the water molecules inside the yam to produce the heat which drives the drying process from within the yam. The more the water content of the yam, the more water molecules are agitated and as such the rate of removal of water increases. This indicates that for microwave drying of yam, the rate of drying of the yam increases with the water content of the yam and as such the time required for complete drying of the yam is not changed significantly.
The result of the simulation of the model for different initial mass of the yam slabs assuming constant wet moisture content of 0.6521 and thickness of 1cm is shown in Figure 4. From Figure 4 it is observed that the graphs for the different initial mass follow the same trend.

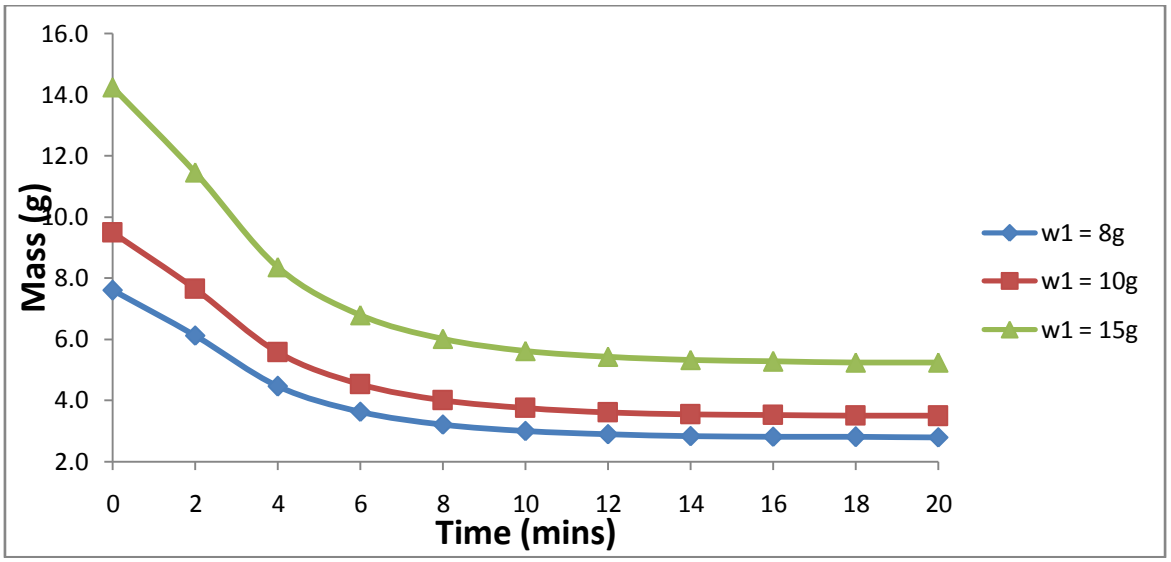

Figure 4. Graph of mass of yam slab against drying time for different initial mass of the yam.

This can be attributed to the corresponding increased area for transfer of water molecules available to the yam slabs of bigger initial mass. This indicates that during the microwave drying of yam, the amount of water expelled per unit area is constant.

IV. CONCLUSION

The reduction in the mass of the yam slab with time at medium low conditions of a microwave oven was investigated. A theoretical model that describes the drying of the yam slab in the microwave was developed and validated using the experimental data. The effective diffusivity of water molecules in yam slab in medium low condition of the microwave oven was calculated to be 5.83 x 10^{-8} m^2/s and the wet moisture content of yam was estimated to be about 65%. Simulations of the model reveals that for microwave drying of yam slabs, the time for complete drying of the yam is independent of the moisture content of the yam and the initial mass of the yam slab but is very sensitive to the thickness of the yam slab. As the thickness of the yam slab increases the time for complete drying of the yam slab increases. It was also observed that the rate of drying of the yam slab increased as the moisture content of the yam slab increased and that the amount of water expelled per unit area of a uniform yam slab is constant during microwave drying.

REFERENCES

[1] Oliveira M.E.C and Franca A.S. Microwave heating of foodstuff; Journal *of Food Engineering*, 53: 347-359, 2002.
[2] Haghi A.K. A mathematical model of the drying process; *ActaPolytechnica*, 4 1(3): 20-25, 2001.
[3] Severini C. Baiano A. Pilli T. De, Carbone B. F and Derossi A. Combined treatments of blanching and dehydration: study on potato cubes, *Journal of Food Engineering* 68 (3), pp. 289-296, 2005.
[4] Sahin, A. Z., Dincer I., Yilbas, B. S. and Hussain M. M. Determination of drying times for regular multi-dimensional objects, *International Journal of Heat and Mass Transfer*, 45, pp. 1757 – 1766, 2004.
[5] Zogzas N.P., Maroulis Z.B. and Marinos K.D. (1996) Moisture diffusivity data compilation in foodstuffs; *Drying Technology*, 14: 2225-2253, 1996.
[6] Krokida M.K., Maroulis Z.B. and Saravacos G.D. The effect of the method of drying on the colour of dehydrated products; *International Journal of Food Science and Technology*, 36(1): 53-59, 2001.
[7] Sharma G.P. and Prasad S. Effective moisture diffusivity of garlic cloves undergoing microwave convective drying; *Journal of Food Engineering*, 65: 609-617, 2004.
[8] McMinn W.A.M., Khraisheh M.A.M. and Magee T.R.A. Modelling the mass transfer during convective, microwave and combined microwave convective drying of solid slabs and cylinders; *Food Research International*, 36: 977-983, 2003.
[9] Dincer I. and Dost S. An analytical model of moisture diffusion in solid objects during drying; *Drying Technology*, 13 (1/2): 425-435, 1995
[10] Dincer I. and Dost S. A modeling of moisture diffusivities and moisture transfer coefficients in drying of solid objects; *international Journal of Energy Research*, 20(6): 531-539, 1996.

American Journal of Engineering Research (AJER)
e-ISSN : 2320-0847 p-ISSN : 2320-0936
Volume-02, Issue-11, pp-272-275
www.ajer.org

Research Paper Open Access

Automotive (Car Paint): From Local Raw Material Castor Seed Oil (Ricinius Communis), As Plasticizer

Oragwu Ifeoma P.
Department Of Pure &Industrial Chemistry, Anambra State Unversity, Uli.

Abstract: - Drying oils have found applications in almost all decorative, communication and surface coatings. Castor seed oil had been assessed as a plasticizer and film former in automotive paint making. The moisture content of the seed meal was low, therefore, good quality for glossy auto-paint. Soxhlet extraction method was used to extract the oil at 315 ^{0}C, while simple distillation method was used to separate the solvent from the pure oil. The viscosity, refractive index, specific gravity were 0.425 at 26 ^{0}C, 1.471, 2.00 g/cm^3, respectively, and are within range for automotive paint application. The mill charge, stabilization and let-down, processes, were carried out within the laboratory conditions. Different colours of paint were prepared from the original formulation by substituting the base pigment with another as desired. The opacity, viscosity, wash-ability, flexibility, compatibility and other quality control tests carried out on the castor oil plasticized auto-paint, compared very well to the Berger auto-fine car paint standard.

Keywords: - *Castor seed oil, pigments, plasticizers, alkyd-resin, auto-paints.*

I. INTROUDUCTION

Castor seed oil (ricinius communis), as one of the drying vegetable oil is derived from the castor oil plant seed, of the family euphorbiaceae. It is one of the most widely used film-forming oil with applications in decorative, communication and surface coatings. The seed plant is wide spreading throughout tropical regions of Africa, India and Mediterranean areas, where they are cultivated as ornamental flowering plants[1].The spring fruit which is greenish to reddish-purple capsule when matured, contains the large oval shiny bean-like poisonous seed[2]. The seed oil is colorless to pale yellow with mild odour, tastes, and commonly referred to as "Palma Christi" or "palm of Christ" due to their medicinal treatments for constipation, wounds,skin diseases etc,[3]. The presence of ricinoleic acid (a mono-saturated compound) with 18 carbon fatty acid having hydroxyl group on the 12th carbon which makes derivatization of other compounds like alkyd resins, possible [4,5, 6]. It is one of the drying oil that could cross-link on exposure to air to form a solid dry film, a property that makes it unique component in automotive paint making.

Paints, generally are pigmented solutions, liquefiable or mastic, which after application to a substrate, dry, to form solid films. The early paints of the Egyptians, were made from egg-shell, insects, plants, animals, minerals, powdered rocks as pigments, resins and water as the commonest solvent, had been improved upon to give better quality and durable coats[6]. Reports had shown that modern paints had been prepared to add shape, beauty, quality and durability to both exterior and interior finishes in automotive vehicles by incorporation of plasticizers[7]. Automotive paint technology are more sophisticated and are composed of blends of resins, fillers, additives, curing agents or extenders, to inhibit rust, cracks, resist fire or light effect on substrates, and designed to withstand other environmental conditions. Environmental Regulation Agencies had advised automotive paint industries to reduce solvent emission in their paint products to check-mate air pollutions [8]. This is because conventional solvents in paints could evaporate into the air during the drying process to release the green house gases that could cause global warming and are detrimental to health [9]. Plasticizers are inert polymeric materials with high boiling point and functions by embedding themselves between the paint components to enhance their cross-linkages[10]. They are dispersants or additives that could increase the plasticity, flexibility, compatibility, washability and durability of auto-paint or gloss paints in general [11]. Studies had shown that plasticizers had been used to improve the strength of glass-fiber reinforced plastic motor cases, concrete clays and related products[12]. An unplasticized surface coats result into loss of flexibility,

emblittlement and cracking within a short period of time[13]. Serious negligible damages had been observed as it concerns maximum average loss in burst strength in motor cases without plasticizers than those with plasticizers [14]. Medical reports had also shown that plasticizers are also used to improve hormone-like and estrogenic activities in the body[15]. Researchers had compared other drying oils and proved castor oil good for most chemical or medical products like in the production of cosmetics, coatings, etc [16]. As part of my contributions to improve the economy, health standard, minimize solvent emission of dangerous gases from paints and increase the quality of automotive paints, I embarked on the extraction and application of castor oil as a plasticizer in auto-paints, as an alternative to the expensive and imported linseed oil for applications in automotive or gloss paint making generally.

II. MATERIALS AND METHODS

The apparatus include; soxhlet extraction sets, stopwatch, leveling cup, viscometer cup, refractometer, Hegman finess grinding-guage, water bath, thermometer, heating mantle, steel-metal panels etc. The materials include: titanium dioxide, xylene, white spirit, nitrocellulose, alkyd resin, etc.

2.1: METHODS:

The castor oil seeds were obtained from afor market, Akwaeze in Anaocha local government Area of Anambra State. The hard back, with white spotted shells were carefully separated and the seeds weighed, ground to seed meals of 2.15 mesh and the moisture content taken. The extraction of the oil was carried out at 315 ^{0}C using soxhlet extractor and petroleum ether as the solvent.

The physico-chemical analysis were carried out on the oil sample to ensure its suitability in automotive paint making, according to the ASTM (2010), standard. The viscosity testing was carried out on the oil using Ford #4 viscometer cup at 25 ^{0}C and a stop watch to monitor the flow resistance of the oil. The refractive index was recorded using the Abbe refractometer of AR200 model, while specific gravity test was carried out at the pressure of 1 atm and the value calculated using the formular; specific gravity(SG) = volume of oil sample divided by volume of water. The boiling point was carried out using - 4 to 360 ^{0}C capacity thermometer.

2.2: Preparation of Auto-paint; This process was carried out in three stages:-

The milling stage;

This involves dispersion of 23.65 wt % of titanium dioxide in 70ml of white spirit , using 1000ml ceramic mortar and pestle. The process lasted for 45 minutes while testing the fines of the pigments using Hegman's fines-gauge, until 5.67cm^3/10.5µm fines was achieved, according to the American Society of Testing Material (ASTM) standard(D817-96(2010)[102]) for automotive paints.

The stabilization stage; The temperature of the dispersed pigments was lowered to 25^{0}C by addition of 70ml of xylene while stirring to increase the intermolecular distance and prevent aggregation of the particles. 90 ml of Alkyd resin was added to the paint mixture to ensure good quality .

The let down stage; Involves incorporation of other additives like cyclohexanes and nitrocellulose , plasticizers (castor seeds oil), etc, to increase the flexibility, brushability, plasticity to prevent curing of the paint solution. The temperature of the finished paints were allowed to drop from 78^{0}C to 26^{0}C before storing in an air tight container.

2.3: Quality control tests:

The quality control tests were carried on the paint samples and compared to the commercial Berger auto-paint sample in relation to opacity, drying time, washability, specific gravity, etc. The specific gravity test was carried out on the research sample according to ASTM standard (2007). Opacity testing was performed by spreading the paint on an opacity white paper with black lines across them, and the hiding ability of the research paint was observed visually. The viscosity testing was done using a Ford #4 viscometer cup at 26 ^{0}C and a stop-watch to record the time for the last drop of the paint samples. The paint sample was thinned down for easy brushing before spraying on the metallic panels using a spray gun, while the storage temperature was also determined by the drying time monitoring[20] .

III. RESULTS AND DISCUSSION

The physico-chemical analysis carried out on the castor seed oil to assess its suitability in automotive paint making is shown on table 1. The values of the refractive index of castor seed oil (1.471) and viscosity (0.425 at 25 ^{0}C), are high as compared to the commercial linseed oil or cedar wood oil which are the industrial standard for auto-paint making according Daniel, (2007). The high viscosity is an advantage to control the melt flow of auto-paints. The higher specific gravity of (2.00 g/cm^3), of the oil sample is attributed to the solvent contamination during the extraction process. The high percentage of castor seed oil, titanium dioxide, alkyd resin, with 20.15, 23.15, 11.42 wt. % respectively, as shown on table 2, was chosen in order to

formulate a characteristic white glossy and plasticized auto-paint. The drying time of the oil was monitored under the atmospheric condition and the period of film formation was recorded at 30minutes, which was quite good for surface coatings, according to Berger paint standard (1998). The opacity result of the castor seed oil plasticized auto-paint as shown on table 3, indicated that the hiding ability is quite better than the unplasticized sample paint compared to the commercial paint. This could be attributed to the cross-linking effect of the castor oil as plasticizer, when exposed to the atmospheric oxygen, Wollensak, et al, [2003].

The viscosity values for plasticized paint sample is lower as shown on table 3, because addition of the castor oil reduces the cohesion of the intermolecular forces along the chains and increases free flow, flexibility, elongation and workability of the paint components. Ibemesi and Attah (1990), had suggested that drying time of plasticized paints are generally reduced, due to the presence of the ricinoleic acid. The stages of dryness, from dust free time to touch dry, through tack dry and hard dry time, as shown on table 3, exhibited satisfactory quality for the research plasticized automotive paint as compared to the unplasticized commercial paint. The castor seed oil plasticized automotive paint exhibited higher gloss, flexibility, increased adhesion, durability, smooth, ruby and provided additional protections to the substrate against corrosion and other weather conditions, as was observed on the coated steel panel, in accordance to the contributions of Needs, et al [1995].

IV. CONCLUSION

Castor seed oil has been proved to be an alternative to the widely used, expensive, imported linseed oil, in paint making. Farmers are also encouraged to embark on the production of castor seed plant, considering its inexhaustible roles in oil paint making, medicine, cosmetics and other industrial applications. The review on the use of castor oil as plasticizers, in automotive paints are now strongly recommended, in order to minimize solvent emission, to check-mate release of green house gases during paint drying which are hazardous to life. Automobile Engineers are also advised to incorporate castor seed oil as plasticizers in the surface coatings to protect their devices/ automobiles against corrosion, cracks, and to improve their attractive appearances.

Table 1: The physico-chemical analysis of the castor seed oil compared to other drying oils:

Tests	Castor Seed Oil	Linseed Oil	Cedar Wood Oil
Appearance	**Colourless to Pale Yellow**	**Golden Brown to Yellow**	**Pale Yellow to Dark Yellow**
Refractive Index	**1.471**	**1.4835**	**1.516**
Specific gravity (g/cm 3)	**2.00**	**0.945**	**0.9250**
Viscosity at 26 0 C	**0.425**	**0.8**	**2000 mPa**
pH	**4.92**	**-**	**-**
Boiling point (0 C)	**330**	**253**	**-**

The comparative values of the castor seed oil sample to the commonly used commercial drying oils .

Table 2: The formulation for the castor seed oil plasticized top coats (finishes)

Raw Materials	Percentage Weight(wt. %)	Volume (ml)
Castor oil	**20.15**	**168.00**
Titanium dioxide	**23.65**	**200.00**
Xylene	**16.52**	**70.00**
White spirit	**7.42**	**70.00**
Cyclo hexane	**6.79**	**45.00**
Trimethyl benzene	**6.40**	**45.00**
Alkyd resin	**11.42**	**90.00**
Methylethylketone	**5.65**	**192.00**
Nitrocellulose	**2.00**	**110.00**
Total	**100.00**	**1000.00**

Table 3: Results of some quality control testes carried out on the paint samples

	Research Paint Sample		Commercial Paint
Tests	**Plasiticized**	**Unplasiticized**	**Unplasticized**
Opacity	**Excellent**	**Fair**	**Good**
Viscosity at 26 ^{0}C	**92.50**	**96.10**	**97.25**
Specific gravity (g/ cm^3)	**1.14**	**1.75**	**1.16**
Dryingtime(minutes);			
dust free time	**2**	**5**	**4**
touch dry time	**3**	**6**	**5**
tack dry time	**4**	**10**	**6**
Hard dry time	**6**	**20**	**10**

Value of some quality testes on the research paint samples

REFERENCES

[1] R.M.R. Philips, (1999), Animal and Biennial Plants, Macmilliam pub., London, 106.

[2] E.P.Sabina, M.K. Rasod, L. Matthew, (2009), Studies on the protective effect of Ricinus Communis Leaves Extract on Carbontetrachloride heptatotoxicity in Albino Rats, *Pharmacology* 2, 905-916.

[3] P. Kalaiselvi, B. Amuradha, C.S. Parameswari, (2003), Protective Effect of Ricinus Communis Leaf Extract against Paracetamol-induced Oxidation of Unsaturated Lipids, Hepato-toxicity, *journal of, (1-2), 97-105.*

[4] M. Ghisari, *Biomedicine*, E.C. Bonafield-Jorgensen,(2009), Effect of Plasticizers and their mixtures on estrogens receptor and thyroid hormonal functions , *Journal of Toxicology, 189(1), 67-77.*

[5] N.J. Frank, (2005), Alkyd Resins, *Ullmann's Encyclopedia of Industrial Chemistry, Willey-VcH, Weinheim, 409.*

[6] P. Slephannie,P.(2011),Oldest Human Paint-making Studio Discovered in Caves, Live Science, 14.

[7] F.C. David and J.H. Christopher (2000), Plasticizers, *Ullmann's E ncyclopedia of Industrial Chemistry, Willey-VcH, Weinheim, 439.*

[8] A.P. Needs, S.E. Caldwell, K.A. Mill, (1995), Mechanism of Free Radical *Lipids*, 30, 277-296.

[9] Sunyer, (2001), "Urban Air Pollution and Chronic Obstructive Pulmonary disease: a review" *European Respiratory journal*, 17(5), 1024-1033.

[10] M. Daniel, (2007), Standard Specification of Linseed Oil for Paints, *Industrial Research and Standard Revision Acts, section 20(25), S.I.159/1949.*

[11] G. Wollensak, E. Spoerl, T.Seiler, (2003), Riboflavin/ultraviolet induced collagen cross linking for the treatment of kertoconus, *American journal of Ophtalmol*, 135 (5), 620- 627.

[12] D.A. Morgan, (1971), Effect of Plasticizers on the Strength of a Plastic Motor Case, *Army Missile Research and Development*, 1, 23.

[13] D.S.Oguniyi,(2006),Castor Oil; A Vital Industrial Raw Material, *Bioresource Technology*, 97(9), 1086-1091.

[14] R.Victor, R.S. Jayalakshamma,(2005),Cost Effective, Qualitative Immersion Oil for Microscopy, *Anatomical Society of India*, 54(2),7-12.

[15] J.A. Ibemesi and J.C. Attah (1990); Solvent Extraction of Oils of Rubber, Melon, Pumpkin and Oil Bean Seeds, *American Oil Chemist's Society, 67(1), 25-27.*

[16] American Society for Testing Materials (ASTM) International, (2010), Chemical Analysis of Paints and Paint Materials, D817-96, [102]. 16.

American Journal of Engineering Research (AJER)
e-ISSN : 2320-0847 p-ISSN : 2320-0936
Volume-02, Issue-11, pp-276-286
www.ajer.org

Research Paper Open Access

Generation Expansion Planning Considering Renewable Energies

Ahmad Rouhani, Gohar Varamini, and Mehdi Nikkhah
(Department of Electrical Engineering, Beyza Branch, Islamic Azad University, Beyza, Iran)

Abstract: - According to need of high investment to construct power plants, the country's generation expansion planning has the particular importance. However, the economic evaluation of distributed generation on power system is an essential step in related studies of this production, in generation expansion planning. In this paper, economic competitiveness of distributed generation and centralized power plants, in the Iranian Power Grid has been analyzed. In order to evaluate the economic justifiably of using these productions, Effective factors in economic justifiably of distributed generation in the development of the power generation system, has been studied using WASP software. Finally, the amount use of the distributed generation capacity and their corresponding costs, Along with the national grid, are compared with each other.

Keywords: - *Distributed Generation, Generation Expansion Planning, Renewable Energy, WASP.*

I. INTRODUCTION

Energy consumption is rapidly increase in development countries, which effects global climate change and global and regional energy management. Among the various kinds of energy carriers, electricity has a special role in helping to attain social and economic development. The problem of power system planning may be classified as generation expansion planning (GEP), transmission expansion planning (TEP), and distribution expansion planning (DEP) [1]. This decomposition is normally performed to make the very highly complex combined problem possible [2].

Generation Expansion Planning (GEP) is considered one of major parts of power system planning issues. The aim of GEP is to seek the most economical generation expansion scheme achieving an acceptable reliability level according to the forecast of demand increase in a certain period of time [3].

The feasibility of the generation structure, the cost of primary energy resources and fuel for the scheme, and the reliability indices of electricity supply, make generation planning a very complicated optimization mathematically [4]. Some of these restrictions have been applied in GEP in the recent literature [5]-[7].

WASP-IV is powerful software developed by International Atomic Energy Agency (IAEA) in which a dynamic programming approach is employed to find an overall optimal required generation capacity for the network so that an index, such as LOLP, is minimized [8].

In using WASP-IV, it is assumed that the fuel cost throughout the geographical distribution of the network is uniform. This assumption is invalid in real life, as allocation of a power plant far from a fuel resource supply center results in high fuel transmission costs. Moreover, in using WASP-IV, a single-node load center is assumed which is not obviously a valid assumption [8]. In other words, while WASP-IV is capable of predicting the overall generation capacity requirements for the grid, it is unable to geographically distribute and allocate the capacities among the areas [1].

Distributed Generation (DG) is an emerging approach to provide electric energy close to load center. Changing economic and regulatory environment and also technological innovations has resulted in a renewed interest for distributed generation in the last decade [9].

DG is a feasible alternative for developing new capacity, especially in competitive electricity networks, from an economic, technical and environmental point of view [10]-[12]. Power system deregulation and the shortage of transmission capacities have led to increase interest in DG sources [13]-[18].

Nowadays, DG is a broadly-used term that covers various technologies; however, it is difficult to find a

unique DG technology that takes into account multiple considerations, such as economic, technical, and environmental attributes [10].

Also, it is known that renewable energy such as wind, hydro, solar, and geothermal are relatively expensive and limited in availability. Anyway, to mitigate the environmental impacts to the planet and the risk of depending only on few sources of energy, there is an increasing interest in renewable energy sources [16]. A multistage model for distribution expansion planning with DG is proposed in [19],[20].

This paper is organized as follows: In Section II, the generation expansion planning is described. Section III shows how the optimization problem is formulated, with details of the objective function and constraints imposed. The detail of Iranian Power Grid is presented in Section IV. This paper ends with a presentation of conclusions.

II. GENERATION EXPANSION PLANNING

Generation expansion planning (GEP) problem plays an important role in planning activities and determines which generating units to be commissioned and when to commit online over the long-term planning horizon [1],[2].

The objective of GEP is to minimize the total investment and operating costs associated with the addition of new units and to satisfy the reliability, fuel mix, and the demand criterion. GEP is a highly constrained, nonlinear, discrete optimization problem. The emerging techniques applied to solve GEP are reviewed in [4]. The different metaheuristic techniques have been applied to solve the single-objective GEP problem [6],[7].

The problem to be solved is a generation expansion planning considering the effect of renewable energies. The aim is analysis the economic competitiveness of distributed generation and centralized power plants, in the Iranian Power Grid.

GEP problem is defined as the problem of determining what capacity, which, and when new generating units should be constructed over a long range planning horizon. To achieve this aim, the WASP software using single nodal generation planning model is employed to satisfy the expected energy demand (Fig. 1.).
The problem is supposed to be solved for several years within a specified planning horizon. In doing so, the following points are worth mentioning:

- The planning problem to be solved is of a dynamic type. In other words, the planning horizon is divided into several stages and subperiods of known duration, so the elements to be installed in each stage should be determined. In addition, it is assumed that the predicted load is known for each stage.
- Load Duration Curves (LDCs) represent the operating conditions of power systems over the time; they are obtained from hourly data of demand over a period of time. It can be used in generation expansion planning when all the load and all the generating units are assumed to be connected at the same node (single nodal point generation planning). LDC consists of several levels, as shown in Fig. 2. It is a linear approximation to practical load during curve.
- Spare or redundant capacities in generation and network facilities have been inbuilt in order to ensure adequate and acceptable continuity of supply in the event of failures and Forced Outage Rate (FOR) of plant, and the removal of facilities for regular scheduled maintenance. Therefore, the total outage in the failure events may be due to a forced outrage or a maintenance outage [21]. Those are not neglected in the proposed approach.
- The reliability of generation system configuration is evaluated by WASP in terms of the Loss of Load Probability index (LOLP). This index is calculated in WASP for each period of the year.

As mentioned before, The WASP model has been enhanced to facilitate the work by electricity planners and is currently accepted as a powerful tool for electric system expansion planning [8]. The response space and constraints for solving GEP problem using WASP-IV is shown in Fig. 3. In this figure, PG_{con} represents the installed generation capacity curve of under construction and downtime generating unit in the network in planning horizon. Increasing the curve in some periods, expresses the increase of the capacity of the network due to installed generating units under construction. On the other hand, reducing the curve meant the outage of generating units due to end of their useful life. According to the mentioned issues, the production should be within the range of S (the feasible solution domain). Therefore, with the loss of the network adequacy since t_0, by doing an optimal GEP, PG_{sch} curve is obtained. It represents the installed generation capacity of new scheduled generating units to restore the generation network adequacy.

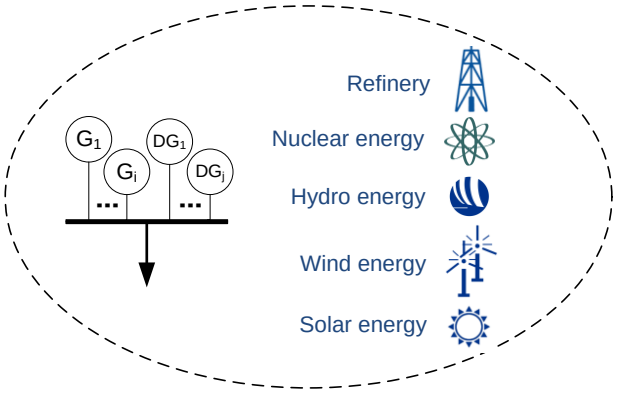

Fig. 1. A single-node sample network.

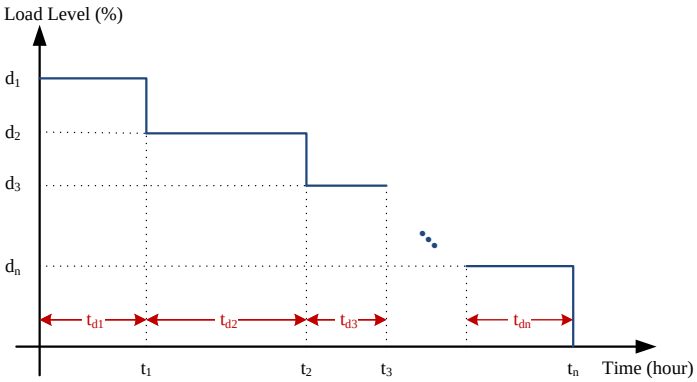

Fig. 2. Linearly approximated load duration curve.

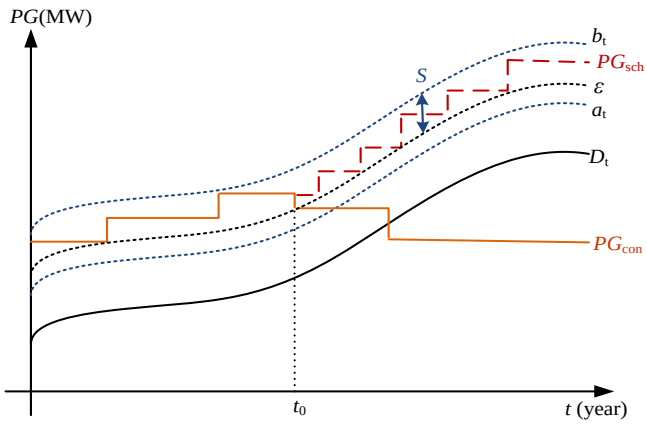

Fig. 3. The feasible solution domain and constraints for solving GEP problem.

III. PROBLEM FORMULATION

The problem as defined in Section II is, in fact, an optimization one to be solved by a proposed solution algorithm. The formulation of the composite expansion planning of generation and transmission line is presented in this section. The objective function terms as well as the various constraints will be discussed in the following subsections.

A. Objective Function

For the long range of planning, the present value of the total cost of engineering project is usually taken as an objective function. Therefore, the objective function to be minimized is the present value of investment and operational costs. This objective function is defined as the total present value sum of the investment cost for new units and the generation costs.

$$z = \sum_{t=1}^{T} \sum_{si} \sum_{b} (I_{tsib} + F_{tsib} + M_{tsib} + O_{tsib} - S_{tsib}) \quad (1)$$

Where I_{tsib}, F_{tsib}, M_{tsib}, O_{tsib}, and S_{tsib} are respectively present value for investment cost in year t in bus b of generating unit si, fuel cost of generating unit si, maintenance cost of generating unit si, operating cost of generating unit si, and salvage value for investment cost of generating. T is number of years in a planning horizon.

B. Constraints

The constraints to be observed during the optimization process are as follows:

Generation capacity: the capacity sum of newly installed and existing generating units are more than or equal to the load demand plus reserve in each year within planning period.

$$(1+a_t)D_{ct} \le PG_{ct} \le (1+b_t)D_{ct} \quad (2)$$

Where a_t and b_t are respectively Lower bound and Upper bound of reserve margin in year t; D_{ct} is forecast peak demand in the critical period of year t; and PG_{ct} is Installed generation capacity in the critical period of year t.

Reliability: the reliability index LOLP is used to evaluate adequacy of generating units.

$$LOLP_{ct} \le \varepsilon \quad (3)$$

Where $LOLP_{ct}$ is LOLP index of critical period in year t and ε is standard level of LOLP index.

The presence of hydro power plants: this constraint expresses the maximum energy obtained from a hydro power plant in the different periods of the planning horizon at different climatic conditions.

$$PG_{hc} \times t_d \le W_{hcdt}^{\max} \quad (4)$$

Where PG_{hc} is installed generation capacity of hydroelectric plant h in hydrological condition c, t_d is duration of subperiod d, and $W_{hcdt}^{\max}$ is maximum energy enhanced from hydroelectric plant h in hydrological condition c in subperiod d in year t.

Fuel constraint: maximum fuel supply of different fuel types of thermal plants.

$$\sum_{i} F_{ifd} \le F_{fd}^{\max} \quad (5)$$

Where F_{ifd} is fuel consumption type f of thermal unit i in subperiod d and $F_{fd}^{\max}$ is maximum fuel type f available in subperiod d.

Emission constraint: maximum production rate of pollution.

$$\sum_{i} E_{iedt} \le E_{edt}^{\max} \quad (6)$$

Where E_{iedt} and $E_{edt}^{\max}$ are total emission type e of generating unit i and Maximum emission type e in subperiod d in year t, respectively.

Repairing time of different types of generating units:

$$Repairing\ time\ for\ each\ unit \ge Required\ maintenance\ time \quad (7)$$

Maximum number of generating units in each period throughout the planning horizon.

$$NG_{it} \le NG_{it}^{\max} \quad (8)$$

Where NG_{it} is number of new generating unit i constructed in year t and $NG_{it}^{\max}$ is maximum number of allowed generating unit i constructed in year t.

IV. IRANIAN POWER GRID

To validate the mathematical model given in section III, the Iranian power grid as a large scale system is considered. Iran is a vast country that has extensive resources of fossil fuels. Major fuel resources are located in the southern part of the country. In the previous years, these resources have been transferred by the oil and gas pipelines to most parts of the country [1].

As Fig. 4 shows, the power plants under construction, cannot supply the system demand until the end of the study period (2025). Due to the complexity of the production facilities technology and electric power transmission, construction of new electrical facilities is very time consuming. Therefore, it is essential that other plants should be added to the production system in addition to the mentioned plants.

Candidate plants specifications considered in this paper, in accordance with the Table I, are introduced into the software. The candidate plants includes the 325 MW steam units (S325), 130 MW big gas units (G130), 400 MW combined cycle units (CC40) and distributed generations (DG30). The WASP software will specify the optimal development of production systems with selecting adequate capacity and types of the candidates, in terms of presence or absence of distributed generations according to system requirements.

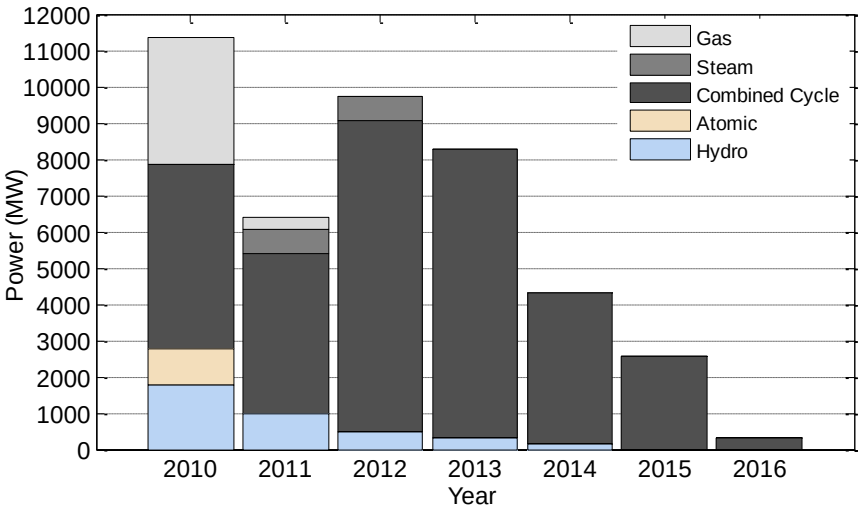

Fig. 4. Approved projects of generation capacity of under construction units by 2016.

TABLE I TECHNICAL AND ECONOMIC ATTRIBUTES OF CANDIDATE GENERATING UNITS

Attributes	Type of Generating Units			
	S325	G130	CC40	DG30
Generation range (MW)	325	130	400	30
Installation lead time (Yr)	5	2	5	1
Life time (yr)	30	15	30	23
F.O.R. (%)	12.9	10.2	13.67	4.95
Maintenance (hr/yr)	56	40	43	7
Capacity factor (%)	92	62	76	69
Efficiency (%)	38.5	33.4	50	51
Investment cost ($/kW)	800	500	850	713
Fix operation and Maintenance cost ($/kw-month)	0.28	0.11	0.11	0.01
Variable operation and Maintenance cost ($/kw-month)	0.36	1.23	0.90	0.018
Allowed installed generating units in RECs	5	10	3	20

Due to global fuel crisis and environmental issues such as restrictions on greenhouse gas emissions, among the technologies used in distributed generation, the renewable energies are especially important. Although renewable energy sources such as wind, photovoltaic, fuel cell and ... Are relatively expensive, but into the reasons mentioned, the increasing desire to develop these resources exist. Although renewable energy sources such as wind, photovoltaic, fuel cell and ... are relatively expensive, but according to the mentioned reasons, the increasing desire exist to develop these resources.

It is known that renewable energies such as wind, solar, and geothermal are relatively expensive and limited in availability. However, to mitigate the environmental impacts to the planet and the risk of depending only on few sources of energy, there is an increasing investment in renewable energy sources. Based on calculations, Iran enjoys only a moderate supply of wind power, though some regions have continuous airflows with sufficient energy to produce electricity. The potential capacity of wind power is figured at about 6500 MW for the country, mostly in the eastern sections [10]

The DG technologies that are considered as alternatives in this comparative assessment are: Wind Technology (WT), Photovoltaics (PV), Fuel Cell (FC) and Microturbine (MT).

In this paper, the mean of technical and economic values of these technologies, according to the Table II, are used as the distributed generation to perform generation expansion planning.

TABLE II TECHNICAL AND ECONOMIC ATTRIBUTES OF CANDIDATE DGS

Attributes	DG Technologies			
	WT	MT	CT	DE
Installation lead time (Yr)	12	1	9	7
Life time (yr)	20	20	30	20
F.O.R. (%)	3.2	6.7	4.2	5.7
Maintenance (hr/yr)	40	20	350	250
Capacity factor (%)	30	95	70	80
Efficiency (%)	40	82	42	40
Investment cost ($/kW)	1000	950	550	350
Fix operation and Maintenance cost ($/kw-month)	0.01	0.01	0.01	0.01
Variable operation and Maintenance cost ($/kw-month)	0.01	0.014	0.024	0.025

The planning horizon is 16 years and each year is divided into four subperiods and considers three load levels. The first stage starts at the base year. The annual rate of interest on capital was set at 10%, with present value factors for the costs of investment and operation. General information required to perform this study is presented in Table III.

With rapid annual growth of 5% - 8% electric consumption, the grid is confronted by a challenging planning problem for the years to come. Table IV gives the peak load ratio for each subperiod. Linearly approximated load duration curve is shown in Fig. 5. In this study, LDC is considered as a three-piece linear approximation.

From 56181 MW installed generation capacity in the Iran Power Grid at the end of 2009, thermal (86.2%), hydro (13.7%), and miscellaneous (1%) are distributed geographic-ally among 16 RECs [8]. Due to the complexity of the generation facilities, the construction of new electrical facilities is very time consuming. If the country is faced with the blackouts phenomenon due to lack of generation facilities, solving the problem in the short term, even with extra spending, is simply not possible. Therefore, new generating units must be added to the grid in addition to the existence units.

TABLE III GENERAL INFORMATION

Parameter	Value
Study period	2010-2025
Planning horizon	2025
Number of periods in year	4
Annual rate (%)	10
Annual rate (%)	10
Minimum reserve margin (%)	10
Maximum reserve margin (%)	30
Critical LOLP (%)	0.05

TABLE IV PEAK LOAD RATIO FOR EACH SUBPERIOD

Period	**Peak Load Ratio**
1	0.8996
2	1
3	0.8936
4	0.8348

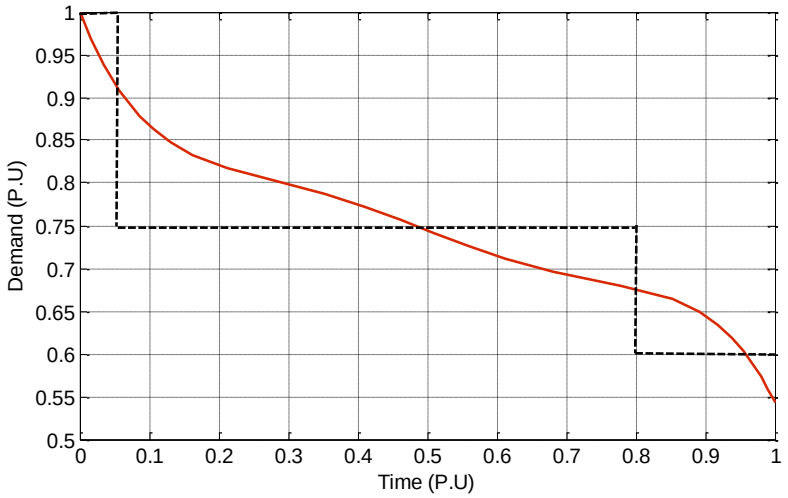

Fig. 5. Linearly approximated load duration curve of the Iranian power grid.

As shown in Fig. 6, total generation capacity of the existence and under construction units, would NOT provide the generation grid constraints until the end of the planning horizon. In this figure, PG_1 represents the installed generation capacity curve of under construction and downtime generating unit in the network in the planning horizon.

V. ANALYSIS OF THE IRANIAN POWER GRID WITH DISTRIBUTED GENERATION

In this section, according to the descriptions and information presented in the previous section, generation expansion planning considering distributed generation have been implemented to Iran Power Grid.
In this section, the results of the WASP software to determine the optimal development scheme of the generation networks with distributed power generation are given in four different scenarios during the period of 2010 to 2025. It is noted that the approved power plans by Ministry of Energy to expand generation capacity by 2016, in accordance with the Fig. 4 is introduced to the software.

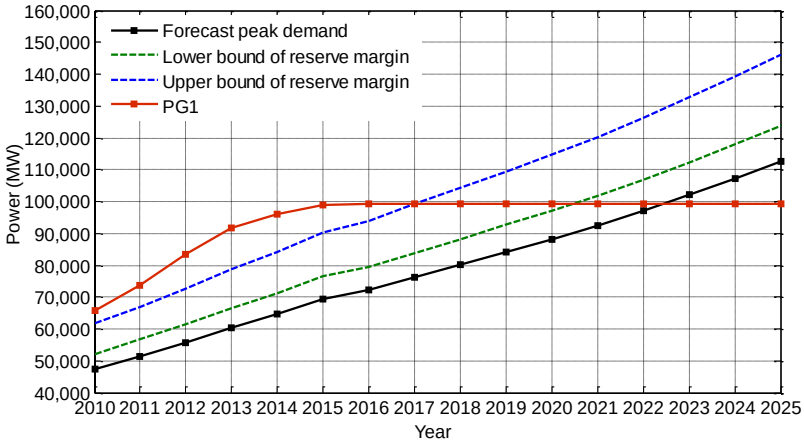

Fig. 6. Iranian Power Grid situation in planning horizon.

Due to the nature of distributed generation, distribution networks are considered as the most appropriate location to connect them to the power system. In addition to distribution feeders, which almost all research done in the field of distributed generation allocation has been assigned to them, the above distribution posts can be suitable for construction distributed generation from the perspective of distribution companies. No need to considerable expansion of the transmission network and reduce the costs related to expansion of these networks, along with reduced losses, are some advantages of the distributed generation.
In this section, with respect to the description of the previous sections, to evaluate the competitiveness of distributed generation on generation expansion planning of power networks, four scenarios have been designed and implemented and their results will be described in the following. For this purpose, at first an option has been selected as the base, then tried to study the justification of the power plant in the different scenarios.

Terms of each scenario are:
Scenario 1) consider the base state of the system
Scenario 2) the effect of non-implementation of the approved construction program
Scenario 3) the impact of increasing transmission costs associated with implementation of centralized power plant
Scenario 4) the combined effects of non-implementation of the approved construction program and increasing trans-mission costs associated with implementation of centralized power plant.
More scenarios features are detailed in Table V.
It can be seen that in the first scenario, 5 steam units, 301 big gas units, and 5 distributed generation units with the total capacity of 40,905 MW are selected and used by 2025 in addition to existing and under construction power plants. The average annual value of LOLP is equal to 0.26, which is equivalent to the blackouts probability of 0.94 day of the year. The cumulative present value of total costs is 38.26 billion dollars that is in fact the lowest cost to develop the system.
Any further capacity intent to improve the reliability or the less capacity to lower investment costs, thereby increasing the total cost of the system. Results of other expansion planning scenarios are presented in the Tables VI and VII.
As is observed, considering the technical advantages, especially the Establishment Location of distributed generations in the fourth scenario, 16 renewable energy units with total capacity of 480 MW by 2025 is scheduled for construction. Figures 7-10 show the new generation capacity planned for each year and Figures 11-14 show the network status of Iran's power grid in every scenario.
By doing the optimal GEP, as shown in Fig. 7, the total installed generation capacities of new scheduled generating units restore the generation network adequacy. It represents with PG_2 in this figure. It is obvious that, with regard to the environmental impacts, feasibility of DGs based on renewable energy technologies, will considerably increase.

TABLE VI GENERATING UNITS AND DGS REQUIRED FOR THE PLANNING HORIZON

	Type of plants	2012	2013	2014	2015	2016	2017	2018	2019	2020	2021	2022	2023	2024	2025
Scenario 1	S325	0	0	0	0	0	0	0	0	0	0	0	4	0	1
	G130	0	0	0	0	0	0	23	36	37	40	41	34	46	44
	CC40	0	0	0	0	0	0	0	0	0	0	0	0	0	0
	DG30	0	0	0	0	0	0	0	0	0	0	0	0	0	5
	LOLP	0.001	0.000	0.002	0.005	0.000	0.203	0.494	0.482	0.495	0.484	0.495	0.500	0.492	0.492
Scenario 2	S325	0	1	0	0	0	0	0	0	0	0	0	1	0	0
	G130	0	6	24	35	25	37	36	36	37	39	41	41	45	46
	CC40	0	0	0	0	0	0	0	0	0	0	0	0	0	0
	DG30	0	0	0	0	0	0	2	0	1	1	2	1	2	7
	LOLP	0.361	0.480	0.498	0.488	0.500	0.492	0.499	0.488	0.495	0.499	0.497	0.495	0.498	0.497
Scenario 3	S325	0	0	0	0	0	0	0	0	0	0	2	1	1	7
	G130	0	0	0	0	0	0	23	36	37	39	37	39	43	31
	CC40	0	0	0	0	0	0	0	0	0	0	0	0	0	0
	DG30	0	0	0	0	0	0	0	0	0	2	0	7	1	3
	LOLP	0.001	0.000	0.002	0.005	0.000	0.203	0.494	0.482	0.495	0.494	0.490	0.0497	0.497	0.496
Scenario 4	S325	0	0	0	0	0	0	0	0	0	0	0	0	2	0
	G130	0	7	25	34	25	37	36	35	37	39	41	43	38	48
	CC40	0	0	0	0	0	0	0	0	0	0	0	0	1	0
	DG30	0	3	0	1	1	0	2	2	2	2	1	2	0	0
	LOLP	0.361	0.494	0.481	0.493	0.496	0.491	0.498	0.497	0.497	0.494	0.499	0.496	0.500	0.499

The Improvement of the proposed approach to determine more details of every region (i.e., R11) is best illustrated by a simple sample as shown in Fig. 8. This figure indicates how to apply the proposed method in the large scale networks.

TABLE V CHARACTERISTICS OF SCENARIOS

Parameters	Scenario 1	Scenario 2	Scenario 3	Scenario 4
Full implementation of construction of thermal units	100 %	50 %	100 %	50 %
Considering the cost of the transmission network	---	---	50 % of Centralized unit	50 % of Centralized unit

TABLE VII RESULTS OF THE PROPOSED METHOD FOR EVERY SCENARIOS

Parameters	Scenario 1	Scenario 2	Scenario 3	Scenario 4
Total cumulative costs ($\$\times 10^6$)	38.26	60.18	44.34	74.96
annual average of LOLP (%)	0.260	0.464	0.260	0.465
Outage period (days per year)	0.94	1.67	0.94	1.67

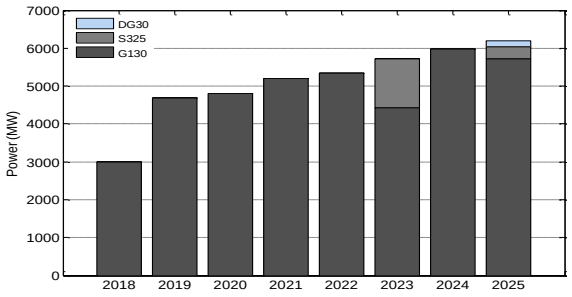

Fig. 7. Capacity of the scheduled power plants in Scenario 1.

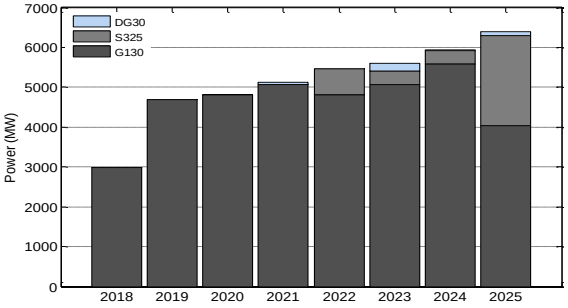

Fig. 9. Capacity of the scheduled power plants in Scenario 3.

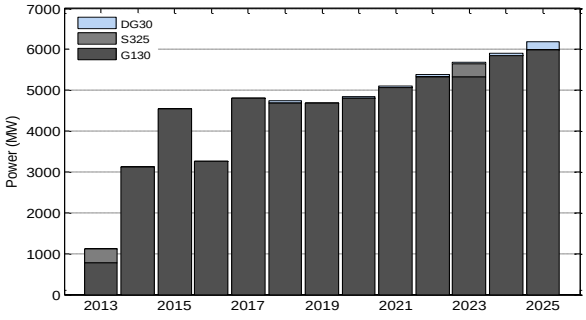

Fig. 8. Capacity of the scheduled power plants in Scenario 2.

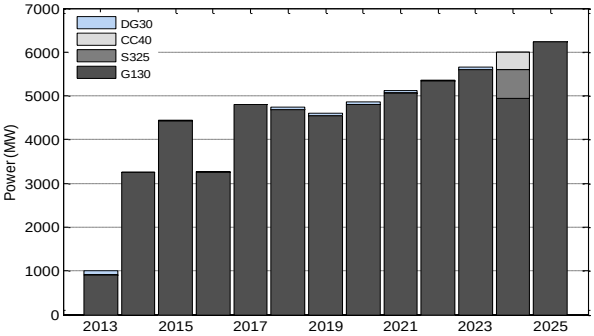

Fig. 10. Capacity of the scheduled power plants in Scenario 4.

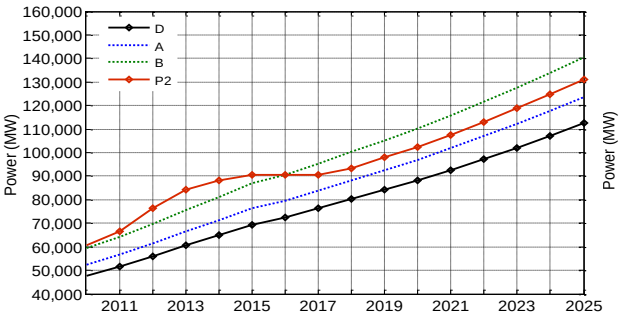

Fig. 11. Expanded Iranian Power Grid situation in planning horizon in Scenario 1.

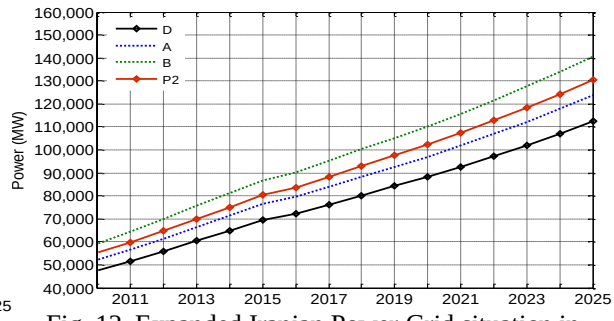

Fig. 12. Expanded Iranian Power Grid situation in planning horizon in Scenario 2.

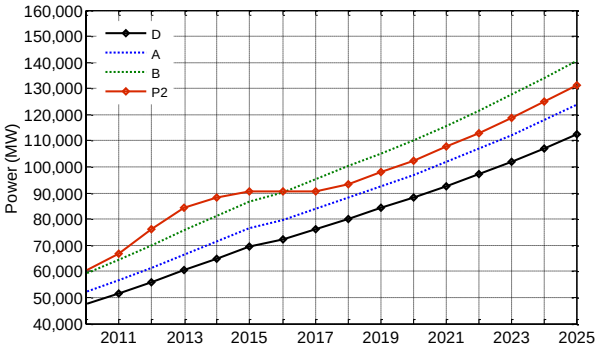

Fig. 13. Expanded Iranian Power Grid situation in planning horizon in Scenario 3.

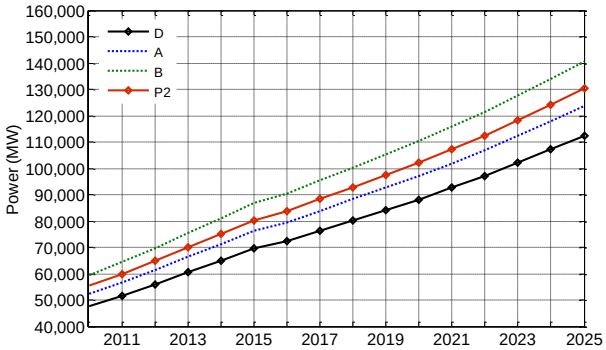

Fig. 14. Expanded Iranian Power Grid situation in planning horizon in Scenario 4.

VI. CONCLUSION

In this paper, the economic competitiveness of distributed generation with centralized thermal power plants was studied in long-term expansion planning. Although the large scale of this issue prevents the use of classical and modern mathematical methods to solve the planning, But in this paper, a part of the facts contained competition distributed generation with centralized power plants included. Due to the importance renewable energies, used these types of technology as distributed generation for long-term generation expansion planning. Considering the technical features of distributed generation in generation expansion planning, especially their construction Location, lead to not additional costs of the transmission network. So, a significant increase of competitiveness between distributed generations with centralized power plants will occur in the country. Therefore if construction of distributed generation done based on technical and economic studies, it would have a significant economic benefit.

VII. ACKNOWLEDGEMENTS

Authors gratefully acknowledge the financial support of Islamic Azad University, Beyza Branch.

REFERENCES

[1] X.Wang and J. R. McDonald, *Modern Power System Planning*. New York: McGraw-Hill, 1994.

[2] M. S. Sepasian, H. Seifi, A. Akbari Foroud, and A. R. Hatami "A multiyear security constrained hybrid generation-transmission expansion planning algorithm including fuel supply costs", *IEEE Trans. Power Syst.*, vol. 24, no. 3, pp. 1609-1618, Aug. 2009.

[3] Li Wenyuan and R. Billinton, "A minimum cost assessment method for composite generation and transmission system expansion planning", *IEEE Trans. Power Syst.*, vol. 8, no. 2, pp. 628-635, May 1993.

[4] J. Wang, M. Shahidehpour, Z. Li, and A. Butterud, "Strategic generation capacity expansion planning with incomplete information", *IEEE Trans. Power Syst.*, vol. 24, no. 2, pp. 1002-1010, May 2009.

[5] J. L. C. Meza, M. B. Yildirim, and A. S. M. Masud, "A model for the multiperiod multiobjective power generation expansion planning", *IEEE Trans. Power Syst.*, vol. 22, no. 2, pp. 871-878, May 2007.

[6] S. Kannan, S. M. Raja Slochanal, and N. P. Padhy, "Application and comparison of metaheuristic techniques to generation expansion planni-ng problem", *IEEE Trans. Power Syst.*, vol. 20, pp. 466-475, Feb. 2005.

[7] J. B. Park, Y. M. Park, J. R. Won, and K. Y. Lee, "An improved genetic algorithm for generation expansion planning", *IEEE Trans. Power Syst.*, vol. 15, no. 3, pp. 916-922, Aug. 2000.

[8] International Atomic Energy Agency (IAEA), Wien Automatic System Planning (WASP) Package, A Computer Code for Power Generation System Expansion Planning, Version WASP-IV User's Manual. Vienna, Austria, IAEA, 2001.

[9] P. Chiradeja and R. Ramakumar, "An approach to quantify the technical benefits of DG", *IEEE Trans. on Energy Convers.*, vol. 19, no. 4, pp. 764-773, Dec. 2004.

[10] A. Zangeneh, S. Jadid, A. Rahimi-Kian, "A hierarchical decision making model for the prioritization of distributed generation technologies-A case study for Iran", *Energy Policy*, vol. 37, no. 12, pp. 5752–5763, Dec. 2009.

[11] S.A.M. Javadian, M.-R. Haghifam, M. Fotuhi Firoozabad, and S.M.T. Bathaee, "Analysis of protection system's risk in distribution networks with DG", *Electrical Power and Energy Systems*, vol. 44, pp. 688–695, 2013.

[12] S.A.M. Javadian, M.-R. Haghifam, S.M.T. Bathaee, and M. Fotuhi Firoozabad, "Adaptive centralized protection scheme for distribution systems with DG using risk analysis for protective devices placement", *Electrical Power and Energy Systems*, vol. 44, pp. 337–345, 2013.
[13] G. W. Ault and J. R. Mc Donald, "Planning for distributed generation within distribution networks in restructured electricity markets", *IEEE Power Eng. Rev.*, vol. 20, pp. 52-54, Feb. 2000.
[14] C. Wang and M. H. Nehrir, "Analytical approaches for optimal placement of distributed generation sources in power systems", *IEEE Trans. Power Syst.*, vol. 19, no. 4, pp. 2068-2076, Nov. 2004.
[15] Z. Moravej and A. Akhlaghi, "A novel approach based on cuckoo search for DG allocation in distribution network", *Electrical Power and Energy Systems*, vol. 44, pp. 672–679, 2013.
[16] A. P. Agalgaonkar, S. V. Kulkarni, and S. A. Khaparde, "Evaluation of configuration plans for DGs in developing countries using advanced planning techniques", *IEEE Trans. Power Syst.*, vol. 21, no. 2, pp. 973-983, May 2006.
[17] R. Ebrahimi, M. Ehsan, and H. Nouri, "A profit-centric strategy for distributed generation planning considering time varying voltage dependent load demand", *Electrical Power and Energy Systems*, vol. 44, pp. 168–178, 2013.
[18] M. Gitizadeh, A. Azizi Vahed, and J. Aghaei, "Multistage distribution system expansion planning considering distributed generation using hybrid evolutionary algorithms", *Applied Energy*, vol. 101, pp. 655–666, 2013.
[19] S. Haffner, L. F. Alves Pereira, L. A. Pereira, and L. S. Barreto, "Multistage model for distribution expansion planning with distributed generation-Part I: Problem formulation", *IEEE Trans. Power Del.*, vol. 23, no. 2, pp. 915-923, Apr. 2008.
[20] S. Haffner, L. F. Alves Pereira, L. A. Pereira, and L. S. Barreto, "Multistage model for distribution expansion planning with distributed generation-Part II: Numerical results", *IEEE Trans. Power Del.*, vol. 23, no. 2, pp. 915-923, Apr. 2008.
[21] R. Billinton and R. N. Allan, *Reliability Evaluation of Power Systems*. 2nd ed., New York: Plenum Press, 1996.

American Journal of Engineering Research (AJER)
e-ISSN : 2320-0847 p-ISSN : 2320-0936
Volume-02, Issue-11, pp-287-292
www.ajer.org

Research Paper Open Access

Model Prediction of The Optimum Production Rate Of An Industrial Lng Plant Using Linear Regression Analysis

Kenneth K. Dagde, Onochie, C. Okonkwo
[1]*Department of Chemical/ Petrochemical Engineering, Rivers State University of Science and Technology, Port Harcourt, Nigeria*
[2]*Department of Chemical/ Petrochemical Engineering, Rivers State University of Science and Technology, Port Harcourt, Nigeria*

Abstract: - This paper demonstrates the applicability of a linear regression model to accurately determine the expected LNG production rate for a functional industrial LNG plant which uses the C3-MR liquefaction process. A total of 501 data points obtained at times of maximum plant LNG production rates were used for the regression analysis. The model showed a maximum deviation of 1.5375% and an average deviation of 0.4197% from the actual LNG production rate of the plant. The coefficient of determination of the model is 0.6033 with a standard error of 49.8T/D LNG. The model also indicated the strong dependence of LNG production rate on the MR gas turbine inlet air temperature (ambient air temperature) and cooling water supply temperature. The linear regression model obtained is peculiar to the plant considered in this study.

Keywords: - Linear regression, Liquefied Natural Gas, Coefficient of Determination, Standard Error

I. INTRODUCTION

The drive to monetize large stranded gas resources coupled with prudent utilization of gas resource and environmental considerations has led to the developments in Liquefied Natural Gas (LNG) due to the fact that the LNG occupies about 1/600th the volume of natural gas [1]. The historical developments of LNG technologies has been discussed by [2] and the different available LNG technologies by [3].

LNG plants are huge energy intensive process plants for the liquefaction of natural gas. The LNG plant considered in this study is a major LNG facility in Nigeria whose liquefaction process is based on the C3-MR liquefaction process and is shown in Figure1, Figure 2 and Figure 3 [4]. Figure 1 depicts the general overview of the C3-MR liquefaction process used in the plant while Figure 2 and Figure 3 describe the propane cycle and the mixed refrigerant cycle respectively.

Accurate prediction of the expected optimum LNG production rates of LNG plants is critical as it enables plant operators to maximize LNG production and efficiency by comparing actual LNG production rates with the expected value and making necessary adjustments if required to certain other parameters to bring actual production rates close to or above the expected value.

Regression analysis is a statistical technique for estimating the relationship between a dependent variable and one or more independent variables. This relationship is the regression model. In this paper, linear regression is employed to obtain the regression model that is fitted using the least square method to the plant LNG production rate. This model yields the expected LNG production rate of the LNG plant based on the cooling water supply temperature and the MR gas turbine inlet air temperature (Ambient air temperature).

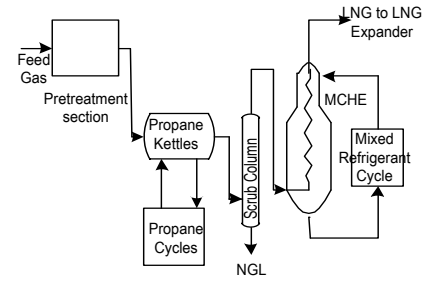

Figure 1 Schematic representation of LNG plant C3-MR liquefaction process

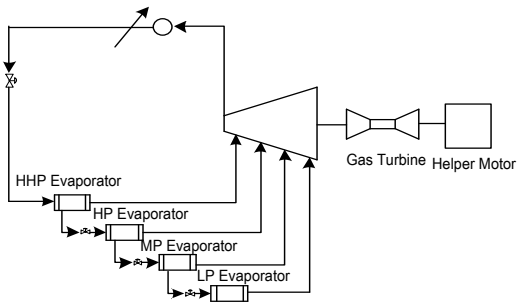

Figure 2 Schematic representation of propane cycle

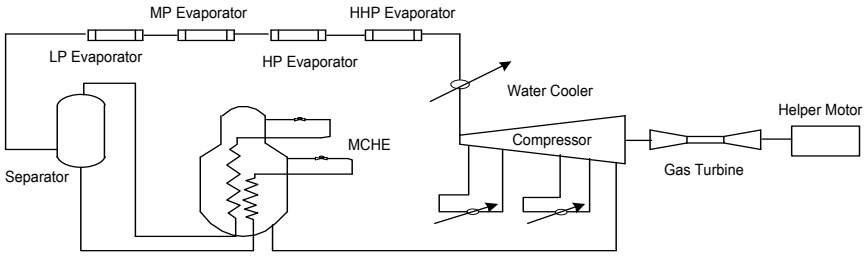

Figure 3 Schematic diagram of mixed refrigerant cycle

Dagde and Okonkwo, [4] developed, validated and simulated a thermodynamic model predicting the LNG production rate of a functional industrial LNG plant using exergy analysis. The model developed showed a maximum deviation of 3.06%. The thermodynamic efficiency of the plant was also calculated to be 45.1%. Previous literatures related to this research have been based on rigorous thermodynamic analysis, process simulation, design and optimization using thermodynamic models constructed in process simulation software. And these studies were limited to the calculation of thermodynamic efficiency, investigation of various approaches to improve thermodynamic efficiency and optimization to minimise energy consumption in various liquefaction processes ([5], [6], [7], [8], [9], [10], and [11]). Sutton [12] had used regression analysis on raw data to obtain second order fits for the pseudo critical properties of natural gas based on 264 different gas samples.

While Dagde and Okonkwo [4] focused on developing a predictive model based on thermodynamic analysis of an LNG plant, this paper demonstrates the applicability of a linear regression model to accurately predict the optimum expected production rate of a functional industrial LNG plant. The knowledge of the optimum expected LNG production rate from an LNG plant will assist plant operators in maximizing their LNG output since the actual plant LNG production rate can be compared to the expected value. Regression analysis of a particular plant data gives results that are peculiar to the plant due to different operational and environmental conditions. Therefore to obtain the regression model for the optimum LNG output of another LNG plant there is need for a regression analysis of the plant data during periods of optimum operations.

II. MATERIALS AND METHODS

The linear regression model describing the LNG production rate ($\dot{m}_{LNG}$) is of the form;

$$\dot{m}_{LNG} = A + BT_{a,MR} + CT_{cws} \qquad 1$$

where, *A*, *B* and *C* are constant coefficients, $T_{a,MR}$ is the MR turbine inlet air temperature (^{o}C), T_{cws} is the cooling water supply temperature. A, B and C are to be obtained by linear regression analysis.

A total of 501 data were obtained during the periods of maximum LNG plant production rates for the regression analysis. These periods represents the periods when the plant is operating most efficiently without any anomalous constraints. Although the data obtained includes LNG composition, MR helper motor power, MR turbine inlet air temperature, cooling water supply temperature, NGL extraction temperature, Feed gas pressure, LNG temperature and LNG production rate only the MR turbine inlet air temperature and the cooling water supply temperature as shown in Table 2 proved useful in obtaining the regression model.

The parameters in the regression model were selected after evaluation of the scatter diagrams of LNG production rate against different independent parameters for indication of reasonable correlation. Figure 4 and Figure 5 shows the scatter diagrams of LNG production rate against cooling water supply temperature and MR

gas turbine inlet air temperature. Although the C3-MR liquefaction process used by the plant has both the propane cycle and the MR cycle with their dedicated gas turbine and helper motor, the MR cycle parameters were preferred because the MR cycle is limiting i.e the propane cycle has some excess capacity. The data was analysed and the constants A, B and C obtained using the regression tool in the analysis toolPak of Microsoft Excel Spreadsheet.

III. RESULTS AND DISCUSSION

Figure 4 and Figure 5 show the scatter diagram of the LNG production rate (T/D) against cooling water temperature (^{o}C) and MR inlet air temperature (^{o}C).

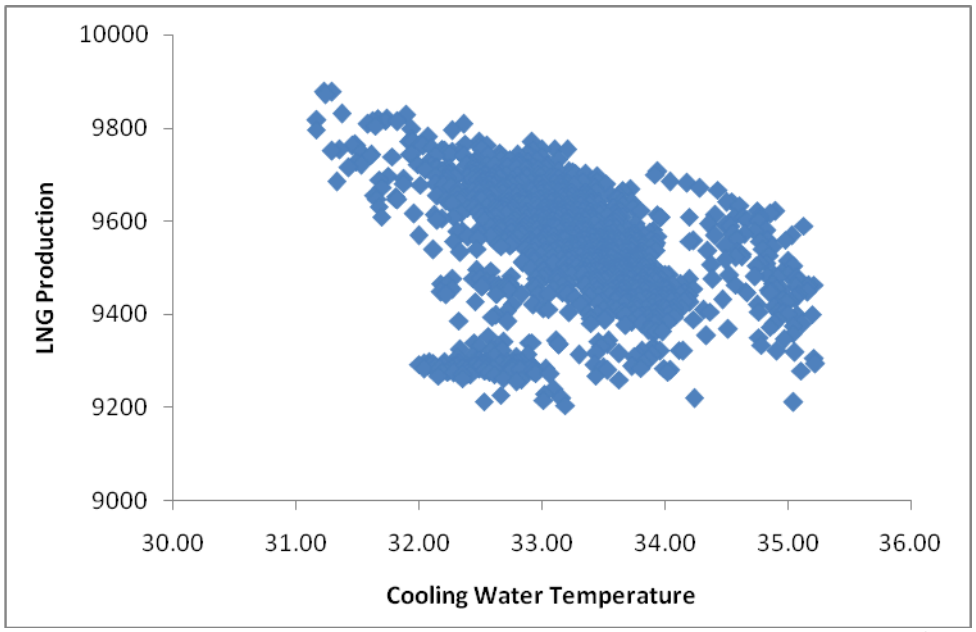

Figure 4: Scatter diagram of LNG production (T/D) to cooling water temperature (^{o}C)

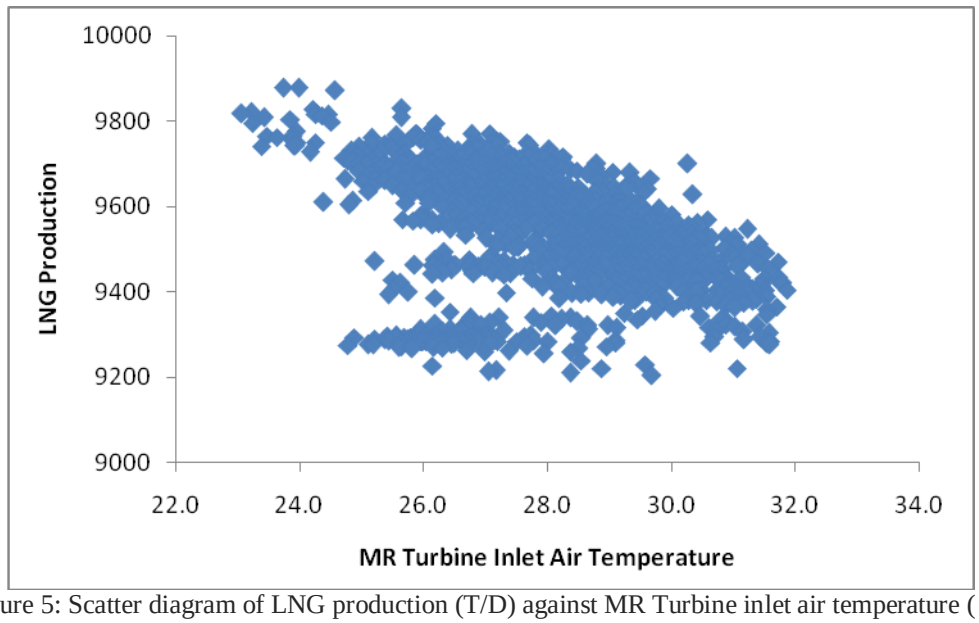

Figure 5: Scatter diagram of LNG production (T/D) against MR Turbine inlet air temperature (^{o}C)

Figure 4 and Figure 5 show a significant correlation of LNG production rate to cooling water temperature and MR turbine inlet air temperature. This indicates that at maximum LNG production rates, the LNG production depends significantly on these parameters.

From the data analysed, there is no significant correlation between the LNG production rate and the LNG temperature although LNG production rate depends strongly on LNG temperature [4]. There was also no

significant correlation between the LNG production rate and the MR turbine helper motor power, the LNG production rate and the LNG composition, the LNG production rate and feed gas pressure and the LNG production rate and the NGL extraction temperature as suggested by Dagde and Okonkwo, [4]. These can be explained by the very low variation in the data for these parameters. They were essentially constant and therefore variations in LNG production rate did not depend on them. Optimisation of the LNG temperature and NGL extraction temperature of the plant had fixed the LNG temperature and NGL extraction temperature for the plant, MR helper motor power and feed gas pressure are at the maximum and the LNG composition does not vary significantly due to LNG specification.

The values of the constant coefficients A, B and C, its respective standard error and its lower and upper values at 95% confidence level obtained from linear regression analysis of the plant data is shown in Table 1.

Table 1: Coefficients and Standard error of coefficients in linear regression model

Coefficients	*Value*	*Standard Error*	*Lower 95%*	*Upper 95%*
A	11662.17	115.4272	11435.39	11888.96
B	-26.4672	2.008292	-30.413	-22.5214
C	-39.4378	4.399538	-48.0817	-30.7938

Substituting the values of the constant coefficients A, B and C into equation 1 yields,

$$\dot{m}_{LNG} = 11662.17 - 26.47T_{a,MR} - 39.44T_{cws} \qquad 2$$

Equation 2 is the linear regression model which predicts the optimum expected LNG production rate for the LNG plant considered in this study. The linear regression model indicates that LNG production rate is increased when the MR gas turbine inlet temperature is lower (lower ambient temperature) and when the cooling water supply temperature is lower in agreement with Dagde and Okonkwo, [4].

Table 2 compares the plant data and the predictions of model [Eq. 2]. It may be seen from Table 2 that the predicted data agree reasonably well with the plant data.

Table2: Comparison of Plant data and Model Prediction

MR turbine inlet air Temperature (^{o}C)	Cooling Water Supply Temperature (^{o}C)	Plant LNG (T/D)	Predicted LNG (T/D)	% Deviation
23.73	31.23	9878	9802	0.7665
23.98	31.30	9877	9793	0.8494
23.22	31.67	9821	9799	0.2232
23.07	31.17	9817	9822	0.0499
23.24	31.17	9796	9818	0.2268
23.94	31.94	9775	9769	0.0602
23.47	31.48	9765	9800	0.3554
24.26	31.30	9750	9786	0.3687
24.84	32.48	9731	9724	0.0738
24.92	31.53	9720	9759	0.4026
25.55	32.53	9708	9703	0.0508
26.02	32.46	9694	9693	0.0060
28.02	31.88	9681	9663	0.1804
25.71	32.54	9668	9698	0.3095
27.04	32.94	9655	9647	0.0788
25.18	31.82	9647	9741	0.9706
27.40	33.39	9632	9620	0.1255
27.77	33.28	9611	9614	0.0367
26.51	32.58	9600	9676	0.7921
29.02	33.28	9587	9582	0.0519
28.25	33.76	9573	9583	0.1095
28.46	34.98	9559	9529	0.3106
29.55	33.93	9538	9542	0.0491
30.12	33.70	9511	9536	0.2651
27.96	33.82	9498	9588	0.9476

The maximum deviation of the model prediction from the plant LNG production is 1.5375% (150 T/D) and its average deviation is 0.4197% (40 T/D) for the entire data used in the regression analysis. This indicates that this linear regression model accurately predicts the expected optimum LNG production rate from the LNG plant. Therefore the expected LNG production rate for this LNG plant strongly depends on the ambient temperature and cooling water supply temperature. The deviations from the plant LNG production rates are due to the presence of other parameters not accounted for in the regression model.

Table 3 shows the results obtained from the linear regression analysis of the plant operating data. The coefficient of determination (R square) is 0.6033 with a standard error of 49.8T/D LNG. This indicates a good fit of the linear regression model to the plant LNG production rate as shown in Figure 6.

Table 3: Regression Results

Multiple R	0.7767
R Square	0.6033
Adjusted R Square	0.6017
Standard Error	49.8027
Observations	501

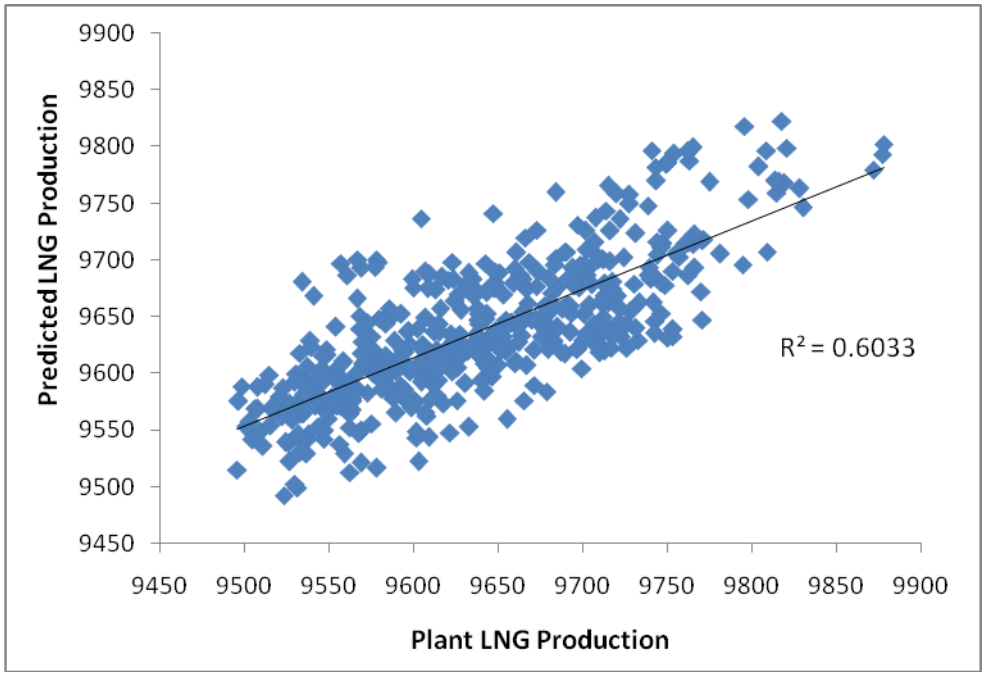

Figure 6. Graph of Predicted LNG production rate (T/D) to Plant LNG production rate (T/D)

The linear regression model explains about 60% of the variation of the LNG output. The actual LNG production rate from the plant is within ± 98 T/D of the regression model prediction within a 95% confidence interval as calculated from the standard error. This also indicates that the model is accurate and reliable to calculate the expected LNG production from the plant.

IV. CONCLUSION

The statistical method, linear regression, was used to analyse 501 data points obtained from a functional industrial LNG plant during periods of maximum LNG production. A linear regression model which accurately predicts the expected LNG production rate from the plant was developed and validated. The maximum and average % deviation of the model prediction to the plant LNG production rate is 1.5375% and 0.4197% respectively. The model indicates that the expected LNG production rate from the plant depends strongly on the ambient air temperature (MR turbine inlet air temperature) and cooling water supply temperature. The coefficient of determination of the model was 0.6033 with a standard error of 49.8T/D LNG. The actual LNG production rate from the plant is within ± 98 T/D of the regression model prediction within a 95% confidence interval.

REFERENCES

[1] R. Khalilpour, I. A. Karimi, Evaluation of Utilization Alternatives for Standard Natural gas; *Energy*, 40**,** 2012, 317-328.

[2] P. Bosma, R.K. Nagelwort, Liquefaction Technology: Developments through History, *Proceedings of the First Annual Gas Processing Symposium*, Doha, Qatar, 2009, 1-13.

[3] T. Shukri, LNG Technology Selection, *Hydrocarbon Engineering*, 9, (February), 2004 71-74.

[4] K.K. Dagde, O. C. Okonkwo, Development of Predictive Thermodynamic Model for Liquefaction of Natural Gas using the C3-MR Refrigeration Process; *International Journal of Engineering and Technology*, 2(11), 2012, 1861-1871.

[5] G. Tsatsaronis, T. Morosuk, Advanced Exergetic Analysis of a Refrigeration System for Liquefaction of Natural gas; *International Journal of Energy and Environmental Engineering*, 1, (Fall), 2010, 1-17.

[6] V. Ravavarapu, J.H.Oakley, C.C. White, Thermodynamic Analysis of a Baseload LNG Plant; Proceeding of the Chemical 96: Excellence in Chemical Engineering: 24th Australian and New Zealand Chemical Engineering Conference and Exhibition: 1996, 143-148.

[7] M. Konoglu, Exergy Analysis of Multistage Cascade Refrigeration Cycle used for Natural Gas Liquefaction; *International Journal of Energy Research*, 26, 2002, 763-774.

[8] P. Rodgers, A. Mortazavi, E. Eveloy, S. Al-Hashimi, Y. Hwang, R. Radermacher, Enhancement of LNG Plant Propane Cycle through Waste Heat powered Absorption cooling, *Applied Thermal Engineering*, 48, 2012, 41-53.

[9] M. Wang, J. Zhang, Q. Xu, Optimal Design and Operation of a C3MR Refrigeration System for Natural Gas Liquefaction; *Computers and Chemical Engineering*, 39, 2012, 84-95.

[10] A. Alabdulkarem, A. Mortazavi, Y. Hwang, R. Radermacher, P. Rogers, Optimisation of Propane Pre-cooled Mixed Refrigerant LNG Plant; *Applied Thermal Engineering*, 31, 2011, 1091-1098.

[11] A. Aspelund, T. Gunderson, J. Myklebust, M. P. Nowak, A. Tomasgard, An Optimisation-Simulation Model for a Simple LNG Process; *Computers and Chemical Engineering*, 34, 2010, 1606-1617.

[12] R.P. Sutton, Compressibility Factor for High Molecular Weight Reservoir Gases; SPE 14265, *paper presented at the SPE Annual Technical Conference and Exhibition*, Las Vegas, NV, 1985.

NOMENCLETURE

T_{cws}	Cooling Water Supply Temperature
$\dot{m}_{LNG}$	LNG Production Rate
$T_{a,MR}$	MR Gas Turbine Inlet Air Temperature
C3-MR	Propane Pre-cooled Mixed Refrigerant
LNG	Liquefied Natural Gas
MR	Mixed Refrigerant

American Journal of Engineering Research (AJER)
e-ISSN : 2320-0847 p-ISSN : 2320-0936
Volume-02, Issue-11, pp-293-299
www.ajer.org

Research Paper Open Access

Performance Analysis of LTE in Rural Environments Considering the Combined Effect of Different Download Scheduling Schemes and Transmission Modes

Md. Ariful Islam, Israt Jahan, Md. Reduan Hossain, Mahmudur Rahman, Abdullah-al-Mukit, Mr. Md. Jakaria Rahimi
[1,2,3,4,5,6](*Department of Electrical and Electronic Engineering, Ahsanullah University of Science & Technology, Bangladesh)*

Abstract: - Long Term Evolution (LTE) is the new standard specified by Third Generation Partnership Project (3GPP) on the way towards the 4G mobile network. The LTE introduces enhance data link mechanisms to support successful implementation of new data services across the network. The incorporated scheduling mechanisms can significantly contribute to this goal. In this paper, we have compared the performance of Best Channel Quality Indicator (Best CQI) and Proportional Fair (PF) which are the two most popular scheduling algorithms used in LTE. The performance was compared in rural environment using Transmit Diversity (TxD) and Open Loop Spatial Multiplexing (OLSM). The results of simulation show that both the Best CQI and PF perform fairly well for transmit diversity. It is due to the fact that variation in channel quality is not so significant in rural environment. On the other hand, throughput and Block Error Rate (BLER) are not improved using OLSM. It was not surprising as the effect of multipath signal is less in rural environment. OLSM can improve throughput only in rich multipath environment.

Keywords: - *Transmit Diversity, Spatial Multiplexing, Best CQI, Proportional Fair, Scheduling.*

I. INTRODUCTION

The 3gpp LTE is designed to meet high speed data & voice support along with multimedia broadcast services. The scheduler in the Medium Access Control (MAC) layer of the eNodeB attempts to make appropriate apportionment of the resources with certain objectives like,

- Required Quality of Service (QoS) for applications.
- Optimized spectral efficiency ensuring high cell throughput under existing channel conditions.
- Fairness among User Equipment's (UEs) and applications.
- Limiting the impact of interference through special handling of cell edge users.
- Load balancing among cells.

There are six downlink channels. They are: Physical Broadcast Channel (PBCH), Physical Control Format Indicator Channel (PFCICH), Physical Downlink Control Channel (PDCCH), Physical Hybrid-ARQ Indicator Channel (PHICH), Physical Downlink Shared Channel (PDSCH) and Physical Multicast Channel (PMCH). In this paper, the Physical Downlink Shared Channel (PDSCH) channel is taken into consideration. This channel can use various Multiple Input Multiple Output (MIMO) techniques, e.g. spatial multiplexing, transmit diversity and beam forming to improve the throughput and data rate. Under this channel, seven transmission modes are defined in Release 8. In this paper, the impact of transmission mode 2 and 3 is demonstrated which represent Transmit Diversity (TxD) and Open Loop Spatial Multiplexing (OLSM) respectively. For the apportionment of downlink resources, the following information is made available with the scheduler for consideration.

- Channel Quality Indicator (CQI) reports from UEs to estimate the channel quality.
- QoS description of the EPS bearers for each UE. This is available in the eNodeB from the downlink data flow.

The throughput of a UE may vary significantly with scheduling algorithm used, distance from eNodeB, multipath environment, multiple antenna techniques and UE speed. The effect of UE speed in the transmission mode performance is already discussed in [1]. The effect of scheduling algorithm, distance and transmission modes 1 and 2 in throughput performance is considered through LTE system level simulations in [2].In this paper, we have focused mainly on the effect of TD and OLSM on Throughput and Block Error Rate (BLER) of LTE specially in rural environment. This report is organized as follows: in section-2 The Downlink Resource scheduling, LTE Transmission Modes are discussed in section-3, section-5 contains the simulation results, and finally conclusion in the section-6.

By analyzing these scheduling algorithms we will easily understand that, which method is useful and cost effective for the rural environment.

II. DOWNLINK RESOURCE SCHEDULING

LTE uses Orthogonal Frequency Division Multiple Access (OFDMA) for downlink transmission. In this case, a time-frequency resource grid is considered using sub-carriers in the frequency axis and symbols in the time axis. A resource element represents one sub-carrier and one symbol resource in the time-frequency resource grid.

Data is allocated to the UEs in terms of Resource Blocks (RB). In time, the length of a RB is one slot which is equal to 0.5 ms (millisecond). With 15 kHz sub-carrier spacing, the number of symbols in one slot is 6 and 7 for normal cyclic prefix and extended cyclic prefix respectively. In frequency, the length of a RB is 180 kHz. The number of sub-carriers in the 180 kHz span is 12 for 15 kHz sub-carrier spacing.

The eNodeB allocates different RBs to a particular UE in either localized or distributed way. The eNodeB uses DCI format 1, 1A, 1B, 1C, 1D, 2, 2A or 2B on PDCCH to convey the resource allocations on PDSCH for the downlink transmission [1]. The eNodeB uses one of the following three types of resource allocation for a particular UE [3].

- Resource Allocation Type 0
- Resource Allocation Type 1
- Resource Allocation Type 2

The scheduler at eNodeB attempts for appropriate apportionment of the resources among UEs. The Channel Dependent Scheduling can be made in both time and frequency domains. In this case, the scheduling adapts to channel variations and link adaptation is achieved. A user with better channel quality is given more resources as the user can make good use of these resources leading to higher cell throughput. The channel dependent scheduling allows transmitting at fading peaks. The Channel Dependent Scheduling (CDS) requires that sufficient information on uplink and downlink channel conditions is made available with the eNodeB. In order to perform Channel Dependent Scheduling (CDS) in frequency, the information about the radio channel needs to be frequency specific. The eNodeB can configure a more frequency specific information but it requires usage of more resources for this information. Also, the eNodeB can configure the availability of the information more frequently in time so that it can represent the variation of radio channel better but again at the cost of more resources for this information.

The UE reports CQI which helps eNodeB estimate the downlink channel quality. The eNodeB can configure if the CQI report would correspond to the whole downlink bandwidth or a part of it which is called sub-band. CQI reporting for different sub-bands requires more uplink resources. The eNodeB can configure CQI reporting in the following ways [3].

- Wideband Reporting: The CQI reported corresponds to the whole downlink bandwidth
- eNodeB Configured Sub-Band Reporting
- UE Selected Sub-Band Reporting

The channel dependent scheduling leads to higher cell throughput and on the other hand, the scheduling should maintain some fairness among the users in their resource allocations. There is a tradeoff between fairness and cell throughput. The scheduler can exercise various methods as shown below in order to address this tradeoff.

- Best CQI: The CQI value can be expressed as a recommended transport-block size instead of expressing it as a received signal quality. It can be used for the scheduling. Best CQI scheduling algorithm uses these values as a reference for making decision of scheduling.
- Proportional Fair (PF): The scheduler can exercise Proportional Fair (PF) scheduling allocating more resources to a user with relatively better channel quality. This offers high cell throughput as well as fairness satisfactorily. Thus, Proportional Fair (PF) scheduling may be the best option.
- Scheduling for Delay-Limited Capacity: Some applications have very tight latency constraints and so, their QoS require certain guaranteed data rate independent of the fading states. This guaranteed data rate is called delay-limited capacity. The scheduler can allocate resources considering such special requirements.

III. LTE TRANSMISSION MODES

PDSCH is configured with one of the following transmission modes according to Release 8 [4]. The choice of transmission mode may depend on the instantaneous radio channel conditions and the transmission mode may be adapted semi-statically.

- Transmission Mode 1: Using a single antenna at eNodeB
- Transmission Mode 2: Transmit Diversity
- Transmission Mode 3: SU-MIMO Spatial Multiplexing: Open-Loop
- Transmission Mode 4: SU-MIMO Spatial Multiplexing: Closed-Loop
- Transmission Mode 5: MU-MIMO Spatial Multiplexing
- Transmission Mode 6: Beam forming using Closed-Loop Rank-1 Precoding: It can also be seen as a special case of SU-MIMO Spatial Multiplexing.
- Transmission Mode 7:Beam forming using UE-Specific Reference Signals

The following sections briefly describe the transmission modes which are simulated for evaluation purpose.

3.1 Transmit Diversity (TxD)

In TxD Figure 1(a), Space Time Block Codes (STBC) are used to provide improvement against the channel deteriorating effects.Alamouti STBC is considered to be the simplest space-time block codes. It is well known that Alamouti codes [5] can achieve full diversity and full code rate simultaneously. But for MIMO Systems having more than two transmit antennas diversity and orthogonality can only be achieved at the cost of slower date rates. Therefore we cannot achieve high data rates beyond a certain value and powerful coding schemes are required to achieve higher data rates as the SNR (Signal to Noise Ratio) $\rightarrow \infty$. Another issue with TxD is that it is single rank i.e. it does not support multi stream transmission [6].

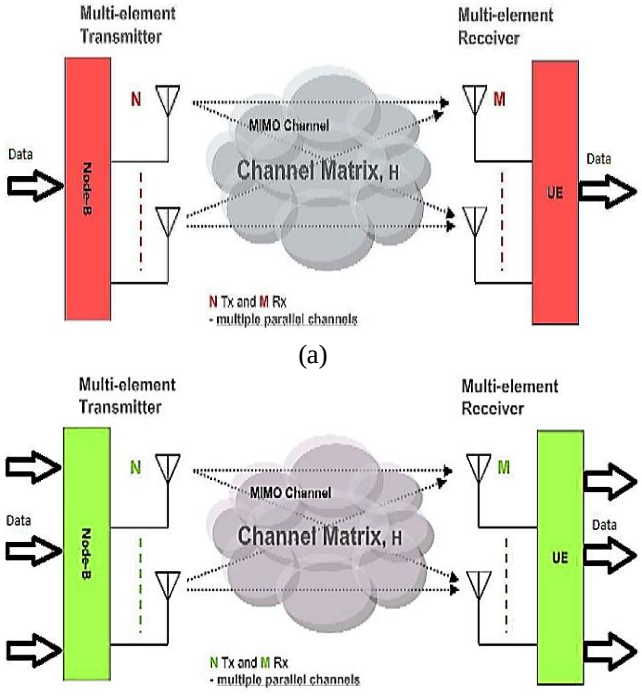

Figure-1: (a) Block diagram of a MIMO transmission using Transmit Diversity (b) Block diagram of a MIMO transmission using OLSM

3.2 Spatial Multiplexing(SM)

SM provides extra gain as compared to TxD [7]. Independent data streams are transmitted from the NT transmit antennas in spatial multiplexing. There are two classes of spatial multiplexing, they are open and closed loop spatial multiplexing. OLSM is discussed in Figure 1(b). OLSM transmits the independent data streams without deploying any feedback algorithm. High data rate is achieved as compared to TxD as multiple independent streams are transmitted. This endorses high BLER. To compensate this BLER Closed Loop Spatial Multiplexing (CLSM) is used. In CLSM, essential amount of CSI is used as feedback which enables us to achieve high throughput with lower BLER. But the CLSM is not considered in this paper.

IV. SIMULATION RESULTS

LTE system level simulator [8] was used with parameters shown in the table-1. Five UEs are placed randomly in one sector of a cell. Performance with Best CQI and Proportional Fair scheduling has been observed for five UEs at various distances from the eNodeB. The throughput has been determined for transmission modes 2 and 3 for rural propagation model.

Table 1: Simulation Parameters

Parameters	***Assumptions***
Transmission bandwidth	2.0GHz
Inter-site distance	5MHz
Thermal noise density	500m
Receiver noise figure	9dB
Simulation length	5000 TTI
UE speeds of interest	5km/hr
UEs position	5UEs/sector, located in target sector only.
BS antenna pattern	$A(\theta) = -\min[12(\frac{\theta}{65°})^2, 20dB],$ $-180 \le \theta \le 180$
BS antenna gain	15 DBi [1]
Scheduler	Best CQI, Round Robin,Proportional Fair
Thermal noise density	-174dBm/Hz
TXmode	1, 2
nTX x nRX antennas	2 x 2
eNodeB TX power	43dBm
Subcarrier averaging algorithm	EESM
Uplink delay	3TTIs
Macroscopic path loss model	Rural, given as, L=128.1+37.6log$_{10}$(R)

The results are presented as graphs for all three scheduling algorithms i.e. Best CQI, Proportional Fair and Round Robin for three different transmission modes. For each scheduling algorithms, we have observed the THROUGHPUT and BLER for the 5 users.

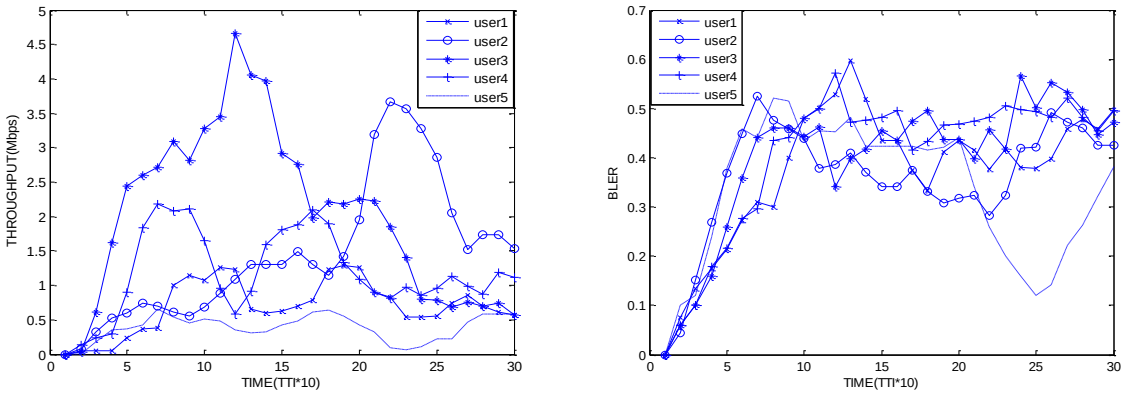

(a) (b)

Figure-2: (a) THROUGHPUTgraphs of 5 users of Best CQI in transmission mode 1(5MHz Bandwidth)
(b) BLER graphs of 5 users of Best CQI in transmission mode 1(5MHz Bandwidth).

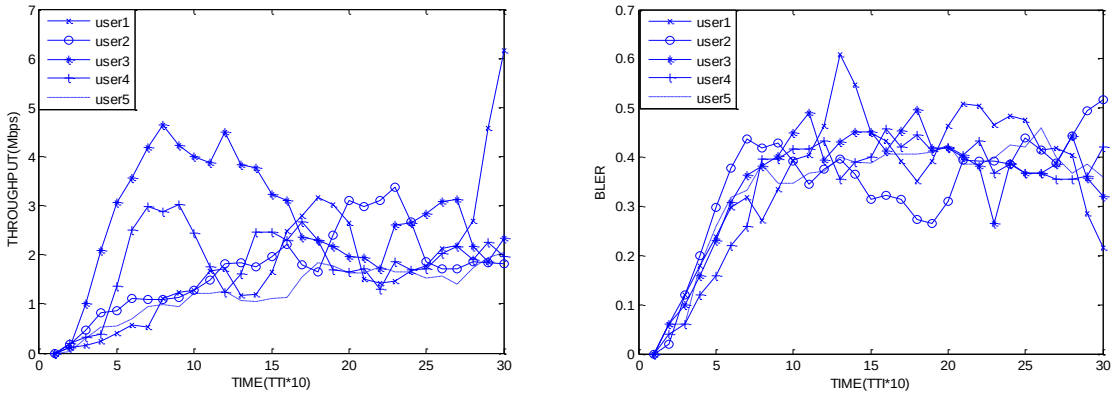

(a) (b)

Figure-3: (a) THROUGHPUT graphs of 5 users of Best CQI in transmission mode 2(5MHz Bandwidth)
(b) BLER graphs of 5 users of Best CQI in transmission mode 2(5MHz Bandwidth).

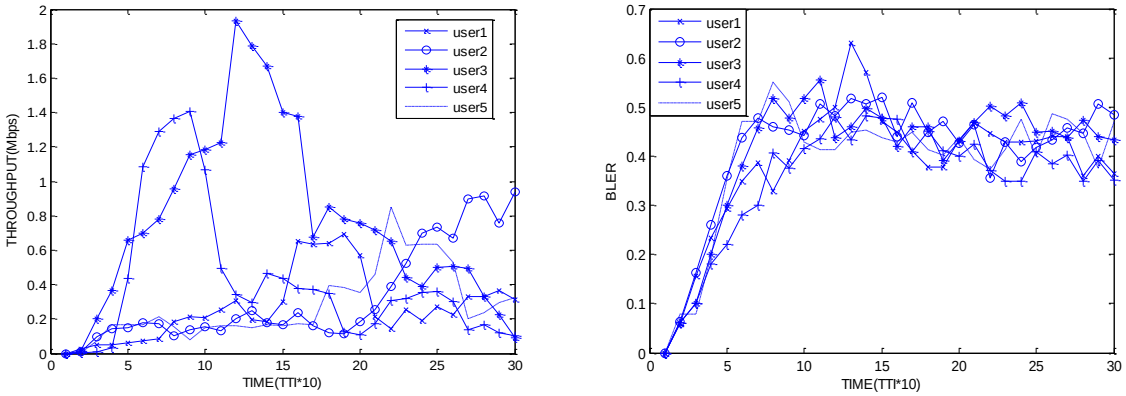

(a) (b)

Figure-4: (a) THROUGHPUT graphs of 5 users of Best CQI in transmission mode 3(5MHz Bandwidth)
(b) BLER graphs of 5 users of Best CQI in transmission mode 3(5MHz Bandwidth).

From the figure 2(a), 3(a) and 4(a) we can easily observe that, at transmission mode 2, i.e. using transmit diversity we are getting slightly higher throughput than transmission mode 1(where the transmission mode 1 is SISO or Single Input Single Output) but significantly higher than transmit mode 3(where the transmission mode 3 is OLSM or Open Loop Spatial Multiplexing).
From the figure 2(b), 3(b) and 4(b) we can easily observe that, the BLER is not much affected by the different transmission modes (here we used transmission mode 1, 2 and 3).

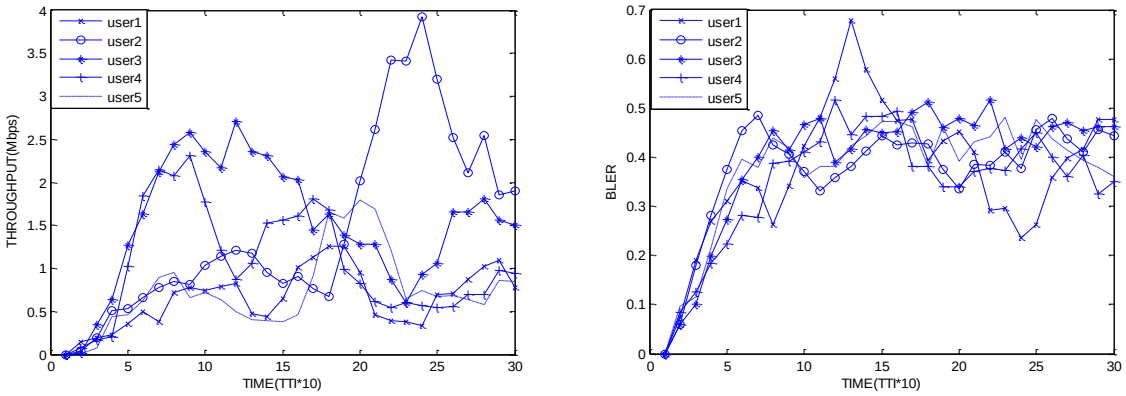

(a) (b)

Figure-5: (a) THROUGHPUT graphs of 5 users of Proportional Fair in transmission mode 1(5MHz Bandwidth)
(b) BLER graphs of 5 users of Proportional Fair in transmission mode 1(5MHz Bandwidth).

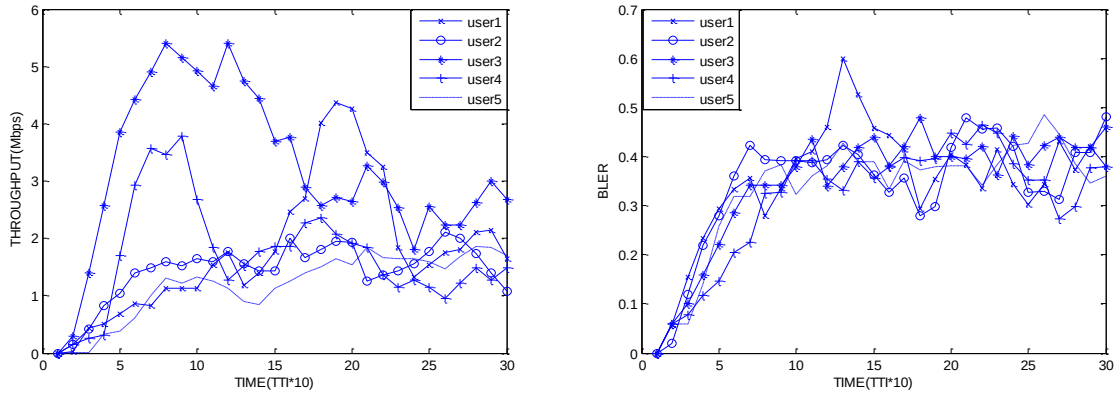

(a) (b)

Figure-6: (a) THROUGHPUT graphs of 5 users of Proportional Fair in transmission mode 2(5MHz Bandwidth) (b) BLER graphs of 5 users of Proportional Fair in transmission mode 2(5MHz Bandwidth).

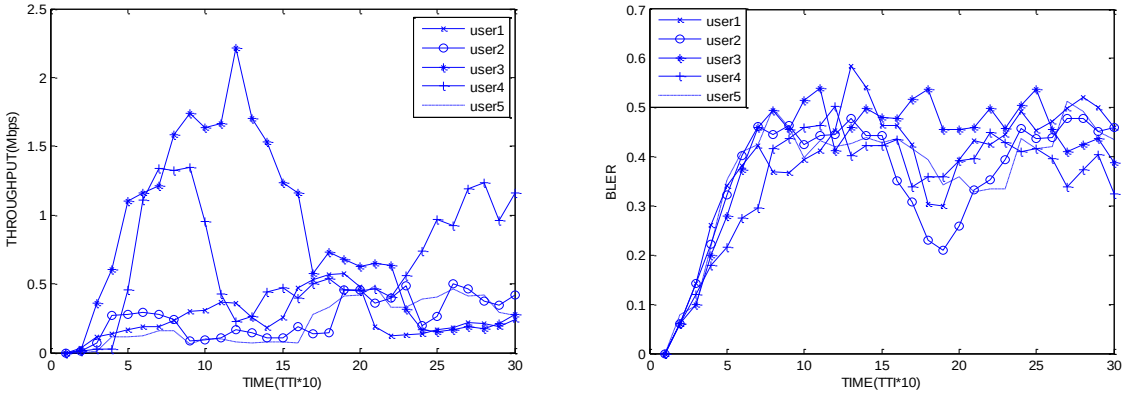

(a) (b)

Figure-7: (a) THROUGHPUT graphs of 5 users of Proportional Fair in transmission mode 3(5MHz Bandwidth) (b) BLER graphs of 5 users of Proportional Fair in transmission mode 3(5MHz Bandwidth).

From the figure 5(a), 6(a) and 7(a) we observed that, at transmission mode 2, i.e. using transmits diversity we are getting significantly higher throughput than transmission mode 1(where transmission mode 1 is SISO). Using the transmission mode 3 or Open Loop Spatial Multiplexing (OLSM) the throughput gets decreased in comparison with the other two transmission modes. Finally, it is observed that the BLER is not heavily affected by the different transmission modes.

From the figure 5(b), 6(b) and 7(b) we can easily see that, there is a significant change in the BLER. BLER is affected by the different transmission modes. According to theory, the BLER is decreasing from transmission mode 1(SISO) to transmission mode 3(OLSM).

V. CONCLUSION

From the simulation results we get fairly good Throughput and BLER for both Best CQI and Proportional Fair schedulers in three different modes. But the analysis of the simulation graphs show that Proportional Fair scheduler has highest throughput values in transmission mode 2. At low BLER values Proportional Fair scheduler performed more efficiently than other scheduler algorithms. On the other way, the OLSM failed to show any significant improvement in Throughput. It is due to the fact that OLSM takes advantages of multipath environment. In rural environment the multipath environment is not so rich, that's why OLSM is not effective here. We also observed the Throughput and BLER of Round Robin, but did not get any expected results. The Round Robin shows drastically lower Throughput and specially the higher BLER from transmission mode 1 to transmission mode 3 which is undesirable. If we want just high Throughput then the Best CQI schedulers will be a good choice for the system. But if high Throughput and lower BLER is a major consideration in the service requirement of the system then the Proportional Fair idea will be a better choice. It is also worth noting that the difference in the throughput results of the Best CQI and Empirical is not low and cannot be used to justify the argument for Proportional Fair as a better algorithm.

REFERENCES

[1] HarriHolma and AnttiToskalaI, *LTE for UMTS - OFDMA and SC-FDMA based radio access* (2009 John Wiley & Sons, Ltd. ISBN: 978-0-470-99401-6).

[2] Mohammad T. Kawser, Abduhu. R. Hasin,Hasib M. A. B. Farid, Adil M. J. Sadik, Ibrahim K. Razu, Performance comparison between Round Robin and Proportional Fair scheduling:Methods for LTE,*Procedia Engineering,28-30 December 2011*, Dubai, UAE.

[3] 3GPP Technical Specification 36.213, 'Evolved Universal Terrestrial Radio Access (E-UTRA); Physical Layer Procedures', www.3gpp.org accessed in September 2013.

[4] StefaniaSesia, IssamToufik and Matthew Baker, *LTE- the UMTS long term evolution: from theory to practice* (2009 John Wiley & Sons, Ltd. ISBN: 978-0-470-69716-0).

[5] "Switching between open and closed loop multi-stream transmission,"Swedish Patent WO 2011/115 532 A1, 2011.

[6] J. Guan, X. Ye, and P. Tian, A robust scheme for transmit diversityand spatial multiplexing: Based on channel spatial correlation,*In InternationalConference on MultiMedia and Information Technology*, 2008.

[7] G. Wetzker, "Definition of spatial multiplexing gain," in Electronic Letters, 2005, accessed in August 2013.

[8] LTE System Level Simulator v1.0r295 by Institute Of communication and Radio Frequency Engineering, ViennaUniversity of Technology, Vienna, accessed in November 2012.

American Journal of Engineering Research (AJER)
e-ISSN : 2320-0847 p-ISSN : 2320-0936
Volume-02, Issue-11, pp-300-308
www.ajer.org

Research Paper Open Access

Immunization of Urban Spaces in Saqqez city, Iran

Dr. Gholam Ali Khammar, Akbar Heydari
[*1] *Assistant professor of Geography and Urban Planning, University of Zabol, Zabol, Iran*
[2] *Ph.D. Student of Geography and Urban planning, Ferdowsi University of Mashhad, Mashhad, Iran*

Abstract: - Saqqez is the regional city of the Kurdistan region, the Northwest province of Iran. In recent years many transformations have occurred in Iranian society and women and girls still have a lot to worry about comes to urban public spaces. In order to, the aim of current research is examine the women's participation in urban spaces safety by PUA model in case study region. Methodology is based on library, documental and field studies. Results showed that the index of city street furniture in Republic street with providing more favorable conditions of women's satisfaction with (0.563) of the Quds street, south Imam Khomeini street with (0.513) and (0.448) were in north Imam Khomeini street. Other indicators also had a similar situation. Finally, presented some solve ways using SWOT model.

Key words: - *PUA Model, Female-centric Land use, Saqqez city, Women Participation*

I. INTRODUCTION

Saqqez is the regional city of the Kurdistan region, the Northwest province of Iran. It has a 987 km common border with Iraq country. The Western border of Iran was specified by the border commission according to the Goldsmith Plan in September 1871 (Taheri, 1977). In land use planning, urban open space is open space areas for "parks", "green spaces", and other open areas. The landscape of urban open spaces can range from playing fields to highly maintained environments to relatively natural landscapes. They are commonly open to public access, however, urban open spaces may be privately owned. Areas outside of city boundaries, such as state and national parks as well as open space in the countryside, are not considered urban open space. Streets, piazzas, plazas and urban squares are not always defined as urban open space in land use planning (Sykes, 1984 & Kurdish encyclopedia, 1975)

Planning and designing safe public spaces for women and girls means creating public spaces with features that enhance women's safety and feelings of safety, and detract from features that cause women's insecurity and feelings of insecurity (Kiani & Heydari, 2011). While planning and designing safe public spaces for women, planners, designers and architects place special focus on lighting, landscaping, visibility, motorized traffic, pedestrian traffic, urban furniture, potential hiding spots, signage, security personnel, proximity to other public spaces, proximity to emergency services, and access to public transportation. Each of these areas is given particular consideration from the perspective of the women and girls who use public spaces (Plan International, 2010). Safety planning and design also involves more than just the concrete, physical features of a space, although interventions at this level may occur first in a safe cities for women program (Werkerle, 2000). It is a necessarily participatory process whereby community members (especially women) work together to create spaces that accommodate strong social relations. In order to be successful, planners and designers must pay attention to how people express themselves in, and interact with, public space (Weingartner, 2010; Rahnama & Heydari, 2013; Kyung-Hwan, 2002). The urban public spaces have important role in urban development programs. This is due to the effect of these spacing in reinforcing the cultural – social aspects of the city and as the result of the production of social capital. The main features of these spaces, gathering people with different cultures and with individual and social characteristics. It means that the city and its urban spaces are the place of use and showing groups and various sectors of society that each of them based on specific social and cultural features of each individual has different expectations from these spaces. Men, women, children, adults and disabled people are the main users of urban areas that the percentage and use rate of each of them from spaces represents ability of the space in meeting their needs. The important point about the women, children, adults and

disabled people is their vulnerability in urban areas against threats to the environment. Hence it is important to pay attention to these people in an urban area (Khammar & et al, 2011; Kolbel, 2008). Public space should belong to everyone and everyone should have a right to use it – girls should feel free to use the soccer field and boys should feel free to sit under the tree. Thus, planning and designing safe public spaces for women and girls also means analyzing the various uses of public spaces, who uses them, when, and for how long (Hickman, 2005; Banister, 2005). This kind of planning and design also focuses on who doesn't use a particular public space, when, and why. This is because when certain groups, like women or girls, do not use a space, it is usually an indication that the space feels insecure to members of that group (Hesse, 2001; Habibi, 1996). In order to, Planning and designing safe public spaces for women and girls requires constant attention to physical and social characteristics of space. It also requires constant evaluation of the social and physical implications of the planning and design process. The planning and design of a space has the potential to either reinforce gender inequality or to advance gender equality. For this reason, the planning and design process is a crucial facet of creating safe cities for women and girls.

This paper deals with one of the more important changes to occur in the contemporary Kurdish city, one that has been identified in the literature as the 'privatization of public space'. This restructuring of the urban landscape has been facilitated by the interlocking components of the real estate, finance, construction and design sectors, and reflects the influence of the latter at the expense of municipal oversight. In conceptual terms, this may be of only limited importance, insofar as cities in the Iran have been both shaped and produced by corporate interests for a very long time (Kohn, 2004; Kirby, 2008). Barker, the founder of the theory of ecological psychology assesses the behavioral patterns of women in space safety. He believes that there is a relation between physical and behavioral aspects which is expressible, considering the implication that fits the environment. He believes that by being in a different manner camps, an individual can take on certain social roles (Barker, 1960). The important point about the women, children, adults and disabled people is their vulnerability in urban areas against threats to the environment. Hence it is important to pay attention to these people in an urban area. Women because of their specific characteristics lead to differences in the urban area that if this area is considered, it can be free from fear and distress for all groups (except disabled). Raggers (2003) is a scholar with consistency tendency and in his work as "cities for a small planet" defines public realm as an encouraging factor in social mobility because he believes that a sustainable city should be characterized by justice, beauty, creativity, ecology, compactness or multicenter, diversity and finally easy information exchange in a way that both face-to-face and electronic information be exchanged (Raggers, 2003). On the other hand it can be said that the need for traffic safety in public spaces is one of the basic needs and has different dimensions itself. In various sources, safety has been considered as an optimal benchmark in determining proper locations for urban usages, in addition of other criteria such as fitness, comfort, efficiency and utility, (Saeednia, 2008). In terms of urban planning, urban safety includes all precautions and doings that can be applied in short, medium and long term programs in order to protect life and property of the citizens (Zangi Abadi & et al, 2008).

II. BACKGROUND

Urban planners and other municipal officials tend to consider public space as "gender neutral". In other words, they consider public space as being experienced in the same way by women and men. However, to plan public spaces that are safe for everyone, space must be "de-neutralized". That is, public spaces cannot be considered to be the same for everyone everywhere (CAFSU, 2002). For example, spaces which might seem safe and enjoyable for young men may seem dangerous and unpleasant for elderly women (Raju, 2006; Sakthivel, 2009). Alternatively, spaces which seem fun and exciting for children may seem complicated and inaccessible to people in wheelchairs. Because space is experienced differently by different people (including men and women), people can create spaces that either promote or impede gender equality. For example, in spaces that are designed to be safer, easier to use and more accessible for men than for women, gender equality is impeded. Conversely, in spaces that are designed to be safe, easy to use and accessible for both men and women, gender equality is promoted (Todkari, 2010). Urban planners and other actors involved in the design of public spaces need to think about how the spaces will be used and by whom. The characteristics of a space (i.e. whether it is cramped or spacious, well-lit or poorly lit, full of people or empty) actively contribute to how social relations will evolve in that space. In other words, the same space may be safe or unsafe for women and girls depending on who uses it and why. For example, if a confined space like an elevator is filled with people for only a short period of time, it might not feel threatening to a woman at all. Designers of public space should be aware of how men and women use spaces together, and incorporate features that promote appropriate gender relations (Alaguraja & et al, 2010).

As a result of most land use and zoning decisions, different types of spaces with different uses are kept far apart from each other (Tavakoli & Heydari, 2012). This approach is based on the belief that spaces work more efficiently if they are divided into separate areas for recreation, work and housing. Unfortunately, this kind of spatial separation has compounded the traditional division between the public and the private spheres. The

separation of public and private spheres is problematic because it can limit women's abilities to move between different spaces in the city (Pant, 2013). For example, for women who are responsible for domestic tasks in the private sphere, including care-giving for children and/or elderly relatives, buying and/or growing food, maintaining the family home, and doing all number of errands and juggling resources, it can be virtually impossible to also squeeze in a trip to a separate part of the city for recreational activities. As a consequence, women simply may not be able to enjoy leisure time in spaces designated for recreation (Gopalakrishnan, 1997). In another example, women may have to decline an employment opportunity if it is located in a public area that is far away from their other daytime responsibilities in the private realm (e.g. family-related chores, care-taking roles). Conversely, women may opt or be oblited to take a job (e.g. due to poverty, to make a living) even if it is inconveniently located, and are thus forced to take long journeys early in the morning and late at night through areas where they feel insecure and their safety is at risk (Xang & et al, 2013).

Jacob believes that the presence of people in urban spaces will have issues such as safety and social security as its followings. Reliance on public oversight in urban space designing, creating a spatial focus, increasing intensity and mixing and utilization of the space and the proper skeletal organization, all form the sustainable and qualitative aspects of public realms. Public spaces must be open to all classes, age and gender groups and social minorities at all hours of the day. They must be safe and easy transportation must be provided. According to Golmoradi's research in university of Kermanshah, the raise of urban insecurity attracted many socialists' attention. He conclude that factors such as rate of cultural promotion (r=0/17), rate of urban authenticity, rate of participation in subjective and objective dimension have a positive and significant correlation with the decrease of insecurity (Golmoradi, 2011). Zokin in his book –culture of cities- says urban spaces are not safe enough for citizens to participate in creation of public culture. So according to Zokin the main index is citizens' partnership in creating of urban spaces in a way that users can both use it and try to make it a safe place (zokin, 2011). Hiller believes that the movement patterns of private spaces will be increased by safety of users who present in such spaces. He projects the term" rate of the capability of urban spaces and locations in attracting citizens' participation" and says that there is a direct correlation between social crime commitment and delinquency in different age and generation groups and the safety which is the result of favorable interaction of citizens (Hiller, 2011).

According to the urban planning program of Britain, there are nine influencing factor in measuring the quality of public spaces:

1- Both city officials and citizens try to keep public spaces, clean.
2- Considering accessibility principle, with respect to citizens' mobility and spatial behavior.
3- Functionality of various urban works in space.
4- Comfort and attractiveness of urban landscapes and public spaces.
5- The rate of inclusion, i.e. urban spaces is designed for which groups or what purposes?
6- Considering factors such as refresh and mobility when designing urban spaces.
7- Considering safety and security of urban spaces.
8- Considering the difference of urban spaces in designing and urban planning.
9- Reconstructing and upgrading urban public spaces (according to Hanifi-e-Asl, 2009 & OUPUK, 2011).

In Britain, the institution of "women against violence" published a book titled "women and security of the society" which was about planning to have more safe societies. It is stated in this book that 60% of women complained that they are afraid of walking alone, 76% were afraid of waiting for public transportation, 83% were afraid of going to their cars in parking lots and 39% were afraid of staying at home alone, early at nights. These finding were generalizable in most societies of the world, regardless of cultural issues. Urban spaces and its inclusions have effects on each other. Spaces get their form, function and identity from human beings and their social-cultural relations and the space organization reshapes these relations. Therefore designing and structuring of urban spaces impact the process of social life and must have benefits both physically and mentally for citizens (Hanifi-e- Asl, 2009).

III. CHANGES OF POPULATION IN KURDISH CITIES

The number of Kurdish cities increased from 6 in 1976 to 23 (10 main cities and 13 minor cities as subset cities) in 2012. In the different National development plans in before and after revolution point on increase urbanizations related to industrialization of these urban Settlements in these areas. Cerate cement factory in Bijar city was the first step to access this purpose in after Islamic revolution and caused the migration of hundreds of thousands of villagers to the cities and also growth of private subdivisions. On the one hand, a cheap workforce for economic activities in cities in industrial and building services was provided; on the other hand, production and consumption within the villages was subsumed into the urban capitalist economy. During the implementation of these plans, most of industrial activities in Sanandaj and Saqqez and its surrounding areas

have been centralized. In this period, both the urban and the master plan had a great impact on physical changes of Sanandaj city as a big city in Kurdistan province. The foreign engineers and consultants along with their indigenous colleagues with modernizing tendencies tried to make a master plan. As a result, the act of owning apartments was approved in 1996 (Habibi, 1996),

IV. CASE STUDY

Saqqez city is located between 46°13'-46°16' eastern longitude and 36°11'-36°15' northern latitude within north-west of Kurdistan province in northwest of Iran and covers of approximately 1474.8 ha. At the 2006 census, the city's population was 135037, whereas its current population is about 145000. Building area was 618.26 ha. The average elevation of the city is about 1496 m above mean sea level. Saqqez is characterized as a mountainous area which is located within Zagros Mountains rages from south-east to north-west. This area comprises about 15.5% of Kurdistan province. The difference of height between the highest elevation point (Chehel-Cheshme Mountain, 3173 m and Symone-Rood basin, 1150 m above mean sea level) is about 2023 m. Saqqez River emanates from western mountains (Khan valley) and continues its path across the city toward north-east. Fig. 2 shows location of study area in Kurdistan province, Iran (Rahimi, 2012). Also it has a 987 Km^2 common border with Iraq country. Western border of Iran was specified by the border commission according to the Goldsmith Plan in September 1871 (Taheri, 1977). This borderline has separated parts of Kurdistan from Iran (Sykes, 1984) and today a majority of the Kurdish population (about 25 million people) live within Turkey (a group of Kurdish people also lives in Iran, Iraq and Syria Countries.(Kurdish Encyclopedia, 1975). Kurdistan province within the Iran has the lowest level of Development (Rahnama & Heydari, 2013; Heydari & Tavakoli, 2012).

Table 1 Population information of Saqqez city in 1996 to 2016.

Divisions	Are	Population of 1996	Population of 2006	Residential Area	Number of households 2006	Gross density 2006	Net Density 2006	Population estimate 2016
District 1	179.56	13427	13427	43.73	3570	75	307	5150
District 2	183.92	24700	23599	59.6	5686	128	396	27500
District 1	363.48	40954	37026	103.37	9256	102	358	49150
District 3	372.53	38965	46127	116.99	10792	124	394	54500
District 4	211.07	9637	13262	34.91	3056	63	380	20000
District 2	583.61	48602	59389	151.90	13848	102	391	74500
District 5	311.36	18103	20224	40.01	4357	65	505	34000
District 6	274.92	7735	14710	41.81	3406	54	352	20500
Region 3	586.28	25838	34934	81.83	7763	60	427	54500
Total	1533.27	115394	131349	337.10	30867	85.66	389.64	178150

Note: Statistics Organization of Iran 1976, 1986, 1996, 2006 and estimate of 2016.

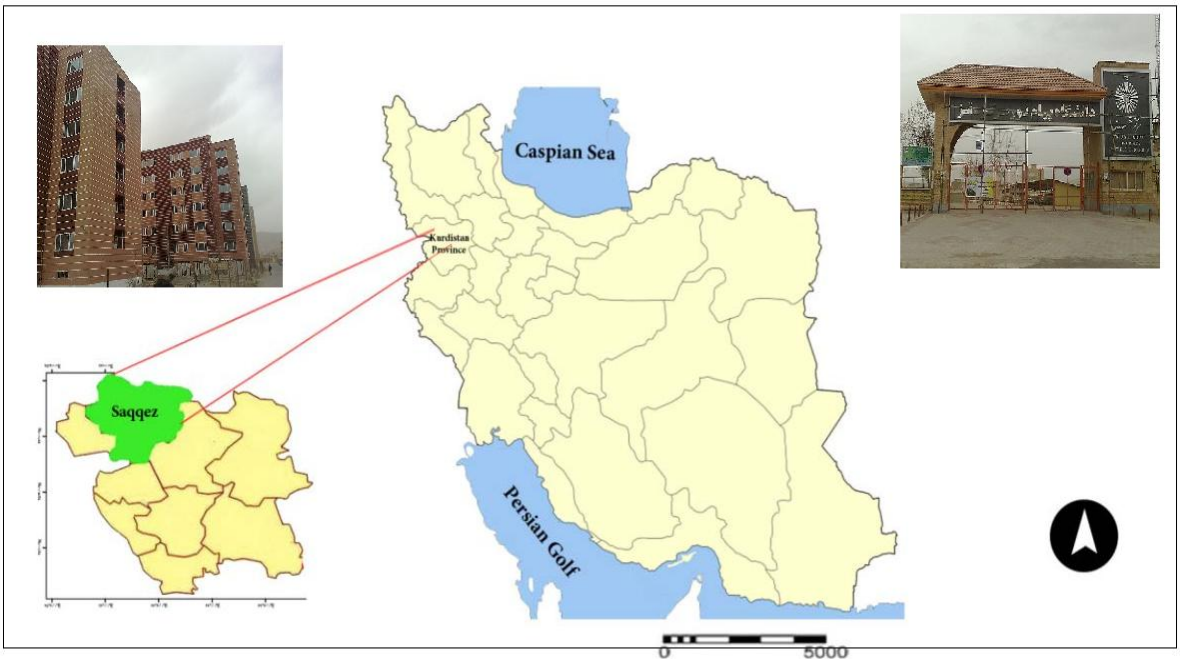

Fig. 1. A landscape of case study region. Source: Authors, 2013.

V. MATERIAL AND METHODOLOGY

The research method we have used is based on the descriptive- analytical approach. We used a documental method to collect information. In order to applied methodology is based on correlation, field and survey methods. Statistical society of current research was including 200 citizens, experts and urban officials. According to characteristics of population, sampling method is simple random sampling without replacement and each expert is considered as a sample. Morgan's sample size estimation table was used to determine size of sample, so 59 experts were selected as final sample. In final presented some solve ways. A precondition for this methodology lies in the fact that the transport and land-use system can be influenced or should be controlled by policies and regulations, although it has been suggested that the regulatory influence may be unelectable. However, the argument here is to develop a methodology which can control, steer or ‘‘govern’’ the transport system, as required principally by approach. The topical constraint to ‘‘empirical research’’ does not need to be required and can also be applied to ‘‘strategies’’, for yielding successful actions.

VI. RESULTS

Interest in the issue of women communication with city and the view that perception and experience of women in city areas may be quite different from men was created from "second wave" of feminist efforts to overcome the sociological theoretical model in 1970. Critics have highlighted the failure of social theory and began investigating of the structural differences of gender and gender inequality. This fight was made not only just in further symbolic composition and materialistic interior of space and family atmosphere but also was required for the claims based on that presence in public space.

Table 2 Physical Division of Saqqez city according to Zone, district and Sector

Zone one		Zone two		Zone three	
Subdivisions	**Area (ha)**	**Subdivisions**	**Area (ha)**	**Subdivisions**	**Area (ha)**
District One	**179.4**	**District Three**	**369.50**	**District Five**	**301.13**
Sector 1	69.98	Sector 8	95.45	Sector 16	
Sector 2	53.29	Sector 9	56.2	Sector 17	
Sector 3	56.13	Sector 10	30.15	Sector 18	
		Sector 11	42.84	Sector 19	
		Sector 12	37.03		
		Sector 13	107.83		
District Two	**184.2**	**District Four**	208.56	**District Six**	**271.51**
Sector 4	52.38	Sector 14	124.66	Sector 20	117.60
Sector 5	53.33	Sector 15	83.9	Sector 21	63.11
Sector 6	28.38			Sector 22	90.80
Sector 7	50.11				
Total area of Zone one: 363.60		**Total area of Zone Two: 578.06**		**Total area of Zone Three: 572.64**	
Total area of Saqqez city: 1514.31 ha					

Source: Authors, 2013.

Claims of representation, identity claims, demands of public rights and citizenship, demands on public life were based on the demands for visibility in public space. Feminists believe that men with the public realm and women with the private sector are identified. It has been argued that the conflict between public and private, and the seemingly comprehensive order, egalitarian and its individualist has caused that subordination of women to men remain hidden. The problem caused public world or in other words, civil society has been raised as a separate entity from the private realm of home and thus it is ignored in theory, while in reality these areas are closely related and world of work and world of home life cannot be separated from each other. In fact, "the field of house living is located in the heart of civil society, not apart from it." Similarly, with the further presence of women in the public realm of work and policy, the natures of public field and opposite forms of are changing. The sample size of the present study includes 200 women’s which living and working in Saqqez city. Therefore for more comprehensive of the sample, 50 were selected from 17-34 year old women, 50 from 34-51 year old women and 50 from 51- 65 year old women and 50 up to 65, for field studies and taking part in PUA meetings. The present study has considered different factors with respect to current usage status of the studied area. In the first step, a questionnaire was distributed and women were asked to specify level of their satisfaction, using a qualitative range: excellent, very good, good, acceptable and weak.

Table 3 The results of women's satisfaction in age 17-65 year's old resulted analysis of usage conditions in studied areas:

Age 17-65 years old				
indexes	Northern Imam ST	Southern Imam ST	Jomhoori ST	Quds ST
recreational spaces	Acceptable	Acceptable	Good	Good
negative sense of the place	Weak	Very good	Good	excellent
Parking lots	Excellent	Weak	Weak	Very good
Places without social usage	Good	Good	Acceptable	Acceptable
Protect children	Excellent	Very good	Weak	Acceptable
Urban Safety	Weak	Acceptable	Weak	Weak
diversified places	Excellent	Good	Acceptable	Excellent

Resource: Authors, 2013.

According to the obtained data, the land uses in general, as one of the quality indexes was not in a good state. According to the women views in this study, lack of recreational spaces in addition of work places, negative sense of the place, non-diversified places, tourism usage, lack of social usage, limited places for children and oldness of the urban spaces were the main mentioned issues.

Table 4 Quantitative results of providing women's satisfaction in case study streets according to studied indexes:

Age / **Ranking** / **Indexes**	**17- 34**	**34- 51**	**51- 65**	**Older than 65**
recreational spaces	30%	26%	30%	32%
negative sense of the place	46%	32%	28%	28%
Parking lots	25%	8%	20%	34%
Places without social usage	26%	24%	18%	18%
Protect children	16%	16%	32%	26%
Urban Safety	10%	34%	52%	2%
diversified places	14%	8%	16%	22%

Resource: Authors, 2013.

VII. URBAN FURNITURE OF SAQQEZ CITY

A "gendered perspective" occurs when planners, designers, decision-makers and community actors look at problems with the needs of both women and men in mind. In the planning process, this means that all policies and design interventions should be reviewed by women and by officials in order to determine whether or not they will make women's lives safer and more convenient. Women and men experience the city differently. This difference is due in part to the different roles in society that men and women are expected to fulfil. Actors involved in any planning project should consider what opportunities women have to use, enjoy and work in public spaces. These opportunities will define women's perceptions of whether a place is safe or unsafe. In addition, women's personal experiences with private and public forms of violence will influence their use of space. All of these points should be taken into consideration at the outset of any planning project. For example, middle-aged men might use a park with groups of other men on their lunch break from work. Young mothers might use the same park in the morning with their children and other young mothers. At night, teenaged boys might use the park with their friends as a social meeting place. For older women, the park might not feel like a safe place in the afternoon or evening because it is filled with men and/or teenaged boys.

In order to, in relation to the status of urban furniture of Saqqez City, some meeting were held and there, urban furniture was defined for women and they were asked to write the related problems in a piece of paper, starting with the most important ones. The first problem that was mentioned by women was that the urban furniture was not compatible with cultural status and identity of residents. Most of this furniture was designed regardless of climate elements of the region, so for example one urban element was not compatible with other elements. In Jomhoori Street, from Kosar Institute to Adami, there were suitable places for sitting, but they were not enough, especially for women, because of high number of users. Most of women complained about the inappropriate distribution of taxi stands and bus stops across the city, for example in Imam Khomeini Street, there is no place for sitting and waiting for bus. Just in Jomhoori Street and in two points far from each

other, few places are provided for waiting for bus and resting. This is the same, in Quds and Northern Streets. Thus in the studied area, taxi stands and bus stops are not distributed appropriately and women have to cross the streets several times to access them. Another problem is that zebra crossings are not just close to taxi or bus stops to make traffic, easier.

After complementary studies were done, the following results obtained as shown in figure (2).

The following results will be taken from figure (2):

1- In the case of lack of urban furniture, Northern Imam Khomeini Street had been the worst (35% out of 100%) and Quds street was the best (18% out of 100%).
2- In the case of light at night, Southern Imam Khomeini Street was the best (40% out of 100%) and Northern Imam Khomeini Street was the worst (6% out of 100%).
3- In the case of disharmony of used elements in a place, Northern Imam Khomeini Street was the worst (35% out of 100%) and Quds street was the best (18% out of 100%).

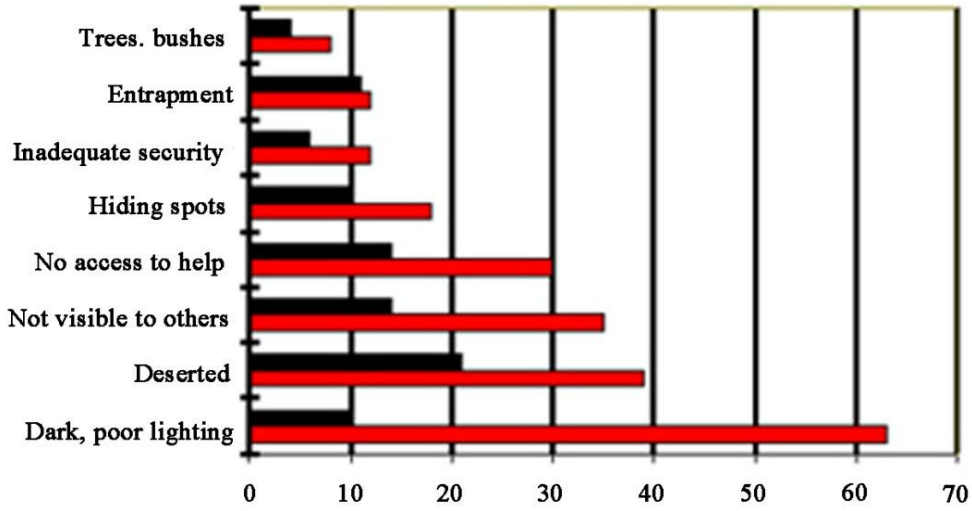

Fig.2. Percent of women's satisfaction of urban furniture's in Saqqez city.
Resource: Authors, 2013.

Analysing the designe of women's favorable spaces:

People who plan and design public spaces need to be aware of all of the ways the space will be used. Planners and designers can take measures to combat space being used in ways that feel threatening to women and girls. For instance, in the case of the park, planners and designers might include different areas for different groups of people – by providing an area for men to get together with their friends that is separate from exercise equipment that could be used by women. This way men and women could use the park independently, but at the same time. In order to avoid gender roles being prescribed by public space, spatial planning and design can be linked to the objective of achieving gender equality. It seems that gender structure or the way that social duties are divided between men and women and its consequences during the history, are all based on the assumption of a requiered relation of normal sex. Thus women are linked to private spaces and men to public spaces. on the other hand, in cities public spaces were always dominated by men. But today, women's presence at work or other public activities has changed the dominant norms of the society and as its concequence, the space organiztions have changed too.The most important problems about designing women's favorable spaces that were mentioned by women, included:

1- multiplicity of visual symbols , 100 out of 200 women considered Southern Imam khomeini Street as the worst, 44 women (Jomhoori Street) 33 women (Northen Imam khomeini Street) and 25 women (Quds Street).
2- Disharmony of residential and commercial buildings in terms of oldness, frontage and height. The results showed that 13 women out of 200, considered Southern Imam khomeini Street as the worst, 47 women (Northen Imam khomeini Street), 55 women (Quds Street) and 85 women (Jomhoori Street).
3- Absence of special rooms for mothers and their children an also absence of places for sitting or studying in bus stops or crowded places were other indexes mentioned by women. Questionnaire data showed that 87 women considered Northen Imam khomeini Street as the worst, 55 women (Southern Imam khomeini Street), 45 women (Quds Street) and 13 women (Jomhoori Street).
4- Most of the women in the present study, believed that when walking in the street (in the afternoons or when going to work), diversity in color and type of used tiles, roughnesses, the difference in the ramp of adjacent

sidewalks and atreets, are the main threatening factors in relation to womens' phisycal and mental health. Thus in respect to his , 85 women considered Quds Street as the worst, 5 women (Jomhoori Street), 45 women (Northen Imam khomeini Street) and 65 women (Southern Imam khomeini Street).

VIII. CONCLUSION

The first hypothesis that this study is going to prove its truth or falsity is: "The physical body and conditions of the central part of Saqqez is not providing comfort and safety for women in the current conditions" According to our results, although there are differences between the considered ideal quantities and the current situation, but women's safety and comfort in the central part of the town as well as in the studied area have been provided to an acceptable level. The negative effects have not been limited to a specific group of users of these spaces. Thus, the first hypothesis was rejected with certainty.

The second hypothesis investigated in this study was "There is a significant difference between the current status and the ideal status of women's participation in the urban spaces of Saqqez, with respect to qualitative indexes of participation."

In relation to this assumption, the field and the participation studies in the area have shown that there is a significant difference between the present situation indexes and that of the ideal situation of these indicators and the potential participation of women is not only actualized but also due to the existence of different definitions and sometimes violating each other the capabilities were not understood and no efforts has been done to achieve the majority of these indicators. These problems in different dimensions such as shortage of comfortable furniture, excessive density of urban elements in a special area, and lack of some in another neighborhood, failure to meet the needs of clients and combination of usages of lacking of parted area and etc. have hindered the comfort and convenience of users of urban spaces, especially women. As the result, according to the data obtained, the second hypothesis of the study was proved.

IX. SUGGESTIONS

After reviewing the current status in in all fields and discovering the truth about each of the indicators, it is necessary to provide guidelines for the second hypothesis of the present study. In this context, the Executive and practical proposals will be presented to resolve problems and to utilize the opportunities in the best way.

1. Attention to the construction and development of recreation usages and places to sit (seats located at bus stations, parks).
2. Optimal distribution of parking in the area, particularly in Quds and Jomhoori Streets which are in lower positions in this respect.
3. Removing the flaw in lighting systems especially at night, and in the areas leading to Southern Imam Streets and its secondary streets.
4. establishing some furniture matched to local and cultural identity the local people that match.
5. Attention to eliminating visual distortion caused by the multiplicity of urban symbols which threaten women's comfort, safety and welfare.
6. Providing region and climate based urban designing and the compatible architecture.
7. Reducing traffic and population by planning in a suitable way in relation to usages for the studied area.
8. Designing of paved streets and pedestrian pathways in a safe way.

REFERENCES

[1] **Alaguraia, W. Varessi, H. Raggers, H. 2010.** Sociological of stop women's from participatory. Tehran, Center of basic researches, 81.

[2] **Banister, D. 2000.** Sustainable urban development and transport a Euro vision for 2020. Transport Reviews 20, 113–130.

[3] **Barker, G. 1960.** Urban geography of Iran. Payam Noor University Press.

[4] **Golmoradi, K. 2011.** Architecture and urban design. Zorikh, Architecture colleague, 101- 102.

[5] **Gopalakrishnan, N. 1997.** Historical political relations of Iran and England. Tehran: National Works Society., 952.

[6] **Habibi, M. 1996.** From Shahr to Shaar. Tehran (Persian): University of Tehran Press.

[7] **Hannifi-e- Asl, Y. 2009.** Women safety in Urmia. University of Zabol, Zabol, Iran.

[8] **Hesse, M., 2001.** Mobility und verkehr in suburban context. Dangschat, SuburbanisierunginDeutschland.Aktuelle Tendenzen.Oladen,Leske+Budrich..

[9] **Heydari, A. and M. Tavakoli, 2012.** Urbanization in Kurdish cities after Islamic revaluation of Iran, A case of Saqqez city, SCS Journal, pp.: 25-29.

[10] **Hickman, R., Banister, D. 2005.** Reducing travel by design: what about change over time? In: Williams, K. (Ed.), Spatial Planning, Urban Form and Sustainable Transport. Alders hot, Ash gate.

[11] **Hiller, B. 2011.** Do burgles understand defensible space? New evidence on the relation insecurity, Chicago School.
[12] **KAFSU, L. (2002).** The Economic Approach to Social Capital." Working Paper No. 7728, National Bureau of Economic Research, Cambridge, MA, USA: 14.
[13] **Khammar GH, Heydari A, Shahmoradi L. 2011**. Analysis of the status of traditional knowledge and technology in energy improvement: The case of Sistan Region, Iran. J. Geogr. Regional Plann. 4(10):28.
[14] **Kiani A, Heydari A. 2011.** Urban management in Kurdish cities with point on Saqqez city. Journal of Geography and Regional Planning Vol. 4(10), pp. 578-585.
[15] **Kirby, A.** 2008. The production of private space and its implications for urban social relations. Political Geography 27
[16] **Kohn, M. 2004.** Brave new neighborhoods. New York: Routledge.
[17] **Kolbel, R., 2008.** A strategic planning methodology. Journal of Transport Policy, 15: 273-282. 19.
[18] **Kurdish Encyclopedia. 1975.** inside Kurdistan. Sanandaj: Royal Book. p. 97.
[19] **Kyung-Hwan, K. 2002.** China CDS Performance Indicators: Final Report: UN-Habitat Fukuoka Office.
[20] **OUPUK. 2011.** Women's and public spaces, Edinburg College, engineering Department: 41.
[21] **Pant, V. 2013.** . Social theory in modern age, translated by Salehi, M. Tehran, Science Press: 144.
[22] **Plan international, 2010.** National sense of place: South Khorosan. Entezami knowledge magazine, 56.
[23] **Raggers, H. 2003.** "An Introduction to Transit-Oriented Development", the New Transit Town; Best Practices in Transit-Oriented Development. Edited by Hank Dittmar & Gloria Ohland, Washington, London, and Island Press: 43.
[24] **Rahimi, E. 2012.** Iranian new towns and Iranian regime. SDS Journal, Vol (45), p.p 123-n 156.
[25] **Rahnama, MR. Heydari, A. 2013.** North West border cities of Iran and regional development: A case of Kurdistan Province, Journal of Geography and Regional Planning, Vol. 6(5), pp. 184-192.
[26] **Raju, K. 2006.** Urban management. Urban planning studies centers. Country ministry.
[27] **Saeednia, A. 2008.** Urban management. Urban planning studies centers. Country ministry.
[28] **Sakthivel, P. 2009.** Do burgles understand defensible space? New evidence on the relation insecurity, Chicago School.
[29] **Sykes, P. 1984.** Travel, 10,000 miles in Iran. Tehran: Loha Publishers. (Transl. by Hossein Saadat Nouri, 1st print).
[30] **Taheri, A. Gh. 1977.** History of political relations of Iran and England. Tehran: National Works Society. p. 952.
[31] **Tedkari, A. 2010.** Socilogical Theories. Tehran, Samt Press.
[32] **Weingartner, M. 2010.** Analyzing the Sustainable City: Nature, Urbanization and the Regulation of Socio-environmental Relations in the UK. Urban Studies, 40, 1183–1206.
[33] **Werkele. M. 2000.** End of history pass of Islam and China. USA foreign ministry, 20.
[34] **Wong, Y., Ochoa, J. J., Shah, M. N., & Zhang, X. 2013.** The application of urban sustainability indicators -A comparison between various practices. Habitat International, 35, 17-29.
[35] **ZangiAbadi, A. Mohammadi, J. Safai, H. Rahmati, S.** 2008. Justifying exclusion: the politics of public space and the dispute over access to McIvers ladies. Geography and Development Journal. 63.
[36] **Zokin, Z. 2011.** Home and city design for women's. China, company home, 45.

American Journal of Engineering Research (AJER)
e-ISSN : 2320-0847 p-ISSN : 2320-0936
Volume-02, Issue-11, pp-309-317
www.ajer.org

Research Paper Open Access

Design & Realization of Non-Volatile Sram Based On Magnetic Tunnel Junction

B.PradeepSathyaKumar,M.E., Dr.A.Sabanayagam, S.Ellammal.M.E.,
First Author- Dr.A.Sabanayagam, M.E.,Ph.D.,MBA.,FIETE,FIE (PRINCIPAL) Sri Vidya College of Engg.,&Tech,INDIA.
Second Author-B.PradeepSathyaKumar,M.E., Sri Vidya College of Engg.,&Tech
Third Author-S.Ellammal.M.E., HOD/ECE Sri Vidya College of Engg.,&Tech

Abstract: - In the last 10 years, FPGA circuits have developed rapidly, because of their flexibility, their ease of use and the low cost to design a function with them. However, the internal memories used in FPGA circuit could limit their future use. Most FPGA circuits use SRAM based flip-flop as internal memory. But since SRAM is volatile, both the configuration and information stored is lost. Internal Flash technology is sometime used to replace the external memory. However, it's slow re-programming and its limited number of writing cycles (up to 10^6) prevents its use to replace SRAM. By working at high writing and reading speed, MRAM (Magnetic RAM) technology is one of the best solutions to bring complete non-volatility to the FPGA technology while keeping the power dissipation low. An MRAM can be re-programmed 10^{12} times and has a large retention time up to 10 years. The objective of our project is to contribute one such storage device by making Non-Volatile SRAM based on Magnetic Tunnel Junction (MTJ). The circuit has been implemented using Tanner Tools using 0.25µm technology and the output waveforms are obtained.

I. INTRODUCTION

Normally the SRAM memory is volatile memory. Its store data during power is ON.When power is OFF,stored data is loss.The aim of this proposed model to change VOLATILE SRAM into NON-VOLATILE SRAM using MTJ(Magnetic Tunnel Junction).This Proposed design is designed by TANNER TOOL,Which is used to design Realization model of Non-Volatile SRAMbased on MTJ.The design of this model explain here.

II. STATIC RANDOM ACCESS MEMORY

Static Random Access Memory is a type of semi-conductor memory where the word static indicates that, unlike DRAM it does not need to be periodically refreshed, as SRAM uses bi-stable latching circuitry to store each bit. SRAM inhibits data remanence but is still volatile in the conventional sense that data is eventually lost when the memory is not powered. Each bit in an SRAM is stored on four transistors that form two cross-coupled inverters. This storage cell has two stable states which are used to denote 0 and 1. Two additional access transistors serve to control the access to a storage cell during read and write operations. A typical SRAM uses six MOSFETs to store each memory bit.

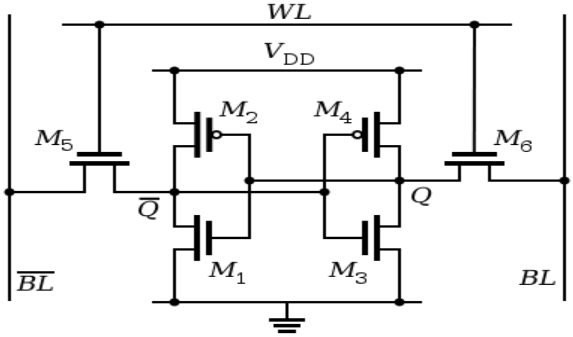

Figure 1:SRAM CELL

Access to the cell is enabled by the word line which controls the two access transistors M_5 and M_6 which, in turn, control whether the cell should be connected to the bit lines: BL and $\overline{BL}$. They are used to transfer data for both read and write operations. Although it is not strictly necessary to have two bit lines, both the signal and its inverse are typically provided in order to improve noise margin. During read accesses, the bit lines are actively driven high and low by the inverters in the SRAM cell. This improves SRAM bandwidth compared to DRAMs.

In a DRAM, the bit line is connected to storage capacitors and charge sharing causes the bitline to swing upwards or downwards.

The symmetric structure of SRAMs also allows for differential signalling, which makes small voltage swings more easily detectable. Another difference with DRAM that contributes to making SRAM faster is that commercial chips accept all address bits at a time. By comparison, commodity DRAMs have the address multiplexed in two halves, i.e. higher bits followed by lower bits, over the same package pins in order to keep their size and cost down. SRAM is used in personal computers, workstations, routers and peripheral equipment.

III. SENSING CIRCUIT IN SRAM

A sense amplifier is an amplifier that senses the output on the bit lines and amplifies it. The sense amplifier that is used in the design is the 'Differential Voltage Sense Amplifier'. It takes small signal differential inputs (i.e. the bit line voltages), and amplifies them to a large-signal single-ended output. The differential approach presents numerous advantages over its single-ended counterpart. One of the advantages is the common mode rejection. It means that such an amplifier rejects noise that is equally injected in both the inputs.

The impact of those noise signals can be substantial, especially since the amplitude of the signal to be sensed is generally small. The effectiveness of a differential amplifier is characterized by its ability to reject the common noise and amplify the true difference between the signals. The signals common to both inputs are suppressed at the output of the amplifier by a ratio called the common-mode-rejection-ratio (CMRR) [4].

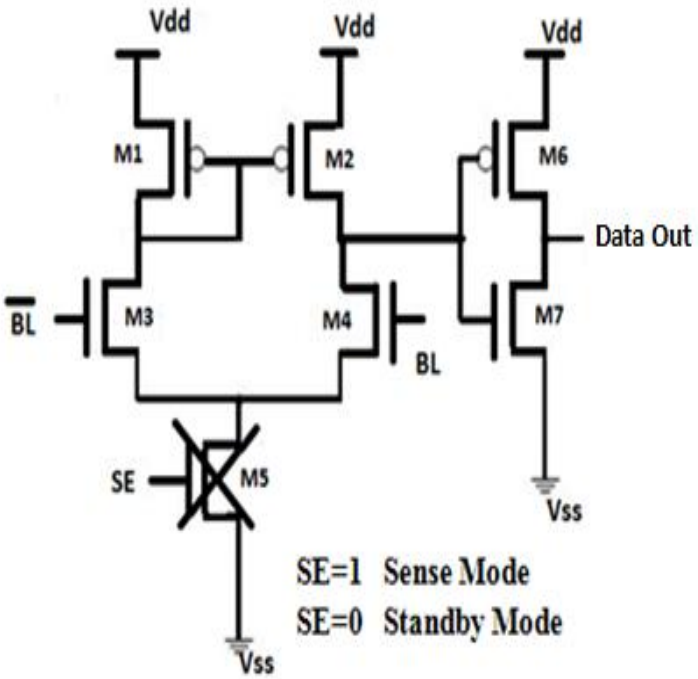

Figure2: Differential Sense Amplifier

IV. MAGNETIC TUNNEL JUNCTION

MTJ uses differentiate between the two logic states. It contains two Ferro-magnetic layers which are separated from each other by a thin layer of insulator also known as barrier. The Ferro-magnetic layers are made up of Cobalt-Ferrous-Boron (CoFeBo). In Fig 3.2, Insulator layer or the barrier is made up of Magnesium-Oxide (MgO) is shown.

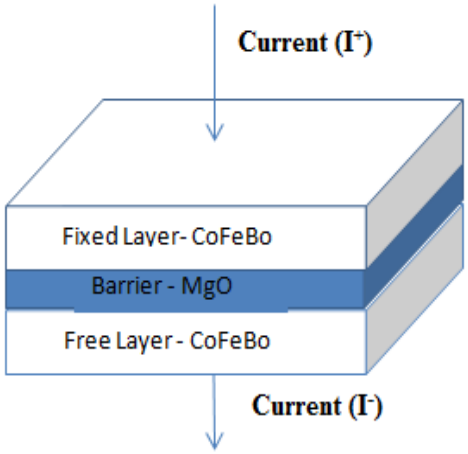

Figure3: Magnetic Tunnel Junction

V. TUNNEL MAGNETO RESISTANCE (TMR)

The ratio between the two resistances at zero bias is called as TMR ratio. Higher the TMR ratio, lower the resistance area.

$$TMR = \frac{R_{AP} - R_P}{R_P} \times 100\% \quad (1)$$

Where, R_{AP} is the electrical resistance in the anti-parallel state and R_P is the electrical resistance in the parallel state.

The fixed layer in MTJ is a permanent magnet whereas the free layer has Ferro-magnetic material that can be magnetised by passing a current (I) through it. Based on the field formed in the free layer the fields forms between the two layers. If both fields are in anti-parallel direction then high resistance is formed between the two layers .

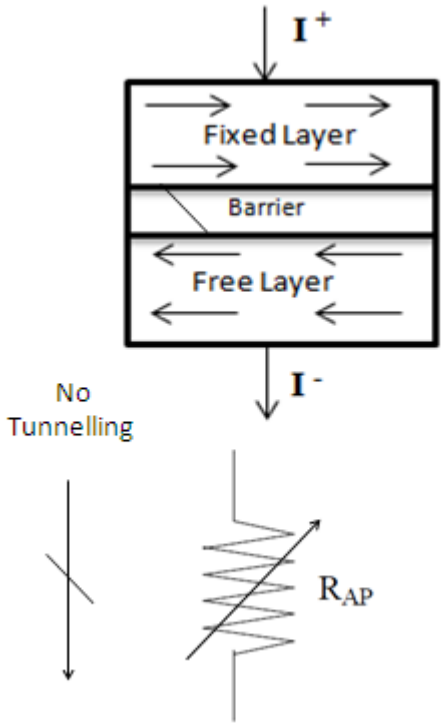

Figure4: Anti-parallel field formed between the two layers.

Whereas when the fields formed between the two layers is parallel then low resistance is formed between the two layers and hence tunnelling occurs.

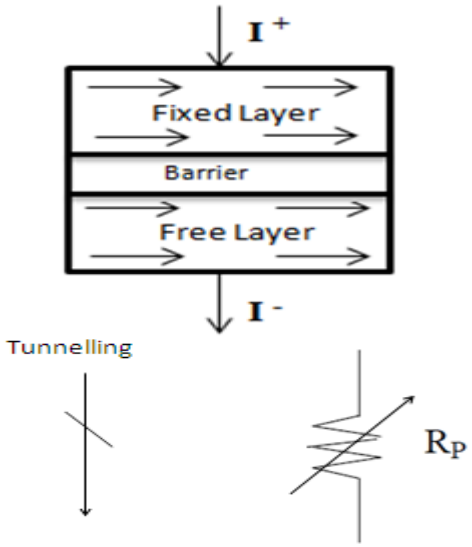

Figure5: Parallel field formed between the two layers.

The two states of an MTJ can be formed by passing current. Fig 4. explains about the anti-parallel field formed between the two layers where as Fig 5. explains about the parallel fields formed between the layers. TMR ratio is used to determine the difference between the two resistances formed in the MTJ. Higher the difference between them, easier it will be to differentiate between the two resistances. The TMR decreases with both increasing temperature and increasing bias voltage [10].

VI. THEORETICAL ANALYSIS OF MTJ

BARRIER CONDUCTANCE

Electron tunnelling through a thin insulating layer between two normal metal electrodes has been studied theoretically and experimentally for almost 40 years. Calculations based on rectangular and trapezoidal potential barriers using various approximations have shown that the tunnelling current should be directly proportional to the applied voltage for voltages very much lesser than the barrier height and should increase exponentially with voltage when the voltage becomes comparable to the barrier height [11].

We take a trapezoidal barrier shape and consider the two extreme cases of

- The WKB approximation.
- Perfectly sharp boundaries between metal and insulator.

VII. CALCULATION OF BARRIER CONDUCTANCE

Consider two metals a and b separated by an arbitrary potential barrier ϕ(x) [10]. Assuming the WKB approximation inside the barrier the tunnelling current density is given by

$$j = \frac{4\pi e}{\hbar}\Sigma\int_{-\infty}^{\infty} dE_{x\rho a}(E)_{\rho b}(E - eV)P(E_x) \times [f(E) - f(E - eV)] \quad (1)$$

where, $E_{\rho a}$ and $E_{\rho b}$ are the densities of states for a given transverse momentum and total energy E for system a and b respectively. The f (E) is the usual Fermi distribution function. E_x is the total energy in the direction perpendicular to the barrier. P (E_x) is the tunnelling probability which has the form.

$$P(E_x) = A\exp\{-\frac{2}{\hbar}\int_0^d \{2m[\varphi(x`, V) - E_x]\}^{1/2} dx`\} \quad (2)$$

where, d is the barrier thickness and $\varphi(x, V)$is the barrier height at the voltage V and the position x in the barrier. The pre-exponential factor A may depend on E_x.

VIII. APPROXIMATION USED BY SIMMONS

The approximation used by the Simmons is to replace the barrier $\varphi(x, V)$by an average barrier $\bar{\varphi}(V)$ hence it is constant throughout the barrier and the tunnelling probability is simply reduced to

$$P(E_x) = A\exp\{(-(\frac{8m}{\hbar^2})^{1/2}\beta[\bar{\varphi}(V) - E_x]^{1/2}\int_d^0 dx^1\} \quad (3)$$

The correction factor β is assumed independent of E_x in order to perform the integration. By applying this approximation all the information about barrier asymmetry is lost [12].

The tunnelling behaviour is usually modelled using the Simmons theory for tunnel junctions. The general equation for this theory is given below.

$$J = J_o\{\bar{\emptyset} \times \exp\left[-A\bar{\emptyset}^{\frac{1}{2}}\right] - (\bar{\emptyset} + eV) \times \exp\left[-A(\bar{\emptyset} + eV)^{\frac{1}{2}}\right] \quad (4)$$

Where, $J_o = \frac{e}{2\pi h (t_{ox})^2}$, $A = \left(\frac{4\pi t_{ox}}{h}\right)\sqrt{2m_e}$

Where 'e' is the charge of the electron, 'm_e' is the mass of the electron. '$\bar{\emptyset}$' is the potential barrier height which is found to be 0.4 for MgO. t_{ox} is the height of barrier in MTJ. 'h' is the Planck's constant which is 6.626×10^{-34}Js.

$$J = \frac{e}{2\pi h (t_{ox})^2}\{\bar{\emptyset} \exp\left[-\left(\frac{4\pi t_{ox}}{h}\right)\sqrt{2m_e}\bar{\emptyset}^{\frac{1}{2}}\right] - (\bar{\emptyset} + eV) \times \exp\left[-\left(\frac{4\pi t_{ox}}{h}\right)\sqrt{2m_e}(\bar{\emptyset} + eV12(5)$$

By ohm's law it's knownthat $V = R \times I$ (7)

Where V is the applied voltage, R is the resistance and I isthe Current flowing through it.

And Current Density $J = \frac{I}{A}$ (8)

Where A is the area of the cross section.

Now, the conductance physics model using the above equations, formed by Brinkman in 1970 is given below. It features the voltage bias dependence and is deeply influenced by the height of the barrier [13].

$$G(0) = \frac{3.16 \times 10^{10} \times \bar{\emptyset}^{\frac{1}{2}}}{t_{ox}} \times \exp[-1.025 \times t_{ox} \times \bar{\emptyset}^{\frac{1}{2}}] \quad (9)$$

$$\frac{G(v)}{G(0)} = 1 - \left\{\frac{A_0 \times \Delta\emptyset}{16 \times \bar{\emptyset}^{\frac{3}{2}}}\right\} eV + \left\{\frac{9}{128} \times \frac{A_0^2}{\bar{\emptyset}}\right\}(eV)^2 (10)$$

where, $A_0 = \frac{4 \times (2m_e)^{\frac{1}{2}} \times t_{ox}}{3 \times h}$ (11)

Here, $\Delta\emptyset = 0$ since barrier is symmetric.

The simplified resistance equations of the above equations (8) and (9) are given below which are used to express the resistance performance of an MTJ.

$$R(0) = \left\{\frac{t_{ox}}{223.76 \times \bar{\emptyset}^{\frac{1}{2}} \times \text{Surface}}\right\} \exp[1.025 \times t_{ox} \times \bar{\emptyset}^{\frac{1}{2}}] \quad (12)$$

$$R(V) = \frac{R(0)}{1 + \left[\frac{t_{ox}^2 \times e^2 \times m_e}{4 \times h^2 \times \bar{\emptyset}}\right] \times V^2} (13)$$

R(0) is the higher value of resistance which is obtained due to the anti-parallel fields formed between the two ferromagnetic layers given by equation (12).

Whereas R(V) is the lower resistance value which is formed due to the tunnelling effect that occurs between the ferromagnetic layers through the insulating layer due to the parallel fields that are formed between the two ferromagnetic layers given by equation (13) [14].

IX. THEORETICAL DESIGN OF MTJ

In this design, an example of MTJ has been worked out and the two resistance values have been calculated by using simplified resistance equations (11) and (12). The diagram of the MTJ is given below.

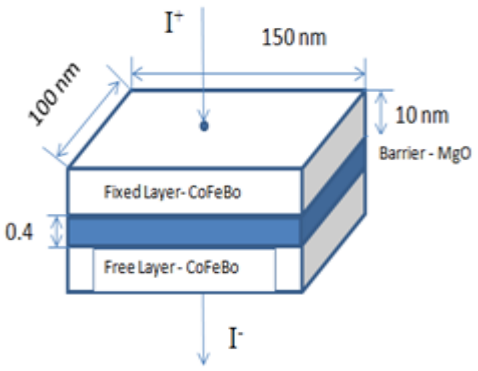

Figure 6: MTJ Design

For this model the following parameters have been considered,
Length of free layer = 150nm,
Width of free layer = 100nm,
Height of barrier = 100Å.

Surface area = (150×100) nm^2= $1.5\times10^{-14}m^2$
The two resistances calculated by putting the above values in equations (13) and (14) are obtained as,

R (0) = 1.415 KΩ
R (V) = 345.5 Ω

X. TO CALCULATE TMR RATIO

TMR ratio is the difference between the two resistances formed in the MTJ. Resistance formed at the anti-parallel field is the higher resistance whereas the resistance formed at the parallel field is lower resistance. The higher the TMR ratio, lesser will be the resistance area (R_A) [15]. And hence it will be easier to differentiate between the two logic states. Hence the higher TMR ratio is desirable.
From equation (1),

$$TMR = \frac{R_{AP} - R_P}{R_P} \times 100\%$$

TMR = 309.55%
Here a high TMR ratio is obtained which is desirable. Hence it becomes easy to differentiate between the two resistances.

XI. NON-VOLATILE SRAM BASED ON MTJ

Realization Design by Tanner Tool

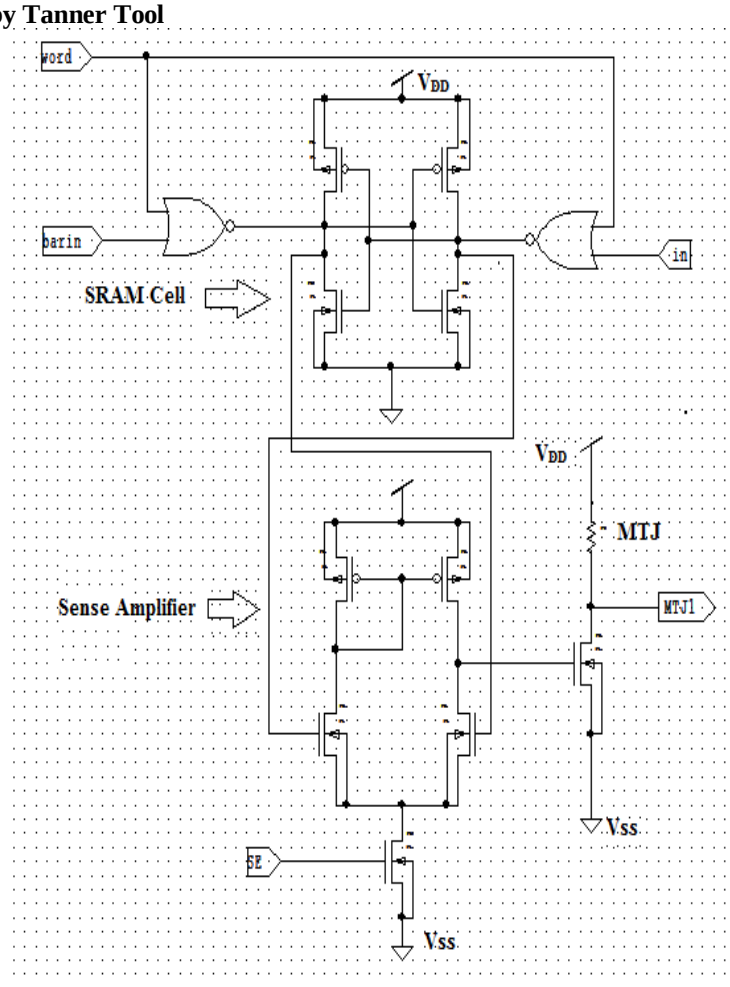

Figure 7: Non-volatile SRAM based on MTJ

XII. FOUR BIT NON-VOLATILE SRAM USING MTJ

A four-bit Non-Volatile SRAM is designed using Tanner Tool (0.25µm) technology. The circuit diagram of Non-Volatile SRAM cell is given in Fig-7 .This figure contains four SRAM cells each connected to an MTJ. The inputs are given to the SRAM cells from where it is fed into the sense amplifier.

The output of the sense amplifier is fed into the MTJ. The detailed diagram of a single cell of SRAM is given in Fig-1. The data is given to the SRAM cell in which it is stored. The output of SRAM is taken with the help of differential sense amplifier. Its output is then fed into the MTJ.

The waveforms of the output of SRAM cell, MTJ output is taken by simulating it in Tanner Tools. The input to the SRAM cell is given as 0110 as shown in Fig 9. and is fed into the sense amplifier. The output of the sense amplifier is given in Fig 10. The output of MTJ is taken as logic '0' when its output voltage is less than 90mV and it is taken as logic '1' when it is more than 200mV.

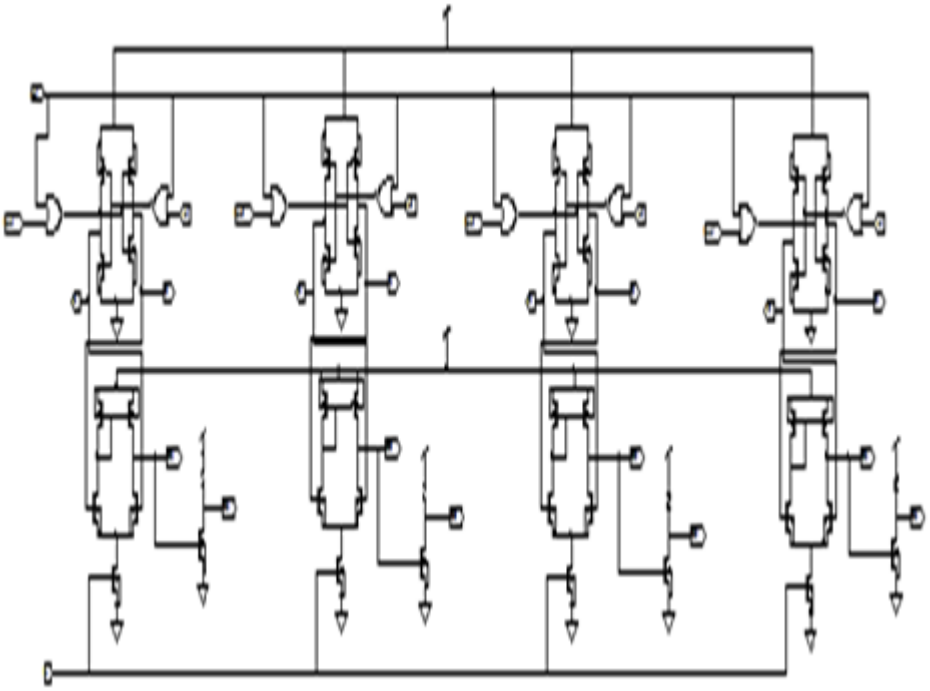

Figure 8: Four bit non-volatile SRAM.

The following graphs are obtained from the simulation of the SRAM cell with the MTJ realization. The input 0110 given to the SRAM cell as shown in Fig 9.

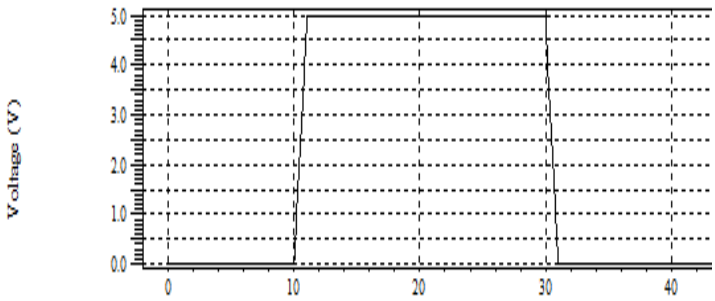

Figure9: Input to SRAM cell (0110)

The output of the SRAM cell is given to the sense amplifier which cancels the common noise and amplifies the difference between the two signals.

The output of the sense amplifier is then fed to the input of the realized MTJ. This MTJ stores the result. The output of the MTJ is given in Fig 10. The output voltage range that is obtained in this circuit is from 90mV to 220mV. The output logic takes it as logic '0' when the output of MTJ is less than 90mV and it takes it as logic '1' when its output is greater than 200mV.

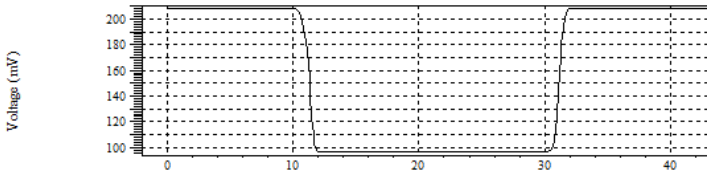

Figure 10: Output voltage across MTJ

The two distinct resistances are found using the tanner tool simulation. The higher resistance which denotes the resistance formed due to the parallel field formed between the two layers is found to be 1.2kΩ and the lower resistance that is formed due to the parallel field formed between the two layers is found to be of 260Ω as shown in Fig 11.

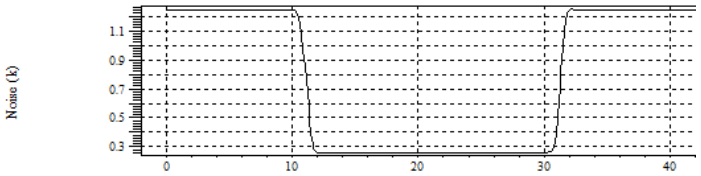

Figure 11: Resistance of MTJ

Drain current through the MTJ is also found out from the simulation. It is given in Fig 12. The range of current is found to be 160µA to 360µA.

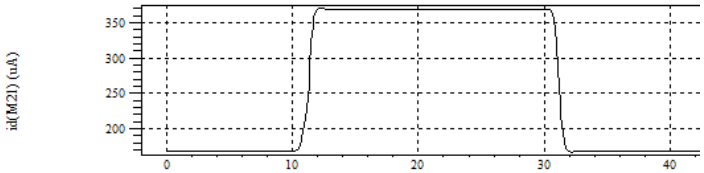

Figure 12: Drain current at MTJ

The power consumption of the MTJ is also calculated using tanner simulation. It is found to be 50µW for higher resistance whereas it is 110µW for the lower resistance. It is shown in Fig 13.

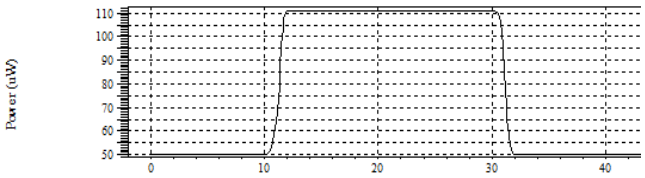

Figure 13: Power consumption of MTJ

TABLE I: Result of NV-SRAM at differ.,input bit

Input Bits	Output Voltage (mV)		Drain Current (µA)		Resistances (Ω)		TMR ratio (%)	Power (µW)	
	Logic '0'	Logic '1'	Logic '0'	Logic '1'	Logic '0'	Logic '1'		Logic '0'	Logic '1'
1010	210	90	160	360	1200	260	314.45	50	110
1001	210	90	160	360	1200	260	314.45	50	110
0110	210	90	160	360	1200	260	314.45	50	110
1110	210	90	160	360	1200	260	314.45	50	110
1011	210	90	160	360	1200	260	314.45	50	110

Hence the higher value of resistance which is the anti-parallel field resistance of MTJ is found to be 1.2KΩ and the parallel field resistance is obtained as 260Ω. And the power consumption of MTJ is found to be as low as 50µW for higher resistance and 110µW for lower resistance.

XIII. CONCLUSION

Most FPGA circuits use SRAM based flip-flop as internal memory. But since SRAM is volatile, both the configuration and information stored is lost. Hence a Non-volatile SRAM is designed using a Magnetic Tunnel Junction and is simulated in the Tanner Tools. The two resistances are calculated and are found to be1.2kΩ for logic '0' and 260Ω for logic '1'. The currents flowing through the MTJ during the two states are easily differentiable. At logic '0', 120μA current flows whereas at logic '1',0.3mA current flows. Thus the maximum current flow is as low as 360μA which is very low.The TMR ratio of 314.45% is obtained. The more the TMR ratio, the more will be the resistance area in the MTJ,hence it is easy to differentiate between the two logic states at the output of MTJ. The power consumption of the Non-Volatile SRAM differentiate between the two logic states at the output of MTJ. The power consumption of the Non-Volatile SRAM is found to be 50μW for higher resistance and 110μW for the lower resistance. Hence the SRAM cell which has been designed and realized using MTJ is a non-volatile device and can be used to store the data from the output of the SRAM cell as tabulated in Table I

The application of full adder has been done and the two outputs (SUM and CARRY) are stored in two MTJs. The drain current flowing through it is found and the two resistances are obtained as shown in Table I. The drain current flowing through the MTJ is obtained as 100μA for logic '0' and 270μA for logic '1' and the voltage obtained across the MTJ is 95mV for logic '1' and 550mV for logic '0'. The two resistances obtained are $R_H(0)$ for logic '0' and $R_L(1)$ for logic '1'. Where $R_H(0)$ is 5.5kΩ and $R_L(1)$ is 330Ω. The input voltage supplied to the MTJ is 0.8 volts.

REFERENCES

[1] Bryan John Baker, (2003) 'A model for the behaviour of Magnetic Tunnel Junctions', , IOWA state University.

[2] HaoMeng and Jian Ping Wang, (2005) 'Spin Transfer Effect in Magnetic Tunnel Junction with a Nano Current Channel layer in free layer', IEEE transactions on Magnetics, Volume 41, No. 10,

[3] J. C. Slonczewski, (1989) 'Conductance and exchange coupling of two ferromagnets separated by a tunnelling barrier', Physical Review, Volume 39, No 10,.

[4] Morgan Madec, Jean Baptiste and Fabien Pregaldiny, (2008) 'Compact Modelling of Magnetic Tunnel Junction', IEEE transactions.

[5] Saied Tehrani and Brad N. Engel(2003.), 'Magnetoresistive Random Access Memory using Magnetic Tunnel Junction', Proceedings of the IEEE, Vol.91, No.5, May

[6] W. F Brinkman, R. C. Dynes and J. M. Rowell, (1970) 'Tunnelling Conductance of Asymmetrical Barriers', Journal of Applied Physics, Volume 41, No. 5,.

[7] W. Zhao, E.Belhaire, Q.Mistral and E.Nicolle,(2006). 'Integration of Spin RAM technology in FPGA circuit', IEEE publications,

[8] W.Zhao and Eric Belhaire,(2007). 'Spin-MTJ based Non-Volatile Flip Flop', Proceedings of the 7th IEEE International Conference on Nanotechnology, Hongkong,

[9] W.Zhao, EBelhaire and Q.Mistral, (2006)'Macro-model of Spin transfer torque based Magnetic Tunnel Junction device for hybrid Magnetic-CMOS design', IEEE transactions.

[10] www.wikipedia.org/MRAM.